

THE UNIVERSITY OF NOTTINGHAM
DEPARTMENT OF
ELECTRICAL AND ELECTRONIC ENGINEERING

A VERY HIGH SPEED
SWITCHED RELUCTANCE GENERATOR

BY

MOHAMMED TAHA EBRAHIM, BSc(Eng), MSc

THESIS SUBMITTED TO THE UNIVERSITY OF NOTTINGHAM
FOR THE DEGREE OF
DOCTOR OF PHILOSOPHY

JANUARY 1995



LIST OF CONTENTS

TITLE
LIST OF CONTENTS
LIST OF APPENDICES
LIST OF FIGURES
ACKNOWLEDGEMENTS
ABSTRACT

CHAPTER ONE	INTRODUCTION
1.1 Objective	1
1.2 SR Machines	3
1.2.1 Basic Operation	3
1.2.2 Flux Linkage-Current Characteristics and Energy Conversion . .	5
1.2.3 Power Converters and Control	7
1.3 SR Generators	13
1.4 High Speed Generators- Alternative Types	15
1.4.1 The Wound Rotor Brushless Synchronous Generator	16
1.4.2 The Permanent Magnet Generator	16
1.4.3 The Homopolar Inductor Alternator	19
1.4.4 The Induction Generator	21
1.4.5 The Reluctance Generator	23
1.5 Advantages of High Speed SR Generators	27
1.5.1 SR Generator Versus PM Generator	28
1.5.2 SR Generator Versus Reluctance Generator	30
1.6 Previous Work on SR Generators	32
1.8 Preview of Thesis Layout	39

CHAPTER TWO	MODELLING AND PERFORMANCE PREDICTION
2.1 Introduction	40
2.2 Review of Methods	41
2.3 Simple Quasi-Linear Model	44
2.3.1 Neglecting Fringing/Leakage Flux	44
2.3.2 Including Fringing/Leakage Flux	47
2.4 Simple Equivalent Circuit for Currents $i \geq I_{sat}$	51

CONTENTS

2.5 Equivalent Circuit for Currents $i \leq I_{sat}$	53
2.6 Computation of Current waveforms for Generation	54
2.7 Computer Programme for Determining Current Waveform and Estimated Power and Efficiency	55
2.8 Conclusion	55

CHAPTER THREE THE SRG ELECTROMAGNETIC DESIGN

3.1 Introduction	56
3.2 Choice of Stator	57
3.2.1 Introduction	57
3.2.2 Stator Geometry	57
3.2.3 Stator Material Data	59
3.3 Design of Rotor	60
3.3.1 Introduction	60
3.3.2 Choice of Pole Number and Number of Phases.	61
3.3.3 Air-Gap Design	66
3.3.4 Physical Dimensions of Chosen Profile	66
3.3.5 Rotor Material Choice and Properties	69
3.4 Design of Phase Winding	71
3.4.1 Introduction	71
3.4.2 Number of Turns / Generator Voltage	71
3.4.3 Choice of Wire Gauge	73
3.4.4 Phase Resistance	75
3.4.5 Current Rating	75
3.5 Predicted Performance	76
3.6 Estimation of Core Losses	84
3.7 Conclusion	86

CHAPTER FOUR THE SRG MECHANICAL DESIGN AND ASSEMBLY

4.1 Introduction	88
4.2 Stress Analysis for The Rotor	90
4.2.1 Background	90
4.2.2 Description of Finite Element Programme	93
4.2.3 Results for Target Speed 100,000 rpm	95
4.2.4 Results for Higher Speeds	97

CONTENTS

4.2.5 Investigation of Different Profiles 99

4.3 Rotor Laminations Assembly and Machining 102

4.3.1 Introduction 102

4.3.2 Insulation and Assembly of Laminations 104

4.3.3 Machining of Rotor Laminations 107

4.3.4 Preparation of the Stub Shaft and Shrink Fit to Laminations .. 110

4.4 Stator Core Machining and preparation 116

4.6 Rotor Position Sensor, Mechanical Details 117

4.7 Conclusion 119

CHAPTER FIVE

THE POWER CONVERTER AND ELECTRONIC CONTROLLER

5.1 Introduction 123

5.2 Selection of Power Converter Topology 123

5.3 Selection of The Switching Components 127

5.4 Power Circuit Layout and Assembly 127

5.5 The Electronic Controller 130

5.5.1 Principles of the Electronic Controller 130

5.5.2 Overall Control Schematic and Operation 131

5.5.3 The Rotor Position Sensor 137

5.5.4 The Phase Locked Loop and the Counters 139

5.6 Power Transistor Gate Drive Circuit 140

5.7 Preliminary Tests and Operation 143

CHAPTER SIX **THE AIR SUPPLY SYSTEM AND THE TURBINE**

6.1 Introducing The Overall System 147

6.2 Turbine Selection and Preparation 150

6.3 Bearings Set-Up 155

6.4 The Air Blower 157

6.5 Electric Motor Drive and Speed Control 161

6.6 Mounting the SR Generator 164

6.7 Tests of the Air Supply System 167

6.8 Conclusion 168

CONTENTS

CHAPTER SEVEN EXPERIMENTAL TEST SYSTEM AND PROCEDURE

7.1 Introduction	169
7.2 Static Tests	169
7.2.1 Introduction	169
7.2.2 Set-Up and Results of Static Tests	170
7.2.3 Phase Resistance Determination	174
7.3 Introducing The Experimental Test System For Dynamic Tests.	175
7.4 Instrumentation	177
7.4.1 Basic Instrumentation	177
7.4.2 Auxiliary Voltage Regulator	179
7.4.3 Blower Speed Measurement	181
7.5 Estimation of Power Output and Efficiency	182
7.6 Test Procedure	183
7.7 Conclusion	185

CHAPTER EIGHT

DYNAMIC TEST RESULTS

8.1 Introduction	186
8.2 Power and Efficiency Diagrams	186
8.3 Comparison With The Model Results	198
8.4 Phase Current Traces	202
8.5 Conclusion	209

CHAPTER NINE

DISCUSSION AND GENERAL CONCLUSIONS

9.1 Introduction	210
9.2 General Operation and Behaviour of The Test System.	211
9.3 Comparison of Power density With Published Work	214
9.4 Power Versus Speed and The Appropriate Voltage	216
9.5 The Case of an All-Steel SRG	221
9.6 Alternative Stator Geometry	222
9.7 Considering The Effect of Size and Cooling	224
9.8 Conclusions and Suggestions For Further Work	226

APPENDICES

LIST OF REFERENCES

LIST OF APPENDICES

APPENDIX - CHAPTER 1

- APPENDIX A1.1 General Theory of Torque Production in SR Motors. (pp 1-5).
- APPENDIX A1.2 Review of Control and Power Converters of SR Machines. (pp 1-7).

APPENDIX - CHAPTER 2

- APPENDIX A2.1 Development of The Modelling Programme. (pp 1-7).
- APPENDIX A2.2 Listing of C programme for Simple Model of The SRG. (pp 1-8).

APPENDIX - CHAPTER 3

- APPENDIX A3.1 Review of Soft Ferrites and Their Use in Electric Machines- With Manufacturer Data Sheets of The Core Material. (pp 1-6).
- APPENDIX A3.2 Review of Amorphous Metals and Their Use in Electric Machines- With Manufacturer Data Sheets of The Selected Alloy. (pp 1-7).
- APPENDIX A3.3 Investigation of Different Rotor Configurations Based on Results of The Modelling Programme. (pp 1-8).
- APPENDIX A3.4 Results of The Simple Modelling Programme At Different Operating Conditions. (pp 1-9).
- APPENDIX A3.5 Estimation of Eddy Current Losses. (pp 1-7).

APPENDIX - CHAPTER 4

- APPENDIX A4.1 General Description of The PAFEC Package With an Illustrated Listing of The Data Input for Stress Analysis on 45° Segment of The Rotor. (pp 1-4).
- APPENDIX A4.2 Data Input Listing for Finding Stresses On The Complete Rotor Structure at 100,000 rpm. (pp 1-4).

CONTENTS

APPENDIX - CHAPTER 5

- APPENDIX A5.1 Determination of The Heat Sinking Requirements for The Power Switches. (pp 1-2).
- APPENDIX A5.2 PCB Production Diagrams of The Controller of Figure 5.7. (pp 1-2).
- APPENDIX A5.3 Details of The PLL Design. (pp 1-2).
- APPENDIX A5.4 PCB Production Diagrams of The MOSFET Gate Drive Circuit of Figure 5.11. (pp 1-2).

APPENDIX - CHAPTER 6

- APPENDIX A6.1 Volume and Weight of The Electromagnetic Unit. (pp 1-2).
- APPENDIX A6.2 Data of The Gas Turbine and Determination of The Air Supply Demand. (pp 1-5).
- APPENDIX A6.3 Air Blower Details, Selection and Determination of Drive Demands. (pp 1-5).
- APPENDIX A6.4 Data for The Balancing Procedure of The Rotor of The SRG. (pp 1-2).

APPENDIX - CHAPTER 7

- APPENDIX A7.1 Tables for Static Test Measurement Results for Determining The Magnetic Characteristics of The SRG. (pp 1-2).

APPENDIX - CHAPTER 8

- APPENDIX A8.1 Tables for Dynamic Test Measurement Results. (pp 1-22).
- APPENDIX A8.2 Some Results of The Modelling Programme for Comparison With Dynamic Tests Results. (pp 1-3).

APPENDIX - CHAPTER 9

- APPENDIX A9.1 Model Results For Some of The Alternative Cases of Stator Size, Material, and Pole Configuration. (pp 1-4).

LIST OF FIGURES

CHAPTER 1

- Figure 1.1: Typical SR Machine and Converter.
 Figure 1.2: Typical Ψ - i - θ characteristics and energy conversion loop.
 Figure 1.3: Basic components of the SR drive.
 Figure 1.4: Phase current, voltage, and inductance.
 Figure 1.5: Torque-speed characteristics of the SR motor.
 Figure 1.6: Classic type power converter.
 Figure 1.7: Split supply converter.
 Figure 1.8: C-Dump Converter.

CHAPTER 2

- Figure 2.1: Quasi-linear magnetic characteristics.
 Figure 2.2: Overlapped stator-Rotor poles.
 Figure 2.3: Magnetisation characteristics for the quasi-linear model neglecting fringing/leakage flux.
 Figure 2.4: Stator-rotor poles in overlapping showing fringing flux.
 Figure 2.5: Significant rotor pole positions showing reference for angular position.
 Figure 2.6: Low current inductance profile for a two-phase SRG.
 Figure 2.7: Magnetic characteristics for the quasi-linear model of the SRG.
 Figure 2.8: Equivalent circuit for SR machine- one phase, for currents $i \geq I_{sat}$.
 Figure 2.9: Expected phase current waveform and inductance profile showing important angular positions.

CHAPTER 3

- Figure 3.1: Cross section of the ferrite stator core. Dimensions are in mm.
 Figure 3.2: Cross section of a stator core with improved slot.
 Figure 3.3: Possible 16/16 Stator-Rotor pole configuration resulting in a single phase SRG.
 Figure 3.4: (a) Expected inductance profile & (b) Expected current waveform. For the machine of Figure 3.3.
 Figure 3.5: Possible 16/8 Stator-Rotor pole configuration. A two phase machine. The selected geometry for the high speed SRG.
 Figure 3.6: Possible 16/12 Stator-Rotor pole configuration resulting in a four phase machine.
 Figure 3.7: Basic terms in relation to the magnetic flux path.
 Figure 3.8: Cross section of the rotor lamination of the selected geometry. Dimensions in mm.
 Figure 3.9: (a) Available space for winding in one stator slot.
 (b) Top view of stator pole.
 Figure 3.10: Phase inductance profile for the SRG considering an extended stator pole arc.
 Figure 3.11: Ψ - i - θ characteristics for the quasi-linear model of the SRG.
 Figure 3.12: Example of fully-opened flat-topped current waveform. $\theta_{dly}=5.3^\circ$, and $\theta_c=27.8^\circ$.
 Figure 3.13: EC-loop for the example of fully opened current waveform.

CONTENTS

- Figure 3.14: Output of the programme for the example case. Speed = 50,000 rpm and supply voltage = 38 volts.
Figure 3.15: Assumption for flux distribution in the rotor.

CHAPTER 4

- Figure 4.1: Elementary rotating disk for radial and tangential stresses calculation.
Figure 4.2: Typical stress-strain relationship for amorphous metal.
Figure 4.3: Stress analysis results at 100,000 rpm.
Figure 4.4: Stress analysis results at 255,00 rpm.
Figure 4.5: Stress analysis results at 100,000 rpm and 12 mm bore radius.
Figure 4.6: Stress analysis for different rotor profile at 180,000 rpm.
Figure 4.7: Cutting and Stacking the sprayed laminations.
Figure 4.8: Rotor laminations and stub shaft assembly to turbine.
Figure 4.9: Shaft-Hub dimensions. Exaggerated dimensions before assembly. Front view after shrink fit.
Figure 4.10: Opto-device and rotating disk arrangement.
Figure 4.11: Dimensions for rotor position sensor disk.
Figure 4.12: Photo showing the stator core inside the steel tube and its assembly to the air turbine.
Figure 4.13: Photo-1; The stator, the rotor, and the sensor disk.
Figure 4.14: Photo-2; The stator, the rotor, and the sensor disk.

CHAPTER 5

- Figure 5.1: Selected supply circuit for the high speed SRG.
Figure 5.2: Basic configuration of the split supply converter.
Figure 5.3: Power circuit layout for reducing stray inductance. Connections to one phase winding are shown.
Figure 5.4: Photo for the power circuit layout.
Figure 5.5: Function diagram for the electronic controller circuit.
Figure 5.6: Signal diagram for the controller of Figure 5.5.
Figure 5.7: Function diagram of the selected electronics controller.
Figure 5.8: Signal diagram for the controller of Figure 5.7.
Figure 5.9: Circuit diagram for the opto-switch used for rotor position sensing.
Figure 5.10: A photo for the rotor position sensor.
Figure 5.11: Power transistor gate drive circuit.
Figure 5.12: Upper: Signal B in Figures 5.7 & 5.8.
Lower: Gate-Source signal on a resistive load of 1 k Ω .
Figure 5.13: Upper: V_{gs} on the power transistor.
Lower: Pulse train for the *on* period.
Figure 5.14: Upper: V_{gs} on the power transistor.
Lower: Pulse train for the *off* period.
Figure 5.15: Upper: Current in phase B.
Lower: Current in phase A. Poles for phase A are in fully aligned position.
Figure 5.16: Upper: Current in phase B.
Lower: Current in phase A. Poles for phase A are in fully un-aligned position.
Figure 5.17: Upper: Current in phase winding B.
Lower: Voltage across phase winding B.

CONTENTS

CHAPTER 6

- Figure 6.1: The Turbine and the air blower in the overall testing set-up of the SRG.
Figure 6.2: (a) Main components and dimensions of the air turbine.
Figure 6.2: (b) Photo-1 showing the Air Turbine before assembly.
Figure 6.2: (c) Photo-2 showing the Air Turbine before assembly.
Figure 6.3: (a) Basic Layout of the assembly of the turbine, the bearing set-up and the SRG converter circuit.
Figure 6.3: (b) Photo showing the actual layout of the turbine, bearing set-up, and SRG assembly.
Figure 6.4: Bearings arrangement for a high speed turbine.
Figure 6.5: Photo showing the outlet silencer and connection pipe to turbine.
Figure 6.6: Photo showing the Air Blower, the Inlet Silencer and the driving D.C. Motor.
Figure 6.7: Armature and field circuits of the 18.5 kW D.C. Motor.
Figure 6.8: Function diagram of the field current controller.
Figure 6.9: Pin connection diagram of the F/V and PWM IC's for motor field current control.
Figure 6.10: photo of the turbine after mounting the rotor (and the rotor disk) and balancing the shaft.
Figure 6.11: Safety cage around the turbine and the SRG.

CHAPTER 7

- Figure 7.1: Circuit diagram for approximate inductance and flux measurement.
Figure 7.2: Photo showing the rotor locking arrangement for the static tests.
Figure 7.3: The magnetic characteristics of the SRG resulting from static tests measurements compared with those resulting from the model (dashed).
Figure 7.4: Circuit for dynamic test set-up.
Figure 7.5: Photo showing instrumentation used for taking measurements of the SRG test rig.
Figure 7.6: Circuit diagram for the auxiliary voltage regulator.

CHAPTER 8

- Figure 8.1: Power & Efficiency diagram for 40,000 rpm and 30 volts.
Figure 8.2: Power & Efficiency Diagram for 40,000 rpm and 40 volts.
Figure 8.3: Power & Efficiency Diagram for 50,000 rpm and 40 volts.
Figure 8.4: Power & Efficiency Diagram for 50,000 rpm and 50 volts.
Figure 8.5: Power & Efficiency Diagram for 60,000 rpm and 50 volts.
Figure 8.6: Power & Efficiency Diagram for 60,000 rpm and 60 volts.
Figure 8.7: Power versus speed at 40 volts and at different excitation voltages.
Figure 8.8: Comparison, Power/Angle diagram for 40,000, 50,000, and 60,000 rpm at 40 volts for $\theta_{on}=22^\circ$. Values of efficiency and phase current (r.m.s.) are shown.
Figure 8.9: Comparison Power/Angle diagram for results of maximum power at different speeds and voltages.
Figure 8.10: Measured and predicted results at 40,000 rpm, 30 volts.
Figure 8.11: Measured and predicted results at 40,000 rpm, 40 volts.
Figure 8.12: Measured and predicted results at 50,000 rpm, 40 volts.
Figure 8.13: Measured and predicted results at 50,000 rpm, 50 volts.
Figure 8.14: Measured and predicted results at 60,000 rpm, 50 volts.
Figure 8.15: Measured and predicted results at 60,000 rpm, 60 volts.

CONTENTS

- Figure 8.16: Upper: Phase B current. Peak is 16.4 A. For 1 div on the trace=1/0.3 Amp. Lower: Switch current for phase A. Angles set is $\theta_{dly}=8$, $\theta_{on}=22$.
- Figure 8.17: Phase current trace. $I_{pk} = 18$ Amp for 10/22 angle set.
- Figure 8.18: Phase current trace. $I_{pk}=7.6$ Amp. Continuous rating for 6/20 angle set.
- Figure 8.19: Phase current trace. $I_{pk}=12.8$. Continuous rating for 8/22 angle set.
- Figure 8.20: Phase current trace. $I_{pk}=20.6$ Amp, peak rating. 8/22 angle set.
- Figure 8.21: Phase current trace. $I_{pk}=22.8$ Amp, peak rating. Angle set 10/22.
- Figure 8.22: Phase current trace. $I_{pk}=9.7$ Amp for angle set $\theta_{dly}/\theta_{on}=18/14$. $\eta=87.3\%$.
- Figure 8.23: Phase current trace. $I_{L-rms}=5$ Amp, and $I_{pk}=8.76$ Amp for 10/18 angle set. $\eta=87.8\%$.
- Figure 8.24: Phase current. Model result for comparison with Figure 8.22. $P_g=99$ W, $\eta=88\%$.
- Figure 8.25: Phase current. Model result for comparison with Figure 8.23. $P_g=143$ W, $\eta=88.5\%$.
- Figure 8.26: Phase current trace. Dashed trace refers to sink voltage of 60 volts and source voltage of 50 volts. Normal trace for 50 volts both. $I_{pk}=13$ Amp.

CHAPTER 9

- Figure 9.1: Model results for power versus speed for continuous and peak operation with the voltage selected to result in maximum power at each speed.
- Figure 9.2: Model and available experimental results showing power versus speed at fixed voltage of 40 volts.
- Figure 9.3: Model results showing power versus speed at fixed voltage of 60 volts.

APPENDIX - CHAPTER 1

- Figure A1.1: Energy determination for case 1, fixed rotor position.
- Figure A1.2: Energy determination for case 2, change in rotor position.
- Figure A1.3: Energy determination for the dynamic case considering constant current for each step of θ .

APPENDIX - CHAPTER 3

- Figure A3.1: (a) Manufacturer's Data sheets for the material of the selected ferrite core.
- Figure A3.1: (b) Manufacturer's Data sheets for a higher grade core material.
- Figure A3.2: (a) Mechanical and general material properties for several amorphous alloys. Note the selected alloy is 6025.
- Figure A3.2: (b) More properties of the Vitrovac range of amorphous alloys.
- Figure A3.3: (a) B/H characteristics and Core losses for a toroidal core for a similar alloy to the 6025.
- Figure A3.3: (b) Core losses for C-cores made of a similar amorphous alloy to the one selected.
- Figure A3.4: Model result: Phase current of the 2-phase SRG at 50,000 rpm, 50 V.
- Figure A3.5: Model result: Phase current for the 4-phase SRG at 50,000 rpm and 38 V. $P_{gen} = 245$ watts and Efficiency is 67%.
- Figure A3.6: Model result: Phase current of the 1-phase SRG at 50,000 rpm and 200 V. $P_{gen} = 200$ watts and Efficiency = 95%.

CONTENTS

- Figure A3.7 - Figure A3.14: Phase current waveforms for results of various operating points of the programming model.
- Figure A3.15: Flux distribution in the rotor.
- Figure A3.16: Flux waveform in the stator pole.
- Figure A3.17: Rotor flux waveform at full power.
- Figure A3.18: Rotor flux waveform at reduced power.
- Figure A3.19: Geometry of the rotor strip assumed to be carrying the rotor flux.

APPENDIX - CHAPTER 5

- Figure A5.1: Covering sheet. Components and IC function definition for the controller of Figure 5.7.
- Figure A5.2: Upper layer of the PCB diagram of the controller circuit.
- Figure A5.3: Bottom layer of the PCB diagram of the controller circuit.
- Figure A5.4: PLL connection diagram for the controller of Figure 5.7.
- Figure A5.5: Covering sheet. Components and IC function identification for the MOSFET gate drive circuit.
- Figure A5.6: Upper layer of the PCB diagram for the gate drive circuit.
- Figure A5.7: Bottom layer of the PCB diagram for the gate drive circuit.

APPENDIX - CHAPTER 6

- Figure A6.1: Dynamometer performance curves for determining air supply demand.
- Figure A6.2: Manufacturer's data: Basic data of the Holset gas turbine.
- Figure A6.3: Manufacturer's data: Results of dynamic tests of the gas turbine.
- Figure A6.4: Manufacturer's Data: General information on the Peabody Holmes Air Blowers.
- Figure A6.5: Manufacturer's Data: Selection sheet for a range of available air blowers.
- Figure A6.6: Manufacturer's Data: Blower package Unit description and dimensions.
- Figure A6.7: Blower performance sheet used for the determination of the required drive for the blower.

ACKNOWLEDGEMENTS

The author would like to express his thanks and gratitude to the project supervisor Mr. W.F. Ray for continuous help and advice and many helpful discussions throughout the course of this work.

Thanks are also due to the following:

- Professor Brian Tuck, head of Department of Electrical Engineering at The University of Nottingham for personal advice and encouragement and for help in using the departmental facilities.
- Mr. Rex Davis, former senior lecturer in the Dept. of Elect. Eng. at The University of Nottingham, for enthusiastically supervising the initial part of the work and for administering contacts with the various firms involved in the project.
- The technical staff in the department and in particular Mr. Barry Robinson for carrying out first class technical jobs.
- Philips Components Ltd. for providing samples of their ferrite core rings; Holset Eng. Ltd. for providing the turbine free of charge; Rolfe Industries for providing a free sample of their amorphous alloy strip and in particular Mr. Jim Nunn for many helpful discussions; and Mr. Kieth Dunn of Galchrist Lubricants Ltd. for helpful advice.
- Finally, I would like to thank my parents, and my wife Yasmin for her continuous support and encouragement in exceptional circumstances; the work is dedicated to her and to my children Ebrahim and Yussra.

ABSTRACT

The thesis investigates a high speed switched reluctance (SR) generator suitable for applications such as aerospace and turbo-charged ground vehicles.

The generator is two-phase with 16-8 stator-rotor poles. The stator is 70 mm OD by 25 mm core length made of soft ferrite. The rotor comprises 30 μ m laminations of amorphous alloy chosen for its mechanical strength. The rotor of the generator was mounted on the protruding shaft of an air turbine and extensive tests were performed at a variety of speeds and supply voltages. The generator is shown to be capable of delivering around 280 Watts to a resistive load at 60,000 rpm, and 60 volts , with an estimated efficiency of around 77%.

The thesis describes in detail the electromagnetic and mechanical construction of the generator and presents a comprehensive survey of operating waveforms and performance measurements. The design utilises a simple magnetic model for the SR generator based on a quasi-linear flux-current characteristics which are shown to provide a very useful tool for performance prediction.

CHAPTER ONE

INTRODUCTION

1.1 Objective

By virtue of their simple and robust rotor construction without embedded permanent magnets or electrical windings, switched reluctance (SR) machines are mechanically capable of very high speed operation. Furthermore, their specific output is reputedly high. There is therefore an attraction in using SR machines for high speed generator applications where weight and space are important considerations. Specific applications include aerospace and road vehicles for which a turbocharger could be used as the source of mechanical power.

Despite many recent publications on the use of SR motors for variable speed drives, relatively little attention has been given to SR generators, whether very high speed or otherwise. At very high speeds, in addition to the mechanical constraints, there are electrical constraints on the frequency of switching for extracting the generated power from the machine windings.

The basic objective of the work described in this thesis is therefore to investigate the mechanical and electro-magnetic design of high speed SR generators and to build and test a particular example operating, if possible, up to a speed of 100,000 rpm, and providing generated power of several hundred watts. The application in mind, though it was not intended that this should dominate the project, was the above mentioned turbo-charger vehicle generator for which an output power of a few kW would have been more appropriate. However, as will be seen from the later description, the stator cores did not enable power in excess of 1 kW (at the most) to be generated, and furthermore the corresponding power to supply the air-turbine driving the generator would have been excessive. It was therefore

necessary to limit the power expectation to a few hundred watts.

Since generators of this power rating and speed are very small, the possibility arose of using ferrite, or some other magnetically low-loss material, for the stator. This would significantly reduce the operating flux density and hence increase the size of the generator, but the generator would still be acceptably small and both the cost and magnetic losses would be reduced. Furthermore, the use of ferrite enhances the novelty aspect of the work. It was therefore decided to proceed on this basis provided a suitably moulded stator could be obtained.

The specific objective was therefore to identify a suitable ferrite stator and, based on the stator geometry, to design, build and test a small SR generator with a target of delivering approximately 500 W at 100,000 rpm. The most important performance aspects are power output and efficiency and instrumentation to measure these is required. A secondary and not insignificant objective is to design and build a prime mover, comprising a motor, compressor and air-turbine for driving the generator.

A detailed description of the design and assembly of both generator and prime mover, and experimental test results, are provided in the remaining chapters of the thesis.

Before proceeding further with project description, the remainder of chapter 1 provides a background review of the operation of SR machines followed by a presentation of the main design differences between SR motors and generators. Alternative types to the high speed SRG are fully discussed with concluding remarks on the advantages of the SRG. The limited previous work available in the literature in connection with high speed SRG, is reviewed in a special section. Finally, the thesis general layout is given at the end of the chapter.

1.2 SR Machines

This section seeks to review the basic principles of switched reluctance (SR) machines, by defining their basic distinct characteristics, their operation, supply and control considerations. The discussion is, however, brief due to the fact that SR machines are becoming more widely understood.

1.2.1 Basic Operation

Figure 1.1 shows a typical SR machine configuration, comprising a single stack of laminated stator, a laminated rotor, and a power converter. Concentrated coil windings exist only on the stator. These coils may be interconnected in various ways, a common one is shown in Figure 1.1, where diametrically opposite stator poles carry coils of one phase winding. Two coils are connected in series. One phase winding is shown in the figure for simplicity. Pulses of current are supplied to each phase winding in synchronism with the position of the rotor salient pole with respect to stator salient pole. This necessitates a feedback signal to indicate the rotor position to the firing circuit of the power switches. At the correct instant, the d.c. supply is connected across the phase winding by closing switches S_1 and S_2 . The nearest rotor pole to the excited stator pole is then magnetised, and reluctance torque is produced, depending entirely on magnetic attraction between the poles, thus pulling the rotor in the direction of increasing magnetic flux linkage. The machine is a singly excited one, as the rotor carries no windings or permanent magnets. At the end of the torque production period, energy stored in the magnetic circuit is usually returned back to the supply via the power diodes after turning S_1 and S_2 off. Other phase windings of the machine are identical and usually independent, depending on the configuration of the power convertor. A continuous rotation at a desired direction, torque and speed is achieved by supplying

the machine phases with current pulses in a particular sequence, at a particular instant and frequency and for a particular duration. Excitation sequence ABCA will give the rotation in the direction shown in the figure.

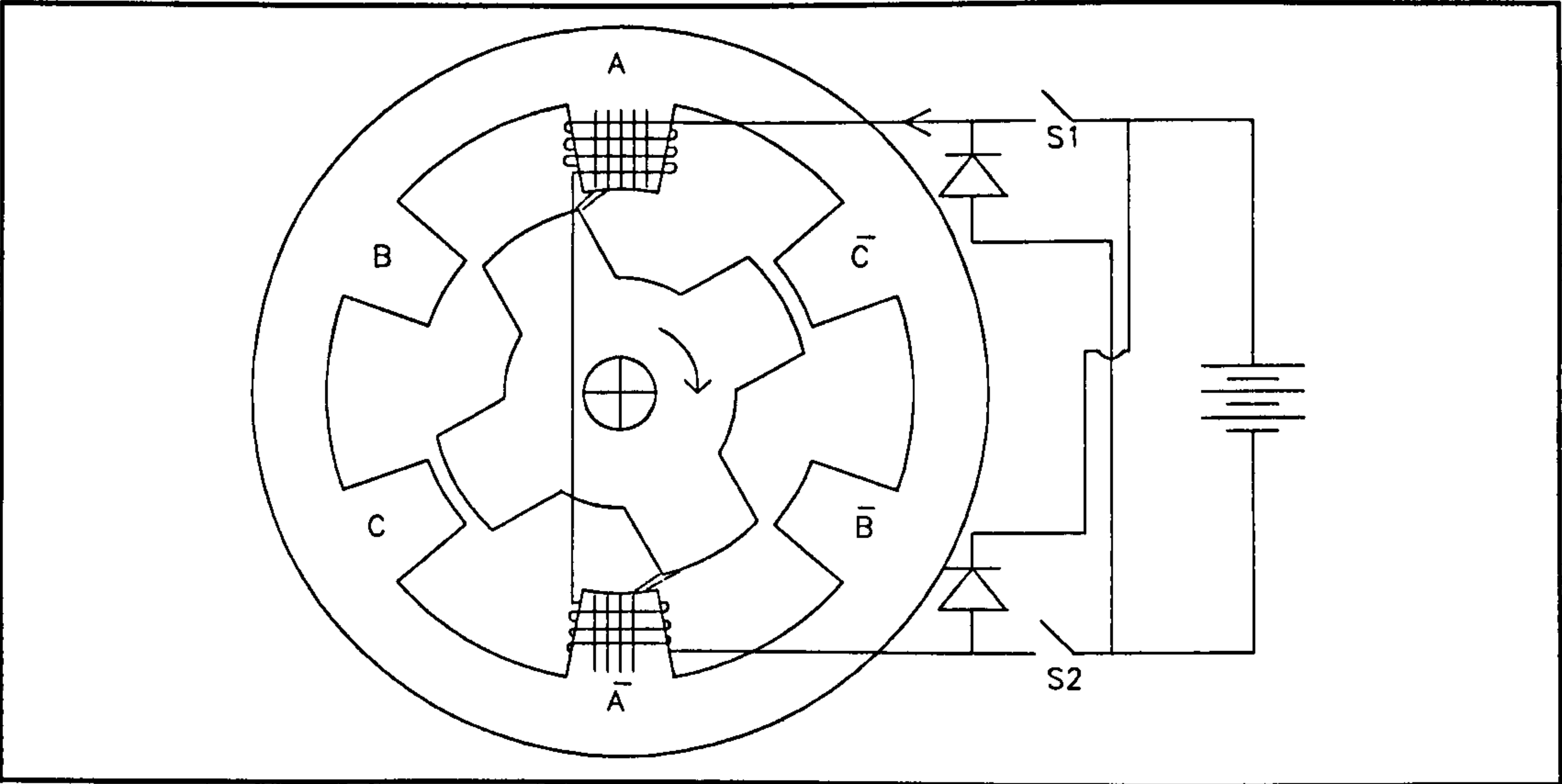


Figure 1.1: Typical SR Machine and Converter.

Stator and rotor poles are unequal and even in number. There is a wide range of possibilities for the machine configuration specifications such as number of poles on both members, number of phases, pole arcs and winding arrangements with some constraints [1].

In some respects the SR machine is a synchronous machine in that it produces net torque only when the rotor motion is synchronous with the applied stator m.m.f. However unlike conventional synchronous machines, this synchronous relationship may be complex depending on the number of poles and phases [2]. Furthermore, the SR machine does not normally run or start from an a.c. voltage source [3][4]. The commutation between phases is electronically implemented so that power electronics are essential to the operation of the machine, one reason why the simple theory of the machine waited more than 100 years [1][5] for the advent of power switches before it could realise its true potential. Thus the SR machine is a brushless machine making it superior to conventional d.c. machines and very similar in its overall behaviour to the d.c. brushless drive [6].

¹ In many respects.

1.2.2 Flux Linkage-Current Characteristics and Energy Conversion

The flux linkage/current characteristics shown in Figure 1.2, also known as magnetisation characteristics, represent the variation of flux linkage Ψ with excitation current i for a set of rotor angles θ . These Ψ - i - θ characteristics are unique for an SR machine with certain geometry and magnetic circuit design. Dynamic behaviour of the machine can be described on the flux linkage/current diagram by defining a locus of the point with (i, Ψ) coordinates during each step or what is known as the working stroke. This locus is known as the operating flux linkage/current trajectory [11] or energy conversion (EC) loop.

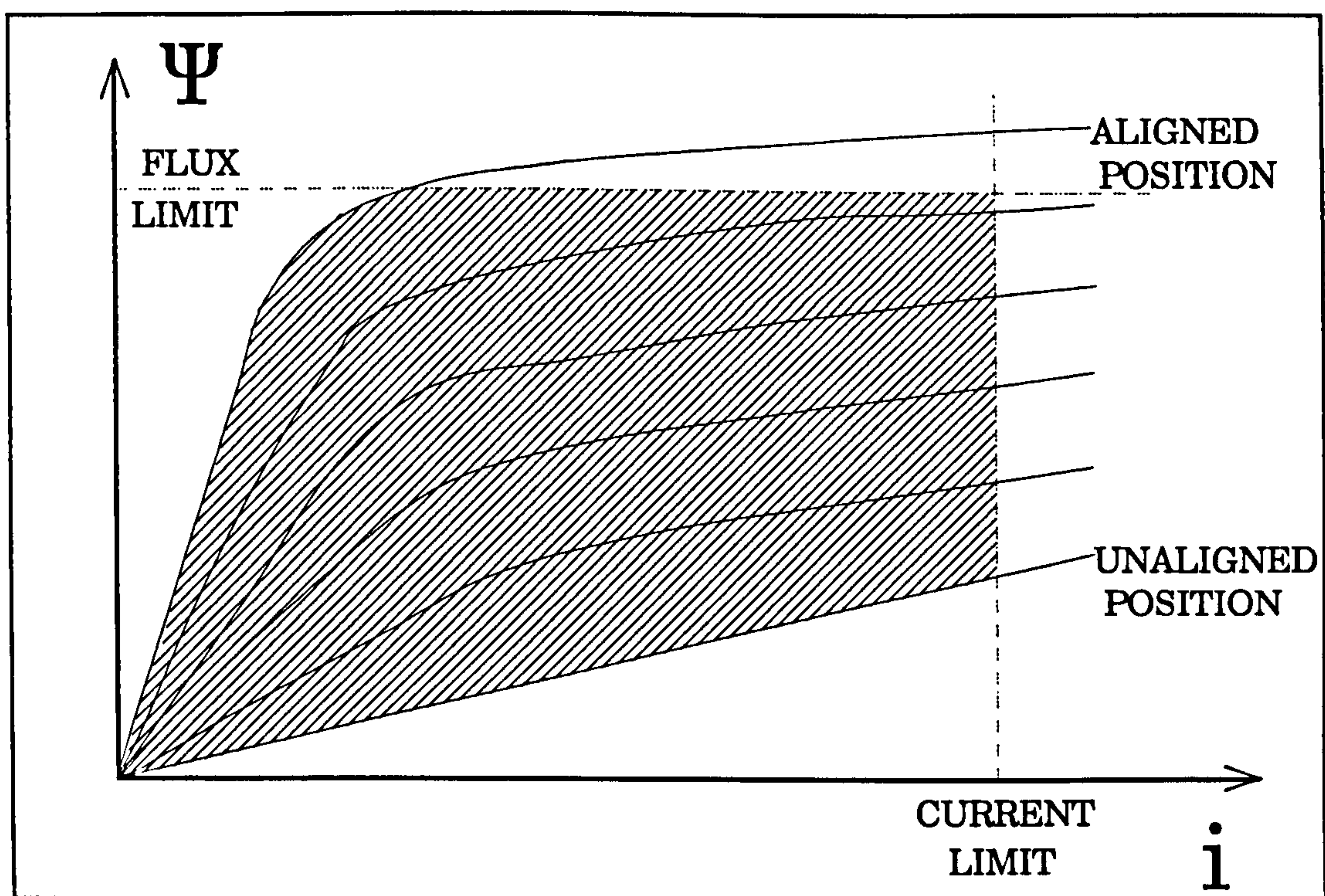


Figure 1.2: Typical Ψ - i - θ characteristics and energy conversion loop.

The operating flux linkage/current trajectory in Figure 1.2 defines an area (shown shaded in the figure) which represents the maximum energy available for conversion with limitations on both flux linkage and current. In practice, the maximum current is limited either thermally or by the electronic converter ratings. Maximum flux linkage may be limited even before saturation by core losses and the tendency towards a spiky current waveform and noisy operation [3].

The slope of the magnetic curves is minimum at what is known as the un-aligned position (between the excited stator pole and the rotor pole), and maximum at the aligned position (at low values of current). This gives rise to two values of phase inductance, L_{\min} and L_{\max} , respectively, which are used to define an inductance profile, indicating L variation with θ . The $L(\theta)$ profile at low currents is a useful tool in design and performance prediction. The inductance is approximated as constant at L_{\min} at no poles overlap and approximated as linearly rising when poles overlap progresses, then linearly falling when poles are coming out of alignment.

Magnetic saturation local to the pole tips of the SR machine at the beginning of overlap and during partial overlap [10] is the normal working condition of the machine. It is considered beneficial to the operation in terms of improving the specific torque and power output (improvement is limited, however, by bulk saturation within the SR machine), and in terms of reducing the VA requirements of the power converter and improving its efficiency [11].

The flux linkage/current trajectory can be expressed as the path integration $\oint i d\Psi$ which is used to find the average torque and the average electromagnetic power converted. For any SR machine, in one revolution, each phase conducts as many steps (or working strokes) as there are rotor poles N_r . Hence, for m phase windings, the EC loop will be swept (mN_r) times per revolution.

After accounting for mechanical and core losses, the average electromagnetic power converted will then depend on the swept area and the rotor speed f_r in rev/sec:

$$P_e = m N_r f_r \oint i d\Psi - [P_{L-mech} + P_{L-core}] \quad (1.1)$$

Mechanical losses $P_{L\text{-mech}}$ includes friction and windage, while core losses $P_{L\text{-core}}$ includes hysteresis and eddy current losses. The equation shows that to increase P_e , the swept area of the EC loop should be maximised within the limits of both current and flux linkage.

The introduction of the co-energy term and its use in the general theory of torque production in SR motors is reviewed in Appendix A1.1.

1.2.3 Power Converters and Control

Power electronic converters involve power sections, which may include rectification from a.c. input, and control sections. A typical SR machine system is illustrated in Figure 1.3. It shows the SR machine connected to its supply and control. This is typical of an SR motor drive.

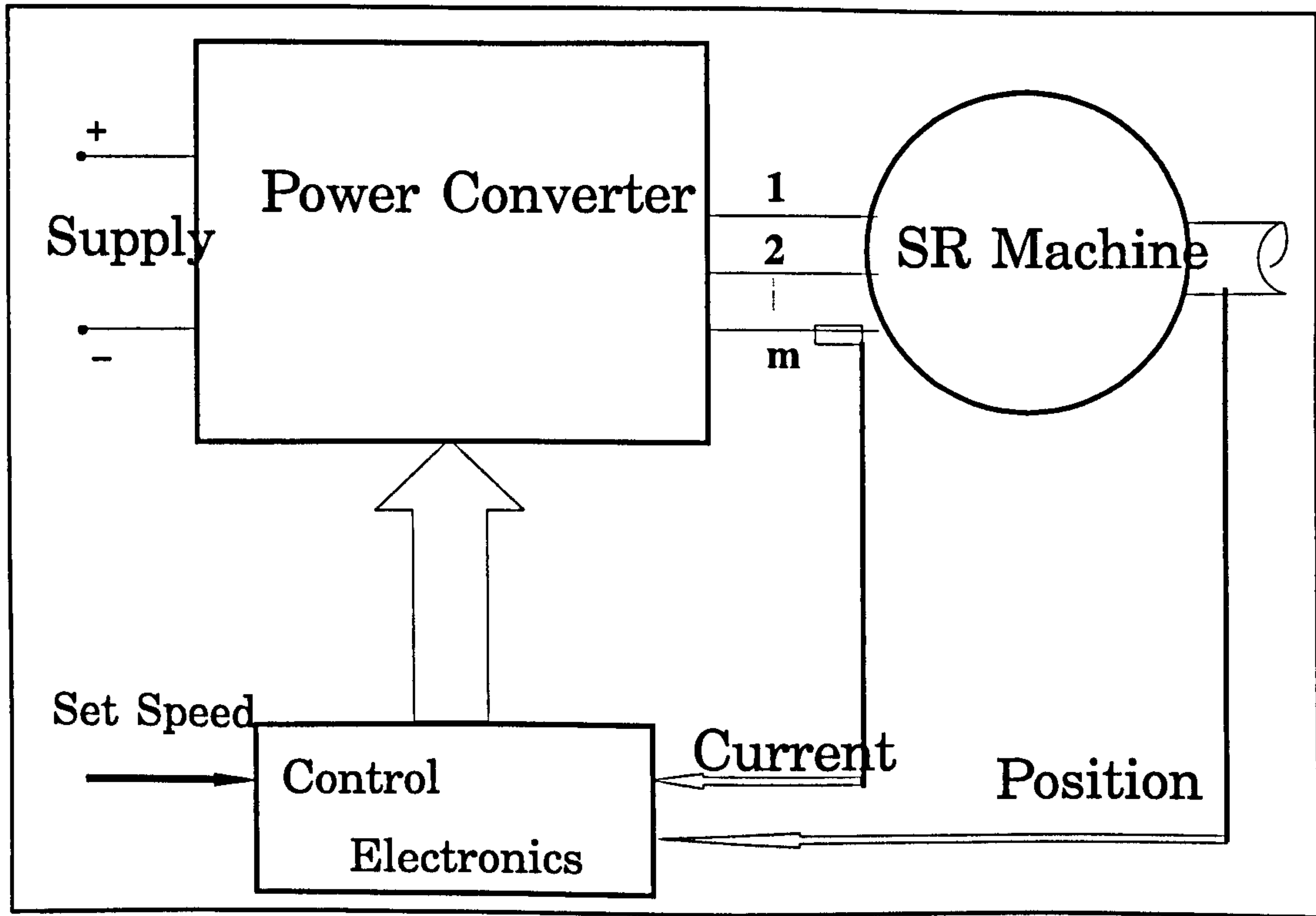


Figure 1.3: Basic components of the SR drive.

The feedback consists of a stream of pulses generated by a rotor position detector (e.g. optical sensor, Hall effect or inductive) and also a current monitoring signal from a current transducer. If switching instant is only determined by rotor position (i.e firing angles are kept constant as well as the supply voltage) the SR motor will simply develop a torque-speed characteristic similar to those of a series-connected d.c. machine. These are known as the natural characteristics of the SR machine [1]. Torque will be inversely related to the square of the speed (limited at low speeds by peak flux). Other than the natural characteristics of the machine, two distinct modes of operation exist. First, is the low speed mode, where the time associated with the rotor angle duration of increasing, or decreasing, phase inductance is relatively long. Back e.m.f. is low and current rises rapidly. This necessitates the use of current feedback to switch off excitation when the current reaches a set level, then switch on again and so the current waveform is chopped several times before the excitation is removed from that phase and commutated to another phase. As a result, the power converter acts as a chopper supplying controlled magnitude of current to the machine. This is shown in Figure 1.4(a) for low speed motoring and is known as the chopping mode. As speed increases there will be less chops per working stroke until the second mode is established where one pulse of current occurs in a working stroke. This corresponds to high speed operation shown in Figure 1.4(b) for motoring and Figure 1.4(c) for generating. In this case the time associated with the rotor angle duration of increasing, or decreasing, phase inductance is relatively short. Back e.m.f. is high enough to limit the phase current and the flux falls as less time is provided for flux rise. Excitation should be advanced to give ample time for the current build up and operation is controlled using angle control.

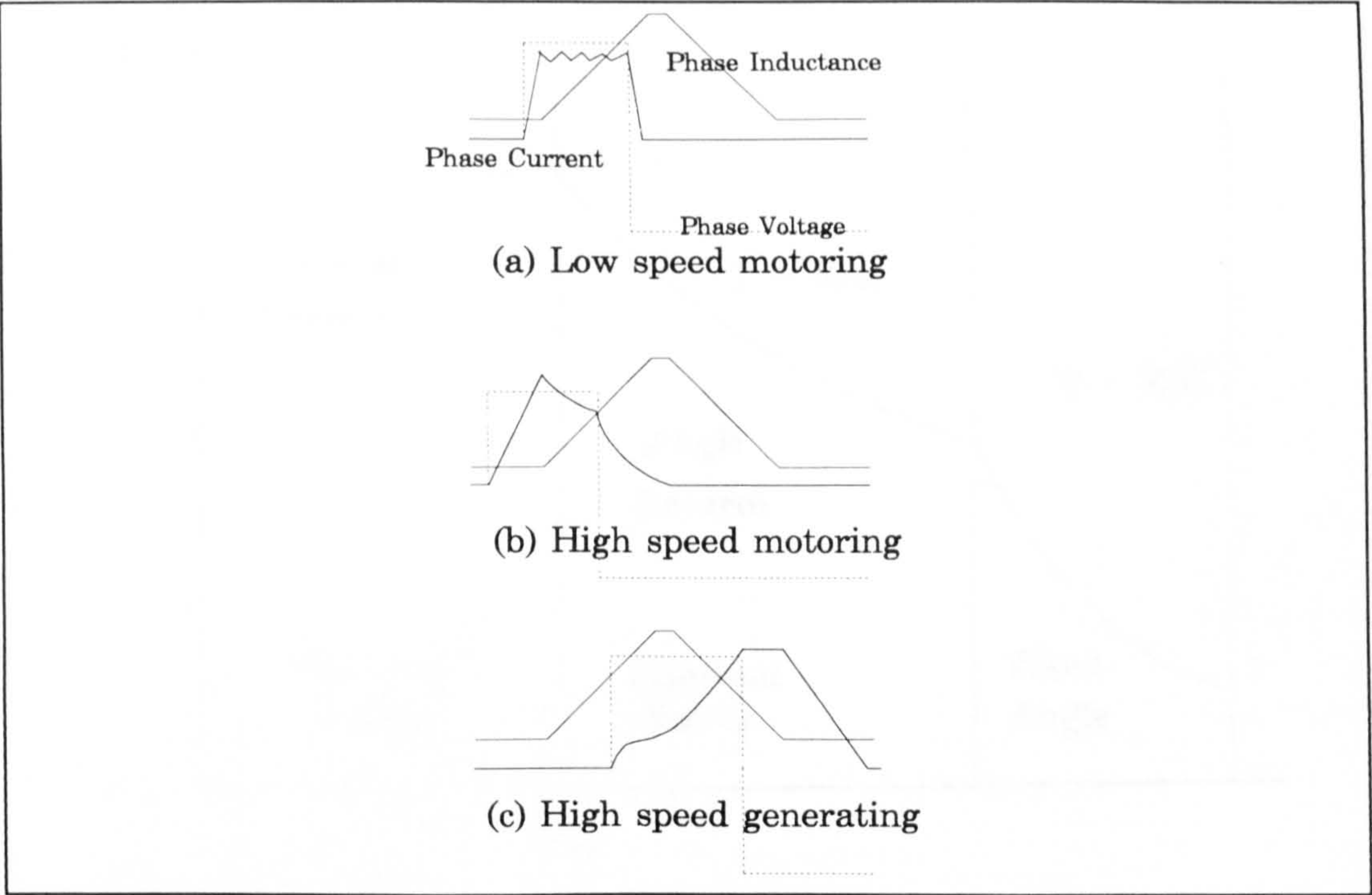


Figure 1.4: Phase current, voltage, and inductance.

Figure 1.5 shows typical torque/speed characteristics of the SR motor. These are obtained by altering the control scheme of the phase energisation timings. The control scheme of the first region is that of the chopping mode. It gives a constant torque characteristics by controlling the amplitude of current. However, it is possible to obtain higher starting torque if the application demands. The speed ω_b , the base speed, is the lowest possible speed for the motor to operate at its rated power as it corresponds to maximum current at maximum supply voltage. Using angle control beyond this speed can give the motor a constant power characteristics as torque is made inversely proportional to speed. This continues until a limit is reached for the phase conduction angle beyond which fixed supply and fixed switching angles will give the machine its natural characteristics.

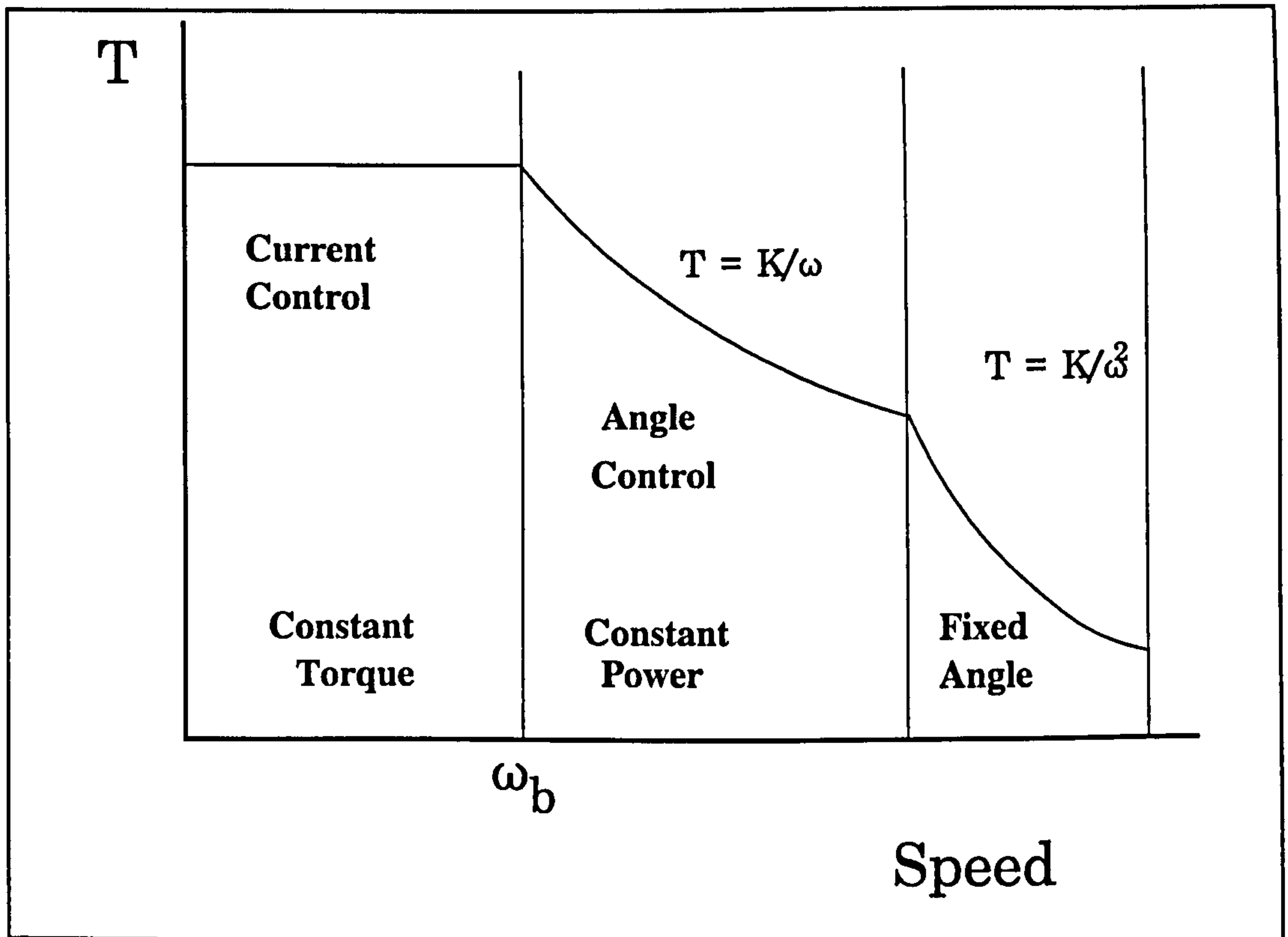


Figure 1.5: Torque-speed characteristics of the SR motor.

A literature review, conducted by the author, regarding control strategies of SR machines and their implementations as well as details of power converters review are given in Appendix A1.2.

The converter in Figure 1.6 is considered as a classic type converter, also known as the asymmetric half bridge. It utilises two switches per phase thereby giving extra control flexibility. The phase winding is connected to the d.c. supply via switches S1 and S2. When the energised phase is disconnected from the supply, both switches are off and diodes are forward biased. The phase winding will "see" a negative voltage $-V_g$ causing the flux to collapse more quickly. It is also possible with this converter to turn-off one of the switches. The phase winding then sees zero voltage and the energy will freewheel through the other switch and one diode. This gives better performance than chopping both switches [12]. A filter is normally required to reduce harmonics in the mains supply.

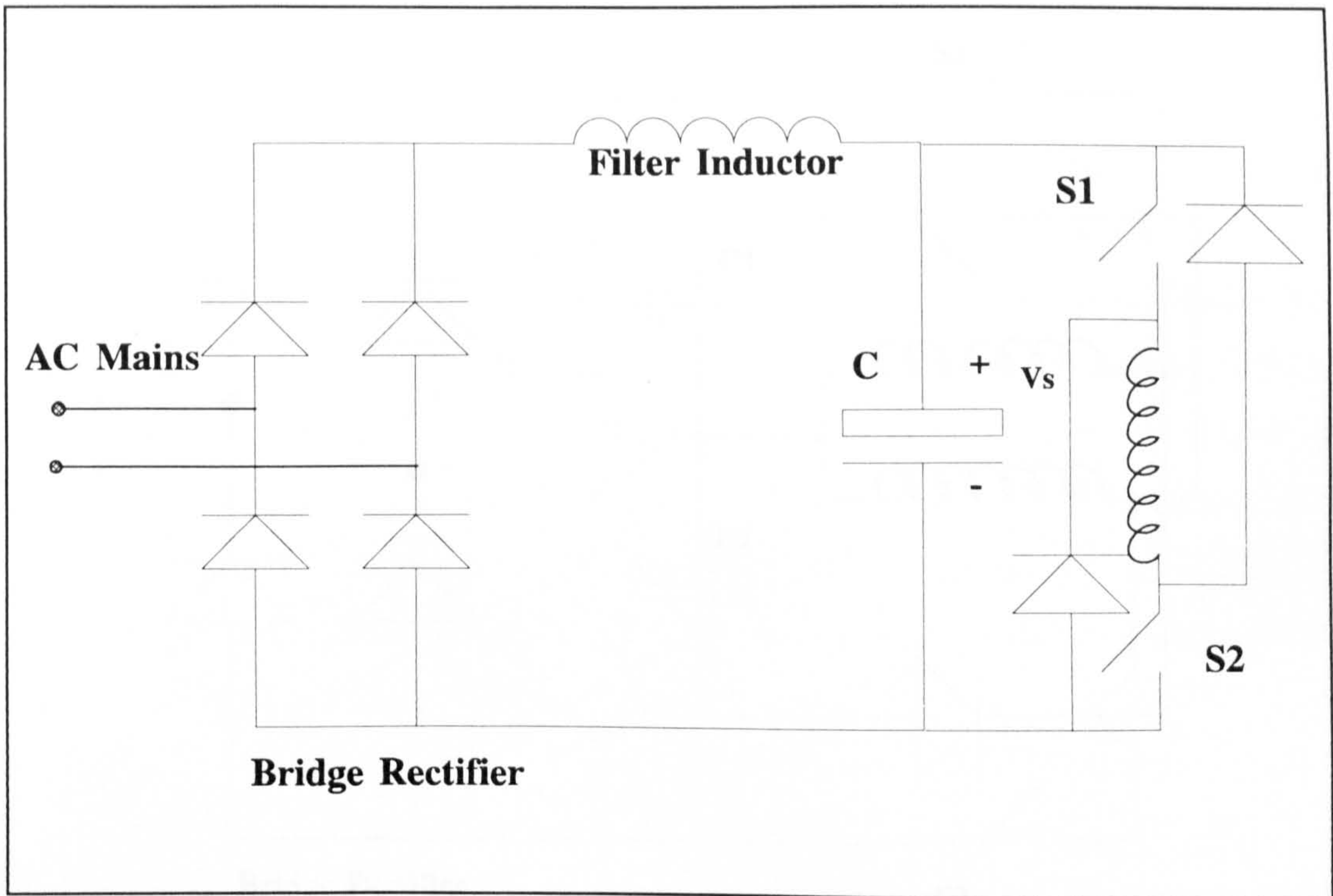


Figure 1.6: Classic type power converter.

A split supply converter, Figure 1.7, is used to supply the machine through one switch and diode per phase. This is making use of the unidirectional current requirement of the SR machine. However, two equal capacitors are required and phase number must be even in order to keep the circuit balanced. Two phase windings are shown in Figure 1.7. Though it requires half the number of switches of the classic converter, the current rating of the switches is double. This converter is more attractive at high voltages because the d.c. supply is centre tapped [37].

A C-dump converter, Figure 1.8, also uses one switch per phase. For proper operation, however, it needs a chopper control section [24] which means an extra switch, diode, power converter as well as the dump capacitor. It has advantages in terms of phase current control and good efficiency at low voltage levels [24]. Further discussion of other interesting designs of various converter topologies as well as the factors effecting the choice of a particular converter are found in the literature review of Appendix A1.2.

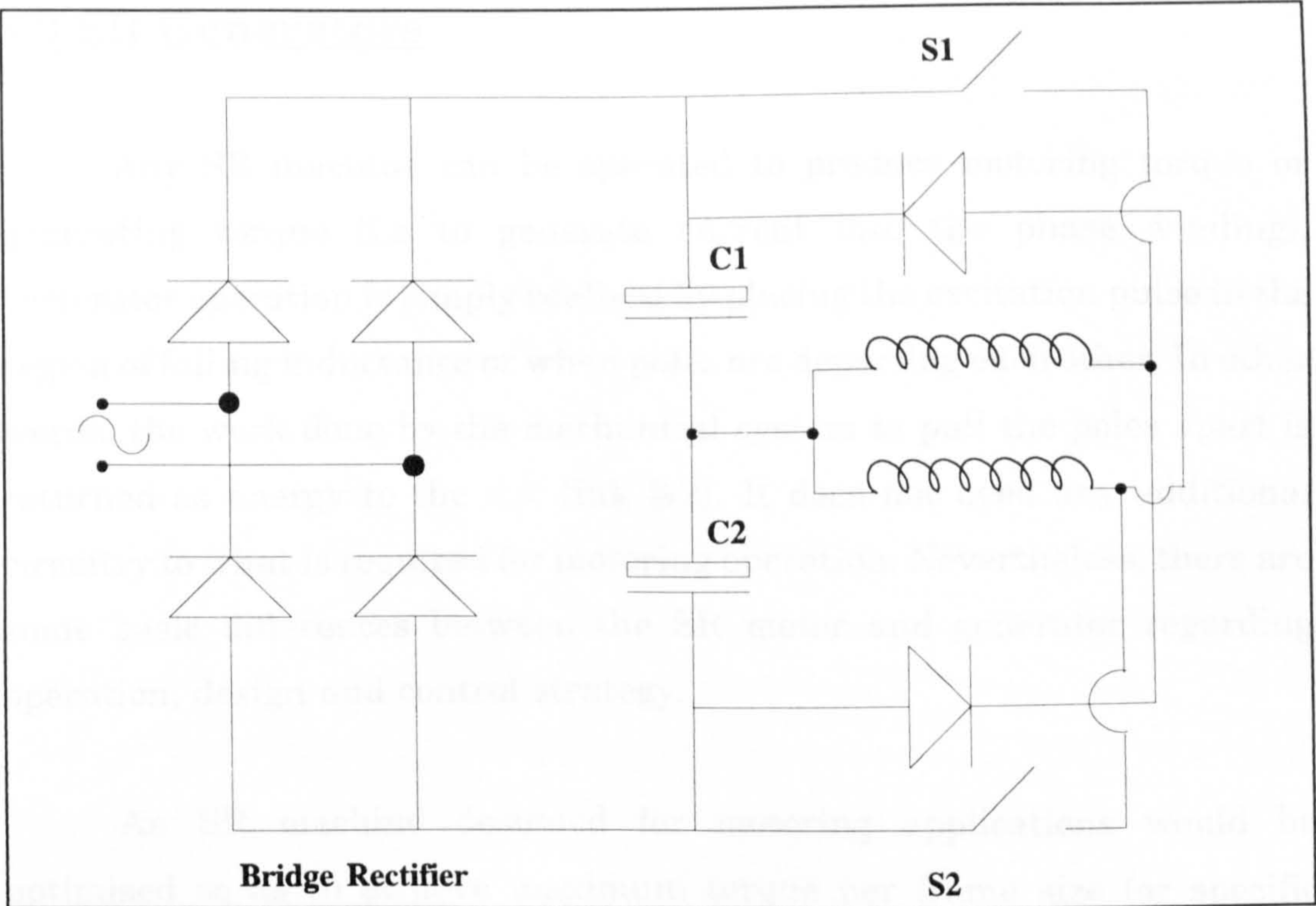


Figure 1.7: Split supply converter.

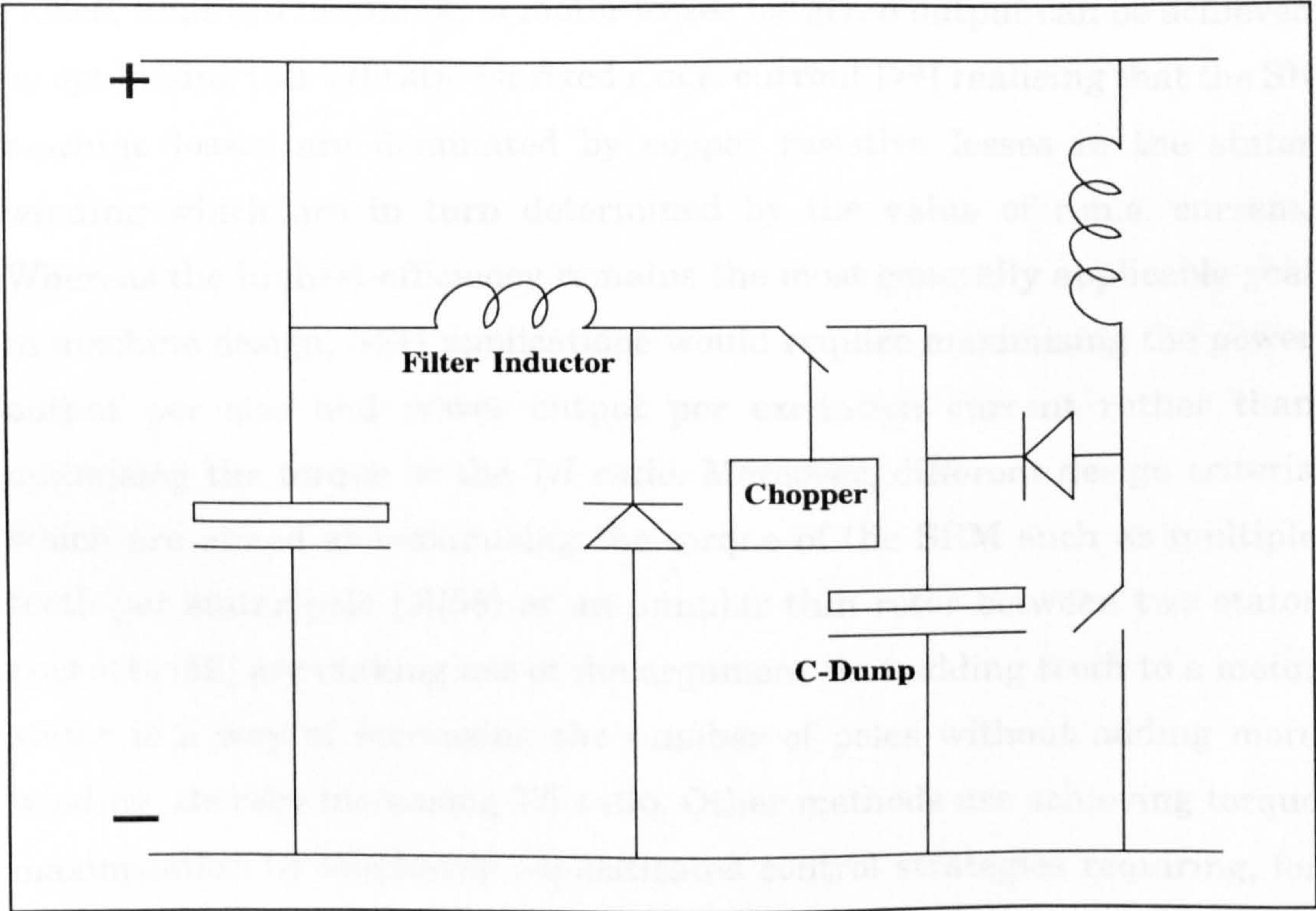


Figure 1.8: C-Dump Converter.

1.3 SR Generators

Any SR machine can be operated to produce motoring torque or generating torque (i.e to generate current into the phase winding). Generator operation is simply realised by placing the excitation pulse in the region of falling inductance or when poles are departing each other. In other words, the work done by the mechanical system to pull the poles apart is returned as energy to the d.c. link [42]. It does not need any additional circuitry to what is required for motoring operation. Nevertheless, there are some basic differences between the SR motor and generator regarding operation, design and control strategy.

An SR machine designed for motoring applications would be optimised so as to achieve maximum torque per frame size (or specific torque) coupled with high efficiency. Often this can be expressed as optimising the ratio of torque per r.m.s. ampere of excitation current. Hence, finding a minimum of motor losses for given output can be achieved by optimising this T/I ratio for fixed r.m.s. current [57] realising that the SR machine losses are dominated by copper resistive losses in the stator winding which are in turn determined by the value of r.m.s. current. Whereas the highest efficiency remains the most generally applicable goal in machine design, SRG applications would require maximising the power output per size and power output per excitation current rather than optimising the torque or the T/I ratio. Moreover, different design criteria which are aimed at maximising the torque of the SRM such as multiple teeth per stator pole [9][58] or an annular thin rotor between two stator pole sets [59] are making use of the argument that adding teeth to a motor stator is a way of increasing the number of poles without adding more winding, thereby increasing T/I ratio. Other methods are achieving torque maximisation by employing sophisticated control strategies requiring, for example, instantaneous torque control [15].

By considering the fact that high torque is related to low speed operation applications of SRM and the fact that SRG potential as a brushless robust generator is better utilised at high speeds rather than low or medium speeds; it becomes apparent that torque maximising methods are not important for the SRG design and that power and efficiency maximisation at very high speeds are the design criteria which should be investigated and implemented.

Starting is obviously not a problem with the SRG. Consequently, the options for phase number are wider, for machines used only as generators, than that of the SRM. The rotor position detector is also quite simple. Waveform interrogation techniques or sensorless position detection is easily employed.

The power converter is basically the same for motor drive applications. Nevertheless, the choice of a topology which will be suitable for a high speed generator must take into account several considerations. These are discussed later in chapter five.

Depending on the specific application of the SRG, control of output parameters is different from that of the SRM. For the SRG, a constant voltage output on the load is normally required which may or may not equal the excitation voltage depending on the power converter topology and the application being sought. Hence an output d.c. chopper may be employed in this case to regulate the output voltage, or a power system controller may account for load voltage regulation. If specific power demands at maximum efficiency is required, then feedback control would be employed to adjust the firing angles accordingly. Control requirements for an SR machine working as a generator are generally simpler than those for SR motor drive applications.

1.4 High Speed Generators- Alternative Types

Direct drive operation enables the elimination of the gearbox and all losses that correspond to it. Further, it provides a reliable light-weight and compact generating unit. It is known that for a given power, the size decreases almost in direct proportion to the increase of speed [65]. Many rotating mechanical machines such as turbines, compressors and machine tools will gain better performance at high speeds. Therefore, a direct coupling to the electrical machine would be advantageous [65].

Applications of direct-driven high-speed generators are found in aerospace, ground vehicles, marine ships, unmanned airborne vehicles and others. The common requirements of direct driven alternator systems (demanded by such applications) are; high power density, high efficiency, high speed capability, brushless excitation, simple construction and ability to perform in hazardous environments.

Once the need for high speed is accepted, the number of suitable machine types is severely restricted; the choice of alternator type would be limited to one that is ruggedly constructed and capable of high speed operation. Machines requiring the transfer of electrical power to or from the rotor are inferior and in some applications immediately unapplicable, because brush wear is excessive at high speeds, so both d.c. generator and wound rotor WR generator can be ruled out [69]. The feasible options can then be:

- 1- Wound rotor brushless synchronous generator WRG.
- 2- Permanent magnet generator, PMG.
- 3- Homopolar inductor alternator, HIA.
- 4- Induction generator, IG.
- 5- Reluctance synchronous generator, RG.
- 6- Switched reluctance generator, SRG.

Other types of machines which have been used as high speed generators may be briefly referred to during the discussion of the above prominent types. The SRG advantages are dealt with in a separate concluding section in 1.5.

1.4.1 The Wound Rotor Brushless Synchronous Generator

Compared with the IG, the WRG is often electrically a better choice. It has the relative advantages of small rotor losses, good efficiency and easy magnetisation. The excitation current is fed from a shaft exciter via a "rotating" full wave bridge rectifier. A gas turbine driven WRG has been in use in power plants to supply 250 kW at 30,000 rpm [74]. It has also been in use as an aircraft generator as a workhorse for producing 400 Hz a.c. electric power -in conjunction with a cycloconverter- for many years [75]. However, it has limitations due to rotating windings and rotating rectifiers. The windings are exposed to great mechanical stresses and they may have to be supported, properly, at the ends of the shaft with carbon fibre bands and in grooves with dove tail joints. Still, to make the winding robust enough against mechanical stresses may be difficult. Furthermore, the winding may become uneven in manufacture, making the balancing of the rotor difficult. Fault tolerance is not available. This point will be further discussed in section 1.5.

1.4.2 The Permanent Magnet Generator

The PMG is increasingly replacing the WRG especially in aerospace and ground vehicles applications [69][76][77]. The on-going development of permanent-magnet materials alloys combining rare earths and cobalt (principally samarium cobalt SmCo) as well as neodymium-iron-boron NdFeB, has produced materials with impressive energy products much higher than earlier magnets such as the AlNiCo 9 [77]. In addition, the

coercive strength, or resistance to demagnetisation of SmCo and NdFeB [78], makes them ideal for motor and generator applications. However, high production costs for these materials hinders them from wider use. Permanent magnet ferrites, or hard ferrites, offer cheaper options but also lower performance as their energy product is about 1/8 that of NdFeB. While the latter has the highest energy product, it suffers from temperature instability compared to SmCo [79]. They can only be operated at temperatures below 150°C. Therefore some trade-off exists when considering the selection of a particular magnet for the machine.

PM generators have shown to be capable of tremendous power densities [80] and high efficiencies, due to the fact that exciting windings (and their related I^2R losses) and d.c. supply are dispensed with, so that rotor losses are much less than in other machines such as IG and WRG. In addition, the elimination of rotating rectifiers, rotor cooling devices, rotor winding and losses, and the auxiliary alternators required for brushless operation, has resulted in a machine package which exhibits significantly improved reliability and rotor life [76]. The efficiency has been shown to be flat over a wide range of current [81] which is a desirable feature in many applications.

PM generators may take different forms regarding magnetic circuit configuration; conventional radial field, axial field, flux squeezing, etc. [69]. They may be of internal or external rotor types [62] or may take a rotor disc form to improve power density and high speed capability [82]. The stator is often a standard laminated slotted core which carries the armature core, similar to an induction machine stator. However, toothless stator designs for PMG have been reported [83] in order to eliminate core losses in the stator and reduce weight. Nevertheless, the most interesting improvement rests with the properties of PM materials which are claimed to realise improvements similar to semiconductors [62].

PM generators, however, suffer from several drawbacks:

- 1- Present cost of permanent magnet materials.
- 2- Because it is not possible to vary the excitation of a PM generator, a potential disadvantage is poor voltage regulation [69]. This deficiency may only be removed by using a dual rotor construction with relatively varying rotor positions to obtain desired output voltage under changing load and speed [84].
- 3- In the event of a winding fault, the generator can only be de-energised by mechanically decoupling the generator from the engine or prime mover [77]. Alternatively, fault tolerance can only be made available by providing separate sets of armature windings with the associated permanent magnet field [75].
- 4- High temperature (above 300°C) environment in particular applications may prohibit the use of PM generators unless sufficient cooling can be supplied. This is mainly due to a limitation in the maximum application temperatures of rare earth magnetic materials [80].
- 5- PM generators inherently produce variable voltage variable frequency (or wild voltages and frequencies). If constant voltage is required, which is normally the case, then a static power converter must be used to regulate the output voltage. This is not a serious drawback, however, as the required power conditioning electronics are considered as relatively simple [85].
- 6- There will be lower efficiencies and higher losses at light loads and specially at no-load ¹ [76]. In general, PM machines have high impedances and must be operated near their maximum output [86].

¹ Compared with conventional a.c. generators.

- 7- The placement of permanent magnets on the surface of the rotor causes problems in spinning the rotor at very high speeds (above 15,000 rpm) [87]. A more adequate mechanical strength may be provided for the rotor by using a can, which may consist of magnetic or non-magnetic material, to contain the rotor. This, however, is likely to reduce the overall output of the machine [88].
- 8- Magnet corrosion and possible demagnetisation are potential hazards not present with other technologies [89].
- 9- The machining required for all the available magnets is hard, and consequently expensive, as these materials are known to be brittle. The NdFeB is, however, an exception [90].

1.4.3 The Homopolar Inductor Alternator

This type of generator has several advantages over conventional machines, making it suitable for very high speed operation. In its most usual form, it is a homopolar machine [91] provided with two axially spaced stator laminations wound with a common a.c. output winding, the armature. A stationary solenoidal d.c. field winding is positioned between the two stator laminations to charge the rotor teeth magnetically north-south along its length. The rotor is a solid magnetic steel alloy shaped to cyclically interrupt the flux produced by the stator field (therefore the name, flux switched, is sometimes used). The cross section of homopolar inductor alternators appears similar to the SR machine both having unequal number of stator and rotor poles, however, the principle of operation is rather different due to the existence of two sets of windings in the case of the HIA. The flux variation in the air gap is obtained by a variation of the reluctance due to the succession of teeth and slots on the wheels. As both sets of armature and field windings are on the stator, the

machine has no slip rings or brushes. This feature, coupled with the typical solid construction of the machine rotor, makes the inductor alternator particularly adaptable to very high speed applications. The homopolar IA would certainly be preferred for very high speed applications over both WR and PM generators on the grounds of more rugged mechanical construction [93]. Electrically, the generator is both self exciting (assuming a battery for initial priming) and suitable for use with a simple rectifier converter [93]. One of the significant advantages of this alternator, over other high speed alternators, is the flexibility in controlling the magnetic flux, hence the induced voltage, which simplifies the overall generator system and inverter [94]. Furthermore, since the \vec{n} -rotating field of the HIA has no polarity reversal, as flux is unidirectional, rotor pole leakage flux and core loss in the back iron are minimised. Therefore, hysteresis and core losses are claimed to be smaller than those normally found in heteropolar generators [55].

Nevertheless, in applications which require high specific power, the PMG offers a better choice. Generally, the power/mass ratio of a homopolar machine is lower than that of a heteropolar one because of relatively low utilisation of the magnetic circuit [95],[96]. Moreover, compared to all the other types of machines considered here -except the WR generator- the construction of the HIA is complex [96]. Another drawback is the requirement of very powerful cooling for the stator laminations; direct water cooling of the laminations is usually employed [95].

1.4.4 The Induction Generator

Induction machines are reliable, cheap, rugged and require little maintenance [97],[98]. They have proved to be quite useful in autonomous/standby power generation and wind energy systems [97],[99],[100]. Despite the fact that the mechanical construction of an IG is relatively simple and well adapted to high speeds (with respect to WRG), tough requirements are often imposed on the rotor and these are usually contradicting each other. The most important requirements are:

- Simple structure and ease of production.
- Mechanical stability.
- Small losses.
- Good electrical properties.

The last two requirements could well be provided by a rotor with a cage winding and a laminated core. However, this would not grant the requirement for good mechanical stability. The alternative is to construct the rotor out of solid steel. The rotor would then consist of a single shaft forging in which slots are machined for the bars . Electrically, the solid rotor structure is inferior. One solution is to machine the rotor face with radial and axial grooves to enhance the electrical properties [74]. In any case, the need for secondary conductors on the rotor and short-circuit end rings connecting the ends of the secondary conductors is a drawback in very high speed applications. The rotor is subjected to very high centrifugal forces acting on the entire circumference to cause the secondary conductors to gradually detach until finally the rotor is destroyed.

Electrically, the main drawback of the IG is the need for an external network to supply the reactive power. If this network is replaced by a variable external capacitor, self-excited operation becomes possible [97]. The basic condition for self-excitation is residual magnetism in the rotor.

When capacitors are connected to the machine, a resonance circuit is formed due to continuous energy exchange between the electric field (capacitor) and the magnetic field (machine). As the load varies randomly, the capacitor and control resistances must be varied to obtain the desired voltage and frequency regulation. Self regulation may be possible using an auxiliary stator winding with a shunt capacitor and a series capacitor with the main winding [100]. However, all the above solutions require an additional network. For aerospace applications, in particular, cascade connected induction machines were considered for aircraft generation due to their reliability. This was later found unfavourable against the single frame cascaded IG [101].

Another drawback is that the operation of IG is not stable especially when operating over a wide speed range and when feeding varying loads. Moreover, IG's do not provide fault tolerance capability which is an essential requirement for aerospace applications [75].

To conclude, the induction generator is not considered as a good candidate for aerospace applications [75] or ground vehicles [102]. This will be clarified even more when the rest of electrical machines are discussed below. The solid rotor machine, however, will need further consideration as it has always been possible to improve its electrical properties [74],[103],[104] and its simple construction and high speed capability are valuable potentials in aerospace and ground vehicle applications.

1.4.5 The Reluctance Generator

Reluctance machines have been known as early as induction machines but they were not developed and exploited until the early sixties [105]. The reason for lack of attention in the early days was mainly due to their poor overall performance compared with well established and developed squirrel-cage induction machines. Moreover, earlier applications of reluctance machines have been rather specialised, hence performance was of secondary importance. As is the case with the IG, because the RG can only be used with a leading power factor, it had to await the development of static VAR sources with solid-state controls before its practical application could widely succeed.

The principle of operation is based on the existence of variable reluctance in the air gap; high reluctance in the quadrature q-axis and low reluctance in the direct d-axis. The reluctance machine differs from what has been described earlier (sections 1.2 and 1.3), the SR machine, by being of basically singly salient structure as well as having the same number of stator and rotor poles. The stator is very similar to an a.c. machine stator with an a.c. winding, thus sinusoidal a.c. power can be generated when distributed windings are used. The rotor is essentially of salient structure similar to the salient pole synchronous machine but carries no field windings and no magnets.

Some similarity exists between the RG and the IG which often leads to performance evaluation conducted on a comparative basis between the two generators [98]. Both generators are simple in construction, cheap in cost, robust and require little maintenance; both produce a.c. power; both are suitable for low power applications; and both need a supply of reactive power or capacitors for self-excitation.

Due to the saliency of RG, the air gap flux is rotated at the same speed as the rotor. Thus the frequency of the RG is directly proportional to the actual speed of the rotor without any slip as in the induction generator [106]. It follows that the synchronous operation of the RG and the fact that the fundamental magnetic flux through the rotor is only a direct component, lead to a high reduction in the rotor iron losses when compared to the IG. Indeed, if harmonics are neglected there will be no iron loss in the rotor and iron losses will only be generated in the stator [107]. Moreover, copper losses in the RG are claimed to be negligible with respect to the IG [106].

The reluctance machine can be used as a self-excited RG when suitable capacitors are connected across the stator terminals to initiate self-excitation. The manner of build up of voltage in the RG is similar to that of the self-excited IG. The final build up value (or equilibrium) is determined by the saturation curve of the machine and by the capacitive reactance of the connected capacitor [106],[108].

Most attempts to improve the performance of the RG have been centred on modifying the rotor magnetic circuit so as to achieve high saliency ratios [105]. Increasing this ratio should also improve the poor power factor of the RG [109]. Segmented rotor designs aiming at enhancing the saliency ratio were shown to outperform the conventional salient rotor [108]. Axially laminated anisotropic (ALA) rotor designs were also reported [110] in an investigation which covered such rotor designs for other machines as well. High speed generators with ALA rotors have not yet found their way into practice, but their potential has been exclusively indicated in [110]. Present fabrication costs may prevent the ALA machines

from immediate development into wider practice. In the case of axially laminated structures, the laminations are bent to produce paths of minimum reluctance in the direction of laminations and maximum reluctance in the path normal to laminations. The result is high ratio of L_d/L_q such as 7-8 [111]. More improvements of RG performance are expected by the proper design of the rotor magnetic circuit in order to give higher magnetic saliency ratio as well as less saturation effects [98].

The load characteristics of RG are very similar to a d.c. shunt generator [105] and there exists an optimum combination of capacitance and rotor speed resulting in maximum output power. When the load characteristics of both the RG and IG are compared, the RG yields a higher output power and efficiency than those of the IG at the same operating conditions [98]. Moreover, regarding stability, the RG is considered as more stable than the IG since the rotor speed is equal to the synchronous speed [98]. The RG can be made to handle almost any type of load, provided that the loads are compensated to present unity power factor characteristics to the generator [106]. In [109] a voltage source inverter VSI was used to act as a controllable leading power factor load and to supply a controllable exciting current to a very high speed RG. A system for direct output power control using a PWM converter was presented with test results in [112].

Similar to the SRG, the obtainable power from the RG is subject to a maximum current constraint. This maximum current is determined by the rating value of the machine (insulation type etc.) or the converter. The lowest speed is limited also by the maximum current. This is also typical of an SRG. However, in order to provide a certain power with increased speed, the load angle should be increased and eventually the maximum speed is reached at the maximum value of the load angle [107]. This is irrelevant for an SR generator since the maximum speed is only determined

by mechanical constraints as long as the applied voltage, or d.c. link voltage, can be elevated to provide the required power.

The efficiency of the RG is not so good especially when it is compared with the PMG. This is mainly due to the large excitation current. Efficiency is expected to improve, however, only with increased rotational speeds [107].

Capacitor rating requirements of the RG to satisfy self-excitation and to maintain the terminal voltage constant under different load conditions, seem to be higher than the capacitor ratings for the IG. This may be attributed to the lower magnetising reactance of the RG [98].

1.5 Advantages of High Speed SR Generators

Since the work of this thesis is concerned with the SR generator, it is naturally desirable to conclude the discussion of alternative machine options of the previous section by comparing these in the reference frame of the SR generator.

From the discussion in section 1.4 above and from the general description of SR machines given in 1.2 and 1.3, it becomes apparent that a high-speed SR generator may well outperform:

- 1- the wound rotor synchronous generator (see 1.4.1) mainly on mechanical considerations, reliability and operation in harsh environments, which are major drawbacks for the WR generator. Open circuit failure of the WRG exciter leads to a total loss of power. The generator therefore lacks fault tolerance in open and short circuits [75]. For high temperatures, the rotating rectifiers become the limiting factor as they can not sustain more than 150-200°C. On the other hand, the SRG is known to provide a fault tolerant machine and converter as well as a robust rotor design and stator winding which allows very high temperatures. In terms of low cost and high efficiency the SRG also has an advantage.
- 2- the homopolar inductor alternator (see 1.4.3) on the basis of higher power output (due to better utilisation of the magnetic circuit in the case of SRG).
- 3- the induction generator (see 1.4.4) on the basis of mechanical considerations, instability of IG operation over wide range of speeds and loads [75], and less overall weight (machine and electronics) for

the SRG at the same power [89].

This leaves two contenders to the SR generator from among the alternatives discussed in 1.4. These are the permanent magnet PM generator and the reluctance generator RG, and they will need more careful consideration to set the right balance for a particular application and requirements whenever a comparison is made.

1.5.1 SR Generator Versus PM Generator

In general, the PMG will outperform the SRG for two main reasons:

- 1- Higher specific power due to the development of permanent magnets with a high energy product.
- 2- The permanent magnets produce a doubly excited machine with no excitation power loss, therefore the efficiencies normally expected with the PMG are even higher than the SRG. Efficiencies of PM generators typically range between 96 and 98% [62].

Despite that, the SRG has some merits over the PMG. Generally, the SRG does not suffer from the nine drawbacks mentioned earlier in 1.4.2, but more specifically:

- 1- The absence of the permanent magnet produces a more reliable rotor in terms of mechanical stability and thermal robustness. The SR machine has the potential to run in very high temperature environments. because it has no permanent magnets, the maximum operating temperature of the machine is limited primarily by the insulation system.

2- Inherent fault tolerance is exhibited by the SRG, while in the case of the PMG fault tolerance is available only by providing separate sets of armature windings with the associated permanent magnet field [75]. The fault tolerance capability of the SR machine is enabled by the following features:

(i) Magnetic independence of machine phases and the circuit independence of the inverter phases. This minimises the possibility of phase-phase faults and also the failure of one phase does not effect the operation of other phases, and the generator can continue operation, at lower power, with one or more phases disabled.

(ii) Since there is no excitation source on the rotor, the machine cannot generate power into a faulted phase.

(iii) Since the machine winding is in series with the power switches, there is no shoot-through fault as is found in a.c. inverter drives.

The fault tolerance capability of the SR machine is claimed to be unmatched by other types of electric machines [113]. In [113] an implemented fault detection and management system for SR machine was tested.

3- PM generators operating at 100,000 rpm have been reported [65],[69], however, higher speeds may be difficult to realise for mechanical reasons. In the case of an SRG, it is mechanically possible to increase the speed to values higher than 100,000 rpm where it is expected to achieve impressive power densities -and efficiencies if proper amorphous laminations are used- which might exceed those of the PMG. This is, however, a potential "theoretical" advantage which is still to be proved.

- 4- Inverter designs for SR machines are simpler compared to PM machines. This makes possible significant weight reduction. For example, a 300 KW inverter for a PM machine would weigh about 65 pounds, whereas an inverter for an SR machine would weigh only 50 pounds [114].

1.5.2 SR Generator Versus Reluctance Generator

The SRG is inferior to the RG in several aspects such as:

- 1- The SRG will suffer from higher rotor losses since the rotor flux switching is the same as in the stator. The switching frequency of the winding of the SRG is: $mN_sN_r/2$ where m is the number of phases, N_s is the number of stator poles and N_r is number of rotor poles and they are not equal. For the RG the switching frequency of the winding is $mN/2$ where $N=N_s=N_r$. Moreover, at very high rotational speeds, the windage losses is also expected to be higher for the SRG as compared to the RG due to the difference in rotor profile.
- 2- The SRG does not generate a.c. power. Instead, the power generated is always a rectified d.c. So, when an a.c. load is to be fed, a power inverter is needed. However, there are still many appliances on aircrafts or ground vehicles that would desire a constant d.c. output voltage.
- 3- Noisy operation of the SRG [89].
- 4- Power switches in the SR machine inverter are exposed to higher voltage levels than for a conventional machine inverter such as those used in conjunction with the RG and IG for machines with well regulated voltage [52].

On the other hand, the SRG will outperform the RG for the following reasons:

- 1- Better saliency utilisation in the case of the SRG. Therefore, there is no need for complex rotor geometries to improve X_d/X_q as is normally the case with the RG.
- 2- If required as a motor-starter, there are no additional circuits required and no cage winding for self starting in the case of the SRG. Excitation is quite simple with wide range of options of power converter topologies to suit different applications.
- 3- No maximum speed limit of load angle as may be the case with some of the RG applications.
- 4- No essential need for a PWM controlled converter.
- 5- Concentrated stator winding giving greater simplicity and better thermal characteristics. However, if the windings are air-cooled rather than liquid-cooled, then distributed winding will be cooled easier. End turns are also fewer in the case of the SRG stator winding. The concentrated stator windings of the SRG can be externally form wound and then slipped over the salient stator poles, making the stator assembly process simple and inexpensive.
- 6- As mentioned before, the SRG is fault tolerant whereas in the case of the RG, fault tolerance feature is not available [75].

1.6 Previous Work on SR Generators

The potential of the SRG to generate electricity reliably with high power density was perceived in an early date of the SR machine [54]. However, this did not motivate any world-wide interest in the commercial applications of the machine as a generator. This lack of interest may be attributed to; first, the fierce competition from the successful PMG in aerospace applications; second, the audible noise of the SRG, which may still require improvement before the generator can be widely accepted for ground vehicles applications; and third the fact that many performance characteristics of the SR machine, despite its simplicity of operation, were not fully understood [115].

Most of the previous work [62],[75],[80],[89],[114] on the SRG was of investigatory nature, highlighting its potential.

In [62] the non-conventional high speed direct drive alternators are reviewed. These are mainly for power applications above 100 KW but at gas turbine speed. The review included the SR generator. Simplicity of construction, low cost to build and high speed capability are noted. The review concluded by giving the preference to the inductor alternator for standby duty and to the PMG for continuous duty. However, the SRG potential as another alternative approach is nevertheless indicated.

In [75] a similar review is carried out for electric machines as generators for aerospace applications. The SRG is commended for its reliability in operating at high temperatures, high speed and fault tolerance. The study concludes that the selection of a proper electric machine for aerospace generating applications must be based on overall system constraints of weight, performance and cost.

In [80] a generating system for unmanned airborne vehicles was suggested. This was based on a switched reluctance generator directly driven by a gas turbine at a speed of 100,000 rpm. The alternator is mainly sized to generate the pulse power required for mid course correction of the unmanned airborne vehicle and also other loads depending on the mission profile of the vehicle. The SRG was preferred over the HIA and the PMG mainly for its high temperature capability. The environment temperature of the application was about 650°C with a prospect of being increased further. Details of the specific SRG for this particular application were not demonstrated.

One of the early designs of reluctance generators which resembled the SRG in several ways was introduced in [116]. It resembles the SRG in that:

- (i) the generated voltage depends on inductance variation as the machine is of variable reluctance structure.
- (ii) no windings on the rotors.
- (iii) field excitation is from a constant voltage source.
- (iv) it produces d.c. power output.

It differs from the HIA by being of a heteropolar type, i.e. flux lines through the machine are bidirectional. But it also differs from the SRG by having two sets of windings on the stator; a primary (field) winding and a secondary (armature winding). There is no need for electronic switching or rotor position sensing. The resultant machine is an induction generator despite being considered as bulky and considerably heavier than conventional machines. The machine phases are completely separated and there is no mutual coupling between the phases for all rotor positions. The machine is of multi-stack type as the several rotors (four) are mounted on the same shaft but displaced from each other by 90 degrees. The

performance was later improved by introducing a feedback system. Later development of electronically commutated generators made such designs obsolete.

The work presented in [117],[118] by Cameron and Lang contributes to the design of a voltage controller of a direct current power system supplied by an SRG [117]. The generator and its inverter were treated as a current source which is dependent on its voltage and the inverter firing angles. The voltage at the load is regulated by adjusting the firing angles of the inverter. The controller is based on a simplified model of the power system and the SRG taking one phase in isolation. The operation of the simple power system is simulated over one electrical cycle with a specific pair of firing angles; turn-on angle and conduction angle. A total average current is then computed and mapped as a function of the source voltage and the firing angles. During the controller operation a turn-on angle is first selected (from the map) so that the contour of the current as a function of the conduction angle passes through the peak. The operation is obviously performed in conjunction with continuous measurement and closed-loop feedback of the load voltage. Finally, it is the turn-on and conduction angles that are passed to the inverter as control commands. Although was not shown in their work, the selection of the firing angles on the basis of maximising the efficiency for a given speed, voltage, and desired current was suggested as a possibility. The model was based on a classic inverter and incorporated a distribution network. The controller was designed to show that it can regulate the load voltage with minimum transients due to load changes and minimum ripple.

In [118] an optimisation procedure for the design of an SRG is presented based on a synthesis of a computer aided design system. The output of the design is a data base containing dominant generator designs with the corresponding performance of the power system. The input is

composed of selection of requirements such as power output, load voltage and operating speed; identifying constraints such as maximum current density and maximum voltage ripple at load; and specifying of attributes which included the volume of the SRG and the efficiency of the power system. The design variables are then selected so as to satisfy the requirements and constraints. Several designs are then synthesised, analyzed and finally evaluated until dominant designs are stored with the corresponding performance of the power system. A specific example of an SRG for test purposes was presented in [118]. The 5-phase 10/6 generator is capable of delivering 10 kW to a resistive load at a speed of 10,000 rpm and 270 volts. The current density in the phase windings was constrained to less than 10 A/mm².

Reports on projects carried out at General Electric (GE) in the USA on SR machines in aerospace technology are the most significant and distinguishable in this field so far.

In [119], the application of SR machine in aerospace technology was thoroughly investigated. Although the application concerned a motor drive system rather than a generating system, the requirements of high-power density, high-speed, fault-tolerance and a small-size machine were predominant and thus quite relevant to an SRG in an aircraft generator application. Tests on a breadboard system of a 25,000 rpm, 120 hp SRM for the fuel pump system of an aircraft were carried out and results were given. Interesting and promising outcomes were presented concerning the use of MLC capacitors and snubber-less paralleled units of IGBT's which significantly reduced the size of the drive system and improved its reliability. Using cobalt-iron for both rotor and stator with high saturation flux density in conjunction with water-cooled windings, the electromagnetic unit provided a power density of 9 kW/kg which could be increased further by doubling the speed to 50,000 rpm. The design approach did not seem,

however, to consider efficiency optimisation whether in the hardware design stage or in the implementation of the control. The project emphasis had rather been placed on packaging and the construction of a high power, high current inverter.

The work of GE on SR generators is outlined in [56] and [120]. The work concerned the design and test of a very high speed SR motors and generators for aircraft engine applications. The control of such a system over very wide speed range was given in [120].

In [121] also by GE, the selection of switched reluctance machine systems for future aircraft engine applications projected for the year 2000 and beyond was justified and the risks were outlined. The selection of the SRG is based on its high power density and fault tolerance capability and reliability of inverter and machine operation represented by independence of phases and self-protection against shoot-through failures which are common with a.c. machines. The selection is also based on the temperature capability of the SRG and the fact that its rotor configuration is significantly less temperature sensitive than the rotors of other conventional machines which carry either rotor windings or permanent magnet yet the SRG still achieves most of the performance attributes of these high power density machines. It is also noted in [121] that higher operating temperature capability permits system weight reduction -thus higher power density- through reduced coolant flow. The main risk for selecting the SR machine for a high performance power conversion system for aircraft applications is given as the little experience that existed up to the date of the project (1988), for the machine in such an application. Therefore presently unknown shortcomings would need to be discovered by hardware testing before final implementation.

In [56], the high speed SRG starter-generator is fully described and

reasons for preferring the SRG over the PMG in particular are outlined. The generator provides 32 kW d.c. power at a speed range of 26,000-50,000 rpm. In terms of power per size, the machine had a total power/volume ratio of about 200 watts/in³. The machine is directly mounted on the shaft of the engine gas turbine, and the cooling and lubrication systems of the SRG are integrated directly into those of the engine. Both rotor and stator are cooled by the engine lubricating oil. Rotor heat is conducted to the hollow shaft, where it is carried away by oil flowing in the shaft. Stator heat is removed by oil flowing in grooves machined in the stator OD, and also by oil flowing in non-magnetic cooling tubes at the top of the stator slots. The result of all these arrangements is obviously a quite efficient cooling system which helps to push the thermal limit of the machine. The same material (iron-cobalt alloy) was utilised for the rotor and stator but the laminations of the rotor were annealed at a lower temperature to allow for better mechanical strength as the rotor laminations should endure high mechanical stresses at high rotational speeds. Unfortunately, this procedure resulted in higher core losses in the rotor than if a higher temperature anneal was used. Magnetically, the material is excellent with a saturation flux density of 2.2 Tesla. A review paper [115] for some GE projects claimed (for this project of [56]) a generating efficiency of 82%. Although there is much room for development and enhancement of power density and efficiency of the starter-generator system of [56] particularly if new materials with better mechanical and electrical properties are used, the results indicate that the SRG is a highly reliable, cost competitive generator. A further development based upon the work of [56] was recently published in 1994 in [164]. Magnetic poles were doubled by using a 12/8 stator/rotor pole configuration giving four magnetic poles. The winding was arranged in parallel phase groups and test results for both parallel and single phase groups were presented. The test results are still incomplete and additional results are needed to establish the usefulness of this aspect of winding arrangement.

The control of the system of [56] is given in [120]. The controller is a microprocessor based digital control system that includes some dedicated hardware for very high bandwidth functions. Because of the high machine speeds involved, it is impractical for the microprocessor to track the rotor angle and control phase commutation directly. A digital commutator circuit relieves the processor of this task while retaining great flexibility for the processor to control the placement and duration of the phase current pulses. Moreover, the processor performs the control function of torque control, generator voltage regulation, engine and aircraft control interfacing and background protectives such as d.c. link over-current, over-voltage, and over-speed monitoring. Control in the generating mode is achieved by combining two methods in order to regulate the voltage and run the system at the maximum possible efficiency. Unlike the controller of [117] reviewed earlier, the control strategy of [120] is designed to linearise the d.c. link current output as a function of command current, and to provide high efficiency, independent of machine speed, by establishing a constant current turn-off level. The output of the controller is a turn-on angle command giving a very linear transfer function relating d.c. current to turn-on angle over large variations in d.c. current and machine speed. A method for optimising the efficiency at low d.c. currents by fixing the turn-on angle while varying the conduction angle is also applied by the controller.

1.8 Preview of Thesis Layout

Chapter 2 introduces the theory of a simple magnetic model which is used (later in chapter 3) to predict the performance of the SRG. The electromagnetic design of the ferrite SRG and the main decisions of stator and rotor profile and material selection are given in chapter 3. The mechanical considerations given to the high speed aspect and the mechanical design and assembly of the SRG are given in chapter 4. Chapter 5 deals with the power converter and electronic controller design and testing. Chapter 6 introduces the selection, design and preparation of the turbine and the air blower used to drive the generator. The arrangements for static and dynamic tests of the high speed SRG are described in chapter 7 with results of the static tests. Dynamic testing results are presented and explained in chapter 8 with comparison between these and the model predictions. Some comments on the results are also given in the same chapter. Finally chapter 9 concludes with some general remarks on the achievements of the project, problems encountered and suggestions for further work. Appendices are presented as supplements to different chapters. Each appendix is related to the work described and referred to in a particular chapter of the thesis. Appendix A3.2, for example, is the second supplement to chapter 3 and so on. A list of references which have been used before and during thesis preparation is provided at the end. The general layout of the thesis largely followed the chronological order of the actual development of the design and building of the high speed SRG test system.

CHAPTER TWO

MODELLING AND PERFORMANCE PREDICTION

2.1 Introduction

The objective of the project was to construct, test and evaluate a high speed SR generator rather than engage in a detailed theoretical analysis. Due to the practical content of the work, sufficient time was not available to engage in the accurate magnetic modelling of the machine. Nevertheless, a simplified model is both useful and necessary at the design stage to predict performance, and at the evaluation stage to assess whether the measured performance is to be expected. The main purpose of this chapter is to develop a simple quasi-linear model, taking into account magnetic saturation, which meets the above objective. However, before this is examined, a review is presented of existing modelling methods.

An SR machine model should yield; phase current waveforms, electromagnetic torque curves, various machine and converter losses (snubber circuits may be involved as well as input filter), and output power and efficiency, accurately under different speeds. An accurate model would also prove useful to support optimal excitation and control design [42].

Despite attempts to include the SR machine in unifying approaches to modelling and performance prediction [43][44], prediction of performance of the SR machine presents a more difficult problem than it is for other types of machines commonly used in industry [45]. The main reason for the difficulty is that, when compared with classic types of machines, the magnetic circuit and excitation pattern for the SR machine are unusual. The magnetic circuit operates under varying levels of excitation, and the

field inside the machine is highly saturated for improved EC efficiency [41][45]. As a result, all of the electrical and magnetic variables (voltage, current, flux, torque) have non-sinusoidal waveforms. The modelling is further complicated by the close inter-relationship between machine parameters and switching strategies.

2.2 Review of Methods

There is no universal method for modelling the SR machine. Requirements which motivate the modelling may vary from application to another. The requirements are often contradictory between accuracy and excessive use of computer time and storage. Some methods may prove quite accurate, yet, may also demonstrate difficulty to include, for example, dynamic behaviour, mutual effects or speed variation [42]. It is required that a modelling approach would *need* a performance calculation that is accurate enough with a computation time that is small enough to allow modern optimisation techniques to be also used for SR machines. This is important for obtaining designs which represent a good compromise between many variables involved. The model should then include as many parameters as possible.

In order to obtain accurate performance prediction, the model for an SR machine must include magnetic non-linearities or the effects of saturation, both local and bulk. Earlier methods, which are described as linear, neglected the magnetic saturation and approximated the characteristics with straight lines [1],[26]. Another method is by storing the magnetic information or the position dependant flux linkage/current characteristics in a tabular form or a look-up table. Interpolation within the magnetic data is performed in the process of determining instantaneous torques and currents for the machine operation [7]. The method was further

developed in [46] to provide a better representation of the input data $\Psi(i,\theta)$ using "customised spline functions" thus allowing a more efficient computation of the steady state current and torque waveforms.

Finite element FE analysis is often used to determine the value of the magnetic flux in different parts of the machine at different rotor positions [8],[9],[47]. The FE method is used to predict the instantaneous and steady state torque of the SR motor [48]. However, a careful approach is needed when applying FE techniques to the SR machine due to the effects of both the shape of elements in the narrow air gap region and the choice of rotor steps and their impact on the accuracy of the overall solution [41].

Analytical methods for predicting the static magnetisation characteristics of the machine for general rotor positions have also been discussed to develop a design of the machine based on calculated magnetic characteristics rather than measured ones [49],[50]. The method is obviously less accurate, nevertheless, it may prove a useful design tool for an SR machine blueprint starting from scratch.

Another analytical approach to predict the performance of the SR machine by numerically calculating force and permeance versus apparent pole flux density curves is illustrated in [45]. The calculations are size dependant as they are based on the so called unit doubly salient structure UDSS. The approach is claimed to be easier to implement than non-linear functions, yet provides sufficient accuracy including prediction of starting torque and current as well as iron losses determination.

Models based on piece-wise linear characterisation of the magnetic non-linearities were also developed and resulted in an accurate prediction of the time-average torque, but, because of errors imbedded in the relationship between flux linkage and current, peak currents and

instantaneous torque are not predicted with accuracy [42]. As a result, these models are not helpful in predicting the power converter ratings and losses.

Despite the accuracy of models based on numerical field solutions, they use excessive computer time and are not always suitable for optimum design purposes which requires repetitive performance calculations. Therefore, it is naturally important, from a designer view point, to develop a quick and accurate performance prediction tool. Some quick and useful methods for preliminary design, though not quite accurate, are those based on the piece-wise linear model which divides the flux-current plane into two regions (linear and saturated) and approximate the characteristics in the saturated region with a set of parallel lines. This is illustrated in Figure 2.1 and is known as the quasi-linear flux-linkage/current characteristics [51][52].

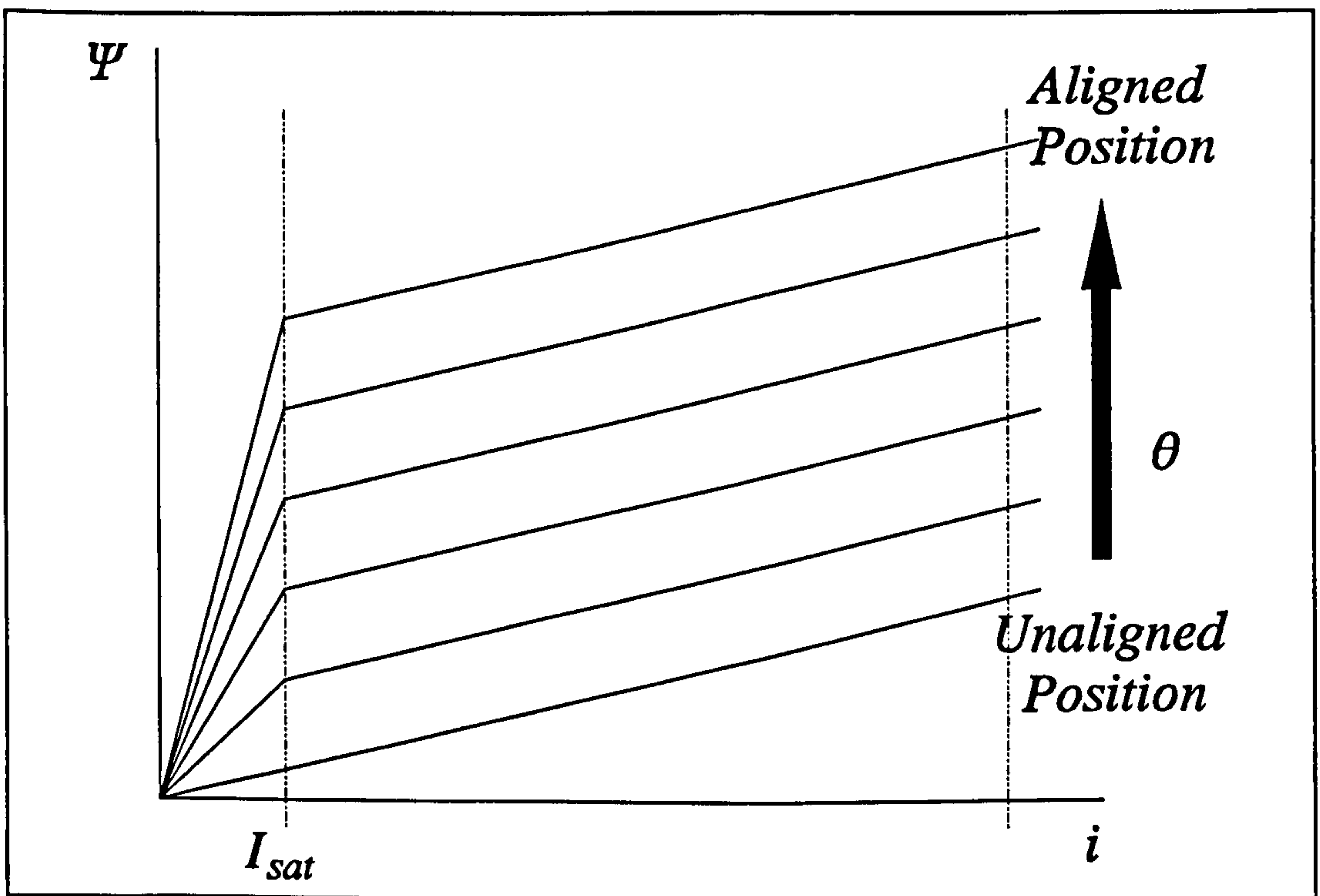


Figure 2.1: Quasi-linear magnetic characteristics.

The relationship between this simple magnetic model and the actual geometry is developed in the next section.

2.3 Simple Quasi-Linear Model

2.3.1 Neglecting Fringing/Leakage Flux

Consider a single stator-pole with a concentrated coil of NI ampere-turns, supporting the flux Φ in the small air gap between the pole and overlapping rotor pole as shown in Figure 2.2, where the rotor-pole width is not less than the stator pole width.

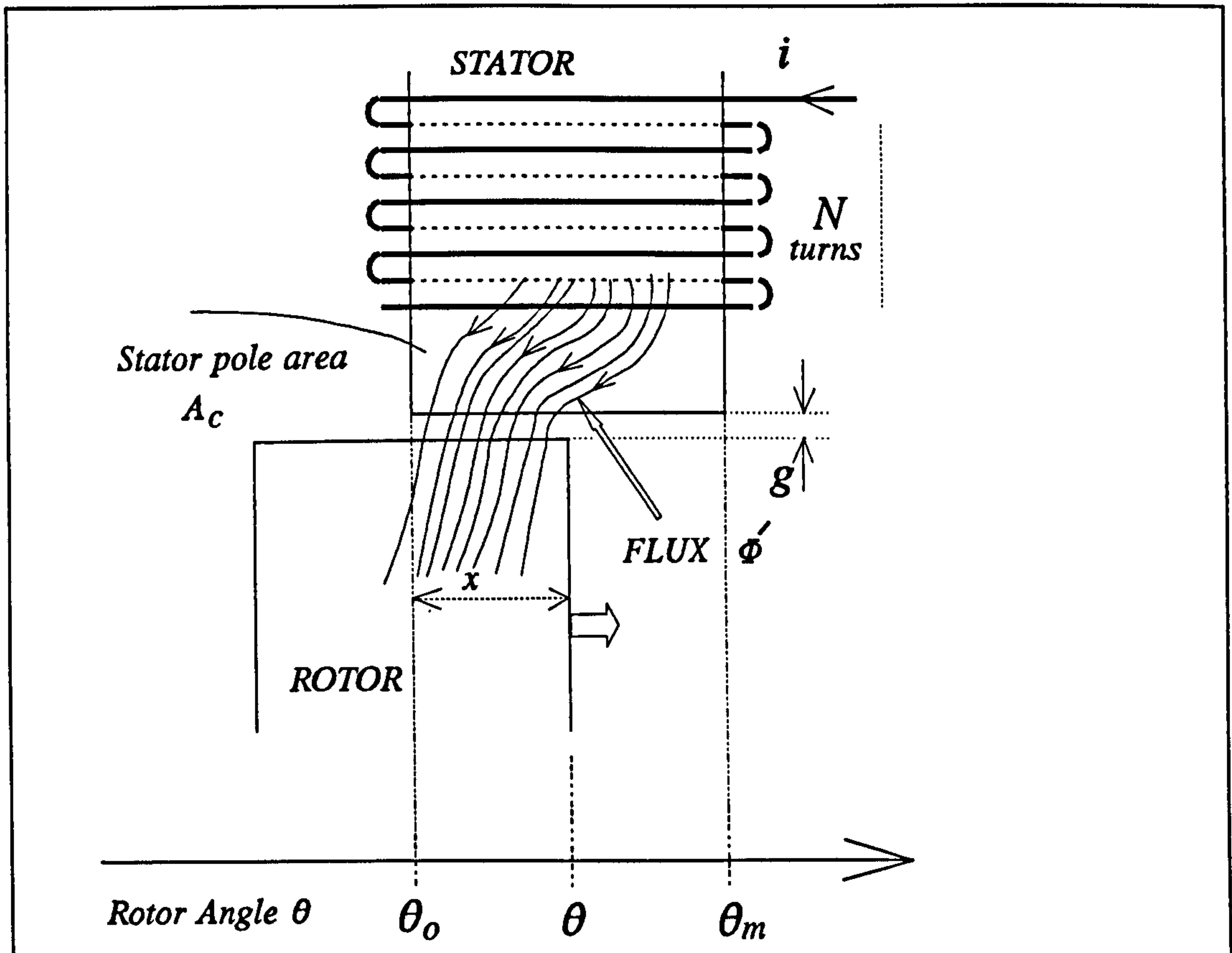


Figure 2.2: Overlapped stator-Rotor poles.

Furthermore, assume at this stage that the reluctance of the circuit is entirely due to the overlapped part of the air gap and that the leakage or fringing flux is negligible.

The overlapped area is proportional to the rotor angle θ and is given by:

$$A(\theta) = A_c \frac{\theta - \theta_o}{\theta_m - \theta_o} = A_c K (\theta - \theta_o) \quad (2.1)$$

Provided that the flux density in the air gap is below the saturation level, B_{sat} for the stator and rotor material, the phase flux-linkage $\Psi' = N_c N \Phi'$ is given by:

$$\Psi'(\theta) = L'(\theta) i \quad (2.2)$$

$$\text{where, } L'(\theta) = \frac{\mu_o N_c N^2 K (\theta - \theta_o) A_c}{g} \quad (2.3)$$

and N_c is the number of stator-pole coils connected in series to form the phase winding.

Alternatively, it is convenient to express equations (2.1) and (2.2) as:

$$\Psi'(\theta) = K (\theta - \theta_o) L'_{\max} i \quad (2.4)$$

$$\text{where, } L'_{\max} = \frac{\mu_o N_c N^2 A_c}{g} \quad (2.5)$$

However, if saturation occurs, $\Psi'(\theta)$ will be:

$$\Psi'(\theta) = N_c N \Phi = N_c N B_{sat} K (\theta - \theta_r) A_c$$

and is constant for a given value of θ .

The limiting value of current for saturation to occur is given by:

$$i = I_{sat} = \frac{B_{sat} g}{\mu_o N} \quad (2.6)$$

and is independent of θ .

Hence for saturation, $\Psi'(\theta)$ can be expressed in terms of L'_{\max} and I_{sat} as:

$$\Psi'(\theta) = K (\theta - \theta_o) L'_{\max} I_{\text{sat}} \quad (2.7)$$

The resultant Ψ - i - θ characteristics for the coil are therefore as shown in Figure 2.3.

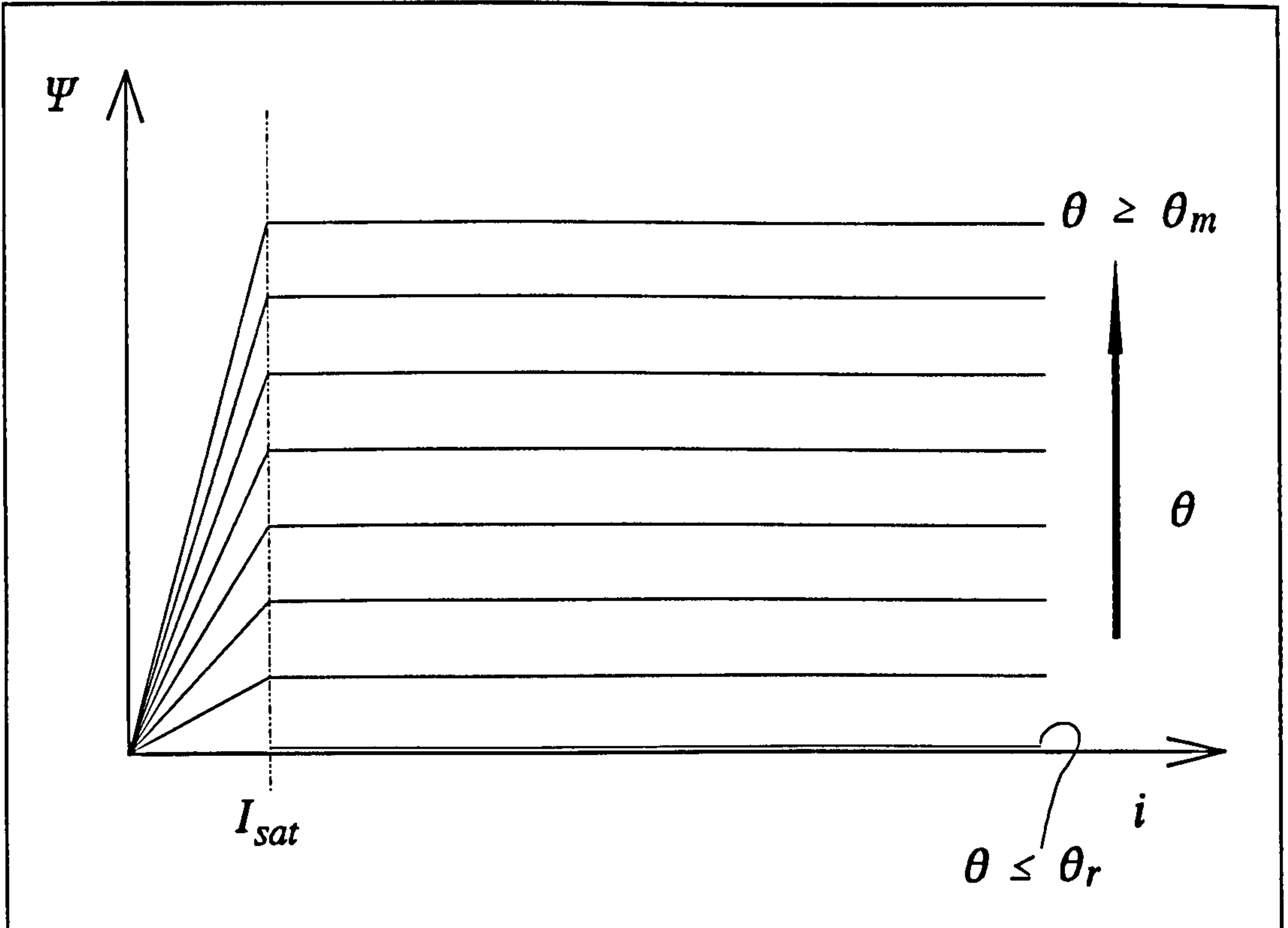


Figure 2.3: Magnetisation characteristics for the quasi-linear model neglecting fringing/leakage flux.

With the assumptions made, for $\theta \leq \theta_r$, the flux linkage is zero.

However this model, whilst being useful in developing approximately the main flux-linkage associated with a phase winding, is too simplistic and the effect of leakage/fringing flux must also be taken into consideration.

2.3.2 Including Fringing/Leakage Flux

Figure 2.4 shows an excited stator pole overlapping with a rotor pole. The fringing flux Φ'' has two main effects:

1- The effective angle of overlap is higher than just $(\theta - \theta_o)$. This is illustrated in Figure 2.5 where significant rotor pole positions are defined for a two-phase machine. These are later used to construct an inductance profile for one phase of the machine.

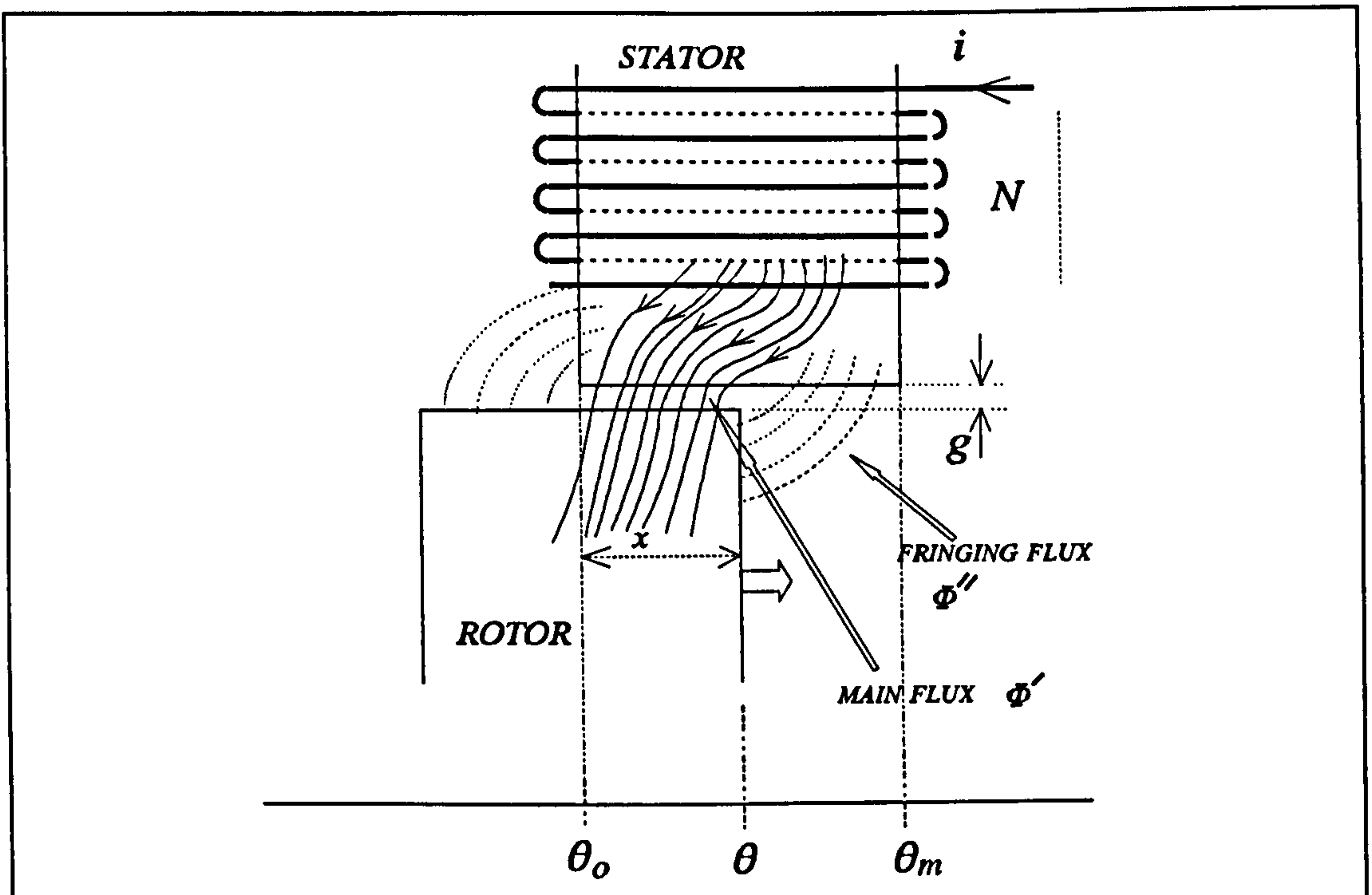


Figure 2.4: Stator-rotor poles in overlapping showing fringing flux.

The reference for rotor pole position ($\theta = 0$) is taken from the fully aligned position of the rotor pole with the previous stator pole (of the other phase in this case) as shown Figure 2.5(a). The shaded stator pole is the one of interest. In (b), of the same figure, the rotor pole has moved to the right but not yet started actual overlap with the excited stator pole. The angular position of the rotor pole is designated θ_r , indicating the point at which phase inductance starts to rise. Due to the fringing flux there is a difference between this point and the one shown in (c) designated θ_o . This difference can not be determined exactly since in practice the assumption for L_{\min} as

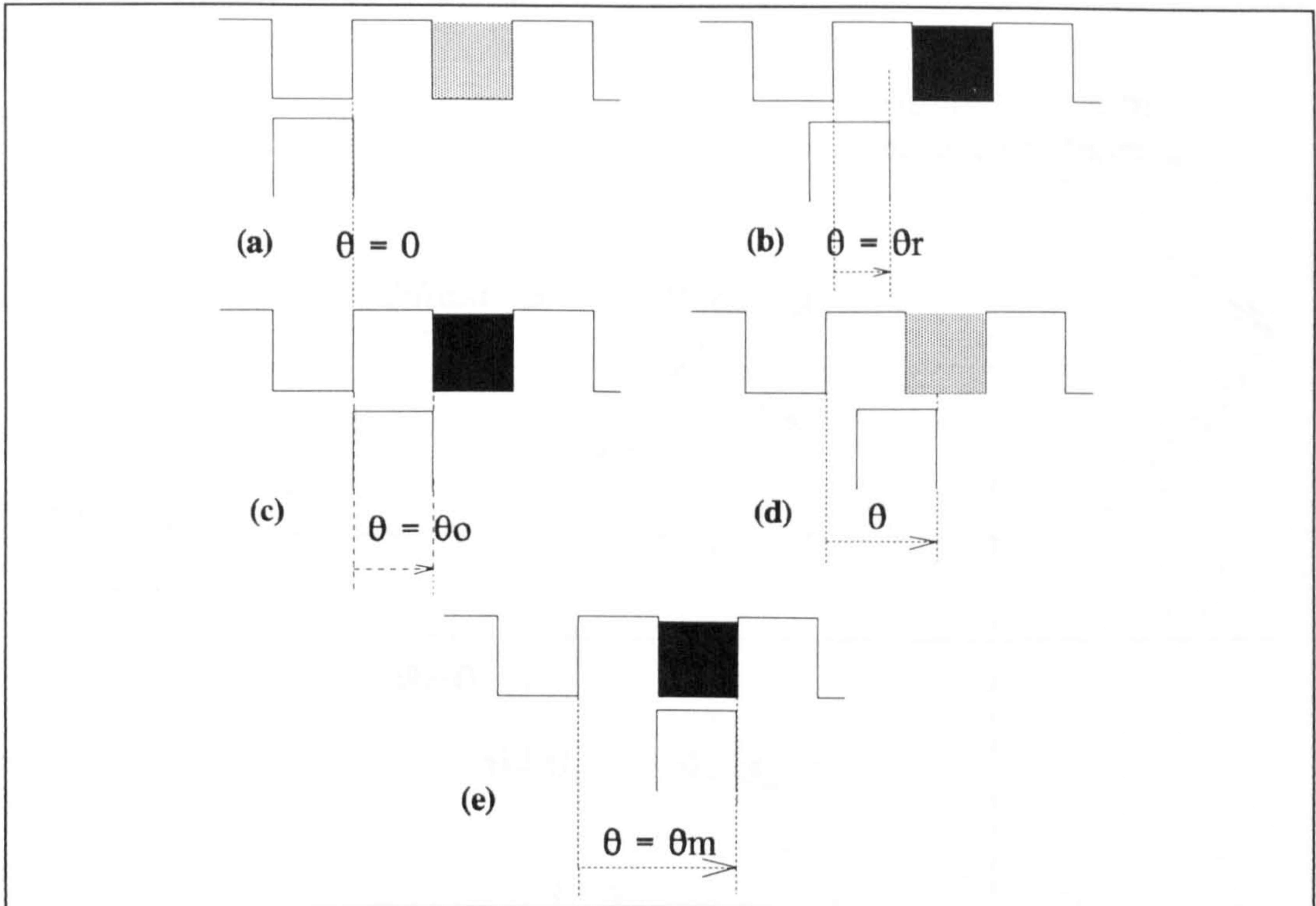


Figure 2.5: Significant rotor pole positions showing reference for angular position.

being constant is only an approximation [140]. As a reasonable estimate, $(\theta_m - \theta_r)$ is approximately $1.25(\theta_m - \theta_o)$, but this will depend on the relative geometry of pole arc to pole pitch to air gap. In (d) the overlap is any value of θ , and in (e) the rotor pole reaches full alignment with the excited stator pole where the angular position is designated θ_m indicating the point at which the phase inductance is maximum or L_{\max} .

With the adjustment for fringing effect equation (2.1) becomes:

$$A(\theta) = A_c \cdot \frac{\theta - \theta_r}{\theta_m - \theta_r} = A_c \cdot K (\theta - \theta_r) \quad (2.8)$$

Based on the above, Figure 2.6 introduces an inductance profile for the unsaturated (or low current) phase inductance of the SRG with respect to rotor pole position or θ . Inductance profile for the other phase is also shown. If fringing is neglected, the dotted line underneath phase A profile would then represent the resulting profile.

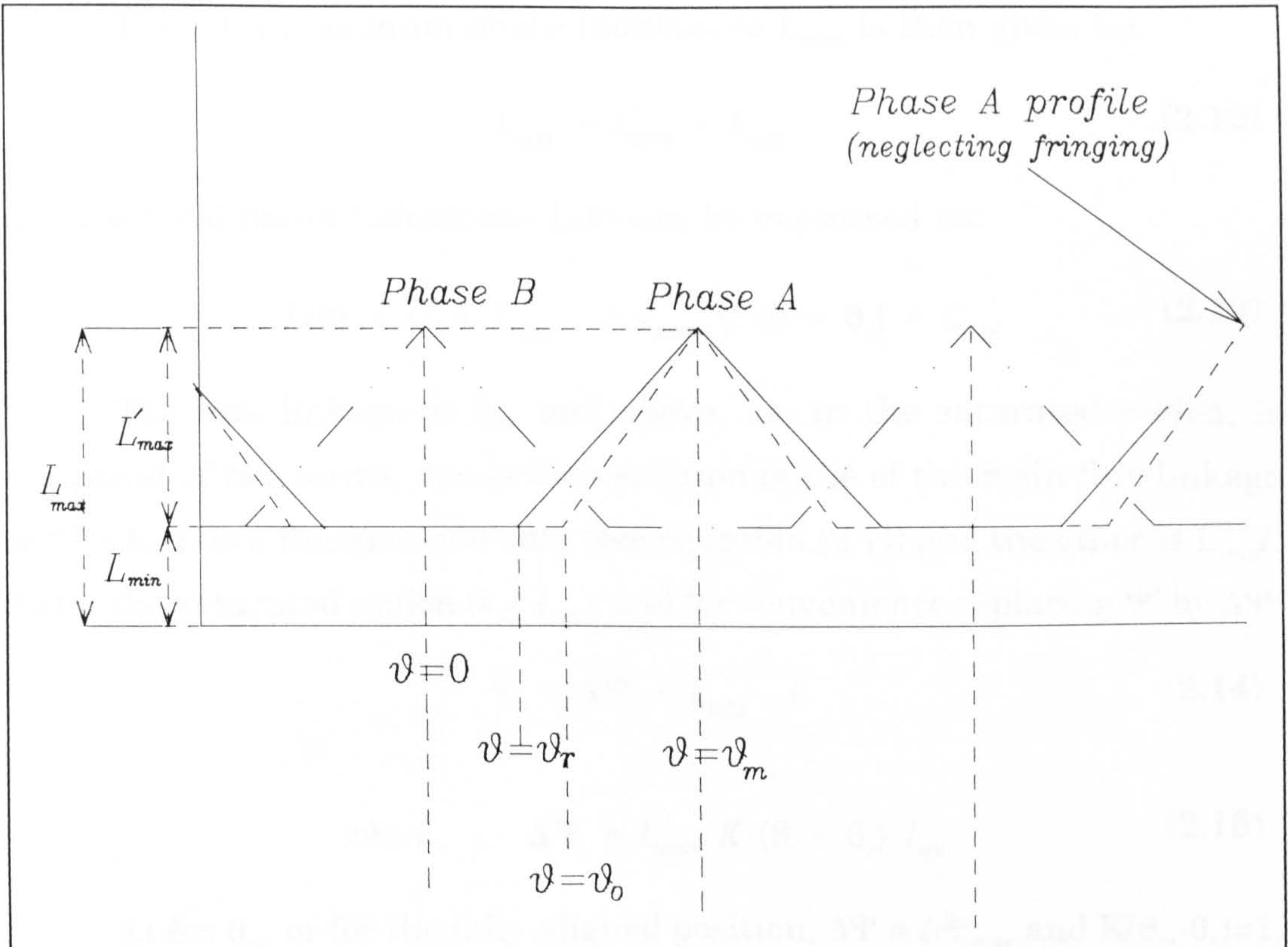


Figure 2.6: Low current inductance profile for a two-phase SRG.

2- The second effect of the fringing flux Φ'' is that it adds to the main flux Φ' so that, in terms of flux linkage:

$$\Psi(\theta) = \Psi'(\theta) + \Psi''(\theta) \quad (2.9)$$

The fringing flux (which also includes leakage flux) represents the non-saturating component flux. If the convenient albeit approximate assumption is made that the flux Ψ'' is independent of θ - i.e. the same Ψ'' exists for a given current for the minimum inductance (un-aligned) position as for the maximum inductance (aligned) position, then:

$$\Psi'' = L_{\min} I \quad (2.10)$$

and utilising equation (2.2) for currents i below I_{sat} :

$$\Psi = L'_{\max} K (\theta - \theta_r) i + L_{\min} i \quad (2.11)$$

The total maximum phase inductance L_{\max} is then given by:

$$L_{\max} = L'_{\max} + L_{\min} \quad (2.12)$$

and the total phase inductance $L(\theta)$ can be expressed as:

$$L(\theta) = L' + L_{\min} = L'_{\max} K (\theta - \theta_r) + L_{\min} \quad (2.13)$$

The flux linkage at I_{sat} and above, i.e. in the saturated region, is composed of two terms, one is the variation of the of the main flux linkage or Ψ' which is a function of θ only (see equation (2.7)) and the other is $L_{\min}i$. So for the saturated region ($i > I_{\text{sat}}$), and for convenience replacing Ψ' by $\Delta\Psi$:

$$\Psi = \Delta\Psi + L_{\min} \cdot i \quad (2.14)$$

$$\text{where, } \Delta\Psi = L'_{\max} K (\theta - \theta_r) I_{\text{sat}} \quad (2.15)$$

At $\theta = \theta_m$, or for the fully aligned position, $\Delta\Psi = \Delta\Psi_{\max}$ and $K(\theta_m - \theta_r) = 1$.

$$\text{Hence, } \Delta\Psi_{\max} = L'_{\max} I_{\text{sat}} \quad (2.16)$$

The resultant Ψ - i - θ quasi-linear characteristics for this simplified magnetic model are shown in Figure 2.7.

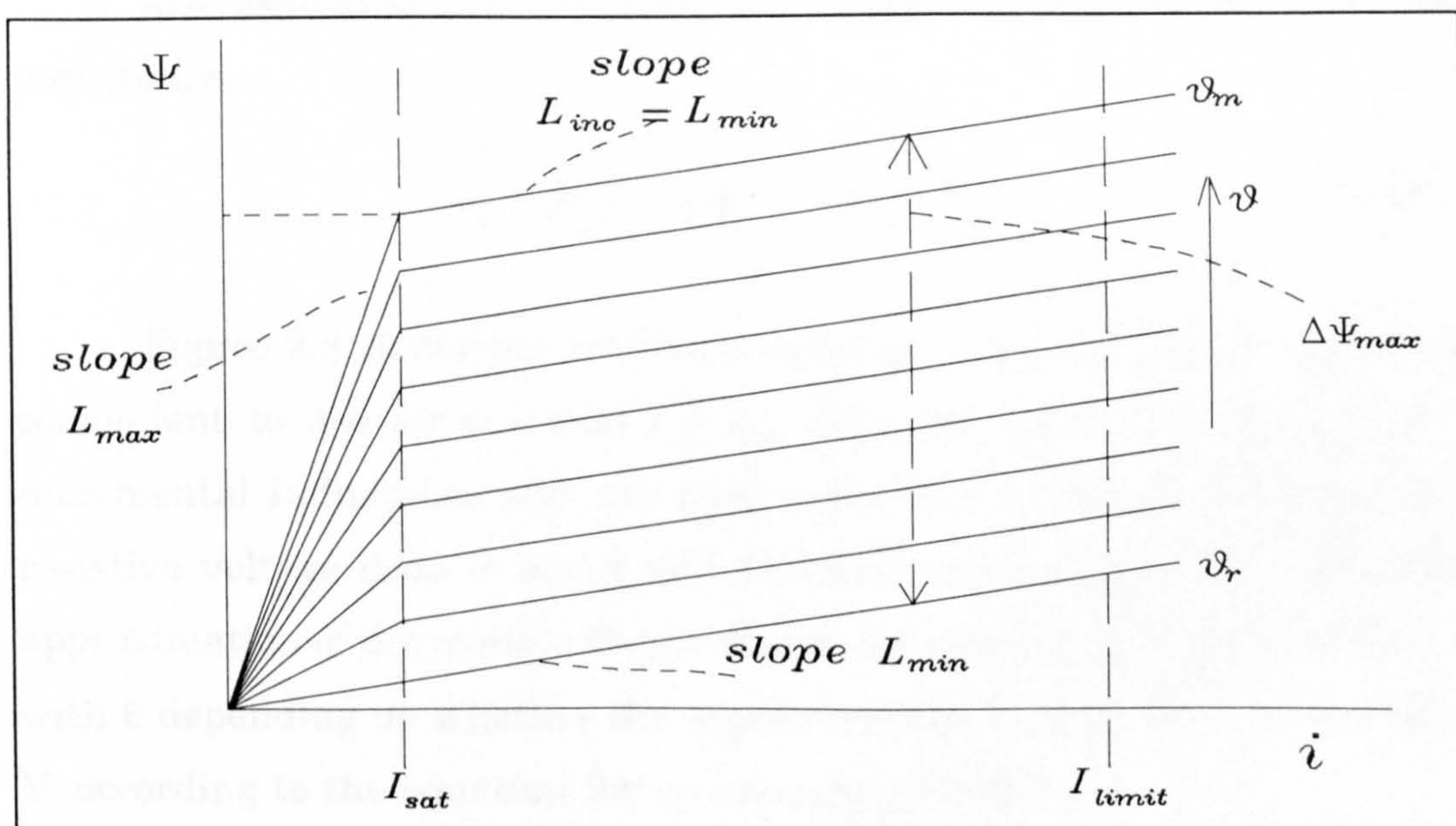


Figure 2.7: Magnetic characteristics for the quasi-linear model of the SRG.

2.4 Simple Equivalent Circuit for Currents $i \geq I_{sat}$

The terminal voltage equation of the SR machine is:

$$V_s = i R + \frac{d\Psi}{dt} = i R + \frac{d\Psi}{d\theta} \cdot \frac{d\theta}{dt} \quad (2.17)$$

where V_s is the supply voltage, and R is the circuit resistance comprising the winding resistance and the resistance of any semiconductor switches in series with the winding.

The term $d\theta/dt$ represents the rotational speed ω in rad/sec. If (2.15) above for Ψ ($i \geq I_{sat}$) is differentiated with respect to θ , V_s will be:

$$V_s = i R + L'_{max} K I_{sat} \omega + L_i \frac{di}{dt} \quad (2.18)$$

The second term in the right hand side of the equation refers to the induced back e.m.f. designated here as V_i , where:

$$V_i = L'_{max} K I_{sat} \omega \quad (2.19)$$

Also assuming the incremental inductance L_i equal to the minimum inductance,

$$V_s - V_i = i R + L_{min} \frac{di}{d\theta} \omega \quad (2.20)$$

Figure 2.8 shows the resultant equivalent circuit. This is extremely convenient to use for currents $i \geq I_{sat}$ since, at a given speed, both the incremental inductance and the back e.m.f. are constant. Assuming the resistive voltage drop is small and therefore can be ignored (within the approximation of the model), the current i will linearly increase or decrease with θ depending on whether the supply voltage V_s is greater or less than V_i according to the equation (by re-arranging (2.20)):

$$\frac{di}{d\theta} = \frac{V_s - V_i - i R}{\omega L_{\min}} \quad (2.21)$$

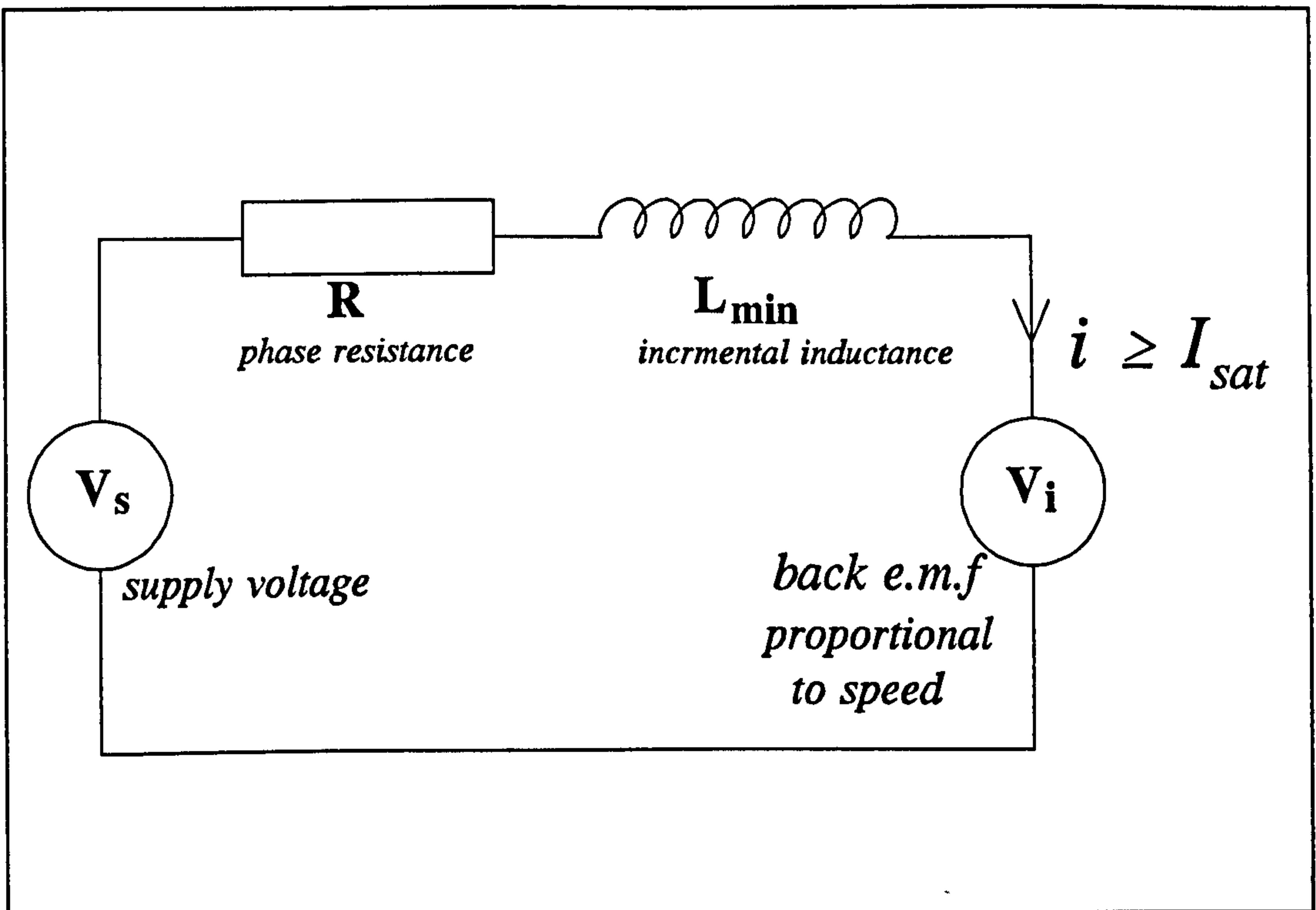


Figure 2.8: Equivalent circuit for SR machine- one phase, for currents $i \geq I_{\text{sat}}$.

2.5 Equivalent Circuit for Currents $i \leq I_{\text{sat}}$

For this case, and for θ within the rising or falling inductance regions, the incremental inductance is no longer L_{min} and must be replaced in Figure 2.8 by $L(\theta)$ according to (2.13) and further the back e.m.f. ($V_i = L'_{\text{max}} K i \omega$) and is a function of both current and speed.

For current waveforms which are representative of the rated conditions (i.e. occupying the majority of the angular phase period), currents $i \leq I_{\text{sat}}$ often only occur in the minimum inductance region for which the back e.m.f. $V_i=0$ and the inductance is L_{min} . Changes of current are then determined using (2.21). If this is not the case for $i \leq I_{\text{sat}}$ then:

$$\frac{di}{d\theta} = \frac{V_s - L'_{\text{max}} K i \omega - i R}{\omega [L'_{\text{max}} K (\theta - \theta_r) + L_{\text{min}}]} \quad (2.22)$$

Equation (2.22) can be solved by small step integration. Alternatively, i and L can be approximated as being constant over the relatively small change of θ over which i increases from 0 to I_{sat} .

2.6 Computation of Current waveforms for Generation

A typical fully-opened current waveform as predicted by the quasi-linear model is shown in Figure 2.9. θ_{dly} is the supply turn-on (or delay) angle and θ_c is the commutation angle. The value of V_i is negative during the falling and positive during the rising inductance region. It will be zero when L is constant at L_{min} or in the maximum inductance dead zone should there be one. The supply voltage is positive before θ_c and negative after it. Since equation (2.22) includes i and θ in the right hand side, it is solved by computer by assuming a value for θ , increasing it and finding the subsequent current at each θ . By doing this, the mean value of current can be determined in order to find power output. The r.m.s. value of the current can also be determined in order to estimate losses and hence efficiency.

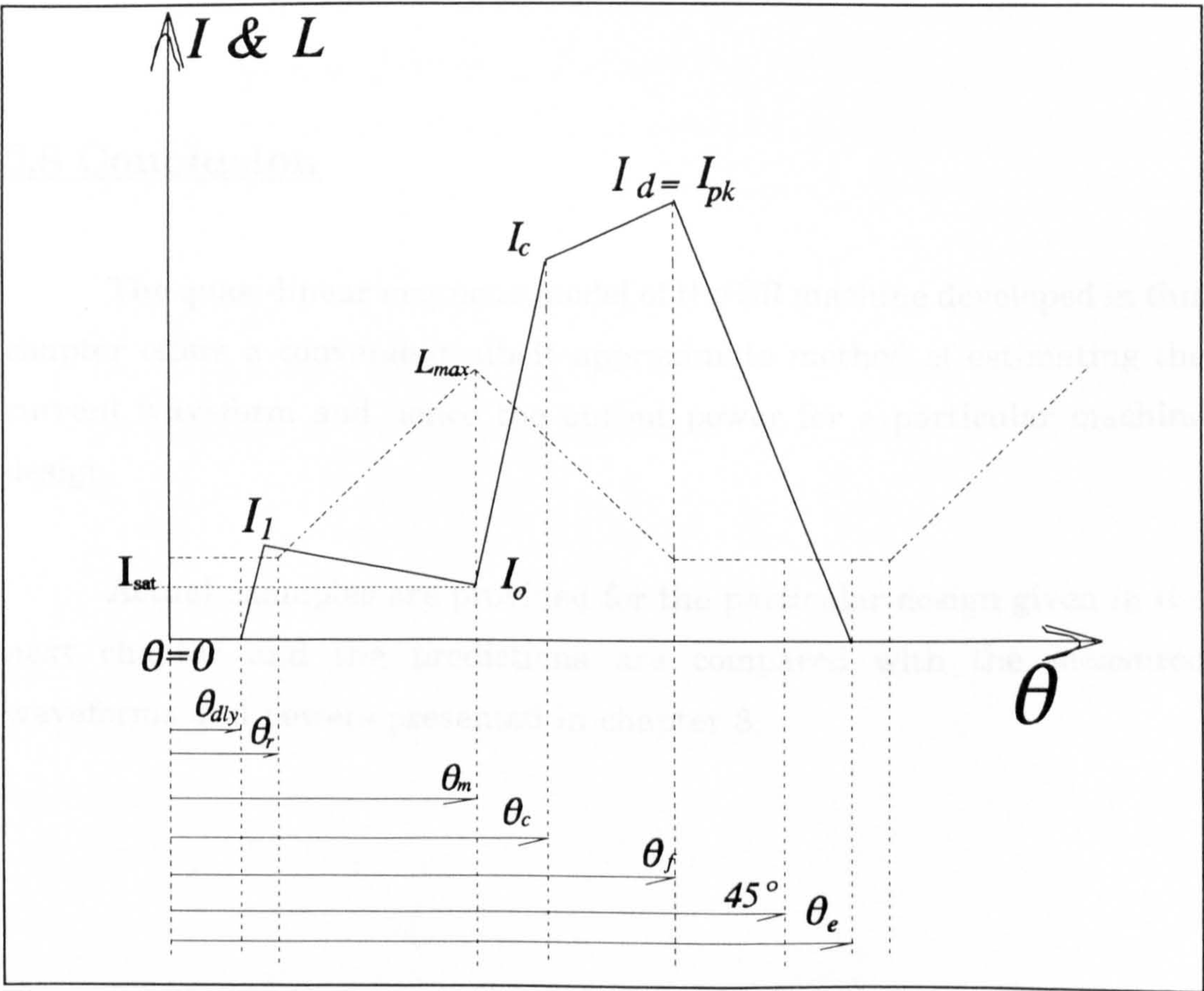


Figure 2.9: Expected phase current waveform and inductance profile showing important angular positions.

2.7 Computer Programme for Determining Current Waveform and Estimated Power and Efficiency

On the basis of equations and assumptions above, a simple computer programme in C was developed. The calculation of current is based upon sub-dividing the current waveform, such as the one shown in Figure 2.9, into several regions. "Flags", or constants that may either take the value of 1 or 0, are used to account for the region of zero back e.m.f. Also other constants are required to insert the value of I_{sat} (and to make $L=L_{\text{min}}$) whenever the current reaches into the saturation region. Development of the computer programme based on the work of this chapter is presented in Appendix A2.1. A listing of the computer programme in C, is given in Appendix 2.2.

2.8 Conclusion

The quasi-linear magnetic model of the SR machine developed in this chapter offers a convenient albeit approximate method of estimating the current waveform and hence the output power for a particular machine design.

Actual examples are provided for the particular design given in the next chapter and the predictions are compared with the measured waveforms and powers presented in chapter 8.

CHAPTER THREE

THE SRG ELECTROMAGNETIC DESIGN

3.1 Introduction

This chapter seeks to explain the sequence of decisions that were made in arriving at the final electromagnetic design of the high speed SR generator. The remaining steps concerning the mechanical design and the electronic drive circuit for the SRG, explained in the next two chapters 4 and 5, are largely a consequence of the basic choices which are introduced in this chapter.

Once the magnetic geometry is fixed, the output power and efficiency for different speeds and working voltages can be estimated based on the simplified quasi-linear model and computer programme in C introduced in chapter 2. Estimated waveforms and predictions are given in this chapter.

Simple static tests were performed on the generator after it had been built to establish maximum and minimum inductances and the approximate inductance profile at low current. Results of these tests are presented in chapter 7.

The time constraints on the project did not allow more than one high speed generator to be built. However, the computer programme enabled other magnetic configurations to be examined and the predicted values of output and efficiency are also presented although these could not subsequently be collaborated by experimental testing.

3.2 Choice of Stator

3.2.1 Introduction

At the outset of the project, it has been decided to find a suitable ferrite core of approximate dimensions which would be sufficient, on appropriate machining, to provide up to 1 kW output power. The most suitable core that could be found was a ferrite ring core manufactured by Philips Components as a TV receiver deflection magnet. This surprisingly has 16 salient poles which approximately fitted the geometry of an SR machine. The dimensions of the unit core were not sufficiently large to enable powers of 1 kW to be reached but nevertheless by combining two or more cores a suitable power could be achieved.

3.2.2 Stator Geometry

Figure 3.1 shows a cross section with all dimensions given in millimetres. It should be noted that these dimensions are for the machined core rather than the originally supplied core which had longer salient poles of about 10 mm. The core was machined by internal grinding to be concentric within a tolerance of 0.03 mm. The axial length of the ring is 12.5 mm. It was originally thought that a machine with an axial or core length of 75 mm (i.e. six ferrite rings) would be required to provide an approximate output power of 1.5 kW at 50,000 rpm. However only two rings were utilised in the final design, with a total core length of 25 mm. The reason for this was to enable the machine to be directly mounted onto the shaft of the driving turbine thereby avoiding the need for separate bearings. This will be explained in more detail in chapter 6.

The cross section in Figure 3.1 shows a core with 16 slots. It should be noted that the shape of these slots is not optimised for phase winding coils to be inserted into a maximum possible space. This is expected to

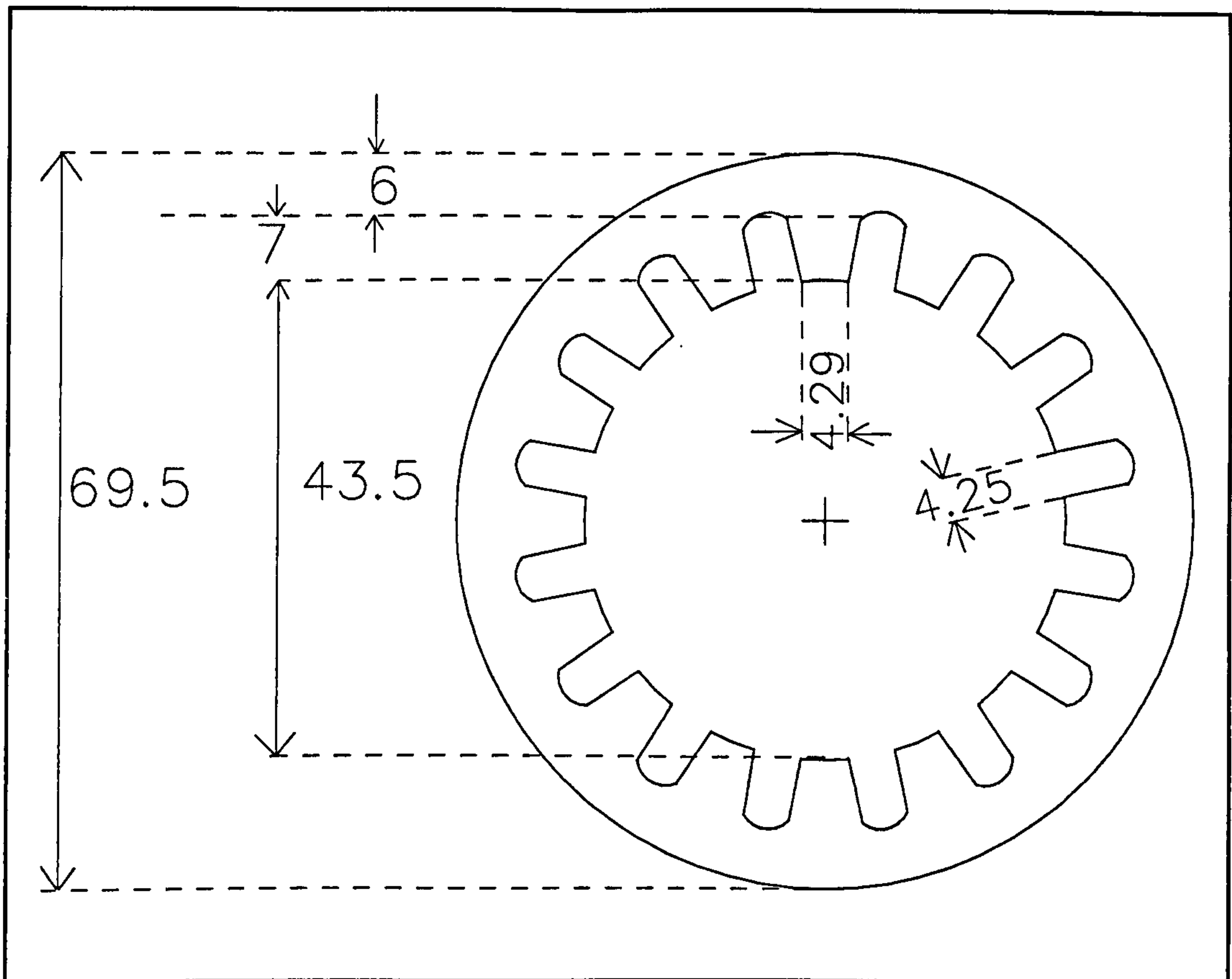


Figure 3.1: Cross section of the ferrite stator core. Dimensions are in mm.

reduce the current density figure of the generator and to have a negative effect on cooling. A better shape for the winding slots would be similar to what is shown in Figure 3.2. However, after moulding the ferrite ring, machining the small slots would be very demanding.

The internal grinding of the core, to achieve concentricity, would reduce the stator pole length from the original 10 mm to about 7 mm. A comparative study [160] of stator cross sections similar to the stators in Figures 3.1 and 3.2 showed that the first ensures that areas of saturated "iron" and high m.m.f. drop are always concentrated in short lengths of the magnetic circuit. This means that the resultant ratio of L_{\max}/L_{\min} is higher for the first stator. This may balance the disadvantage of the slot shape shown in Figure 3.1, although the stator of Figure 3.2 can have more ampere-turns. Finally for Figure 3.1, the stator yoke is of sufficient width

to prevent bulk saturation of the machine back ferrite before saturation of the stator poles.

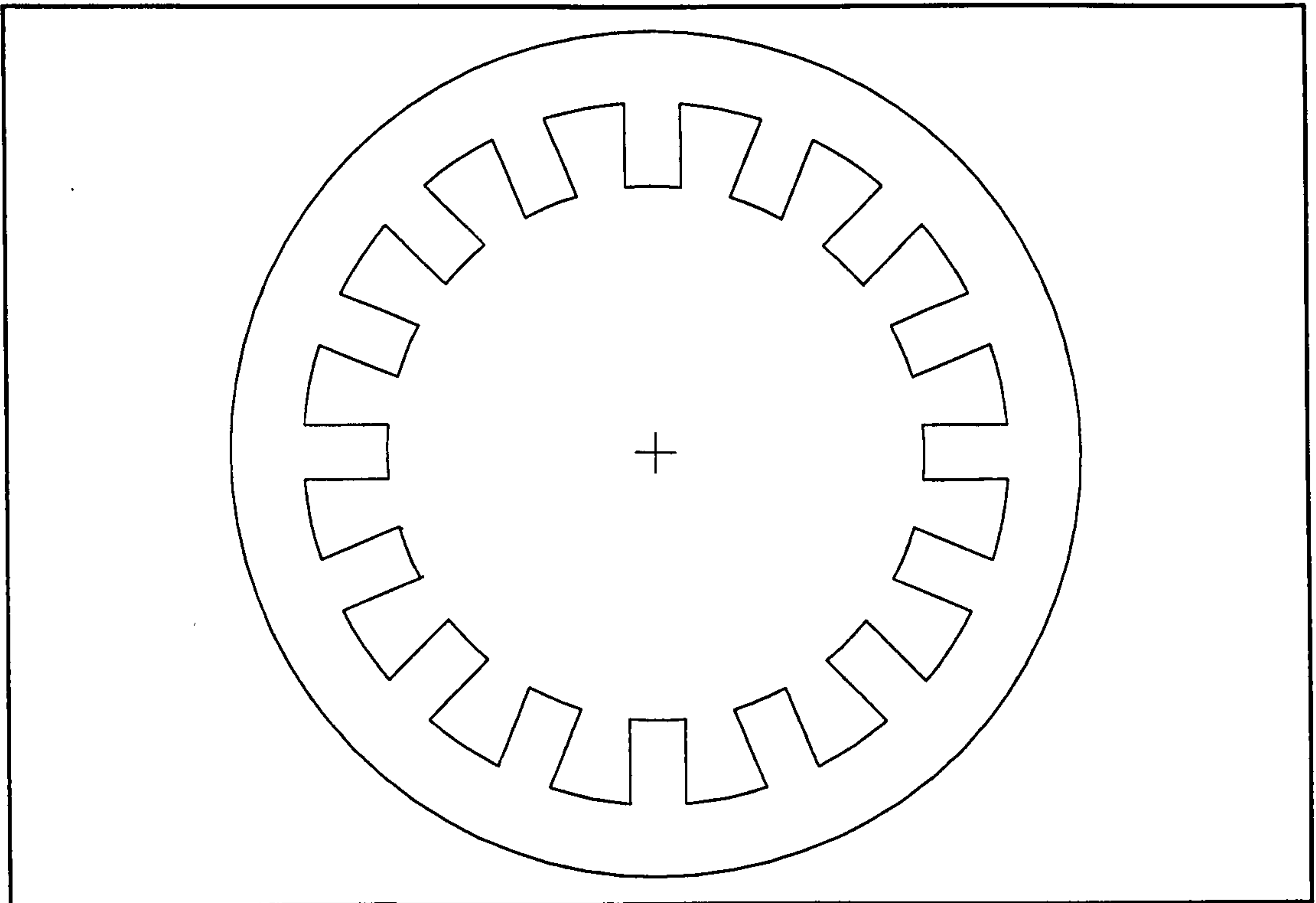


Figure 3.2: Cross section of a stator core with improved slot.

3.2.3 Stator Material Data

The chosen core is made of a Mn-Zn compound. These cores are usually made in different grades and are often used in power converters and low frequency filters. Compared with other ferrite cores, they have a relatively low resistivity such as $1 \Omega\cdot\text{m}$. The type of ferrite material can be of either high or low grade. Data of both grades are given in Appendix A3.1 (which also includes a review of the use of soft ferrites). The particular Philips core used was low grade core type 3C2. Its maximum flux density is 0.25 tesla at 25°C which reduces to 0.2 tesla at 100°C . The Curie temperature of the core is 150°C at which B_{sat} drops down to zero. The initial permeability μ_i is approximately 1000 for most of the operating temperature range. Some of the material specifications are frequency dependant. The figures above are true for frequencies up to 10 kHz.

3.3 Design of Rotor

3.3.1 Introduction

The electromagnetic design of the rotor part of the machine involves only rotor profile design and selection of proper rotor material. This simplicity of rotor design stems from the fact that the SR machine rotor has no winding, permanent magnet, slip rings or cage bars. Therefore, the major decisions for the design of the rotor of the SRG are relatively straightforward.

The firstmost and main decision is the number of rotor poles and the appropriate number of phase windings. Because the stator geometry is already fixed, this choice may be different than would be the case if both stator and rotor were to be specially made.

In addition there are special requirements for the rotor design taking the high speed into consideration:

- 1- A laminated rotor is required with the minimum possible thickness of laminations in order to keep down core losses in the rotor.
- 2- A material with sufficient tensile strength is required in order to endure the high centrifugal stresses caused by the high rotational speed as examined in the next chapter.
- 3- A generous shaft diameter is required in order to avoid shaft bending and vibration at critical speeds. This necessitates that the central hole, or the hub, of the rotor be sufficiently large within the constraint that, if it is made too large, it will weaken the mechanical structure of the rotor.

- 4- Rotor poles are required to have a shape that is mechanically suitable for high speed rotation (i.e. without discontinuities which may cause excessive stresses). Rotor profiles of SR machines are generally designed to provide high reluctance when stator and rotor poles are not aligned but these designs may prove unsuitable from the mechanical viewpoint.

The last two requirements are obviously related to the mechanical design of the rotor rather than the electromagnetic design. However, they are mentioned here briefly in order to emphasise the importance of considering high speed prerequisites in an early stage of rotor design.

3.3.2 Choice of Pole Number and Number of Phases

The choice of pole number and number of phases for the SR machine design in general is open to a variety of combinations [1]. It is logical to examine first the possible pole combinations for various phase numbers.

Due to the already available 16-pole stator, only one-phase (16/16), two-phase (16/8), and four-phase (16/12) are contenders. There are some requirements for the project in this connection which are derived from the project objectives outlined in 1.1. The objective is to maximise output power whilst minimising power-electronic circuitry. This requires the selection of low number of phases unless it is disadvantageous from an output power viewpoint.

To facilitate the comparison procedure, the EC-loop principle or the area $\oint id\Psi$ is used. The main criteria for output power is the number of work-cycles per stator pole per revolution. If an equal EC-loop area for each case is assumed, then this would indicate that the best design has the highest number of rotor poles (i.e. the single phase case).

Possible alternative choices for rotor pole number and phases are as examined below:

- 1- 16 stator poles and 16 rotor poles. This arrangement can result into a single phase SRG as shown in Figure 3.3. Phase winding coils can be arranged to provide, upon excitation, alternate north and south magnetic stator poles. In one revolution there will be 16 work-cycles per stator pole. However, a disadvantage of this configuration is a relatively large value of L_{\min} . This would effectively result in the EC-loop area being probably not better than 50% of the two-phase case. Moreover, due to the expected inductance profile of this arrangement sketched in Figure 3.4(a), the phase current in Figure 3.4(b) will almost be continuous upon excitation. This will make it difficult to build up the current to the required value unless fairly large excitation voltages are introduced. Continuous current operation needs to be avoided for stability reasons.

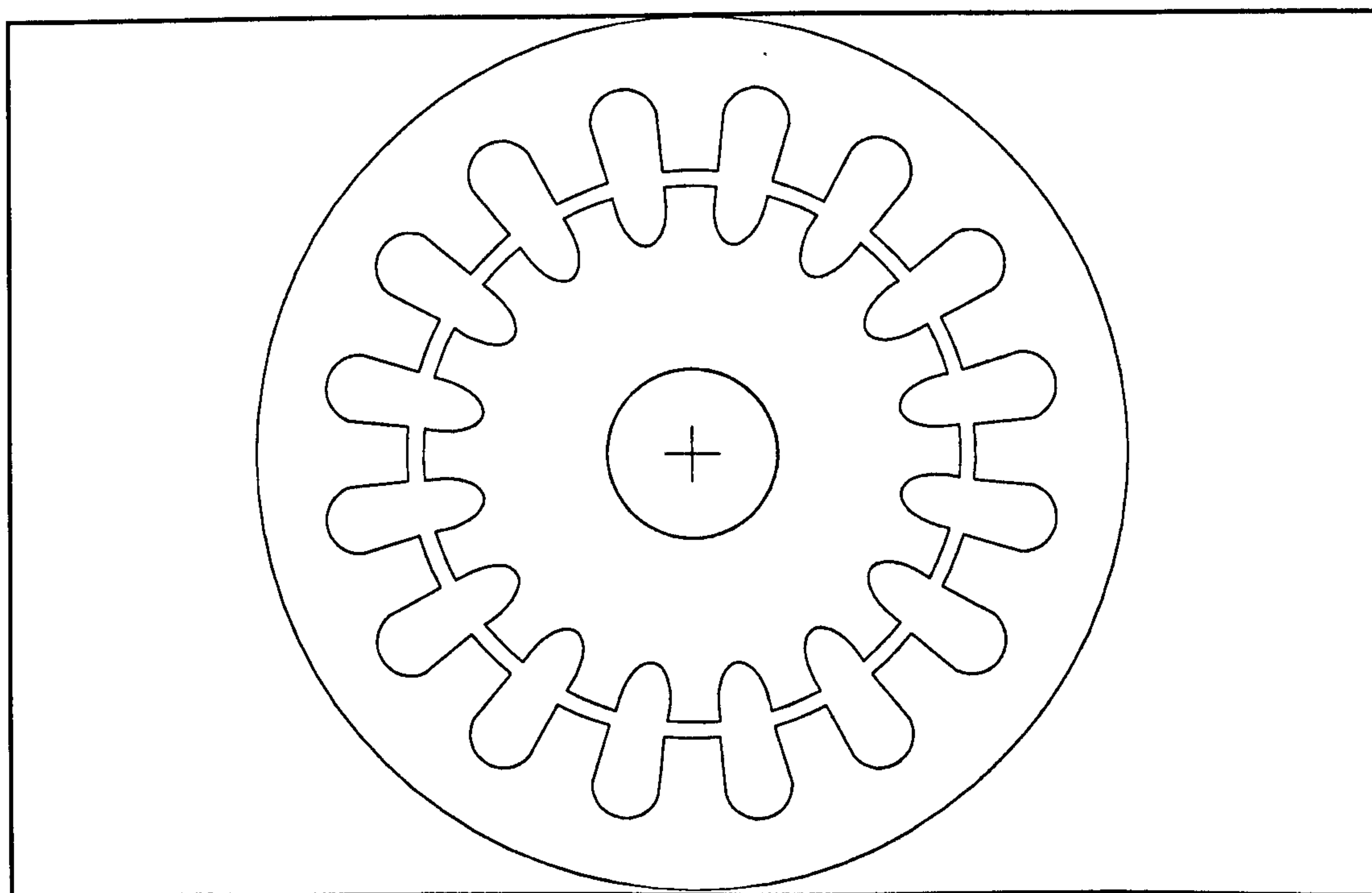


Figure 3.3: Possible 16/16 Stator-Rotor pole configuration resulting in a single phase SRG.

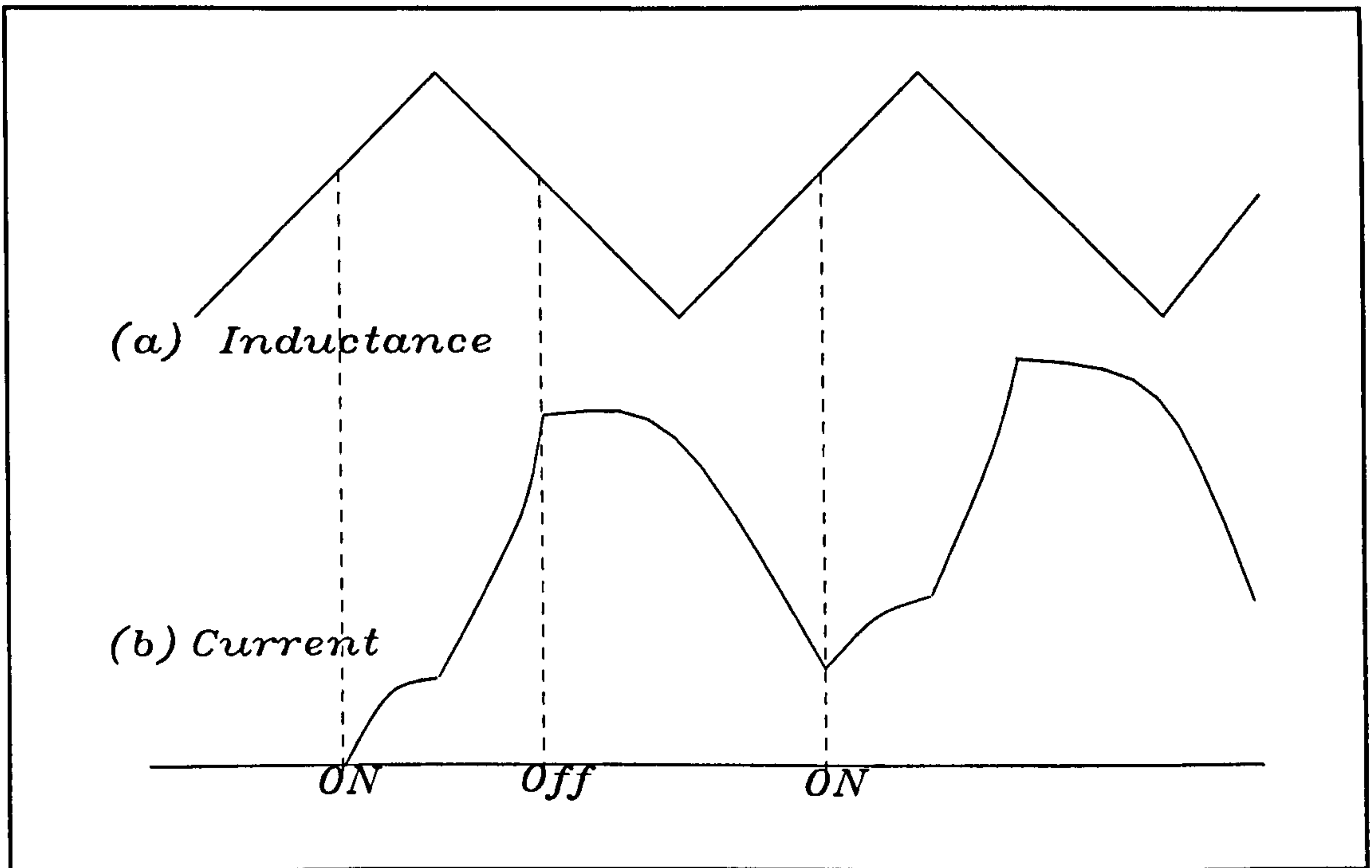


Figure 3.4: (a) Expected inductance profile & (b) Expected current waveform. For the machine of Figure 3.3.

- 2- 16 stator poles and 8 rotor poles. This is shown in Figure 3.5. The arrangement will result in a minimum of two phases with a step angle of 22.5° . There will be eight stator poles per phase, i.e. eight coil windings are connected in series on eight stator poles spaced 45° from each other to form a machine phase. The arrangement gives lower value of L_{\min} than the other two alternatives which results in a relatively larger EC-loop area. Its other advantage is the requirement of two phases only.

- 3- 16 stator poles and 12 rotor poles. This is shown in Figure 3.6. The arrangement will result in a minimum of four phases. There will be four stator poles per phase, i.e. coil windings are connected in series on four stator poles spaced 90° from each other to form a machine phase. Although the EC-loop area for this arrangement is probably smaller than the 16-8; in one revolution, there are 50% more work-cycles per stator pole. Output power could therefore be slightly greater.

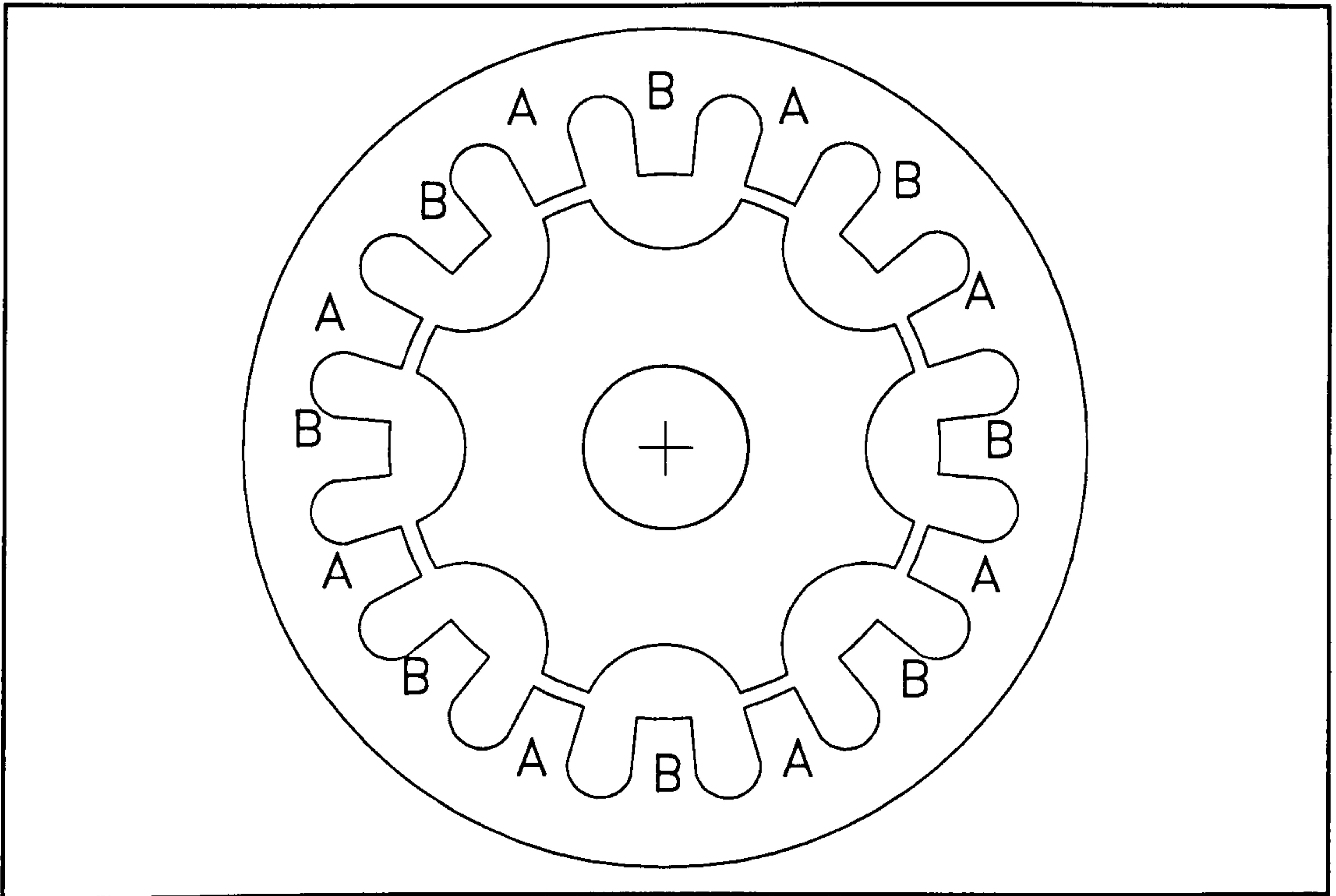


Figure 3.5: Possible 16/8 Stator-Rotor pole configuration. A two phase machine. The selected geometry for the high speed SRG.

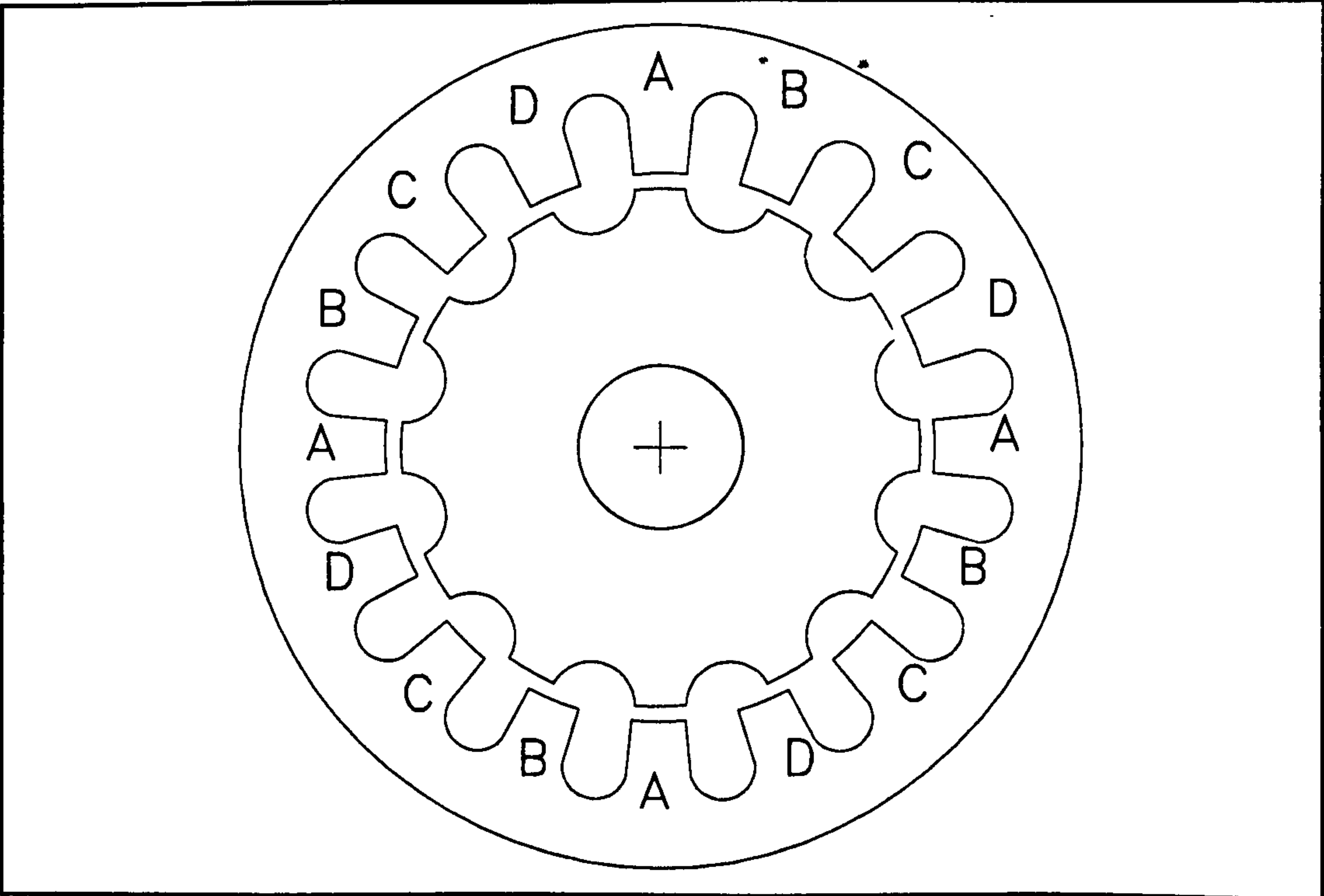


Figure 3.6: Possible 16/12 Stator-Rotor pole configuration resulting in a four phase machine.

The possibility of slightly greater output power for this configuration than the previous one is investigated by the simple model described earlier in chapter 2. Assumptions that were made and the results of the comparison are given in Appendix A3.4. Moreover, the argument may be supported by the findings reported in [128] in connection with the influence of the ratio of pole arc to pole pitch. In the study it was suggested that a ratio of rotor pole arc to rotor pole pitch, rpa/rpp of 0.4 is optimum as far as co-energy production in the SR machine is concerned. Assuming the same value of rpa for both 16/8 and 16/12 equalling the stator pole arc (s_{pa}), the first results in a ratio of 0.25 whereas the second is 0.375.

Note that 16 stator poles and 4 rotor poles will result in a minimum of four phases with a large step angle of 67.5° . There will be four stator poles per phase with winding arrangement similar to 3 above. This arrangement is ruled out since it would provide much poorer power output as there only half the number of working cycles of the 16/8 with no matching improvement in the area of the EC-loop.

Despite the possibility of slightly greater output power for the 16/12 configuration, it was decided to choose the two-phase (16/8) for:

- (i) Simplicity of power electronic circuit.
- (ii) Traditionally favourable for high speed applications.
- (iii) Lower frequency and iron losses (assuming these to be of significance).
- (iv) Having eight poles per phase rather than four is advantageous in terms of providing shorter flux paths, thus less m.m.f. drop across the back core [127], as well as resulting in more balanced radial forces.

3.3.3 Air-Gap Design

At least for small and medium sized SR machines, in general, the air gap should be as small as possible so as to maximise the inductance when the stator and rotor poles for a given phase are aligned and to enable the maximum flux per stator pole to be achieved with as little ampere-turns as possible.

In practice, the air gap size g is limited by mechanical considerations. Further, a disadvantage of a very small air gap is that, with machining tolerances, it may vary significantly from pole to pole thereby giving unbalanced radial forces and unbalanced inductances for the phases. Ultimately, some compromise on minimum air gap size may be necessary. The chosen figure of g for the high speed generator is 0.1 mm. Hence, due to this very small air gap, concentricity of the stator ID and the rotor is essential. This can only be achieved by careful machining of both rotor and stator at tolerances of at least ± 0.03 mm. Moreover, for operation at very high speeds envisaged (100,000 rpm), the rotor must be carefully balanced around its centre of rotation.

3.3.4 Physical Dimensions of Chosen Profile

Figure 3.7 shows an enlarged section of the selected geometry of Figure 3.5 with a single line of flux path for the aligned position is shown for simplicity. This flux pattern is expected when the winding configuration -discussed in the next section- is arranged so as to yield alternative north and south magnetic poles per phase.

In the figure, the stator pole arc (spa) and the rotor pole arc (rpa) are shown equal at 11.25° . Stator pole width (after machining) is 4.29 mm and rotor pole width is 4.25 mm. Since the stator pole pitch (spp) is $360/16=22.5^\circ$, the ratio of spa/spp (pole arc to pole pitch) will be 0.5. The

corresponding ratio for the rotor is 0.25.

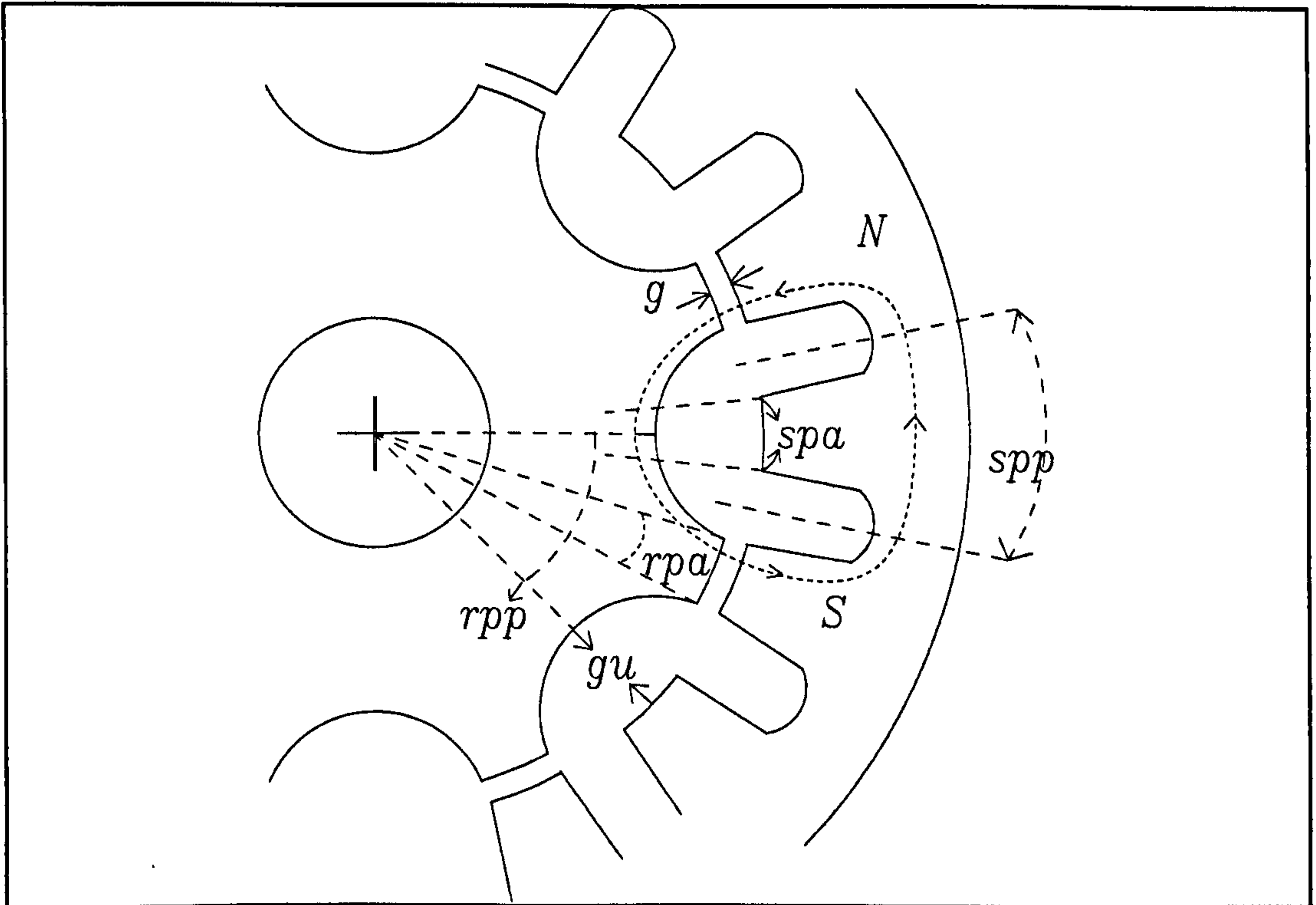


Figure 3.7: Basic terms in relation to the magnetic flux path.

The (rpa) needs to be at least as large as the (spa) if the maximum flux capability of the stator pole in the aligned position is to be utilised. If the (rpa) is greater than the (spa), this introduces some inductance dwell in the phase inductance-rotor angle profile at the expense of less minimum inductance dwell. Some maximum inductance dwell has no particular merit and is more likely a disadvantage. Equal pole arc for rotor and stator were chosen.

A cross section of the rotor lamination of the selected profile is shown in Figure 3.8. Dimensions are in mm. The dimension gu is generally favoured to be as high as possible to increase the ratio L_{\max}/L_{\min} . It is, however constrained by mechanical stability and machining difficulty. As for machining, the selected gu suited the drilling method and the available tools that were later used.

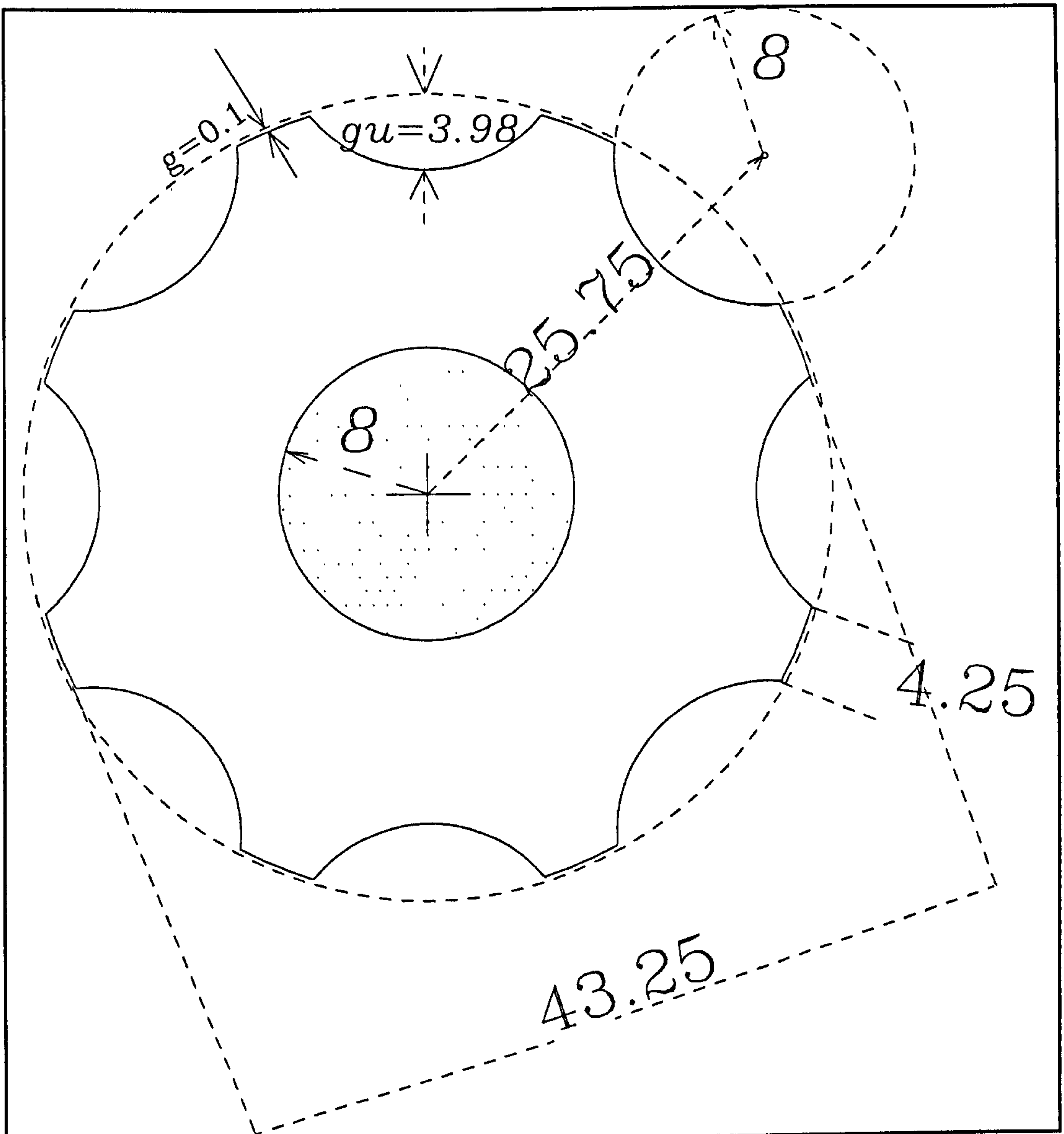


Figure 3.8: Cross section of the rotor lamination of the selected geometry. Dimensions in mm.

The central hole of the rotor, or the hub, dimension was aimed to be in the range 15-20 mm. The dimension which was found suitable for the shaft of the selected turbine (chapter 6) is 16 mm. The rotor was only machined after a suitable turbine was located. The effects of the hub dimension on the strength and stability of the rotor were investigated using stress analysis (see chapter 4).

3.3.5 Rotor Material Choice and Properties

The choice of rotor material is based primarily on mechanical considerations. There are no strict magnetic requirements apart from low core losses, since the use of the ferrite core is already limiting the saturation flux density to a low level (typically 0.25 tesla).

Materials most widely employed in wound or stacked cores are the electrical steels (low-carbon silicon-iron alloys) and the specially processed carbon steels designated as magnetic lamination steels. Nickel-iron alloys are also common in power applications. These conventional materials are characterised by high B_{sat} values such as 1.97 tesla for silicon steel and 1.6 tesla for Ni-Fe alloys. Higher B_{sat} values such as 2.5 tesla are obtained using cobalt based iron, Co-Fe alloys. They are also characterised by high Curie temperatures, above 700°C for silicon steel, and above 400°C for Ni-Fe. Nevertheless, their mechanical properties are not quite suitable for high speed applications in particular at ultra high speeds such as 100,000 rpm where the centrifugal stresses may be quite high. Some exceptions are possible, as it has been shown that heat treatment is more effective for smaller dimensions, so it does not seem impossible to obtain better steels for small machines with, for instance, ultimate strength of 1000 N/mm² [94].

Amorphous metals and alloys provide a very good alternative for conventional steel laminations, as they possess exceptional mechanical properties. Further, cores can be made out of very thin laminations 0.003-0.05 mm, with different widths of strips.

Amorphous alloys are broad alloy compositions containing about 75-85 atomic percent of transition metal elements such as iron, cobalt, and nickel which when combined with a 15-25 atomic percent mixture of metaloids can be quenched from the liquid state rapidly enough to avoid the normal, equilibrium crystalline structure and retain the disordered,

amorphous structure of a glass. Hence, they are frequently referred to as metallic glasses [131]. More details on these alloys and their applications are given in the review of Appendix A3.2.

The selected core material for the rotor of the current project was the Vitrovac® 6025. This alloy was selected mainly for its high tensile strength, typically 1500-2000 N/mm². Machining and assembly of laminations are considered in the next chapter. The magnetic properties of the alloy are very appropriate for the application. Manufacturer's data sheets are given in Appendix A3.2. Different shapes of hysteresis curves are obtained by simple annealing or heat treatment procedure of the stamped core. The annealing procedure is only necessary for applications with certain magnetic requirements. Therefore, the alloy is usually supplied as a semi-finished product which is an un-annealed thin strip of nominal thickness of 30 µm and 50 mm width. This suits the rotor diameter requirement of 43.25 mm. The 6025 alloy is cobalt based with B_{sat} value of 0.55 tesla which is the lowest in the range of Vitrovac® products but this does not matter as the stator core is already limiting the operation of the generator to 0.25 tesla maximum. It is also noted from the data that the Curie temperature is quite low (210°C) compared with steel laminations. The magnetic properties of the alloy are claimed to be very slightly influenced by mechanical stresses [134].

3.4 Design of Phase Winding

3.4.1 Introduction

SR machines invariably use a concentrated copper coil winding on each stator pole. Once the number of stator poles per phase, or the number of coils per phase, has been decided, the design of the phase winding will depend on the voltage of the machine to determine the appropriate number of turns and the available winding space to determine the wire diameter. The coils may be interconnected in a variety of ways and a multi-layer winding and/or a multi-strand of wires connected in parallel may be used. For convenience of interconnection, in the current project, the stator pole coils for each phase are connected in series. However, for the number of winding layers per coil there is no wide range of possibilities as will be shown, and the choice is largely dependent upon the available slot area.

3.4.2 Number of Turns / Generator Voltage

It was decided to choose the number of turns per stator pole, N , such that the internal generator voltage at 50,000 rpm lay in the approximate range of 40 to 50 volts. The design was based at 50,000 rpm since it was not certain whether 100,000 rpm would be achieved. At 100,000 rpm, the corresponding voltage would be approximately 100 volts. Higher voltages are inconvenient for MOSFET based power electronics design.

The simplified quasi-linear model introduced in chapter 2 was used for the estimation of voltage. It was shown, in equation (2.19) and Figure 2.8, that the back e.m.f. V_i at a specified speed ω rad/sec for currents in excess of the saturation value I_{sat} is given by:

$$V_i = \frac{\Delta \Psi_{max}}{\Delta \theta} \omega \quad (3.1)$$

where $\Delta\Psi_{\max}$ is the flux-linkage excursion from minimum to maximum and $\Delta\theta = \theta_m - \theta_r$ is the corresponding change in rotor angle.

Furthermore, $\Delta\Psi_{\max}$, for a phase comprising eight stator-pole coils of N turns each connected in series is given by:

$$\Delta\Psi_{\max} = 8 N A_c B_{sat} \quad (3.2)$$

where $B_{sat} = 0.25$ Tesla is the saturation flux density, and $A_c = 4.25 \times 25 = 106 \text{ mm}^2$ is the stator pole area.

The estimated value for $\Delta\theta$ for this particular design of SRG is $14.5^\circ = 0.253 \text{ rad}$.

At a speed of 50,000 rpm (5236 rad/sec), the back e.m.f. is therefore given by:

$$V_i = \frac{8 \times N \times 106 \times 10^{-6} \times 0.25 \times 5236}{0.253} = 4.4N \quad \text{volts} \quad (3.3)$$

A choice of $N = 10$ giving an internal generator voltage of approximately 44 volts was made.

3.4.3 Choice of Wire Gauge

Figure 3.9(a) shows a stator slot with dimensions (in mm) showing the available space for winding in one slot. Whereas Figure 3.9(b) shows a top view of a stator pole for finding the length of turn and thus the required length of coil per phase.

A reasonable stacking factor for stacking a wire of diameter d (area $d^2\pi/4$) with a total number of turns per coil N in an available slot area of $5 \times 2 \text{ mm}^2$ shown shaded in Figure 3.9(a) is taken to be 0.4. This factor takes into account the shape of the available area for winding as well as difficulties which may be encountered in tightening the coil turn around a quite brittle ferrite-made pole.

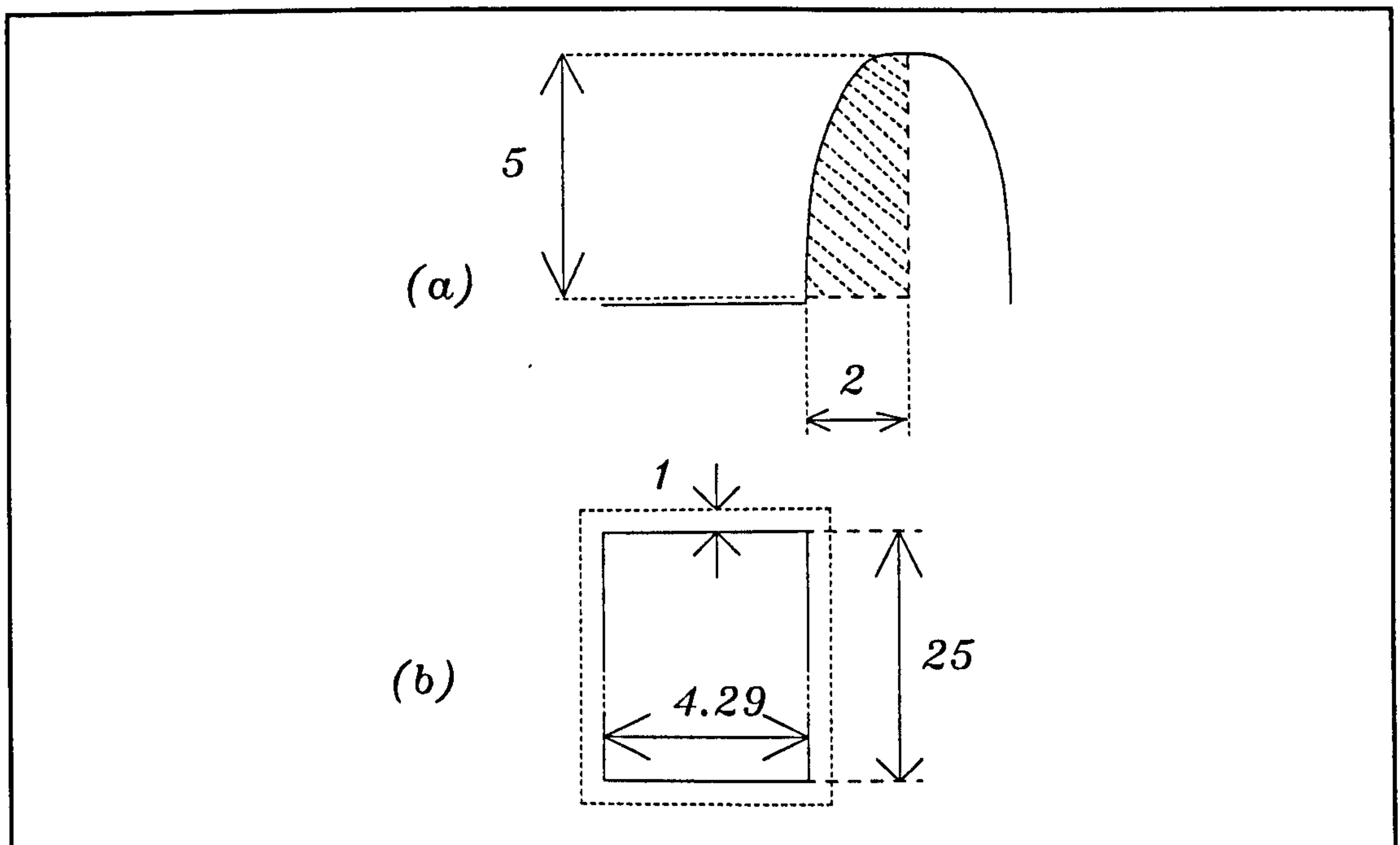


Figure 3.9: (a) Available space for winding in one stator slot.
(b) Top view of stator pole.

$$\text{Hence, } 0.4 \text{ (st.Factor)} \approx \frac{10 \times d^2 \frac{\pi}{4} \text{ mm}^2}{5 \times 2 \text{ mm}^2} \quad (3.4)$$

giving $d \approx 0.714 \text{ mm}$. The copper enamled wire selected was SWG22 with an OD of 0.711 mm, using two layers of 5 turns for each coil.

The coils were individually wound in situ on each stator pole. They were then connected in series on alternative stator poles in such a direction as to provide two phases each phase having alternative north-south stator magnetic poles upon excitation as shown in Figures 3.5 and 3.7.

In order to find the required length of the selected wire per coil, Figure 3.9(b) is used to find the length of a single turn. The clearance of 1 mm is to allow for the wire diameter:

$$\begin{aligned} \text{Turn length} &= 2 \times (6.29 + 27) = 66.6 \text{ mm} \\ \text{Length of 8 coils} &= 8 \times 10 \times 66.6 \text{ mm} = 5.3 \text{ m} \end{aligned} \tag{3.5}$$

Before coils were interconnected, an insulating layer was used to contain individual coils and to help absorbing the resin that was later used. Sixteen small strips of mica, each 25 mm long were pressed on the coil sides in each slot in order to help the resin to firmly hold the coils in place. Coils of each phase were interconnected by brazing.

3.4.4 Phase Resistance

The resistivity of copper, ρ at 25°C is 0.0175 $\Omega\text{mm}^2/\text{m}$. The cross section A_w of 22 SWG copper wire is estimated at about 98% of the nominal diameter of the wire (0.711 mm) to account for the insulation around the copper wire. Therefore:

$$A_w = \left(\frac{0.696}{2}\right)^2 \pi = 0.38 \text{ mm}^2 \quad (3.6)$$

The total length of the phase winding wire l_w can be considered to be 6 m if end connections to the power circuit are taken into consideration. Substituting for ρ , A_w and l_w results in a phase winding resistance R_w of 0.28 Ω .

3.4.5 Current Rating

A continuous current rating of 5 Amp r.m.s. will give a winding current density of: $5/0.38 = 13 \text{ Amp/mm}^2$ which is acceptable for this size of machine. The equivalent power loss for the two phases is: $2 \times 0.28 \times 5^2 = 14$ watts.

For short term operation, a current density of about 30 Amp/mm^2 would not be inappropriate. This is equivalent to an r.m.s. current rating (short term) of 11.4 Amp r.m.s. and a total copper loss of 73 watts.

3.5 Predicted Performance

The quasi-linear model of chapter 2 was used to make a preliminary prediction of typical phase current waveforms and power based on the geometric data for the machine. The basic data of the high speed SRG are given in Table 3.1, which represent the actual machine parameters obtained after building the SR machine. Although it was aimed to design the machine with certain values, in practice, it was difficult to achieve all the required specifications.

Number of coils per phase N_c	8
Number of turns per coil N	9.5
Saturation flux density B_{sat}	0.23 Tesla
Stator pole area A_c	106 mm ²
Stator pole arc ($\theta_m - \theta_o$)	11.34°
Stator pole pitch	22.5°
Extended stator pole arc ($\theta_m - \theta_r$)	14.5°
Air gap g	0.125 mm
Inductance ratio L_{max}/L_{min}	6.5

Table 3.1: Basic Data of the SRG.

The number of turns per coil was considered 9.5 to take into account the fact that some stator poles were in practice wound with 10 and others with 9 turns per pole. The air gap was measured using feeler gauges and found to be 0.125 mm. The maximum flux density was taken as 0.23 tesla to account for temperature rise to about 65°C in the core. Finally, the inductance ratio L_{max}/L_{min} was taken as 6.5, based upon a simple inductance measurement using an LCR bridge.

The model parameters were estimated as follows; with reference to the equations (2.5), (2.6), and (2.16) of chapter 2:

$$I_{sat} = \frac{B_{sat} g}{\mu_o N} = 2.4 \text{ A} \quad (3.7)$$

$$L'_{max} = \frac{\mu_o N_c N^2 A_c}{g} = 0.78 \text{ mH} \quad (3.8)$$

$$\Delta \Psi_{max} = L'_{max} I_{sat} = 1.87 \text{ mVs} \quad (3.9)$$

Since the model is only approximate, the values above have been suitably rounded. The extended stator pole arc represents the arc for rising inductance giving the profile shown in Figure 3.10, when $\theta = 0^\circ$ represents the unaligned stator-rotor pole position.

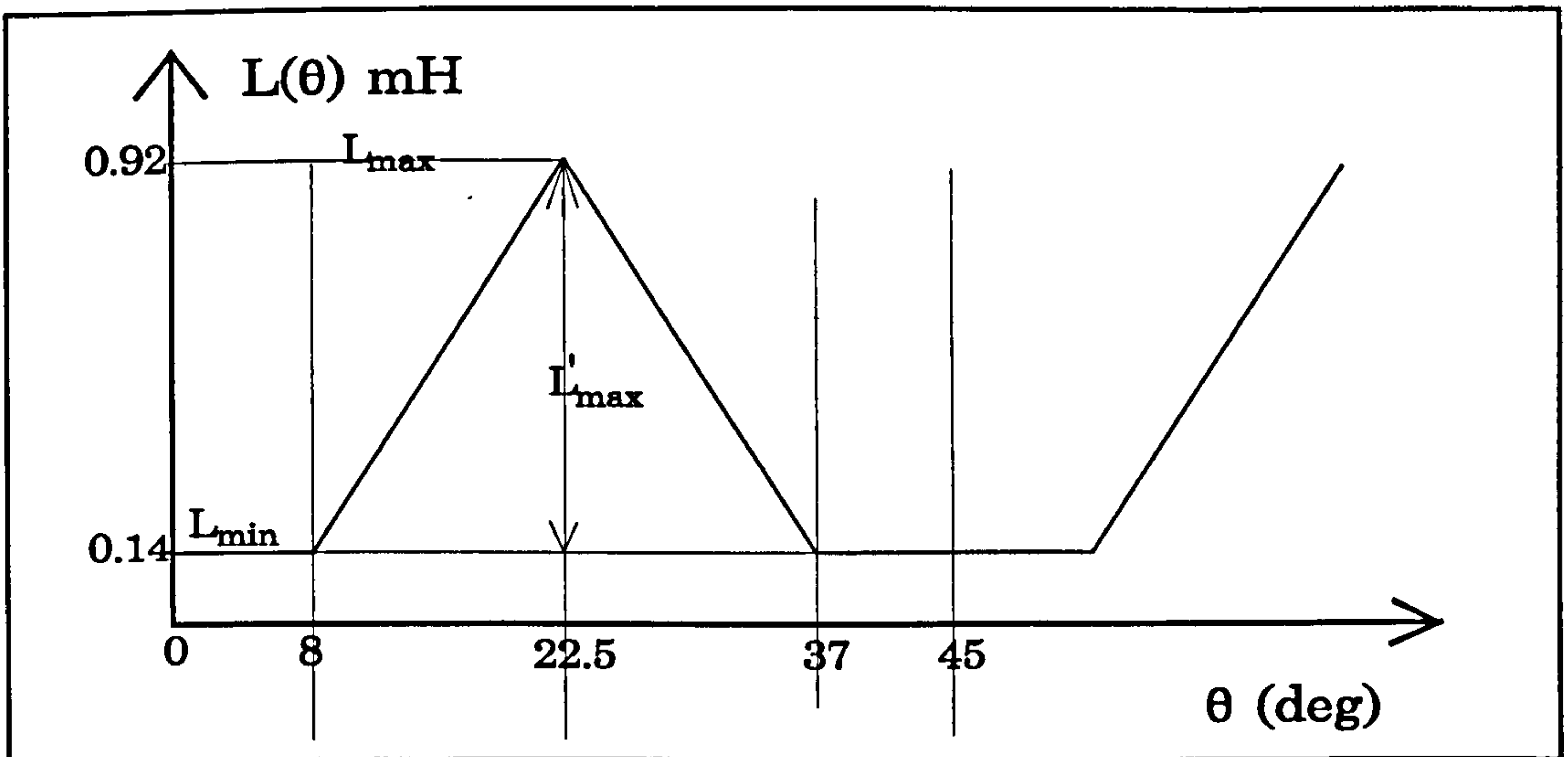


Figure 3.10: Phase inductance profile for the SRG considering an extended stator pole arc.

The resultant estimated Ψ - i - θ characteristics are shown in Figure 3.11.

The back e.m.f. constant for the equivalent circuit of Figure 2.8 is given by $\Delta \Psi_{max} / (\theta_m - \theta_r) = 1.87 \text{ mVs}/14.5^\circ$. At 50,000 rpm ($= 300^\circ/\text{ms}$), the back e.m.f. $V_i = 561/14.5 \approx 38$ volts.

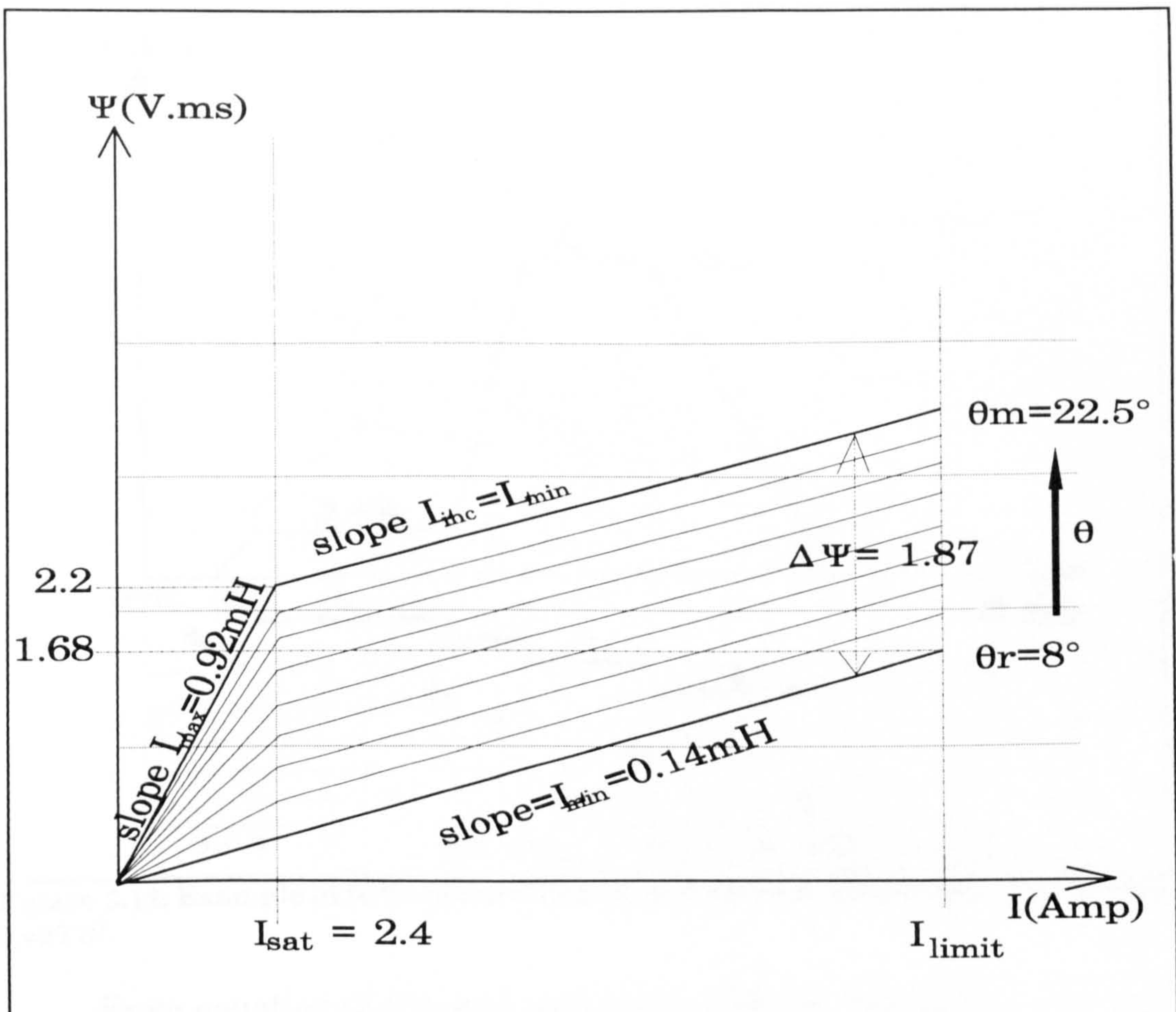


Figure 3.11: Ψ - i - θ characteristics for the quasi-linear model of the SRG.

For an estimate of high power generation at 50,000 rpm, a fully opened phase current waveform that occupies a rotor pole pitch of 45° is shown in Figure 3.12. This is used to estimate the power available for conversion for a typical condition with a supply voltage of 38 V which equals to the back e.m.f. voltage V_i at that speed.

The firing angle at which phase current is switched on, θ_{dly} , is selected as 5.3° to give rise to what is known as the flat topped current waveform. Therefore, θ_c is known for this current waveform as $\theta_{dly} + 22.5^\circ = 27.8^\circ$. Note that higher values of current and power conversion can be obtained with earlier delay angle (i.e. $\theta_{dly} < 5.3^\circ$).

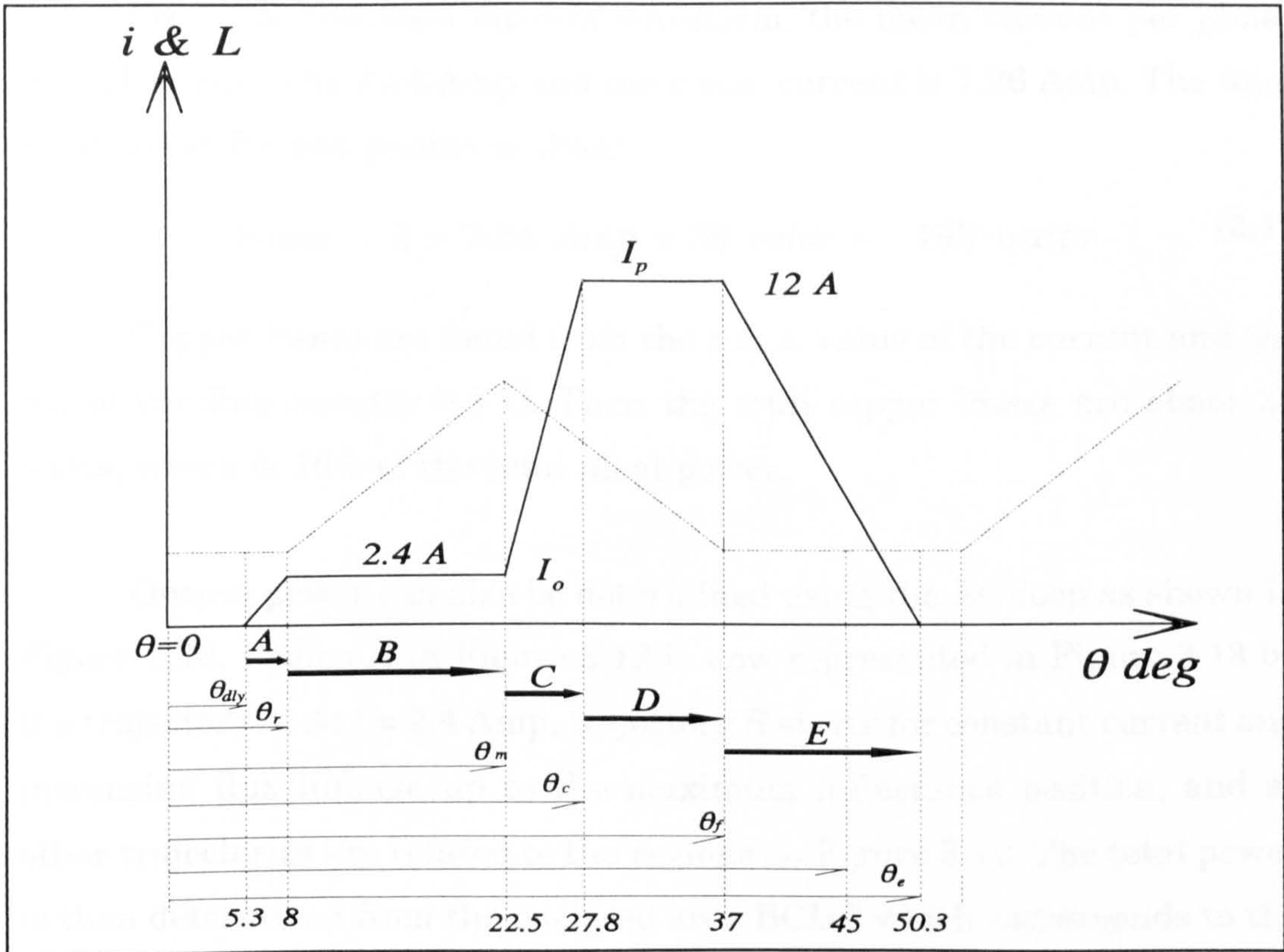


Figure 3.12: Example of fully-opened flat-topped current waveform. $\theta_{dly}=5.3^\circ$, and $\theta_c=27.8^\circ$.

From equation (2.21), and neglecting resistive volt-drop;

$$\frac{di}{d\theta} = \frac{V_s - V_i}{\omega L_{\min}} \quad A/degree \quad (3.10)$$

where $\omega = 300^\circ/\text{ms}$ and $L_{\min} = 0.14 \text{ mVs/Amp}$.

$$\text{Hence} \quad \frac{di}{d\theta} = \frac{V_s - V_i}{42} \quad A/degree \quad (3.11)$$

The rate of rise of current during region A of Figure 3.12 is found by substituting for $V_s = 38$ volts, and $V_i = 0$. The result is shown in the figure. The 2.4 Amp current will stay constant during region B as $di/d\theta$ is zero. The current rise in region C is $(76/42) \times 5.3 = 9.6$ Amp since $V_i = -38$ volts. For region D, the current is flat topped since $V_s = V_i = -38$ volts. For region E, the current fall is -0.9 Amp/deg since $V_s = -38$ volts and $V_i = 0$, requiring 13.3° for the current to fall from its peak value of 12 Amp to zero.

From the resultant current waveform, the mean current per phase¹ is worked out to be 2.54 Amp and the r.m.s. current is 7.26 Amp. The total ideal power for two phases is then:

$$Power = 2 \times 2.54 \text{ Amp} \times 38 \text{ volts} = 193 \text{ watts} \quad (3.12)$$

Copper losses are found from the r.m.s. value of the current and the phase winding resistor 0.3 Ω . Then the total copper losses are about 32 watts, which is 16% of the total ideal power.

Output power can also be determined using the EC-loop as shown in Figure 3.13. Region A in Figure 3.12 is now represented in Figure 3.13 by the trajectory A. At $i = 2.4$ Amp, trajectory B starts for constant current and increasing flux linkage up to the maximum inductance position, and so other trajectories are related to the regions on Figure 3.12. The total power is then determined from the enclosed area BCDE which corresponds to the energy times the phase switching frequency f_s :

$$Power = f_s \times \oint i d\psi \quad (3.13)$$

$$as \quad f_s = 8 \times \frac{50,000}{60}$$

The area BCDE is found from Figure 3.13 as:

$$\oint i d\psi = \frac{\Delta\psi_B + \Delta\psi_D}{2} \times \Delta i \quad (3.14)$$

$$= \frac{1.87 + 1.19}{2} \times (12 - 2.4) = 14.7 \times 10^{-3} \text{ joules}$$

Total power from (3.14) is then, for two phases, 196 watts. This figure will be less by about 20% if the effect of winding resistance is considered, as the enclosed EC-loop will be smaller. The gross generated power (i.e. $\oint i d\psi$) will therefore be approximately 157 watts. If losses are also considered, the net power generated will be about 118 watts for an estimated efficiency of 75%.

¹ Taking the direction into account.

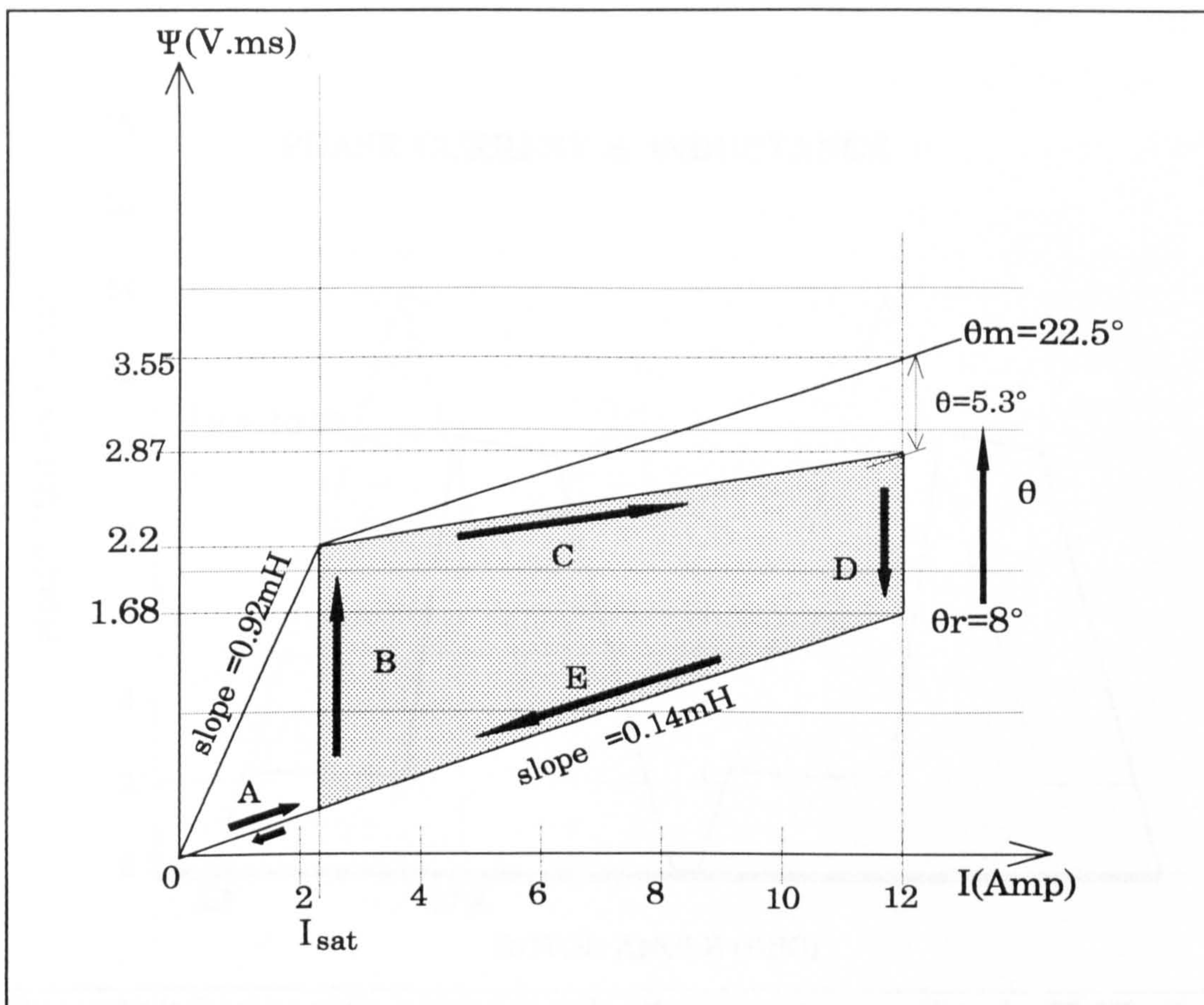


Figure 3.13: EC-loop for the example of fully opened current waveform.

The above example of current waveform in Figure 3.12 has only been provided for illustration. If winding resistance is included, the peak current value and the generated power will be reduced.

Figure 3.14 shows the current waveform for the same condition with winding resistance included. The waveform was obtained using the computer programme described in chapter 2 and in Appendix A2.1, and Appendix A2.2.

Higher values of output power, equivalent to the short term limit on current of 11.4 Amp r.m.s., can be obtained using earlier delay angles (exciting the phase winding earlier). The power obtained for this example case using the computer programme was 134 watts at an efficiency of 83%.

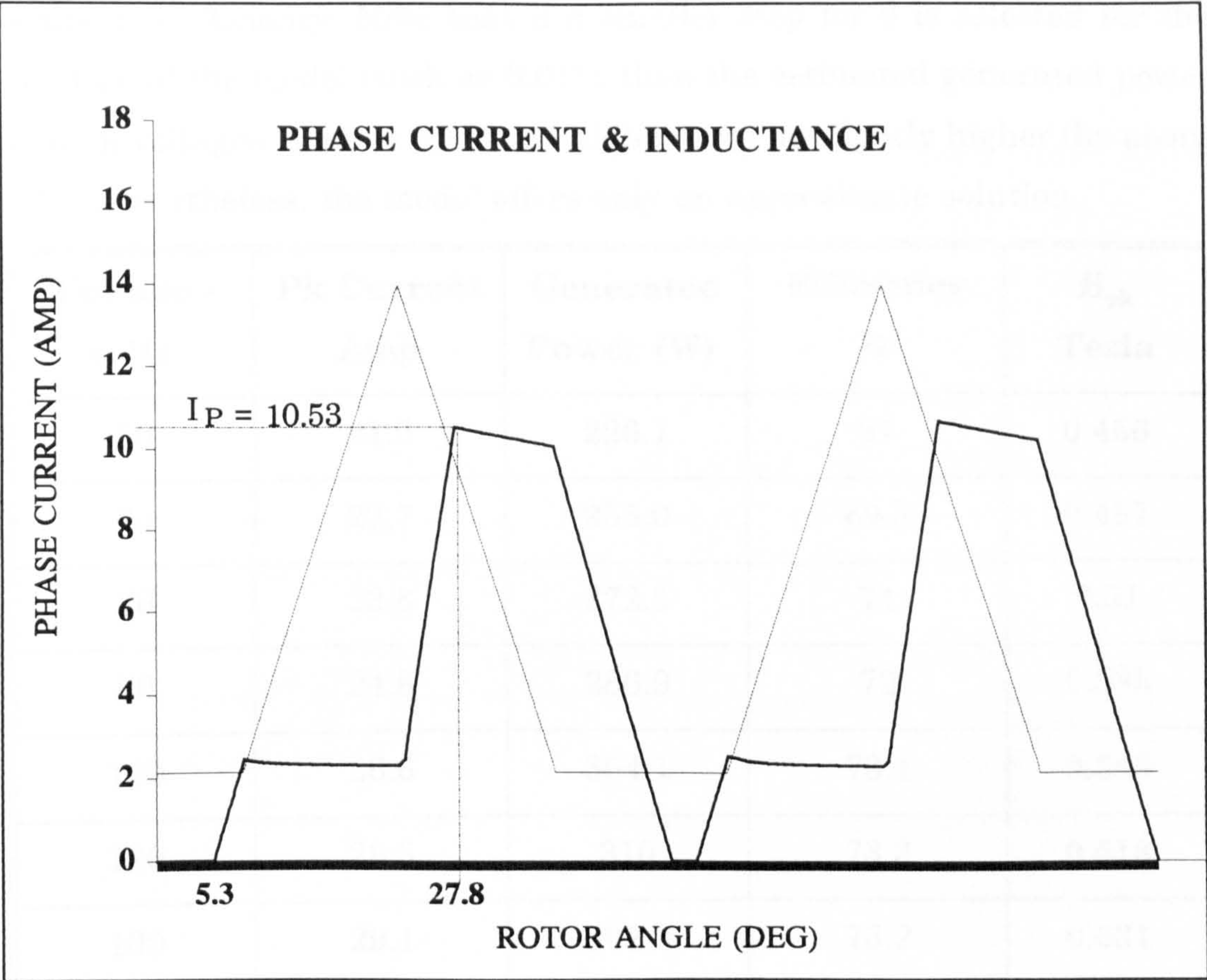


Figure 3.14: Output of the programme for the example case. Speed = 50,000 rpm and supply voltage = 38 volts.

Results from several other runs of the programme at different voltages and different firing angles which are selected to give a peak power operation at a rated phase current of about 11.4 Amp are presented in Appendix A3.4.

A summary of these results is given in Table 3.2 below, for a rated phase current of 11.4 Amp r.m.s, and a speed of 50,000 rpm.

These results show that the power output of the generator and efficiency increase with increased excitation up to a certain level. However, the rate of the increase diminishes and more stress is put on the power switches as peak current and voltage ratings increase. At an excitation of 130 volts, the power is less than in the case of 120 volts and so is the

estimated efficiency. Note that if a smaller step for θ is selected for the solution of the model (such as 0.01°), then the estimated generated power at high voltages (such as 80 V and higher) will be slightly higher (by about 5%). Nevertheless, the model offers only an approximate solution.

Voltage - volts	Pk Current Amp	Generated Power (W)	Efficiency %	B _{pk} Tesla
50	21.6	226.1	67	0.456
60	22.7	255.0	69.5	0.487
70	23.8	272.5	71	0.51
80	24.8	286.9	72	0.535
100	26.6	304.1	73.1	0.583
120	28.5	310	73.3	0.618
130	29.1	308.2	73.2	0.631

Table 3.2: Results of the simplified model of the SRG.

Estimated values of peak flux density B_{sat} are also determined for each case by the model. It is shown from these values that stator poles are driven heavily into saturation particularly at high voltages. However, this is to be expected with SR machines operating at maximum output.

3.6 Estimation of Core Losses

Core losses in the SR generator are composed of hysteresis iron losses and eddy current losses. Attention will be paid to estimating the latter, since the effect of eddy current is likely to dominate at high speeds. If eddy current loss is found to be insignificant, which may be intuitively expected, then hysteresis loss can also be ignored. Also, if the analysis shows that losses in the rotor part of the machine are insignificant, then stator losses can also be considered insignificant since at 50,000 rpm the frequency of the stator pole flux is only 6.67 kHz which is quite low for ferrites.

The objective is then to show that compared with the estimated generator output of 200 watts (or more) at 50,000 rpm, the eddy current loss in the rotor is negligible. At 50,000 rpm with a stator pole configuration of NNSSNN.., as shown in Figure 3.14, the rotor frequency for flux density B_r is 3.33 kHz (which is equal to four times the shaft frequency) and this is not unduly high. Furthermore, the thickness of the rotor lamination is only 30 μm and the volume material is small. Nevertheless, it should be shown that the expected loss is negligible.

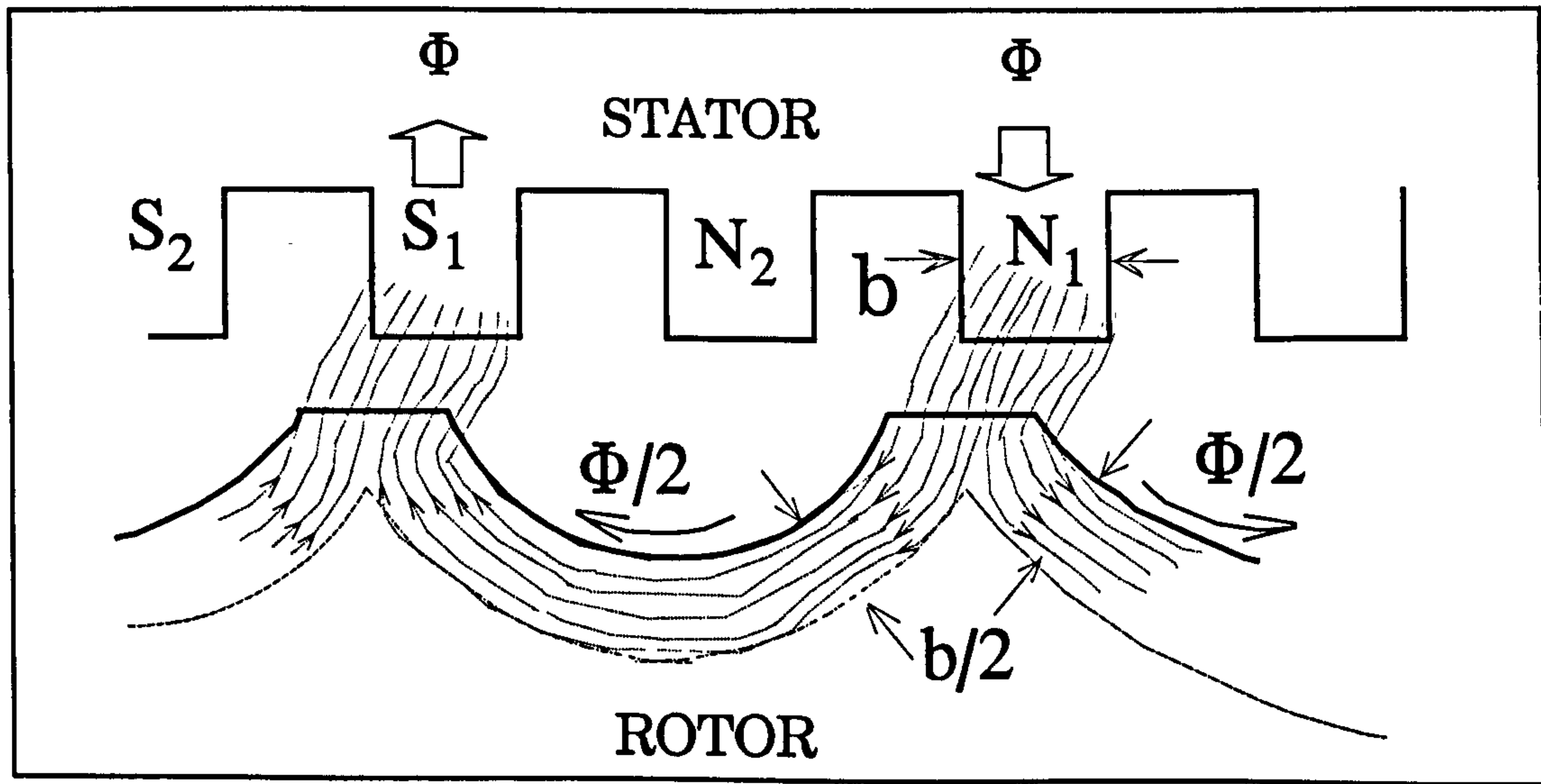


Figure 3.15: Assumption for flux distribution in the rotor.

The formula for determining power loss per volume due to eddy currents is:

$$\frac{Power_{eddy}}{volume} = \frac{\pi^2}{6} \frac{B_{pk}^2 f^2 t^2}{\rho} \quad (3.15)$$

where B_{pk} is the peak value of the flux density in the particular element of rotor under consideration, ρ is the electrical resistivity for the rotor material which is $1.35 \times 10^{-6} \Omega m$, f is the frequency of flux variation and t is the lamination thickness which is $30 \times 10^{-6} m$.

However, for the SR rotor, the flux density does not vary sinusoidally with time, and hence the more general equation may be used to estimate eddy current losses:

$$\frac{Power_{eddy}}{volume} = \frac{B_{rms}'^2 t^2}{12\rho} \quad (3.16)$$

where $B' = dB/dt$.

The main assumption for the flux distribution in the rotor is that the stator flux is evenly carried by the rotor as shown in Figure 3.14. Other simplifying assumptions to determine B' in the rotor resulted in an R.M.S value of B' as 14.1×10^3 Tesla/sec for full power case, and 10,000 Tesla/sec for reduced power. These assumptions are given in Appendix A3.5. Assumptions for the determination of the volume of the rotor flux-carrying part resulted in an active volume of 5.48 cm^3 . Maximum rotor losses at full power and 60 volts supply were thus determined using (3.16). This was found to be 0.06 watts at 50,000 rpm speed which is expectedly small. Details of the calculations and flux waveforms are given in Appendix A3.5.

3.7 Conclusion

The electromagnetic design of the SRG has started with locating a suitable ferrite stator of fixed geometry of 70 mm OD and 16 salient poles, which limited the number of possible phase winding arrangements and rotor geometries. An eight-pole rotor resulting in a two-phase machine has been found to be the most suitable in terms of power conversion and simplicity of power electronics.

Material wise, the low magnetic saturation flux density B_{sat} of the ferrite stator core (0.25 Tesla) has made the magnetic properties of the amorphous iron rotor not particularly important; the Vitrovac® 6025 amorphous iron was basically chosen for its mechanical properties. However, having a higher B_{sat} of 0.55 Tesla for the rotor material is advantageous since the stator poles will certainly be driven heavily into saturation at B values twice B_{sat} of the ferrite or more.

A very small air gap is generally required between stator and rotor poles for increasing power conversion, yet this should not be on the expense of mechanical tolerances. A compromise for this resulted in the selection of 0.1 mm air gap.

The design of the phase winding was based on a speed of 50,000 rpm and a voltage of around 50 volts. This resulted in 10 turns per pole of SWG 22 wire gauge wound in two layers. At 50,000 rpm, the internal voltage of the generator will be 44 volts. Eight coils were connected in series on alternative stator poles to comprise a phase winding, which upon excitation would charge the stator poles with NSNS etc. magnetic polarity.

The continuous rating of the SRG is 5 Amp, giving a current density of 13 Amp/mm², and the peak (short term) rating is 11.4 Amp, giving 30 Amp/mm².

Using the basic design data of the SRG (after adjusting for the actual achieved specifications), its performance could be predicted by utilising the quasi-linear model of chapter 2. Predictions of the power gave an estimate figure for the appropriate level of the generator voltage as 60-70 volts at a speed of 50,000 rpm. Based on the peak rating of the machine, the expected power of the SRG would be 250 watts at 60 volts with an estimated efficiency of 70%.

It has also been shown that the core losses in the SRG are insignificant. Though this may be expected, an approximate method of estimating these losses has been devised. The result has shown that rotor losses would approximately be 0.06 watts at 50,000 rpm and 60 volts for peak power operation.

CHAPTER FOUR

THE SRG MECHANICAL DESIGN AND ASSEMBLY

4.1 Introduction

Once the electromagnetic design of the SRG is realised, the next step is to give proper attention to the mechanical design of the experimental testing system bearing in mind the high rotational speeds envisaged, since the failure of rotating parts, in such cases, is particularly hazardous. The principle requirements of a high speed electrical machine arrangement are discussed below:

- 1- At high speeds (above 20,000 rpm) the stresses due to centrifugal forces become excessive particularly at the bore of the rotor. This requires the selection of a rotor material with an ultimate strength high enough to endure these stresses. It also puts a limit on the maximum diameter of the rotor. Stress analysis is required using finite element analysis especially if the rotor is profiled.
- 2- The rotor and all other rotating parts of the machine should be dynamically balanced, having their centre of mass on the axis of rotation to avoid vibration and possible bending of the shaft at very high speeds.
- 3- The rotor length should be restricted due to critical speeds. The maximum length is expressed as the ratio of the maximum length to the maximum rotor radius. In practice this ratio should not exceed 5 [90][94].

- 4- If an interference fit is used to mount the rotor on the shaft, then the shaft should maintain this fit during operation.
- 5- Bearings and lubrication need careful choice. The choice of lubricant depends on the load, the speed and the temperature. This will be further discussed in chapter 6.

This chapter is concerned with the mechanical design of the SRG. The first step is to carry out a stress analysis aiming to find the likely stress distribution in the rotor due to the centrifugal forces. Other sections of the chapter deal with the machining and assembly of both the rotor laminations and the stator ferrite core. Direct or indirect coupling in high speed machinery requires careful approach; therefore some consideration is given to the description of fitting the rotor directly on the shaft of the driving turbine. To complete the description of the testing arrangement, the mechanical details of the disk used for rotor position sensing are introduced.

4.2 Stress Analysis for The Rotor

4.2.1 Background

The case of centrifugal stress determination over the surface of a rotating disk with a central hole is well known in stress analysis. A brief review of the basic relations is presented with the aid of Figure 4.1, which shows a disk in the x - y plane rotating around the z -axis with an angular speed of ω . The disk has an outer and inner radii r_o and r_i respectively.

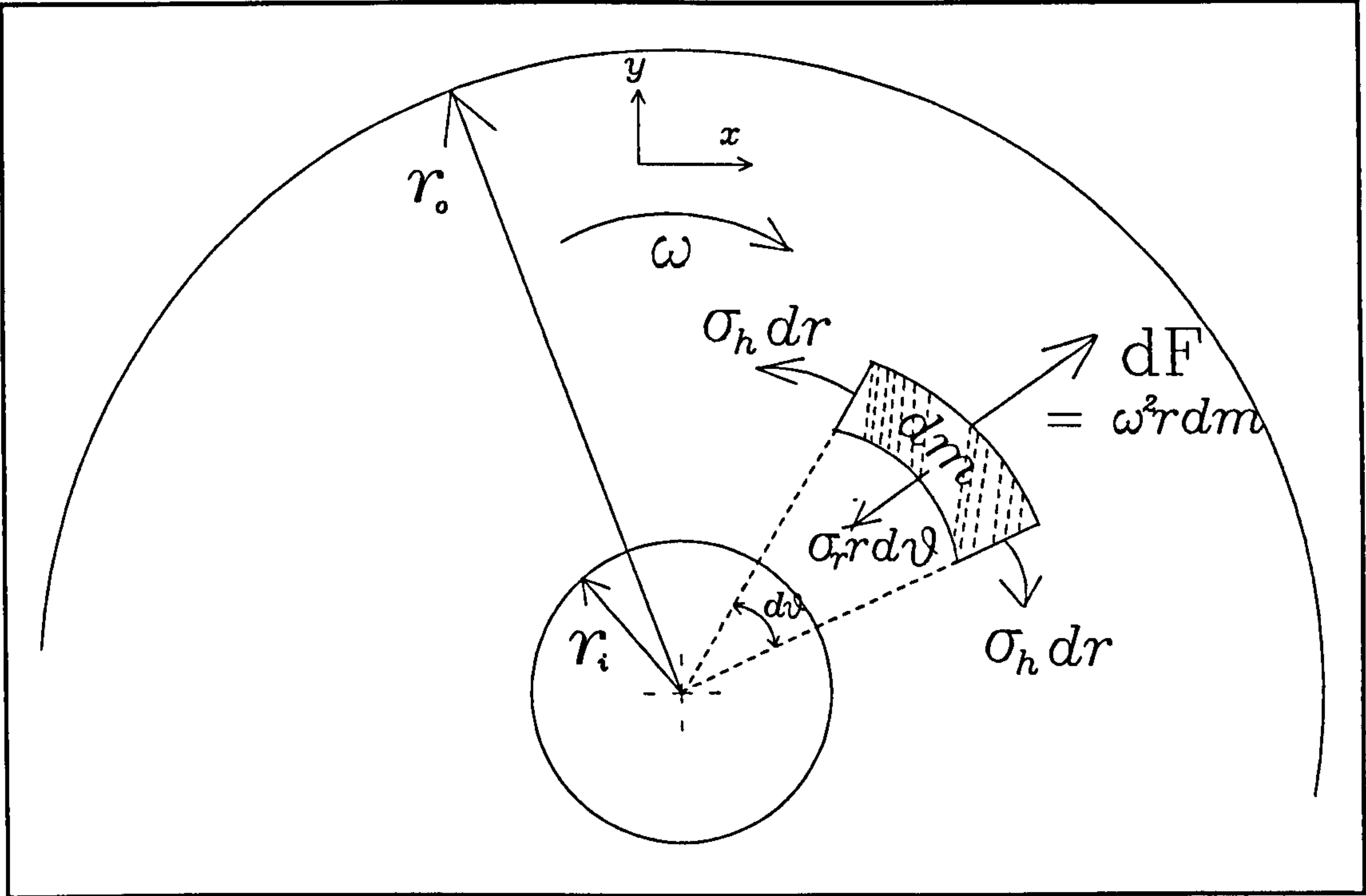


Figure 4.1: Elementary rotating disk for radial and tangential stresses calculation.

It is assumed that the radial and hoop (tangential) stresses are constant through the thickness of the disk and that there is no stress in the z -direction. Mass element dm , in the x - y plane, and given by $dm = \rho r dr d\theta$, where ρ is the density, is subjected to radial stress σ_r and hoop stress σ_h . The problem reduces to one in statics where the centrifugal force exerted on element dm is counter-balanced by the stress forces which pull the element towards the centre of rotation.

The radial stress σ_r distribution, subject to the boundary constraints that $\sigma_r=0$, for $r=r_o$ and $r=r_i$ is given by:

$$r^2 \frac{d^2 \sigma_r}{dr^2} + 3r \frac{d\sigma_r}{dr} + (3+\nu) \rho \omega^2 r^2 = 0 \quad (4.1a)$$

and the hoop stress σ_h is related to σ_r by:

$$\sigma_h = r \frac{d\sigma_r}{dr} + \sigma_r + \rho \omega^2 r^2 \quad (4.1b)$$

These equations may be solved to find relationships for σ_r and σ_h as a function r , from which the maximum values can be obtained.

$$\sigma_{h \max} = \frac{3+\nu}{4} \rho \omega^2 r_o^2 (1 + b) \quad \text{at } r = r_i \quad (4.2)$$

$$\text{where } b = \frac{1-\nu}{3+\nu} \left(\frac{r_i}{r_o} \right)^2 \quad \text{and is generally } < 1$$

and,

$$\sigma_{r \max} = \frac{3+\nu}{8} \rho \omega^2 r_o^2 \left(1 - \left(\frac{r_i}{r_o} \right)^2 \right) \quad \text{at } r = \sqrt{r_o r_i} \quad (4.3)$$

The tangential stress at any point in the structure is higher than the radial stress. Tangential stress is maximum at the bore and should always be less than the ultimate strength or the tensile strength of the material used by some safety margin. From this, the notion known as working stress σ_w is devised. It is important to include in this safety margin any additional boundary loads and residual stresses that may act on the structure under stress. These include shrinkage stresses, impact stresses and stresses caused by operating torques and imperfections in the material [151]. Only shrinkage stress is relevant to the application here, although imperfections in the material may also be relevant if imperfections in the finished stacked laminated rotor are considered.

For the amorphous alloy, the tensile strength is quoted as 1500-2000 N/mm². Tensile strength is a property of a material with the unit of stress, N/mm² or MPa. It is considered as the highest point plotted for a material on the stress-strain curve -see Figure 4.2- when the material is subjected to a tensile test. It should be noted here that, for amorphous metals, from which the rotor is made, the tensile point T shown in Figure 4.2 and the yield point are the same. This means that these alloys do not work harden, and are different from steel in this respect, see [134] and Appendix A3.2. The straight line portion of the graph represents the value of the modulus of elasticity or Young's modulus (E) which is a measure of the inherent rigidity of a material. It is given for the rotor material as 150×10^3 N/mm² [134]. Poison's ratio (ν) is a measure of the unit strain of a material in the directions normal to the applied load. Like E, it is a constant depending on the material in the elastic range. For the rotor material it is taken as 0.3, which is similar to that for steel.

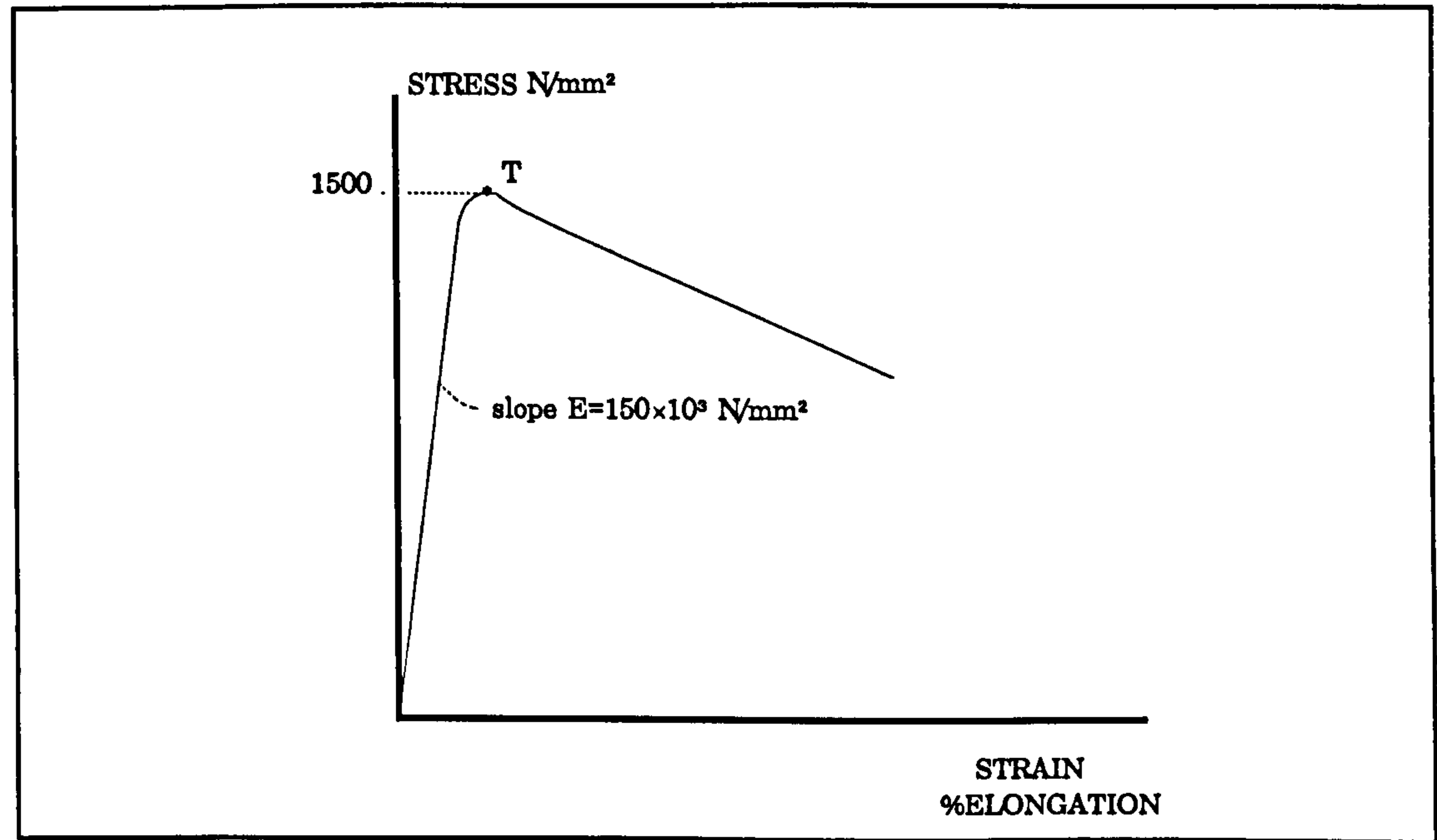


Figure 4.2: Typical stress-strain relationship for amorphous metal.

Therefore, applying (4.2) for 100,000 rpm and for rotor dimensions as designed in chapter 3 (i.e. $r_o = 21.625$ mm, $r_i = 8$ mm, and with $\rho = 7.7 \times 10^3$ kg/m³), the maximum stress is at the bore and equals to 335 N/mm². This

is about one fifth of the ultimate strength of the material used for the rotor. The figure does not include any residual stresses. It is, however, initially still quite safe. It would also be remembered that this gives stresses for a disk with the same outer radius as the rotor. For a more accurate determination of maximum stress and where it occurs, it is necessary to consider the rotor profile. This can only be achieved by using a finite element approach, or other similar field-stress analysis package.

4.2.2 Description of Finite Element Programme

A package suit for solving engineering problems using finite element approach, PAFEC, was used in order to obtain stresses on the rotor of the high speed SRG.

The programme reads the information according to modules. Each module has a specified function and contains a list of information which should be prepared in relation to the specific problem. A listing of a programme used to find stresses on a 45° segment of the rotor at 100,000 rpm is given in the Appendix A4.1. This is introduced as an illustration of the modules, and is preceded by description of the programme phases. Elements should be selected according to the required type which suits the application. A wide range of possibilities is provided by the programme. A quadrilateral eight-node flat element was selected for the data input after consulting the manual [152]. When these elements are selected, stresses in the plane of the cross section of the rotor are determined. All bending or twisting effects acting out of the plane of the element are ignored. Slight distortion from the basic square shape of elements is allowed. However, if the distortion becomes too great, the programme will issue an error signal. There was some difficulty in the beginning regarding defining the region adjacent to the rotor poles due to extreme curvature. It was overcome by proper selection of number and size of elements in that region aiming to

produce as near to square shape of elements as possible.

The geometry of the structure should be defined first in the NODES module. Restraints for a structure under centrifugal force are such that the rotating body does not travel tangentially. The loading is defined in the CENTRIFUGAL module where the speed is given in rev/sec. Material properties required are E , ν and ρ .

The programming suit package is aimed at solving diverse types of engineering problems [152]. Consequently, data modules read by the programme will have to be very specific in order to correctly define the problem to be solved. This will inevitably add some burden during the data preparation stage.

4.2.3 Results for Target Speed 100,000 rpm

A complete rotor structure with material properties, restraints and loadings is defined using the relevant modules. The data input listing for this case is given in Appendix A4.2. The output of the programme is a drawing of the rotor cross section with stress contours superimposed on it. This is shown in the drawing of Figure 4.3. The range of stresses is determined as 65 N/mm²- 321 N/mm². These figures correspond to the maximum principal stresses. The contour which corresponds to the highest values in the stresses range is, as expected, along the bore as shown in the figure. This is similar to the 335 N/mm² found earlier for σ_h by applying (4.2). Hence the effect of the profiling of the rotor by removing material to create the salient poles does not significantly reduce the maximum stress at the bore. The result also shows that at the rotor periphery, the maximum stress is that in the mid-region between rotor poles.

The largest bore displacement determined from the output of the programme is 11.6 μm . This figure of displacement is quite important. It represents the magnitude of the radius enlargement (in the elastic region) due to the centrifugal stress only. This means that a rotor-to-shaft fit must ensure avoiding a loose rotor situation taking into account a diameter enlargement of 23.2 μm at 100,000 rpm. The shrinkage fit is discussed in the next section, but it is worth mentioning here that this fit should also consider a safety factor on the displacements of the rotor including displacement due to high rotor temperature, if found to be not negligible.

E SRG ROTOR STRESS ANALYSIS 100 KPM 0MM IN RAD

PAFEC

VIEW FROM X 0.0000
 Y 0.0000
 Z 0.1000



Z TOWARDS VIEWER

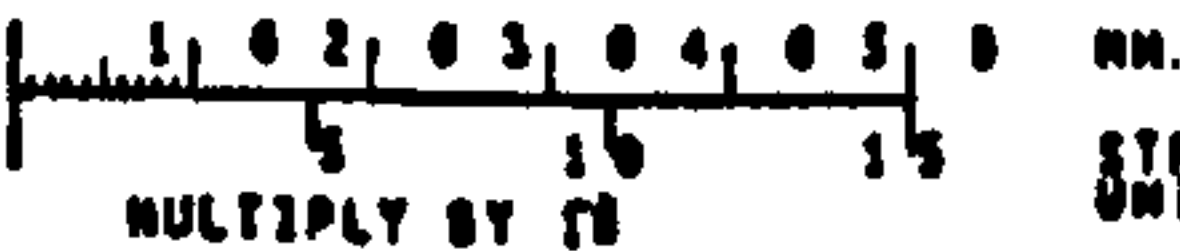
MAXIMUM
PRINCIPAL
(MOST
POSITIVE)
STRESS
(MIDDLE SURFACE)
MULTIPLY
BY 10

64.80	A
93.30	B
121.8	C
150.8	D
178.8	E
206.8	F
235.8	G
263.8	H
292.8	I
320.8	J

LOAD CASE = 1

WHOLE STRUCTURE DRAWN
AS DEFINED IN FRONT. ORDC

ON 19/07/94 AT 23:03:50



MM.
STRUCTURAL
UNITS

DRAWING NO. 2
SCALE = 3 333
DRAWING TYPE= 30

Figure 4.3: Stress analysis results at 100,000 rpm.

4.2.4 Results for Higher Speeds

In order to gain more insight into the effect of increasing the speed beyond 100,000 rpm on the maximum stresses and largest displacements at the rotor bore, the programme was run various times at different values of rotational speeds. Output results for 255,000 rpm are shown in Figure 4.4. Table 4.1 shows the results of the finite element programme for the rotor with the chosen profile at different speeds. In all cases, the stress at the inter-pole region is slightly more than half that on the bore. The ratio of stresses at these two regions are not considerably influenced by increased speed for this profile.

Speed rpm	Stress Range N/mm ²	Displacement on radius µm
100,000	65 - 321	11.6
120,000	73 - 436	16.1
150,000	140 - 694	25.2
180,000	202 - 998	36.3
200,000	259 - 1280	46.6
255,000	330 - 1970	73.0

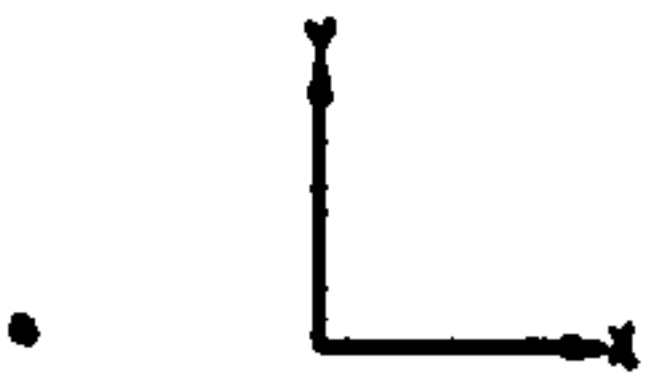
Table 4.1: Results of FE analysis for stress calculation.

If the allowable working stress is taken as 1000 N/mm², which is 50% less than the ultimate stress, then the correspondent maximum allowable speed is 180,000 rpm as given in the table above. However, displacements that might lead to a loose fit situation are still to be considered and may lead to a lower value of maximum allowable speed as will be shown in 4.3.4

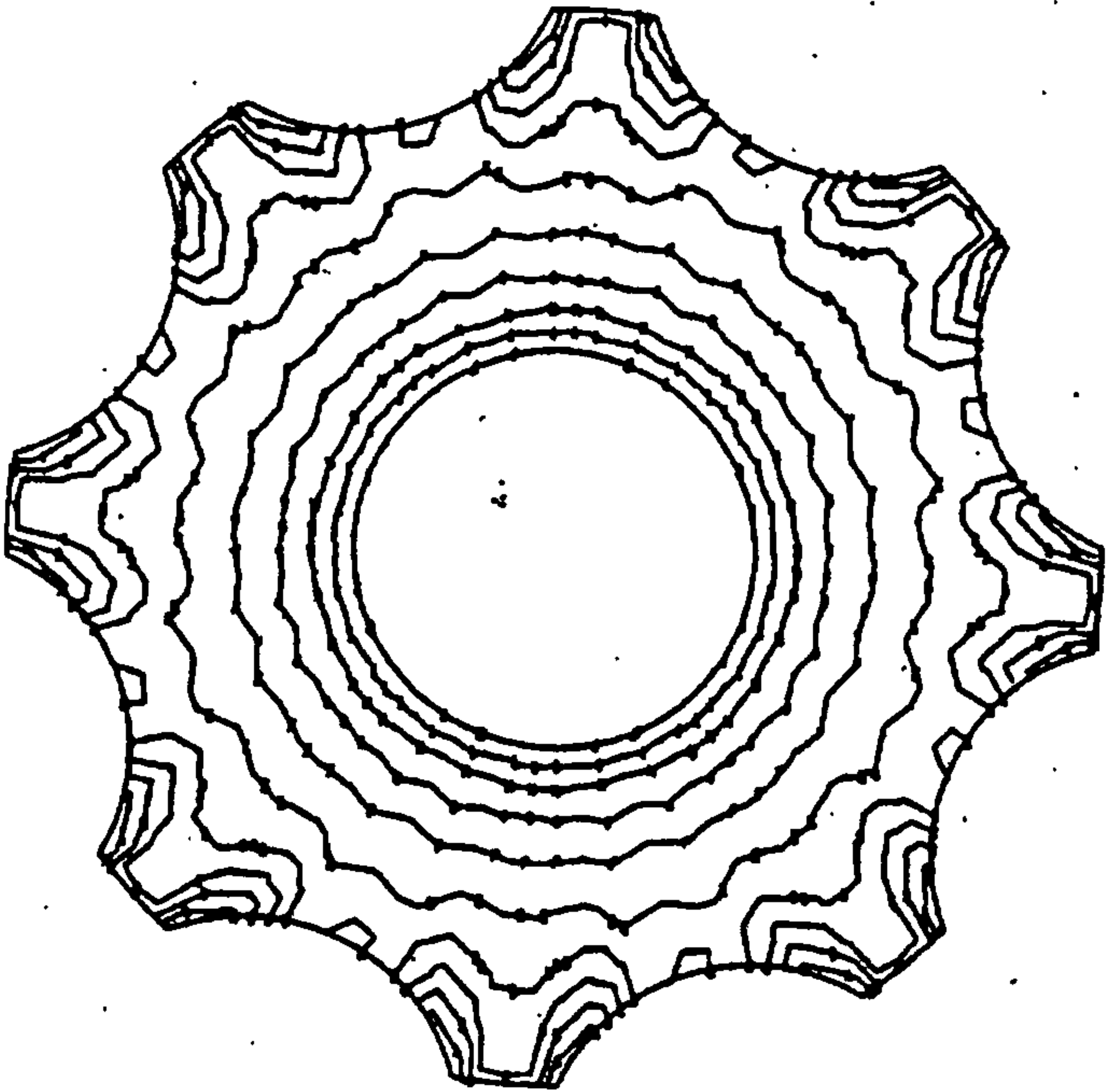
SRG ROTOR STRESS ANALYSIS 255 RPM GURTI

PAFEC

VIEW FROM X 0.0000
Y 0.0000
Z = 1.00



Z TOWARDS VIEWER



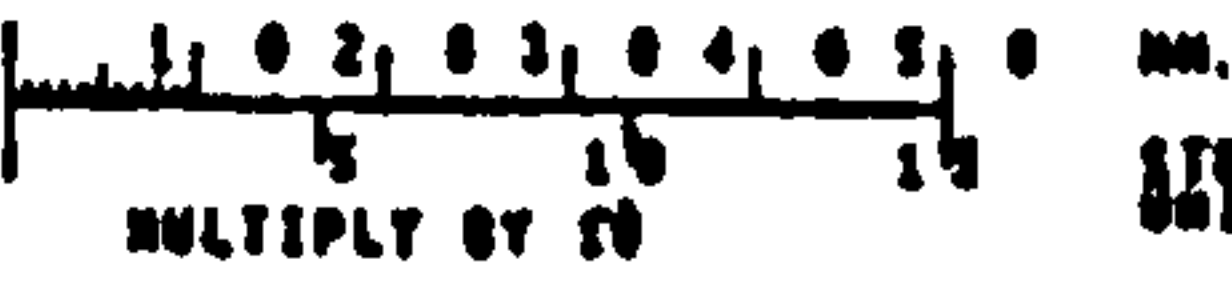
MAXIMUM
PRINCIPAL
(MOST
POSITIVE)
STRESS
(MIDDLE SURFACE)
MULTIPLY
BY 10

329.0	A
511.0	B
693.0	C
875.0	D
1056.0	E
1236.0	F
1416.0	G
1596.0	H
1776.0	I
1956.0	J

LOAD CASE = 1

WHOLE STRUCTURE DRAWN
AS DEFINED IN FRONT. ORG

ON 26/07/94 AT 15:10:27



MM.
STRUCTURAL
UNITS

DRAWING NO. 2
SCALE = 3.333
DRAWING TYPE = 30

Figure 4.4: Stress analysis results at 255,00 rpm.

4.2.5 Investigation of Different Profiles

Using the same approach with modified rotor geometry, an investigation is carried out in order to evaluate the mechanical stability of other geometries at very high speeds. In addition, the same rotor profile was tested in the programme at an increased bore diameter. The bore diameter of the rotor was a design choice, limited in the range of 10-20 mm. The value selected was 16 mm. Nevertheless, the effect of increasing this on lowering the allowable speed is not as serious as increasing the outer diameter. This is not surprising - see equation (4.2) for "b" in particular. For example, the programme was run for a rotor of 24 mm bore running at a speed of 100,000 rpm. The result is shown in Figure 4.5. Maximum stresses are only slightly higher than in Figure 4.3, displacements are 60% higher, but the distribution is quite different. The difference is that stresses at the interpolar region are now 90% of the maximum stresses at the bore.

Finally, a rotor profile which is more common for salient pole machines than the one selected, is investigated by the programme. This is shown in Figure 4.6. The results show that at 180,000 rpm, the presumed maximum allowable speed, stresses are very similar but displacements are slightly larger. However, there is some stress concentration in the area near the pole bottom.

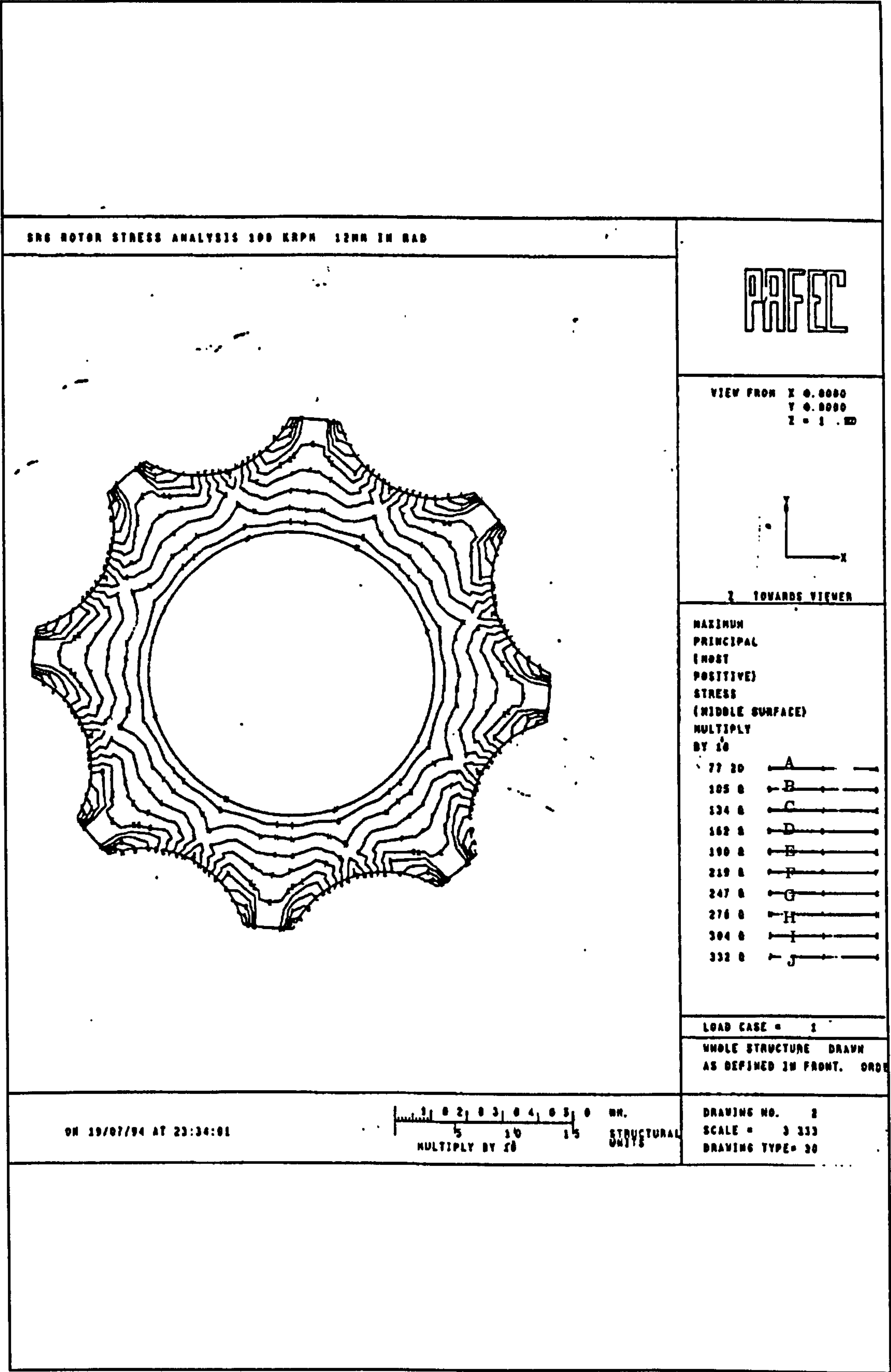


Figure 4.5: Stress analysis results at 100,000 rpm and 12 mm bore radius.

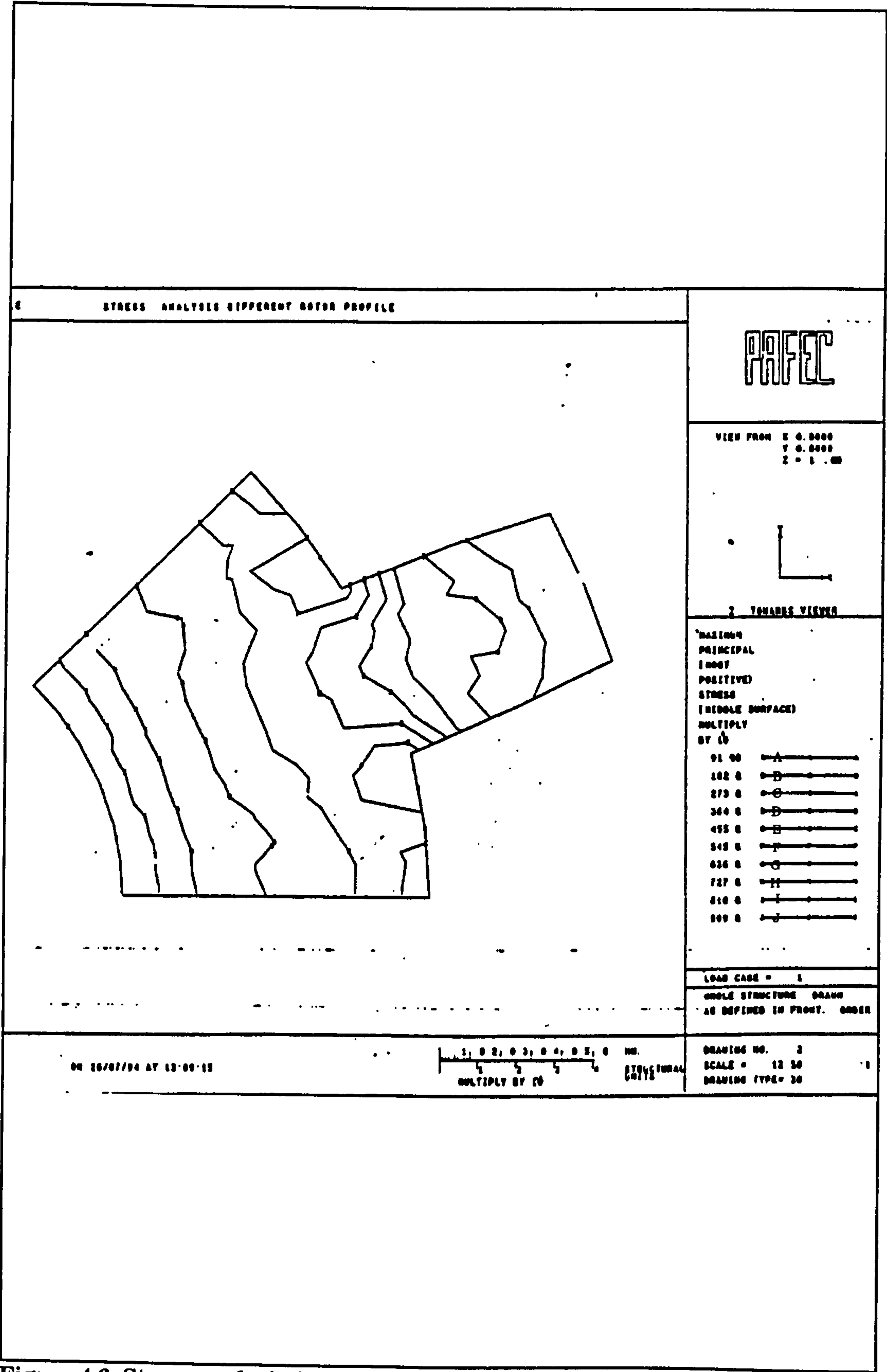


Figure 4.6: Stress analysis for different rotor profile at 180,000 rpm.

4.3 Rotor Laminations Assembly and Machining

4.3.1 Introduction

The rotor material is supplied as a strip and sold by weight. The required strip length to make a 25 mm stack of laminations was determined and given to the supplier which then provided a gift sample of 480 gm or approximately 42 m of Vitrovac® 6025. Since the thickness of the strip is 30 µm, strip width is 50 mm and stacking factor was assumed to be 0.8:

$$\text{No. of Laminations} = \frac{25 \text{ mm}}{30 \text{ } \mu\text{m}} \times 0.8 \approx 667 \quad (4.5)$$

$$\text{Required length} = 50 \text{ mm} \times 667 \approx 34 \text{ m}$$

Therefore, at least 700 of 50 mm squares are required to be cut from the strip. Initially, there was some difficulty with cutting a small strip sample using traditional methods (e.g. scissors, gelatin etc.) without shattering the edges of the cut square. This difficulty was overcome after spraying the strip with resin before cutting. The resin is required for stacking the laminations and insulating them electrically. Fortunately, it also had the advantage of hardening the strip before cutting to the required squares using scissors.

Stages of rotor preparation, which are described in this section were as follows:

- 1- Spraying the strips with resin.
- 2- Cutting to approximately 700 squares.
- 3- Stacking the squares according to an approach recommended by the manufacturer.

- 4- Clamping the stack using face plates.
- 5- Curing the block in a pre-heated oven to activate the resin.
- 6- Removing the face plates and preparing a mandrel.
- 7- Drilling a central hole, followed by reaming for accurate bore dimension.
- 8- With the mandrel in place, a programmable lathe is used to accurately position the block of laminations with respect to the cutting tool for machining away (by drilling) eight circular segments from the surface of the block to form the inter-pole spaces shown in Figure 3.8.
- 9- Reaming the pole surfaces to the correct outer diameter on the finished product with accurate concentricity in relation to the centre of the mandrel.
- 10- Taking off the mandrel and preparing a steel stub shaft with outer dimension only slightly larger than the rotor hub and inner dimension only slightly larger than the turbine shaft.
- 11- Using the formulae of the previous section, calculating the likely stresses due to the shrink, or interference, fit. Thereafter, locating the stub shaft in the rotor hub using shrink fitting.

Mounting the rotor on the turbine shaft and bearings preparation are discussed later on. Details of the rotor disk used in conjunction with a photo-detector for position sensing are given in a separate section.

4.3.2 Insulation and Assembly of Laminations

The amorphous strip was cut into about forty pieces, each is one metre long, for convenience, and attached to a working plate for spraying the resin. The resin which was selected for this purpose would serve as an adhesive for making strong bonding between the laminations and as an insulator to reduce eddy current losses. From among a wide range of adhesives, Araldite was chosen after consulting the manufacturer for the intended application. Araldite is a trade name for a range of epoxy resin adhesives.

Epoxies are attractive as adhesives for a number of reasons [154] given below, with comments on some of the practical steps taken during lamination stacking:

- 1- They exhibit a wide range in viscosity and can easily be formulated to give mixes of low viscosity with improved wetting and spreading action [155]. This was important for the application, as a very thin layer of resin is to be applied to the surface of the thin laminations. This is a reason for selecting spraying as the suitable application method.
- 2- They have high specific adhesion to metals.
- 3- They cure as adhesives with little weight loss or shrinkage during cure [155]. However, it was suggested by the manufacturer that part of the Araldite will evaporate during curing at moderate temperatures.
- 4- A wide range of curing temperatures from room temperature to 177°C. Contact pressure is usually sufficient to make a good bond. In the application, however, two clamping plates were used for the laminations stack to ensure a proper bond.

- 5- The cured resins are good electrical insulators and have good resistance to chemical and environmental degradation [155].

In order to facilitate spraying and avoid forming a relatively thick layer of varnish over the laminations, thinning liquid was needed to be mixed with the araldite and hardener. Cellulose thinners were used. The strips had to be thoroughly cleaned before spraying. Spraying gun operated by a compressor was used. Evenness of applying the mix is essential. It is an advantage that the finished un-sprayed amorphous strip features a rough surface on one of its sides. The spray is better applied to the rough surface side of the strips to help the wetting process.

The thickness of the sprayed laminations measured approximately 45 μm . Due to the non-uniform thickness of the original un-sprayed strips, the process of stacking laminations was carried out with care. In order to avoid the consequence of ending up with a stack that does not have parallel faces top and bottom, each strip of the forty sprayed strips was marked into squares of 50 mm with a dot mark on one side of the square as shown in Figure 4.7. After cutting the individual laminations, stacking was realised by rotating the dot mark in a certain direction, shown as anti-clockwise direction, for example, in Figure 4.7.

The number of squares eventually used in making the stack was approximately 550 to make a stack slightly above 25 mm in length. This margin above the required stack length was provided in order to account for the loss in length due to the evaporating resin (during curing) and the pressing procedure that will follow. Two steel face plates with holes in the corners for bolts connections were used to press the stack by tightening the bolts before curing it in a preheated oven. After taking off the clamping plates, the product is a strong solid block ready for machining.

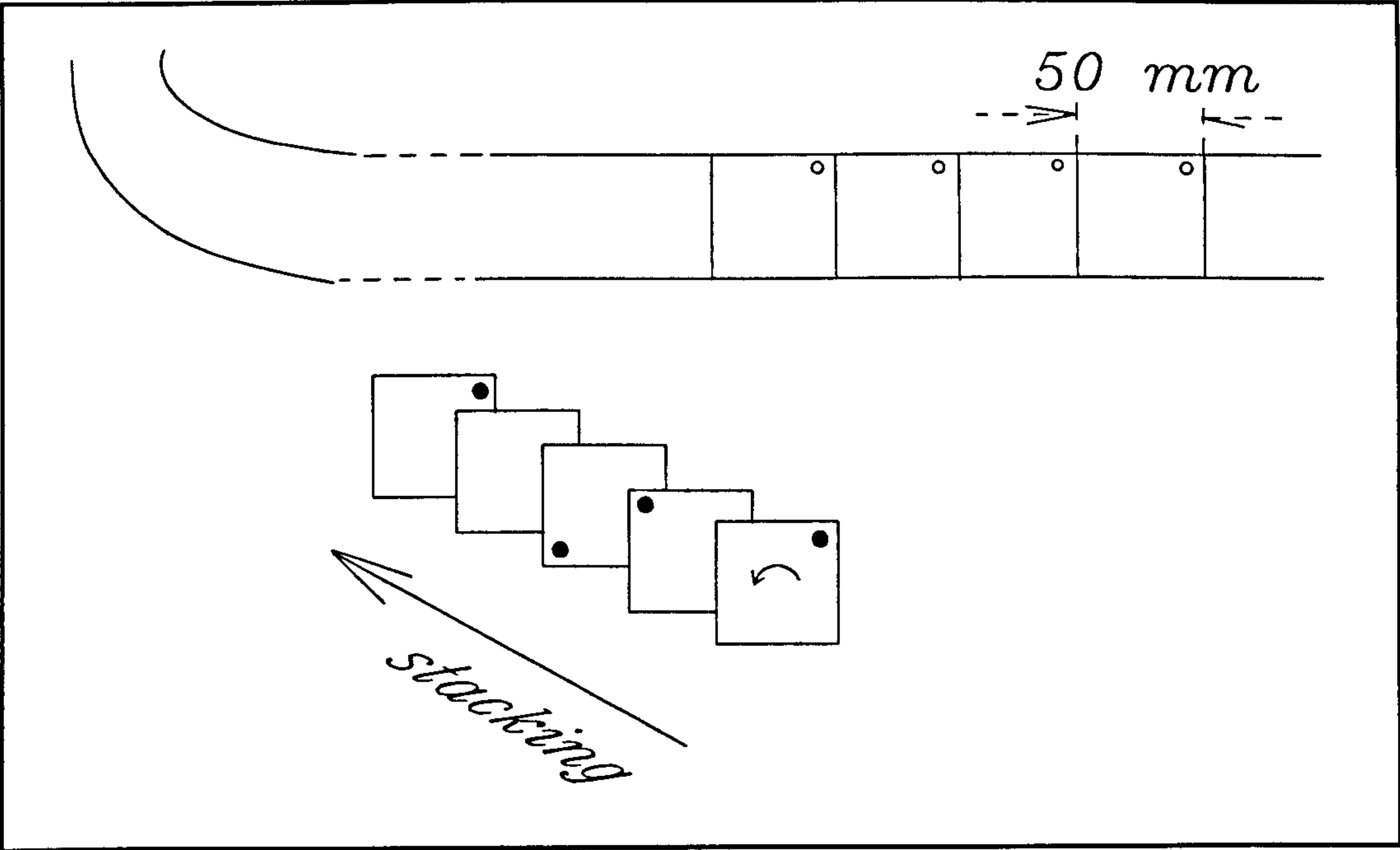


Figure 4.7: Cutting and Stacking the sprayed laminations.

4.3.3 Machining of Rotor Laminations

The actual method that was used for cutting the rotor laminations into the required profile shown in Figure 3.8 was by drilling as has been briefly introduced in section 4.3.1. Before describing the actual process that was used, it is worth mentioning the different cutting methods that were investigated (or tried) for this application.

The required job of cutting the rotor can be considered as one of the applications where metal removal by chip formation is not satisfactory or economical. Although traditional methods were eventually used for cutting the rotor and succeeded, the main reason for considering non-traditional methods first, was due to the fact that the tensile strength of the rotor material and hardness is very high. Furthermore, this is coupled with critical dimensional tolerances, (as it was aimed for $\pm 10 \mu\text{m}$ tolerance). In general, development of non-traditional machining methods was led by requirements, such as cutting a very high tensile material, cutting shapes that are too complex, aiming at better surface finish, and miniaturisation in the electronics industry [156].

The first method that was investigated was laser cutting. Laser radiation can transmit a well-directed beam which may then be focused to spot diameters comparable with the wave length of radiation [157]. The process comprises the conversion of electrical energy into light energy (beam) and then into thermal energy [156]. The process is usually automated by using NC systems to control the movement of the machine table under the laser beam. Most engineering materials can be successfully laser processed. the process is suitable for small-scale cutting operations such as slitting and drilling of very small holes. However, for the application considered here, laser cutting could only be used to cut the laminations before stacking, as the required stack exceeds the maximum thickness that can be laser-cut (which is for stainless steel, for example, is

only 5 mm [156]). In fact, the possibility of cutting the laminations before stacking was investigated first. It was not recommended by the supplier of the rotor material. The reason stems from recent experience of other users of amorphous alloys with laser cutting, (the information here was only conveyed through correspondence with the amorphous manufacturer and supplier). The experience showed that when laser cutting is used for producing laminations, very small globules or beads of the alloy are left on the cut edge of the strip. So, when stacking up the laminations, this makes the edges very tight and the central areas very loose leading to an unsatisfactory and non-uniform mechanical stability.

Chemical photo-etching was also investigated. The method is suitable for cutting laminations before stacking. It has been used successfully in connection with amorphous alloys [131][137]. A contact was made with a specialist, who did not confirm the possibility of achieving the required tolerances. As a post processing result, the procedure leaves, on the surface of the lamination, a very thin layer of insulation known as the photo-resistor, which is an advantage in terms of reducing rotor losses. The method is more suitable and economic when it is used to cut both rotor and stator laminations.

The third method was actually tried. This is the spark machining or, sometimes referred to as, electro-erosion method. It was recommended by the amorphous alloy supplier. The method may be described briefly as the removal of material by means of repetitive high frequency (in the order of 10 kHz) electric sparks which occur between the tool (i.e. the electrode) and the work-piece. In order to achieve erosion, a gap (approximately 0.025-0.05 mm) between the tool and the work-piece has to be maintained by a servo-drive. As the current is discharged across this gap, temperatures in the region of 10,000-50,000°C are developed which evaporates parts of the surrounding dielectric fluid and vaporises the metal, thus forming a small

crater on the work surface [156]. When precision band sawing hard materials, a fine wire wound onto two reels is used, with the dielectric fluid flooding into the work. To prevent wire from breaking and wearing it is continually wound from one reel to the other.

It is possible with spark machining to cut a material after it has been hardened [156]. Thus the laminations block of the rotor, which was fabricated earlier and cured, was prepared in order to experimentally investigate the possibility of having it spark-machined. Wire erosion, described above, was used as the cutting tool. Cutting was not realised due to repetitive wire breaking. Lack of time prevented investigating the problem any further or changing the whole wire with different tool at different size. It was eventually decided to resort to a more traditional method of cutting; chip removal by drilling.

It must be noted that when using traditional methods of cutting, it is not impossible to machine a high tensile material with good precision and critical tolerances, particularly, if well-experienced operator handles the job. The diametric precision required by this job is within 0.01 mm for the central hole and concentricity of outer surface with the centre. A mandrel was prepared after boring the inside of the rotor. The most accurate holes are produced by the following sequence of operations [158]:

- Centring
- Drilling
- Boring
- Reaming

The mandrel is a type of work-holding devices used with machine tools. It is placed inside hollow or tubular workpieces and is used to hold the work-piece that requires machining on both ends or on their cylindrical surface [158]. The assembly was bolted with a mandrel of the gang type. Outer surface finish was finally reamed to the required dimension.

4.3.4 Preparation of the Stub Shaft and Shrink Fit to Laminations

The stub shaft is a hollow shaft made of steel in order to couple the rotor to the shaft of the turbine. The arrangement of the rotor laminations and the stub shaft is known as a hub-shaft fitting. As this shaft is small in dimension, 16 mm outer diameter, it is not expected to be critical in terms of centrifugal stresses. However, it is critical in terms of bore and outer surface tolerances. The latter being more important. It is also required to be longer than the laminations stack, about 33 mm. The arrangement of the rotor laminations and the stub shaft on the turbine shaft is shown schematically in Figure 4.8. Dimensions are in mm.

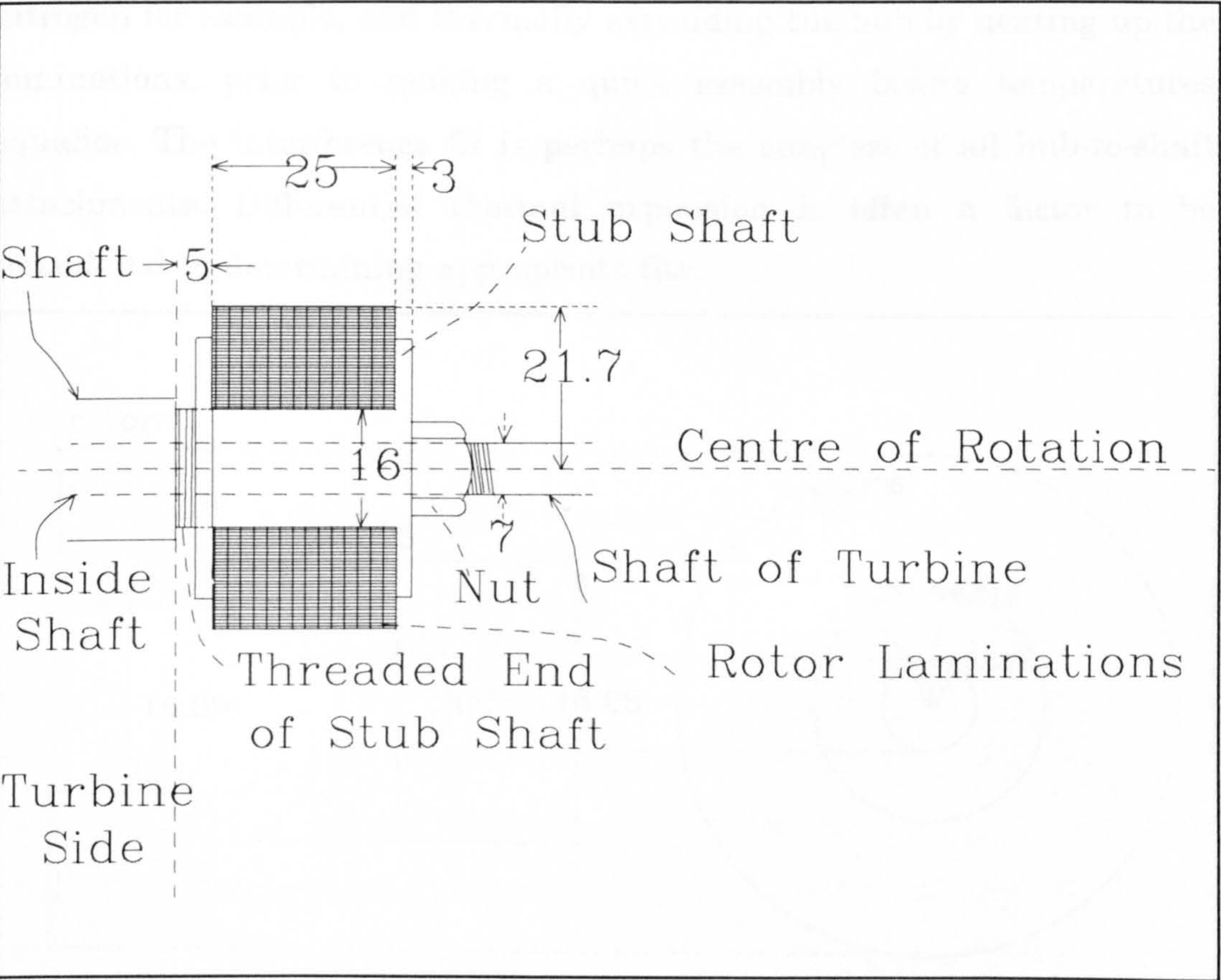


Figure 4.8: Rotor laminations and stub shaft assembly to turbine.

The arrangement shows the stub shaft with a cap for laminations support from one side, on the right, and a face end, an inside threaded steel ring, pressed over the laminations from the other. The stub shaft side near the turbine ends with a left hand thread for laminations support on

the left hand side. The stub shaft itself slides over the original shaft of the turbine which is 7 mm in diameter and ends with a left hand thread and a nut to join the assembly to together.

The inner diameter of the hollow shaft is made 7.03 mm to provide a small clearance for slide fitting. The outer diameter is 16.05 mm. Tolerance for these figures is ± 0.01 mm. Since the laminations bore was reamed at 16.00 mm (with the same tolerance of ± 0.01 mm), the fitting of hub and the shaft would result in a negative clearance, or an interference fit, achieved by thermally contracting the shaft, by cooling it in liquid nitrogen for example, and thermally expanding the hub by heating up the laminations, prior to making a quick assembly before temperatures equalise. The interference fit is perhaps the simplest of all hub-to-shaft attachments. Differential thermal expansion is often a factor to be considered in determining appropriate fits.

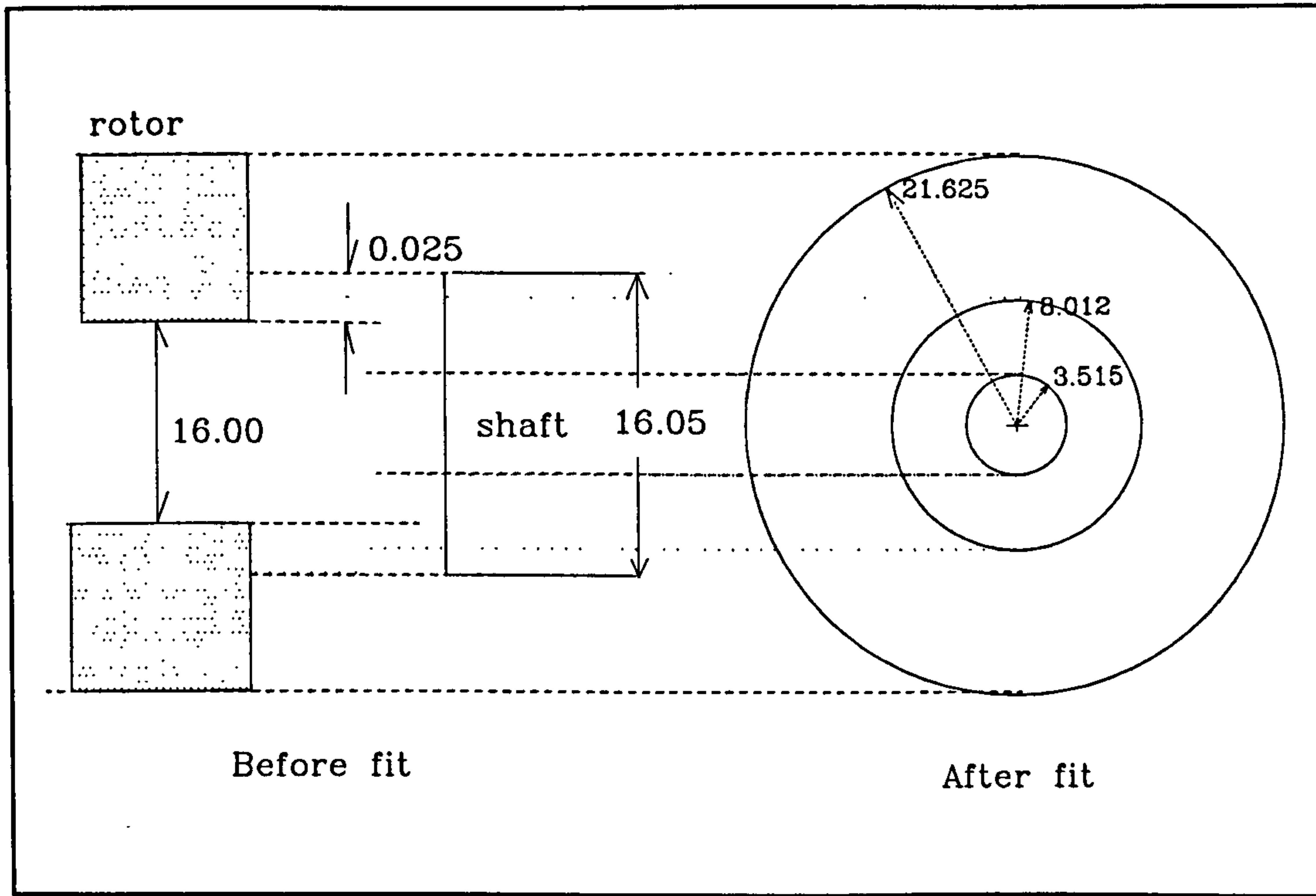


Figure 4.9: Shaft-Hub dimensions. Exaggerated dimensions before assembly. Front view after shrink fit.

Figure 4.9 shows the shaft and hub dimensions before and after the fit. The radial interference dimension δ is 25 μm . By considering the machining tolerances of both the laminations and the stub shaft, the δ dimension could approximately be within the range of 15-35 μm . However, on the grounds of convincing measurements taken by an accurate digital micrometer, after machining, a realistic assumption was made for δ to be no more than 25 μm . Another assumption is that the required clearance for fitting immediately after shrinking the shaft and expanding the hub is about 3-5 μm . This clearance is quite small and would require a push fit type. This sort of fit allows assembly by hand or with light blows [159]. Then, a total diametrical displacement of 50+3 μm is to be obtained from the expanding and the shrinking processes together. For the hub, the thermal coefficient of expansion is $12.5 \times 10^{-6} / \text{K}$, and it is to be heated on a pan at up to 100°C. A uniform heating of the hub increases all its dimensions. Diametrical increase on the hub would be:

$$16\text{mm} \times 12.5 \times 10^{-6} (100-20) = 16 \mu\text{m}$$

The thermal coefficient of the steel shaft is taken as $11 \times 10^{-6} / \text{K}$, and it is to be cooled in liquid nitrogen down to -194°C. The shrinkage in the shaft diameter is:

$$16.05 \text{ mm} \times 11 \times 10^{-6} (20+194) = 38 \mu\text{m}$$

This gives a total clearance of 4 μm if a radial displacement of 25 μm is assumed. The process must be very quick due to the use of liquid nitrogen instead of liquid helium (-271°C). The latter would give ample time and clearances and would certainly result in a more convenient procedure. However, liquid helium was not available at the time.

Upon simultaneous heating of the rotor and cooling of the shaft, the rotor was displayed on a plate of a pressing machine while the shaft was very quickly taken out of the liquid to be pressed by (one push) of light load

into the hub. In fact the process went on as expected with the need of a light blow from the pressing machine. This indicates that the resultant δ dimension obtained for the laminations and the stub shaft is closer to the 15-25 μm range rather than the higher range.

The stresses caused by the interference fit would be determined by finding the pressure P between the two metals. This pressure is known as the contact pressure. A loose fit, or ineffective fit, would result when P is zero. The formula for finding P depends on the value of the radial interference δ . Thus for the hollow shaft the formula is [159]:

$$P = \frac{\delta/2b}{\frac{1}{E_{shaft}}\left(\frac{b^2+a^2}{b^2-a^2} - \nu\right) + \frac{1}{E_{hub}}\left(\frac{c^2+b^2}{c^2-b^2} + \nu\right)} \quad (4.7)$$

Where a , b , and c are the radii of, inner shaft, outer shaft and outer rotor respectively. In this formula, the difference in length between the shaft and the lamination stack has been neglected, though it has some effect of increasing stresses over the side ends of the hub.

Maximum stresses on both the shaft and the rotor at the interference fit are determined from the following formula:

$$\sigma_{shaft} = P \frac{b^2 + a^2}{b^2 - a^2} = 140 \text{ N/mm}^2 \quad (4.8)$$

Where this value represents the tangential stress at the outer diameter of the stub shaft. For the rotor,

$$\sigma_{hub} = P \frac{c^2 + b^2}{c^2 - b^2} = 125 \text{ N/mm}^2 \quad (4.9)$$

These stresses are residual stresses and should be combined with the centrifugal stresses of the dynamic situation. Also, the resultant radial displacements during rotation (due to stresses, as found earlier) must be less than the radial interference, otherwise there will be a loose fit

situation. The speed at which this happens is determined from the formula for displacement due to centrifugal stresses in the hub and shaft:

$$U_{hub} = \omega^2 b \rho \left[\frac{(1-\nu)b^2 + (3+\nu)c^2}{4E_{hub}} \right]$$

$$U_{shaft} = \omega^2 a \rho \left[\frac{(1-\nu)a^2 + (3+\nu)b^2}{4E_{shaft}} \right]$$
(4.10)

There rotor bore will also suffer thermal displacement due to the expansion resulting from temperature rise during operation. An assumption is made for temperature rise ΔT to be 50°C . Then a small radial displacement of $5 \mu\text{m}$ will result. This is added to the displacement due to mechanical stresses in order to estimate the speed at which the fit becomes ineffective.

The speed at which the rotor becomes loose is when:

$$U_{hub} - U_{shaft} = \delta$$
(4.11)

Therefore, the maximum allowable speed for operating the SRG is taken to be 90,000 rpm as is explained below.

By substituting for δ for the worst case of $15 \mu\text{m}$, ω is found to be 93,300 rpm. However, the rotor in these equations has been assumed as a rotating disk, and this may under-estimate the allowable speed. From the finite element FE solution and the results shown in Table 4.1 the speed at which radial displacement equals the minimum radial interference of the fit (of $15 \mu\text{m}$) is 120,000 rpm. In order to take into account the thermal expansion of the rotor during rotation, the maximum radial displacement allowed will be considered as $10 \mu\text{m}$. This corresponds to a rotational speed of even less than 100,000 rpm (95,000 rpm as in Table 4.2). The results of the maximum speed and maximum residual stresses considering allowable displacement δ as 10, 15, 25, and $35 \mu\text{m}$ are given in Table 4.2. The speed that gives a loose fit situation is determined either by applying equation

(4.11), or, more precisely, by running the finite element programme. Both results of finding the speed are given. Maximum residual stresses at the rotor bore (from equation (4.9)), added to the maximum stress in the rotor due to centrifugal loading (from the finite element solution of the correspondent speed), are also given.

$\delta \text{ }\mu\text{m}$	$\omega \text{ rpm}$	$\omega \text{ (FE) rpm}$	$\sigma_{\text{hub}} \text{ N/mm}^2$
10	76,200	95,000	323
15	93,300	120,000	511.3
25	120,500	150,000	819
35	142,600	180,000	1173

Table 4.2: Results for maximum allowed speeds and total maximum stresses for assumed cases of radial interference.

The maximum allowable speed is then taken as 90,000 rpm by considering the worst case of $\delta = 10 \text{ }\mu\text{m}$ (including the effect of rotor expansion during operation) and allowing some safety margin on the figures of the FE analysis above.

4.4 Stator Core Machining and preparation

The moulding of ferrite cores into a required shape is quite simple and cost effective. However, if further machining is required for surface or bore finishing, then ferrite machining is not straightforward. Moreover, if very tight tolerances were desired, as is the case with this project, then the job will be particularly demanding.

Due to the physical nature of ferrites, any subsequent machining of the resulting product from the ferrite making process must be by grinding [157]. With bore tolerances for centralising the inner diameter with the centre of the core being in the order of at least ± 0.03 mm, the abrasive used in the grinding wheel must be very strong.

Abrasives are considerably harder than cutting-tool materials. They allow removal of very small quantities of material from the work-piece surface. Consequently, very fine surface finish and dimensional accuracy can be obtained [158]. Diamond, the hardest substance known,

and cubic boron nitride CBN, are considered super-abrasives. Diamond grinding was then selected for the job.

An appropriate way of handling ferrite during machining is by preparing a die container in which the ferrite core is glued with very strong adhesive. The die container is a short tube of heavy steel appropriately designed to fit into the grinding machine. Each ferrite core ring was handled separately. The two rings were then placed (using glue bonding) into a thick steel tube. This tube was machined to fit on the turbine disk. It was provided with a step at one end and four holes. Special arrangements were made on the tube holes and the turbine disk surface to ensure concentricity of the stator centre with the turbine shaft when making the overall assembly. This will be discussed further in chapter 6.

4.6 Rotor Position Sensor, Mechanical Details

This section concerns the mechanical details of the rotor position sensor. The type of position sensor that was selected is a high speed photo detector. These sensors are widely used in conjunction with SR machines. The requirements of the mechanical job are as follows:

- 1- To prepare a disk of appropriate size made of suitable material considering the high rotational speeds.
- 2- To drill as many small holes or slots in the disk as there are rotor poles. Depending on the electronic circuit, one hole might be sufficient but will impose certain requirements on the electronics.
- 3- To prepare an arrangement for adjusting the position of the opto-device radially and tangentially with regard to a fixed point on the stator. This arrangement is fixed on the steel tube which contains the stator.

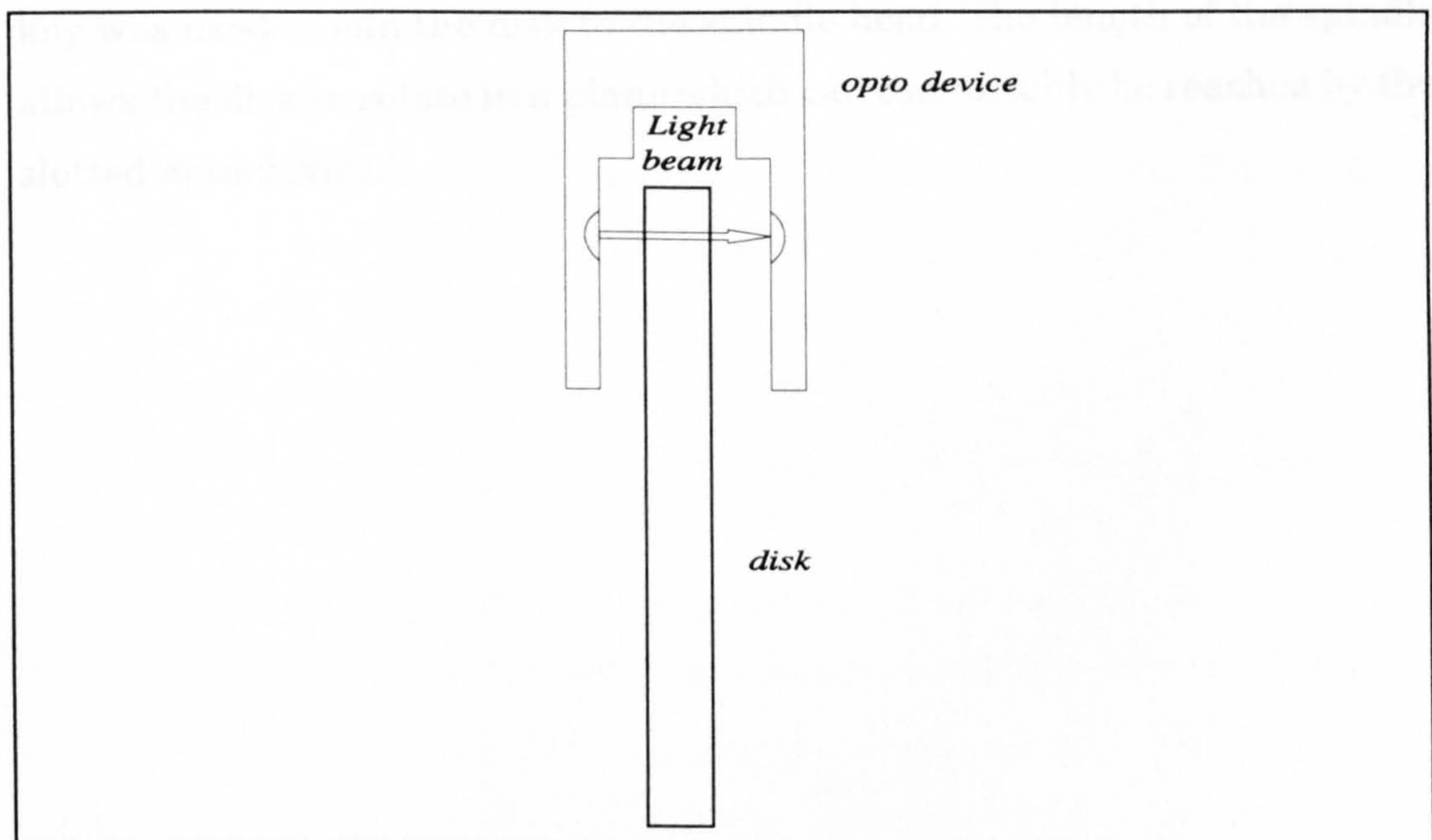


Figure 4.10: Opto-device and rotating disk arrangement.

The opto-device is slotted, as shown in Figure 4.10. One side is a light emitter and the other is a receiver. The output of the device will be "high" upon receiving light on the receiver side. Through this slot the disk holes pass as the rotor rotates, thereby cutting the light beam and generating a short pulse only when light passes through a hole.

The material that was selected for making the disk is an aluminum based alloy with a percentage of copper and small percentage of magnesium. The alloy has a trade name, dural, and is easily available and cheap. It is often supplied as sheets. A sheet with a nominal thickness of 0.914 mm (SWG 20) was obtained, from which a disk with the dimensions shown in Figure 4.11 was made. Dural offers a tensile strength of 380-500 N/mm². However, it is quite light as its density is only 2.8 gm/cm³. It is therefore suitable for high speed rotation, bearing in mind its outer diameter of 25 mm is significantly less than the rotor diameter of about 42 mm.

The disk was connected to the shaft of the turbine using an inside threaded spindle which is 24.5 mm long and 10 mm in diameter. A shaft key was used to join the disk to the spindle head. The length of the spindle allows the disk to rotate in a plane which can comfortably be reached by the slotted opto-device.

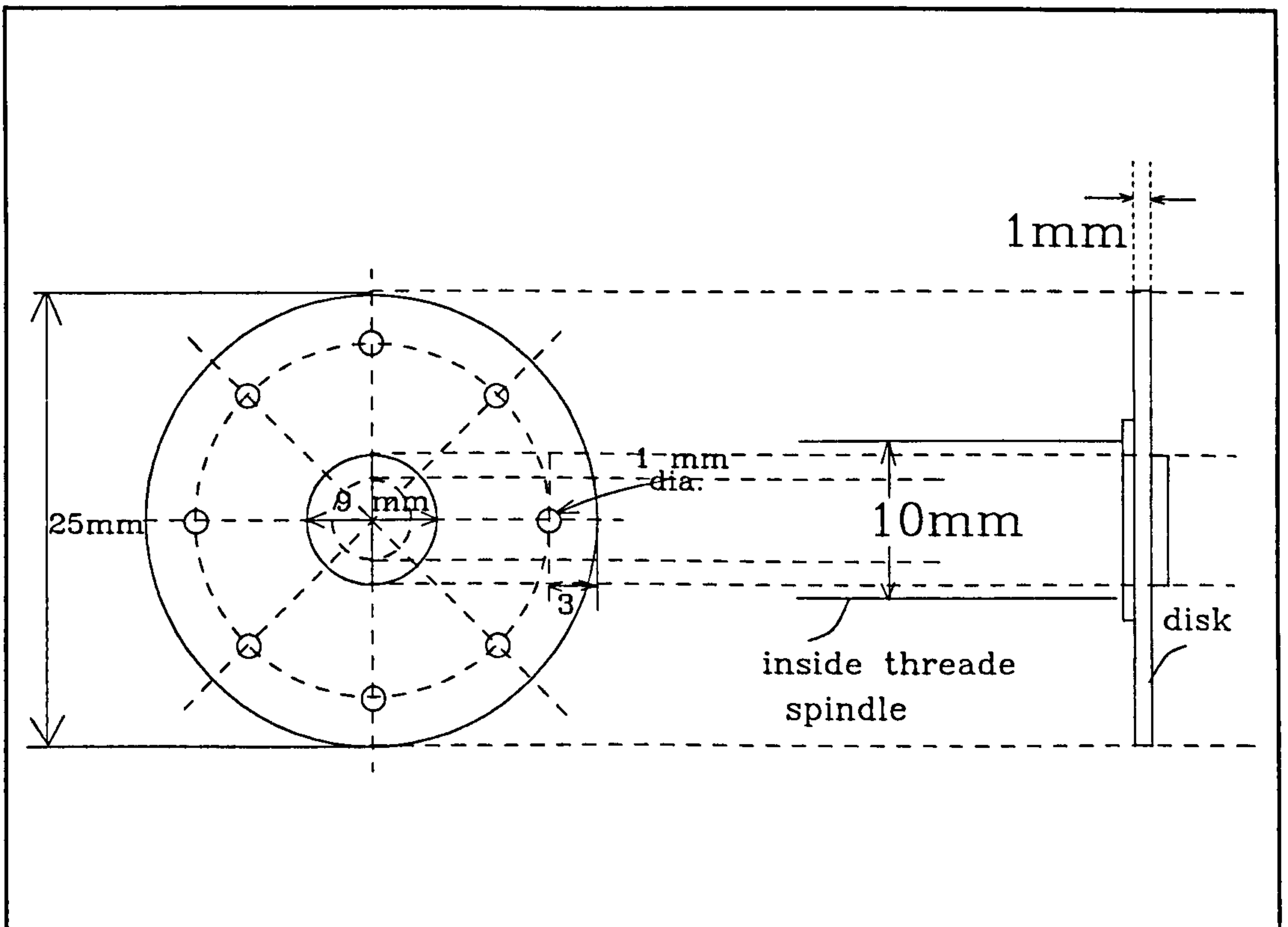


Figure 4.11: Dimensions for rotor position sensor disk.

4.7 Conclusion

The mechanical design of the SRG, taking into consideration the aspect of stresses caused by high speed operation has been discussed. A discussion of the finite element analysis which was used to determine stresses on the profiled rotor ensured the appropriate selection of the amorphous metal, from which the rotor is made, as well as the assurance of the mechanical stability of the rotor as has been designed in chapter 3.

The machining of the varnished stack of laminations has been described in some detail. Drilling was used to profile the rotor according to the required shape followed by reaming of the pole surfaces, however, other methods which were tried or investigated have also been discussed.

The interference fit for assembling the rotor to the turbine shaft, by shrink fitting the rotor to a steel stub shaft has been discussed with calculations for the residual stresses and radial interferences. The maximum allowable speed resulting from this discussion has been found to be 90,000 rpm.

Diamond grinding for machining the stator ferrite core has also been discussed. Finally, the mechanical details of the rotor position sensor have been presented.

The photo of Figure 4.12 shows the amorphous iron strip from which the rotor is cut along side the stator ferrite core. The steel tube is also shown where one ferrite ring (un-wound) is placed inside. The turbine, before assembly (which will be discussed in chapter 6) is shown. The photo of Figure 4.13 shows the stator core (un-wound) inside the steel tube and its assembly with the turbine disk. Photos in Figures 4.13 and 4.14 illustrate the wound stator core, the rotor, and the position sensor disk before assembly.

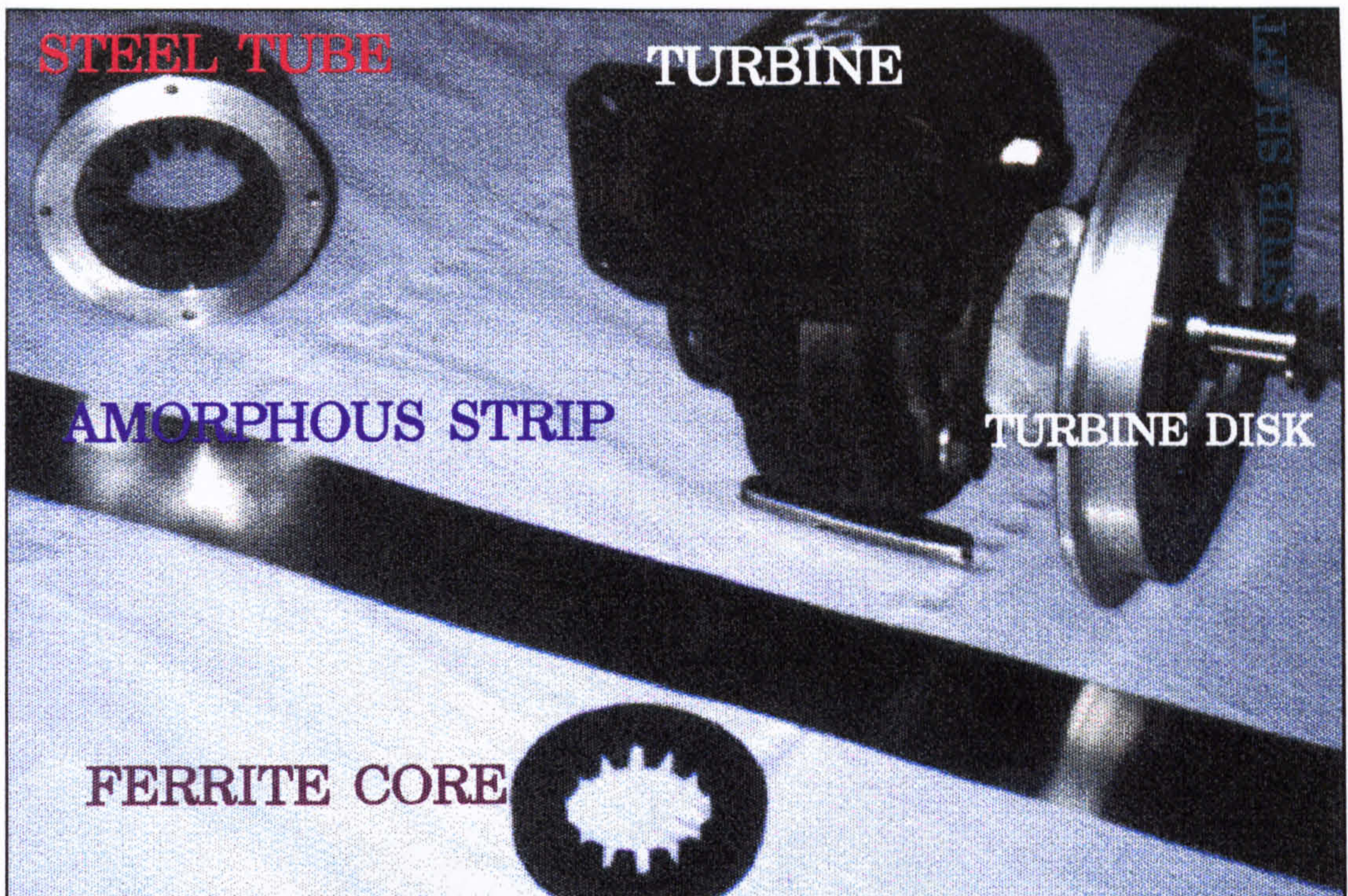


Figure 4.12: Photo showing the amorphous iron strip, the stator ferrite core, the steel tube, and the turbine before assembly.

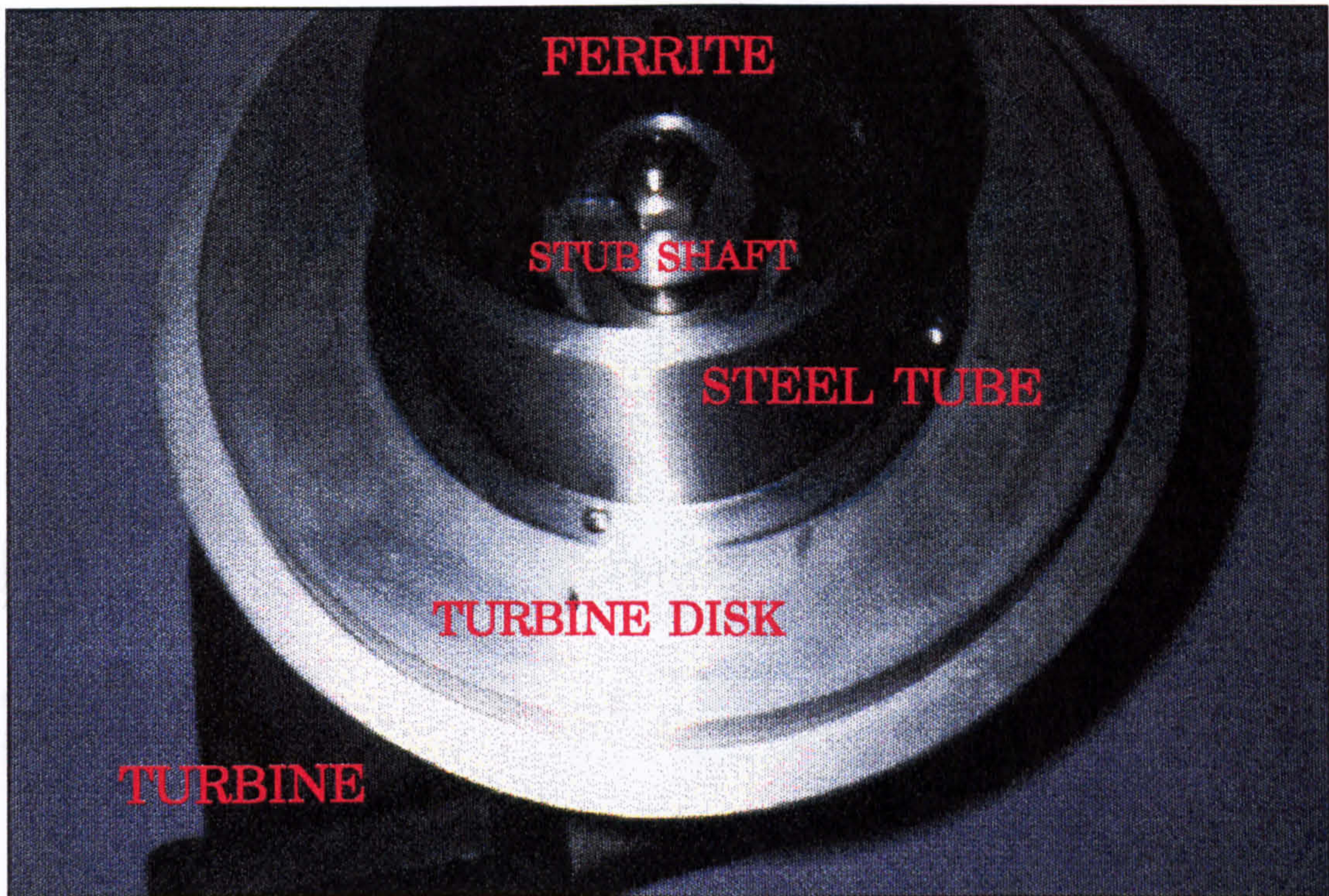


Figure 4.13: Photo showing the stator core inside the steel tube and its assembly to the air turbine.

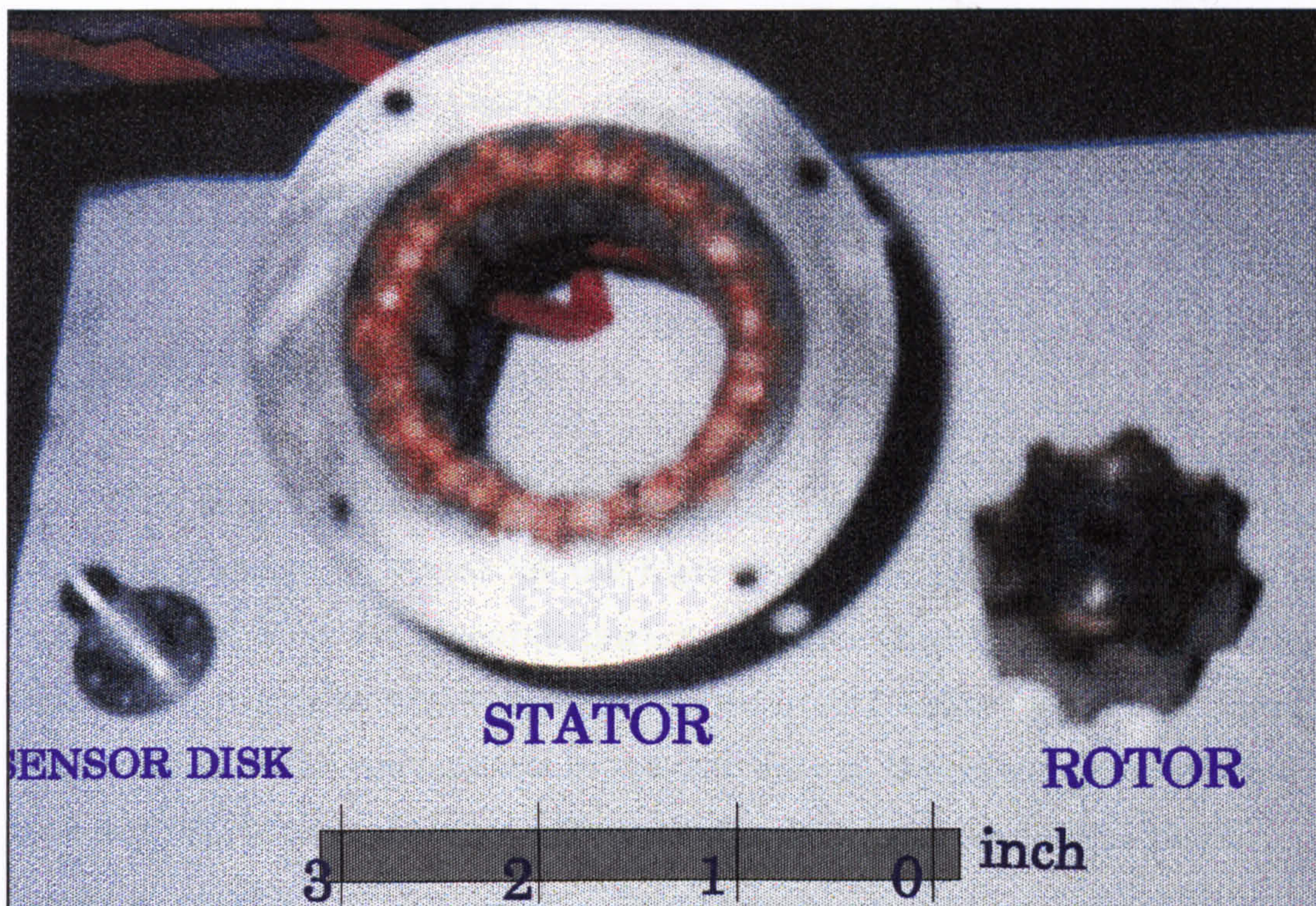


Figure 4.14: Photo-1; The stator, the rotor, and the sensor disk.

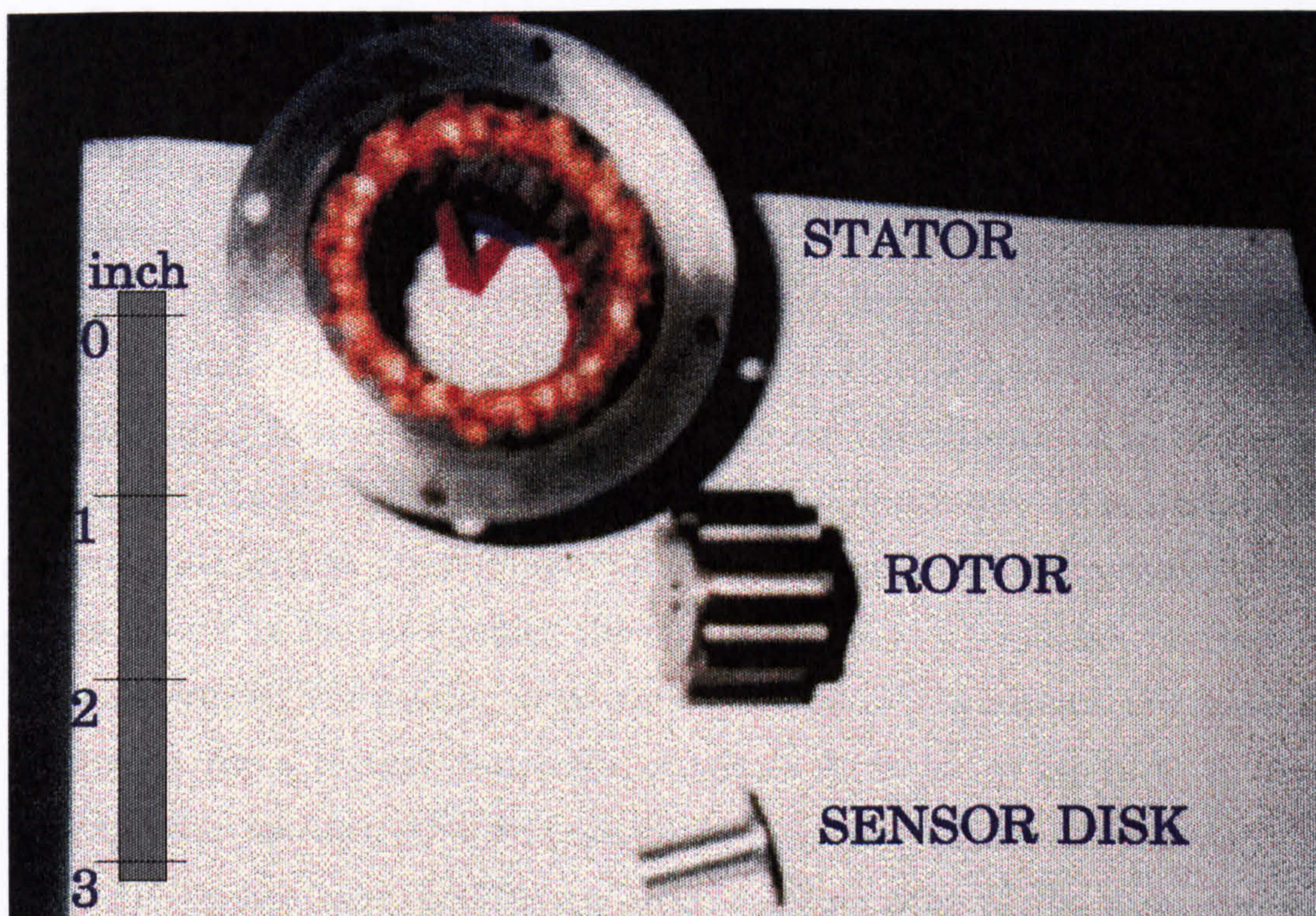


Figure 4.15: Photo-2; The stator, the rotor, and the sensor disk.

CHAPTER FIVE

THE POWER CONVERTER AND ELECTRONIC CONTROLLER

5.1 Introduction

The aim of this chapter is to introduce the basic choices for the design of a power converter for the high speed SRG. Since the machine is designed and built for research purposes rather than for optimum power conversion, a simple and versatile converter and controller are required. The function of the converter is to operate only in the single pulse mode by providing the phase windings with excitation pulses at predetermined firing angles θ_{dly} and θ_{com} .

5.2 Selection of Power Converter Topology

The power converter shown in Figure 5.1 was selected for this project. The circuit is chosen in order to attain simplicity of the power electronics and drive circuits, and flexibility of the power supply. The converter also offers the main advantage of utilising only one switching device per phase. The switching devices are power MOSFETs, and are discussed in the next section. The source terminals of both transistors are connected to a common ground, thus further simplifying the drive requirements. Another advantage of the circuit is that it enables the output (sink or C_o) voltage to exceed, upon generation, the source, or excitation, voltage V_e . It is however required to provide for a voltage regulator to adjust V_o to be equal to V_e in the experimental set-up as this represents the more usual mode of operation for most SR applications. Unlike the basic configuration of the dual supply converter, this circuit enables any phase number to be used. It is therefore

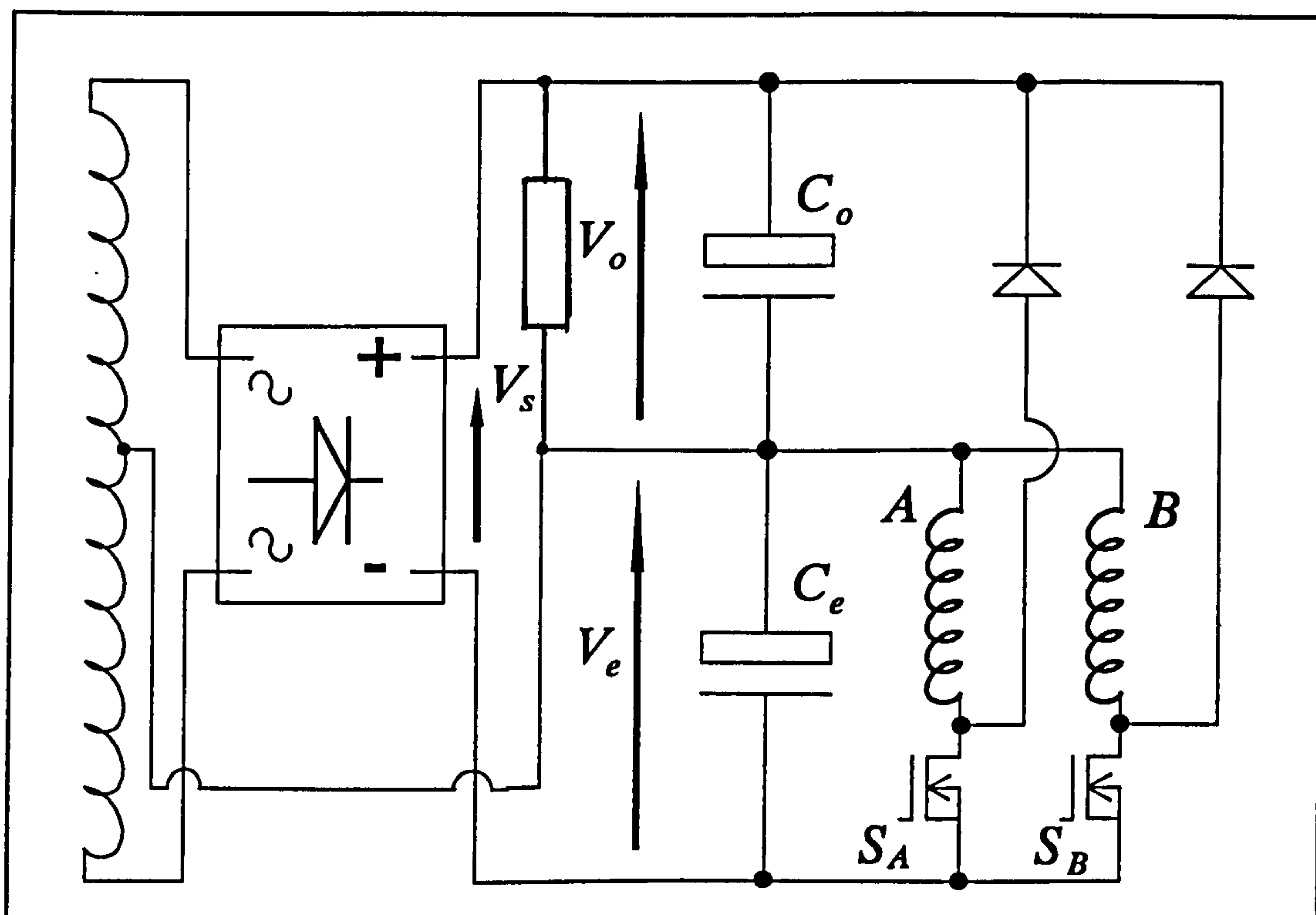


Figure 5.1: Selected supply circuit for the high speed SRG.

acting more like a C-dump converter but without the resonant circuit and the chopper. The circuit is fed from the mains through a single phase variac and a centre tap isolation transformer. In Figure 5.1 only the secondary winding of this transformer is shown. During tests, the circuit will continuously be excited from the supply with the initial output voltage set to equal the excitation voltage. However, the converter could easily be modified by adding a transistor chopper and a circuit (diode and inductor) to the upper capacitor to form a resonant circuit in order to transfer part of the generated energy in C_o to excite C_e .

The circuit does not provide for returning energy to the source, rather, it dissipates the output power in a power resistor across C_o which represents an electrical load for the generator. An advantage of this circuit, however, is that it enables the separate measurement of the power that is taken from the supply and used for excitation, as will be shown in chapter 7, and the power that appears on the output load. The

difference between these two is the net generated power. The benefit of separate measurement of the input electric power and the output power is to investigate the effectiveness of power conversion inside the SRG. Although the circuit is suitable for testing purposes, in real applications a more realistic alternative circuit would be a split-supply converter, or a C-dump converter. A classic converter utilising a two-switch per-phase may also be considered as a good alternative. Some of these alternatives are discussed below.

A dual supply circuit is shown in Figure 5.2, where again a two-phase machine is considered. The circuit allows for energy return to the supply, provided that a further controlled bridge rectifier is used when supplying from a.c. mains. With reference to Figure 5.2, upon exciting phase A by turning S_A on, current is drawn from the top half supply C_A and returned

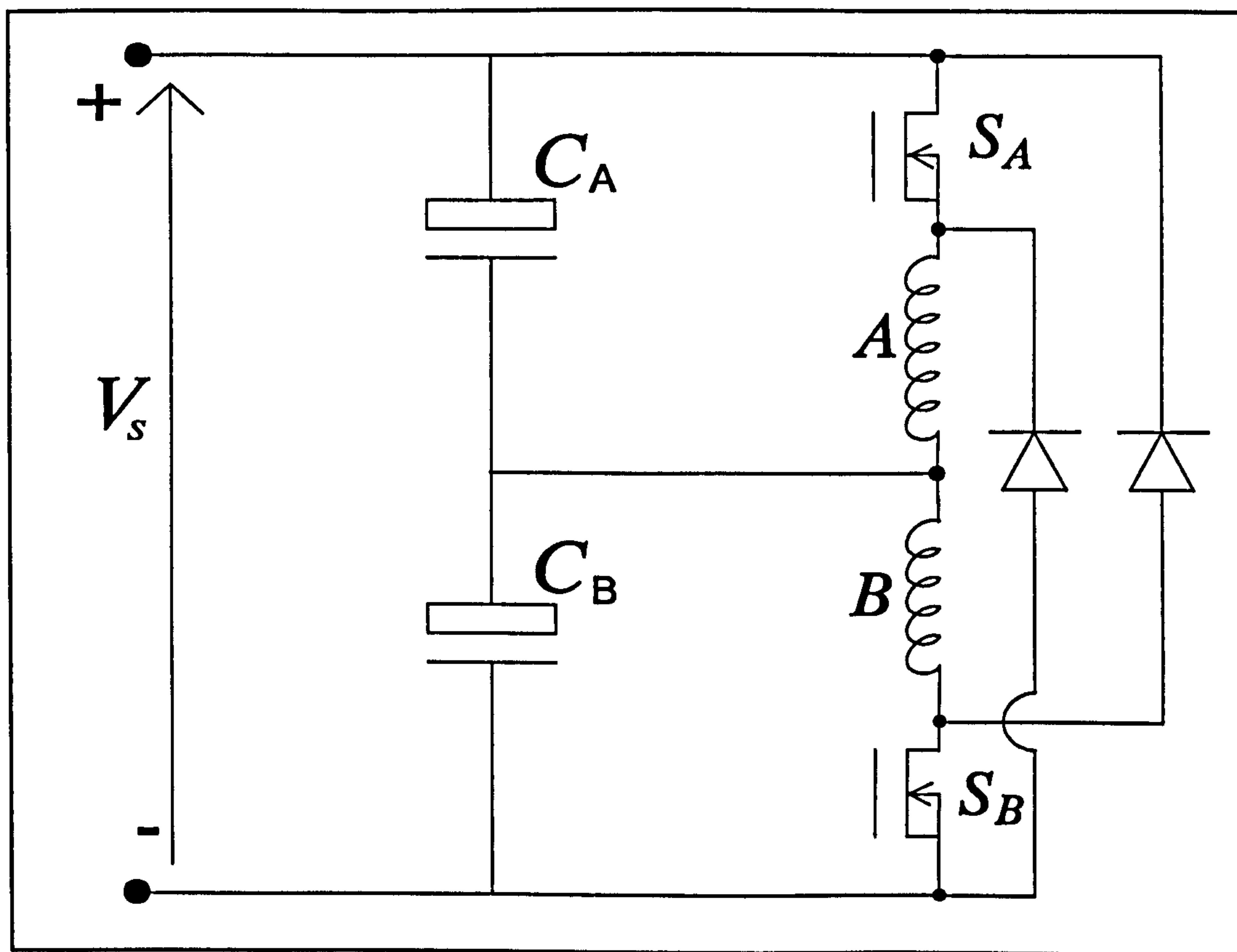


Figure 5.2: Basic configuration of the split supply converter.

to the bottom half supply C_B when S_A is turned off. The converse applies for phase B. In this case if the capacitor voltages are to remain stable at half V_s , then the mean current of the phases should be equal. This circuit is therefore only feasible with even number of phases and suitable for single pulse control for generator applications. Under chopping control, however, the capacitor mid-point is not self-regulating. Phase windings A and B are rated for the capacitor voltage, but each power switch must be rated for full supply voltage, V_s .

Other unipolar converters (with one-switch-per phase) such as the bifilar winding and the C-dump, were not considered suitable for the application despite their simplicity. As for the first, it was considered inappropriate due to extra copper and poor thermal management. The stress on the switching device at turn-off is also a negative attribute of the bifilar converter. As for the C-dump converter, it is not strictly a one-switch-per-phase because of the need for addition of a chopper transistor.

5.3 Selection of The Switching Components

For the SRG, the excitation voltage V_e , in Figure 5.1, is nominally selected as 50 V. This is suitable for applications such as generators for ground vehicles. The winding may be excited at more than this voltage, but there would be no benefit in raising the voltage beyond 120 V as was shown in chapter 3, Table 3.2. The MOSFET is considered as the optimum choice for low power applications up to 2-3 kW [17]. It is characterised by simple gate driving and snubberless operation, and can therefore also be considered as the most economic choice for this application. As for the switching speed, the maximum phase switching frequency at 100,000 rpm is only 13.34 KHz, which is also suitable for the MOSFET transistor. The results of the model in chapter 3 showed that the peak current would not exceed 30 A for a rated r.m.s. phase current of about 10 A. A power MOSFET with 50 A peak and 18 A continuous rating was selected. The conducting losses of power MOSFETs can tend to be high. However, the selected transistor, IRF640, features a low, 0.18Ω , R_{ds-on} which ensures reasonable transistor losses of less than 10 W per phase at the maximum expected transistor current of about 7 A r.m.s. The power switch should be rated for $V_o + V_e$ for the circuit of Figure 5.1. The 200 V rating of the IRF640 switch was found suitable for the application. To protect the transistors and to ensure low conduction losses (since R_{ds-on} is proportional to junction temperature), the transistor of each phase is mounted on a separate heat sink along with the power diode of the relevant phase. Power diode losses are not expected to have an impact on the thermal capability of the heat sink to dissipate the heat from the transistor. Simple calculations which led to the selection of $1.1 ^\circ\text{K/W}$ matt black heat sink are given in Appendix A5.1.

A fast recovery BYT12P-800 diode with 12 A continuous rating and 800 V was selected. The continuous current rating should be slightly higher than that of the power transistor; 12 A is sufficient. The peak current will

exceed that of the transistor in generator applications.

Two electrolytic capacitors with 100 V rating are suitable for the power converter. A suitable value of each capacitor was selected as 10,000 μF capable of 28 A r.m.s for an estimated capacitor r.m.s current of 3 A.

5.4 Power Circuit Layout and Assembly

The main concern for the layout of the power converter is to reduce the effects of stray inductances thereby reducing voltage spikes and stresses on the power switches. This requires the connection of the power capacitors to the phase winding and the power switches to be as short as possible. One possible layout for the assembly was considered and is given schematically in Figure 5.3. The power circuit was kept very close to the machine to avoid using long leads for connections. Photo for the actual layout of the power circuit and the SR machine is given in Figure 5.4.

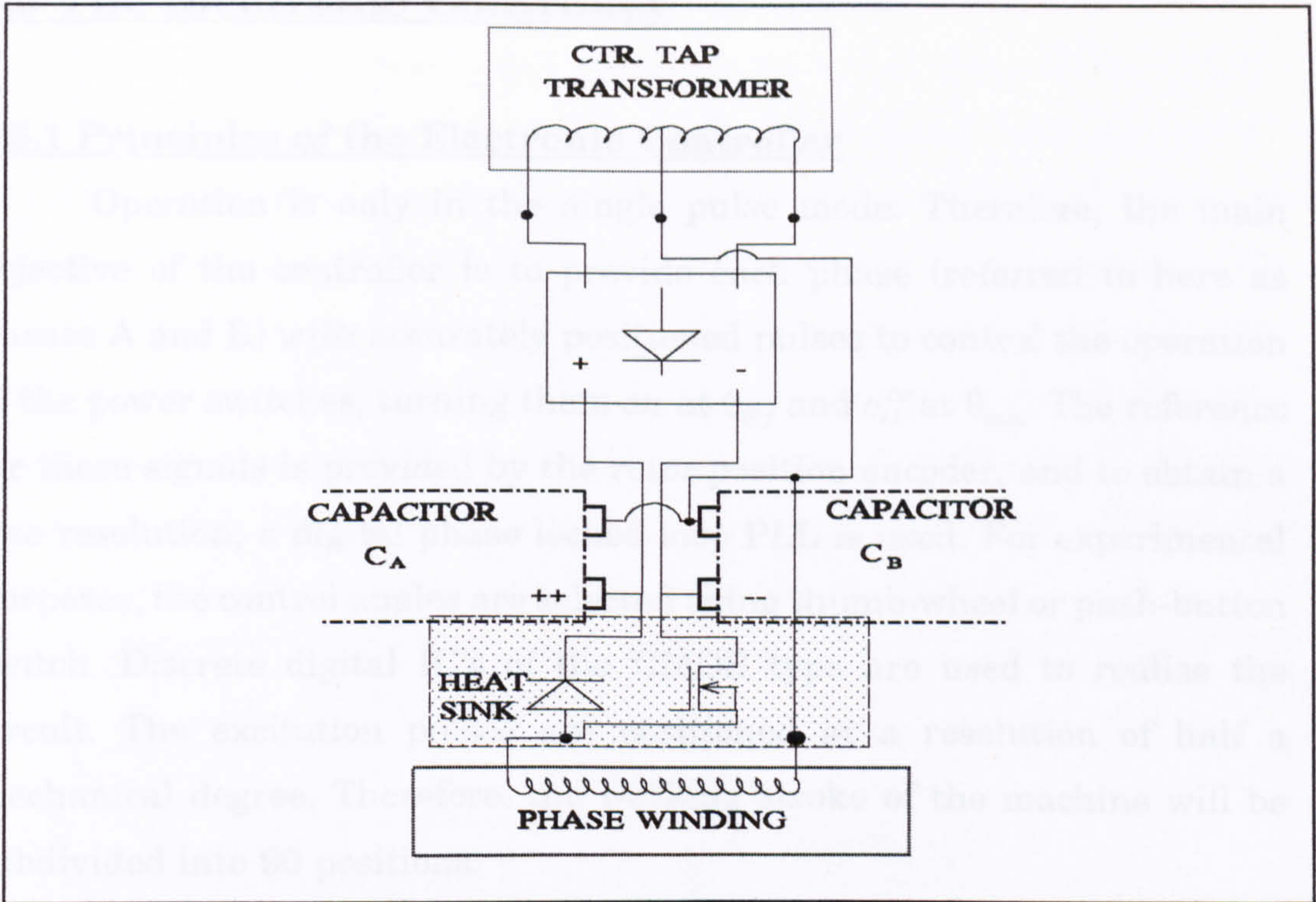


Figure 5.3: Power circuit layout for reducing stray inductance. Connections to one phase winding are shown.

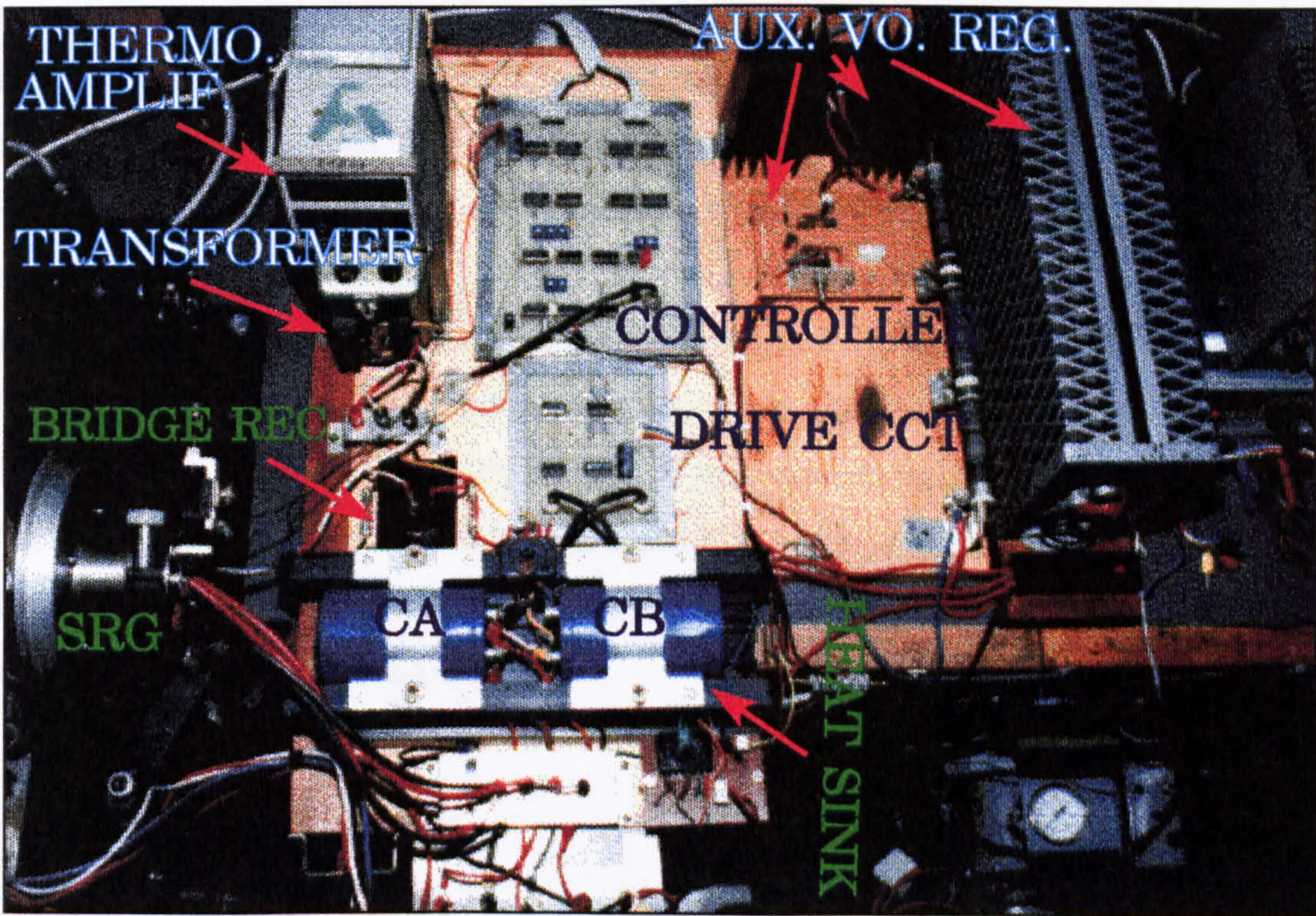


Figure 5.4: Photo for the power circuit layout.

5.5 The Electronic Controller

5.5.1 Principles of the Electronic Controller

Operation is only in the single pulse mode. Therefore, the main objective of the controller is to provide each phase (referred to here as phases A and B) with accurately positioned pulses to control the operation of the power switches, turning them *on* at θ_{dly} and *off* at θ_{com} . The reference for these signals is provided by the rotor position encoder, and to obtain a fine resolution, a digital phase locked loop PLL is used. For experimental purposes, the control angles are selected using thumb-wheel or push-button switch. Discrete digital IC's of the CMOS type are used to realise the circuit. The excitation pulses are positioned at a resolution of half a mechanical degree. Therefore, the working stroke of the machine will be subdivided into 90 positions.

Current sensing is needed for the purpose of measurement of losses, as will be seen in chapter 7, rather than for control purposes. Since the generator is not going to be operated at low speeds, chopping (current) control is not required. However, some form of protection is still needed when the speed of the driving turbine is suddenly reduced or lost for any reason or when excitation is raised before attaining sufficiently high speed for single pulse operation. Fuse protection might help to protect the winding of the machine by cutting off excitation from the mains. However, for a proper design the power switch will need an over-current protection circuit. One circuit was designed, built and tested. It worked during the first stage of testing but later found to influence the normal operation of the converter. It was consequently discarded.

5.5.2 Overall Control Schematic and Operation

Two controllers were used and are described in this section (Figures 5.5 and 5.7). Measurement results were taken using both controllers. However, most of the results were taken while using the second controller, as it uses two stage of the PLL, thus providing a more stable operation. The first controller is used in conjunction with a rotor encoder that provides eight pulses per revolution, whereas the second is used in conjunction with an alternative encoder giving one pulse per revolution. Figure 5.5 shows a function block diagram of a simple electronic controller. Figure 5.6 introduces sketches for the signals of this controller.

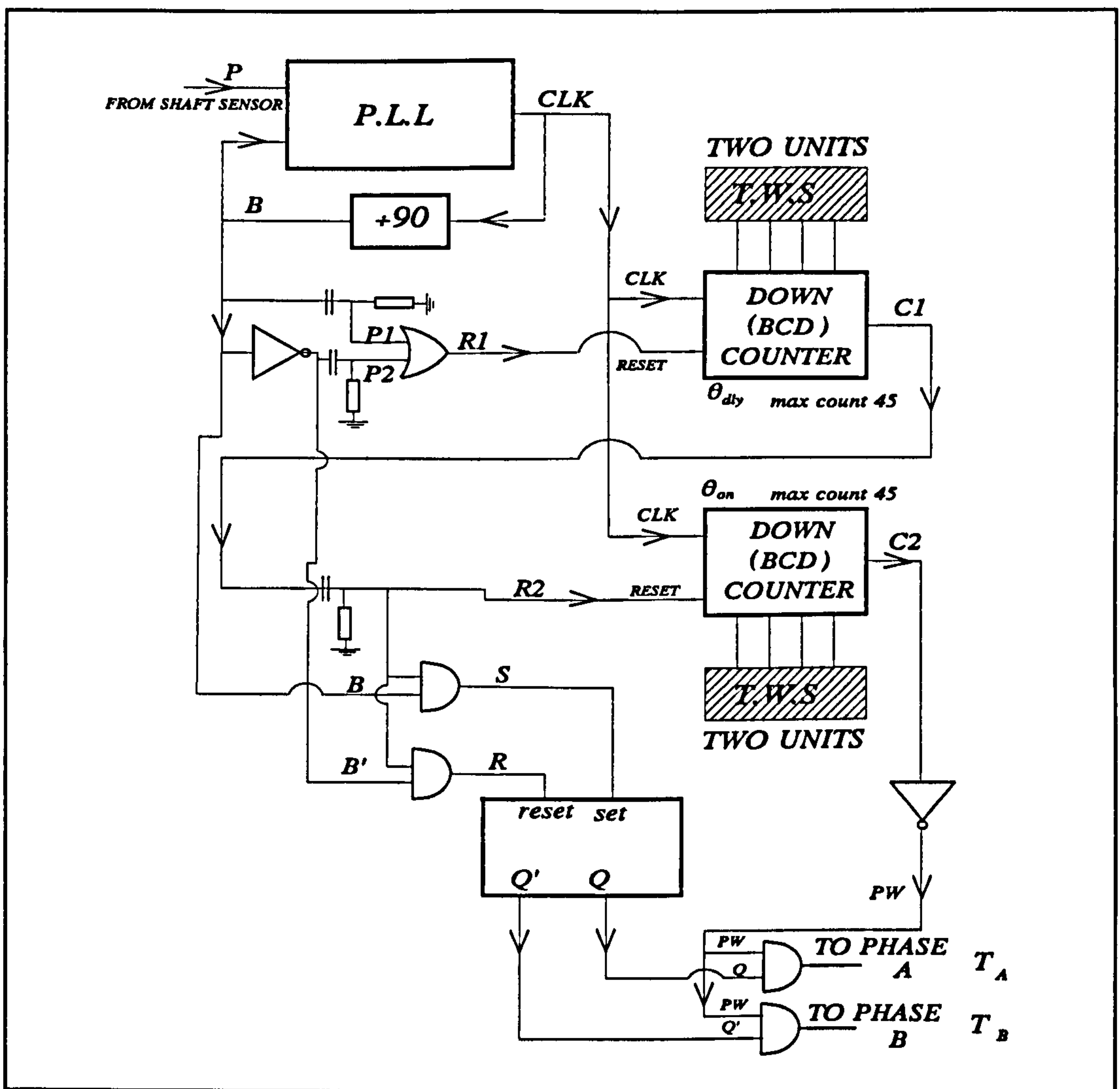


Figure 5.5: Function diagram for the electronic controller circuit.

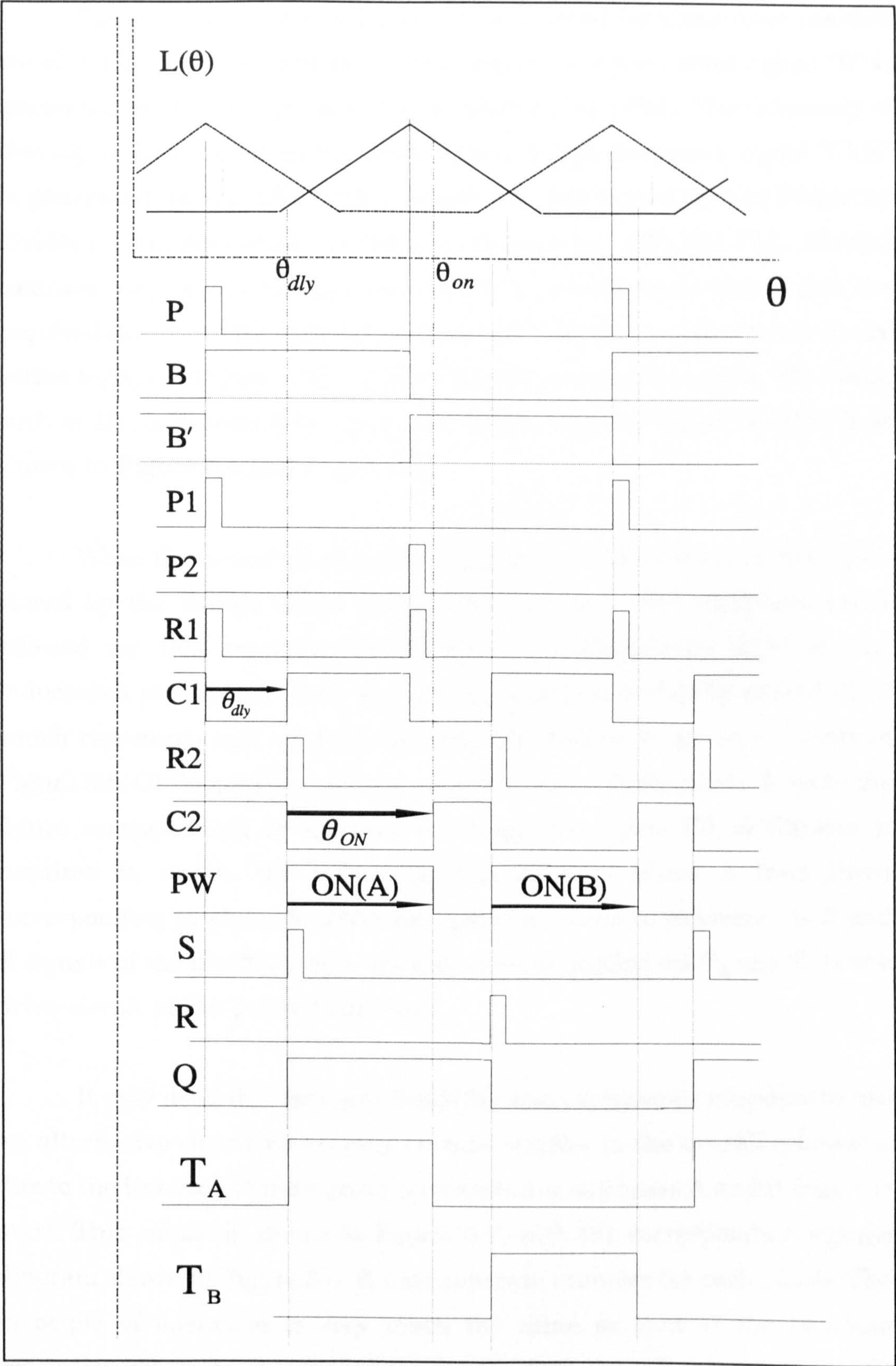


Figure 5.6: Signal diagram for the controller of Figure 5.5.

Signal P (in Figures 5.5 and 5.6) is received from the rotor position encoder which is described in the next section. A square wave signal "B" is generated by the voltage controlled oscillator of the PLL. The frequency of this signal is the same as the input signal. A high frequency signal "CLK" is generated on the PLL with a frequency determined by the frequency dividers (counters) which are used in conjunction with the PLL. Several counters may be used (in this case two) in a cascade connection to give the required division. The clock signal is used for the down-counters which are active high, see Figure 5.6, and are reset by an external signal. The reset, such as R1, is derived from rising and falling edges of B and inverted B as shown in Figure 5.5 and Figure 5.6.

When the counter is reset, it will count down from some number, pre-stored by the thumb wheel switch TWS, to zero. The maximum count allowed for this controller is 45 which corresponds to 22.5° on the inductance profile $L(\theta)$. Both θ_{dly} and θ_{on} may not practically exceed 22.5° which represents half a rotor pole pitch. The output of the first counter in Figure 5.5, C1, is used to reset the second counter which counts down to the figure corresponding to θ_{on} , thus resulting into signal C2. A flip-flop is required to isolate the pulses corresponding to phase A from those corresponding to phase B. AND logic gates are used to generate the S and R signals of the flip-flop, the output of which is applied via T_A and T_B to the drive circuit of the power transistors.

It may be desirable for more flexibility and exploratory purposes to use an alternative circuit which may even be simpler in the overall schematic due to the isolation of the signals corresponding to phases A and B from the start. This circuit is shown in Figure 5.7, with the corresponding signals diagram shown in Figure 5.8. It uses separate counters for each phase. The principle of operation is very much the same as that of the previous controller but without the need for the flip-flop, the OR gate, or the AND

gates. This circuit, however, uses a two-stage PLL. The signal from the rotor position detector in this case is one pulse per revolution rather than eight pulses. This needed modification of the rotor interrupting disk that was originally used with the circuit of Figure 5.5. Details of the circuit configuration and IC's used are given in the circuit diagram used for PCB production shown in Appendix A5.2.

The same disk was used but with all eight holes, except for one, masked by a light thin strip glued firmly to the surface of the disk. The resulting signal is then frequency multiplied by eight in the first stage PLL1. This alteration provided a signal P in the controller of Figure 5.7 which is more stable than P in the previous controller of Figure 5.5. Some jittering and noise in P of the first circuit were transmitted to the power switches, thus causing instability in the operation of the whole system. The utilisation of two-stage PLL helped to provide a more stable operation of the circuit. The thumb wheel switch used with the first controller was replaced by a push button switch which was placed inside a user panel box along with knobs for speed and output voltage fine adjustment. This allows control of the main variables of the system from one small panel box, from a safe distance.

FROM POSITION SENSOR

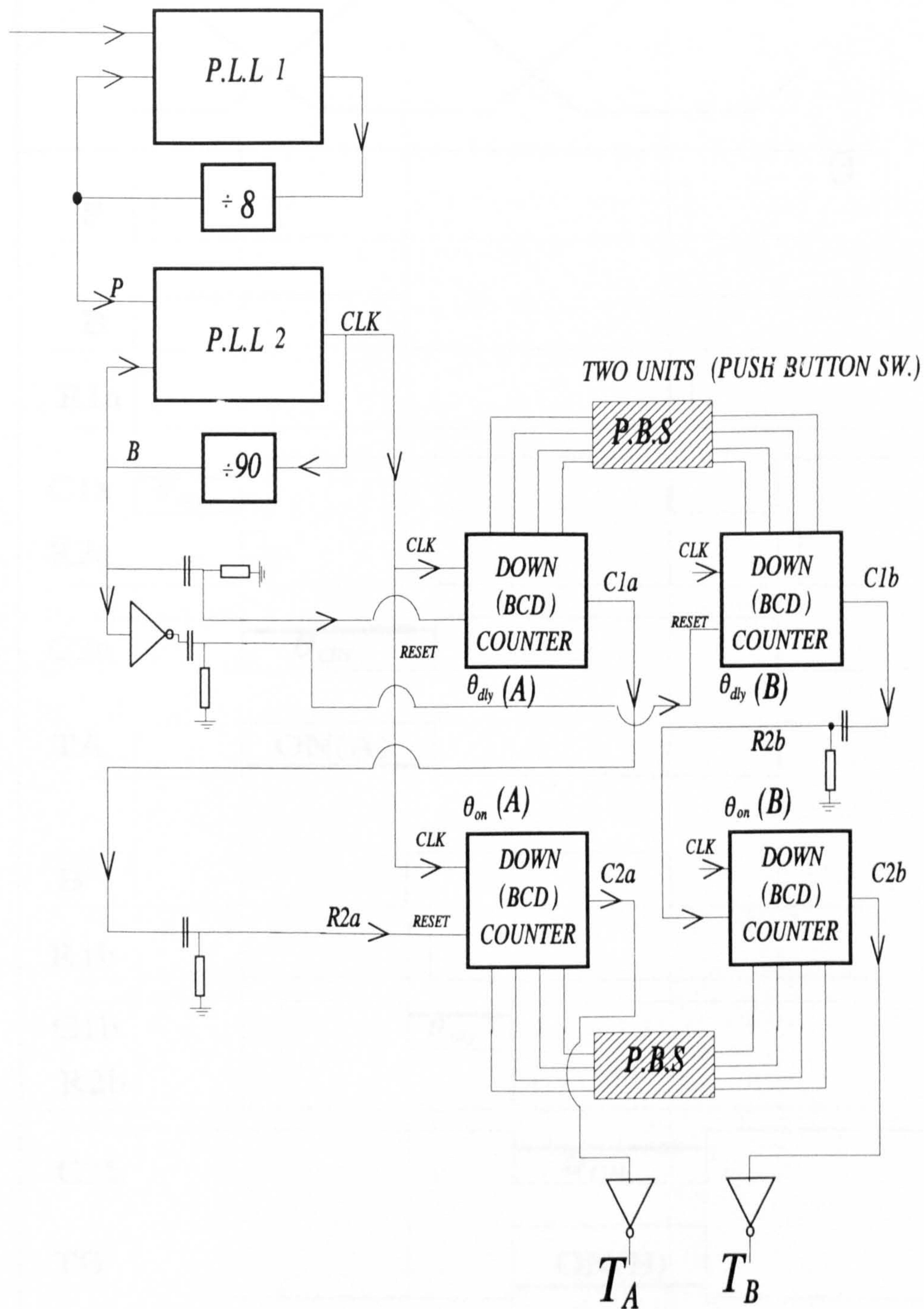


Figure 5.7: Function diagram of the selected electronics controller.

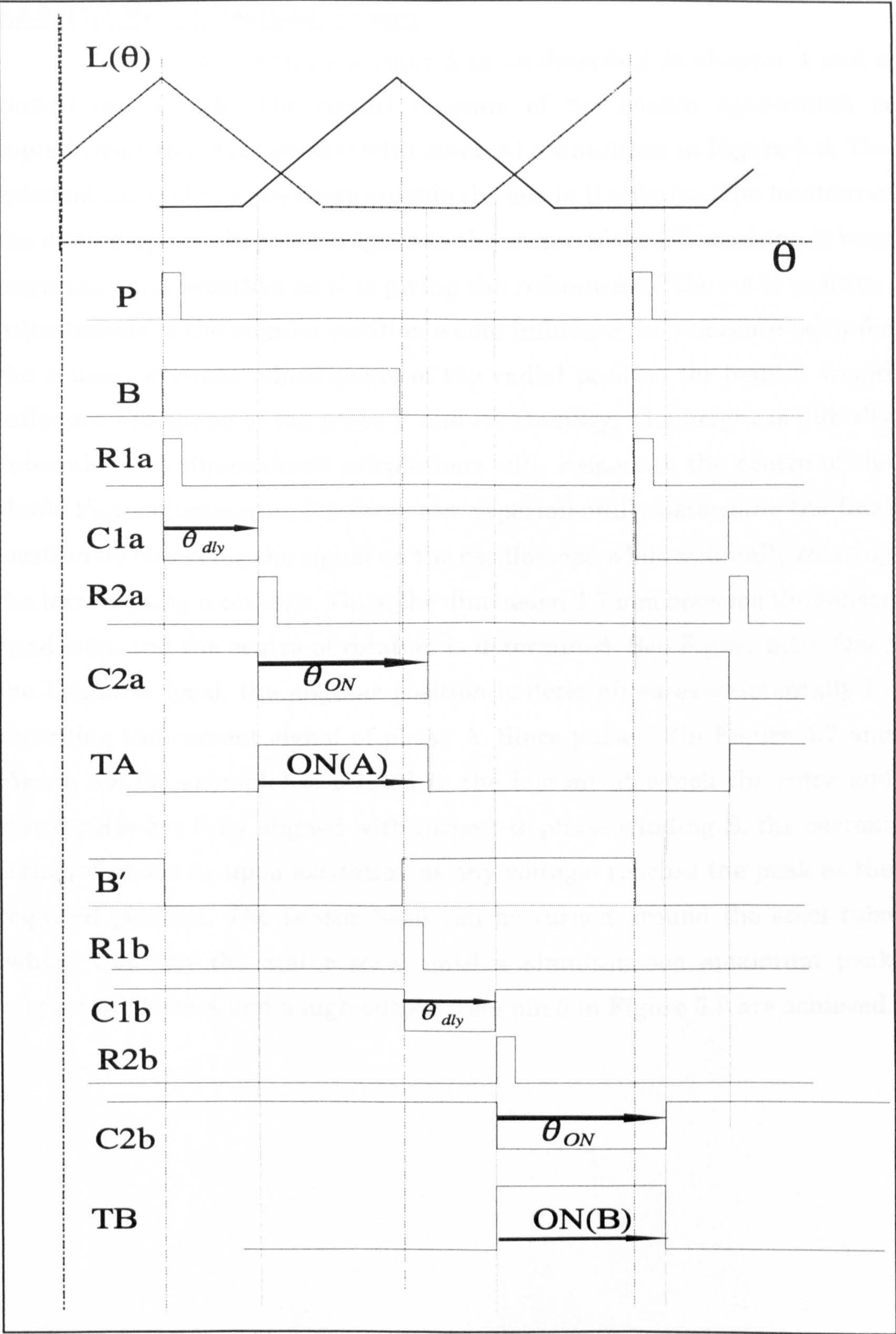


Figure 5.8: Signal diagram for the controller of Figure 5.7.

5.5.3 The Rotor Position Sensor

This device comprises a rotor disk as described in chapter 4 and a slotted opto-switch. The circuit diagram of the chosen opto-switch is reproduced (from data sheets) with external connections in Figure 5.9. The external connections are those outside the box in the figure. The location of the slotted opto-switch with regard to the stator of the SR machine is very important and sensitive as it is giving the reference for the rotor position. Adjustments of the angular position would influence the reference point for the sensor, whereas adjustments of the radial position (or height) would influence the shape of the pulse P and its stability. The height is initially determined by dimensional calculations with respect to the centre of the shaft. Fine adjustments, however, can experimentally determine the final location by observing the signal on the oscilloscope while manually rotating the interrupting rotor disk. Thus, the dimension 6.7 mm between the sensor head edge and the centre of rotation is determined. See Figure 5.10. Once the height is fixed, the angular position is determined experimentally by observing the current signal of phase A. Since pulse P (in Figure 5.7 and Figure 5.8 for example) is related to the instant at which the rotor and stator poles are fully aligned with respect to phase winding B, the current signal of phase A -upon excitation at any voltage- reaches the peak at the required position. The sensor head can be turned around the steel tube (which contains the stator core) until a simultaneous maximum peak current in phase A and a high output from pin 5 in Figure 5.9 are achieved.

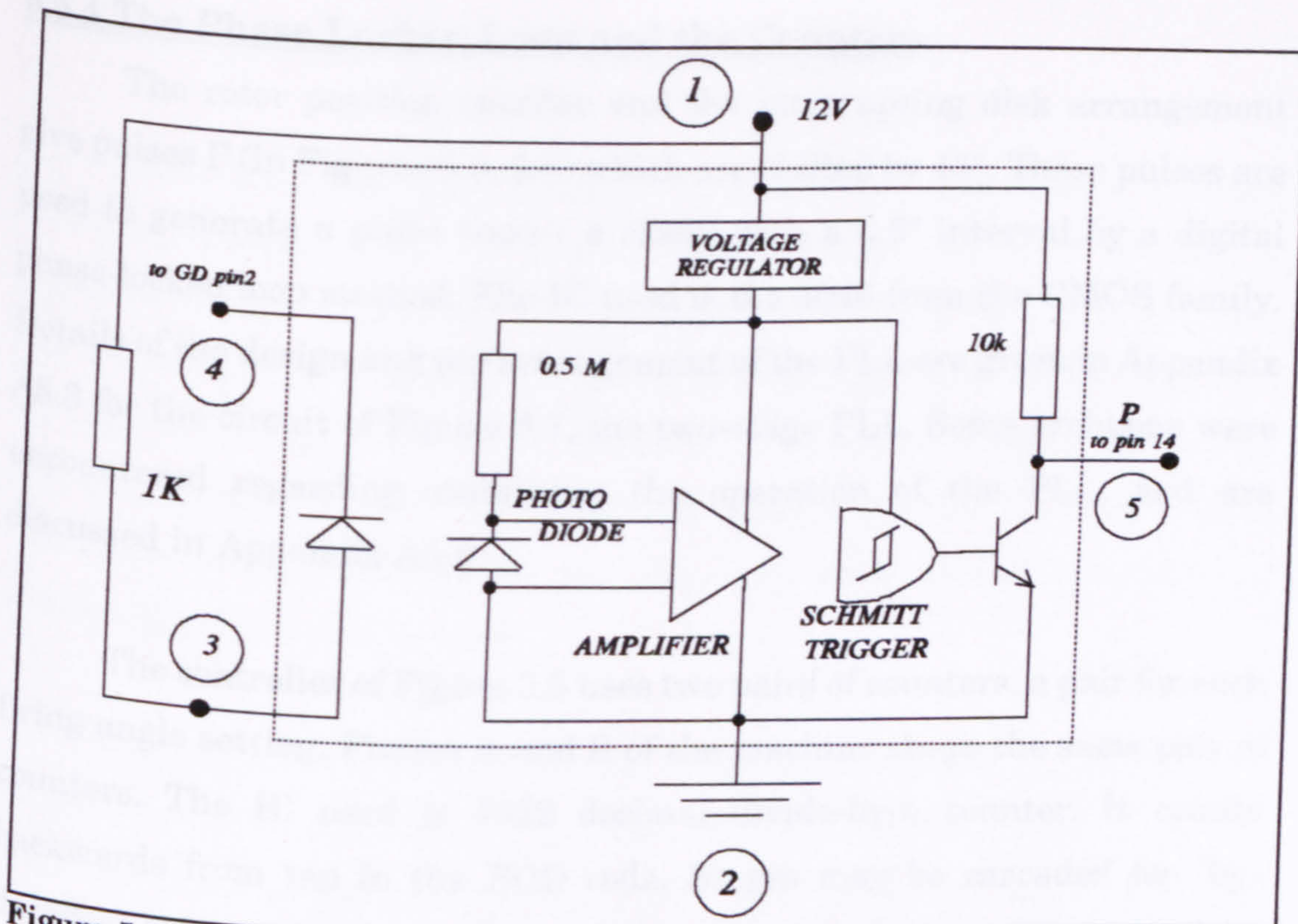


Figure 5.9: Circuit diagram for the opto-switch used for rotor position sensing.

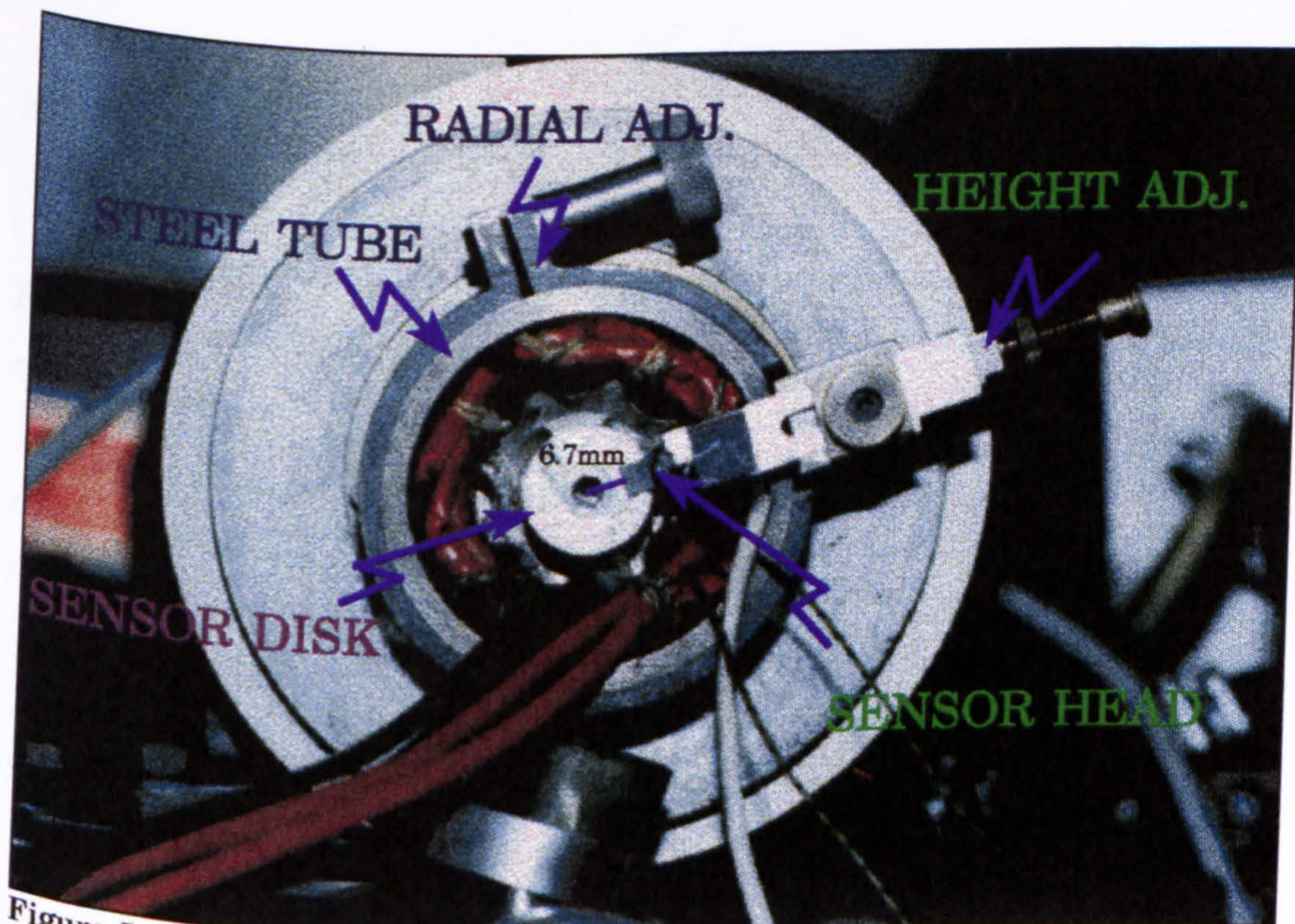


Figure 5.10: A photo for the rotor position sensor.

5.5.4 The Phase Locked Loop and the Counters

The rotor position encoder and the interrupting disk arrangement give pulses P (in Figures 5.5, 5.6) which are shifted by 45° . These pulses are used to generate a pulse train (a clock) with a 0.5° interval by a digital phase-locked loop method. The IC used is the 4046 from the CMOS family. Details of the design and pin arrangement of the PLL are given in Appendix A5.3 for the circuit of Figure 5.7, the two-stage PLL. Some problems were encountered regarding stabilising the operation of the PLL, and are discussed in Appendix A5.3.

The controller of Figure 5.5 uses two pairs of counters, a pair for each firing angle setting. Phases A and B of the machine share the same pair of counters. The IC used is 4522 decimal divide-by-n counter. It counts backwards from ten in the BCD code. Stages may be cascaded for "by-decades" setting of any count. Two IC's are required to provide a counting for θ_{dy} and another two for θ_{on} .

In the controller circuit of Figure 5.7, signals for phases A and B are independent and use a separate set of counters of the same IC 4522.

Two units of BCD code switches are used for each pair of counters. For the controller circuit of Figure 5.7, still two units of switches are required but for two pairs of counters.

5.6 Power Transistor Gate Drive Circuit

MOSFET power transistors are generally easier to drive than other switching devices. They are considered as voltage controlled devices. A sufficient voltage exceeding the threshold of the gate-source requirement, and an initial small charging current for the gate-source capacitor are basically required to drive the transistor. To ensue turning *off* at the required instant, a negative gate-source voltage is often desirable. Good isolation between power circuit connections and electronic circuit is achieved through the drive circuit stage.

One circuit that achieves the drive requirements for the power transistor is shown in Figure 5.11. The circuit generates a train of pulses from the input signals T_A or T_B , which are the output signals of the controller. The pulse train is generated by the hysteresis loop realised by the Schmitt trigger NAND gate loop which is comprised of a diode, a resistor and a capacitor, besides the NAND and NOT logic gates. The invert of the input signal is routed to an identical circuit (if circuit inside the box in Figure 5.11 is ignored for the moment) to generate a pulse train for the OFF period of the input signal. The two pulse trains, of the ON and the OFF periods, are then switched across a pulse transformer via a fast small signal FET transistor. The fact that these pulses are quite narrow means that the pulse transformer can be quite simple and saturation of the transformer core is avoided. A set of four pulse transformers embedded in a small chip and intended for use in data communication isolation purposes suited this application quite well. The transformed pulse train is switched across the upper and lower branches using small low voltage power FETs. These transistors were of the V10KE type which is provided with gate protection. The resulting signal is a train of pulses with a level of 12 V for the ON period of the input signal, and about -12 V at the OFF period. When the power transistor is connected to the G and S terminals, sufficient

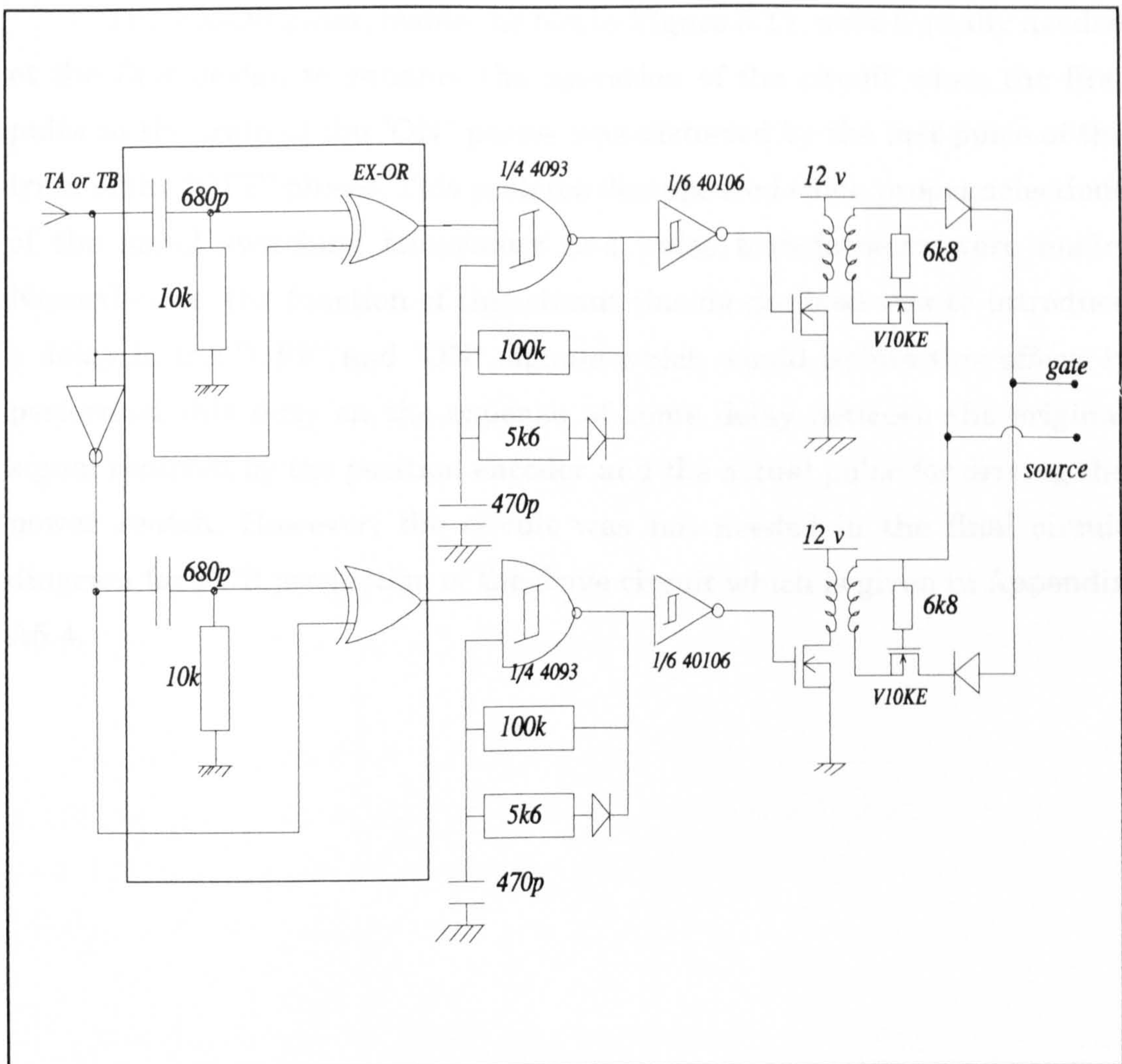


Figure 5.11: Power transistor gate drive circuit.

charging current is provided at the start of the ON pulse train to charge the input capacitor of the transistor.

The circuit offers the following advantages:

- 1- No need for floating power supply to provide negative gate-source voltage at turn-off.
- 2- Pulse transformers requirements are minimal.
- 3- Protection against shorted gate-source.

The EX-OR gates, inside the box in Figure 5.11, were initially needed at the first design to enhance the operation of the circuit when the first pulse in the train of the "ON" pulses was distorted by the last pulse of the train of the "OFF" pulses. This problem disappeared when proper selections of the small switching transistors and pulse transformers were made. Nevertheless, the function of this circuit (inside the box) was to introduce a delay in the "OFF" and "ON" signals which would isolate this effect. It performed this duty on the expense of some delay between the original signal received by the position encoder and the actual pulse for driving the power switch. However, the circuit was not needed in the final circuit diagram for PCB production of the drive circuit which is given in Appendix A5.4.

5.7 Preliminary Tests and Operation

Static tests were made possible by the use of a 555 timer configured as a pulse generator to produce the necessary signal replacing P or the signal from the position detector in the case of zero speed. A toggle switch was provided with the controller to switch operation between static tests and dynamic tests. The tests aimed at checking the operation of the converter as a whole, the electronic controller, and the gate drive circuit of the power switches.

The unit operated as required. Problems with noise and instability of the PLL operation were only faced when running the actual SR machine.

It was observed, at this stage also, that the machine phases are similar to each other to a good degree despite the difficulty of achieving a good degree of similarity for a small machine with very limited slots for the winding and very small air-gap.

Results for the MOSFET gate drive circuit operation are given in Figures 5.12, 5.13, and 5.14, showing oscilloscope traces (transferred to a plotter) for the gate-source signal and the pulse train signals which are used to compose it. Results for the power converter operation are given in Figures 5.15, 5.16, and 5.17, showing oscilloscope traces for currents in both phases in the fully aligned and fully un-aligned positions (regarding phase-A). Figure 5.17 shows the waveform of the current in phase B and the voltage across it.

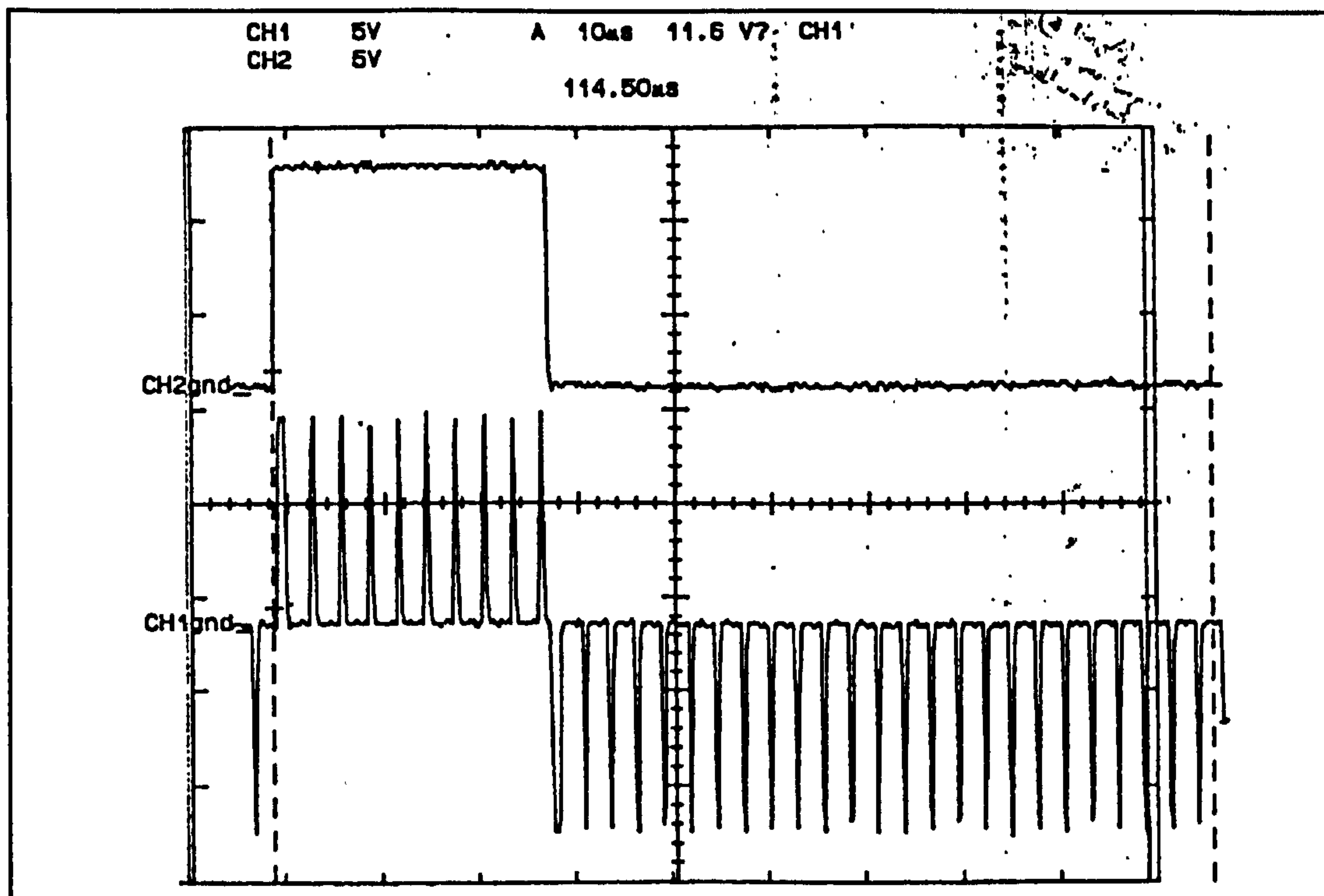


Figure 5.12: Upper: Signal B in Figures 5.7 & 5.8.
Lower: Gate-Source signal on a resistive load of 1 kΩ.

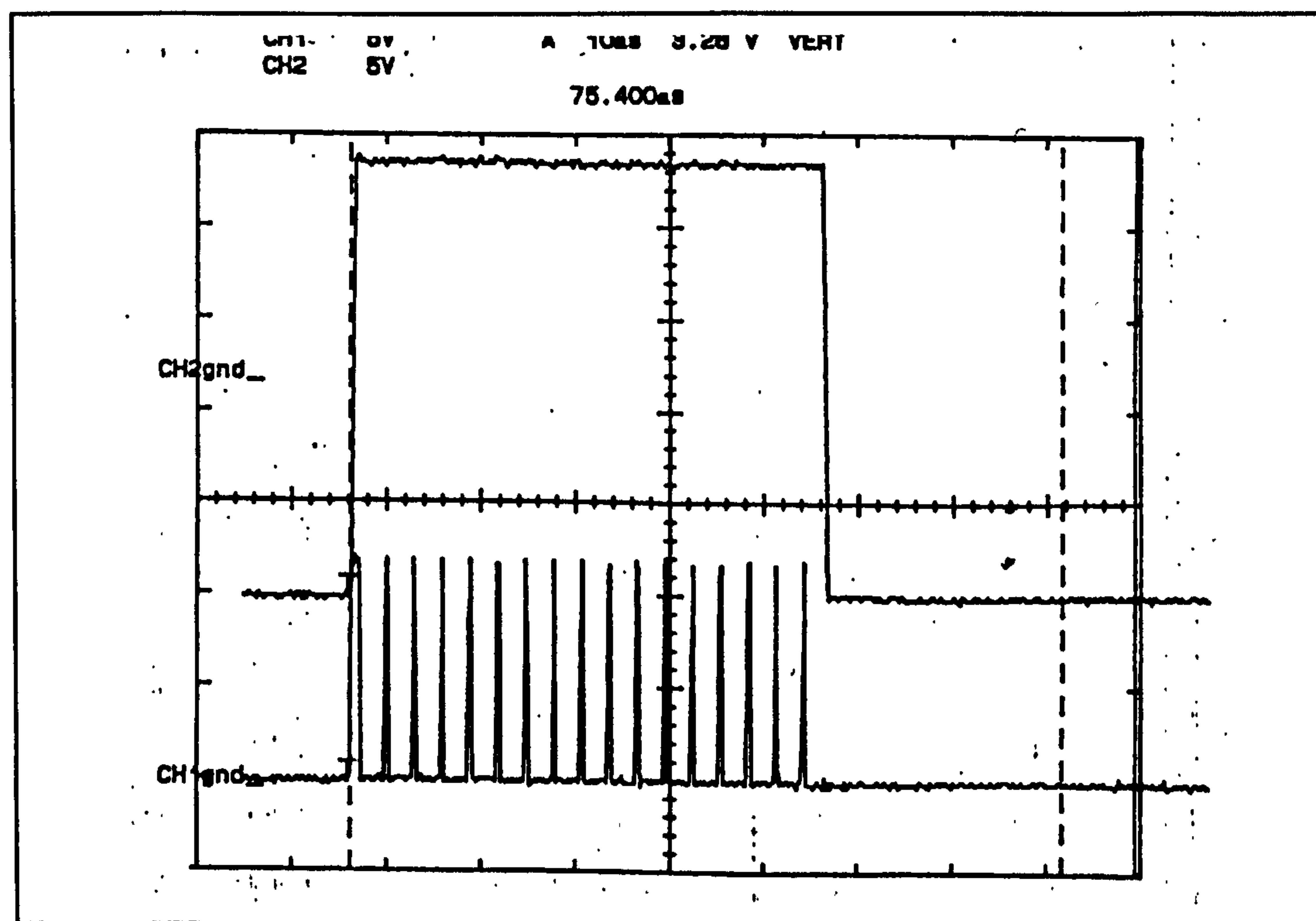


Figure 5.13: Upper: V_{gs} on the power transistor.
Lower: Pulse train for the *on* period.

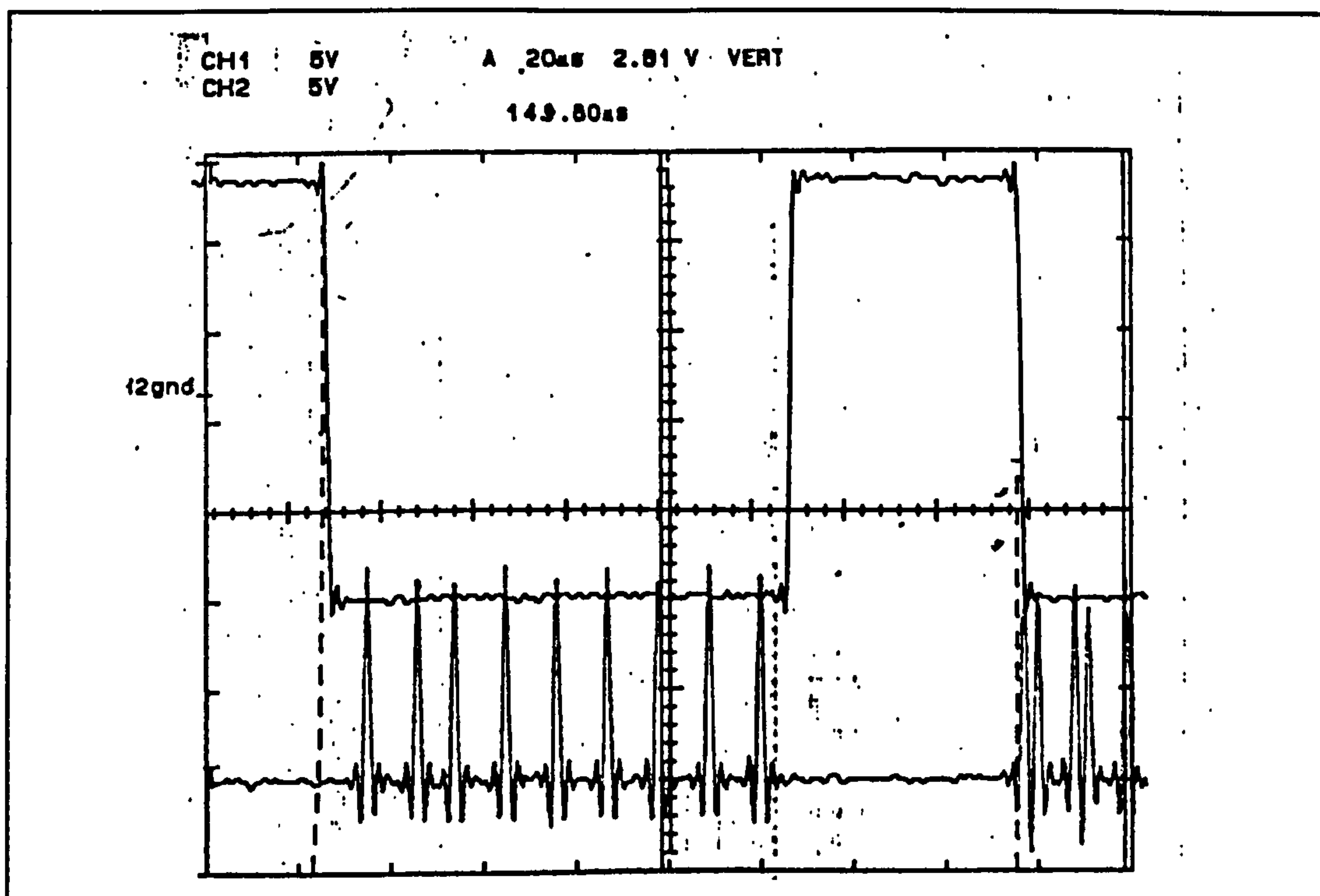


Figure 5.14: Upper: V_{gs} on the power transistor.
Lower: Pulse train for the *off* period.

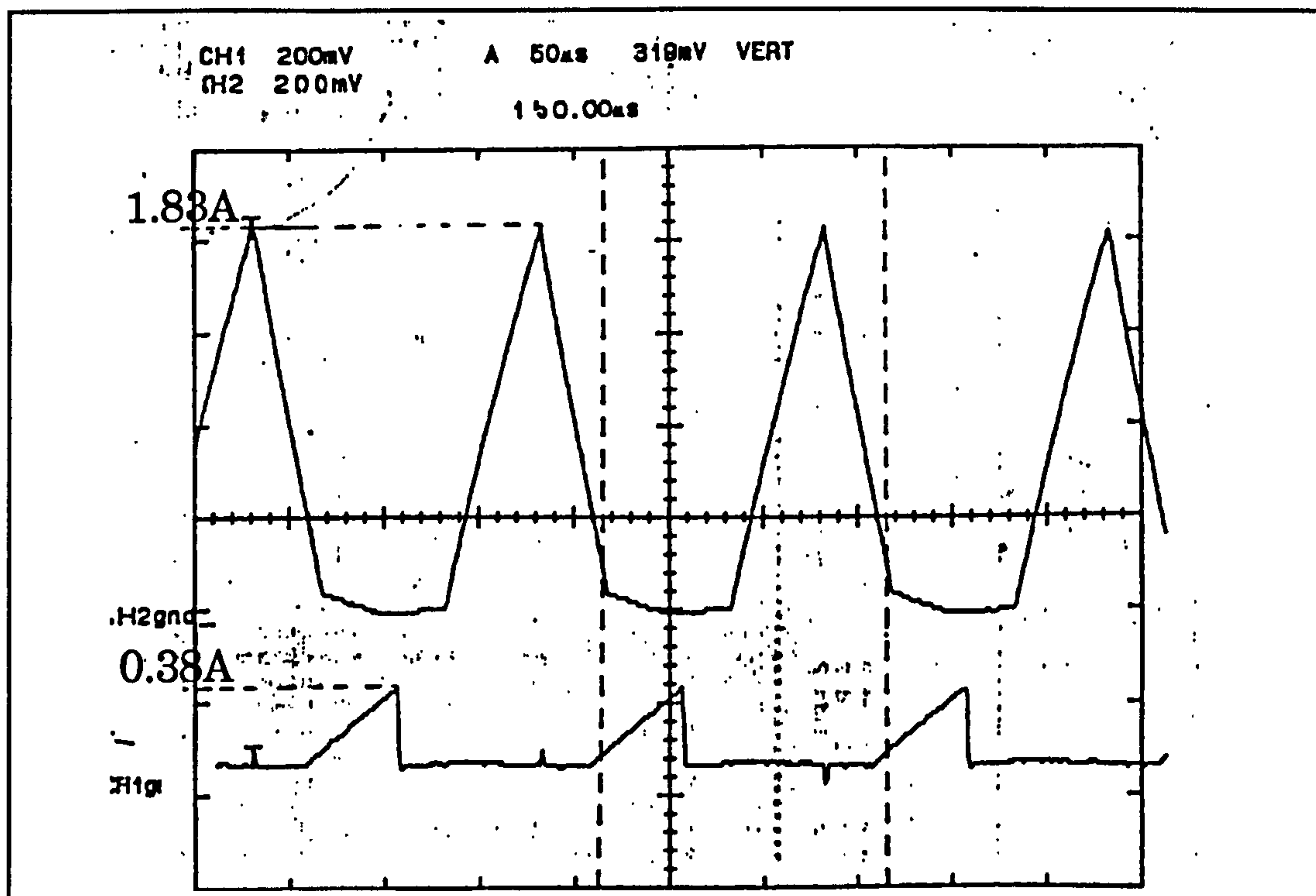


Figure 5.15: Upper: Current in phase B.
Lower: Current in phase A. Poles for phase A are in fully aligned position.

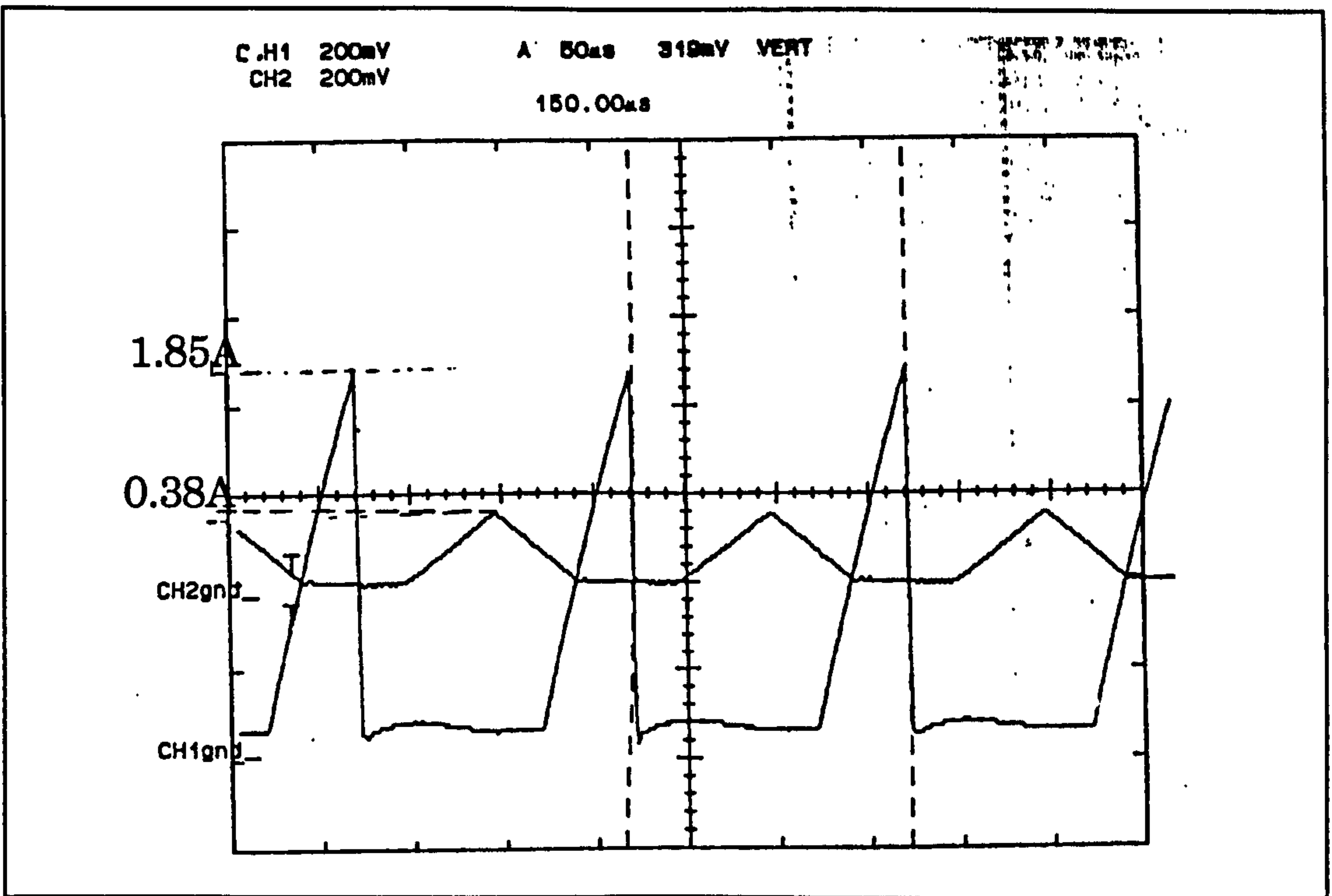


Figure 5.16: Upper: Current in phase B.
Lower: Current in phase A. Poles for phase A are in fully unaligned position.

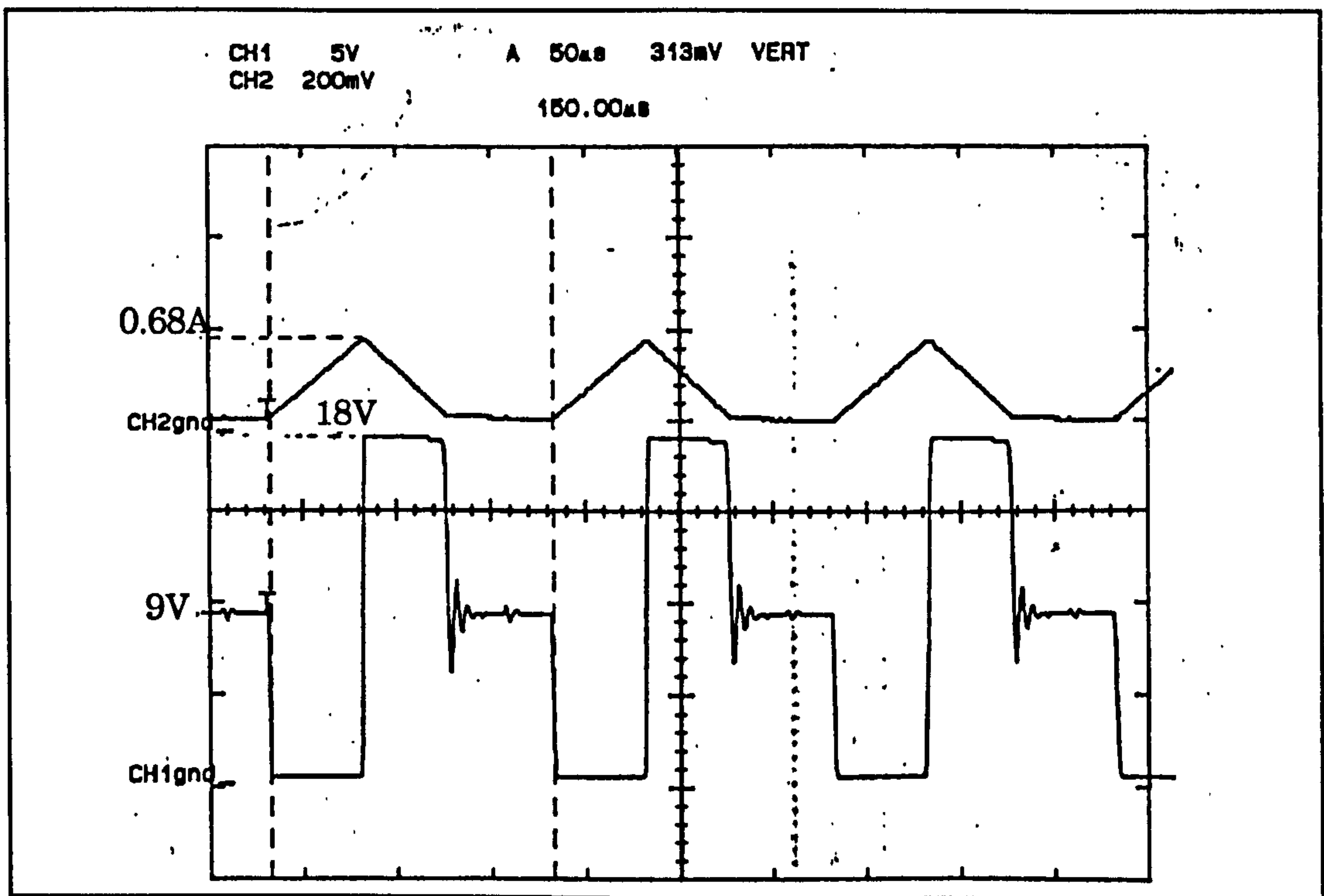


Figure 5.17: Upper: Current in phase winding B.
Lower: Voltage across phase winding B.

CHAPTER SIX

THE AIR SUPPLY SYSTEM AND THE TURBINE

6.1 Introducing The Overall System

A prime mover that provides the mechanical energy input, at high speeds, up to 100,000 rpm, to the SR generator is required. This can either be achieved using an electric system comprising a high speed motor, (such as a high frequency inverter driven induction motor), with a high speed coupling and special high speed bearings for the SR machine, or a gas turbine can be used, whereupon the SR generator can be directly coupled to the shaft of the turbine.

A turbine of a turbocharger unit was selected as a prime mover for the SRG. The availability of a suitable turbine at no initial cost was a major reason for choosing this. However, this is also in accord with the possible application of providing a vehicle turbo-driven generator.

Figure 6.1 illustrates a function diagram of the complete system including the air supply and the turbine. The turbine works in an open cycle, where ambient air is the working fluid. An air blower is used to supply the turbine with compressed air at an absolute pressure of 21.7 psi and air temperature of only about 50°C. By referring to the data of the turbine, it was found that the blower needs to deliver at least 90 Litre/sec of air to the turbine at about 21.7 psi to drive the turbine at 100,000 rpm. The turbine will normally be working with an expansion ratio of no more than 1.5.

The air blower is a positive displacement blower capable of delivering 150 Litre/sec against a discharge pressure of 7 psi (relative pressure) while running at 2929 rpm. However, for 60,000 rpm turbine shaft speed demand, the blower will need to run at only 1380 rpm while absorbing 7 kW from the driving motor.

An 18.5 kW two pole d.c. motor was used to drive the blower through a V-belt. The motor is fed by a rectified three-phase voltage on its armature with a transformer variac on the a.c. side. The variac was used to manually adjust the speed of the blower and thus the speed of the turbine. As the motor field winding is separately excited, a simple feedback circuit was employed for field current control which automatically adjusts the motor speed so as to minimise variations of the turbine shaft speed due to the magnetic loading of the SRG.

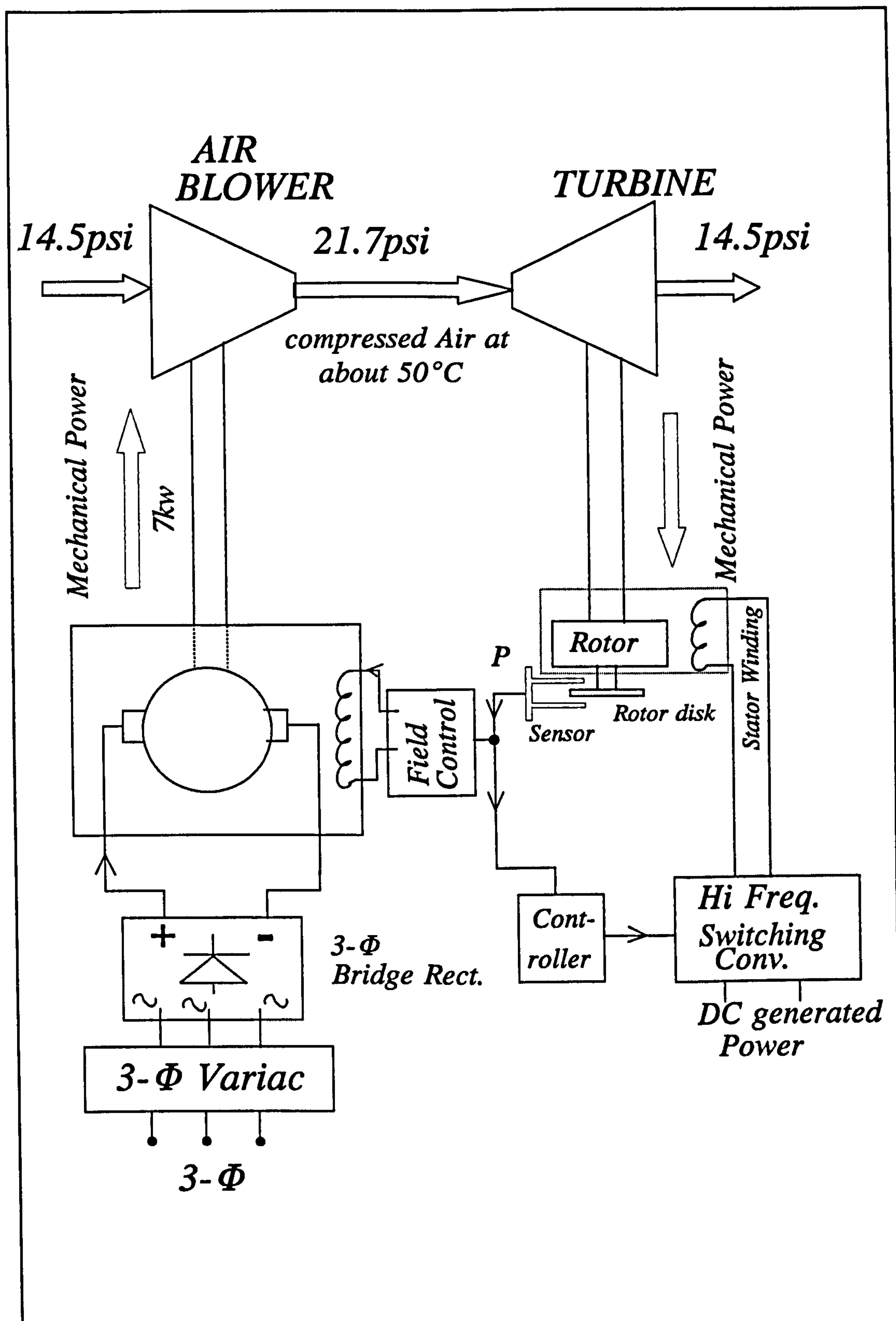


Figure 6.1: The Turbine and the air blower in the overall testing set-up of the SRG.

6.2 Turbine Selection and Preparation

The turbine that used is a medium sized gas turbine originally manufactured as a turbocharger for ground vehicle comprising a gas turbine and a compressor. When the compressor is removed from the turbocharger, a shaft which is 42.5 mm long is available for mounting the 200 gm, 25 mm long, rotor. (See Appendix A6.1 for details of rotor volume and weight determination).

Figure 6.2(a) illustrates the main components of the turbine after removing the compressor. Figures 6.2(b) and 6.2(c) show photos for the turbine before assembling it in the system.

The aluminium disk shown in the figure is normally used in conjunction with the compressor. It was decided not to remove this disk since it was ideal for mounting the steel tube containing the stator of the SRG. Careful machining was required to make an inner groove in the disk which is accurately concentric with the centre of the shaft of the turbine.

The turbine is, as shown, an inward flow device. Gas is normally delivered to the turbine inlet, shown in the figure, at an elevated pressure and temperature towards the turbine wheel. However, in this application, normal air, rather than hot exhaust gases, is used to drive the turbine. The implications of this option are:

- 1- The speed of the turbine will be adjusted by altering the mass or volume flow rate of the compressed air. Fuel feed-rate is normally used for this purpose when the complete turbocharger unit is performing. However, in this application, the speed of the blower only, which determines the flow rate, will determine the speed of the turbine.

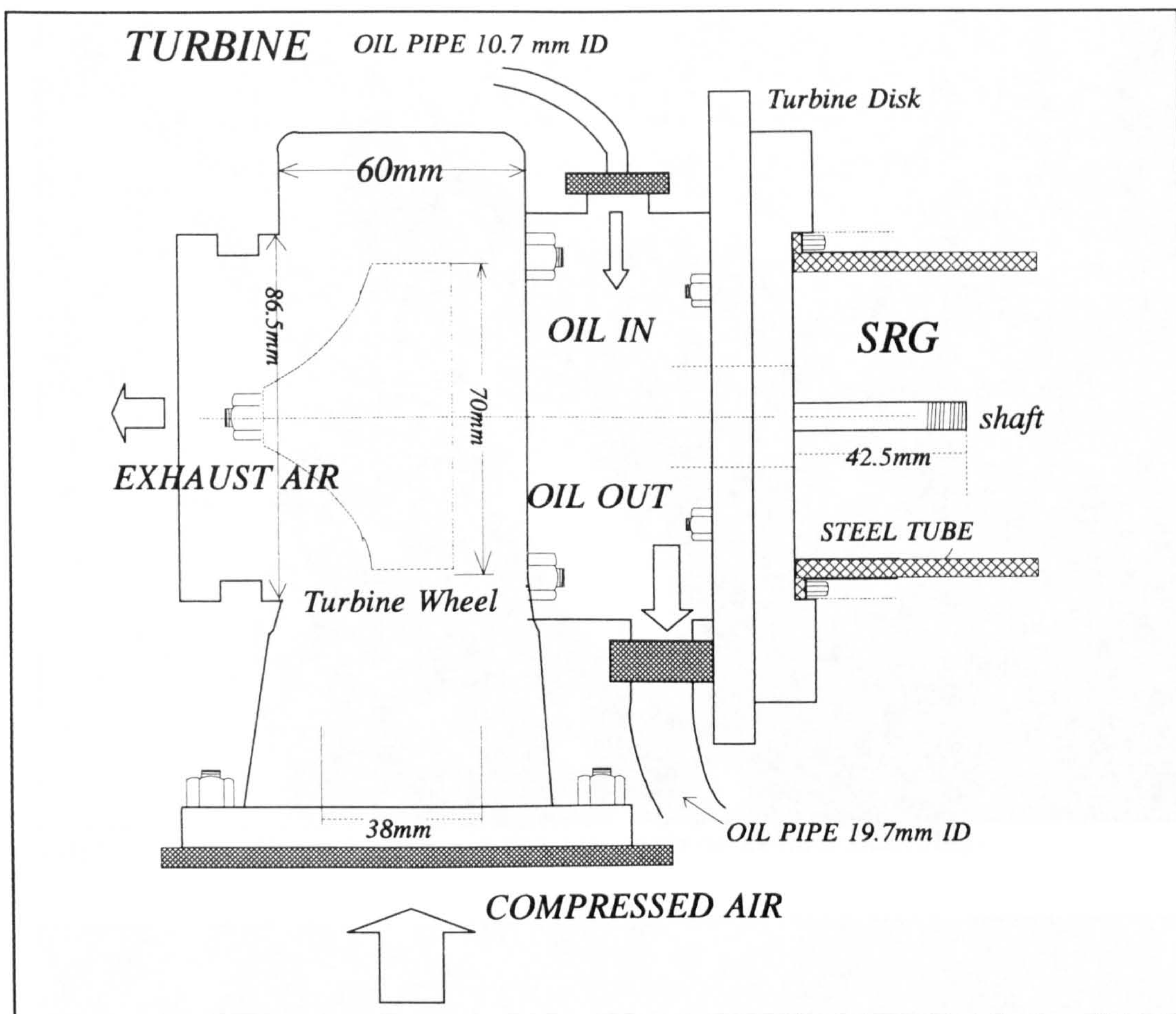


Figure 6.2(a): Main components and dimensions of the air turbine.

- 2- The turbine data related to dynamic tests, supplied by the manufacturer and given in Appendix A6.1, are to be considered for air temperatures which are between 20 to 50°C, rather than 500-600°C. Extrapolation of the dynamometer performance characteristics was necessary to determine a suitable figure for the required volume flow rate (found to be 90 Litre/sec, as in Appendix A6.2).
- 3- The expansion ratio at which the turbine is to be operated was selected as 1.5, suitable for low temperature. Curves corresponding to this ratio were not given in the data sheets. Curves for the nearest ratio, 1.8, were used for the initial design to find the required air flow. The manufacturer was also consulted regarding these selections.

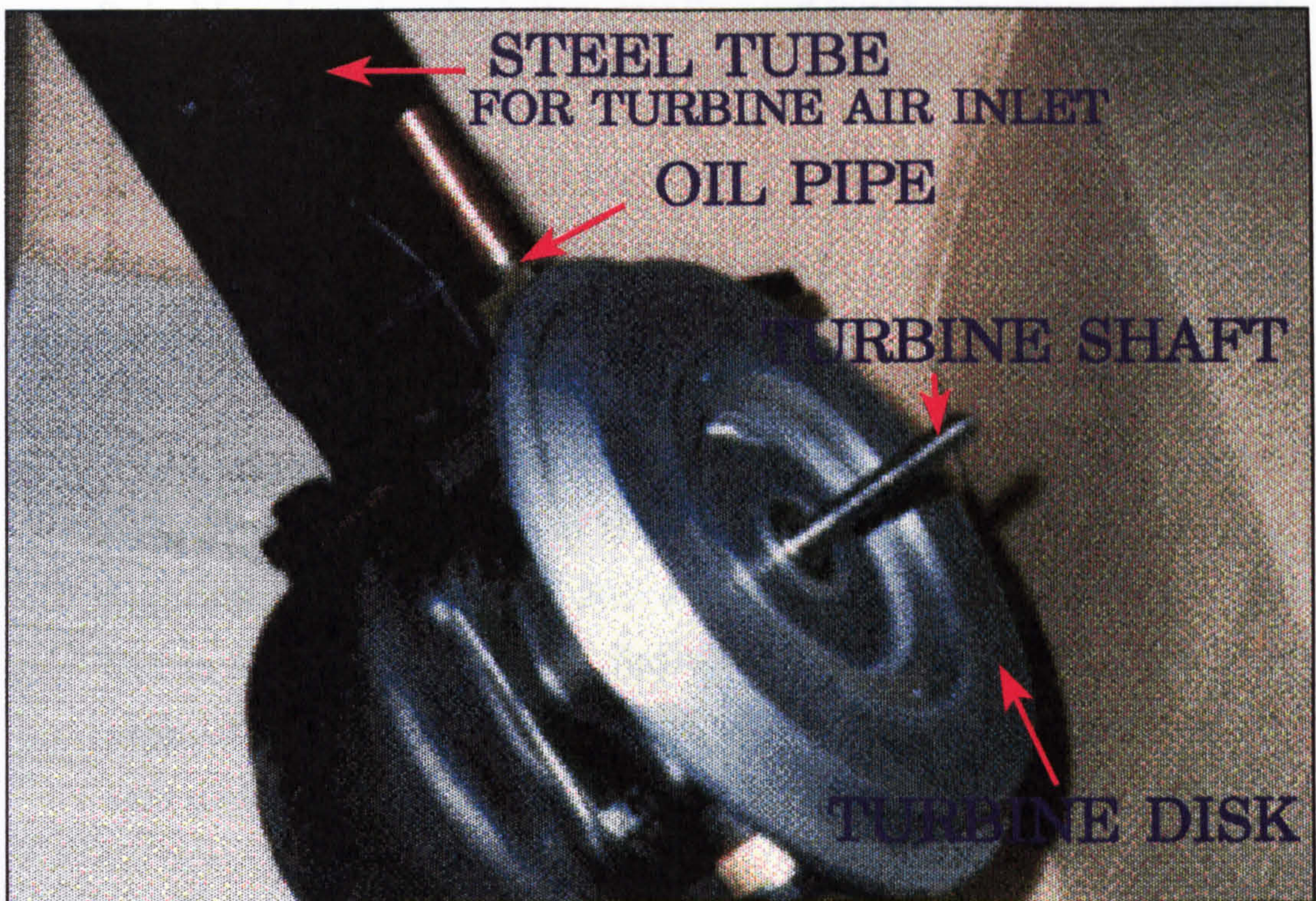


Figure 6.2(b): Photo-1 showing the Air Turbine before assembly.

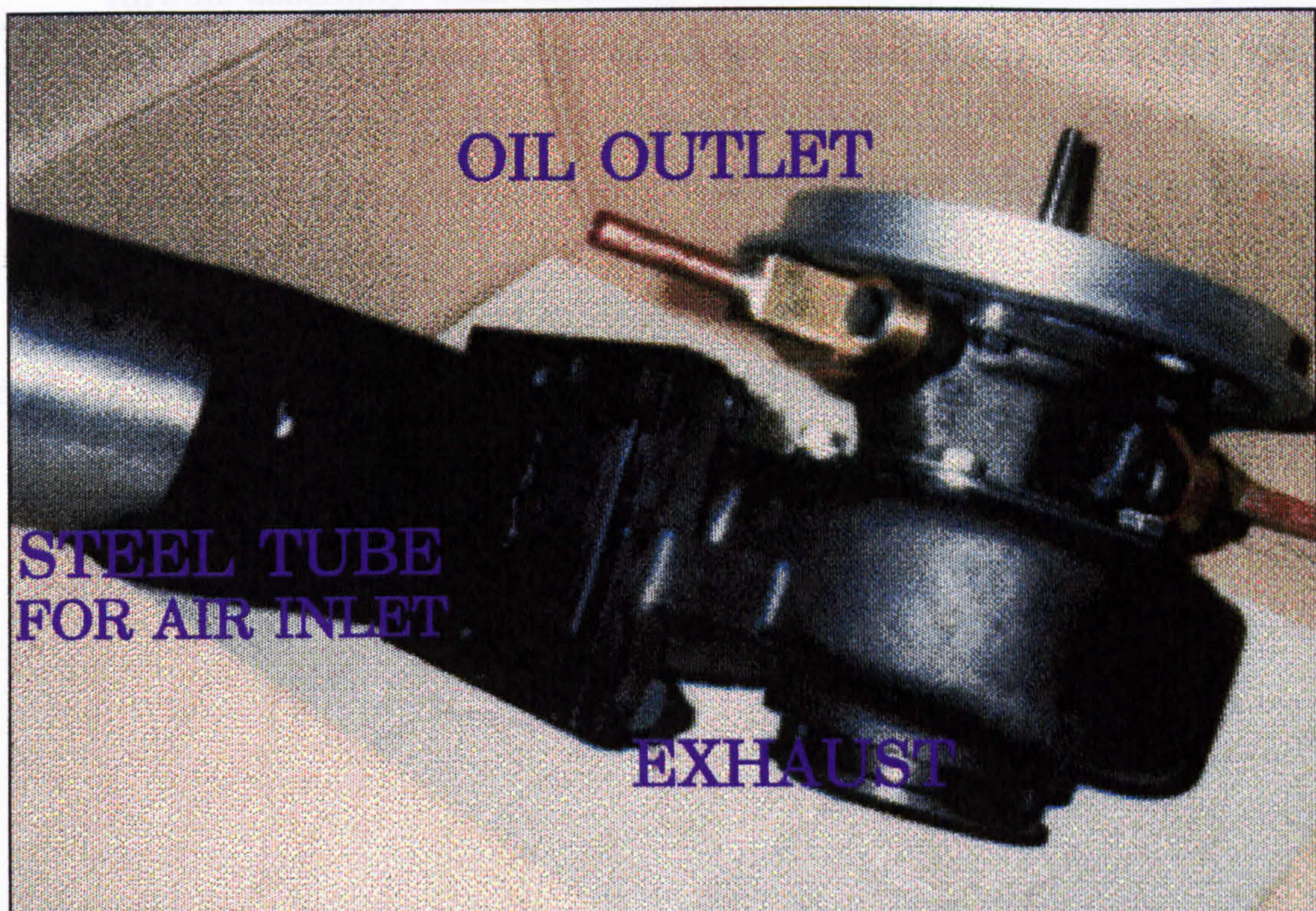


Figure 6.2(c): Photo-2 showing the Air Turbine before assembly.

- 4- Suitable oil grade which is normally used for the bearing is different when the turbine is operated at low temperature. Lighter oil is preferred in this case.

Having decided the air flow required, the pressure, and the temperature, the following preparations were then made for the turbine:

- 1- A special steel tube of about 3 inches diameter and 7 inches long was fixed to the air inlet end of the turbine. This is shown in photos of Figure 6.2(b) and Figure 6.2(c). Flexible pipes were used to join this end to the blower outlet. A flexible pipe is also required from the exhaust end, or the wheel exit end, of the turbine to exhaust at some safe distance from the testing bench.
- 2- A secondary bed plate (7.5 in × 10 in), was prepared for mounting the turbine assembly. This assembly was mounted on a main bed plate (12 in × 24 in) along with an oil pump and a d.c. motor (for the bearing set-up). Figure 6.3(a) shows the layout illustrated by top view of the assembly, dimensions are in inches. Figure 6.3(b) is a photo for the actual layout.
- 3- Rubber wafers were used to join the secondary plate of the turbine to the main bed plate and to the testing bench. These would help to absorb possible vibrations of the whole unit at very high speeds.

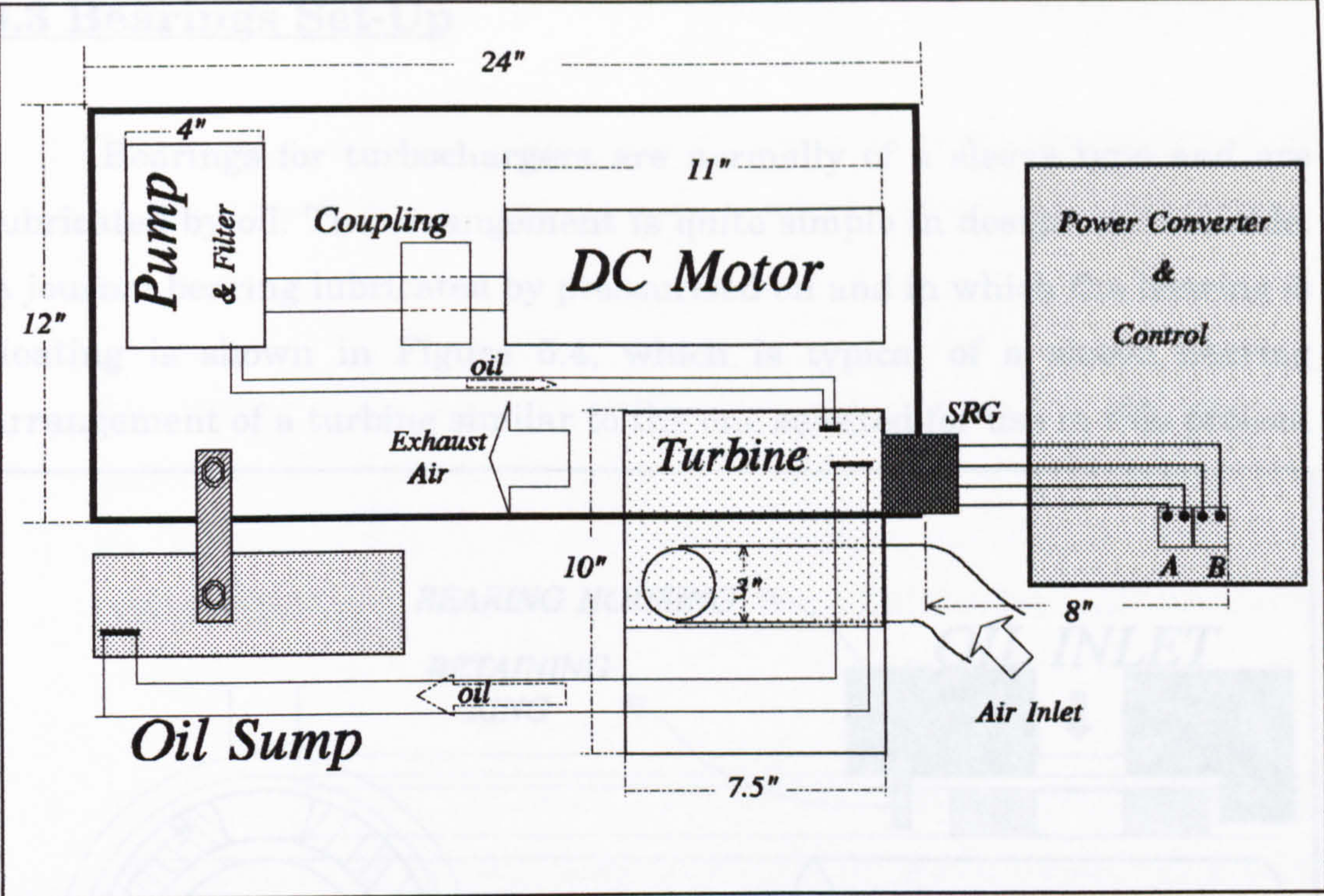


Figure 6.3(a): Basic Layout of the assembly of the turbine, the bearing set-up and the SRG converter circuit.

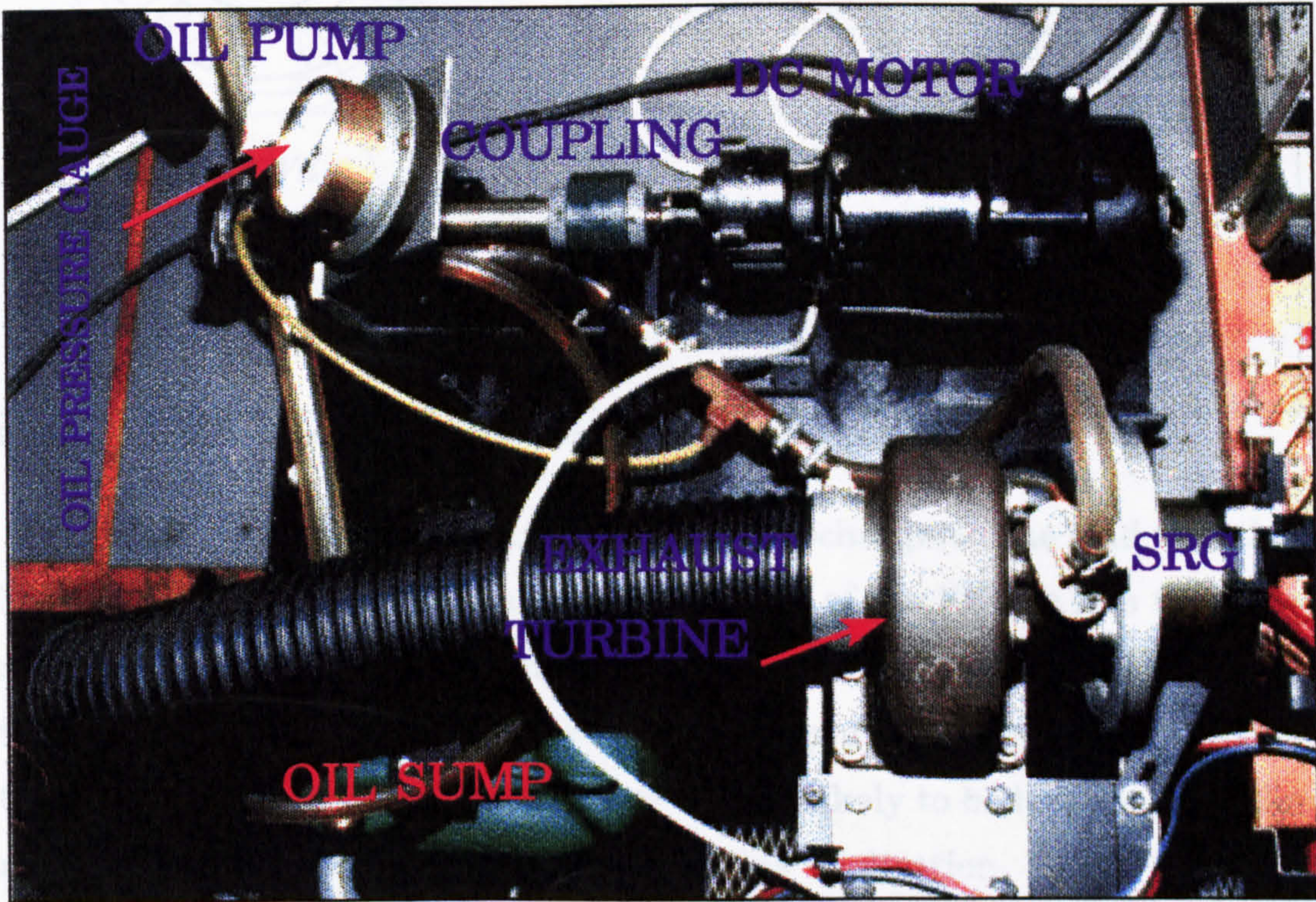


Figure 6.3(b): Photo showing the actual layout of the turbine, bearing set-up, and SRG assembly.

6.3 Bearings Set-Up

Bearings for turbochargers are normally of a sleeve type and are lubricated by oil. The arrangement is quite simple in design and reliable. A journal bearing lubricated by pressurised oil and in which the bearing is floating is shown in Figure 6.4, which is typical of a sleeve bearing arrangement of a turbine similar to the one selected for use in this project.

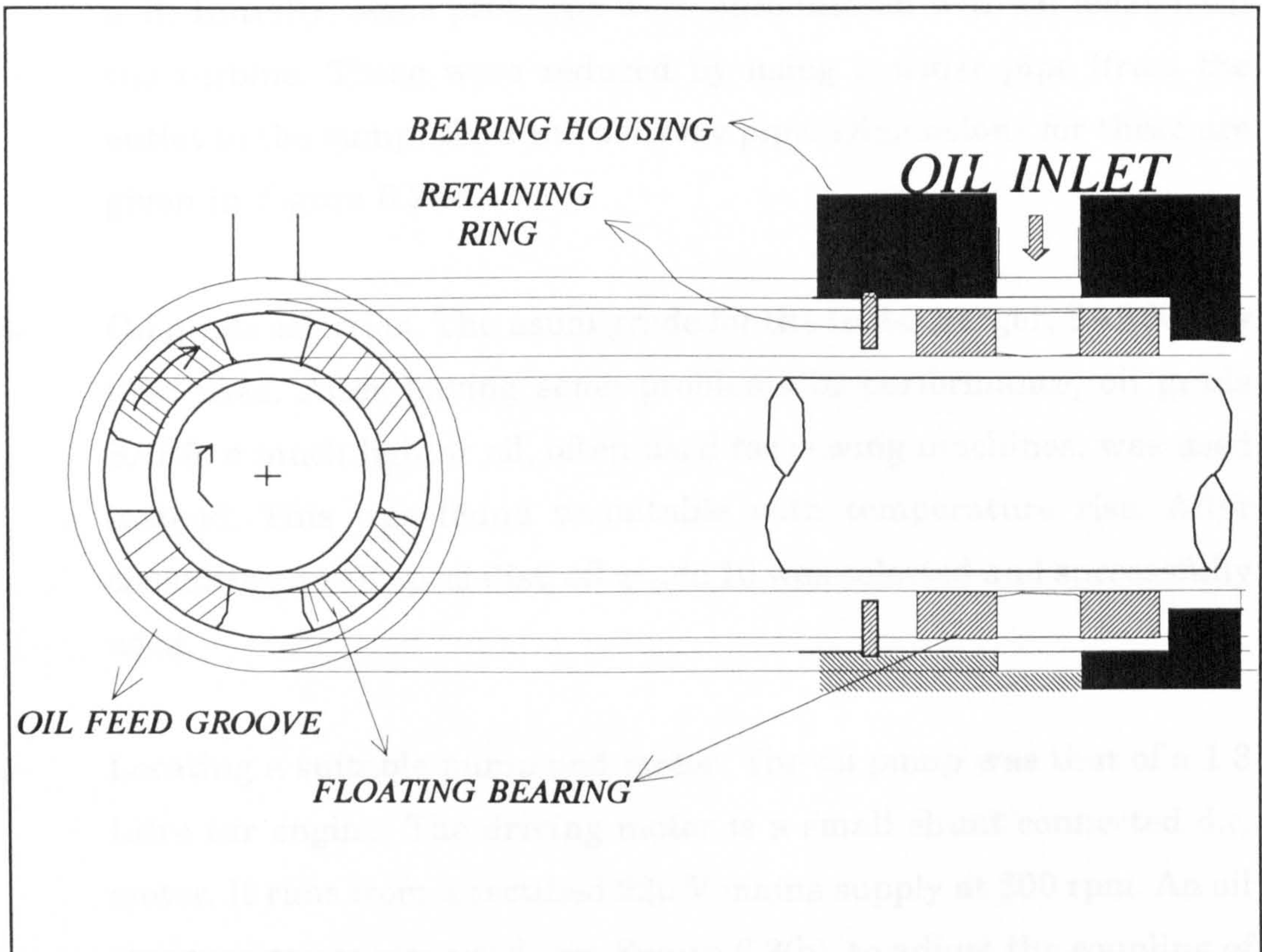


Figure 6.4: Bearings arrangement for a high speed turbine.

This type of bearing is common for turbochargers. The load that this bearing should carry after mounting the rotor of the SRG is less than the normal load of the turbocharger unit. The normal load being represented by the turbine wheel and the impeller of the compressor. The impeller has an OD of 65 mm (from turbocharger data) and is likely to be heavier than the rotor of the SRG which is replacing it in this application.

Preparation of the bearing system required the following steps:

- 1- Preparation of brass connections to the turbine oil inlet and outlet points. These can be shown in the photos of Figure 6.2(b) and Figure 6.2(c).
- 2- Preparation of suitable pipes for oil delivery to the bearing and oil exit. Initially, some problems were encountered with oil leaks from the turbine. These were reduced by using a wider pipe (from the outlet to the sump) than the delivery pipe. Dimensions for these are given in Figure 6.2(a).
- 3- Oil grade selection. The usual grade for the turbocharger, SAE30 was first used. After having some problems in performance, oil grade SAE5, a much lighter oil, often used for sewing machines, was used instead. This was found unsuitable with temperature rise. After consulting an oil specialist, oil grade 10 was selected and successfully used.
- 4- Locating a suitable pump and motor. The oil pump was that of a 1.3 Litre car engine. The driving motor is a small shunt connected d.c. motor. It runs from a rectified 220 V mains supply at 200 rpm. An oil pressure gauge was used, see Figure 6.3(b), to adjust the coupling of the motor and pump such that a pressure of about 40 psi is achieved at 200 rpm.

6.4 The Air Blower

The turbine required an air volume flow rate of at least 90 Litre/sec at 0.5 bar above atmospheric pressure. A suitable air blower was selected from the range of blowers given in Appendix A6.3, by considering a supply demand of 150 Litre/sec at 0.5 bar relative pressure (or 7 psig). This figure was initially set as a target for 100,000 rpm turbine speed and 1.8 expansion ratio for the turbine. The performance characteristics of the blower, given in Appendix A6.3 were then used to determine the required power and speed of the motor used to drive the blower.

The turbine is connected to the blower through an outlet silencer and a flexible pipe. The assembly is shown in the photo of Figure 6.5 (the turbine is not shown). The audible noise that the blower makes requires the use of an inlet and outlet silencers. Reconditioned lorry silencers of 20 cm diameter and 68 cm length were prepared for use as they are of suitable power. Figure 6.6 shows a photo for the air blower, the inlet silencer, and the driving d.c. motor (which is discussed in the next section).

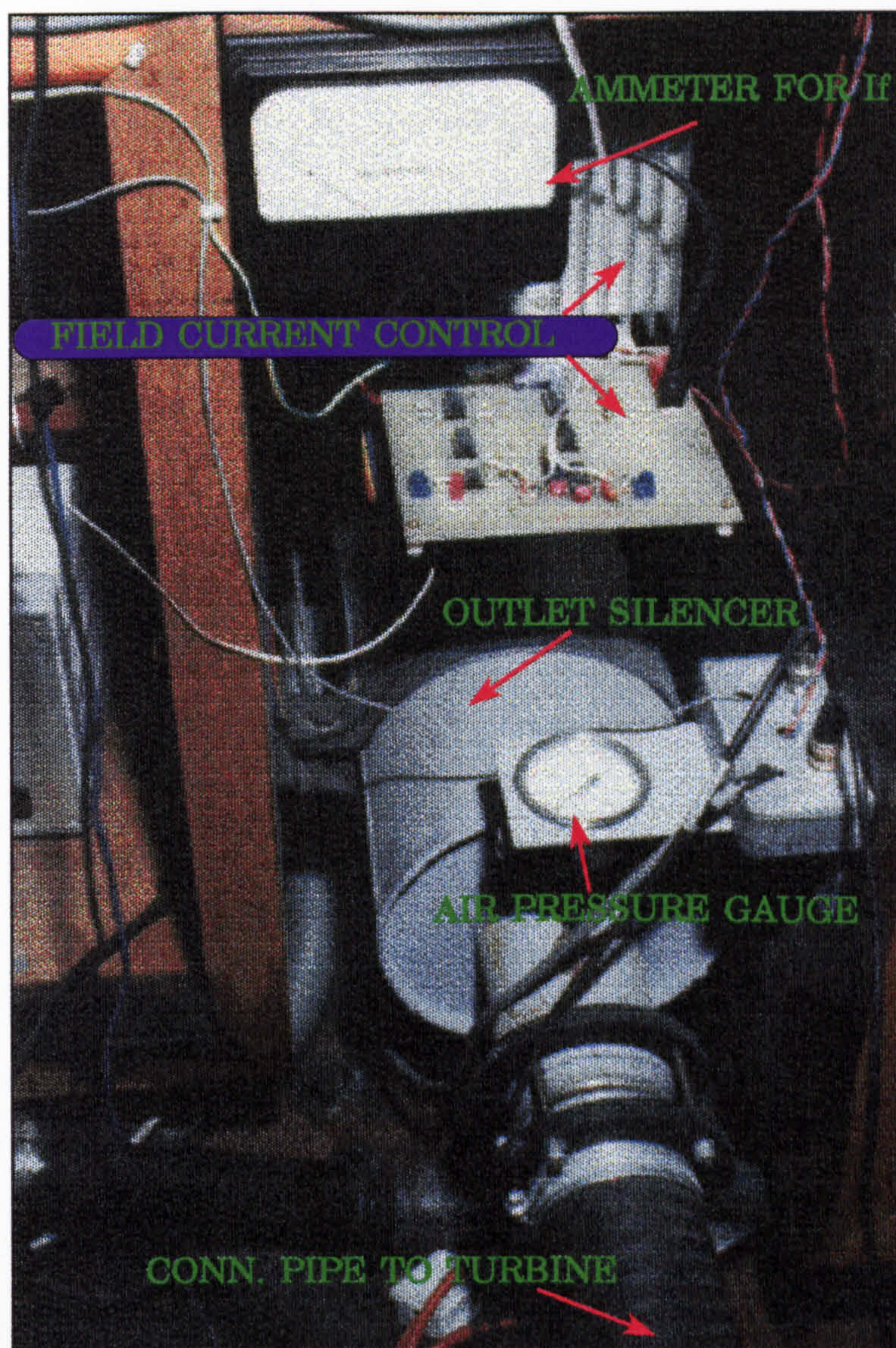


Figure 6.5: Photo showing the outlet silencer and connection pipe to turbine.

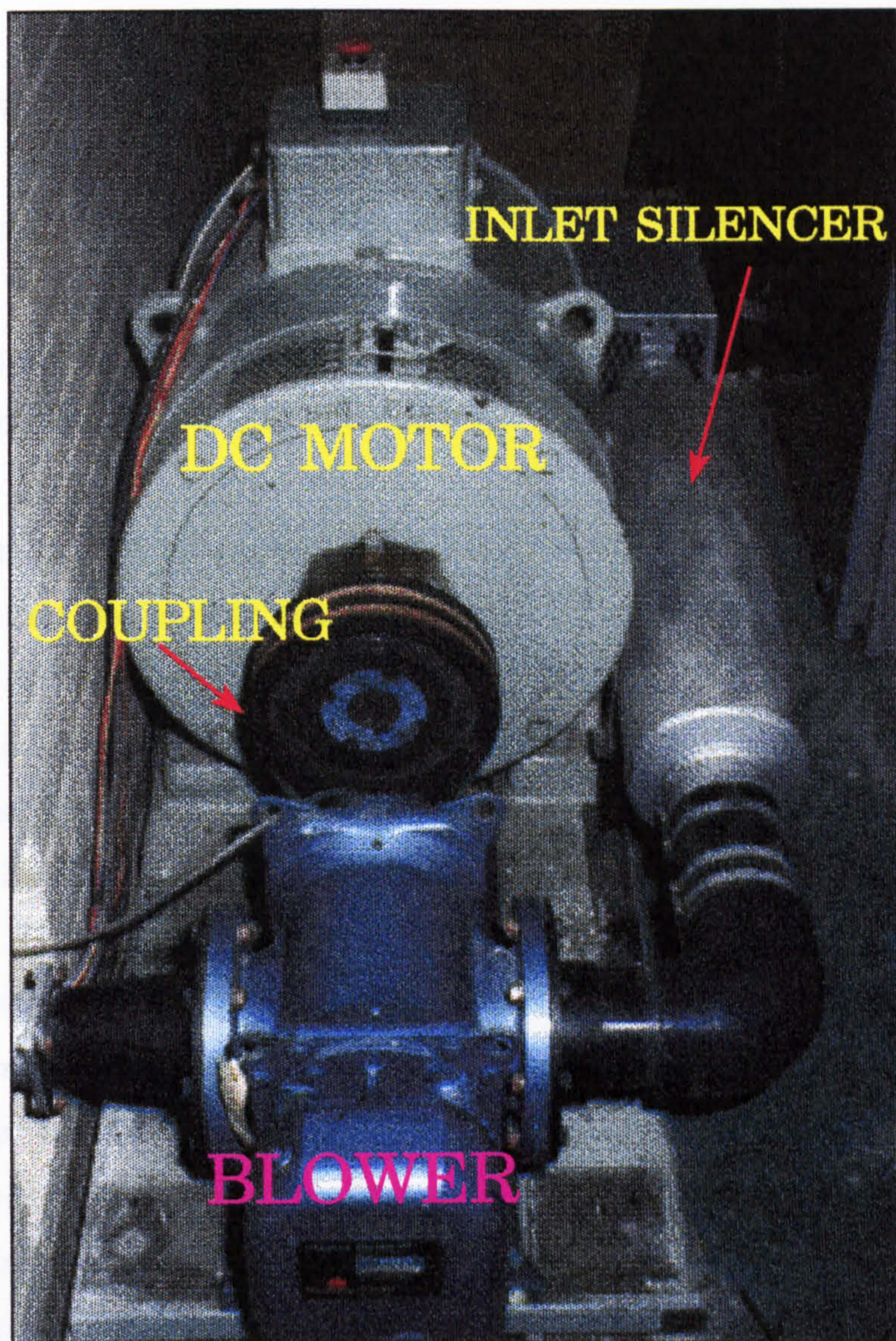


Figure 6.6: Photo showing the Air Blower, the Inlet Silencer and the driving D.C. Motor.

The supplied blower is a positive displacement bare shaft blower. It features a generous shaft diameter of 32 mm, permitting the use of a V-belt to the drive shaft without the need for a double outer bearing.

The following steps were taken for the preparation of the blower:

- 1- Making flange interfaces for connecting the inlet and outlet silencers to the blower sides. Special washers for sealing the compressed air were placed between the blower side and the coupling flange.
- 2- Oil is needed for the gear of the blower. A suitable gear oil was used. Oil level requires regular checking.
- 3- Preparing a coupling between the blower and the motor drive. The motor and the blower are mounted on the same bed plate. The extra belts appearing in the photo of Figure 6.6 were used after experiencing some difficulties, during testing, with slipping of the original belt that was first used. The height of the blower was carefully adjusted for good coupling.

The data concerning blower performance, given in Appendix A6.3, indicates a minimum safe speed for the blower of 1300 rpm. It must be noted that, for turbine speeds of 50,000 rpm and less, the required speed of the blower will be less than this figure. However, for the experimental test procedure, the operation will be for relatively short duty only. For long duty operation, an air pressure valve control could be used.

6.5 Electric Motor Drive and Speed Control

A two pole 18.5 kW separately excited d.c. motor is used for driving the blower. The maximum speed is 3000 rpm which is beyond what is required by the air blower. Figure 6.7 shows the electrical connections of the motor. The armature is supplied from a three-phase bridge rectifier rated at 37 Amp.

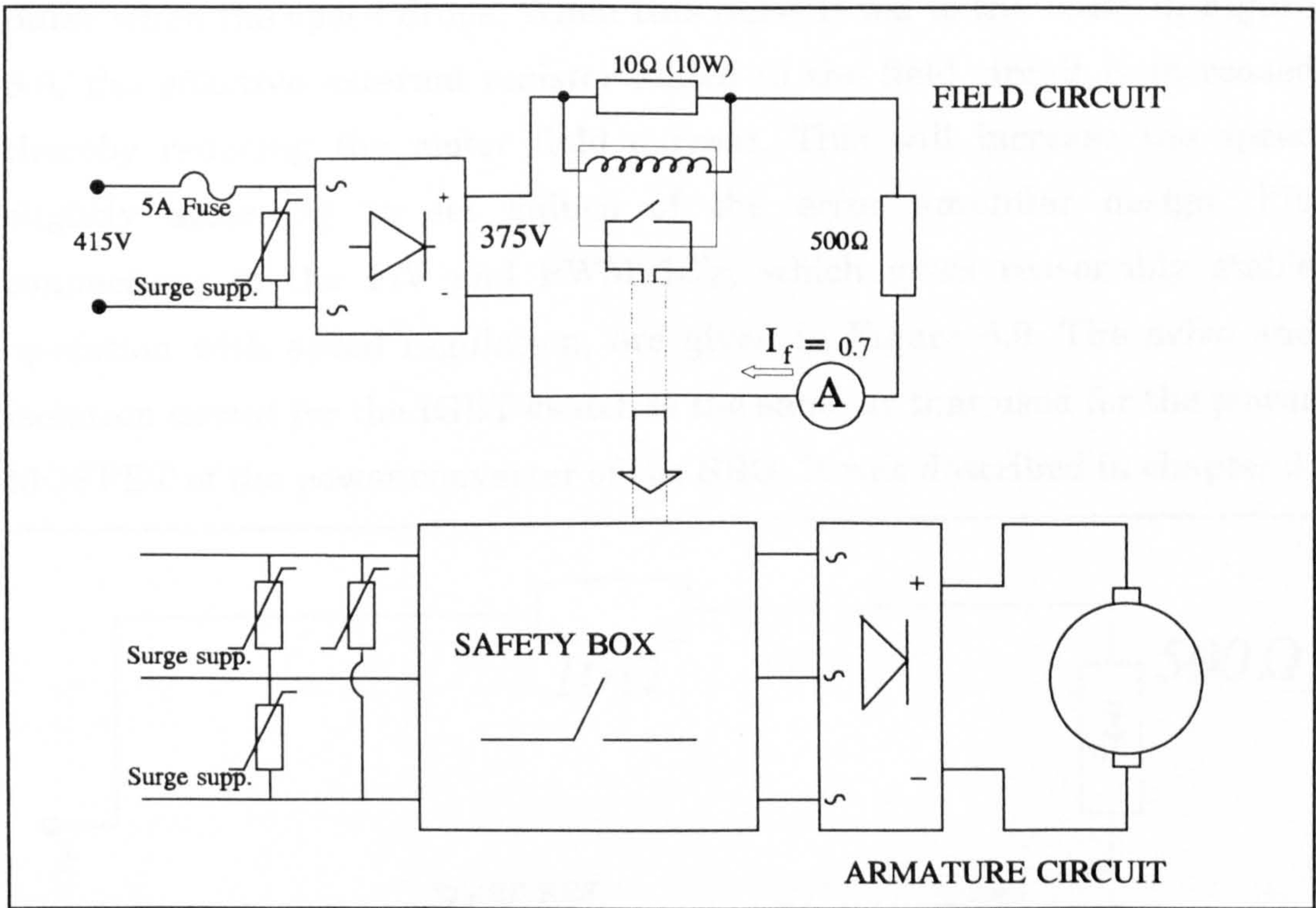


Figure 6.7: Armature and field circuits of the 18.5 kW D.C. Motor.

The field is supplied with 0.7 Amp from a rectified line-line voltage of 415 V using a single phase bridge rectifier. See figure 6.7. The motor field resistance is 500 Ω .

A 5 V relay to protect the motor, the blower, and the turbine, in the case of a sudden loss of the field current is also shown in Figure 6.7. This will trip a circuit breaker in a safety box thereby cutting off the armature supply.

The speed control circuit is required in order to automatically regulate the speed of the turbine during testing. A function diagram of a field control circuit is shown in Figure 6.8. The speed signal, from the position detector, or signal P as given in chapter 5, is converted, via an F/V converter IC-2917, to a voltage signal that makes one of the inputs of the error amplifier of a PWM IC-3524. The error amplifier is arranged to provide a P+I control such that the output of the PWM IC is a narrower pulse when the speed drops. When this pulse is fed to the IGBT in Figure 6.8, the effective external resistor added to the field circuit is increased thereby reducing the motor field current. This will increase the speed slightly according to set values of the error amplifier design. Pin connections of the F/V and PWM IC's, which gives reasonably stable operation with speed regulation, are given in Figure 6.9. The drive and isolation circuit for the IGBT switch is the same as that used for the power MOSFET of the power converter of the SRG. It was described in chapter 5.

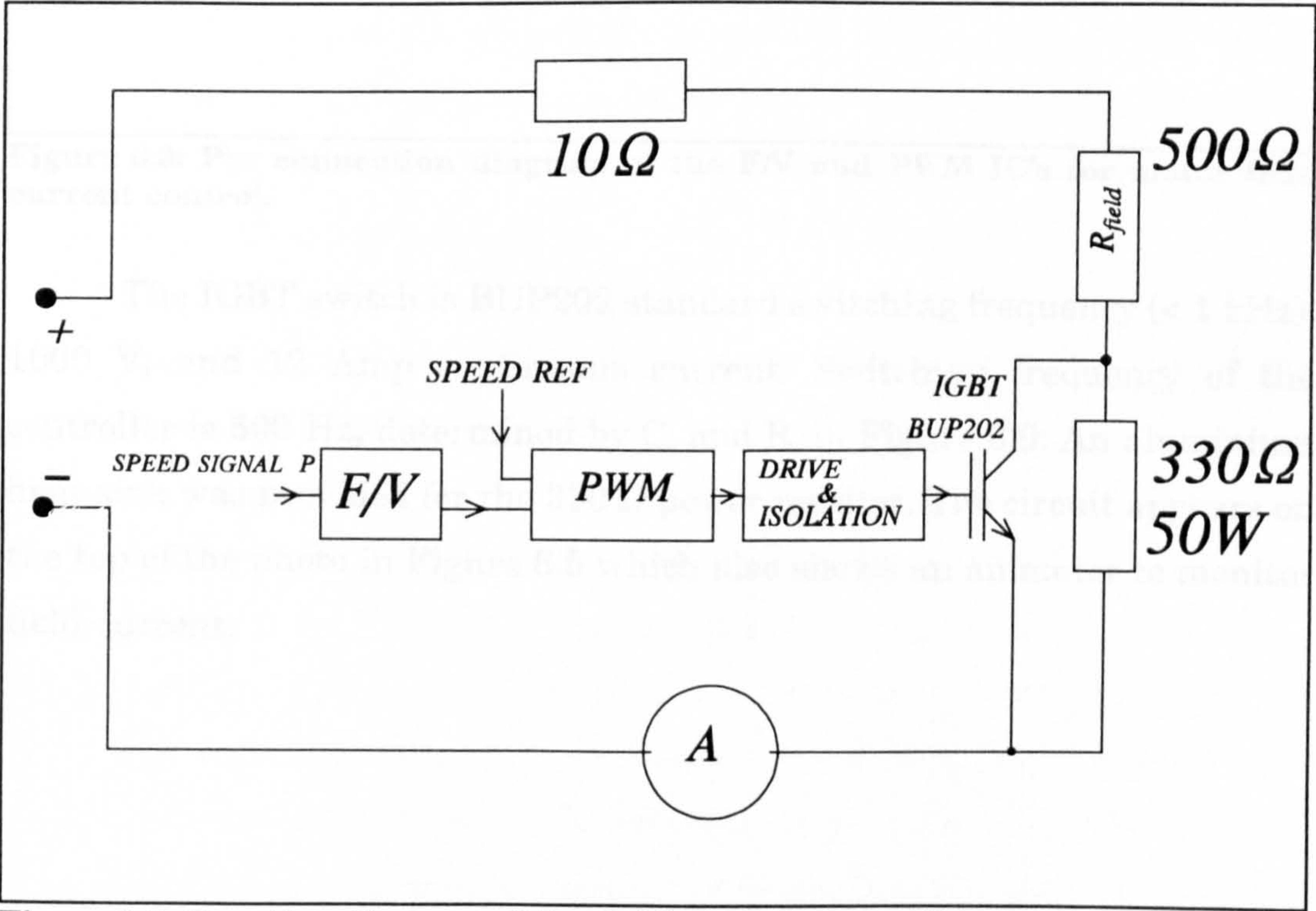


Figure 6.8: Function diagram of the field current controller.

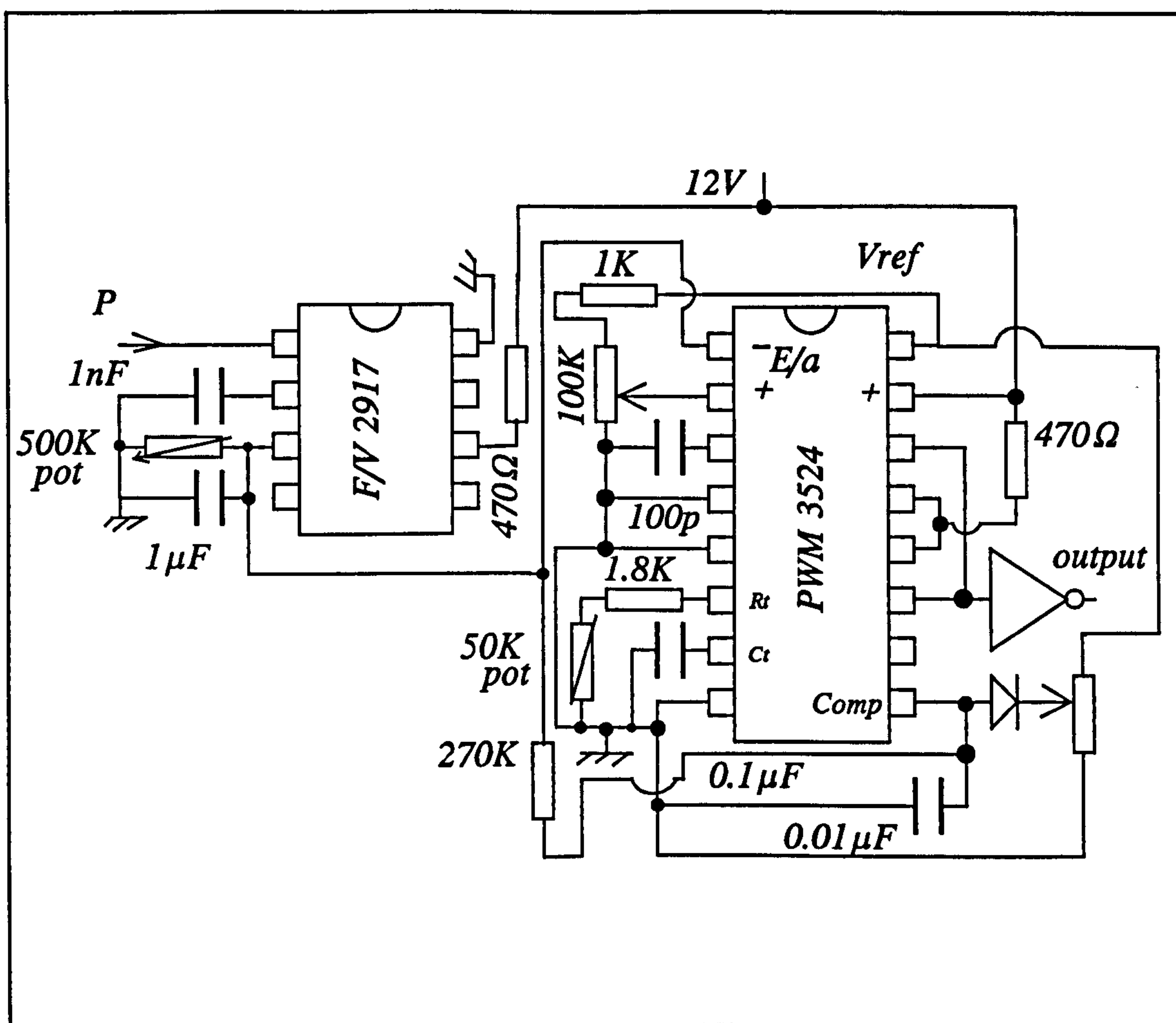


Figure 6.9: Pin connection diagram of the F/V and PWM IC's for motor field current control.

The IGBT switch is BUP202 standard switching frequency (< 1 kHz), 1000 V, and 12 Amp continuous current. Switching frequency of the controller is 500 Hz, determined by C_t and R_t in Figure 6.9. An aluminium heat sink was provided for the 330 Ω power resistor. The circuit appears on the top of the photo in Figure 6.5 which also shows an ammeter to monitor field current.

6.6 Mounting the SR Generator

The photo of Figure 6.10 shows the rotor of the SRG mounted on the turbine shaft. The rotor light-interrupting disk is also shown. The procedure of mounting the rotor requires the preparation of a stub shaft which is shrunk fit with the rotor hub. The assembly then slides over the turbine shaft and held in place using nut joints as has been explained in chapter 4. The shaft must then be balanced at 100,000 rpm. Balancing was carried out by the manufacturer of the turbocharger by taking away material from the stub shaft. Data for the balancing procedure is given in Appendix A6.4.

Mounting the stator of the SRG on the turbine required the following preparations:

- 1- Machining the outer surface of the steel tube round the wider end which fits into the groove of the turbine disk. See Figure 6.2. This machining ensured concentricity with the shaft of the turbine to the required tolerance, 0.03 mm. Careful machining is also required for the contact surface of the tube with the disk surface.
- 2- Machining of the inner groove of the turbine disk concentric with the shaft and polish-machining the surface of the disk.
- 3- Some radial clearance was allowed between the steel tube and the turbine disk. This served to allow for small adjustments of the stator position on the disk while using several feeler gauges with about 0.1 mm thickness to try to achieve a 0.1 mm air gap between the stator and the rotor which is as uniform as possible. This procedure of positioning the stator requires the oil bearing system to be in operation.

- 4- A safety cage was built to house the turbine and the SRG. This is shown in the photo of Figure 6.11. The top and side pieces are made of wood covered by a sheet of steel on the outer surface. The piece in the front of the unit has a window of double layer of Lexon for protection and viewing.

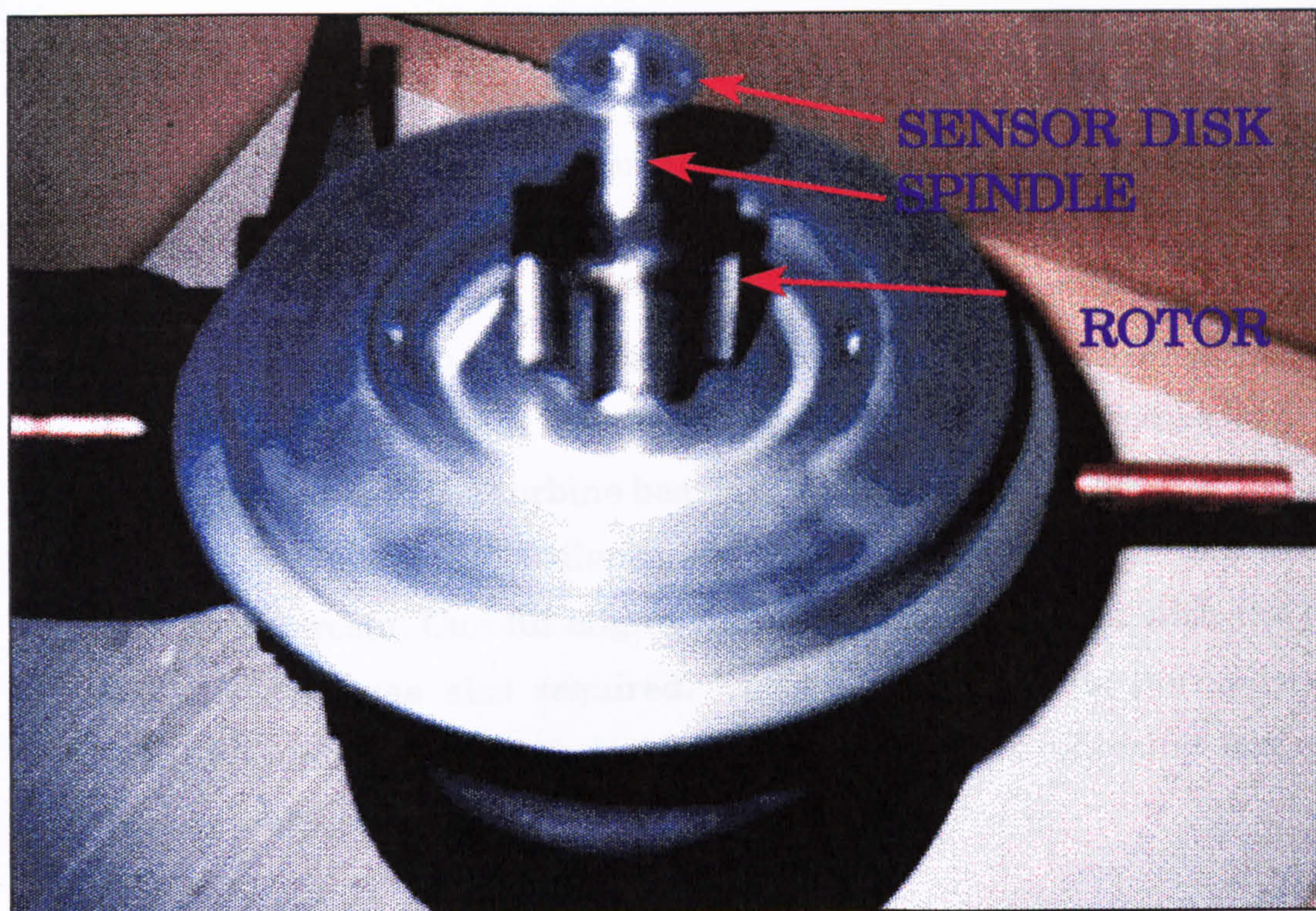


Figure 6.10: photo of the turbine after mounting the rotor (and the rotor disk) and balancing the shaft.

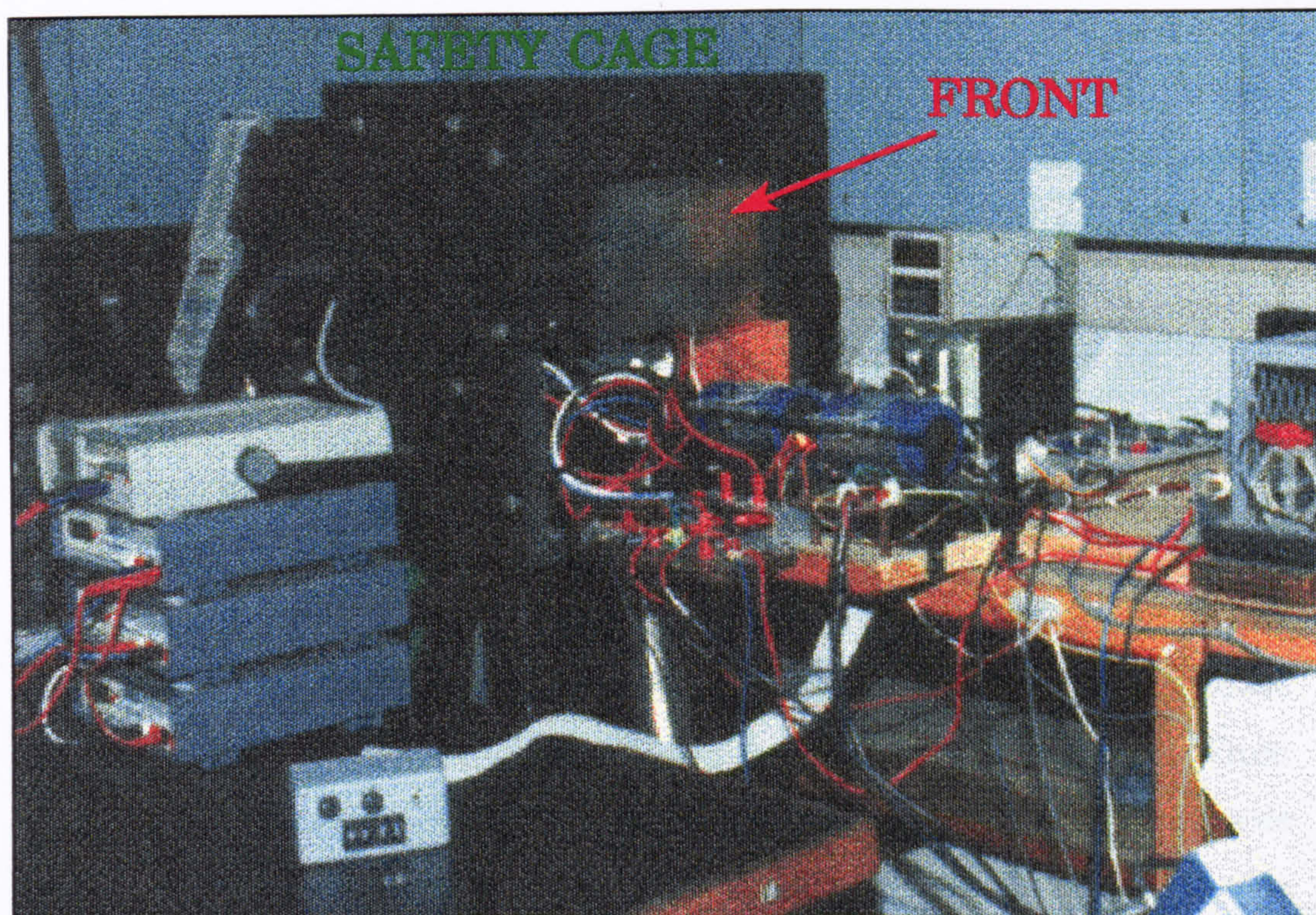


Figure 6.11: Safety cage around the turbine and the SRG.

6.7 Tests of the Air Supply System

To ensure the desired operation of the overall air supply system and the turbine, several tests were carried out:

- 1- The turbine was run at moderate speeds before mounting the rotor on its shaft. The aim was to investigate the blower performance and the performance of the turbine bearing. The high audible noise of the blower, despite the use of silencers, required transferring the unit to an adjacent room. Careful alignment of the outlet exhaust with the blower outlet was also required. The noise problem is normally tackled by placing the whole blower into a special silencing box. However, this was not provided.
- 2- After mounting the rotor, the turbine was run at high speeds up to 60,000 rpm. A high frequency light strobe was used to visibly ensure that vibration is minimum. A critical speed is encountered at a speed of about 10,000 rpm. To avoid problems during tests, the turbine should not be left running at this speed, i.e. this speed should be passed to the higher speeds as quickly as possible by increasing air flow.
- 3- A tachometer was used to measure the speed of the large d.c. motor while recording the turbine speed from a frequency counter of the signal P. At moderate turbine speeds, below 15,000 rpm, the relationship between the two speeds is approximately linear. At higher speeds, however, more power was required to overcome the losses in the coupling, the blower and silencers. A possible increase of leakage of air at higher speed demands is not ruled out. When slippage in the coupling between the motor and the blower was caused by the poor quality V-belt, which was first employed, it was easily detected by this test.

6.8 Conclusion

The design of the air supply system including the air turbine, the blower, and the driving d.c. motor has been presented in this chapter with the technical details of assembly and operation. It can be said that the resulting system performed satisfactorily as required, achieving the required speed of the turbine (60,000 rpm) with a reasonably balanced turbine shaft, and an electronic regulation of the turbine speed. Three main problems were encountered and demanded time and effort; the selection of an appropriate oil for the bearings, the stability of the turbine speed regulator, and the initially improper coupling between the blower and the d.c. motor driving it. Solutions for these problems were also discussed. Rotational speeds above 60,000 rpm could be achievable if the coupling between the d.c. motor and the blower is improved further. Nevertheless, speeds near the mechanical limit of the rotor (90,000 rpm) were avoided for safety reasons.

CHAPTER SEVEN

EXPERIMENTAL TEST SYSTEM AND PROCEDURE

7.1 Introduction

So far, a description of the design and construction of the SRG, and its assembly to the air turbine, has been presented. In this chapter, the experimental test system which aims at providing a preliminary performance evaluation of the SRG is described. Static tests for obtaining the magnetic characteristics of the SRG are discussed first with some results. The test system and the arrangements and procedure for obtaining the dynamic test results are also introduced, whereas the measurement results are discussed in the next chapter.

7.2 Static Tests

7.2.1 Introduction

Static tests for an SR machine include the determination of the magnetisation characteristics of the machine by measuring the air-gap flux levels corresponding to a certain excitation current and rotor position θ . The result is a table of values of flux linkage Ψ , current i , and rotor position θ , or graphical representation of $\Psi/I/\theta$ by a set of magnetisation curves.

Static tests will also include the measurement of the phase resistance R_w and the likely influence of temperature rise and switching frequency on its effective value.

The method that is to be adopted for determination of the magnetic characteristics of the high speed SRG does not have to be unduly accurate, since its function is only to provide an evaluation of the approximate quasi-linear model which was developed in chapter 2. Therefore, the simplest method of measurement at few locked-rotor positions will be considered sufficient.

7.2.2 Set-Up and Results of Static Tests

Figure 7.1 shows a circuit diagram for measuring the flux-linkage current characteristics of the high speed SRG. Figure 7.2 shows a photo for the actual arrangement for static tests. A voltmeter is used to measure the voltage across the phase winding and a current transducer is used for measuring the instantaneous current. The converter is the same one selected for exciting the SRG during its normal operation and was discussed in chapter 5. The rotor is mechanically locked into position and is fitted with a 50 cm arm made of light aluminium. The arm can be set at an angular position as an indicator for the rotor position or the angle θ .

A constant voltage is applied to the winding, and readings for peak current in the phase winding, time duration of voltage pulse Δt , and the voltage level V are taken. The measurement starts with low current values (the linear region). The current can be adjusted using the voltage level or the time duration of the voltage pulse. The voltage is altered using an a.c. transformer which supplies a single phase bridge rectifier (not shown in Figure 7.1) whereas the time duration of the pulse can be altered using the thumbwheel switch for setting the timer counter as described in chapter 5.

Flux is determined approximately using a simplified relation. This is derived from the basic terminal voltage equation. The flux is given as:

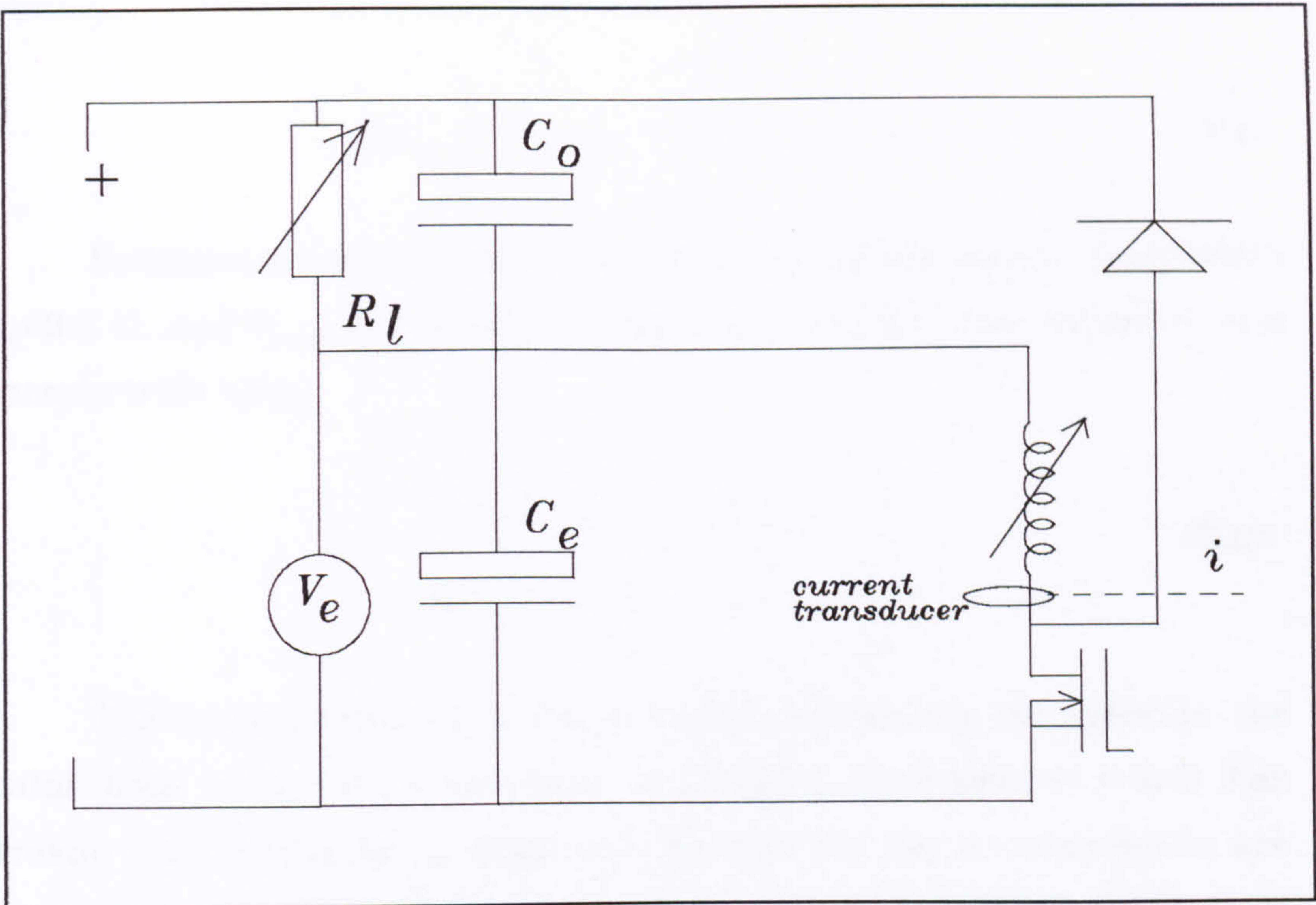


Figure 7.1: Circuit diagram for approximate inductance and flux measurement.

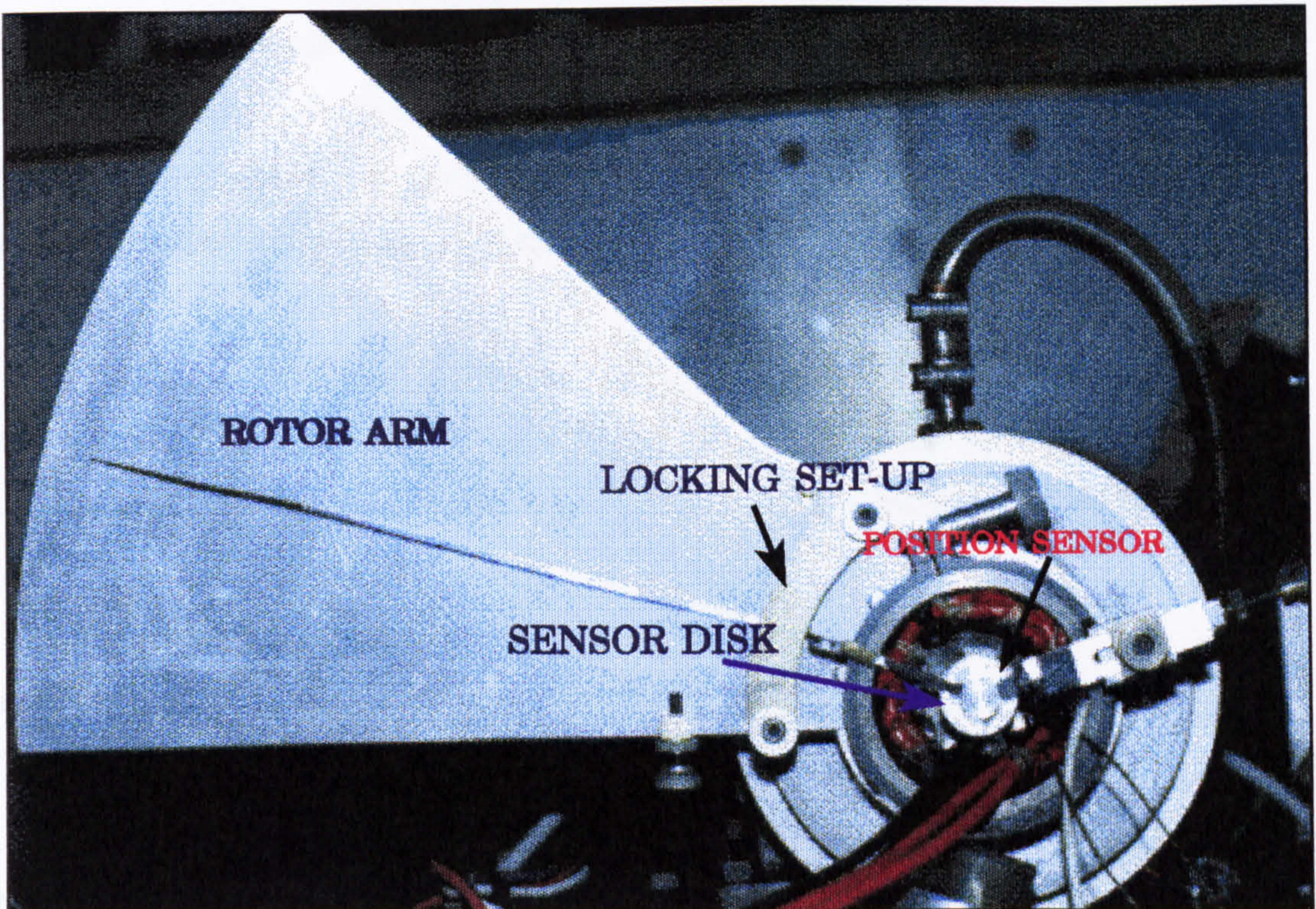


Figure 7.2: Photo showing the rotor locking arrangement for the static tests.

$$d\Psi = \int_0^t [v(t) - i(t) \cdot R] dt \quad (7.1)$$

Substituting the values of winding and power switch resistances $R_w=0.3 \Omega$, and $R_{ds-on}=0.2 \Omega$ respectively, and assuming the current to rise linearly with time:

$$\Psi = (V - \frac{\hat{I}}{2} R) \Delta t \quad (7.2)$$

$$\Psi = (V - \hat{I} 0.25) \Delta t$$

The measurements are taken while centralising the rotor in the stator bore using the pressurised oil bearing arrangement which has already been discussed in chapter 6. Results for the measurements are shown schematically in Figure 7.3 for $\theta=8^\circ$, 12° , 17° , and 22.5° , where $\theta=0^\circ$ corresponds to the fully-aligned position of the previous phase winding with regard to the one in question. The curves are compared with those assumed by the quasi-linear model of Figure 3.11. The effect of the leakage inductance can be seen in Figure 7.3 to give a higher slope of the measured curves than those of the model. Tables giving the results of the static tests measurements are given Appendix A7.1.

The LCR bridge connection was also used for determining the phase inductance at fully aligned and un-aligned positions. The bridge circuit supplies the winding with very low current. The results were as follows:

$$L_{\max} = 870 \mu\text{H}, \text{ at angular position } 22.5^\circ.$$

$$\text{and } L_{\min} = 129 \mu\text{H}, \text{ at angular position } 0^\circ.$$

However, for the angular position where the phase inductance is expected to start the rising inductance region (if leakage/fringing flux is allowed for) which is at about 8° , the minimum inductance L_{\min} is higher

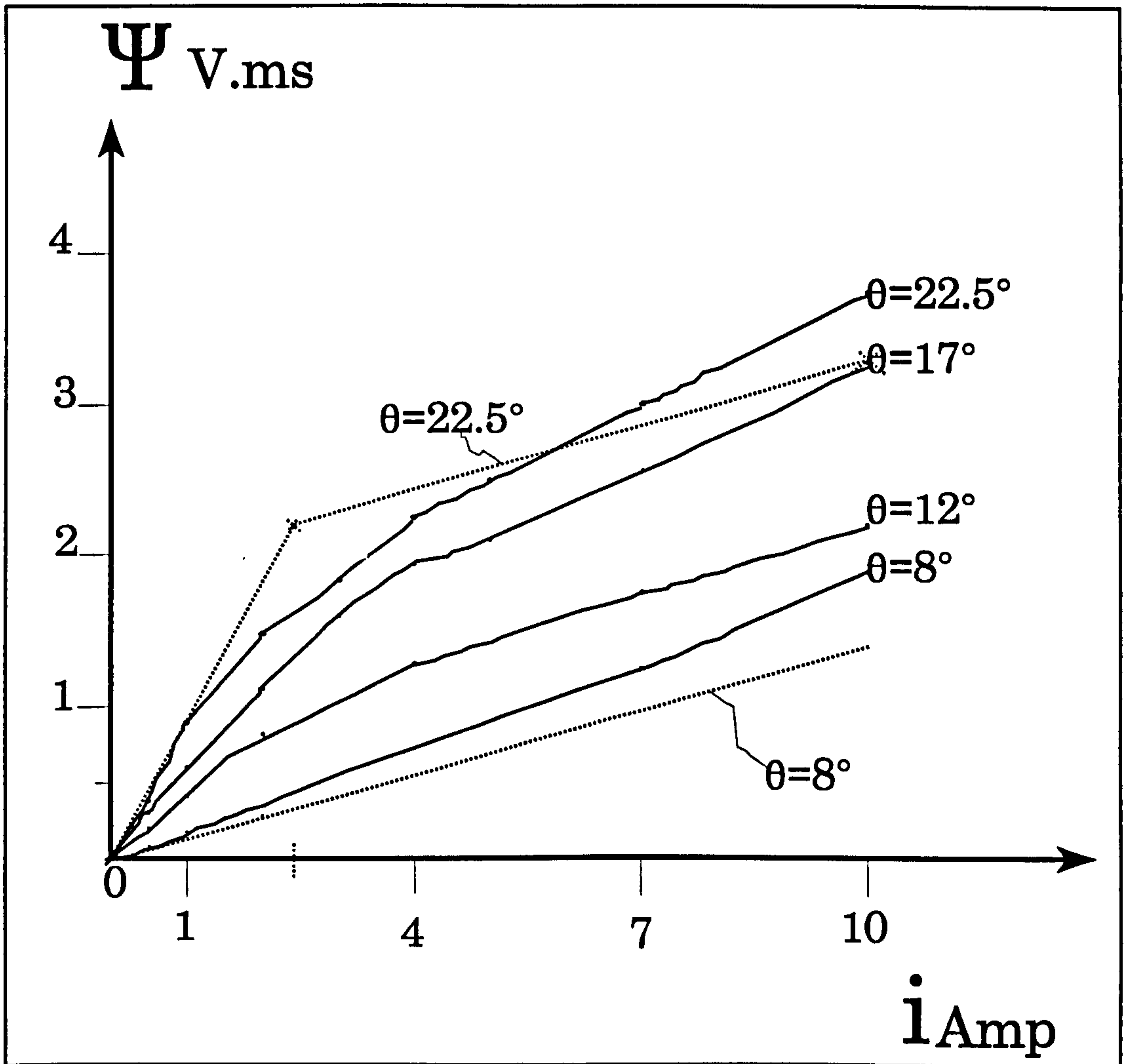


Figure 7.3: The magnetic characteristics of the SRG resulting from static tests measurements compared with those resulting from the model (dashed).

than at 0° (about 170-180 μH as in Table 2 of Appendix A7.1). Although the fit between the measured magnetic characteristics and those assumed by the quasi-linear model shown in Figure 7.3, appears to be poor, the overall Ψ - i area enclosed by typical waveforms give realistic values of power.

7.2.3 Phase Resistance Determination

It is expected that the winding may experience a temperature rise of about 30-50°C during its normal operation.

A simple arrangement for measuring the resistance consists of a d.c. voltage source, a voltmeter across the phase winding and an ammeter. A thermocouple to measure the winding temperature was inserted inside one of the eight coils that comprise the phase winding. By applying a d.c. voltage starting with low voltage and waiting for the temperature of the winding to settle, the resistance dependence on temperature was obtained. Results are shown in Table 7.1

I Amp	3	5	7	8.5	9.8	11	12	13	14
R_w mΩ	275	277	285	294	306	322	333	346	360
T°C	22	25	30	35	44	60	64	76	88

Table 7.1: Phase winding resistance dependence on temperature.

These figures were taken at an ambient temperature of 10°C. The temperature rise is therefore expected to be higher in an ambient of 25°C (at which most dynamic test results were taken). Also, one phase winding was connected during tests. Therefore, it is expected that during operation, winding temperatures, given in the table above, may correspond to a lower value of the phase current.

These results are expected, if the temperature coefficient figure for copper is taken into account. This coefficient is $\alpha = 0.00427 / ^\circ\text{C}$ and is utilised in the following relation in order to estimate the resistance change with temperature rise:

$$R_{t_1} = R_{t_2} (1 + \alpha \Delta t) \tag{7.3}$$

where temperature rise is $\Delta t = t_1 - t_2$.

A sample piece of the copper wire was tested to investigate at what temperature the insulation of the enamled copper wire of the 22 SWG would fail. It was only beyond 100°C, that the insulation began to show signs of failure. Fortunately, It is not expected for the machine to be operated above 80°C.

A simple test was also carried out to investigate the impact of high frequency switching on the effective winding resistance. A 2 kHz frequency signal was superimposed on a d.c. voltage supplying the phase winding. No detectable effect can be reported. Although 2 kHz is a relatively low frequency, the skin depth is approximately 1.6 mm which is large compared with the diameter of the wire. Skin effect would therefore be expected to be negligible. Proximity effect should also be small due to low number of turns.

7.3 Introducing The Experimental Test System For Dynamic Tests

Figure 7.4 shows a schematic diagram of the circuit used for dynamic tests. The main quantities to be directly measured by the test rig arrangement are explained below:

- 1- I_{out} , the output current or the load current. This is the mean current taken from both phase windings of the SR generator and delivered to the load after turning off the power switch of a particular phase. It is equivalent to the sum of the mean value of currents in the power diodes.
- 2- V_o , the output voltage of the power converter or the sink voltage. Since I_{out} will vary during dynamic tests and V_o is required to be kept constant, a variable load resistor or an auxiliary voltage regulator is

necessary (described later in the chapter).

- 3- I_{in} , the input current. This is the mean current drawn by the phase windings of the SR generator during excitation. It is equivalent to the sum of the mean value of current in both power switches.

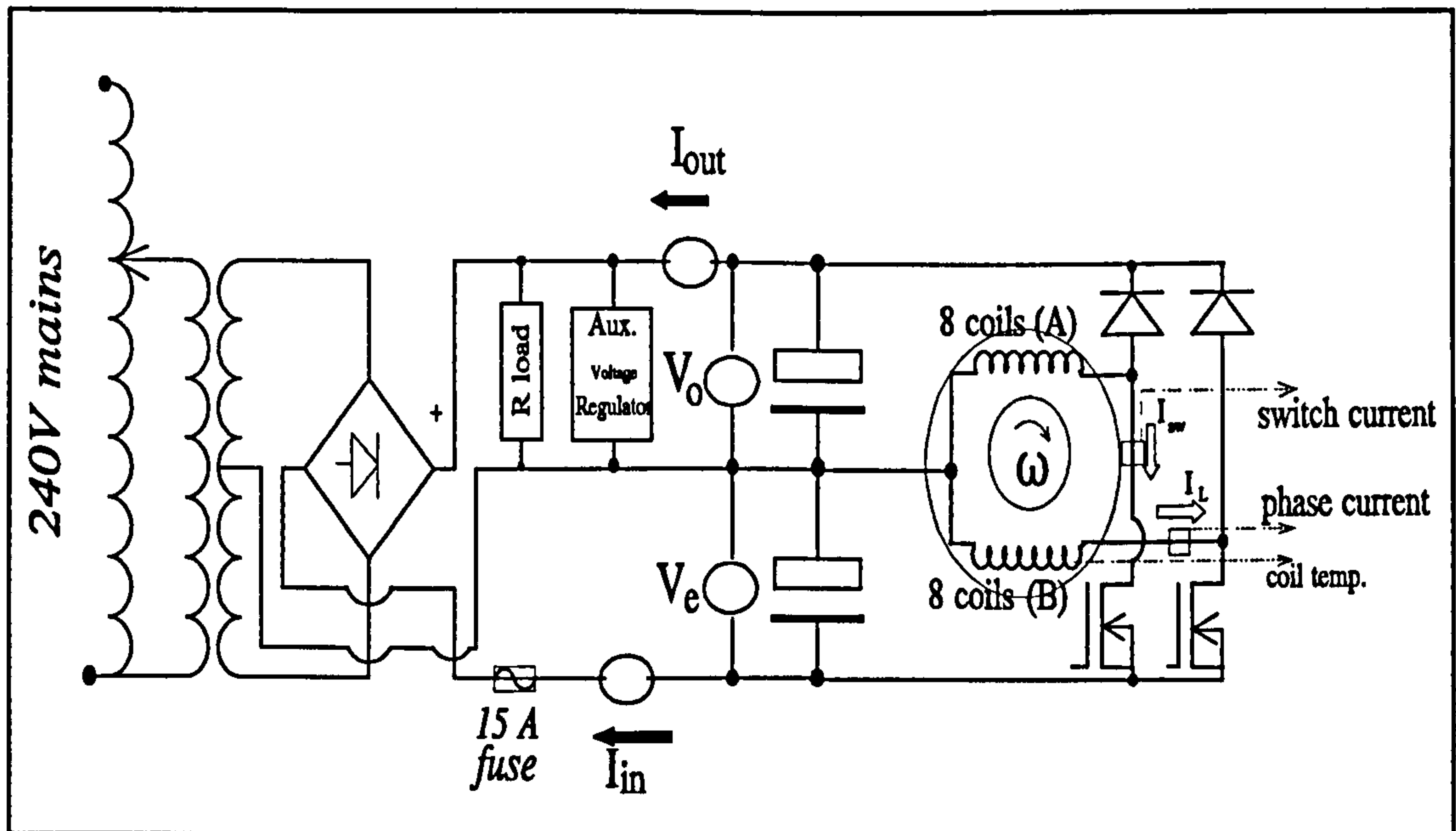


Figure 7.4: Circuit for dynamic test set-up.

- 4- V_e , the excitation voltage of the generator. It is kept constant at the required excitation level by adjusting the single-phase variable transformer supplied by the mains.
- 5- I_{L-rms} , the r.m.s. value of the current in one phase winding, (phase winding B).
- 6- I_{sw-rms} , the r.m.s. value of the current in the power switch which is in series with phase winding A.
- 7- ω , the rotational speed of the rotor of the SRG.
- 8- T_c , the coil temperature.

7.4 Instrumentation

7.4.1 Basic Instrumentation

Figure 7.5 shows a photo for the basic dynamic test instruments. Digital multimeters were used for the measurement of mean currents and voltages. Instrumentation for more precise measurement of the SR machine would use a data acquisition system.

The electric power injected in the SRG to provide the field excitation can be obtained from the readings of the mean voltage across the exciting capacitor V_e times the mean current in the return path I_{in} . These are provided by a digital voltmeter measuring V_e and a digital ammeter measuring I_{in} as shown in figure 7.4 and photo of Figure 7.5.

The electric power output across the load is simply determined from the product of the mean current provided by the freewheeling diodes and the load voltage. Similarly, these are measured by a digital ammeter measuring I_{out} and a digital voltmeter measuring V_o shown in Figure 7.4 and the photo of Figure 7.5.

The r.m.s. measurement facility of the oscilloscope Tektronix 2430A is used to determine the current in the phase winding I_{L-rms} , and the current in the switch I_{sw-rms} .

The current waveform was obtained using two small Hall effect current transducers which can accurately measure instantaneous values up to 50 Amp. The location for each transducer is shown in Figure 7.4. The resolution of each transducer was increased by passing the conductor three times through the centre core such that the current measurement range is reduced to (50 Amp/3) or about 17 Amp. Upon testing the transducer it was found that current values up to 25 Amp may still be measured without

saturating the core of the transducer. However, the accuracy beyond 17 Amp may not be guaranteed by the manufacturer.

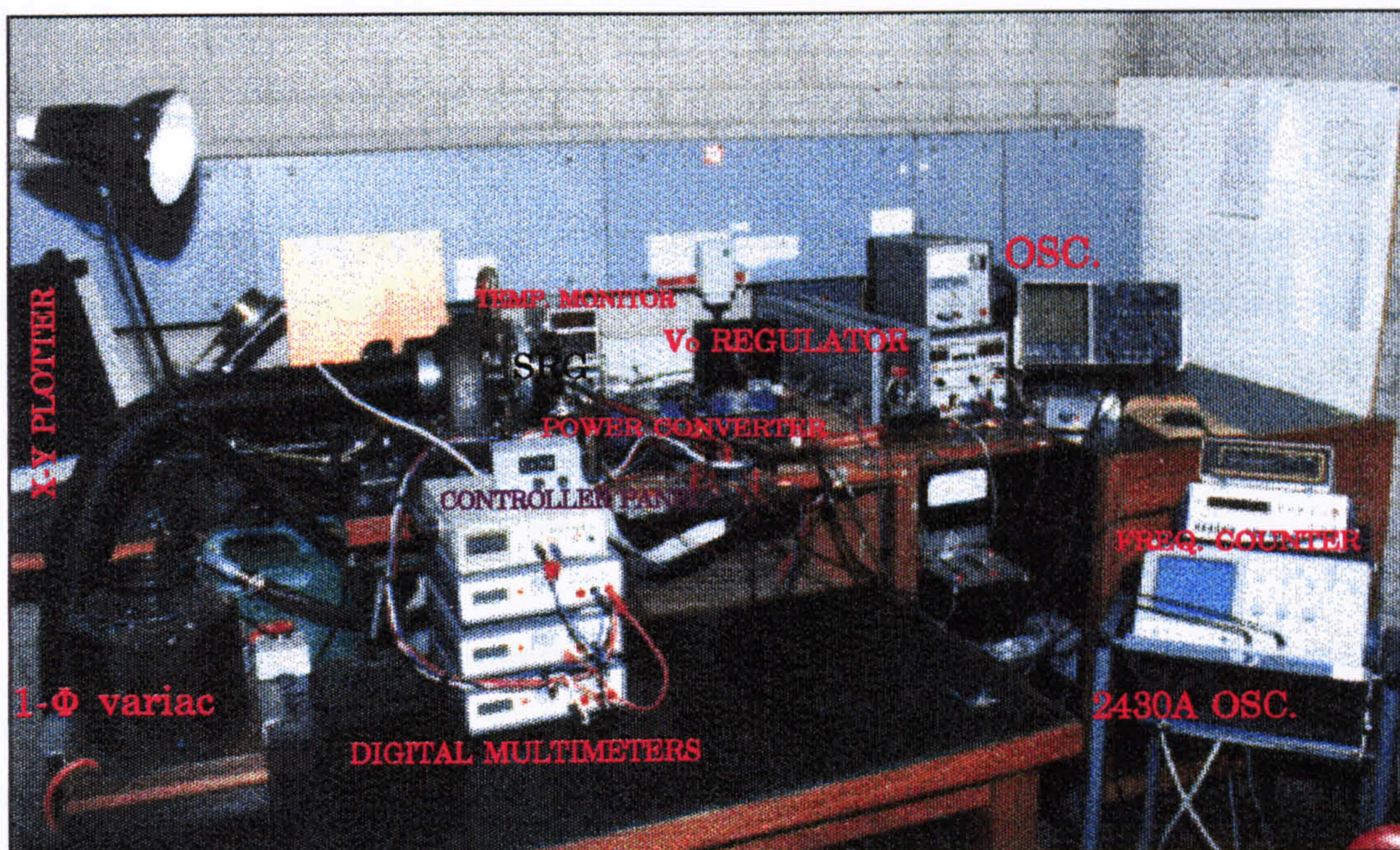


Figure 7.5: Photo showing instrumentation used for taking measurements of the SRG test rig.

Traces of the phase current waveform and switch current waveform were obtained by using a serial port interface between the oscilloscope and an X-Y plotter (also shown in the photo of Figure 7.5). Some examples are shown in chapter 8.

The rotor speed ω is simply measured by applying signal P, the output of the rotor position sensor, to a frequency counter.

Copper losses are determined using the value of the phase winding resistance, found earlier (in section 7.2.3) to be in the range $0.28\text{--}0.36\ \Omega$ for temperature range $22\text{--}88^\circ\text{C}$, and the measured value of $I_{L\text{-rms}}$. It was therefore necessary to monitor the coil temperature continuously during tests using a thermocouple carefully placed inside at least one coil. Two thermocouples were eventually used for measuring the temperature of both phase windings.

7.4.2 Auxiliary Voltage Regulator

As the SR machine starts to generate, the voltage across the load V_o rises due to the additional electric power generated in the system. V_o continues to rise until the peak P_g is reached at some set of firing angles.

As far as the power convertor is concerned, V_o should not exceed the reverse breakdown voltage rating of the power switches. In the present case this rating for the power MOSFET is 200 volts. Hence, the voltage V_o should be limited to 100 volts since double this voltage would appear across the power switch at turning off.

In most practical convertors and drives that employ SR machines as generators or motors, the energy used to excite the machine is returned back to the supply via power diodes. In this case the voltage applied to the winding of the machine is only that of the fixed d.c. supply. There is an obvious advantage, therefore, in testing the SRG as if it is performing in an actual practical system. It would therefore be necessary to regulate V_o so that it is fixed and equal to V_e . An active load regulator has therefore been developed and is shown in Figure 7.6.

The regulator consists mainly of a power transistor of bipolar darlington type MJ11016 mounted on a 0.9°C matt black heat sink. The transistor draws more load current as the current into its base is increased. The means of converting the rise in V_o into higher base current is realised by deriving the required base current from the collector of a small signal PNP transistor. The electrolytic capacitors (shown in Figure 7.6) are needed to filter out the ripples of the switching converter that were interfering with the operation of the regulator causing overheating in the transistor. The regulator performed satisfactorily for V_o values of 30, 40, 50, and 60 volts.

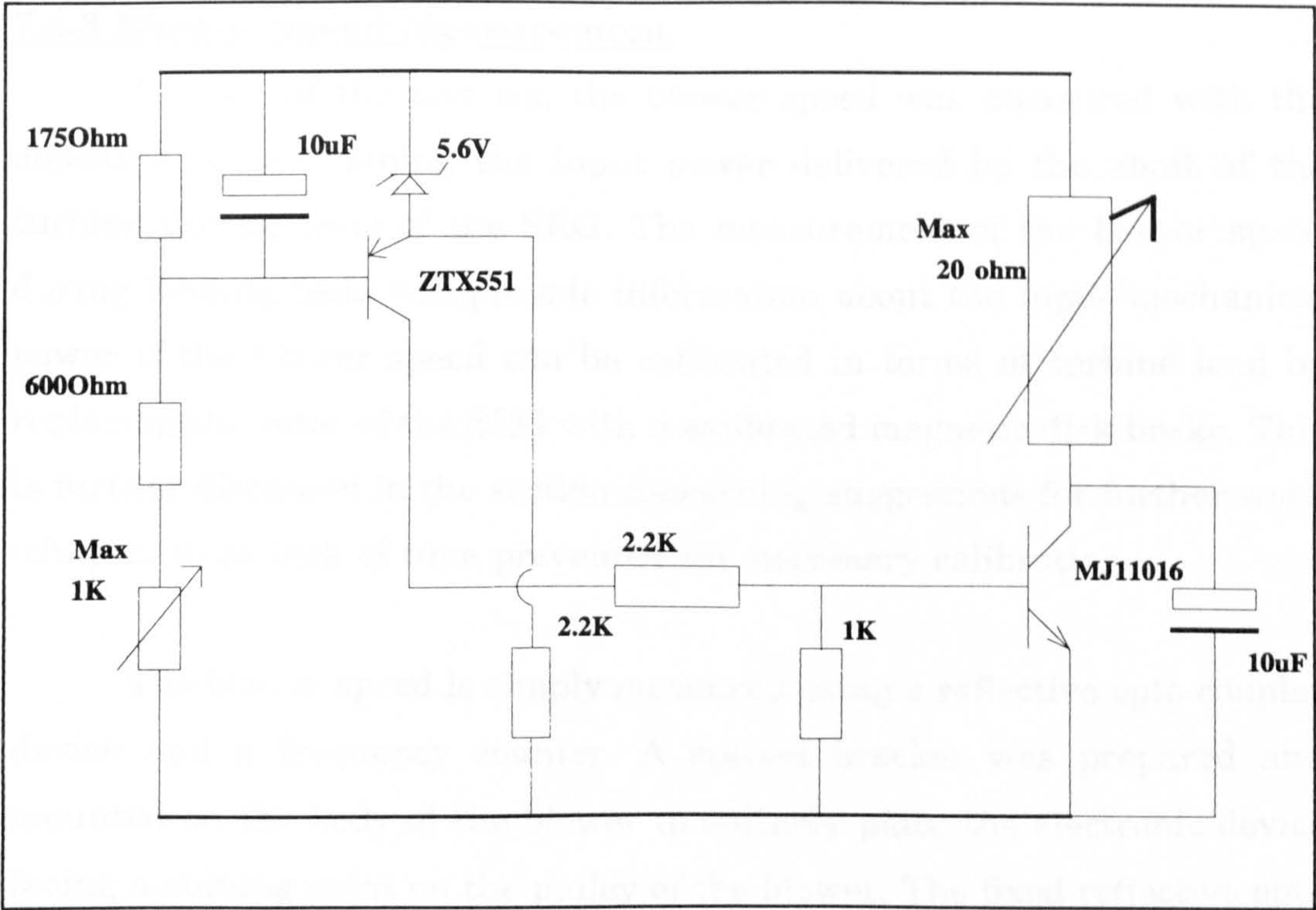


Figure 7.6: Circuit diagram for auxiliary voltage regulator.

7.4.3 Blower Speed Measurement

As part of the test rig, the blower speed was measured with the objective of determining the input power delivered by the shaft of the turbine during tests of the SRG. The measurement of the blower speed during loading tests will provide information about the input mechanical power if the blower speed can be calibrated in terms of turbine load by replacing the rotor of the SRG with a calibrated magnetic disk brake. This is further discussed in the section concerning suggestions for further work (chapter 9) as lack of time prevented the necessary calibration

The blower speed is simply measured using a reflective opto-coupler device and a frequency counter. A special bracket was prepared and mounted on the body of the blower to suitably place the electronic device facing a shining point on the pulley of the blower. The fixed reflective opto will pick up the signals from a rotating shining strip glued firmly on the pulley. It was necessary to have this strip glued onto a small piece of hard rubber to make the shining rotating point project towards the opto device. Experimentally, it was found that this reduced the noise accompanying the output pulses representing the frequency of rotation of the blower. The optimum distance between the device and the 1 cm wide strip was found experimentally to be 4 cm.

Readings of the blower speed were taken during dynamic tests of the SRG. Since the experiment of estimating input power was not performed, these readings are not included in the presentation of testing results in chapter 8, but a sample of these measurements is given, instead, in the Appendix relating to chapter 8.

7.5 Estimation of Power Output and Efficiency

The net generated power is determined from the d.c. measurements of voltages and currents:

$$P_g = V_o \times I_{out} - V_e \times I_{in} \quad (7.4)$$

Efficiency is determined by estimating the losses in the winding (copper losses P_{L-c}) and in the converter (transistor conduction losses P_{L-sw} and diode on-state losses P_d). Therefore, efficiency determination is based entirely on estimating electrical losses in the system. These losses are dominated by copper losses, and for two phases:

$$P_{L-c} = 2 \times I_{L-rms}^2 \times R_w|_{T_c} \quad (7.5)$$

where R_w is the phase winding resistance at the measured winding temperature T_c .

Transistor conduction losses are determined by the r.m.s. current in the switch, I_{sw-rms} , and the conduction resistance of the power transistor (R_{ds-on}). These losses are much less than the copper losses; typically 10-30% of copper losses. On average, the value of R_{ds-on} was taken slightly higher than its initial value at 25°C of 0.18 Ω . During tests, the temperature rise of the power transistor was limited to slightly above 30°C. Therefore, it is possible to consider R_{ds-on} as being 0.2 Ω in all cases during tests. The error resulting from this approximation is indeed very small. Thus P_{L-sw} :

$$P_{L-sw} = 2 \times I_{sw-rms}^2 \times R_{ds-on} \quad (7.6)$$

Diode on-state losses P_d were determined from I_{out} , which is the total mean output current, assuming the average voltage across the diode 0.7 volts. Thus:

$$\text{For both phases: } P_d = I_{out} \times 0.7 \quad (7.7)$$

Switching losses in the transistor (for a 60 nsec fall time for the transistor and 8 kHz switching frequency at 60,000 rpm) were considered to be insignificant (less than 1 watt) compared with the winding loss and were therefore ignored. Capacitor losses are negligible. Therefore, the efficiency will be determined as:

$$\eta \% = \frac{P_g}{P_g + P_{L-c} + P_{L-sw} + P_d} \quad (7.8)$$

7.6 Test Procedure

The measurement results are obtained by executing the following procedure:

- 1- The required speed of the turbine, ω , must be reached before some voltage could be applied to the phase winding. Failing to do so or failure of the air supply system to provide enough supply for high speed running while excitation is applied, would result in excessive currents in the winding. The speed regulator must be adjusted for the required ω by setting the speed reference potentiometer of the control circuit of the d.c. motor field current as has been discussed in chapter 6.
- 2- The firing angles are set using the thumb wheel or push button BCD switch at the required set of θ_{dly} and θ_{on} angles. θ_{on} is fixed first at a low value such as 10° , while θ_{dly} is selected at a value that would give a commutation angle ($\theta_{com} = \theta_{on} + \theta_{dly}$) of 26° . θ_{dly} is then increased by 2° until θ_{com} reaches 38° .

- 3- The excitation is raised to the required level of V_e . Some adjustment might be needed during tests to keep V_o constant as it will fall when θ_{on} is increased. V_e is adjusted using a single phase variable transformer.
- 4- Adjustment of the auxiliary voltage regulator to regulate V_o according to the working level of V_e . Some further adjustments might be needed during tests to ensure that V_o equals to V_e . The resistance value of the resistive load must fall within the range of the expected output current.
- 5- With the required ω , θ_{dly} , θ_{on} and V_e values, readings of output current I_{out} , input current I_{in} , I_{L-rms} , I_{sw-rms} , and blower speed are taken. Meanwhile, ω , V_e , V_o are continuously monitored in case manual adjustment is required. The temperature of the phase windings T_c is also monitored. This temperature was kept at approximately 65°C by using a cooling fan running at 10,000 rpm to blow air towards the side of the steel tube which contains the stator core and the winding. If T_c starts to exceed 70°C, the test will be halted and the fan will continue to cool the winding.
- 6- The test procedure outlined in 2-5 above is then repeated for larger values of θ_{on} in steps of 2°. The maximum value of θ_{on} is 22° which corresponds to about half a rotor pole pitch.
- 7- The test procedure of 2-6 is then repeated for different rotational speeds and excitation voltages.

7.7 Conclusion

A description of the experimental test system (instruments and procedure) for the static and the dynamic tests has been presented in this chapter. The resulting accuracy of the static tests depends on ensuring the locking of the rotor at the required position without movement during tests. Very slight movement of the rotor was inevitable with the arrangement that has been used. Another factor affecting accuracy is the use of the oil bearings while the rotor is stationary. A light load (such as the aluminium arm) on the small rotor of the SRG will inevitably have some influence on the uniformity of the air-gap during tests.

The accuracy of the dynamic tests is determined by the digital multimeters used for reading average voltages and currents. Readings for the voltage were recorded within a random voltage variation of ± 2 volts, whereas for the current, a random variation of ± 0.1 Amp was noticed. These figures were typical for voltages around 50 volts and currents around 5 Amp, thus resulting in random errors of 4% and 2% for voltage and current readings respectively. For P_g , a possible error of about 16% could result, but in practice the error will be much less due to the number of readings taken. The accuracy also depends on the oscilloscope measurements of the r.m.s. currents. The readings were accurate, (accuracy is guaranteed up to about 17 Amp peak) but some d.c. offset (about 0.3 Amp) resulting from the use of the Hall effect current transducers was ignored.

Finally, the efficiency values will be slightly optimistic regarding the estimation of losses in the diode. Due to the high value of average current in the diode, a voltage higher than 0.7 volts in equation (7.7) (such as 0.9-1.1 volts) could give more realistic values for these losses. However, the error is within the uncertainty of loss prediction, particularly regarding copper losses dependence on temperature winding.

CHAPTER EIGHT

DYNAMIC TEST RESULTS

8.1 Introduction

The dynamic testing results presented in this chapter are determined for 40,000 rpm, 50,000 rpm and 60,000 rpm. Two levels of excitation voltages V_e were considered for each speed, resulting in six sets of measurement results.

The wide range of results obtained gives a detailed performance representation of the machine at continuous as well as at peak power ratings. The results are graphically presented with comments on each graph. Phase current traces from the oscilloscope are presented. A comparison between the practical results and the simple model predictions is given. Tabulated results are fully explained and presented in Appendix A8.1.

8.2 Power and Efficiency Diagrams

Figures 8.1-8.6 illustrate curves for generated power P_g versus commutation angle for various θ_{on} (from 10° up to 22° with 2° steps) showing also the values of estimated efficiency for each operating point on the graph. Results of each set correspond to a particular speed and excitation voltage. Values of I_{out} and I_{in} currents are used to determine the effectiveness of power conversion inside the machine. This is the ratio of the converted power to the total output power, and is thus given as:

$$\text{Effectiveness} = \frac{P_{gen}}{P_{out}} = 1 - \frac{I_{in}}{I_{out}} \quad (8.1)$$

The continuous and the peak ratings of the machine which are determined by the thermal limit of the winding are indicated on each graph by defining a contour which corresponds to maximum generated power at each of the ratings. The continuous rating is determined from the tabulated results, given in Appendix A8.1, at the operating points which correspond to 5 Amp r.m.s. phase current. A particular point on the contour may be approximated to the nearest measured points to the 5 Amp rating by referring to the tabulated results of Appendix A8.1. The contour for peak (short-term) rating is determined in a similar manner.

The legend in the Figures 8.1-8.6 corresponds to the values of θ_{on} ranging from 10° to 22° .

The power curves of Figure 8.1 show that maximum power, at each particular θ_{on} , is achieved by operating at a commutation angle θ_{com} of 32° . However, this does not correspond to the maximum efficiency, which occurs earlier at θ_{com} of 28° (and 30° for peak power curve). Delaying commutation to higher values of θ_{com} results in allowing sufficient time for the current to build up, thus higher P_g , yet energy circulation in the converter is increasing resulting in higher losses. Efficiency is maximum for the power curves of Figure 8.1 along the curve which corresponds to θ_{on} of 12° , however, P_g is quite low being just below 30 watts. Peak power is 100 watts and will be used as a reference when comparing with other sets of results. However, in this case, this power level is achieved at a point beyond the continuous rating of the machine as shown in Figure 8.1. The maximum power at the assumed continuous rating is approximately 72 watts at an efficiency of 80%.

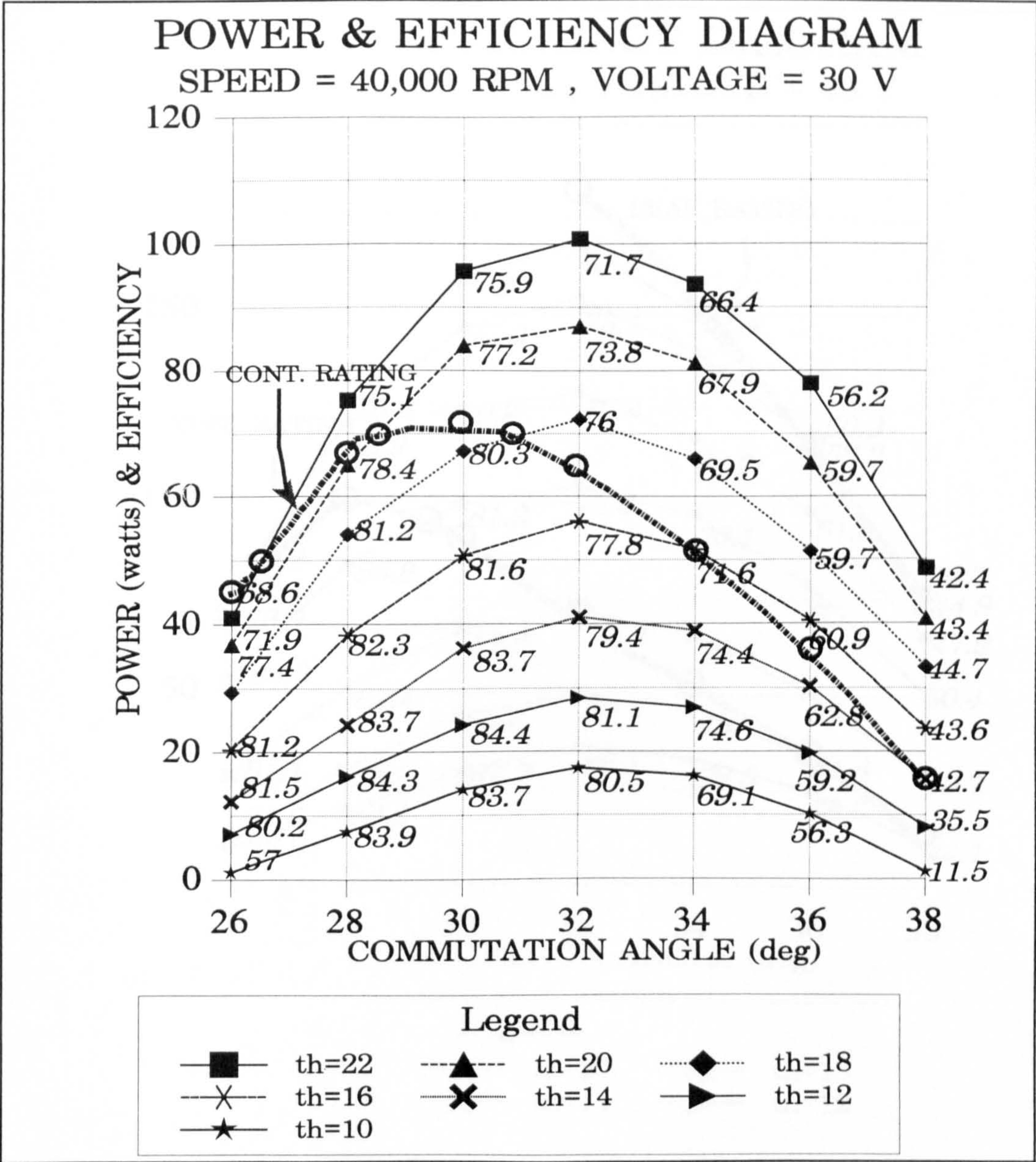


Figure 8.1: Power & Efficiency diagram for 40,000 rpm and 30 volts.

Considering the power diagram of Figure 8.2, the maximum efficiency also occurs at θ_{com} of 28° . If the power diagram of Figure 8.2 is compared to the previous one, then the peak power in the case of Figure 8.1 (100 watts) can be achieved with more than 10% better efficiency by increasing the excitation by 10 volts and changing the operating point to a new set of angles; θ_{on} is approximately 17° , and θ_{com} is 28° . Note that this point corresponds to the maximum power at continuous rating as shown in Figure

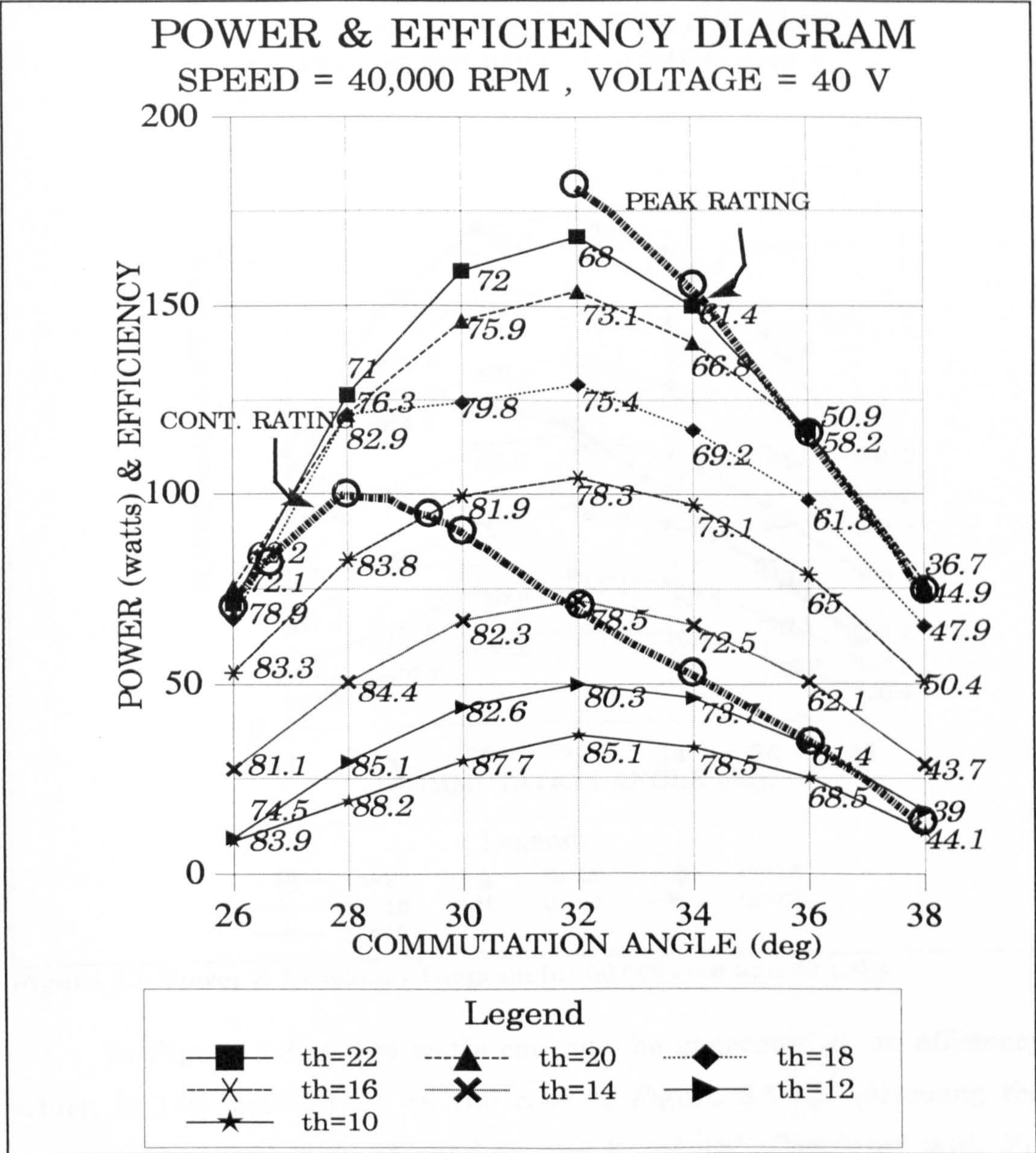


Figure 8.2: Power & Efficiency Diagram for 40,000 rpm and 40 volts.

8.2. The maximum effectiveness factor is found for 30 volts to be 0.54, whereas in the case of 40 volts it is 0.55, both at θ_{com} of 30° . Also, operation is slightly below the peak rating at peak power, which is 168 watts (at $\theta_{com}=32^\circ$) and at which the phase current is 10.33 Amp. The value of θ_{on} was not increased at this point to avoid continuous phase current situation.

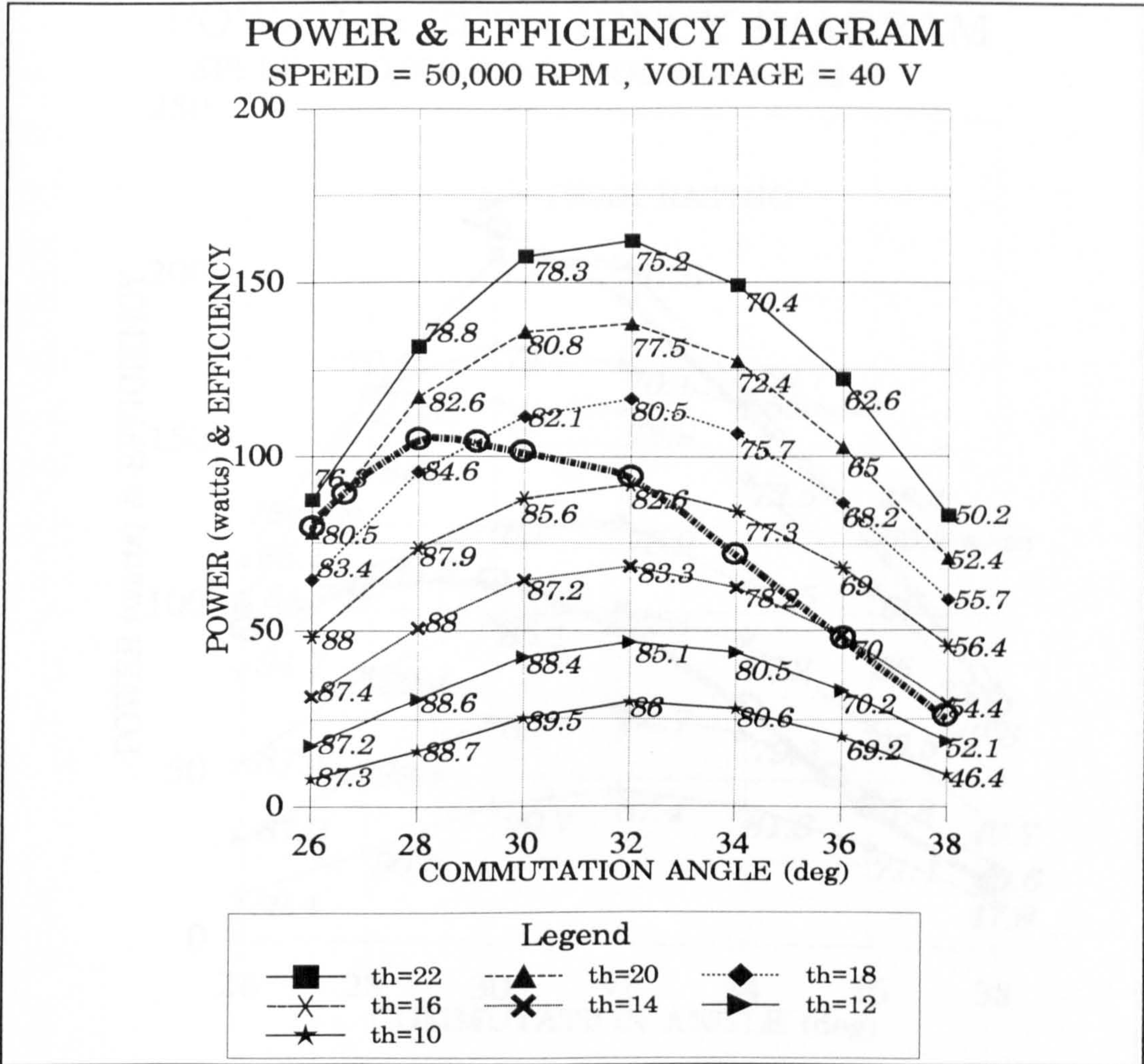


Figure 8.3: Power & Efficiency Diagram for 50,000 rpm and 40 volts.

In Figure 8.3, a 100 watts can now be generated at an efficiency which is 14% better than in the case of Figure 8.1 by advancing the commutation further to 28° and setting θ_{on} at 18°. Compared with the previous case of Figure 8.2, the peak power is now only 3% less when increasing the speed by 10,000 rpm (25%), but the efficiency is improved by more than 7%. However, by increasing the speed at the same voltage the continuous rating contour in the case of Figure 8.3 is only very slightly higher than that in Figure 8.2 with only 1% better efficiency.

The maximum effectiveness factor occurs when θ_{on} is 16°, and this is better than in previous cases, standing at 0.59.

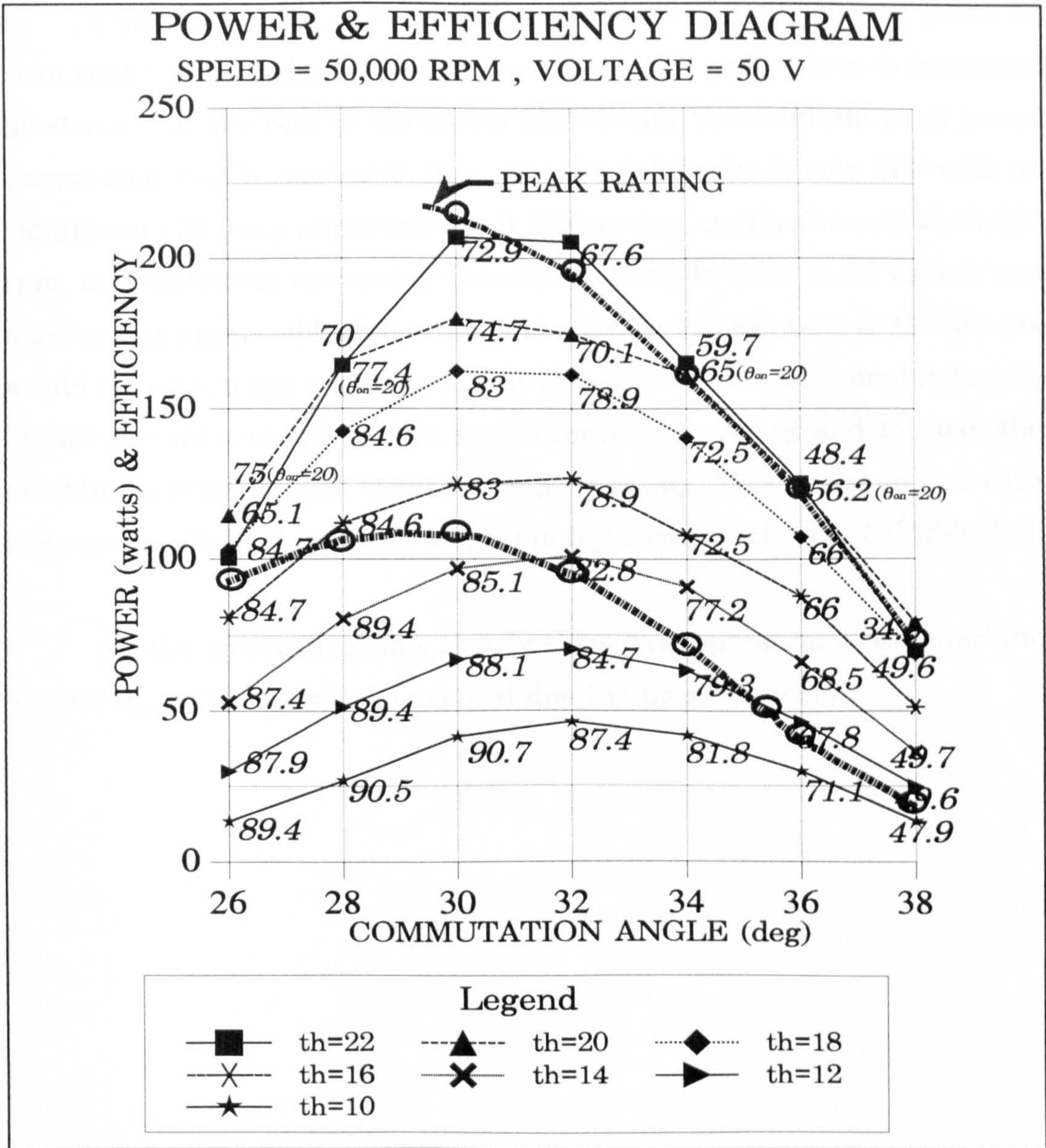


Figure 8.4: Power & Efficiency Diagram for 50,000 rpm and 50 volts.

In Figure 8.4, upon increasing the voltage by 25% at 50,000 rpm, the efficiency for 100 watts case is only very slightly improved over that of Figure 8.3. Furthermore, the maximum effectiveness factor in the case of 50 volts is reduced to 0.54. Also at powers higher than 100 watts, the peak power locus is shifted towards earlier commutation at 30°. It can also be seen from the diagram that the continuous rating in the case of 50 volts in Figure 8.4 is in general not better than the previous one at 40 volts.

Comparing the previous four sets of results, at 40,000 rpm it can be seen that by increasing V_e from 30 to 40 volts the peak power is increased by about 70%, whereas in the case of 50,000 rpm, the resultant peak power improvement of increasing V_e from 40 volts to 50 volts is only 27% with no significant efficiency improvement. It follows that, unlike the case at 40,000 rpm, at 50,000 rpm increasing the voltage from 40 volts to 50 volts is not making any appreciable difference, and a higher voltage such as 60-70 volts would have been more appropriate at this speed as it would enable to give higher powers and efficiencies at the continuous rating and to push the machine operating point towards the peak rating. This is also in line with the results obtained from the programming model in chapter 3 (Table 3.2).

All the power diagrams clearly show that operation of the machine beyond θ_{com} of 32° should be avoided due the poor efficiency.

POWER & EFFICIENCY DIAGRAM

SPEED = 60,000 RPM , VOLTAGE = 50 V

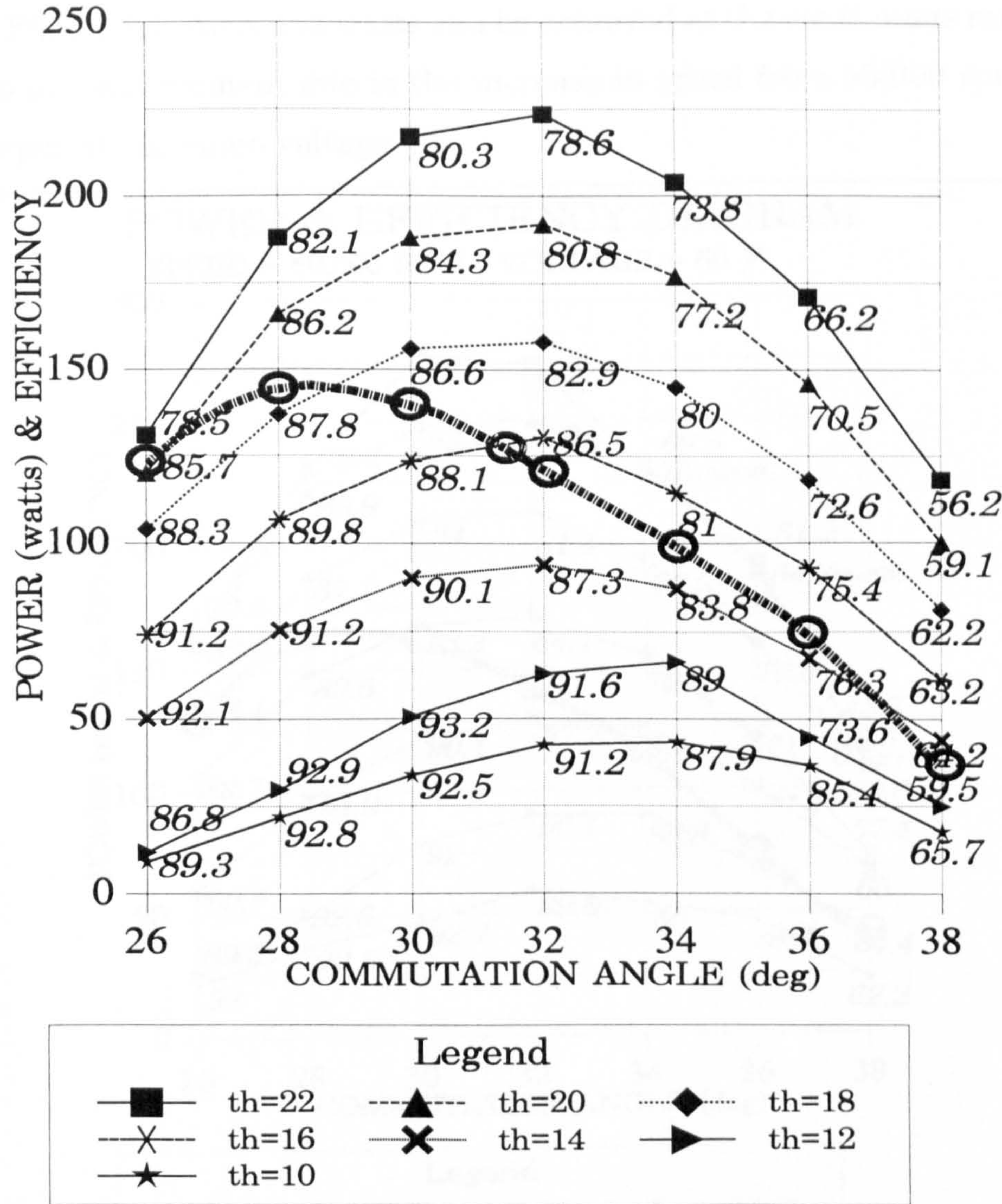


Figure 8.5: Power & Efficiency Diagram for 60,000 rpm and 50 volts.

Figure 8.5 shows higher peak power (by 7%) when the speed is increased from 50,000 rpm to 60,000 rpm at the same voltage, 50 volts. This may be compared to the slight reduction in power resulting from increasing the speed from 40,000 to 50,000 rpm at 40 volts excitation. In the case of 60,000 rpm, the converter is better utilised with effectiveness factor of 0.6.

To compare with other earlier results, the 100 watts power can be achieved in Figure 8.5 with an efficiency of about 90% which is 20% better than in Figure 8.1. Also, 150 watts can be achieved at the continuous rating which is an improvement due to the increase in speed from 50,000 rpm to 60,000 rpm at the same voltage.

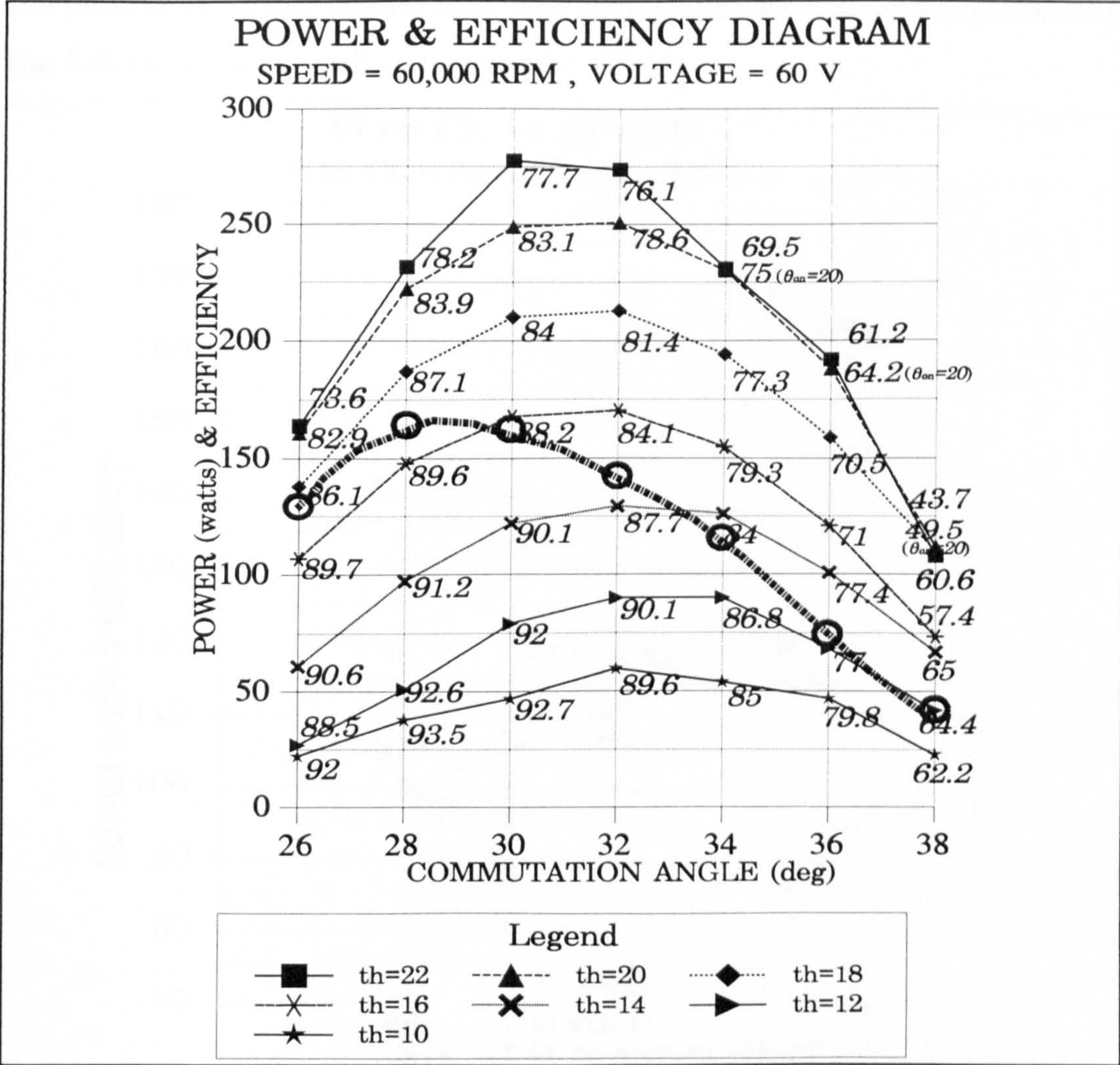


Figure 8.6: Power & Efficiency Diagram for 60,000 rpm and 60 volts.

In the case of Figure 8.6, by increasing the voltage by 20% compared to the previous case at the same speed, the peak power is increased by 25% to 277 watts which is the maximum power measured on this SR generator. On the other hand, the effectiveness factor is reduced from 0.6 to 0.58, whereas the efficiency is improved, for 223 watts for example (the peak power for the previous case), from 78% to 84%.

Figure 8.7 shows a graphical representation of the effect of increasing the rotational speed from 40,000 rpm to 60,000 rpm at the same voltage, 40 volts, and also at increasing voltages with increased speed. The diagram is a result of selecting the operating points that result in maximum power at continuous rating for each speed. To achieve this, an extra set of results for the maximum speed, 60,000 rpm, was obtained at 40 volts and is given with the full tabulated results in Appendix A8.1.

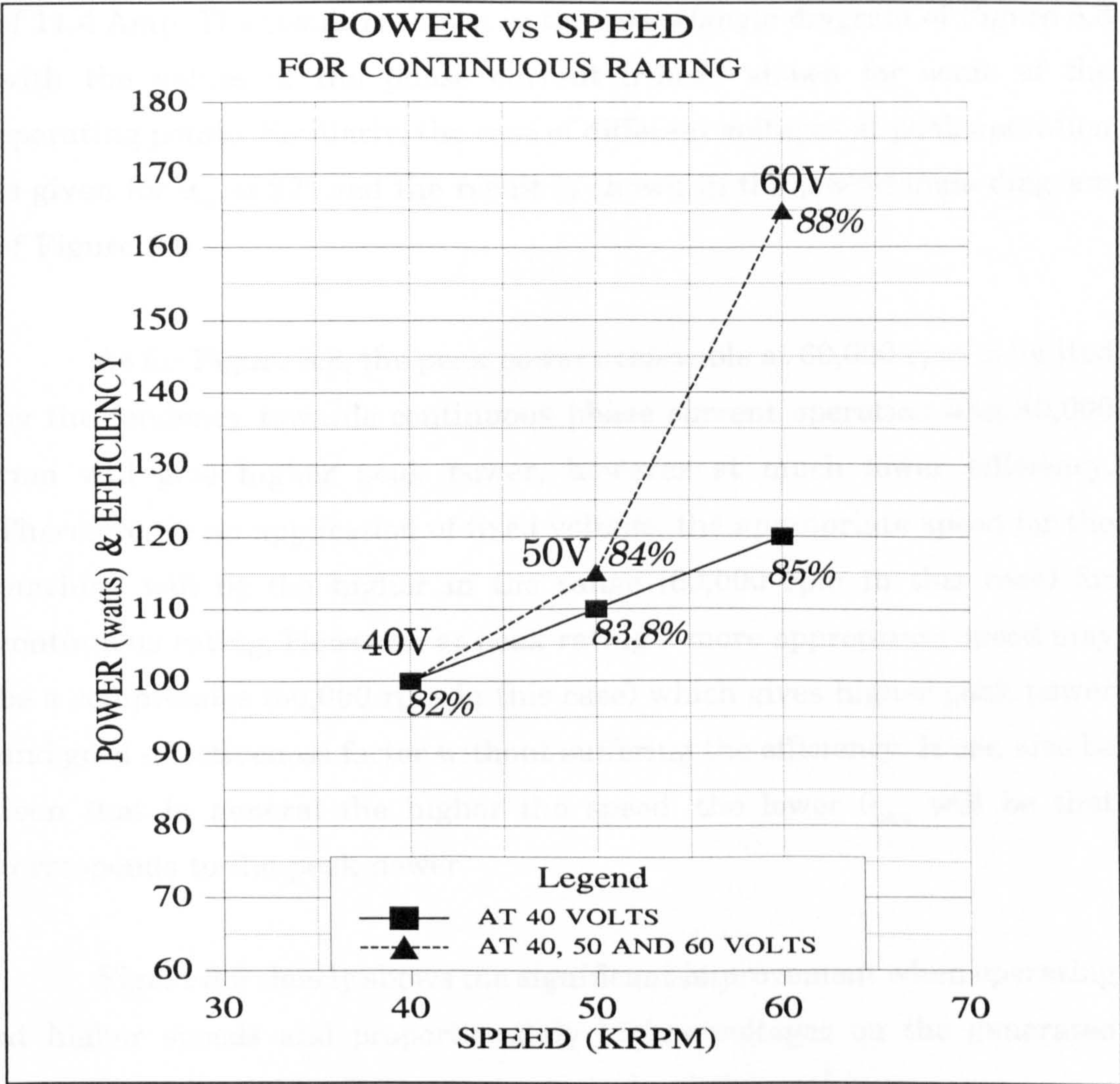


Figure 8.7: Power versus speed at 40 volts and at different excitation voltages.

The results in the Figure 8.7 show that for a constant excitation voltage the increase in the power for increased speed is small and there is some sort of a linear relationship between the speed and the generated power with a slope of 1 watt/krpm. However, at different excitation voltages

the relationship is more of an exponential form with noticeable improvement of the efficiency at an increased speed.

The case of the maximum power achievable at a fixed voltage (of 40 volts as an example) regardless of the continuous rating limit of 5 Amp may be considered for the three speeds by comparing the power results at the maximum θ_{on} of 22° . All the results would be within the peak rating limit of 11.4 Amp. The result is shown in the power/angle diagram of Figure 8.8 with the values of the phase current (r.m.s.) shown for some of the operating points. Similarly, the case of different voltages at peak operation is given for θ_{on} of 22° and the result is shown in the power/angle diagram of Figure 8.9.

As for Figure 8.8, the peak power achievable at 60,000 rpm is limited by the tendency towards continuous phase current operation and 40,000 rpm will give higher peak power, however at much lower efficiency. Therefore, in an application of fixed voltage, the appropriate speed for the machine will be the higher in the range (60,000 rpm in this case) for continuous rating. However, at peak rating a more appropriate speed may be a compromise (50,000 rpm in this case) which gives higher peak power and good effectiveness factor without suffering the efficiency. It can also be seen that in general the higher the speed, the lower θ_{com} will be that corresponds to the peak power.

Figure 8.9 clearly shows the significant improvement when operating at higher speeds and proportionately higher voltages on the generated power as well as the efficiency, particularly at the peak power.

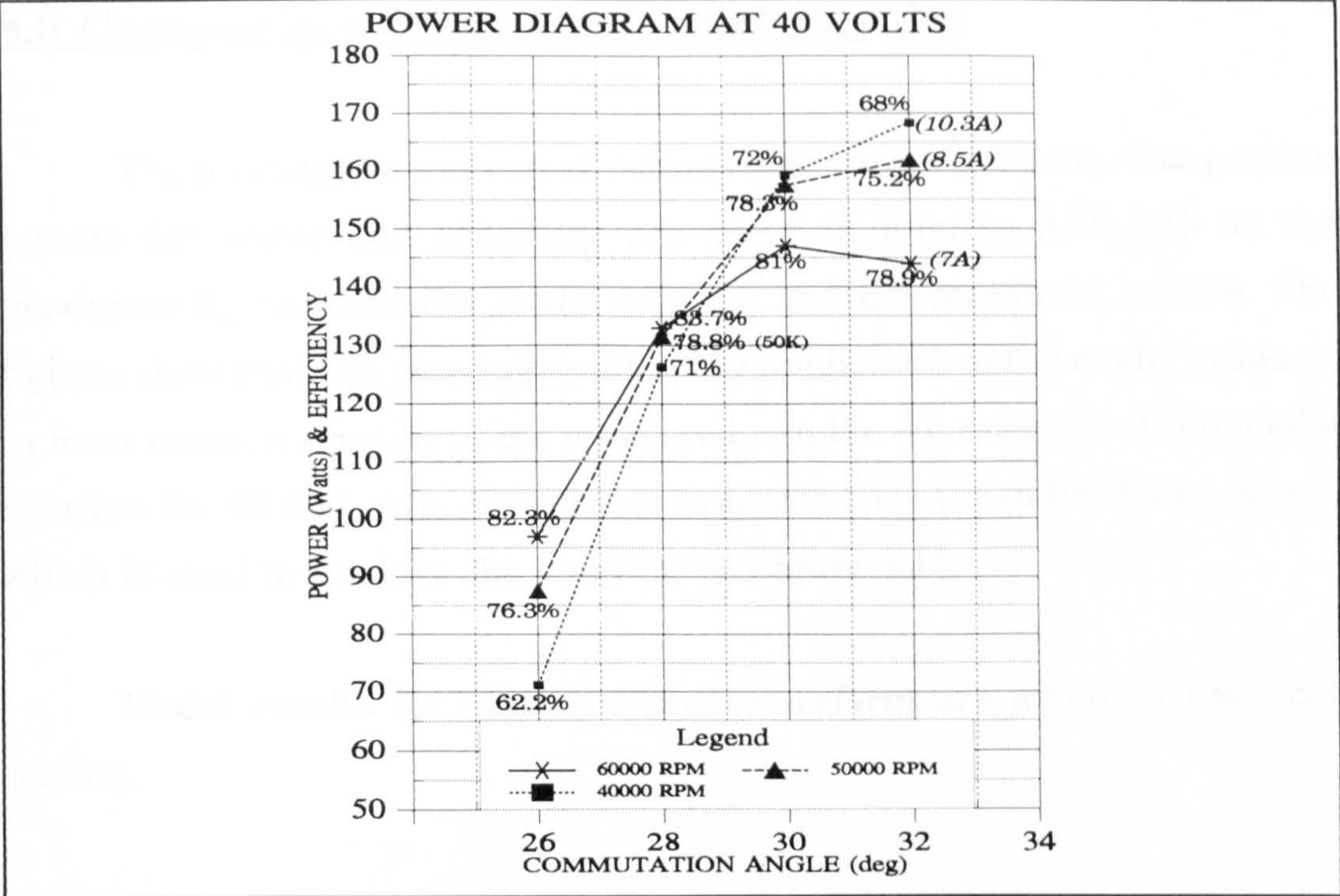


Figure 8.8: Comparison, Power/Angle diagram for 40,000, 50,000, and 60,000 rpm at 40 volts for $\theta_{on}=22^\circ$. Values of efficiency and phase current (r.m.s.) are shown.

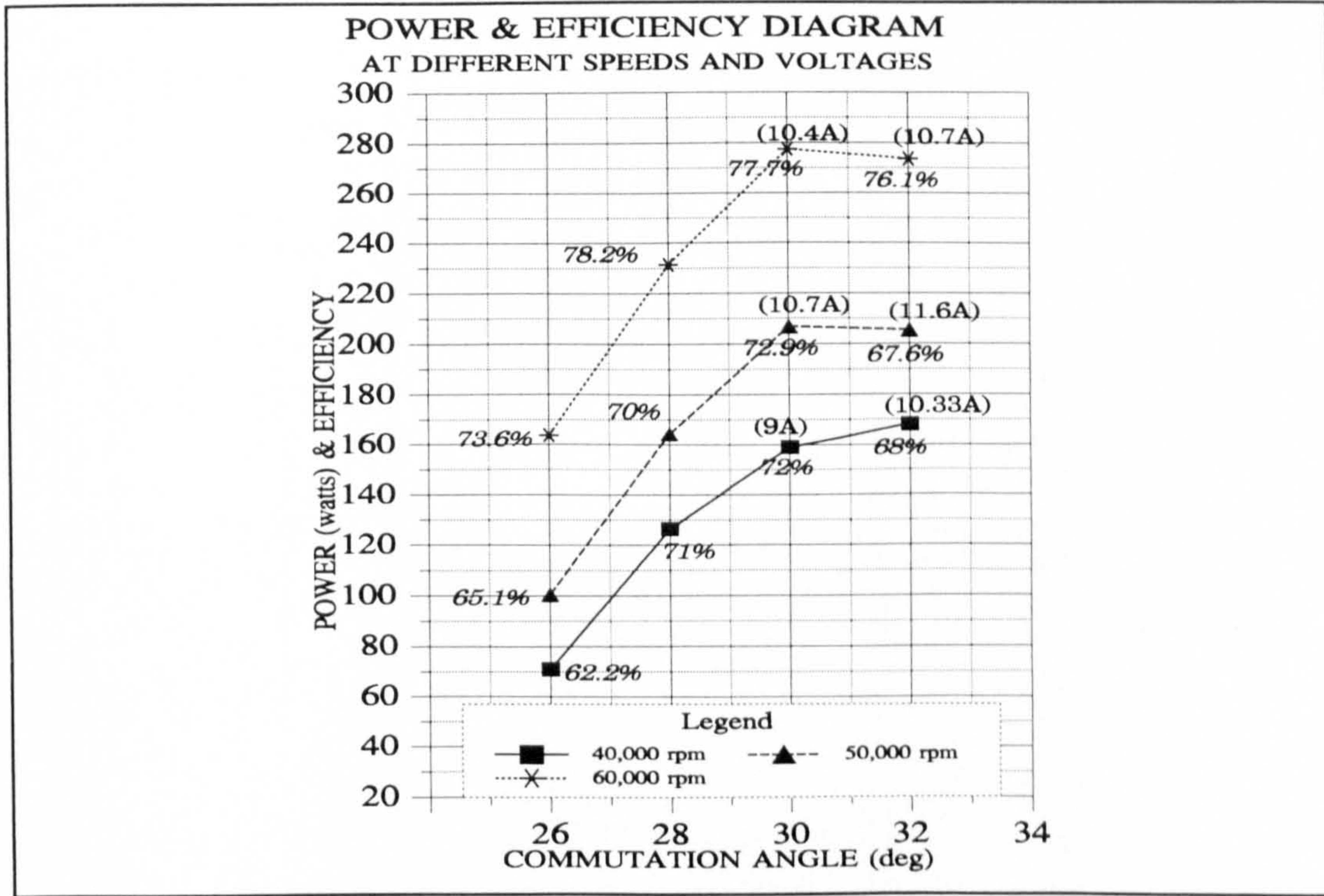


Figure 8.9: Comparison Power/Angle diagram for results of maximum power at different speeds and voltages.

8.3 Comparison With The Model Results

The programme was run at various operating conditions. Comparison results for power and efficiency are given in Figures 8.10-8.15 at the maximum θ_{on} for both the model solution and the measured results. The figures show that the power and efficiency predictions of the model produce, in most cases, a close fit to the measured results. An example of the model solution for 60,000 rpm, 60 volts is presented in Appendix A8.2, case-2, which is used to produce the diagram in Figure 8.15.

Model results for phase current waveform are given in the next section.

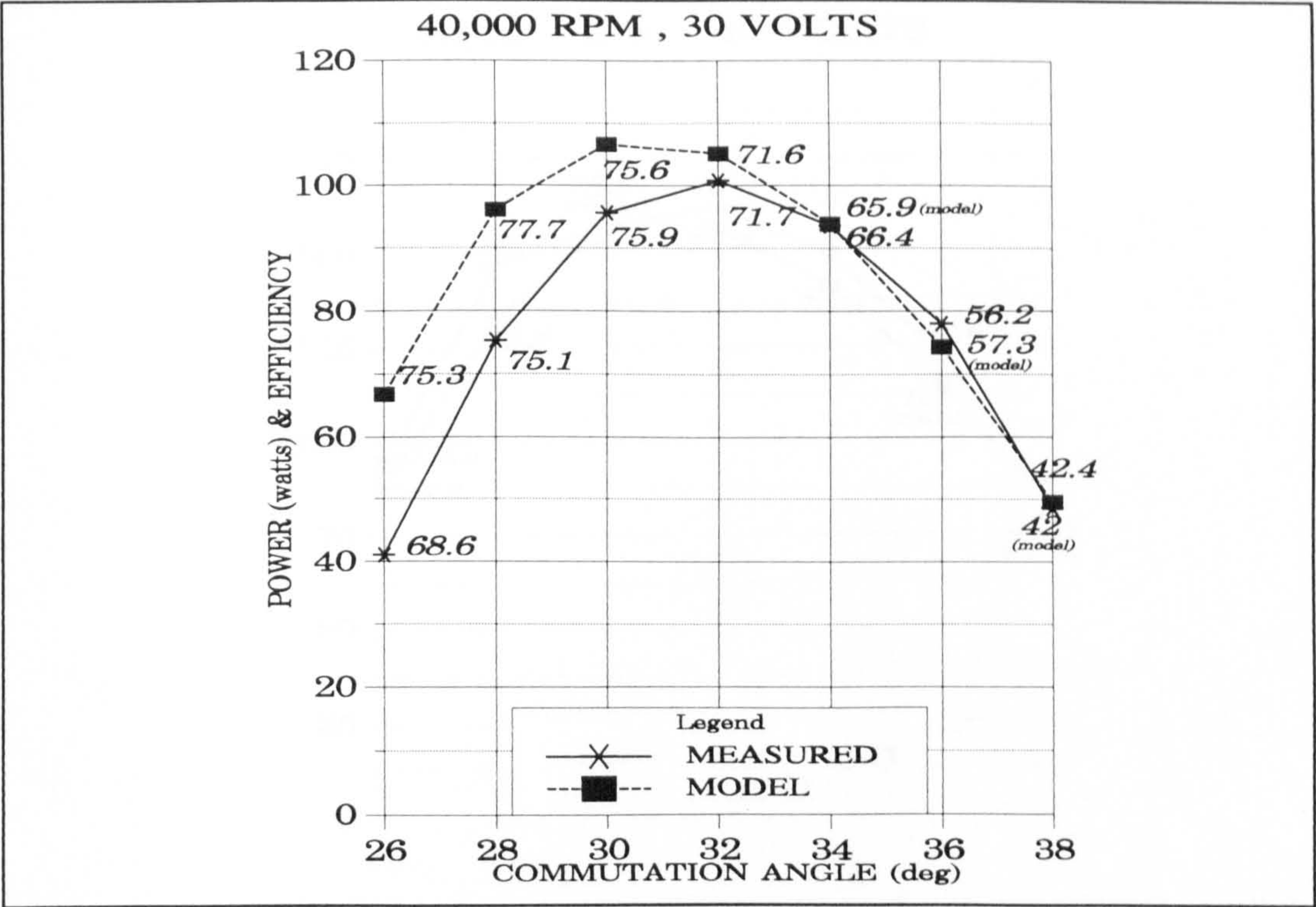


Figure 8.10: Measured and predicted results at 40,000 rpm, 30 volts.

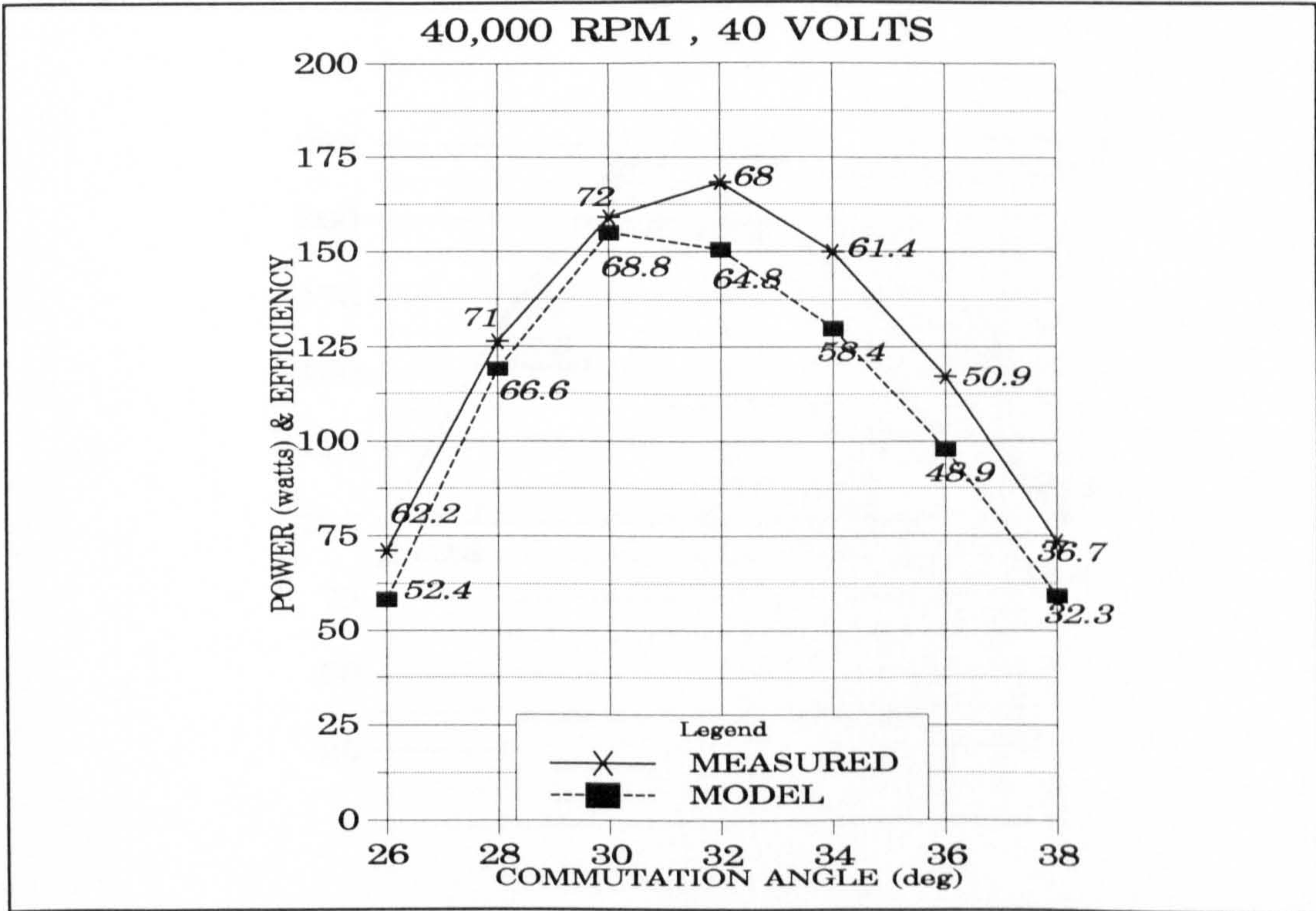


Figure 8.11: Measured and predicted results at 40,000 rpm, 40 volts.

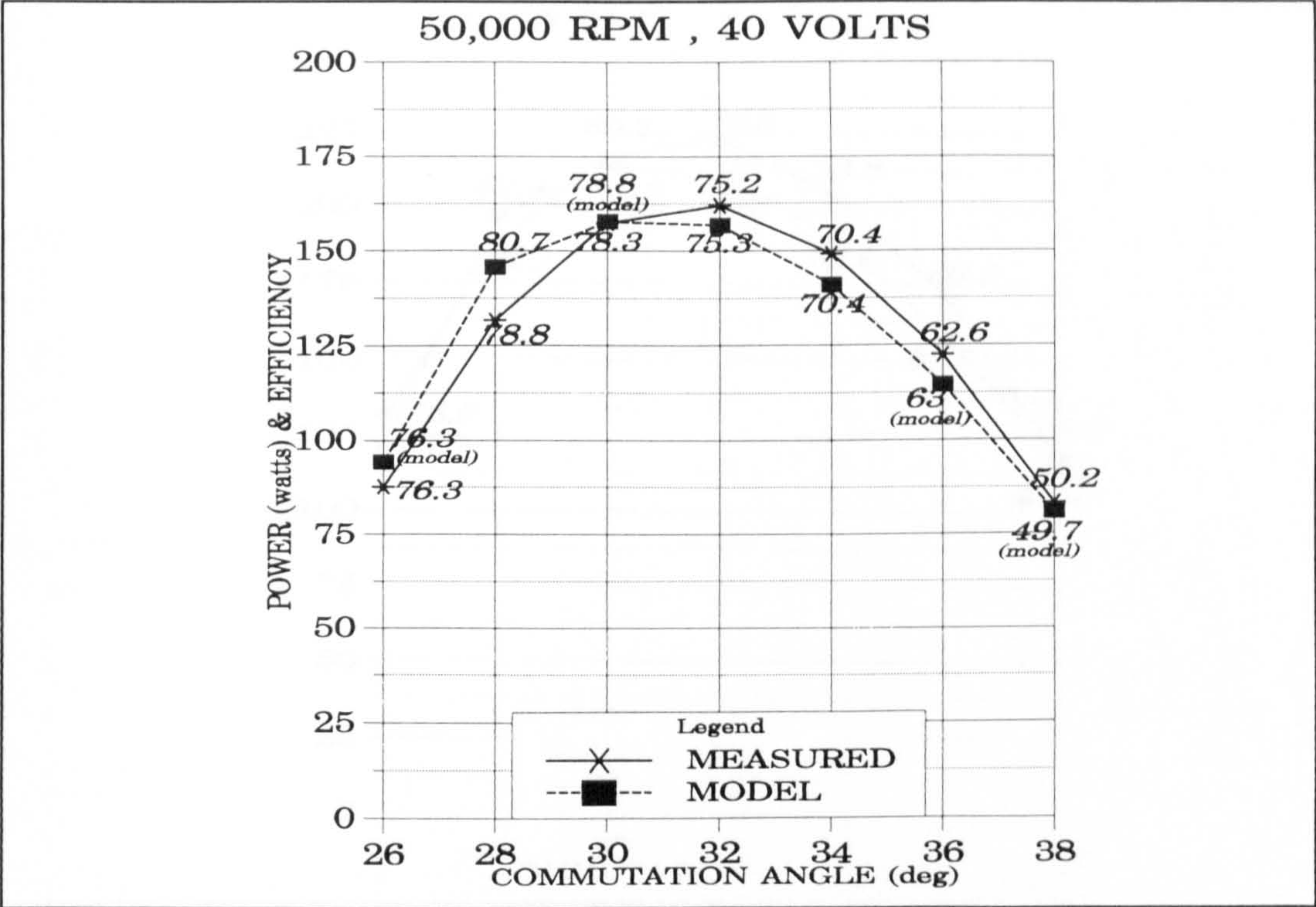


Figure 8.12: Measured and predicted results at 50,000 rpm, 40 volts.

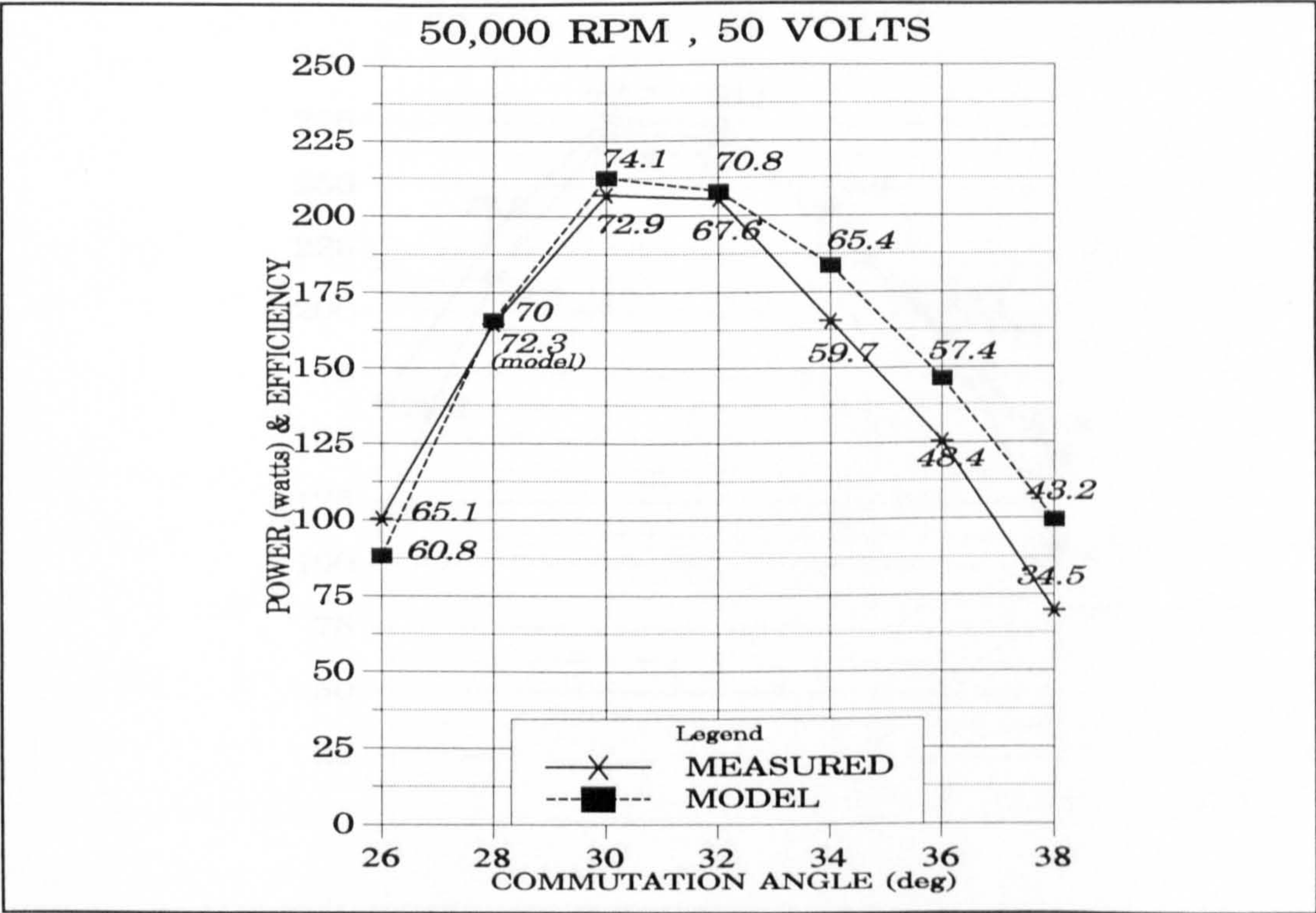


Figure 8.13: Measured and predicted results at 50,000 rpm, 50 volts.

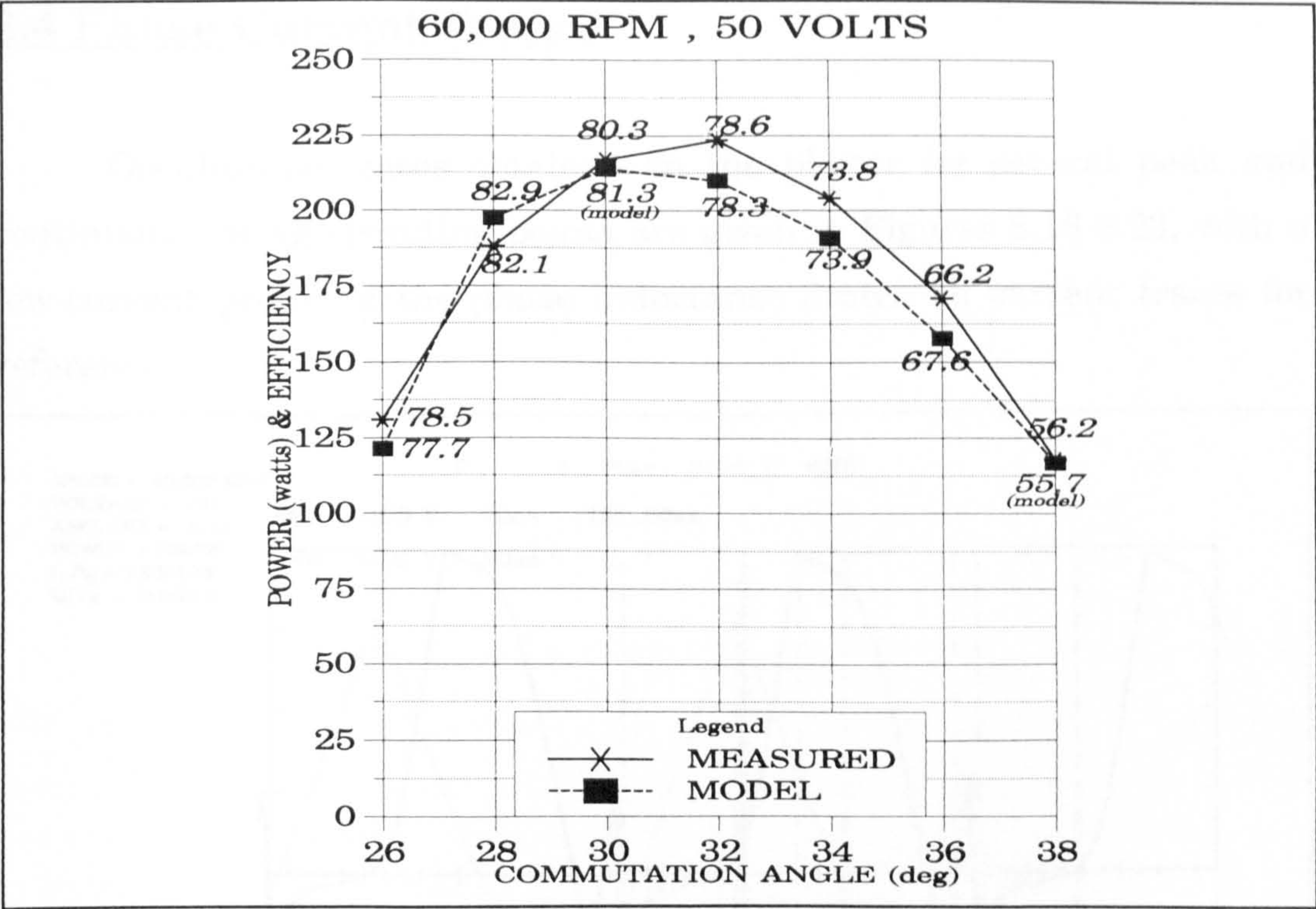


Figure 8.14: Measured and predicted results at 60,000 rpm, 50 volts.

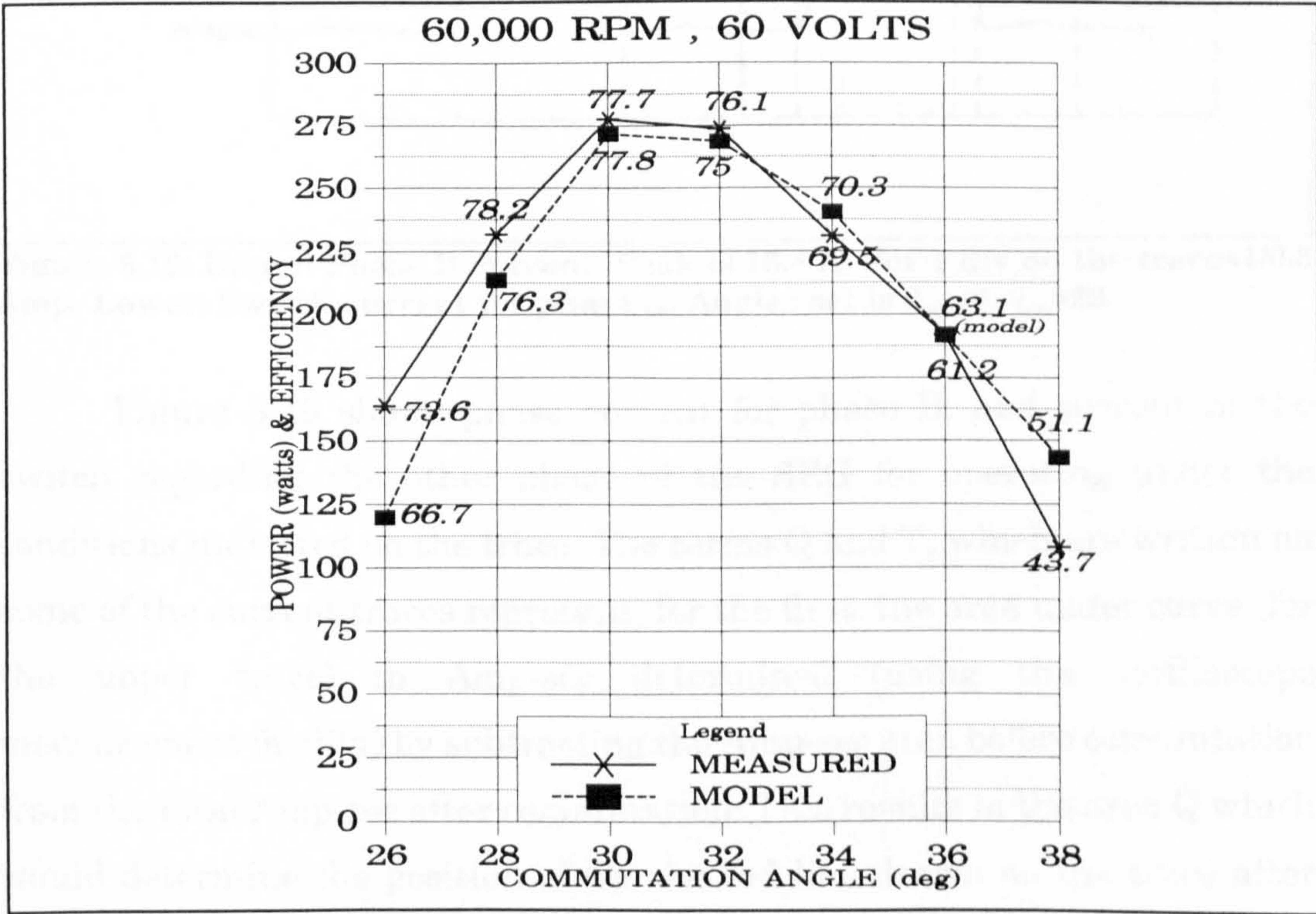


Figure 8.15: Measured and predicted results for 60,000 rpm, 60 volts.

8.4 Phase Current Traces

Oscilloscope traces obtained on the plotter for several peak and continuous rating operating points are given in Figures 8.16-8.23, with a low-current profile of the phase inductance drawn on current traces for reference.

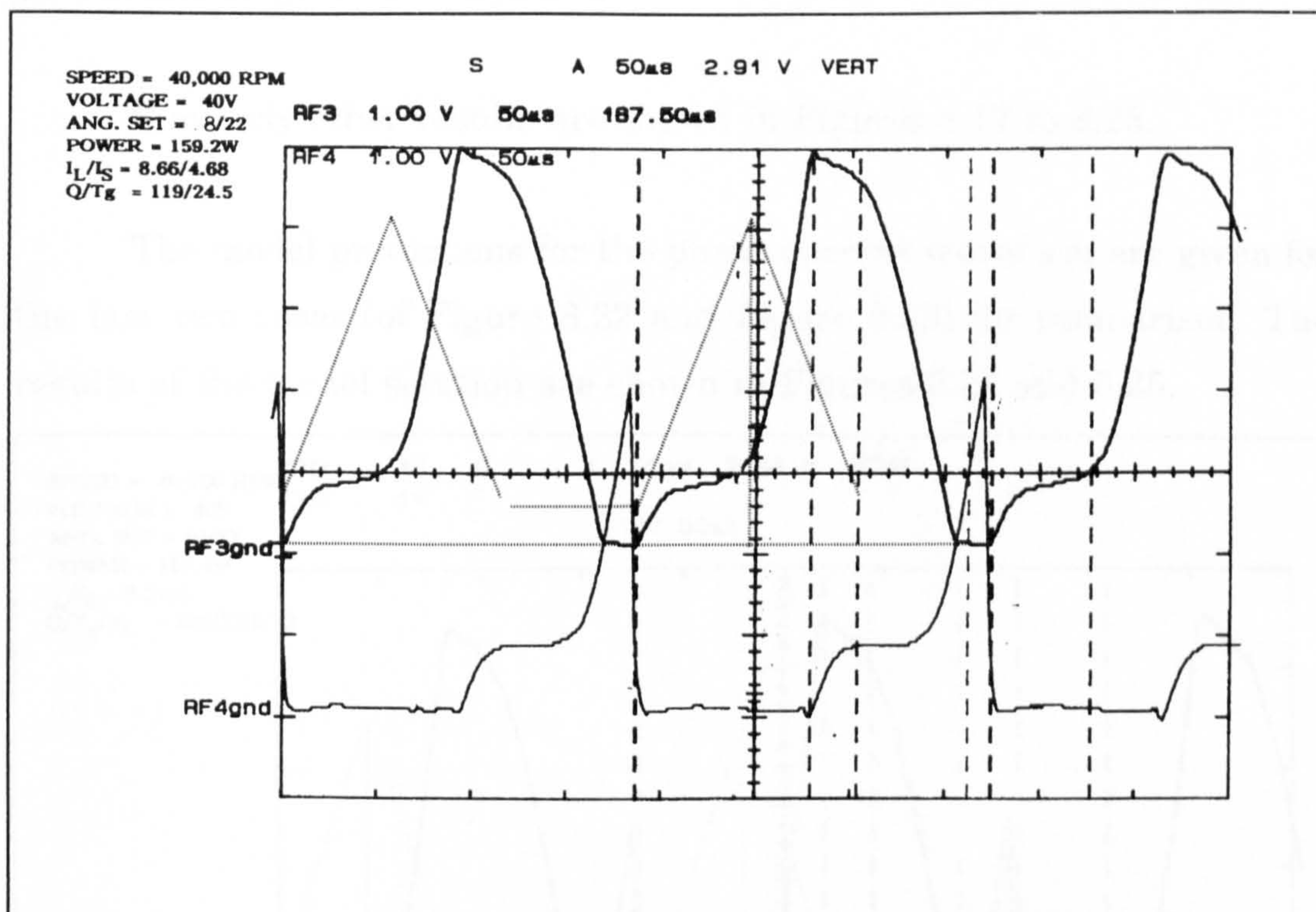


Figure 8.16: Upper: Phase B current. Peak is 16.4 A. For 1 div on the trace=1/0.3 Amp. Lower: Switch current for phase A. Angles set is $\theta_{dly}=8$, $\theta_{on}=22$.

Figure 8.16 shows phase current for phase B, and current in the switch regarding the other phase of the SRG for operating under the conditions indicated on the trace. The terms Q and T_g which are written on some of the current traces represent, for the first, the area under curve (for the upper trace) in Amp-sec determined (using the oscilloscope measurement facility) by subtracting the Amp-sec area before commutation from the total Amp-sec after commutation. This results in the area Q which would determine the position of the dashed line drawn on the trace after commutation on the upper trace. This line is separated from the

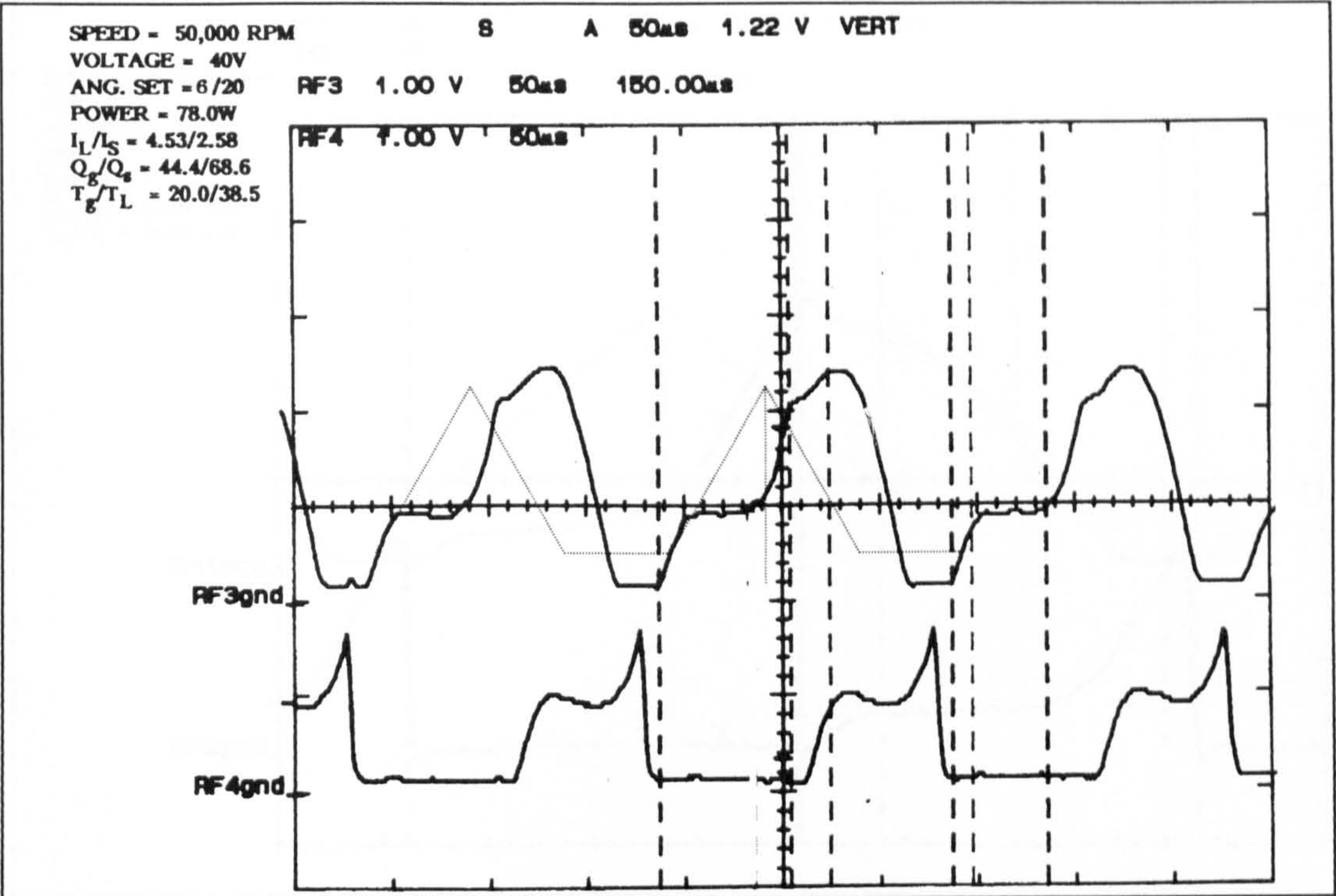


Figure 8.18: Phase current trace. $I_{pk}=7.6$ Amp. Continuous rating for 6/20 deg.

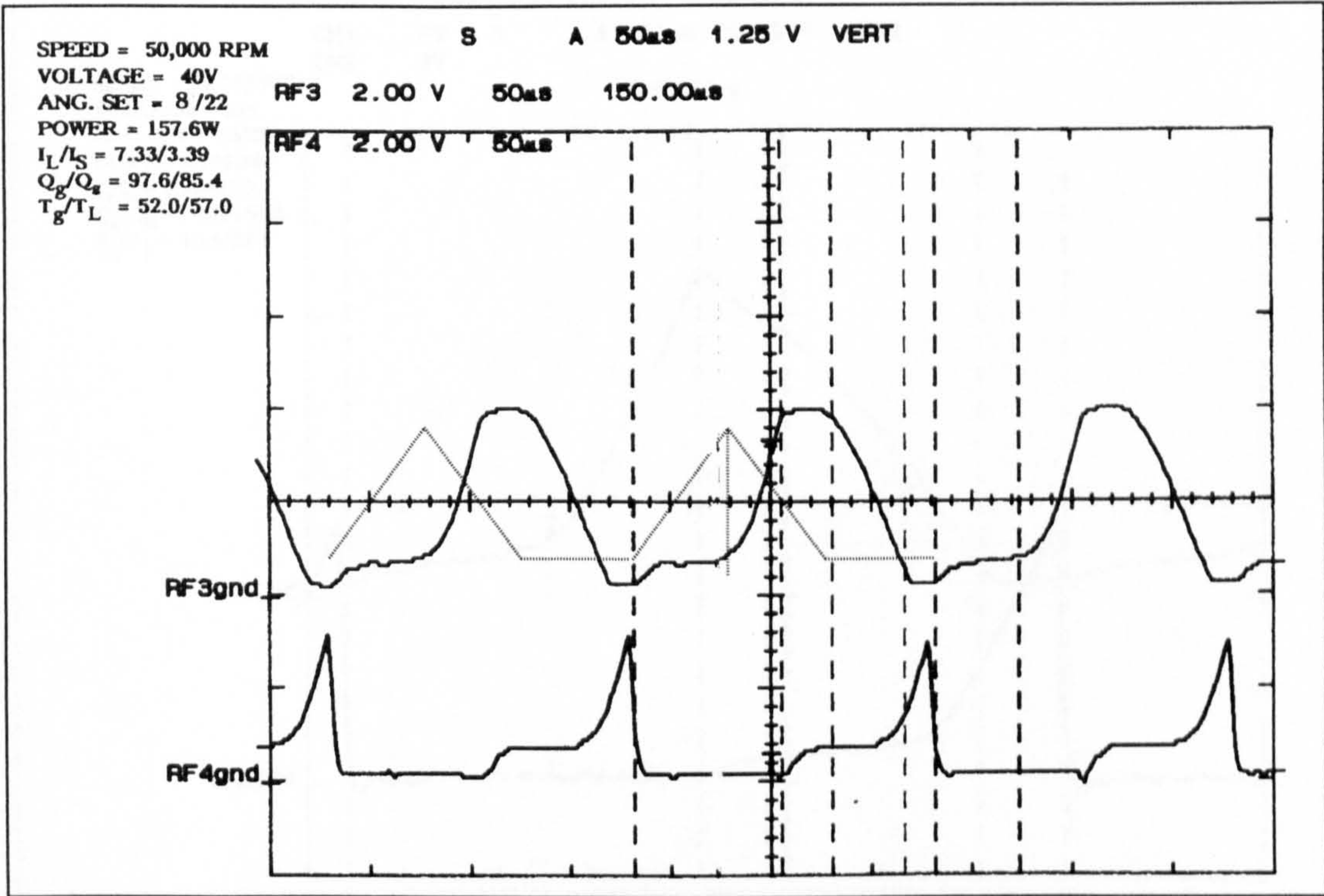


Figure 8.19: Phase current trace. $I_{pk}=12.8$. At 8/22 deg.

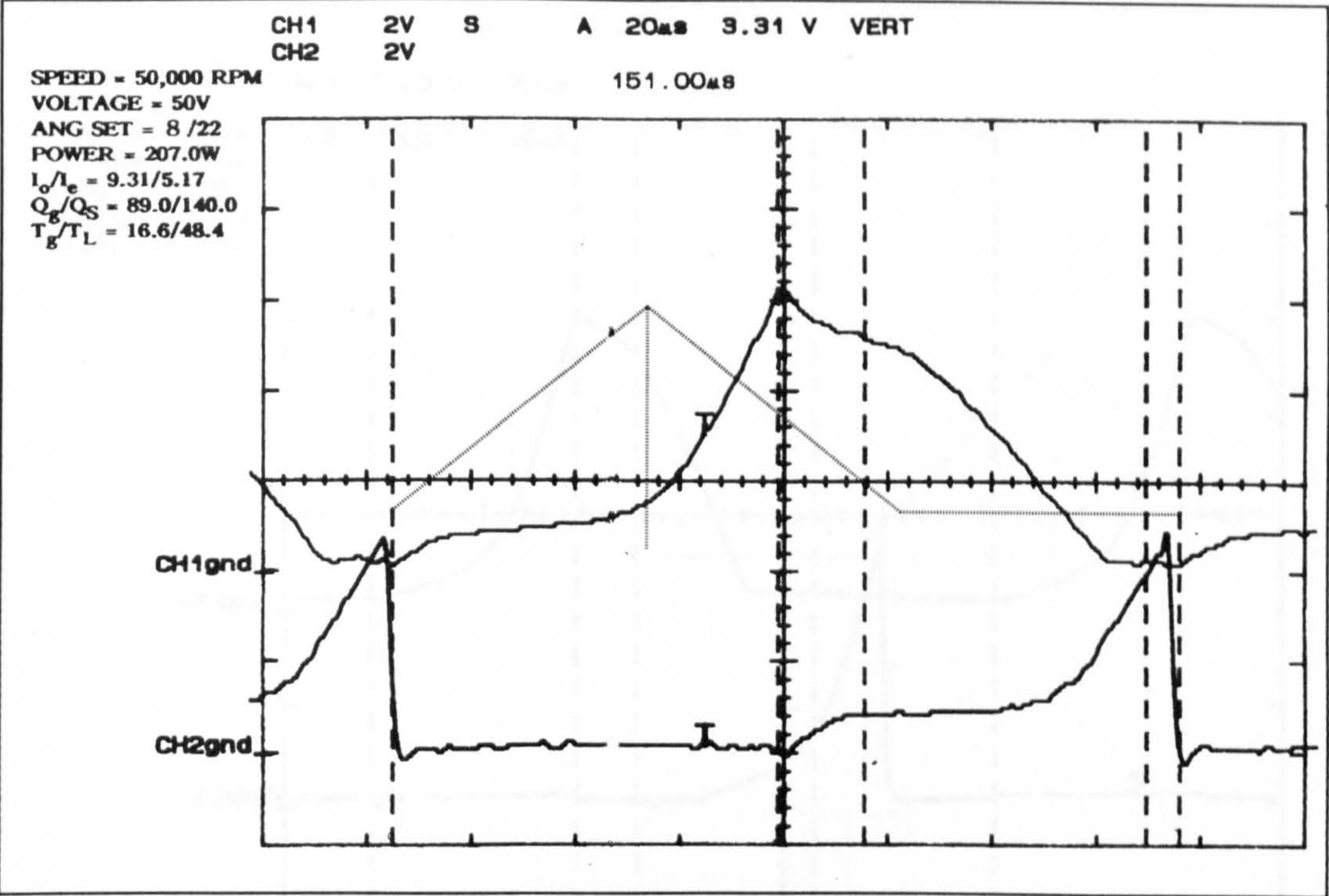


Figure 8.20: Phase current. $I_{pk}=20.6$ Amp. At 8/22.

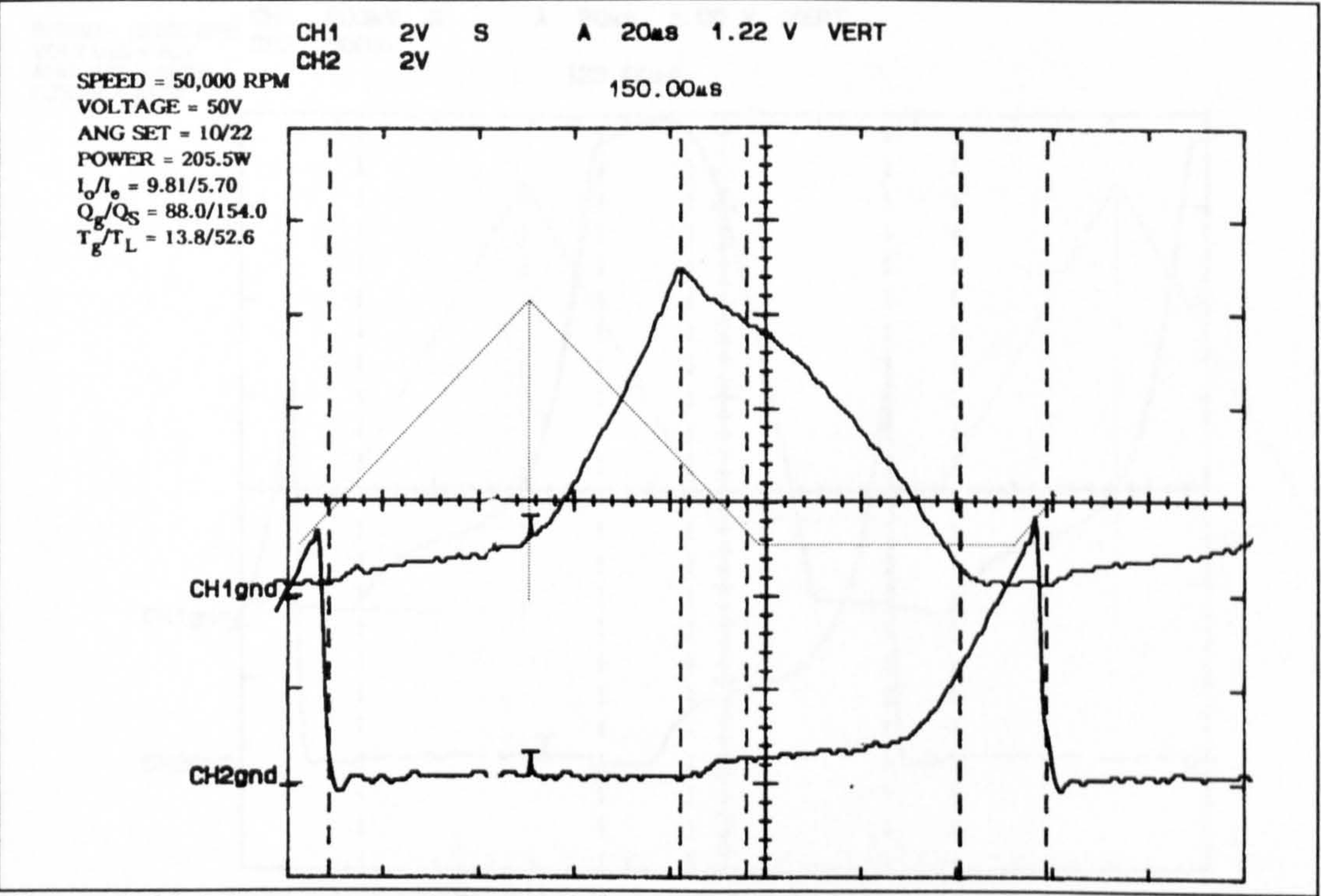


Figure 8.21: Phase current. $I_{pk}=22.8$ Amp, peak rating. Angle set 10/22.

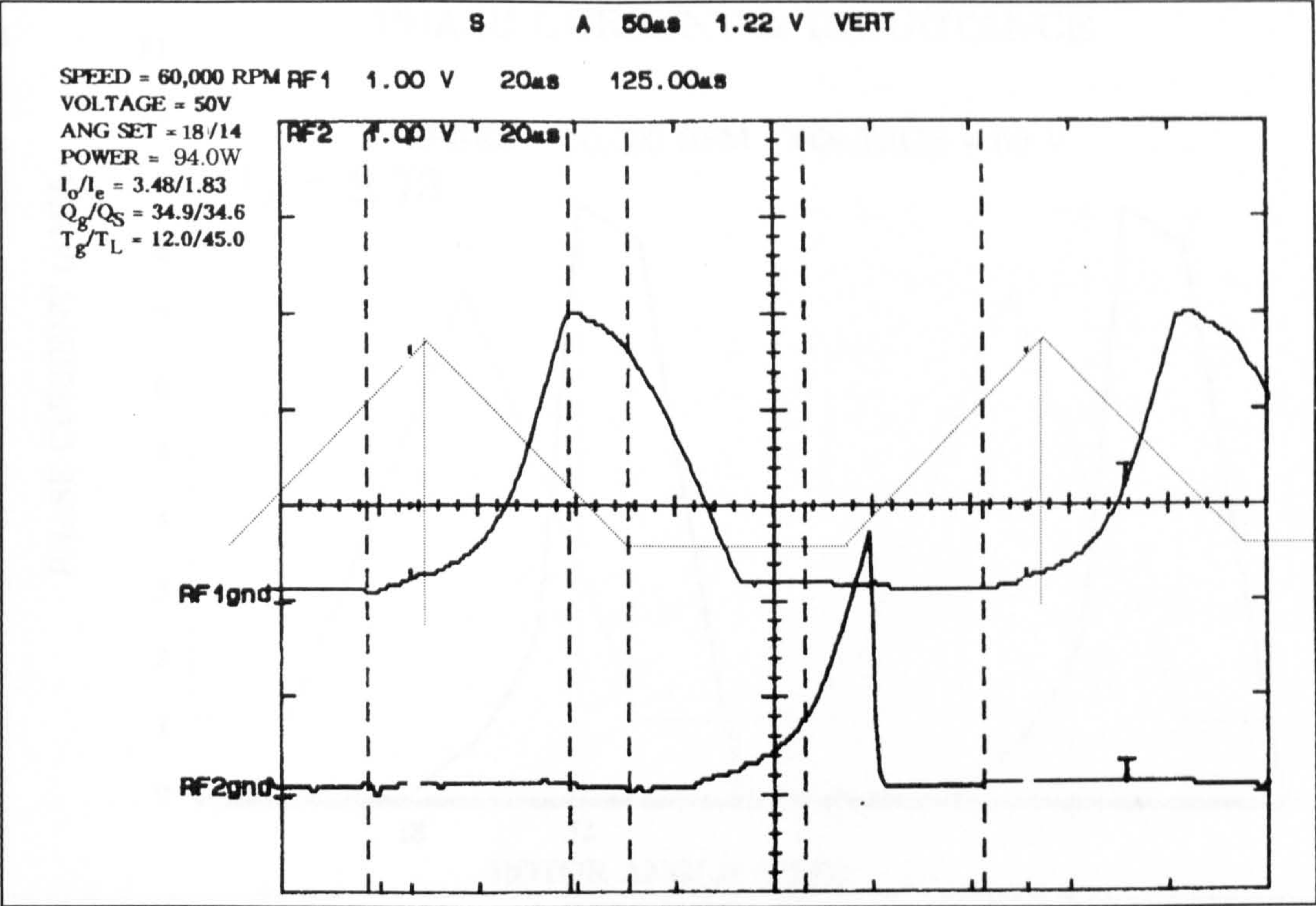


Figure 8.22: Phase current. $I_{pk}=9.7$ Amp for angle set $\theta_{dly}/\theta_{on}=18/14$. $\eta=87.3\%$

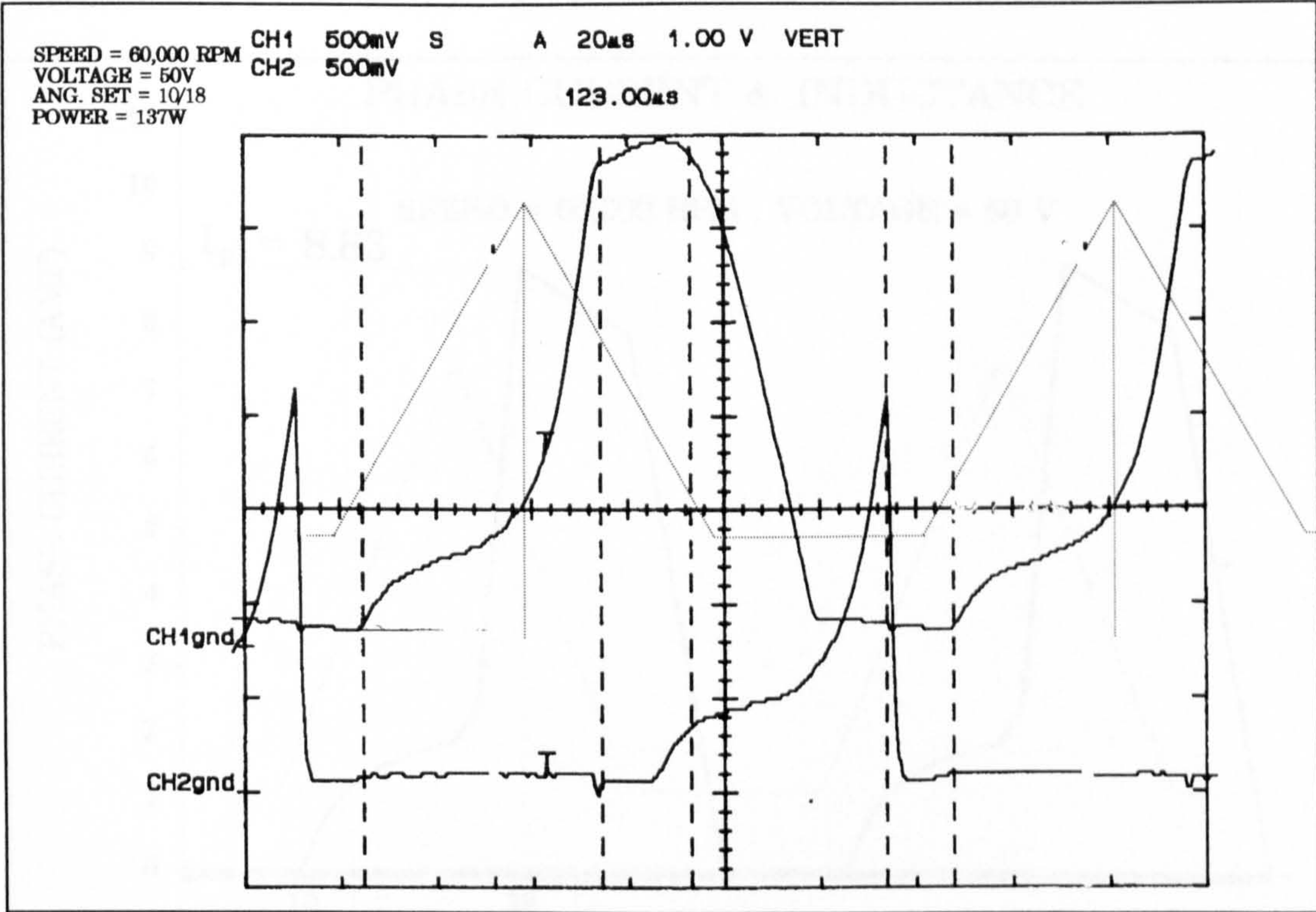


Figure 8.23: Phase current. $I_{L-rms}=5$ Amp, and $I_{pk}=8.76$ Amp for 10/18 angle set. $\eta=87.8\%$.

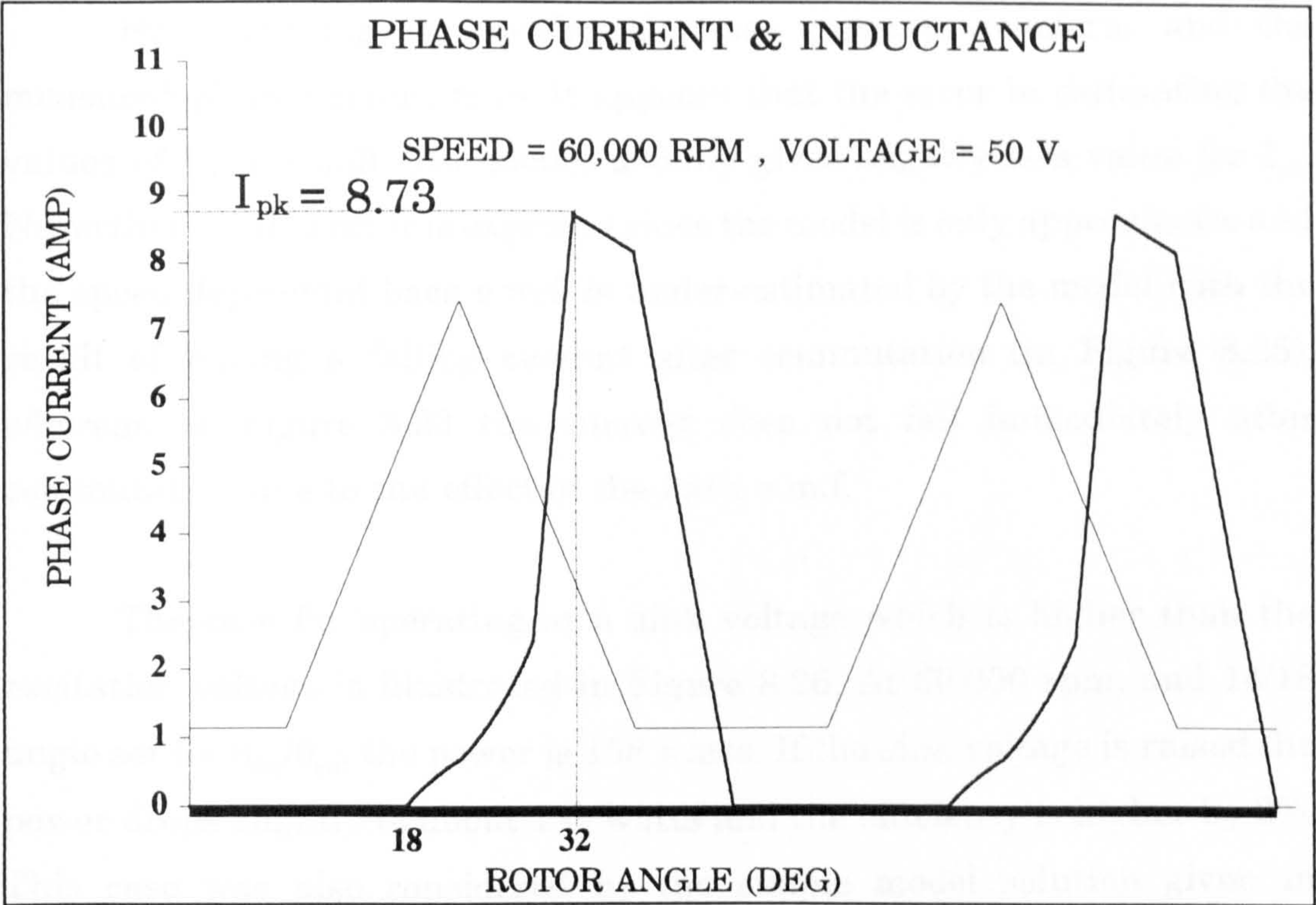


Figure 8.24: Model result for comparison with Figure 8.22. $P_g=99$ W, $\eta=88\%$.

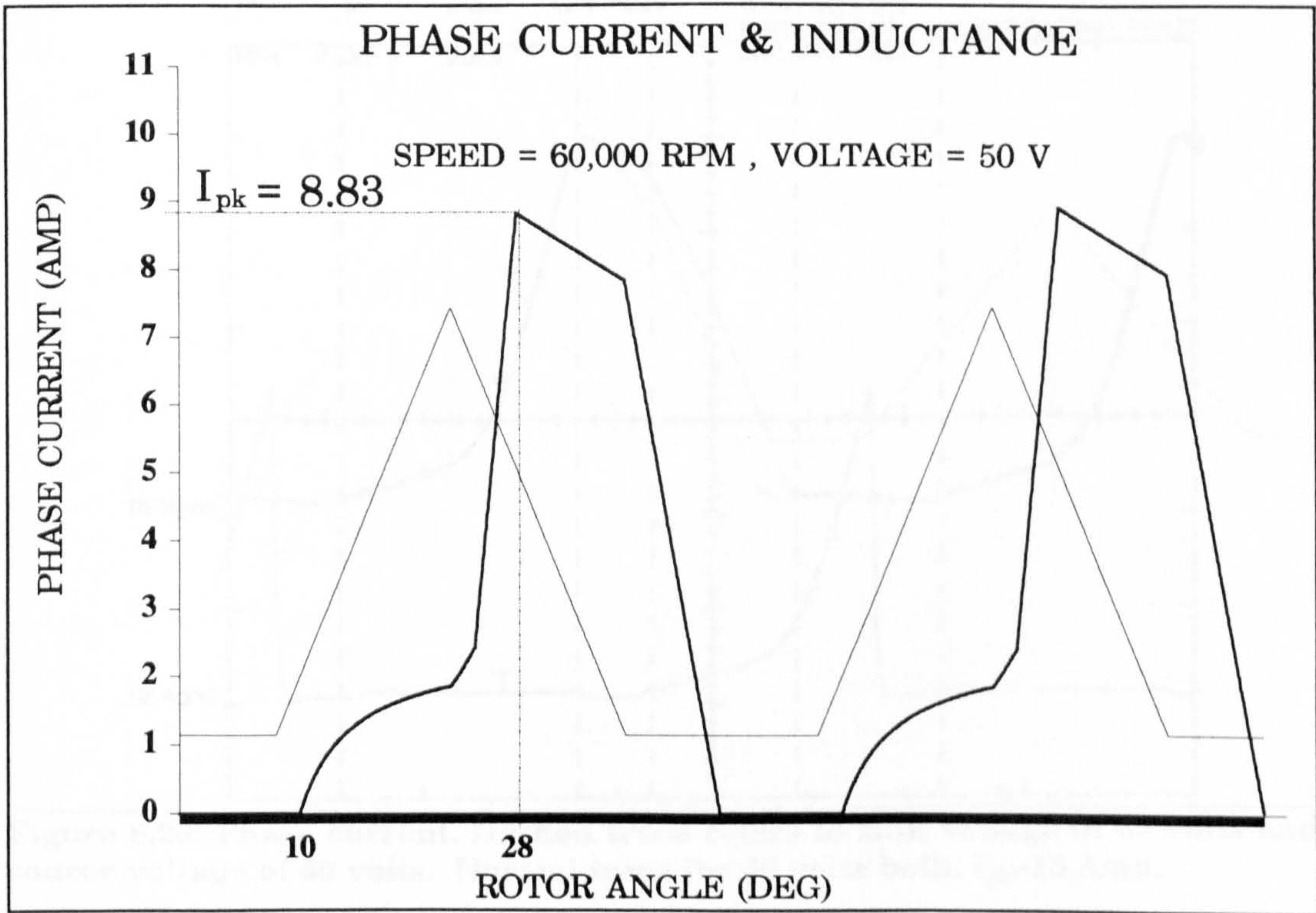


Figure 8.25: Model result for comparison with Figure 8.23. $P_g=143$ W, $\eta=88.5\%$.

By comparing the predicted phase current waveform and the measured phase current trace it appears that the error in estimating the values of I_{pk} is small. The model usually gives slightly less value for I_{pk} . Nevertheless, this error is expected since the model is only approximate and the speed dependant back e.m.f. is under-estimated by the model with the result of having a falling current after commutation (in Figure 8.25), whereas in Figure 8.23 the current does not fall immediately after commutation due to the effect of the back e.m.f.

The case for operating at a sink voltage which is higher than the excitation voltage is illustrated in Figure 8.26. At 60,000 rpm, and 14/18 angle set for θ_{dly}/θ_{on} , the power is 158 watts. If the sink voltage is raised the power drops slightly to about 150 watts and the efficiency is higher by 2%. This case was also considered by the simple model solution given in Appendix A8.2, case-1.

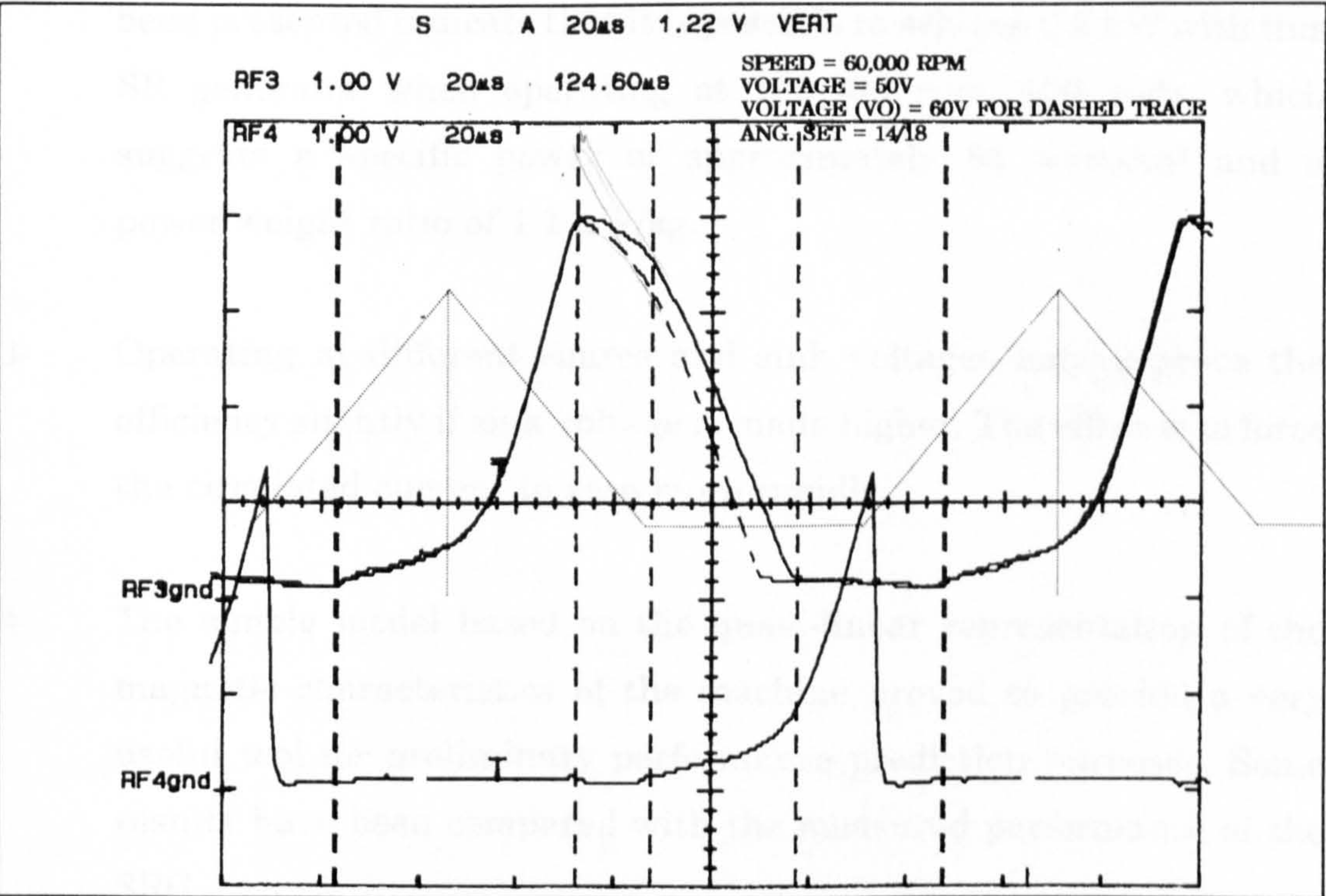


Figure 8.26: Phase current. Dashed trace refers to sink voltage of 60 volts and source voltage of 50 volts. Normal trace for 50 volts both. $I_{pk}=13$ Amp.

8.5 Conclusion

The test results presented in this chapter show the following:

- 1- Upon exciting the generator at the correct θ_{com} , which results into maximum efficiency, the generated power can be controlled using the width of the excitation pulse or the appropriate θ_{on} .
- 2- Increasing the voltage of the generator has an advantage of increasing efficiency up to a certain level, when the increase in voltage becomes disadvantageous regarding efficiency and effectiveness of power converter unless the speed is increased. Operating at an increased speed and proportionately higher voltage significantly improve peak power and efficiency. Although it was not possible to test the generator at 100,000 rpm, the results which have been presented indicate that it is possible to achieve 0.5 kW with this SR generator when operating at 100,000 rpm, 100 volts, which suggests a specific power of approximately 84 watts/in³ and a power/weight ratio of 1.1 kW/kg.
- 3- Operating at different source and sink voltages may improve the efficiency slightly if sink voltage is made higher. The effect is to force the circulated current to zero more rapidly.
- 4- The simple model based on the quasi-linear representation of the magnetic characteristics of the machine proved to provide a very useful tool for preliminary performance prediction purposes. Some results have been compared with the measured performance of the SRG.

CHAPTER NINE

DISCUSSION AND GENERAL CONCLUSIONS

9.1 Introduction

The main findings of the project, which are discussed in this chapter, are primarily based upon the following:

- 1- The electromagnetic design of the high speed SRG which has been described in detail in chapter 3.
- 2- The mechanical design procedure (of chapter 4) taking into consideration the effects of the high rotational speed of the SRG on the material selection and assembly of the whole system.
- 3- The dynamic testing results discussed in chapter 8 which provide an evaluation of the performance of the test system.

The electromagnetic design procedure offers a useful approach for the design of an SRG with a stator of fixed geometry. However, a discussion of a more general case is considered in this chapter based upon the conclusions of chapter 3 and the simple magnetic model based on the quasi-linear representation of the magnetic characteristics which was developed in chapter 2. This will also include investigating other cases such as an all-steel SRG and an SRG with better cooling and/or different size keeping in mind the intended application of a vehicle turbo-driven SRG.

The experience gained from the mechanical design procedure and assembly is quite useful in estimating the mechanical limits of any

alternative design for a high speed SRG.

Finally, the power/speed relationship for fixed or variable output voltages is discussed on the basis of the experimental results of the test system as well as the results of the magnetic model. Time and project funds constraints did not allow the collaboration of all these investigations by experimental testing.

9.2 General Operation and Behaviour of The Test System

The experimental testing system did not aim for very accurate measurement results, nor did it aim for sophisticated operation control or protection. The emphasis had rather been placed on a simple and flexible system for the measurement of power and efficiency. However, to facilitate the measurement procedure of large number of results at different speeds and voltages, some auxiliaries to the testing system were required (see chapter 7) such as the auxiliary voltage regulator and the d.c. motor feedback speed control system.

The experimental system of the high speed SRG enabled the set-up to provide results at speeds up to 60,000 rpm and at voltages up to 60 volts. The main limitation of the rotational speed was the air supply system. The V-belt coupling of the d.c. motor to the air blower could not sustain the high torque demand of the air blower at high speeds of the turbine particularly when the machine is excited and angles are selected for maximising power generation into the phase winding. A turbine speed of 75,000 rpm was possible for only a short time that did not allow measurement results to be taken although the d.c. motor was running at the time at a speed below its rated speed.

It was shown (in the results of chapter 8 and the model results of chapter 3) that the SRG is best operated at voltages around 60-70 volts when running at a speed of 50,000-60,000 rpm. The limitation to the voltage was dictated by the current density of the phase winding of the machine and the tendency towards a continuous phase current operation. However, as was shown in chapter 3, operating at voltages higher than 70 volts did not seem to be of any benefit to the machine or to the power converter. Results at 60,000 rpm and 60 volts show that the machine is operating slightly below its peak power. Liquid cooling of the machine would have enabled it to operate at peak power at 70 volts. Investigation of the voltage influence (whether fixed voltage at variable speed or otherwise) on the power and efficiency of the SRG is given in the next section.

The voltage rating of the power converter is limited by the reverse voltage of the power MOSFET at 200 volts. This means that the maximum allowable voltage is 100 volts. This was sufficient for the voltage levels involved during testing. The selection of the power MOSFET was appropriate for this application. A power converter with higher voltage rating would require paralleling of several devices per phase to reduce the on-state resistive losses of the MOSFET. However, an IGBT may be more appropriate at higher voltages and powers. The current in the converter is limited by the r.m.s. current rating of the power diode at 12 Amp, which is higher than the r.m.s. current at peak rating of the machine given as 11.4 Amp. No heat problems were encountered regarding the power devices. One problem with the power converter is related to destroying the power transistors of one phase due to the accidental application of excitation to the machine at zero speed or the accidental loss of air supply while the excitation is on. An over-current protection circuit should therefore be employed. A suggestion for a simple circuit was considered but was not employed during testing and needs further development as was briefly discussed in chapter 5.

Power converters which may better suit a practical application than the one used for testing should be considered for a serious design of an optimised SRG system. An alternative power converter is the classic -or asymmetric bridge- converter. This converter offers a great degree of control flexibility on the expense of requiring an extra switch per phase. In applications such as the starter/generator where the machine operates as a motor for part of the speed range such converter may be considered ideal. In generator applications this control flexibility may not be required (see chapter 1) and a C-dump circuit, which may be considered as a unipolar converter (see Figure 1.13), may better suit this application.

9.3 Comparison of Power density With Published Work

The dynamic results of the test system of the SRG showed that the generator could provide a maximum power of 277 watts at 60,000 rpm and 60 volts for operation at peak rating. However, the model shows that higher powers could have been achieved had the test system allowed results to be taken at higher speeds, such as 80,000 rpm. At such a speed and at the appropriate voltage (of 100 volts) the model predicts a peak rating power of approximately 450 watts. The phase current is predicted to be 10 Amp r.m.s. and the peak flux density is 0.47 Tesla. The solution for this case is given in Appendix 9.1, case-1. This power could be extracted from the machine on continuous duty if a powerful liquid cooling was provided. This rating gives a power/volume (P/V) ratio for this SRG of 75 watts/in³ and an approximate power/weight (P/W) ratio of 1 kW/kg. These figures are to be compared with the some of the results given in the publications (most of which have already been reviewed in chapter 1) taking into consideration that some of the published work present high speed generators which are optimised for maximum power density and using various methods to push the operation of the machine to the maximum possible electromagnetic, electrical, and thermal limits.

The 3-phase 6/4 starter-generator SRG developed by GE [56] for the use of aircraft engine applications is characterised by a high power density due to the use of vanadium permendur (Fe-Co-V) for the stator and rotor laminations, which has a B_{sat} of 2.2 Tesla. Moreover, the cooling consists of a combination of air and oil through the shaft for the rotor and liquid cooling shroud on the outside of the stator core as well as coolant pipes through the stator slots. This resulted in a P/V ratio of 220 watts/in³ and a P/W ratio of 3.25 kW/kg at 50,000 rpm. As for the other SRG designed by GE and published in [164], the three-phase 12/8 machine gives a P/W ratio of 4.2 kW/kg and the machine delivers 250 kW at 14,000 rpm.

A relatively large 5-phase 18/12 375 kW SRG, also developed by GE [115] for size and weight optimisation, is claimed to provide a P/V ratio of 526 watts/in³ and an impressive P/W ratio of 11.2 kW/kg while running at 10,000 rpm.

A experimental system of a very high speed small gas turbine-driven permanent magnet generator PMG [65] made of NdFeB magnets was reported to have a P/W ratio of 2.5 kW/kg. The generator delivers 25 kW at 100,000 rpm. This does not mean that the PMG will always have lower power densities than the SRG. This will depend on the speed, the magnet material and the optimisation procedure of a particular application. Gas turbine generators running at very high speeds need to use fewer poles and with non-magnetic retaining bands in the air gap which nullifies some of the advantage of using a high speed [89].

Details of the high speed reluctance generator RG system of [107] are given in [109], where the P/V ratio is 57.5 watts/in³. The generator delivers 1.5 kW at 24,000 rpm. The generator is, however, claimed to be designed for research purposes rather than for optimisation of energy conversion.

9.4 Power Versus Speed and The Appropriate Voltage

A useful approach to obtain a power-speed envelope is to expand the power/speed relationship further beyond what has been obtained from the experimental testing system. This relationship would result from operating at various voltages along a speed range of 10,000-100,000 rpm. This is graphically shown in Figure 9.1 for continuous as well as for peak power rating. The operating voltages were selected here to result in the maximum power at each operating speed. On the other hand, Figure 9.2 shows the power-speed envelope for fixed voltage of 40 volts (both continuous and peak rating) and Figure 9.3 for fixed voltage of 60 volts. Model results were used to construct the graphs. However, the testing results from Appendix A8.1 are also shown on the corresponding operating points (of Figure 9.2) for comparison.

POWER - SPEED ENVELOPE

CONTINUOUS & PEAK RATINGS

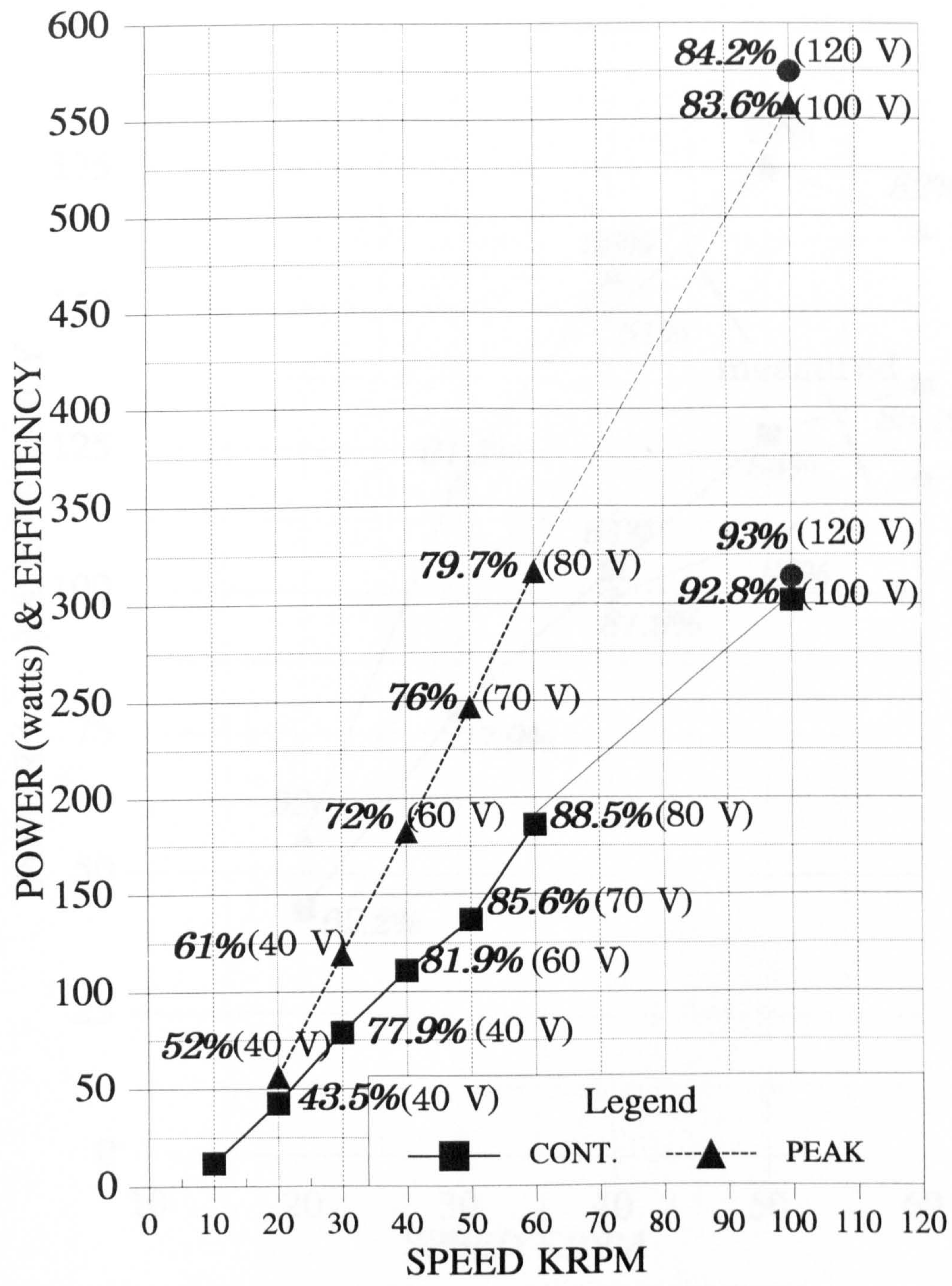


Figure 9.1: Model results for power versus speed for continuous and peak operation with the voltage selected to result in maximum power at each speed.

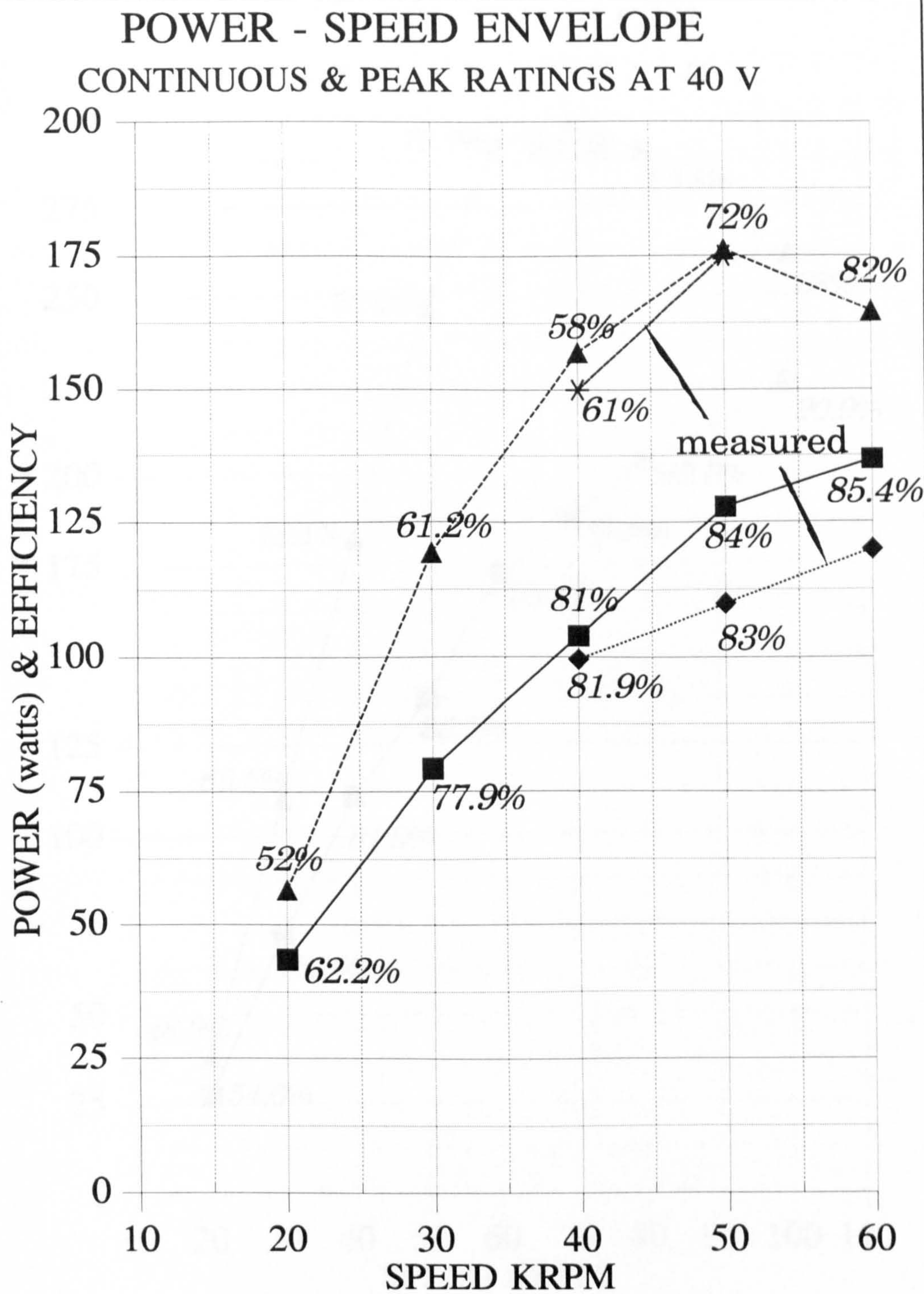


Figure 9.2: Model and available experimental results showing power versus speed at fixed voltage of 40 volts.

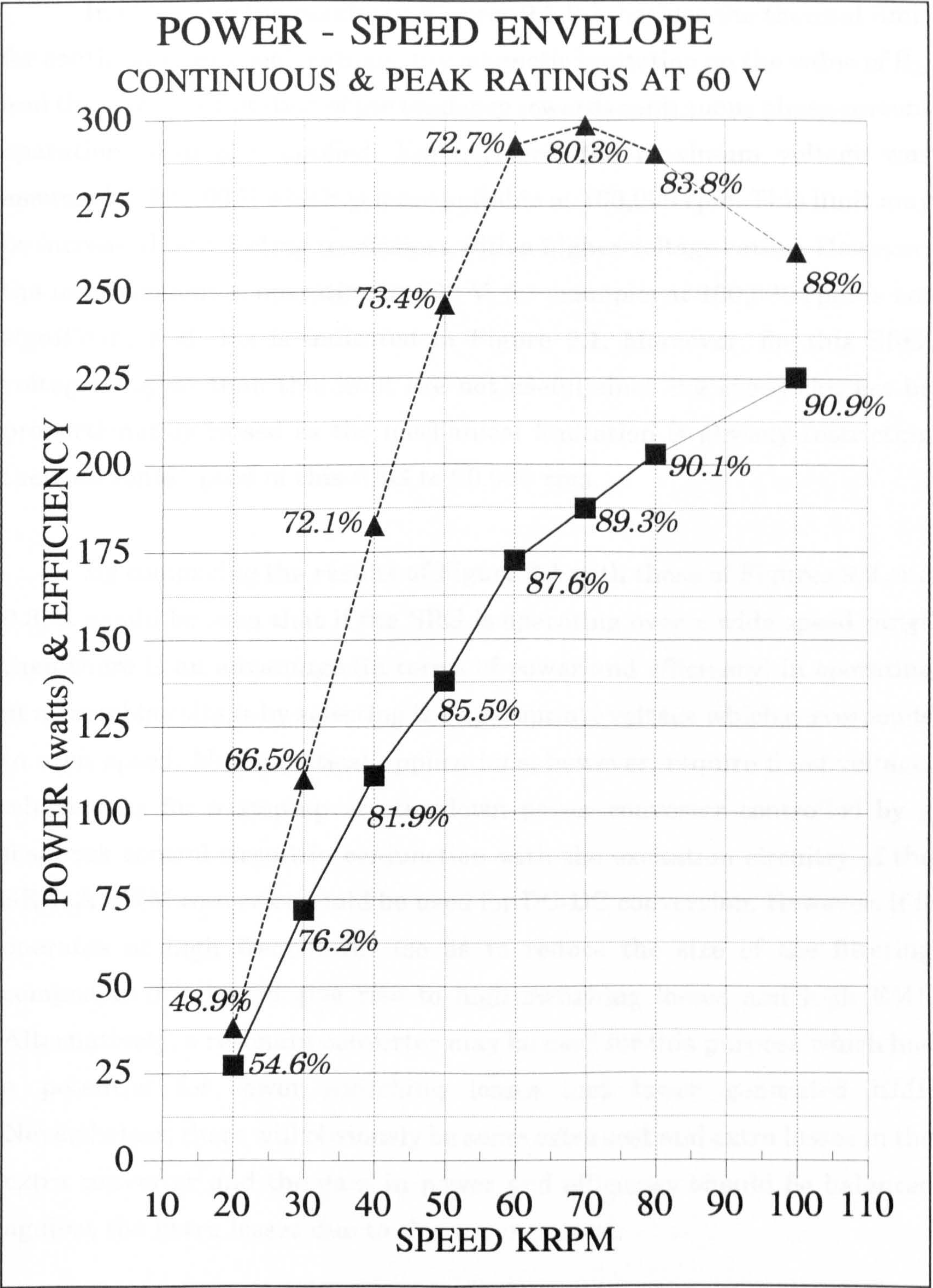


Figure 9.3: Model results showing power versus speed at fixed voltage of 60 volts.

In obtaining the results in Figures 9.1-9.3, besides the thermal limit for continuous and peak ratings, the magnetic limitation on the value of B_{pk} and the electric limitation of the tendency towards continuous phase current operation were also applied. Furthermore, the maximum voltage was assumed to be 100 V which is more suitable at 100,000 rpm. This limit may be increased by selecting transistors with a higher voltage rating. However, the improvement of operating at 120 V, for example, at 100,000 rpm is not significant and this is indicated in Figure 9.1. Moreover, for this SRG, voltages higher than this limit are not useful since the speed can not be proportionately raised as the mechanical limitation is already restricting the rotational speed of this SRG to 90,000 rpm.

By comparing the results of Figure 9.1 with those of Figures 9.2 and 9.3, it would be seen that if the SRG is operating over a wide speed range then there is an advantage (in terms of power and efficiency) in operating at a variable voltage by selecting the appropriate voltage which corresponds to each speed. Most practical applications, however, require fixed voltage, which calls for a step-up or step-down power converter controlled by a feedback control circuit in conjunction with the excitation circuitry of the SRG. A PWM converter could be used for DC-DC conversion. However, if it operates at high frequencies (so as to reduce the size of the filtering components) it would give rise to high switching losses and high EMI. Alternatively, a resonant converter may be used for this purpose which has a potential for lower switching losses and lower generated EMI. Nevertheless, there will obviously be some extra cost and extra losses in the extra converter and the gain in power and efficiency should be balanced against the extra losses due to this arrangement.

9.5 The Case of an All-Steel SRG

The use of the ferrite stator core had the following implications regarding the over-all performance of the SRG, compared to a steel core:

- 1- Limiting the peak flux density to a low value.
- 2- Reducing the over-all weight of the unit.
- 3- Reducing the over-all cost.

The magnetic model was used to investigate the effect of using a steel core with a flux density of 1 Tesla. The dimensions of the SRG are considered to be the same. The rotor is assumed to be of the same core material as the stator. The same specifications of the phase windings are also considered resulting in a similar current density limitation of 5 Amp continuous and 11.4 Amp peak rating. However, since the saturation flux density is now four times greater, the ampere-turns required to saturate the poles would be much higher than in the case of the ferrite SRG. Assuming no thermal limitation on ampere-turns, this means that with the same time constraints and with four times the operating voltage, appreciably more power could be generated. However, in practice the ampere-turns is limited and therefore the only way in which higher fluxes could be obtained for the same geometry is by reducing the air gap by say 75%. Unfortunately, for this size of machine, this reduction in air gap is not mechanically realistic. Some benefit could be obtained by increasing the area available for the winding at the expense of the pole area on the steel core.

For a fixed geometry, as has been the case for this study, and for the small size of generator considered, there is therefore some force to the argument that there is little disadvantage in using a ferrite stator (as compared with steel) which is a surprising conclusion. However, it should be noted that if very powerful cooling is used (allowing the r.m.s. phase current to rise to say 30 Amp) then it is more advantageous to use steel

than ferrite and the expected power could be 3 kW at an efficiency of 79%. The model prediction for this case is given in Appendix A9.1, case-2.

The weight reduction due to the use of ferrite is about 30% (see Appendix A6.1) considering the same winding design on the stator for both cases. Moreover, provided that the correct desirable shape for the stator can be molded out of ferrite, using a ferrite core for the small machine will lead to some cost reduction.

9.6 Alternative Stator Geometry

The stator geometry selection has been discussed in chapter 3. Availability of a suitably molded ferrite core was a prime reason for the selection of the core. Consequently, there was not a choice regarding the suitable number of stator poles, the split ratio, and the stator OD. Assuming that this option was available, the suitable stator geometry is investigated.

The main assumption upon which the investigation is based is that the machine would have the same specifications of the particular SRG that has been built and tested. This includes the main dimensions of the machine, the wire size of the phase winding design and the assumption for the stator core to be also made of ferrite. These assumptions are made to allow for comparison with the particular SRG of the current project. The rotor material is assumed to allow magnetic flux densities higher than those of the ferrite stator.

The choice of stator and rotor pole number for the SR machine is very wide and needs to be confined to few alternatives which are suitable for a particular application. If a high number of stator poles is selected, then the

rotor pole number should also be high in order to increase power conversion inside the machine. This will give rise to high switching frequencies and high core losses unless a low-loss core material is selected for both the stator and the rotor. High power density SR machines need to be built with as many magnetic poles as the air gap geometry permits without loss of inductance ratio. It may be argued that to achieve the goals of high specific power, high efficiency, and simplicity, within each magnetic pole configuration, the lower stator and rotor pole combinations seem preferable [164]. The specific power is related to the weight of the machine which may be reduced by having a lower number of poles on the rotor and the stator especially if the pole design is arranged to give a split ratio and an inter-pole configuration that aims for higher L_{\max}/L_{\min} ratio. However, the specific power is also related to the power conversion capability which will be reduced by having a fewer number of working strokes per revolution at fewer number of poles. Therefore, the choice of magnetic poles depends upon the inductance ratio and weight (stator yoke radial dimension) versus losses trade-offs.

A two-phase 4/2, or even a single-phase 2/2, stator/rotor pole configuration could have been investigated, if the option of stator geometry was available, since starting problems with these configurations are irrelevant regarding generator applications. These configurations will offer a high L_{\max}/L_{\min} ratio. However, for the two-phase 4/2 configuration for example, there will be two coils per phase and thus a large number of turns per pole will be required (such as 70) to give a suitable internal voltage of the generator of about 50 volts. Due to the fewer stator poles, there would be adequate space for 14 layers of 5 turns per layer but since the average turn-length will increase, the phase resistance will be higher and thus higher losses. The phase inductance will also be higher which would result in higher values of B_{pk} at excitation voltages of 50 volts or more. After making the appropriate assumptions for L_{\max}/L_{\min} and the fringing effect of

the flux, the programming model results for the generated power for this configuration suggest less values than those for the tested SRG. The power could be considerably improved if a high B_{sat} stator core is used as a power of about 930 watts is predicted by the model (at 50,000 rpm and 280 volts) if a steel stator core is used thus giving a P/V ratio of 155 watts/in³. The model solution for this case is given in Appendix A9.1, case-3. The limiting factor to the power in this case is the peak value of the flux density as the r.m.s. phase current is predicted to be only 8.7 Amp. If this is compared with the results of the 16/8 all-steel SRG, then the 4/2 configuration (with a core of high B_{sat}) is a better choice for the small machine as it also affords a more tolerable demand for a very small air gap. At high pole numbers, however, it seems that the ferrite SRG is an attractive choice.

9.7 Considering The Effect of Size and Cooling

The influence of increasing the size of the SRG and the provision of powerful cooling is investigated with the aid of the testing results and the programming model.

The size may be increased by increasing the OD of the machine or the axial length or both. Upon increasing the OD of the machine and keeping the same split ratio, the mechanical limit of the machine will be reduced. As it was shown in chapter 4, the maximum allowable speed is inversely proportional to the square of the outer diameter of the rotor. This limit is already critical regarding the appropriate rotational speeds of the car turbocharger (100,000 rpm). Therefore increasing the axial length only will be considered. The result of the model regarding the actual SRG (of 25 mm core length) is a maximum power at peak rating of approximately 250 watts at 50,000 rpm and optimum voltage of 70 volts and an estimated efficiency of 76%. On the other hand, the result for a 75 mm long SRG (with

the same other specifications of the previous one) is a peak power of 850 watts at an efficiency of 81% when operating at the same speed and at an optimum voltage of 180 volts. In terms of specific power this means that the 25 mm long SRG gives 42 watts/in³ whereas for the 75 mm long SRG the corresponding power/volume figure is 48 watts/in³. The model solution for the 25 mm long SRG and the 75 mm one is given in Appendix A9.1, case-4.

The effect of introducing powerful cooling is more pronounced for the case of an all-steel SRG of the same size as the one of the project. For the ferrite generator in order to obtain the maximum power it can be seen that the speed and the voltage should be elevated and the limiting factor to the power will therefore be the saturation flux density of the core material. However, effective cooling should make it possible for the machine to run continuously giving maximum power at 12 Amp. Effective cooling would also have made it possible to test the machine at continuous phase current operation, a case which was avoided during tests. It should also be noted here that the estimate of the continuous rating of the machine as 5 Amp has been rather conservative as the temperature rise at this current was about 40°C. A reasonable 60°C temperature rise would result from about 6.5-7 Amp r.m.s. phase current and this can therefore be a better estimate for the continuous rating for the machine. As a result, the introduction of a very powerful cooling arrangement would not considerably increase the specific power of this particular machine due to the limit on the flux density.

9.8 Conclusions and Suggestions For Further Work

The development of a high speed SR generator seems to be an interesting and rewarding area for research and development due to the significant potential of the machine in particular applications which this thesis aimed to exploit using testing results of a particular example of a novel ferrite small SRG running at 60,000 rpm and a simple, yet very useful, magnetic model based on the quasi-linear magnetic characteristics of flux-linkage versus current.

The mechanical design procedure is based on the finite element stress analysis of the rotor and may also be considered for rotors made of other materials and rotors of different size. The procedure that was given in chapter 4 which included the determination of the mechanical limits (due to centrifugal, thermal, and interference fit stresses) of the rotor of the high speed machine may be quite useful for other designs.

Although the SRG designed and built for this project could only provide electric power in the sub-kW region at the highest possible speed, the mechanical and electromagnetic design procedure in conjunction with the testing results of an actual high speed SRG and simple model results constitute the main contribution of the project by giving an insight into possible means of designing a high power density electric power generator for aerospace and ground vehicle applications. It also raises attention to several points of interest for further research, such as the choice of materials and poles configurations for optimising power conversion and the effect of the mechanical, electromagnetic, and thermal limits on the performance of the machine and discussing various ways to push-up these limits with the aim to increase the specific power of the generating unit. There is much room for development with novelty in this field. Different materials for the rotor and stator, different pole configurations, and

different winding configurations are just but few examples of the areas of interest for general further work. In particular, rotor material selection and processing as well as rotor heat transfer design are key for a successful machine design. The stator winding need to combine liquid cooling and coil separation techniques that reduce the potential for coil-to-coil short circuits, and a coil support strong enough for the pulsating forces.

For this particular project, there are several steps which may be taken towards development although these may seem to be in different directions. Time and project funds did not allow serious consideration for some of this further work; some other areas are also important but were considered to be beyond the scope of the project. Some suggestions for possible further work with this particular SRG are therefore given below:

- 1- The consideration of continuous phase current operation. This operation may initially cause some stability problems but it is worth consideration. The simple programming model was equipped with the facility to calculate a prediction for the current waveform and thus power and efficiency in continuous phase current operation but this could not be collaborated with testing results.
- 2- The magnetic model which is based upon a quasi-linear representation of the machine's magnetisation characteristics could be improved to give a better approximation of these characteristics by considering the convergence of the magnetisation curves at high currents instead of taking parallel lines with a slope equal to the minimum inductance of the un-aligned position.
- 3- The static tests of the SRG were limited to instantaneous currents up to 10 Amp due to some difficulty in achieving higher currents with the simple set-up for static tests. The generator, however,

experienced currents up to 25 Amp. It is useful to extend the static tests to cover the magnetic characteristics of this SRG in this area.

- 4- Better estimate of diode losses is required since the average currents handled by the power diodes during generation are quite high. At the moment these losses were estimated by considering the product of 0.7 times the average current. This decision was explained in chapter 7 yet it may underestimate the losses and will need further consideration.
- 5- The experimental determination of the power extracted from the shaft of the turbine by determining the torque at a given speed using an eddy current brake (a torque calibrating disk). This will enable a more realistic estimate of losses, thus efficiency of the SRG.
- 6- For the given stator ferrite core ring of 16 salient poles, a single phase 16/16 machine is a quite interesting case for experimental investigation. Also, a small SRG but of a longer stack such that it becomes capable of delivering 2-3 kW to the increasing electric loads of the vehicle could be experimentally examined by replacing the turbine by a high speed electric drive and using a special bearings for the machine.

APPENDIX A1.1

GENERAL THEORY OF TORQUE PRODUCTION IN SR MOTORS

The flux linkage associated with a machine phase winding $\psi(\theta, i)$ depends on the rotor position θ and winding current i , and hence for a phase winding resistance of R_w , the voltage v applied to the winding is related to i by the terminal voltage equation of the machine:

$$v = i R_w + \frac{d\psi(\theta, i)}{dt} \quad (\text{A1.1})$$

Then, two cases are considered; static and dynamic energization.

A1.1.1 Fixed Rotor Position θ_A , Static Energization

For any position of the rotor a characteristic of flux linkage ψ against current i can be drawn. This is shown in Figure A1.1.

Let v' be the applied voltage v less the voltage drop iR_w . Then:

$$v' = \frac{d\psi}{dt} \quad (\text{A1.2})$$

Then, ignoring power loss due to iR_w ,

$$\text{Inst. Power supplied} = i.v' = i \frac{d\psi}{dt} \quad (\text{A1.3})$$

For any stationary position the mechanical output is zero and all the useful electrical energy input is converted into field energy. For time t_1 to build flux from 0 to ψ_1 :

$$\text{Energy supplied} = \text{Energy stored } W = \int_0^{t_1} i \frac{d\psi}{dt} dt \quad (\text{A1.4})$$

$$\text{or } W = \int_0^{\psi_1} i d\psi$$

This is represented by the shaded area shown in Figure A1.1.

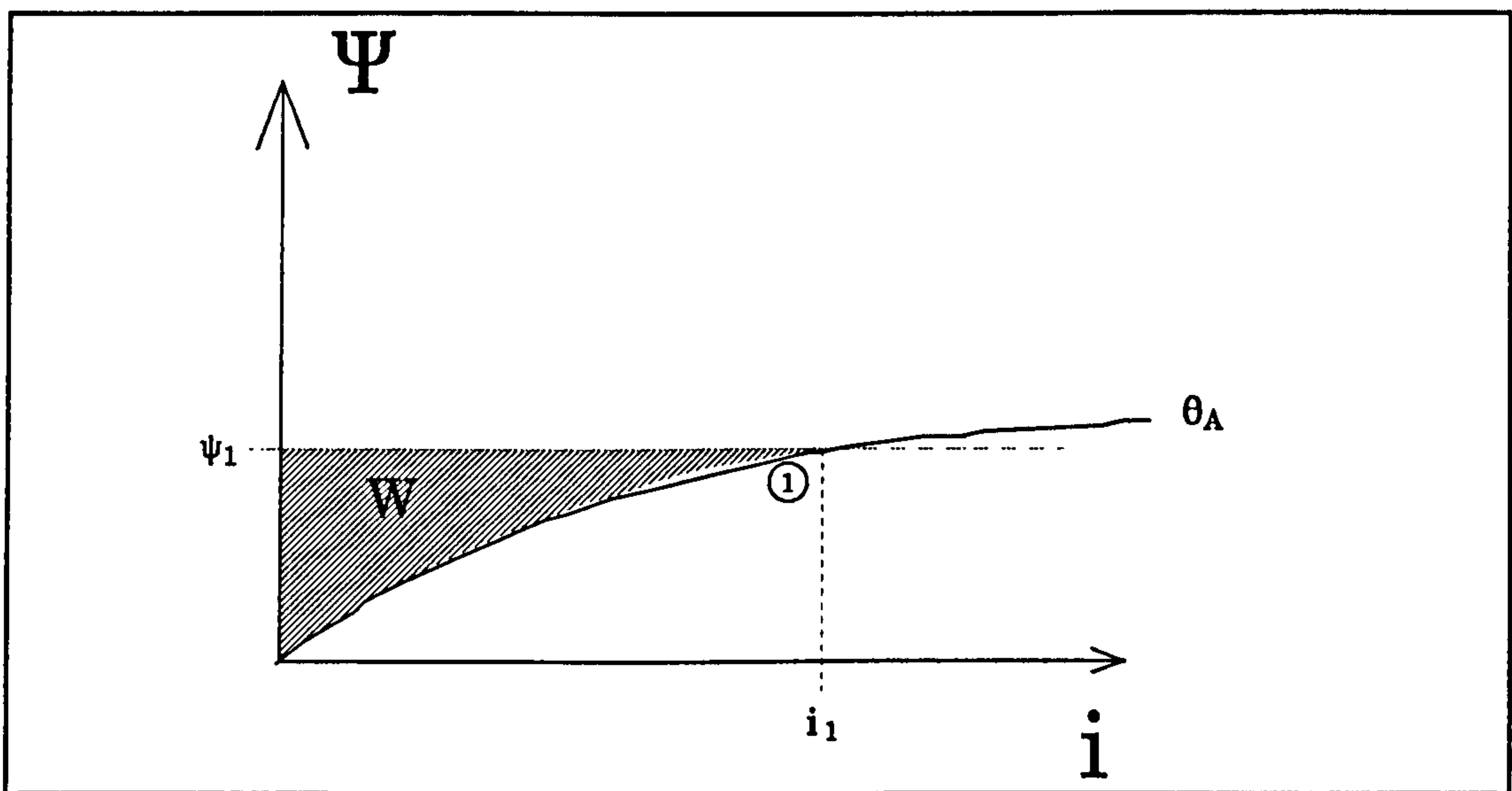


Figure A1.1: Energy determination for case 1, fixed rotor position.

A1.1.2 Change in Rotor Position θ_A to θ_B

Figure A1.2 illustrates energy change for change in rotor position from θ_A to θ_B .

$$\text{Energy Supplied} = \int_{\psi_1}^{\psi_2} i d\psi = \text{area } B + D \quad (\text{A1.5})$$

$$\text{Change in energy stored} = (A+B) - (A+C) = (B-C) \quad (\text{A1.6})$$

$$\begin{aligned} \text{Energy converted to mech. energy} = \\ (B+D) - (B-C) = (C+D) \end{aligned} \quad (\text{A1.7})$$

and this is represented by the shaded area shown in Figure A1.2.

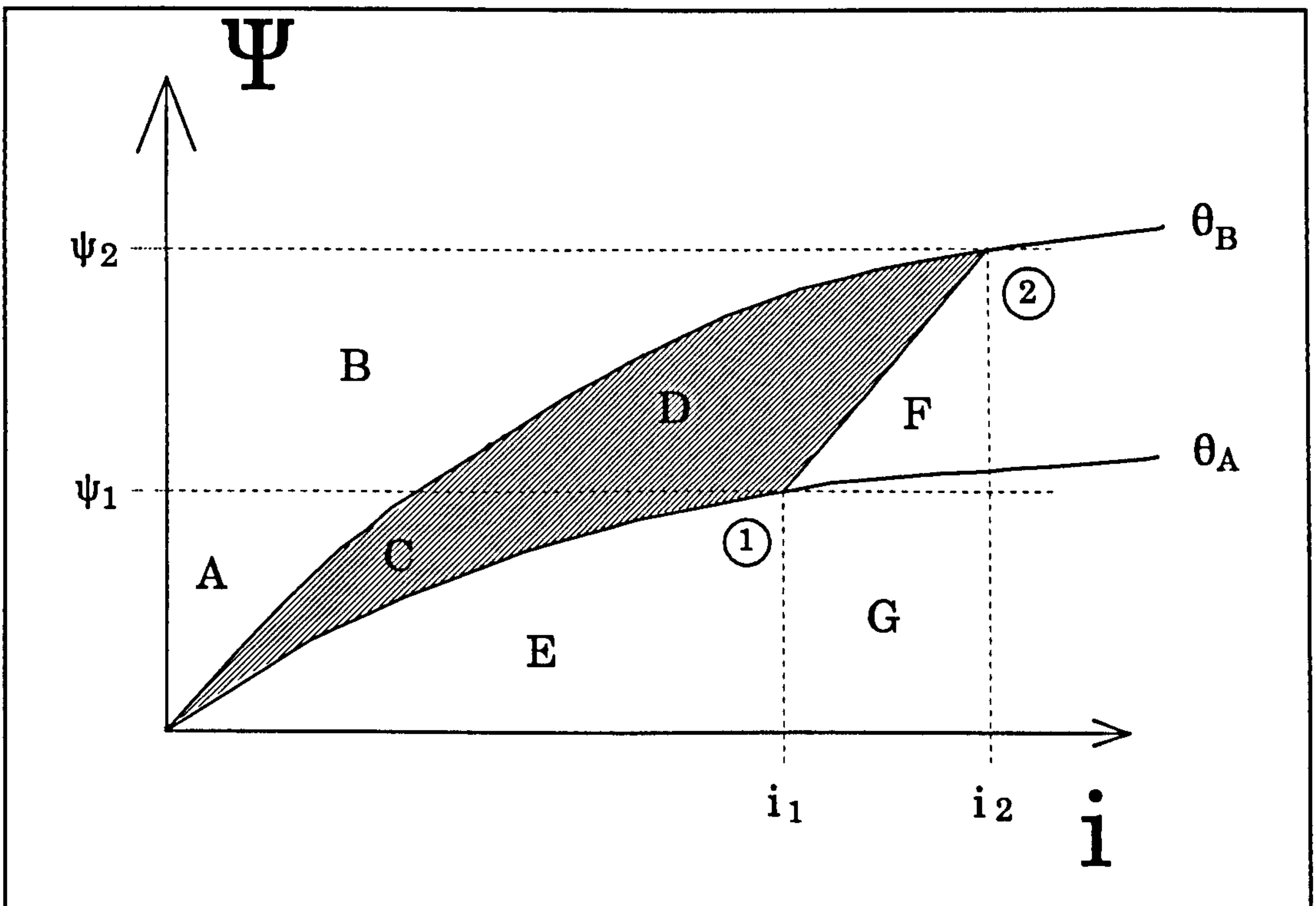


Figure A1.2: Energy determination for case 2, change in rotor position.

$$\text{Let co-energy } W' = \int_0^i \psi \, di \quad (\text{A1.8})$$

Hence, change in co-energy in changing position from 1 to 2 (in Figure A1.2) can be given by:

$$(C+D+E+F+G) - (E) = (C+D) + (F+G) \quad (\text{A1.9})$$

It can be shown that by considering a constant current during the position change of θ from 1 to 2, the change in co-energy given by (A1.9) can be approximated to $C+D$. This is illustrated by Figure A1.3.

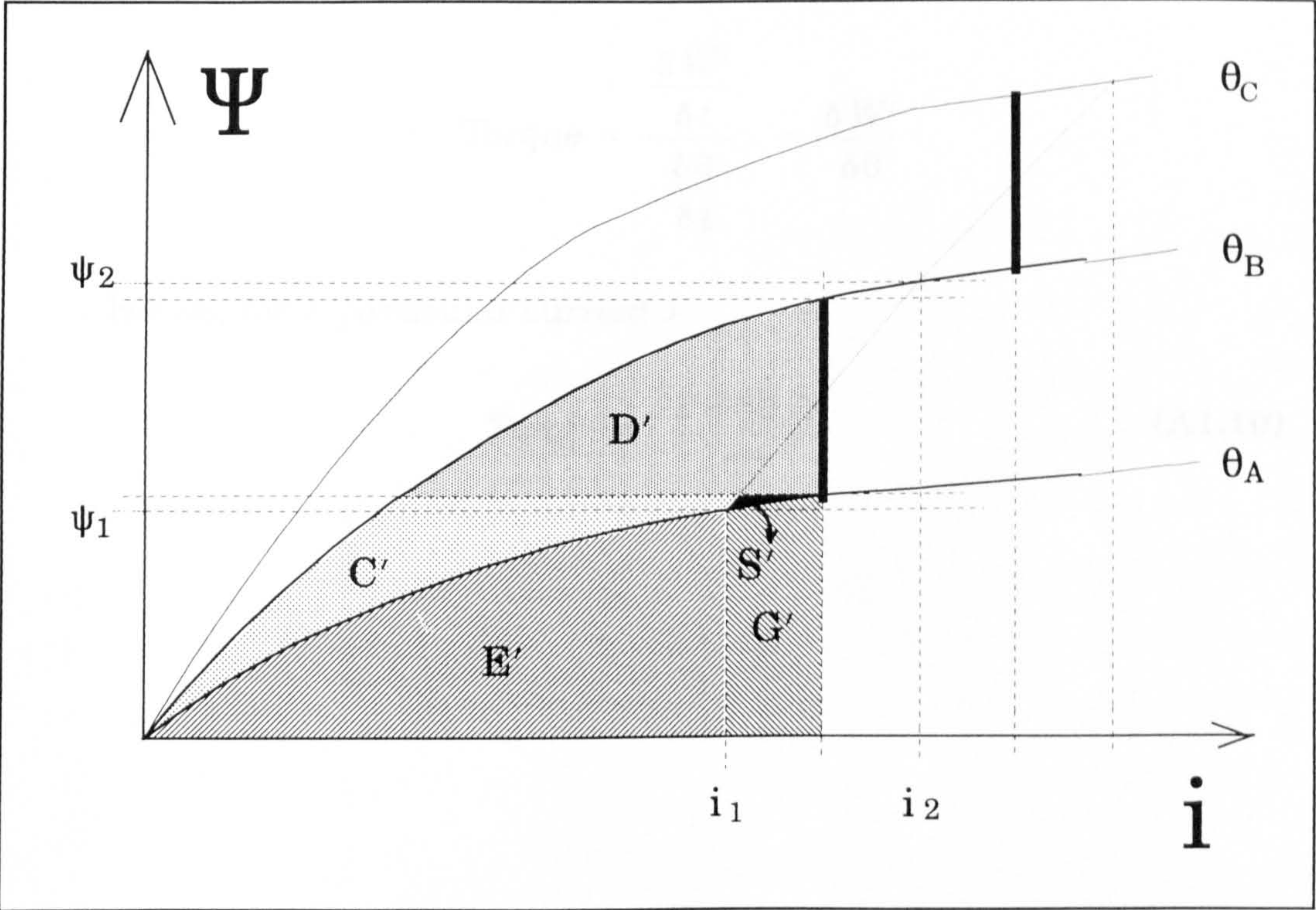


Figure A1.3: Energy determination for the dynamic case considering constant current for each step of θ .

The for a step change of θ from θ_A to θ_B , the current is assumed to be constant between i_1 and i_2 . The same applies for the position change between θ_B and θ_C and so on. The change in co-energy in this case is simply:

$$(C'+D'+E'+G') - (E'+G') = (C'+D') \tag{A1.10}$$

Now $C+D$ can be shown to be only greater than $C'+D'$ by the small area S' shown in Figure A1.3. This small difference can be ignored when the step change is very small, $\delta\theta$. Therefore:

$$\delta W' = C' + D' \approx C + D$$

and mechanical power = $\frac{\delta W'}{\delta t}$

$$\therefore \text{Torque} = \frac{\frac{\delta W'}{\delta t}}{\frac{\delta \theta}{\delta t}} = \frac{\delta W'}{\delta \theta}$$

Hence, for a particular current i :

$$\text{Torque} = \frac{\delta W'(\theta, i)}{\delta \theta} \quad (\text{A1.10})$$

APPENDIX A1.2

REVIEW OF CONTROL AND POWER CONVERTERS OF SR MACHINES

A1.2.1 Control

SR machines have a high degree of controllability for current (hence efficiency), torque, and power over the speed range beyond the simple natural characteristics of the machine. Hence it is virtually possible to give the machine any type of operating characteristics, e.g. constant torque or power [14] with four quadrant drive performance using PWM control [15]. High efficiencies can be maintained over a wide speed range. Instantaneous torque control is also possible with a more sophisticated controller [16]. Consequently, the SR machine is often thought of being "programmable" especially as a controlled speed drive [17] and in servo and near servo applications [18].

Despite the simplicity of the SR machine in its construction- claimed to be the simplest of electrical machines [2]- ; simplicity in its principle of operation [1][2][3][14], and adaptability to a variety of control functions [19], its control strategy is far from simple [2][20]. This is mainly due to non-linearity and the fact that saturation dominates the normal working machine [14]. However, since, initially, no requirement exists for complex control strategies related to the application of pulse width modulation PWM techniques, in the early time of its launch as a variable speed drive, the SR machine controller was based on analogue or digital techniques using simple discrete logic IC's [21]- a type of controller implemented in the work presented in this thesis. As the potential of the machine was further utilised which resulted in control strategies becoming more complicated

with better performance demands, a microprocessor was used to implement the controller [22]. The microprocessor based system is designed in such a way as to allow the implementation of as much of the control functions as possible within the software [13]. Personal computers (PC's) and microcomputers have been proposed to replace microprocessors in order to eliminate the extra peripheral circuitry needed with the microprocessor [23][24][25]. A micro-controller or single chip computer with high performance capabilities and lower cost can also replace the PC [23].

As far as generator applications are concerned, control strategy is quite different in terms of the performance parameters to be optimised, especially if a machine is designed to work as a generator only, or predominantly as a generator, such as direct driven turbo-generators for ground vehicles and aerospace applications.

A control strategy for an SRM is determined by several factors such as intended application, performance requirements and the type of converter topology used for driving the machine. In any case, an integrated approach to the design of the whole system is essential [21][26]. Unlike most conventional machines, SR machines design must be closely related to the design of its inverter and control.

Some applications require the optimisation of the efficiency (and the effectiveness) and the reduction of noise. These are typical requirements for a low voltage SR machine. For such an application optimising the effects of switching angles is carried out. This is achieved by setting up an experimental hardware in order to find optimum switching angles that would yield the required performance. The sets of angles are then stored as functions of rotor speed and torque in a look-up table in an EPROM [27].

Other applications, such as the direct drive SR motors, require essentially the minimisation of torque ripple which is an inherent problem in the operation of SRM. Feedback linearisation techniques were suggested [28] with a follow up development [29] to simplify the complex control algorithm that was given in [28]. The system is based on a dynamic non-linear model of the SR machine. Again, an experimentation set up is required to measure and produce a family of torque-angle curves for small current steps and a family of current-angle curves for small torque steps. A transformation circuit is then used to produce desired (command reference) current trajectories for constant speed and constant torque (ripple free) operation. These current reference signals are applied to a composite control system. The non-linearity of these current reference waveforms is carefully designed to cancel the non-linearity of the torque function, and to eliminate torque ripple during the commutation intervals through which two phases simultaneously produce torque.

In order to simplify -and automate- the measurements of the magnetisation characteristics of the machine required to generate reference signals off-line, self-learning techniques were suggested [30]. The compromise solution aims at minimising the need for knowledge of machine characteristics. It uses an off-line self-learning algorithm for characterising the machine in order to produce a fast on-line torque control.

Such methods, described briefly above, have the disadvantage of necessitating the exact knowledge of the machine characteristics and of often being very complex in implementation. Variable structure control, first suggested for SR motor in [31], is claimed to offer easier implementation of the control scheme while giving the SRM drive the usual benefits of insensitivity to drive parameter variations and disturbances. It aims to

control the SRM, without the pre-knowledge of the machine characteristics, and to reduce torque ripple by compensating for the non-linear torque characteristics.

The use of neural networks has also been recently reported [32]. The technique attempts to minimise torque ripple by learning the required current profiles on-line, thus making it possible to account for effects ignored by other techniques such as magnetic interaction between simultaneously conducting phases, as well as windage and friction effects. In order to produce acceptable solutions, the network must be pre-loaded with accurate solutions of initial current profiles.

A1.2.2 Power Converters

Various circuits can be used to supply the SR machine. What is generally required is a switching converter that would connect the d.c. supply to the phases of the machine in sequence and at carefully timed instants for a carefully timed dwell. After disconnecting each phase from the supply, the inductive energy, or the energy stored in the magnetic field, would be dealt with by various means.

Apart from the basic power converters discussed in the main text of chapter one, other different approaches are also possible, especially those used to tackle specific problems such as pulsating torque or audible noise. Such approaches are found in conjunction with unconventional and novel winding arrangements such as the split coil SR machine [34] and auxiliary winding VRM [35]. New topologies are still being developed for conventional SR machines [36].

Nevertheless, the method used for recovering the inductive energy is uniquely used to define the class of a power converter. In fact every converter configuration is becoming a class of its own bearing in mind the far reaching consequences a configuration may have on the performance of the machine itself. This applies to both SR motor drives and SR generator excitation circuits. Some power converters which were not covered in chapter one are discussed next.

One of the old classical unipolar converters is the bifilar winding converter which uses one switch per phase, i.e half the number required by the classic converter but with at least double the voltage rating. It requires a secondary winding on each coil tightly coupled to the primary [21][26][37]. A circuit suggested by Miller et.al uses one switch per phase and an extra switch which connects all phases at one end [15]. Another unipolar converter uses two diodes per phase with some loss of independence of phases [38] in addition to higher current rating for each switch and insufficient demagnetisation time during phase currents overlap. Its main advantage as a unipolar converter is in the voltage rating of the switches, which is only V_s instead of $2V_s$ as with other unipolar converters.

As the potential range of SR machines is enormously wide [39], from few watts [18] to hundreds and even thousands of kilowatts [40] and for various demands of power, torque and speed in domestic, industrial and traction applications, the choice of converter configuration for certain application depends on a large number of factors including:

- 1- The supply voltage. The supply can either be a battery or, more generally, derived from rectified a.c. mains circuit. Up to few kilowatts, a single phase supply is adequate. At larger power levels,

three phase is used with three phase bridge rectifier. The load seen by the a.c. mains is a rectifier supplying a capacitor bank, i.e similar to the supply of the d.c. link inverter which feeds the induction motor [37]. A second controlled rectifier should be used if regeneration is included.

- 2- The number of phases. In general, any number of phases is possible with SR machines. However, for motor drive applications three phases and more will be suitable for self starting in either direction. For any application, the choice of number of phases will influence power and torque as well as efficiency. In general, the higher the phase number, the more power switches will be required, and this will have to be weighted against weight/size, converter efficiency and cost implications.
- 3- The type of power switching device. These include thyristors and GTO's for high power applications, power bipolars and IGBT's for medium power applications, and power MOSFET's for powers up to 2 kW. The power MOSFET is not suitable for powers above 2 kW as its conduction losses tend to dominate and the IGBT is a better choice. As manufacturing costs are decreasing for new technologies of power semiconductors, the IGBT, which combines advantages of both power MOSFET's and power bipolars with high switching frequency capability, is becoming the optimum option for many applications. For high power applications the new range of MOS-controlled thyristors MCT's is finding increasing use.

- 4- The control strategy. For some applications the control strategy can be quite complex and demanding. Fortunately the SR machine is easily adaptable to microprocessor and microcomputer control. Some control schemes may well dictate a certain type of power converter in order to make use of this easy adaptation.

APPENDIX A2.1

DEVELOPMENT OF THE MODELLING PROGRAMME

On the basis of the equations and assumptions of chapter 2, a simple computer programme in C is developed. The evaluation of the power and the efficiency is based upon sub-dividing the expected current waveform, such as the one shown in Figure 2.9, into several regions. Basic assumptions and equations applicable for each region are given below.

1- Switching *on* at θ_{dly} .

(a) If $\theta_{dly} < \theta_r$: Current is switched on before the onset of the rising inductance. In this case there is no back e.m.f. and the inductance is only L_{min} . The current is initially zero and is expected to follow a straight line. However, provision was made in the programme to account for a non-zero initial current at the second and subsequent current pulses, to take into consideration the case of continuous phase current operation which may result from the selection of particular firing angles. The relation, which is applied during the first inner loop of the programme, to find I_1 (in Figure 2.9) is:

$$I_1 = \frac{V_s - iR}{\omega L_{min}} (\theta_r - \theta_{dly}) \quad (A2.1)$$

where R equals to the phase winding resistance R_w plus on-state resistance of the power switch R_{ds-on} .

(b) If $\theta_{dly} > \theta_r$: The second inner loop. Current switching is delayed until after the onset of the rising inductance region. In order to find I_o , (in Figure 2.9), it is not known in advance when the current will reach the value of I_{sat} which should be known in the programme as given by (2.6). Therefore,

using (2.22), the value of i is determined and tested for reaching I_{sat} . In this case the back e.m.f. opposes current build up. I_o is then:

$$I_o = \frac{V_s - K L'_{max} \omega i c ze - i R}{\omega [K L'_{max} (\theta - \theta_r) z + L_{min}]} (\theta_m - \theta_{dly}) \quad (A2.2)$$

Where c is set in the programme to 1 in the linear region and to I_{sat}/i in the saturated region. z will be zero in the saturation region and 1 in the linear region. ze takes into account the possibility of constant inductance, or dead-zone profile at L_{max} . Note that L'_{max} is given the symbol La in the programme listing.

If the switching starts before θ_r , (A2.2) is applied by considering the initial current to be I_1 , determined from (A2.1).

The current will normally be commutated in the falling inductance region. However, considering the general, though not usually practical case of $\theta_{com} < \theta_m$, a secondary loop is added to the programme after this second main loop. This loop will only be entered upon "breaking" the second loop if during incrementing θ it becomes greater or equal to θ_{com} while still not reaching θ_m . The equation that will apply for $di/d\theta$ from which i is determined using step integration is:

$$\frac{di}{d\theta} = \frac{-V_s + K L'_{max} \omega i c ze - i R_w}{\omega [K L'_{max} (\theta - \theta_r) z + L_{min}]} \quad (A2.3)$$

where $-V_s$ may take the value of $-V_o$ if the case of different source and sink voltages applies. This also takes into account commutating during the dead-zone of L_{max} , if applicable by setting ze to zero.

2- Current between θ_m and θ_{com} : The third inner loop. Since this is in the falling inductance region, the back e.m.f. will assist the supply voltage until the commutation angle. The current will reach its peak value at θ_{com} if the supply voltage is higher than the back e.m.f., V_i . Otherwise, the current will continue to rise beyond the commutation point as long as V_i is higher than the supply voltage. For realistic SR generator, θ_{com} will be somewhere during the falling inductance region, i.e. before θ_r . The increase of θ_{com} beyond a certain point may cause continuous operation which, though may have an advantage, it may also result in overheating and operation instability. Similar to θ_{dly} , the location of the commutation angle should be optimised for efficiency and power conversion. The current I_0 at the start of this region may not have reached I_{sat} , for a general case. It is therefore allowed in the programme to test for the value of i . If i is below the saturation level, the inductance should be $L(\theta)$ rather than the incremental inductance. Since the angular position is being increased, the same relation for L as in (2.13) is no longer valid and a constant is introduced in (2.13) to yield the required value of L making use of the fact that L in the falling inductance region is a mirror image of L in the rising inductance region. The relation used in this case to determine i is:

$$\frac{di}{d\theta} = \frac{V_s + K L'_{max} \omega i c z - i R}{\omega [K L'_{max} \{\theta - \theta_r - 2(y - 1)\delta\theta\} z ze + L_{min}]} \quad (A2.4)$$

The value of z will be zero if $i > I_{sat}$, and ze is zero when θ exceeds θ_r . The counter y starts from 1 and is increased with a step of 1 every $\delta\theta$.

The resultant value of the mean current is obtained at the end of this region in order to find the input (electrical) power by:

$$P_i = \frac{qi}{2 \theta_m} V \quad (\text{A2.5})$$

$$\text{where,} \quad qi = \sum_{\theta_{dly}}^{\theta_{com}} i \, d\theta \quad (\text{A2.6})$$

and $(2 \theta_m)$ represents a complete electrical cycle.

The R.M.S current in the power transistor I_{sw-rms} is determined also at the end of this region:

$$I_{sw-rms} = \sqrt{\frac{r}{2 \theta_m}} \quad (\text{A2.7})$$

$$\text{where,} \quad r = \sum_{\theta_{dly}}^{\theta_{com}} i^2 \, d\theta \quad (\text{A2.8})$$

3- Current is switched off at θ_{com} : This is the fourth loop as indicated in the programme listing. Between the commutation angle and θ_f , the value of V_s is negative and the back e.m.f. effect still exists. Then:

$$\frac{di}{d\theta} = \frac{-V_s + K L'_{max} \omega i c - R_w i}{\omega [K L'_{max} \{\theta - \theta_r - 2(y-1)\delta\theta\} z + L_{min}]} \quad (\text{A2.9})$$

The flag z is unlikely to be 1 in practice, as this would mean that the current falls very quickly from a high value (which may well be its peak I_{pk}) to a low value below saturation level I_{sat} . Note that $-V_s$ is given in the programme as $-V_o$ to allow for different values of the source and sink voltages.

A new variable qt is defined and initialised in this region. It is used to determine the output power when current falls to zero. This variable will have been used already if the secondary loop after the second loop (explained by (A2.2)) has been entered.

4- Current falls to zero: This is the fifth inner loop. At θ_e , the extinguishing angle, the current will reach zero under the influence of negative voltage applied to the winding. This region starts from θ_r up to an unknown angle. The relation is valid as long as $i > 0$. If the fall of the current is in the region beyond θ_r then it will fall linearly as the inductance is constant. $di/d\theta$ will then be:

$$\frac{di}{d\theta} = \frac{-V_s - K L'_{\max} \omega i c z - R_w i}{\omega [K L'_{\max} (\theta - \theta_r - 2\theta_m) z + L_{\min}]} \quad (\text{A2.10})$$

The value of z here will be zero unless θ exceeds beyond the rising inductance region of the next cycle before i reaches zero. This relation shows that if the voltage at the output of the generator network is higher than the supply voltage then it will have an advantage of causing the current to drop to zero at a faster rate.

In this loop, the case for $\theta \geq \theta_{\text{aly}} + 2\theta_m$ is tested. If θ reaches this value before the current reaches zero, then continuous phase current waveform will result in which case the programme must "break" the loop and start calculations for a new electrical cycle. The next current pulse will not then start from zero but from the last value determined for the current. It is therefore required to include in the programme a facility to perform calculations for several pulses of current. The printed output power and phase r.m.s. current will be the average of as many pulses as has been specified in the programme. If continuous operation is detected due to the

selection of certain values of voltage, speed, or firing angles, then the programme will indicate this. Depending on these variables, when the model is run in the continuous operation, the peak current has been seen to settle after few pulses. Values of peak current I_{pk} are also determined by the programme.

Value of peak flux linkage Ψ_{pk} (from which the peak flux density B_{pk} is determined) are obtained from the estimated value of I_{pk} . Using (2.14) and substituting I_{pk} for i , and equations (2.15) and (2.16) for $\Delta\Psi$:

$$\Psi_{pk} = L_{\min} I_{pk} + L'_{\max} I_{sat} K (\theta - \theta_r) \quad (\text{A2.11})$$

At a particular operating point, all parameters in (A2.11) are known, and θ is given as:

$$\begin{aligned} \theta &= 2\theta_m - \theta_{com} & ; \text{ if } \theta_{com} > \theta_m \\ \text{or } \theta &= \theta_{com} & ; \text{ if } \theta_{com} < \theta_m \end{aligned} \quad (\text{A2.12})$$

The peak or maximum operating flux density is normally higher than the saturation flux density value of the core material B_{sat} . The value of B_{pk} may not, however, be higher than $2B_{sat}$. The value of B_{pk} will be:

$$B_{pk} = \frac{\Psi_{pk}}{N_c \times A_c} \quad (\text{A2.13})$$

$$\text{where, } N_c = N \times \frac{\text{stator poles}}{m}$$

where A_c is given in the machine specifications as the area of the stator pole, N is the number of turns per pole, N_c is the number of turns per phase and m is the number of phase windings in the machine.

The output power will then be:

$$P_o = \frac{qt}{2} \frac{V}{\theta_m} \quad (\text{A2.14})$$

$$\text{where,} \quad qt = \sum_{\theta_{\text{com}}}^{\theta_o} i \delta\theta \quad (\text{A2.15})$$

The net generated power will then be:

$$P_g = m (P_o - P_i) \quad (\text{A2.16})$$

The total phase R.M.S current $I_{L\text{-rms}}$ is determined similar to (A2.7) and (A2.8) above:

$$I_{L\text{-rms}} = \sqrt{\frac{r}{2} \frac{1}{\theta_m}} \quad (\text{A2.17})$$

From (A2.7) and (A2.17), the losses in the power switch $P_{L\text{-sw}}$ and copper losses $P_{L\text{-c}}$ are calculated respectively:

$$P_{L\text{-sw}} = m I_{\text{sw-rms}}^2 R_s \quad (\text{A2.18})$$

$$\text{and,} \quad P_{L\text{-c}} = m I_{L\text{-rms}}^2 R_w \quad (\text{A2.19})$$

The diode on-state losses are estimated as follows:

$$P_d = m \frac{qt \times 0.7}{2 \theta_m} \quad (\text{A2.20})$$

The estimated efficiency will then be:

$$\eta = \frac{P_g}{P_g + P_{L\text{-c}} + P_{L\text{-sw}} + P_d} \quad (\text{A2.21})$$

APPENDIX A2.2

LISTING OF C PROGRAMME FOR SIMPLE MODEL OF THE SRG

```
/* Q.C THIS PROGRAM IS A SIMPLE MODEL FOR A SWITCHED
RELUCTANCE GENERATOR*/
/* IT IS AN AMENDMENT OF QUASI.C */
/* IT CONSIDERS CONTINUOUS PHASE CURRENT OPERATION WITH
TRIANGULAR L-PROF.*/
/* WITH PROVISION OF BLOCK SOLUTIONS FOR SEVERAL RUNS IN
SEVERAL SETS */
```

```
#include "input"                                /*TO READ INPUT DATA FROM FILE : INPUT*/

main()                                           /*THE MAIN BODY OF THE PROG. BEGINS*/
{

int    mult, m, z, ze=1, y, steps=1, f=0, cont=0;
int    set=0, run=0, sm=0, rm=0;
int    a, b;
double thm, thr, thm1, thm2, thf;
double thd, thc, thon;
double A, Isat, La, Lmin, L, N_phase, PSI, Bpk;
double k, th, i, di, dith, qi, r, ri, c;
double P_in, Isw_rms, qt;
double P_out, P_gen, IL_rms, I_out, PL_sw, PL_c, PL_d, eff;
double sqrt();
double Ip_k, Ip;

if(prt==1){
printf("*****%c");
printf("\nstator poles = %d", stator_poles);
printf("\trotor poles  = %d", rotor_poles);
    }

mult = 1;                                     /*THIS SEGMENT IS TO DETERMINE THE
APPROPRIATE NUMBER OF PHASE WINDINGS*/
m = stator_poles*mult/rotor_poles;
while ( ( stator_poles * mult) % rotor_poles != 0 )
    mult++;
m = stator_poles * mult / rotor_poles;
```



```

if(prt==1){
printf("\tno. of phases m = %d", m );
printf("\nstator arc  = %3.3f", stator_arc);
printf("\trotor arc    = %5.3f", rotor_arc);
printf("\tFringing factor = %3.3f", fring_factor);
}
if ((stator_arc + rotor_arc) > (360/(float)rotor_poles))    /*WARNINGS ARE GIVEN
                                                             FOR INAPPROPRIATE
                                                             CHOICE OF POLE ARCS*/
{
printf("\n\tInter pole of rotor is less than stator pole arc,\n");
printf("\n\treduce either or both arcs of stator or rotor.\n");
}

thm = 360 /(2*(float)rotor_poles) ;
thr = ( thm- (stator_arc/2 + rotor_arc/2)) / fring_factor ;
thf = 2 * thm - thr ;

if ( rotor_arc > stator_arc )    /*CONSIDERS DEAD ZONE IN THE L-PROF.*/
{ thm1 = thm - ( rotor_arc - stator_arc ) / 2 ;
  thm2 = thm + ( rotor_arc - stator_arc ) / 2 ; }
else
{ thm1 = thm + ( rotor_arc - stator_arc ) / 2 ;
  thm2 = thm - ( rotor_arc - stator_arc ) / 2 ; }

if(prt==1){
printf("\n\tImportant Values of theta in (deg) which define L profile are :\n");
printf("\tthm = %3.3f,\tthr = %3.3f,\tthf = %3.3f\n",
        thm, thr, thf );
}

if ( thm1 != thm2 )
{if(prt==1){
printf("\tthm1 = %3.3f,\tthm2 = %3.3f\n", thm1, thm2 );
}}

if(prt==1){
printf("\nstator inner dia id = %.3E m", id);
printf("\tcore (axial) length = %.3E m", lc);
printf("\nmax flux density B = %.3f Tesla", B);
printf("\tAir gap\t\t g = %.3E m", g);
printf("\nInductance ratio    = %.3f", L_ratio);
printf("\t\ttno. of turns\t N = %3.1f", N);
}

```



```

A = (id * pi * lc * stator_arc)/360 ;
Isat=(B * g)/(muo * N);
La  = ( stator_poles /(float)m )*N*N*muo*A / g ;
Lmin = La /(L_ratio - 1) ;
k = 1/((thm1- thr)*deg);
N_phase = N*stator_poles/(float)m;

if(prt==1){
printf("\n\nA = %E sqm,\tIsat = %f Amp,\nLa = %E H,\tLmin = %E H\t,\tk =
%.3f"
      , A, Isat, La, Lmin, k);
}

if (oneset==1) {set=xsets ; sm=0;}
else {set=1; sm=1;}

while( set <= xsets )          /*"SETS" LOOP STARTS*/
{
if (onerun==1) {run=xruns ; rm=0;}
else {run=1; rm=1;}

    while( run <= xruns )      /*"RUNS" LOOP STARTS*/
    {
thd = thdly + map_step*(run-1)*rm - thon_step*(set-1)*sm ;
thc = thcom + map_step*(run-1)*rm ;
thon= thc - thd ;

if(prt2==1){
printf("\n*****0%c\n");
printf("\nSwitching Angles: Theta_dly = %.2f ,  Theta_com = %.2f"
      , thd, thc);
if((oneset==1)&&(onerun==1)) {
printf(" ** Theta_on = %.2f\n", thon); }
else{
printf("\nSET NO.\t%d\t,\tRUN NO.\t%d\t:\tTheta_on =  %.2f\n", set, run,
thon);
}}

i = 0; th = 0; di = 0; qi = 0; ri = 0; r = 0; qt = 0; Ipk = 0; Ip = 0;
while( f != pulses )          /*MAIN LOOP OF THE CALCULATION BEGINS*/
{
while ( th < thr + 2*f*thm)    /*FIRST INNER LOOP*/
{ if ( th <= thd ) i=0;
  L = Lmin*scale;

```



```

    if(prt1==1){
    printf("%.3E\t%.4f\n", L, i );
        }
    steps += 1;
    dith = (ve-i*(rw+rs)) / ( speed*rpm*Lmin) ;
    i += dith * dth * deg ;
    qi += i*dth*deg ;
    ri += i*i*dth*deg ;
    r += i*i*dth*deg ;
    th += dth;

    if (i >= Ip) Ip=i; else Ipk=Ip;
}

while ( th <= thm2 + 2*f*thm )    /*2ND INNER LOOP*/
{ if (th >= thc+2*f*thm) break;
  if ( i< Isat){ z=1 ; c=1; }
    else { z=0 ; c=Isat/i; }
  if ((th >= thm1 +(2*f*thm))&&(thm1 != thm2))
  { L = (Lmin + La)*scale; ze = 0; }
    else{ L=(Lmin + La*k*deg*(th-(2*f*thm)-thr))*scale;}
  if ( th <= thd ) i=0;
  if(prt1==1){
  printf("%.3E\t%.4f\n", L, i );
      }
  steps += 1;
  dith=(ve-(ze*i*speed*rpm*La*k*c)-i*(rw+rs)) /
    (speed*rpm*(z*La*k*(th-(2*f*thm)-thr)*deg+Lmin));
  i += dith*dth*deg ;
  qi += i*dth*deg ;
  ri += i*i*dth*deg ;
  r += i*i*dth*deg ;
  th += dth;

  if (i >= Ip) Ip=i; else Ipk=Ip;
}

while ( th < thm2 + 2*f*thm )    /*SECONDARY LOOP*/
{ if ( i< Isat){ z=1 ; c=1; }
    else { z=0 ; c=Isat/i; }
  if ((th >= thm1 +(2*f*thm))&&(thm1 != thm2))
  { L = (Lmin + La)*scale; ze = 0; }
    else{ L=(Lmin + La*k*deg*(th-(2*f*thm)-thr))*scale;}
  if(prt1==1){
  printf("%.3E\t%.4f\n", L, i );
      }
  steps += 1;

```



```

    dith=(-vo+(ze*i*speed*rpm*La*k*c)-i*(rw+rd)) /
        (speed*rpm*(z*La*k*(th-(2*f*thm)-thr)*deg+Lmin));
    i += dith*dth*deg ;
    qt += i*dth*deg ;
    r += i*i*dth*deg ;
    th += dth;
    if (i >= Ip) Ip=i; else Ipk=Ip;
}

z=1 ; c=1.0 ; y=0 ; ze=1;
while ( th < thc+(2*f*thm))          /*3RD LOOP*/
{ y += 1;
  if ( th > thf + 2*f*thm ) ze = 0;
  if ( i < Isat ) { z=1; c=1.0;}
                  else { z=0; c=Isat/i;}
  if ( th <= thd ) i=0;
  L =(Lmin+(ze*k*La*deg*(th-(2*f*thm)-thr-thm2+thm1-2*(y-1)*dth)))*scale;
  if(prt1==1){
    printf("%.3E\t%.4f\n", L, i );
  }
  steps += 1;
  dith = (ve + ze*i*speed*rpm*La*k*c - i*(rw+rs))/
    (speed*rpm*(z*ze*La*k*deg*(th-(2*f*thm)-thr-thm2+thm1-2*(y-1)*dth)+Lmin));
  i += dith*dth*deg ;
  qi += i*dth*deg ;
  ri += i*i*dth*deg ;
  r += i*i*dth*deg ;
  th += dth ;

  if (i >= Ip) Ip=i; else Ipk=Ip;
}

if (f==(pulses-1)){
    /*PRINTING INPUT POWER AND RMS CURRENT
    OF SWITCH*/
    P_in   = (qi * ve)/(2*thm*deg*pulses);
    Isw_rms = sqrt(ri/(2*thm*deg*pulses));
}

while( th < thf + 2*f*thm )          /*4TH LOOP; AFTER COMMUTATION AND DURING
    FALLING L*/
{ y += 1;
  if ( i < Isat ) { z=1; c=1.0;}
                  else { z=0; c=Isat/i;}
  if ( i <= 0 ) i=0;
  L =(Lmin + (k*La*deg*(th-2*f*thm-thr-thm2+thm1-2*(y-1)*dth)))*scale;
  if(prt1==1){
    printf("%.3E\t%.4f\n", L, i );
  }
}

```



```

    steps += 1;
    dith = (-vo + i*speed*rpm*La*k*c - i*(rw+rd))/
(speed*rpm*(z*La*k*deg*(th-2*f*thm-thr-thm2+thm1-2*(y-1)*dth)+Lmin));
    i += dith*dth*deg;
    qt += i*dth*deg;
    r += i*i*dth*deg;
    th += dth;

    if (i >= Ip) Ip=i; else Ipk=Ip;
}

```

```

z=0;
while ( i > 0 )                                /*FIFTH LOOP*/
{ if ( th > ( thr + 2*thm + 2*f*thm ))
    { if ( i > Isat ){ z=1; c=Isat/i;}
      else { z=1;}
    }
    if ( th > thd + 2*thm + 2*f*thm ) break;
    L =(Lmin + (z*La*k*deg*(th-2*f*thm-thr-2*thm)))*scale;
    if(prt1==1){
        printf("%.3E\t%.4f\n", L, i );
    }
    steps+= 1;
    dith = (-vo - i*(rw+rd) - i*speed*rpm*La*k*c*z) /
(speed*rpm*(z*La*k*deg*(th-2*f*thm-thr-2*thm)+Lmin));
    i += dith*dth*deg;
    qt += i*dth*deg;
    r += i*i*dth*deg;
    th += dth;

    if (i >= Ip) Ip=i; else Ipk=Ip;
}

```

```

if ( f == (pulses-1)){
    I_out  = (m*qt)/(2*thm*deg*pulses);
    P_out  = (qt*vo)/(2*thm*deg*pulses);
    P_gen  = m*(P_out - P_in);
    IL_rms = sqrt(r/(2*thm*deg*pulses));
    PL_sw  = m*Isw_rms*Isw_rms*rs;
    PL_c   = m*IL_rms*IL_rms*rw;
    PL_d   = I_out*0.7;
    eff    = P_gen/(P_gen + PL_sw + PL_c + PL_d);
    if (thc > thm)
        {a=1; b=-1;}
    else {a=0; b=1;}
    PSI    = (Ipk*Lmin) + ( La*Isat*k*deg*(2*thm*a+thc*b-thr));
}

```



```

Bpk    = PSI / (N_phase * A);
    }

thd = thd + 2*thm;
if ((f==0)&&(prt2==1)){
    if ( i > 0.1 ){ cont=1;
        printf("Continuous Phase Current");
    }
    else {printf("Dis-Continuous Phase Current\t\tI_peak = %.3f Amp", Ipk);}
}

f += 1;
} /*FOR THE WHILE F!=PULSES LOOP*/

f = 0;

if(prt2==1){
    if ( cont==1){
printf("\nI_peak considering %d current pulses is %.3f Amp", pulses, Ipk);
    }
printf("\nStep used for theta = %.3f\t,\tPeak Flux Density Bpk = %.3f",
    dth, Bpk);
    if ( Bpk >= 2*B ){
printf("\nMax Flux Density %.2f is %.2f times Bsat!", Bpk, Bpk/B);
    }
printf("\nNumber of Phase Current Pulses = %d\tInductance Scale = %d",
    pulses, scale);
printf("\nRotor Speed = %d krpm\tExcitation Ve = %d volts\tO/P Vo = %d volts",
    speed , ve, vo);
printf("\nInput Power per phase = %.3f W\tIsw_rms/phase = %.3f AMP\n"
    , P_in, Isw_rms);
printf("Output Load Power/phase = %.3f W\tIL_rms/phase = %.3f AMP\n"
    , P_out, IL_rms);
printf("\nTotal Power generated = %7.3f W\n", P_gen);
printf("\tEFFICIENCY = %.2f%%\t", eff*100);
printf("\tsteps = %d", steps);
printf("\n*****%c\n");
    }
cont = 0;
run +=1;
} /*FOR THE WHILE RUN <= xruns LOOP*/

f = 0; cont = 0;
set +=1;
} /*FOR THE WHILE SET <= xsets LOOP*/

} /*FOR THE MAIN FUNCTION*/

```



```

/* "INPUT" THIS FILE CONTAINS INPUT DATA FOR SWITCHED
RELUCTANCE GENERATOR*/
/* PROGRAMS USING THIS FILE ARE QUASI.C AND Q.C */
#define pi          3.1415927          /* THE VALUE OF PI */
#define deg         17.453293e-3       /* TO CONVERT DEG TO RAD */
#define rpm         104.71976          /* TO CONVERT RPM TO RAD PER SEC */
#define muo         1.2566371e-6       /* FREE SPACE PERMEABILITY */
#define stator_poles 16
#define rotor_poles  8
#define stator_arc   11.34              /* IN DEGREES */
#define rotor_arc    11.25              /* IN DEGREES */
#define fring_factor 1.4                /* TAKES ACCOUNT OF LEAKAGE FLUX */
#define id          0.04374            /* STATOR INNER DIAMETER - BORE */
#define lc          0.025              /* CORE (AXIAL) LENGTH */
#define B           0.23               /* MAX FLUX DENSITY */
#define g           0.125e-3           /* AIR GAP */
#define L_ratio     6.5                /* INDUCTANCE RATIO L-MAX/L-MIN */
#define N           9.50               /* NO. OF TURNS PER POLE */
#define ve          50                 /* EXCITATION VOLTAGE */
#define vo          50                 /* OUTPUT "SINK" VOLTAGE */
#define rw          0.33               /* PHASE WINDING RESISTANCE */
#define rs          0.2                /* SWITCH ON RESISTANCE */
#define rd          0.0                /* DIODE RESISTANCE */
#define speed       50                 /* ROTOR SPEED IN KRPM */
#define dth         0.05              /* STEP THETA */
#define thdly       16.00              /* DEL ANGLE DEG, START OF SWITCH ON*/
#define thcom       26.00              /* COMMUTATION ANG, SWITCH OFF */
#define oneset      0                  /* SELECT 1 IF ONE SET IS REQUIRED */
#define onerun      0                  /* SELECT 1 IF ONE RUN IS REQUIRED */
#define xsets       7                  /* NO. OF SETS FOR THE SAME TH_ON */
#define xruns       8                  /* NO. OF RUNS FOR THE SAME SET */
#define map_step    2.0                /* THD & THC STEP (DEG) MULTI-RUN */
#define thon_step   2.0                /* TH_ON STEP (DEG) MULTI-SET */
#define pulses      2                  /* NO. OF PULSES PROGRAM TO PRODUCE */
#define scale       12000              /* TO SCALE UP THE L FOR DRAWING */
#define prt         0                  /* TO PRINT ADDITIONAL OUTPUT */
#define prt1        0                  /* SELECT 1 TO PRINT th, L, i OUTPUT */
#define prt2        1                  /* SELECT 1 TO PRINT REQ.OUTPUT ONLY */

```


APPENDIX A3.1

BACKGROUND OF SOFT FERRITES - WITH DATA SHEETS OF THE SELECTED CORE MATERIAL

The story of ferrites began with the search for ferromagnetic materials of unusually high resistivity to obtain reasonably low eddy current losses. There is a practical limit to the thickness to which steel laminations can be satisfactorily manufactured. Eddy current loss is proportional to the square of the frequency for ordinary ferromagnetic materials. Ferrites, having electrical resistivity of up to 10^7 Ohm-metre for some cores as compared to 10^{-7} Ohm-metre for iron [122], reduce the eddy current losses in them to negligible values, even at microwave frequencies.

Ferrites, having mixed metallic oxides of high resistivity, are members of the semiconductor family [122]. Their electrical resistivity, which resembles that of the semiconductors, decreases with increasing temperature. They are made by sintering process where the mixture crystallises into a cubic structure. The resulting ferrite has a hard, black and non-porous ceramic appearance. The cores are moulded from a mixture of metallic oxide powders such that certain iron atoms in the basic cubic crystal are replaced by other metal atoms, such as Mn and Zn, to form manganese-zinc ferrite, or by Ni and Zn to form nickel-zinc ferrite [60]. Manganese-zinc ferrite is the material most commercially available and is used in devices below 1.5 MHz. Nickel-zinc ferrites, on the other hand, are used mainly for filter applications above that frequency.

Various applications of ferrites include use as a core material in flyback transformers, inductor cores (pot cores) in telecommunications,

adjustable air-gap inductors, recording heads, deflection yokes (such as those used in the TV picture tubes), and as magnetic memories and switches at frequencies up to 15 MHz.

The ferrite core ring which was obtained by Philips Components Ltd., in connection with the high speed SRG project, is a one that is originally manufactured for applications of frequencies below 1.5 MHz such as low frequency filter coils in power converters, or in some colour TV receivers. The core is made of the Mn-Zn type. On the other hand, ferrites of the nickel-zinc-iron or nickel-manganese-zinc-iron variety are, for example, used for deflection yoke which consists of wire coils wound to fit around the neck of a TV picture tube. The ferrite cores are moulded so that they can be assembled tightly around these coils. The complete structure slips over the neck of a TV picture tube. In general, the Ni-Zn based ferrites are used at higher frequencies since their resistivity is higher than the Mn-Zn range.

Magnetic permeability μ of ferrites may be as high as 10,000. One of the disadvantages, however, is that the Curie temperature T_c is quite low, in the range of 100-300°C. Saturation flux density is generally below 0.5 Tesla. Ferrite materials are available in a variety of compositions which, through processing, can improve one or two magnetic parameters (high B_{sat} , high μ , low hysteresis loss, high T_c) but at the expense of the other parameters [123]. For example, a high permeability in ferrites can be achieved only at the expense of the useful frequency range [122]. It is also known that the resistivity of Mn-Zn ferrites can be increased by the addition of calcium-oxide, which forms an insulating layer at the grain boundaries. However, this is achieved on expense of decreasing the value of permeability [123]. Therefore, compromise over such properties must be made when ferrite cores are manufactured. This leads to the manufacture

of a wide variety of cores with quite different properties, shapes and sizes to suit particular applications. Even the attempts that were made to produce super-ferrites with outstanding magnetic properties were eventually counterbalanced with the high cost of the manufacturing method and difficulties of handling these mechanically sensitive cores.

The use of soft ferrites in electrical rotating machines is not common. This may be attributed to the following:

- 1- Ferrite cores are not currently produced in large bulk volumes. Therefore, large machines are not yet a suitable application for soft ferrites.
- 2- Low values of B_{sat} , typically below 0.5 Tesla. This reduces the machine output. Moreover, the value of B_{sat} will drop much further at higher temperatures as given in the data sheets in this Appendix.
- 3- Machining may be needed for small machines in particular and usually with stringent tolerances. Since ferrite cores are known to be brittle, their machining is expected to be difficult and expensive. Nevertheless, machining cost may sometimes be offset by the low cost of the core production itself.

However, ferrites have been successfully used [124] in secondary applications in rotating machinery such as magnetic wedges (a high permeability material inserted to bridge slot openings in stator slots of ac machines). These are used to reduce pulsation losses in the teeth. Although efficiency improvement was realised in this application, it was limited due to the low B_{sat} value of ferrites. Nevertheless, in some specialised

applications, ferrites can prove quite useful especially if the required core can be manufactured according to specifications including the required cross section with the specified tolerances. The low production cost and the high resistivity are the main advantages in using ferrite cores in high speed small machines.

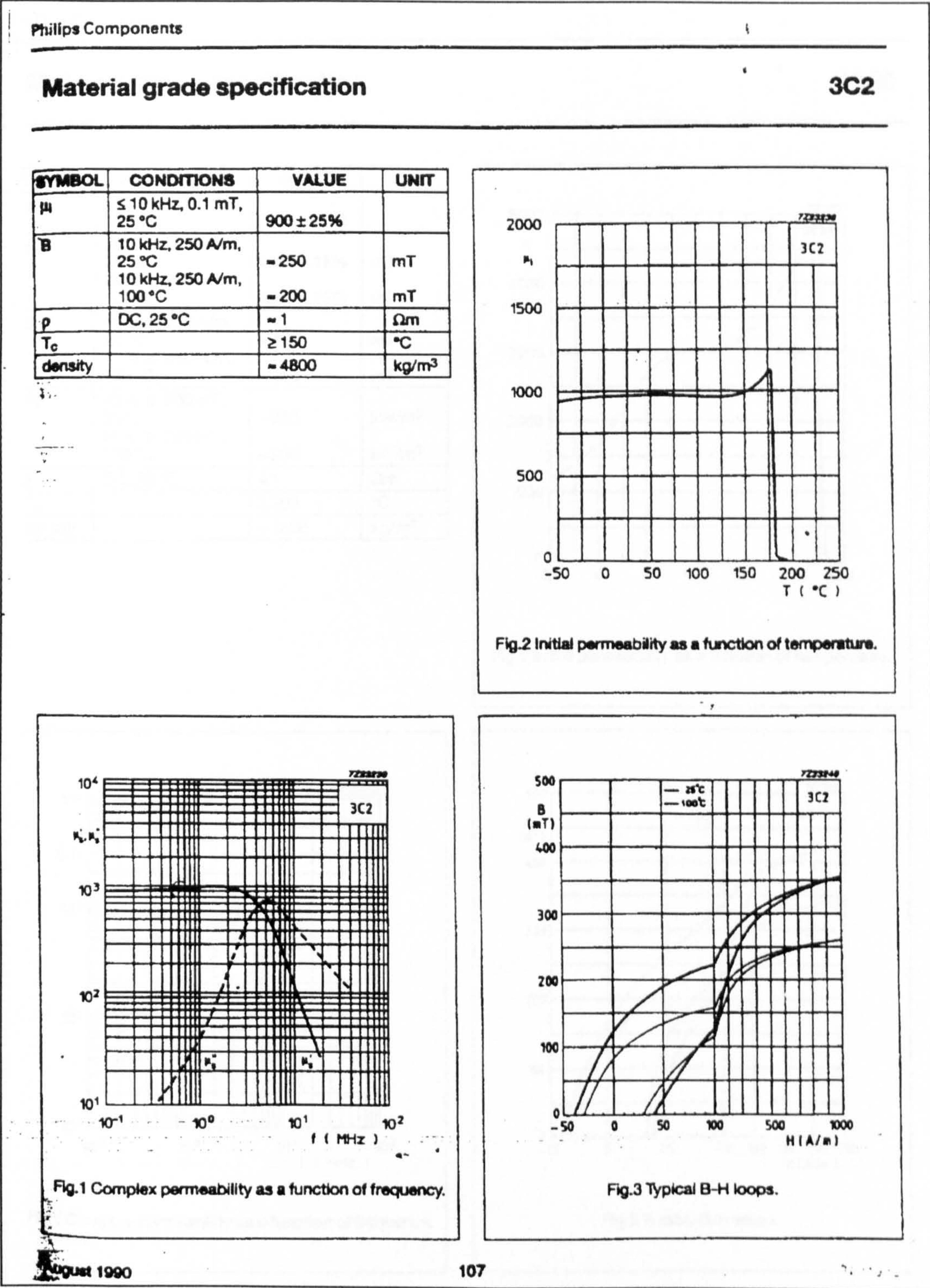


Figure A3.1(a): Manufacturer’s Data sheets for the material of the selected ferrite core.

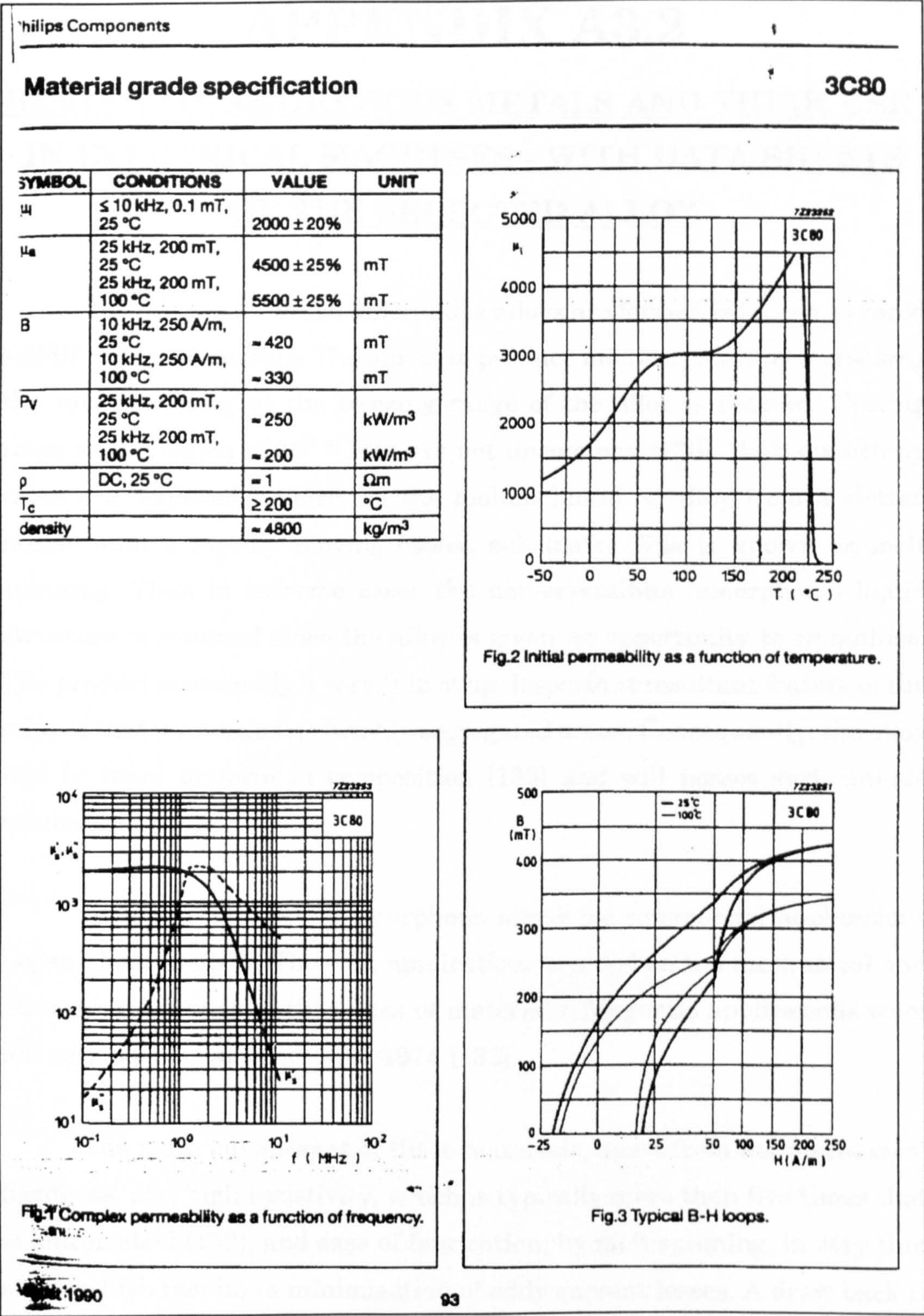


Figure A3.1(b): Manufacturer’s Data sheets for a higher grade core material.

APPENDIX A3.2

REVIEW OF AMORPHOUS METALS AND THEIR USE IN ELECTRICAL MACHINES - WITH DATA SHEETS OF THE SELECTED ALLOY

The process by which amorphous alloys are formed is known as rapid solidification processing. The aim is to produce micro-crystals by increasing the rate of cooling as the freezing range of the alloy is reached. Cooling rates in the region of 10^6 °C/sec are not uncommon [130]. High quenching rates are achieved by ejecting the molten metal or alloy from a slotted nozzle onto a rapidly moving cooled substrate. This is known as melt spinning. Thus in extreme cases the non-crystalline (amorphous) liquid structure is retained since the alloy is given no opportunity to crystallise. The product is normally a very thin strip. Important resultant feature of the alloy is that it contains no heavily segregated areas. Consequently, the alloy will be more uniform in composition [130] and will possess such unique mechanical properties.

Attempts to develop amorphous alloys for commercial applications began about in 1971. The first applications centred on the mechanical and strength properties of this class of materials. Magnetic applications were not seriously considered until 1974 [132].

The main advantages of these materials, apart from the mechanical hardness, are; high resistivity, which is typically more than five times that of silicon steel [132], and ease of fabrication, by melt spinning, in very thin strips which results in minimisation of eddy current losses. A draw back is their lower B_{sat} value compared with silicon steel [133]. Attempts are still

being made on improving the magnetic properties of these materials and some alloys were reported achieving B_{sat} values of up to 1.5 tesla from the METGLAS™ range [129]. Despite the relatively lower flux density, it is believed that there are genuine prospects of worthwhile savings [131],[132],[133]. These savings stem from the fact that core losses in amorphous alloys are estimated at about 25% of losses in silicon steel. Also, since the production method of amorphous alloys involves only one step from the melt to the finished strip, the production costs are projected to be considerably lower than those of silicon steel laminations [132].

Applications of amorphous alloys include transformers, motors and inductors. Most of the activities of applying amorphous alloys to electrical machines were directed at their implementation in fractional horse power machines [131]. The prime reason for this was that the available strip width from which amorphous laminations were cut was limited to approximately 3 cm. The strip width was later increased to 5 cm [134], still it could only grant their application to small machines. Efforts in developing these are now centred on improving their magnetic properties and producing thinner strips. Strips as thin as 3 μm now exist and claimed to offer core losses as low as 40% of those of Mn-Zn ferrites at 1 MHz [135]. However, the width of the strip in this case is only 5 mm making them suitable for making toroidal cores rather than laminations of machine cores.

Larger stator cores than the available strip width does not prevent constructing stators having for example OD of 100 mm from amorphous alloys. In this case, appropriate segment shape is selected and for each lamination two segments of 180° or four of 90° etc. can be cut, stacked and bonded together to form the required stator core. In [131] six segments of 60° of the stator core were chemically etched, fabricated to the required

stack, annealed and bonded.

A super high speed reluctance motor reported in [137] was built using amorphous metal for both stator and rotor of the small motor. The motor OD was 50 mm enabling to use the 50 mm strip to cut the laminations using photo-etching. No heat treatment was necessary for the laminations. The results of [137] showed that the at a maximum speed of 48,000 rpm, core losses in the amorphous-based machine were reduced by a factor of five compared to a silicon-iron based machine.

Despite the success which was reported in the literature in connection with using amorphous metals in electric machines, there are some difficulties in implementing these metals to a wider use in electric machines. First of all, the thin extremely hard strips are not easily stamped into laminations. Further, the stress sensitivity of high induction (B_{sat}) alloys and the lower stacking factor (typically 0.8-0.85 as compared to 0.97 for silicon-iron) of these thin strips also make them more difficult use in conventional methods for manufacturing of motors. Still, the potential energy savings justify attempts to overcome these difficulties [132]. Some of these difficulties have actually been overcome and more improvements are envisaged [134].

Tabelle 1 Physikalische und mechanische Eigenschaften (typische Werte) Table 1 Physical and mechanical properties (typical values)							
Werkstoff	Alloy		6025	6030	6150	7505	4040
Dichte	Density	g/cm³	7,70	7,75	7,84	7,07	7,40
Spez. elektrischer Widerstand	Electrical resistivity	Ω mm²/m	1,35	1,3	1,15	1,35	1,35
TK des Widerstandes (20 °C – 200 °C)	TC of resistivity (20 °C – 200 °C)	10⁻⁴/K	1	0,8	2,1	1,5	2,3
Thermische Dehnung	Thermal expansion	10⁻⁴/K	120	120	120	80	120
Vickershärte	Vickers hardness	HV₀₅	800–1.000				
Kristallisations-temperatur	Cristallization temperature	°C	540	480	415	540	450
Obere Anwendungs-temperatur	Upper application temperature	°C	80 – 100	120	80 – 120	120 – 150	80 – 150
Max. Banddicke	Max. strip thickness	mm	0,03	0,03	0,03	0,03	0,04

Tabelle 2 Magnetische Eigenschaften (typische Werte) Table 2 Magnetic properties (typical values)							
Werkstoff	Alloy		6025	6030	6150	7505	4040
Allgemeine Werkstoffangaben / General material data							
WeSENTliche Bestandteile neben Metalliden	Main constituents besides metalloids		Co	Co	Co	Fe	Fe, Ni
Sättigungsinduktion	Saturation flux density	B _s [T]	0,55	0,82	1,0	1,45	0,8
Curietemperatur	Curietemperature	T [°C]	210	365	485	430	260
Sättigungsmagneto-striktion	Saturation magnetostriction	10⁻⁶	< 0,2	< 0,2	< 0,2	24	8
Bandkerne mit Z-Schleife / Strip-wound cores with Z-loop (high remanence)							
			6025 Z	6030 Z	6150 Z	7505 Z	
Statische Koerzitivfeldstärke	DC coercivity	H _c [mA/cm]	3	8	10	30	
Remanenzverhältnis	Remanence ratio	Br/Bs	0,9	0,95	0,95	0,85	
Verluste (100 kHz, 0,3T)	Core losses (100 kHz, 0,3T)	P _{Fe} [W/kg]	120	600	1200	850	
Bandkerne mit F-Schleife / Strip-wound cores with F-loop (low remanence)							
			6025 F	6030 F	6150 F	7505 F	
Nutzbarer unipolarer Induktionshub	Effective unipolar flux density swing	B _{max} [T]	0,4	0,7	0,9	1,1	
Max. Impulspere-meabilität	Max. pulse permeability	μ _{p max}	70.000 – 100.000	2.500 – 3.500	1.100 – 3.000	4.000 – 8.000	
Verluste (100 kHz, 0,3T)	Core losses (100 kHz, 0,3T)	P _{Fe} [W/kg]	100	110	130	150	

Figure A3.2(a): Mechanical and general material properties for several amorphous alloys. Note the selected alloy is 6025.

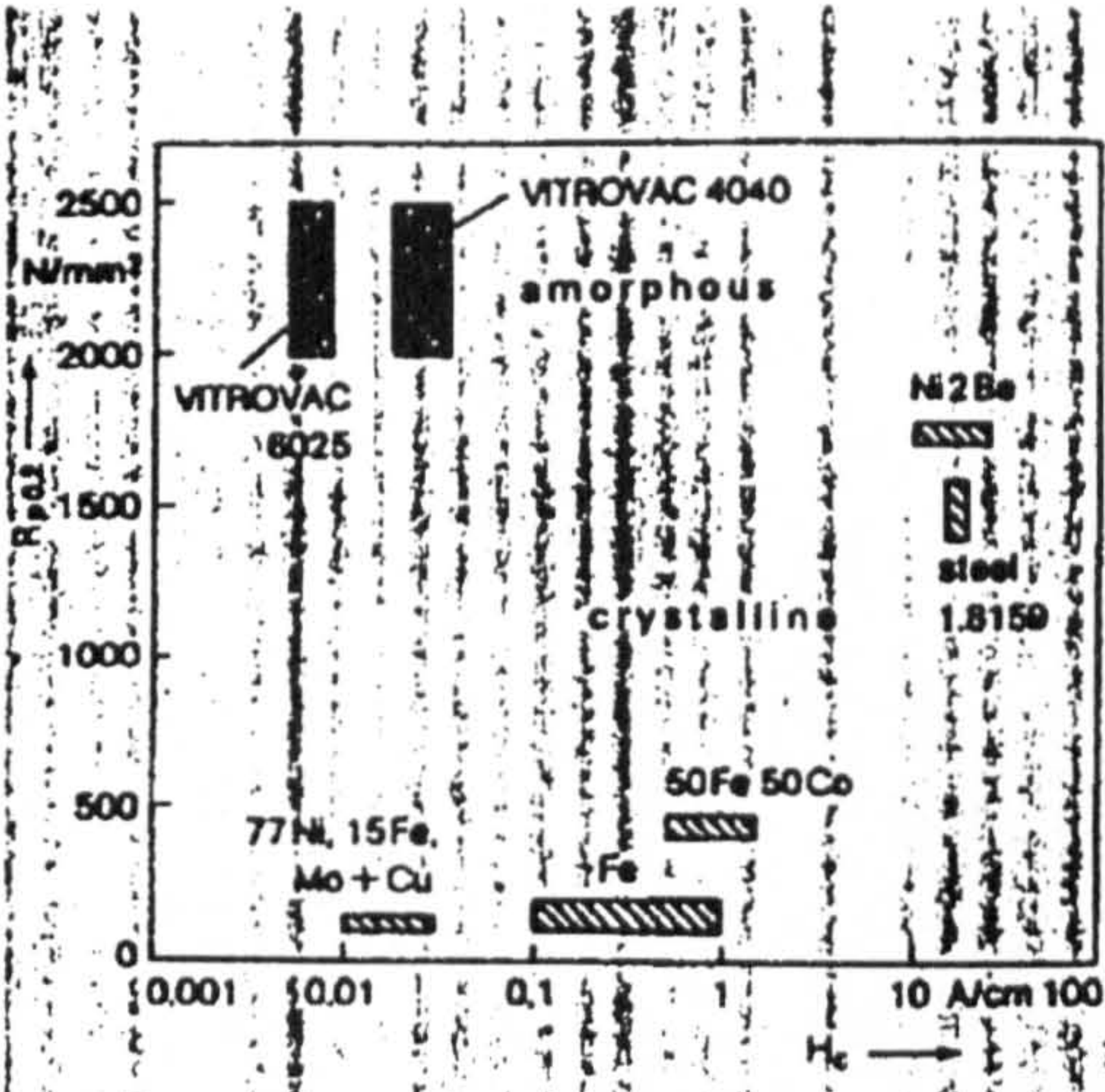


Fig. 4: Yield strength $R_{p0.2}$ and coercivity H_c of amorphous and crystalline materials (values without heat-treatment)

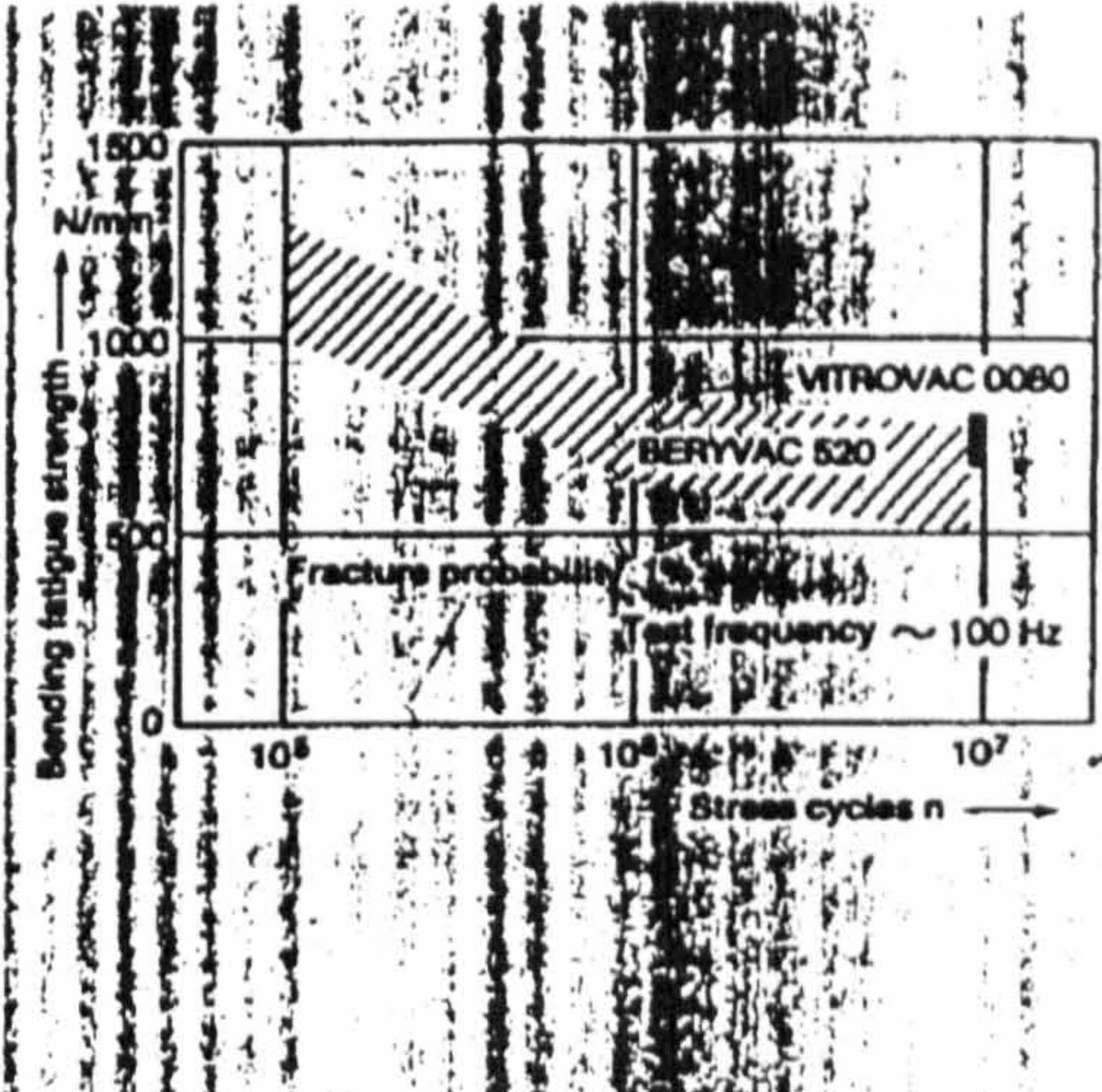


Fig. 5: Bending fatigue strength (Wöhler-curves) of a crystalline spring material (BERYVAC® 520), in comparison with VITROVAC 0080. The areas apply to different material states.

Table 2 Physical and Mechanical Properties (typical values)

Material		VITROVAC 7505	VITROVAC 4040	VITROVAC 6025	VITROVAC 0080
Density	g/cm³	7.1	7.4	7.7	8.0
Electrical resistivity	Ω mm²/m	1.3	1.35	1.35	0.9
TC of el. resistivity (20–200°C)	10⁻⁴/K	2	2.3	1–2	1.2
Thermal expansion	10⁻⁷/K	80	120	125	130
Vickers hardness	HV₀₂	950	800	1000	850
Modulus of elasticity	kN/mm²	ca. 150	ca. 150	ca. 150	ca. 150
Yield strength, tensile strength *)	N/mm²	–	1500–2000	1500–2000	1500–2000
Bending fatigue strength (10⁷ stress cycles)	N/mm²	–	± 700	± 700	± 800
Crystallization temperature	°C	500	450	500	450
Upper application temperature	°C	120	120	80	ca. 200
Max. strip thickness	mm	0.04	0.04	0.05	0.06

The properties apply to the state on production without additional heat treatment.

*) Unlike crystalline materials amorphous alloys do not work-harden; it follows that the yield strength and tensile strength are almost identical.

Figure A3.2(b): More properties of the Vitrovac range of amorphous alloys.

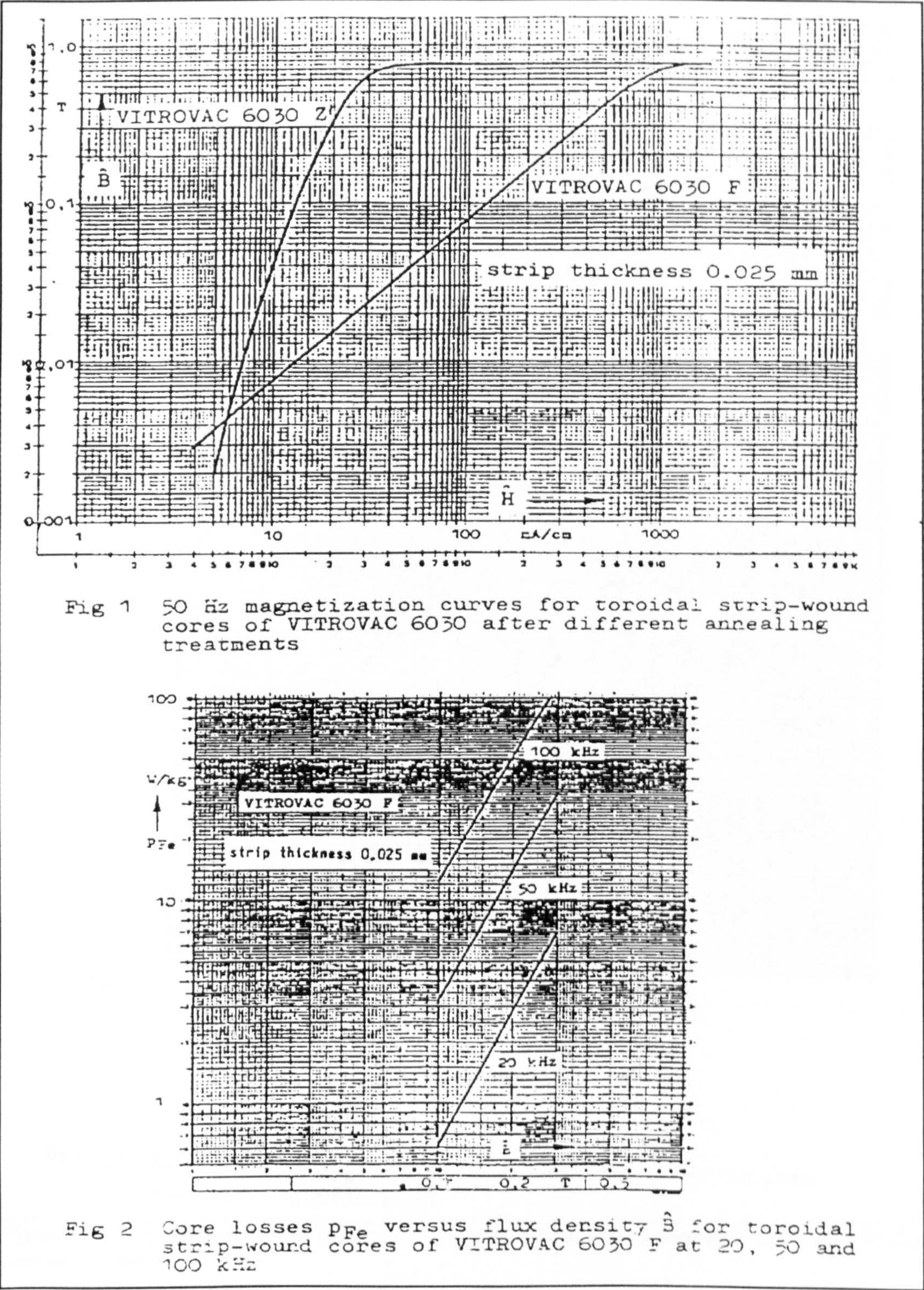


Figure A3.3(a): B/H characteristics and Core losses for a toroidal core for a similar alloy to the 6025.

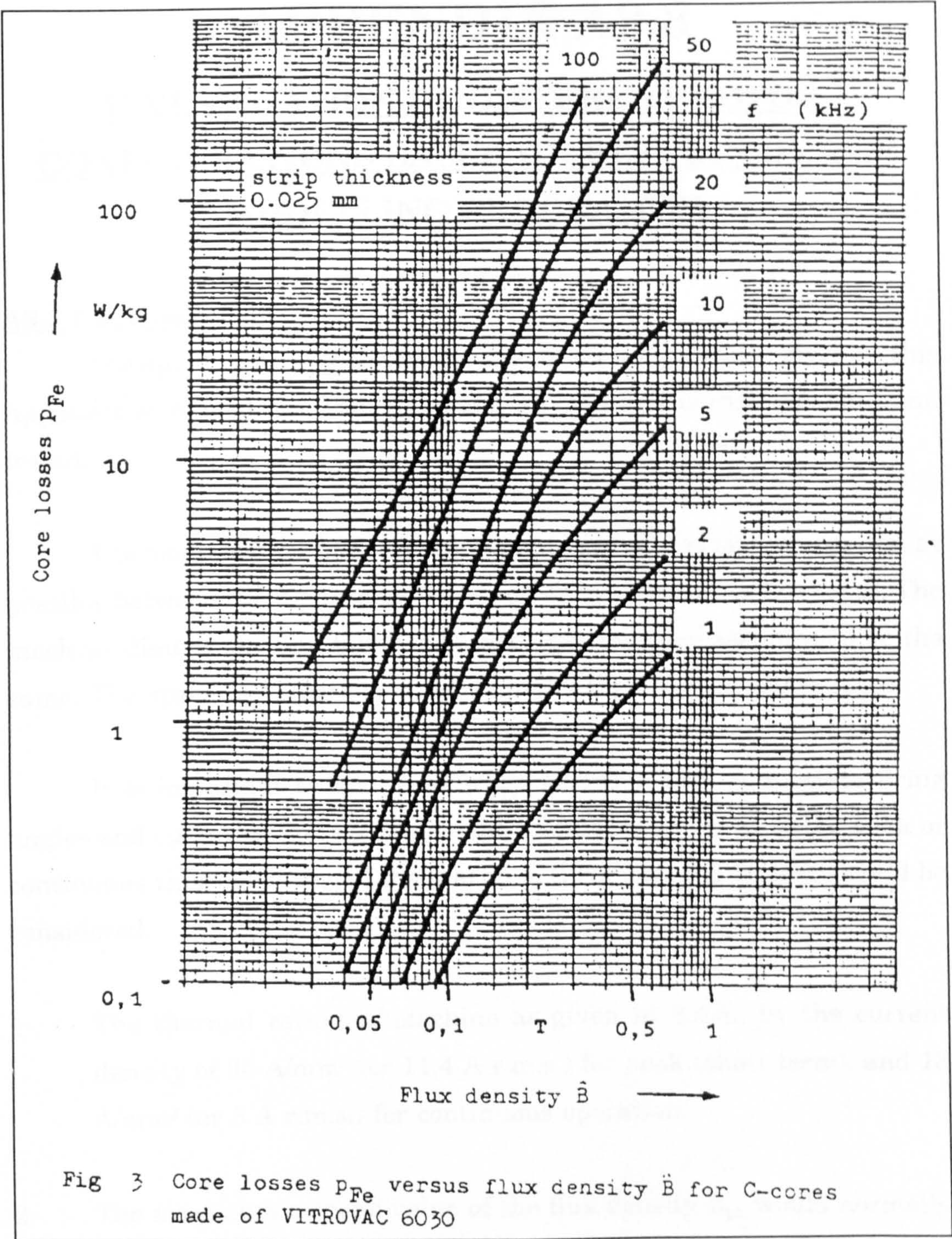


Figure A3.3(b): Core losses for C-cores made of a similar amorphous alloy to the one selected.

APPENDIX A3.3

INVESTIGATION OF DIFFERENT ROTOR CONFIGURATIONS BASED ON RESULTS OF THE MODELLING PROGRAMME

A3.3.1 Introduction

The specifications of the two alternative configurations given in this Appendix were modified from those of the 2-phase SRG that was built and tested.

The modifications of these cases aim to provide as fair comparison as possible between the 2-phase machine and each of the other two cases. The machine dimensions and number of turns per pole are assumed to be the same. The speed of operations is set at 50,000 rpm for the three cases.

It is important to note that when selecting the appropriate firing angles and operating voltage to give the maximum power at either peak or continuous thermal rating of the machine, three limiting factors should be considered:

- 1- The thermal rating of machine as given in 3.4.5., by the current density of 30 A/mm² (or 11.4 A r.m.s.) for peak (short term), and 13 A/mm² (or 5 A r.m.s.) for continuous operation.
- 2- The maximum or peak value of the flux density B_{pk} would normally be higher than B_{sat} value as the poles of the stator are normally driven into heavy saturation, but would not in practice exceed more than $2B_{sat}$. In the model solution, there can only be a warning line in

the output of the programme to state that this figure has exceeded the reasonable limit of the magnetic material.

- 3- The case of continuous phase current should be avoided. Considering this phase of operation was regarded beyond the scope of the project.

The maximum power case is determined after selecting the appropriate voltage and set of firing angles and upon reaching one or more of the above limitations.

A3.3.2 The Reference Case of 16/8 Stator-Rotor Poles, 2-Phase SRG

The specifications of the 2-phase machine case were given in Table 3.1 and explained in 3.5. More results of the model predictions are given in Table 3.2 and are detailed in Appendix A3.4.

(A) Machine Specifications

stator poles = 16 rotor poles = 8 no. of phases m = 2
 stator arc = 11.340 rotor arc = 11.250 Fringing factor = 1.400
 Important Values of theta in (deg) which define L profile are :
 thm = 22.500, the = 8.004, thf = 36.996
 thm1 = 22.455, thm2 = 22.545

stator inner dia id = 4.374E-02 m core (axial) length = 2.500E-02 m
 Sat flux density B = 0.230 Tesla Air gap g = 1.250E-04 m
 Inductance ratio = 6.500 no. of turns N = 9.5

A = 1.082129E-04 sqm, Isat = 2.408266 Amp,
 La = 7.854459E-04 H, Lmin = 1.428083E-04 H , k = 3.965

(B) The Operating Conditions and The Solution

Switching Angles: Theta_dly = 8.00 , Theta_com = 32.00 ** Theta_on = 24.00
 Dis-Continuous Phase Current I_peak = 21.576 Amp
 Step used for theta = 0.050 , Peak Flux Density Bpk = 0.456
 Number of Phase Current Pulses = 2 Inductance Scale = 15000
 Rotor Speed = 50 krpm Excitation Ve = 50 volts O/P Vo = 50 volts
 Input Power per phase = 168.409 W Isw_rms/phase = 6.443 AMP
 Output Load Power/phase = 281.464 W IL_rms/phase = 11.475 AMP

Total Power generated = 226.111 W
 EFFICIENCY = 67.00% steps = 1958

(C) The Phase Current Waveform

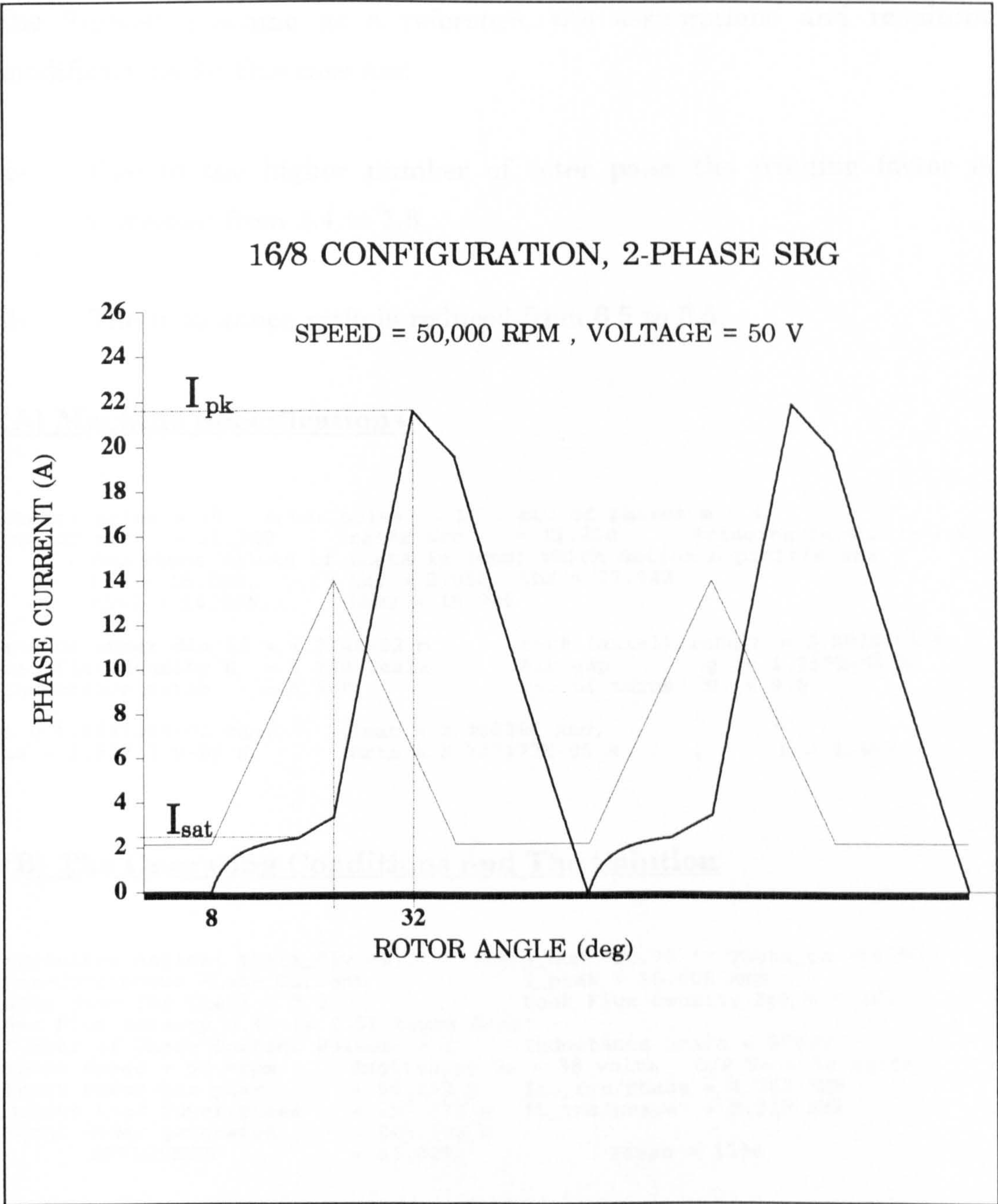


Figure A3.4: Model result: Phase current of the 2-phase SRG at 50,000 rpm, 50 V.

A3.3.3 The Case of The 16/12 Stator-Rotor Poles, 4-Phase SRG

The reasons for studying this case were given in chapter 3. Taking the 2-phase machine as a reference, the assumptions and resultant modifications for this case are:

- 1- Due to the higher number of rotor poles the fringing factor is increased from 1.4 to 1.8.
- 2- The inductance ratio is reduced from 6.5 to 5.5.

(A) Machine Specifications

```

stator poles = 16    rotor poles = 12    no. of phases m = 4
stator arc    = 11.340    rotor arc    = 11.250    Fringing factor = 1.800
    Important Values of theta in (deg) which define L profile are :
        thm = 15.000,    thr = 2.058,    thf = 27.942
        thm1 = 14.955,    thm2 = 15.045

stator inner dia id = 4.374E-02 m    core (axial) length = 2.500E-02 m
sat flux density B  = 0.230 Tesla    Air gap g = 1.250E-04 m
Inductance ratio    = 5.500    no. of turns N = 9.5

A = 1.082129E-04 sqm,    Isat = 2.408266 Amp,
La = 3.927230E-04 H,    Lmin = 8.727177E-05 H    ,    k = 4.443

```

(B) The Operating Conditions and The Solution

```

Switching Angles: Theta_dly =4.70 , Theta_com =20.70 ** Theta_on =16.00
Dis-Continuous Phase Current    I_peak = 15.606 Amp
Step used for theta = 0.050    ,    Peak Flux Density Bpk = 0.461
Max Flux Density 0.46 is 2.01 times Bsat!
Number of Phase Current Pulses = 2    Inductance Scale = 20000
Rotor Speed = 50 krpm    Excitation Ve = 38 volts    O/P Vo = 38 volts
Input Power per phase    = 96.102 W    Isw_rms/phase = 4.703 AMP
Output Load Power/phase  = 157.379 W    IL_rms/phase  = 8.318 AMP
Total Power generated    = 245.106 W
    EFFICIENCY    = 67.02%    steps = 1296

```


(C) The Phase Current Waveform

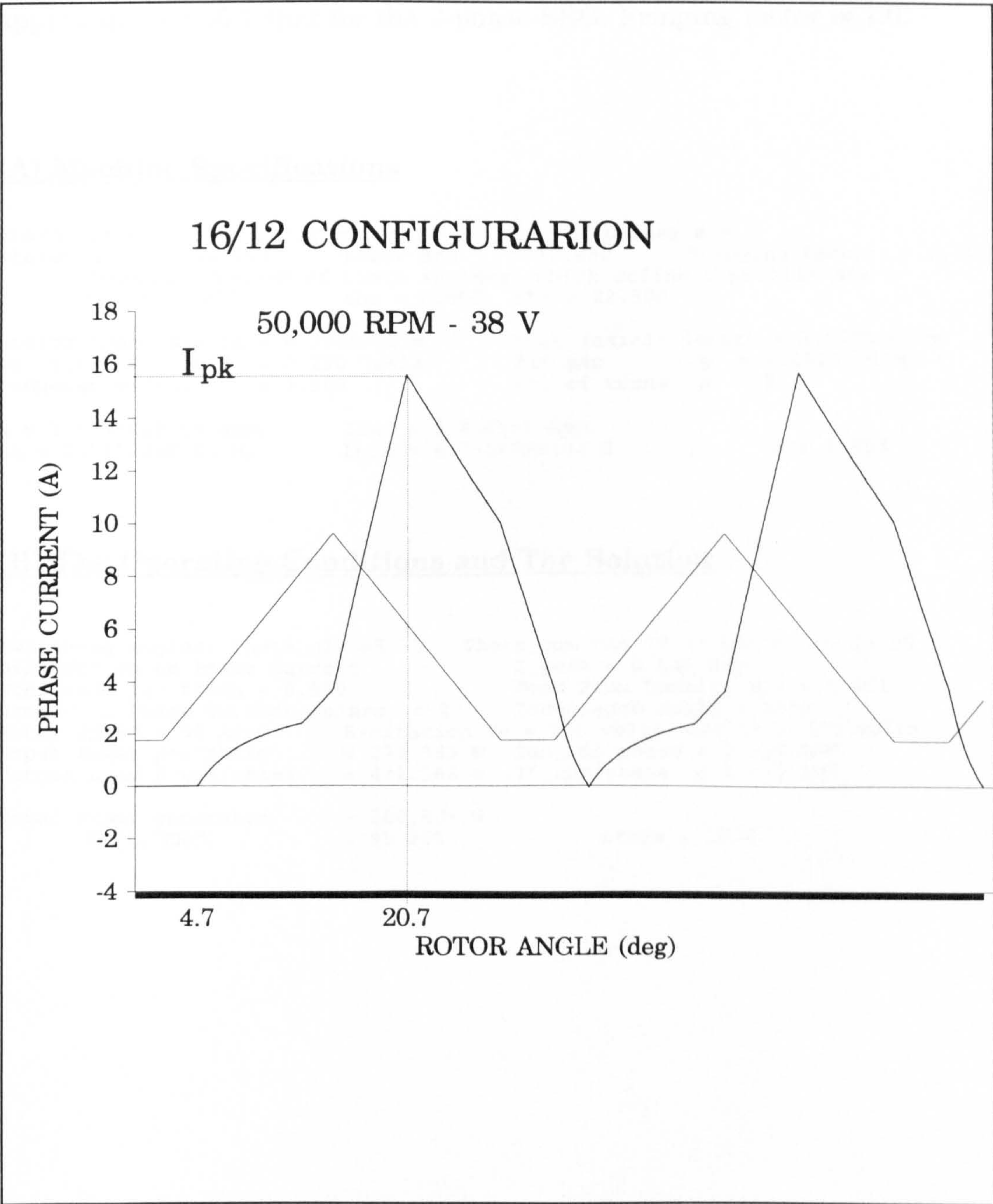


Figure A3.5: Model result: Phase current for the 4-phase SRG at 50,000 rpm and 38 V. $P_{gen} = 245$ watts and Efficiency is 67%.

A3.3.4 The Case of The 16/16 Stator-Rotor Poles, 1-Phase SRG

The assumption is made for this case for the inductance ratio to be approximately 50% that for the 2-phase SRG. Fringing factor is 1.0.

(A) Machine Specifications

stator poles = 16 rotor poles = 16 no. of phases m = 1
stator arc = 11.250 rotor arc = 11.250 Fringing factor = 1.000
Important Values of theta in (deg) which define L profile are :
thm = 11.250, thr = 0.000, thf = 22.500

stator inner dia id = 4.374E-02 m core (axial) length = 2.500E-02 m
sat flux density B = 0.230 Tesla Air gap g = 1.250E-04 m
Inductance ratio = 3.500 no. of turns N = 9.5

A = 1.073541E-04 sqm, Isat = 2.408266 Amp,
La = 1.558424E-03 H, Lmin = 6.233698E-04 H , k = 5.093

(B) The Operating Conditions and The Solution

Switching Angles: Theta_dly =5.70 , Theta_com =16.70 ** Theta_on= 11.00
Dis-Continuous Phase Current I_peak = 8.546 Amp
Step used for theta = 0.050 , Peak Flux Density Bpk = 0.451
Number of Phase Current Pulses = 2 Inductance Scale = 4000
Rotor Speed = 50 krpm Excitation Ve = 200 volts O/P Vo = 200 volts
Input Power per phase = 271.563 W Isw_rms/phase = 2.555 AMP
Output Load Power/phase = 471.968 W IL_rms/phase = 4.610 AMP

Total Power generated = 200.405 W
EFFICIENCY = 95.26% steps = 1020

(C) The Phase Current Waveform

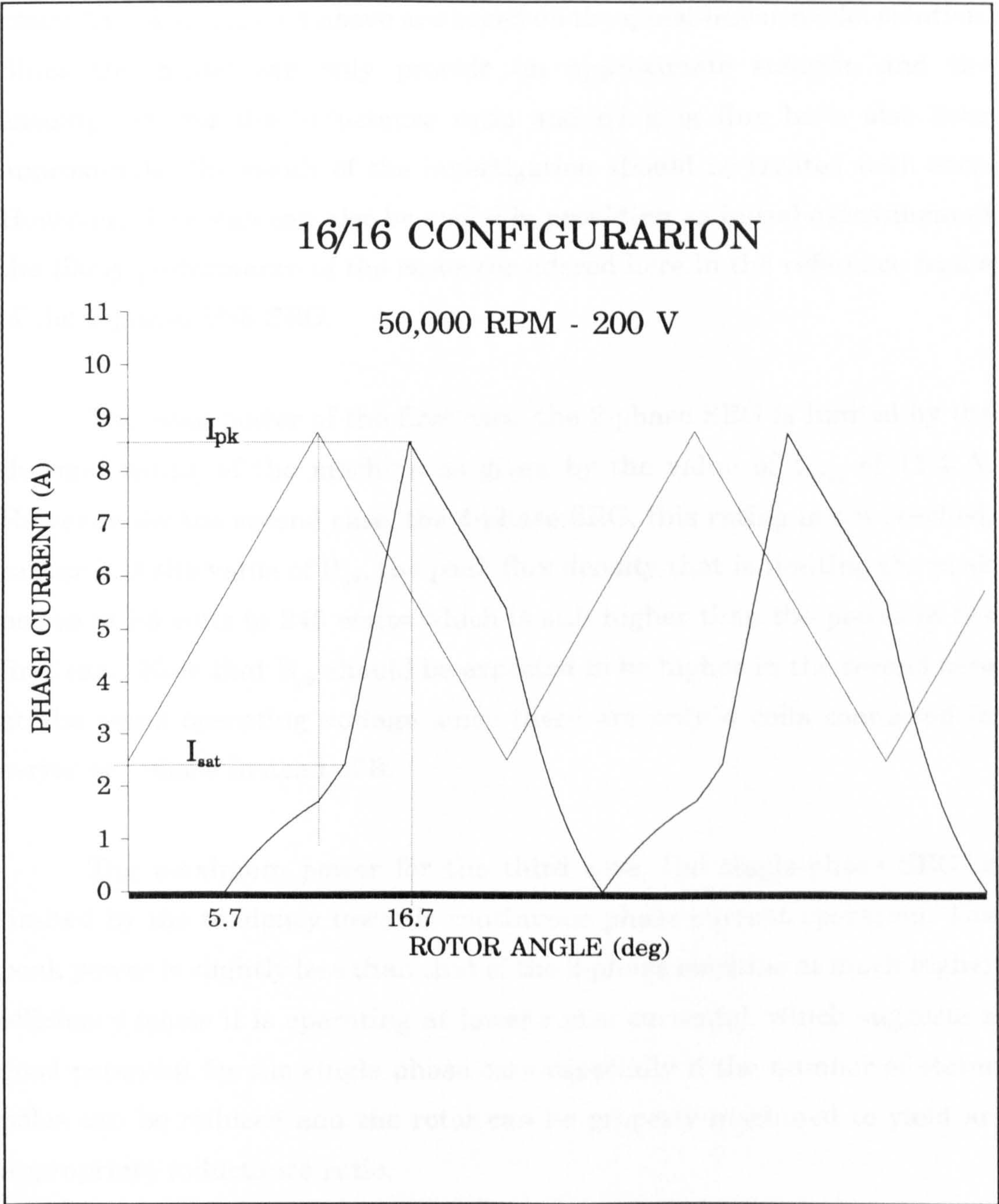


Figure A3.6: Model result: Phase current of the 1-phase SRG at 50,000 rpm and 200 V. $P_{gen} = 200$ watts and Efficiency = 95%.

A3.3.5 Conclusion

The investigation results for the alternative rotor configurations of cases A3.3.3 and A3.3.4 above are based on the quasi-linear model solution. Since the model can only provide an approximate solution and the assumptions for the inductance ratio and fringing flux have also been approximate, the result of the investigation should be treated with care. However, the result can also be useful in providing an initial assessment of the likely performance of the cases considered here in the reference frame of the 2-phase 16/8 SRG.

The peak power of the first case, the 2-phase SRG is limited by the thermal rating of the machine as given by the value of I_{l-rms} of 11.4 A. However, for the second case, the 4-phase SRG, this rating is not reached, rather it is the value of B_{pk} , the peak flux density that is limiting the peak power at 38 volts to 245 watts which is still higher than the power in the first case. Note that B_{pk} should be expected to be higher in the second case at the same operating voltage since there are only 4 coils connected in series per phase instead of 8.

The maximum power for the third case, the single-phase SRG is limited by the tendency towards continuous phase current operation. The peak power is slightly less than that of the 2-phase machine at much higher efficiency (since it is operating at lower r.m.s. currents), which suggests a good potential for the single phase case especially if the number of stator poles can be reduced and the rotor can be properly machined to yield an appropriate inductance ratio.

APPENDIX A3.4

RESULTS OF THE SIMPLE MODELLING
PROGRAMME AT DIFFERENT OPERATING
CONDITIONS

PROGRAMME MAIN SPECIFICATIONS

stator poles = 16 rotor poles = 8 no. of phases m = 2
stator arc = 11.340 rotor arc = 11.250 Fringing factor = 1.400
Important Values of theta in (deg) which define L profile are :
thm = 22.500, thr = 8.004, thf = 36.996
thm1 = 22.455, thm2 = 22.545

stator inner dia id = 4.374E-02 m core (axial) length = 2.500E-02 m
Sat flux density B = 0.230 Tesla Air gap g = 1.250E-04 m
Inductance ratio = 6.500 no. of turns N = 9.5

A = 1.082129E-04 sqm, Isat = 2.408266 Amp,
La = 7.854459E-04 H, Lmin = 1.428083E-04 H , k = 3.965

EXAMPLE OF THE FLAT-TOPPED FULLY-OPENED CURRENT
WAVEFORM GIVEN IN CHAPTER 3

Switching Angles: Theta_dly = 5.30 , Theta_com = 27.80
Dis-Continuous Phase Current I_peak = 10.535 Amp
Number of Phase Current Pulses = 2 Inductance Scale = 15000
Rotor Speed = 50 krpm Excitation Ve = 38 volts O/P Vo = 38 volts
Input Power per phase = 59.516 W Isw_rms/phase = 2.683 AMP
Output Load Power/phase = 126.480 W IL_rms/phase = 6.106 AMP
Total Power generated = 133.927 W
EFFICIENCY = 82.97% steps = 932

CASE 1 , VOLTAGE = 50 VOLTS

Switching Angles: Theta_dly = 8.00 , Theta_com = 32.00 ** Theta_on = 24.00
Dis-Continuous Phase Current I_peak = 21.576 Amp
Step used for theta = 0.050 , Peak Flux Density Bpk = 0.456
Number of Phase Current Pulses = 2 Inductance Scale = 15000
Rotor Speed = 50 krpm Excitation Ve = 50 volts O/P Vo = 50 volts
Input Power per phase = 168.409 W Isw_rms/phase = 6.443 AMP
Output Load Power/phase = 281.464 W IL_rms/phase = 11.475 AMP
Total Power generated = 226.111 W
EFFICIENCY = 67.00% steps = 1958

*****0&

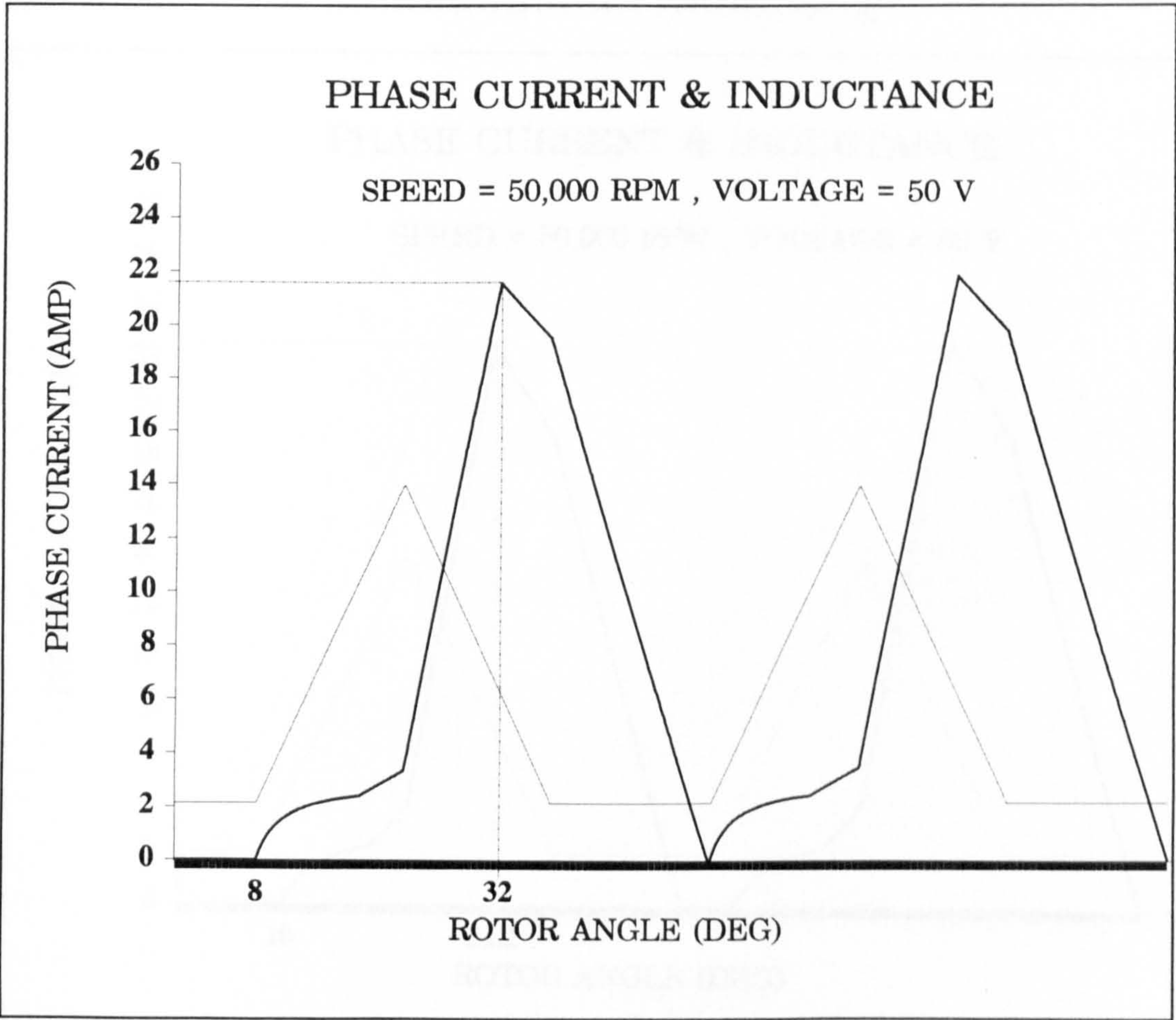


Figure A3.7

CASE 2 , VOLTAGE = 60 VOLTS

Switching Angles: Theta_dly = 10.00 , Theta_com = 31.20 ** Theta_on = 21.20
Dis-Continuous Phase Current I_peak = 22.675 Amp
Step used for theta = 0.050 , Peak Flux Density Bpk = 0.487
Max Flux Density 0.49 is 2.12 times Bsat!
Number of Phase Current Pulses = 2 Inductance Scale = 15000
Rotor Speed = 50 krpm Excitation Ve = 60 volts O/P Vo = 60 volts
Input Power per phase = 192.884 W Isw_rms/phase = 6.531 AMP
Output Load Power/phase = 319.875 W IL_rms/phase = 11.475 AMP
Total Power generated = 253.983 W
EFFICIENCY = 69.51% steps = 1900
*****0l

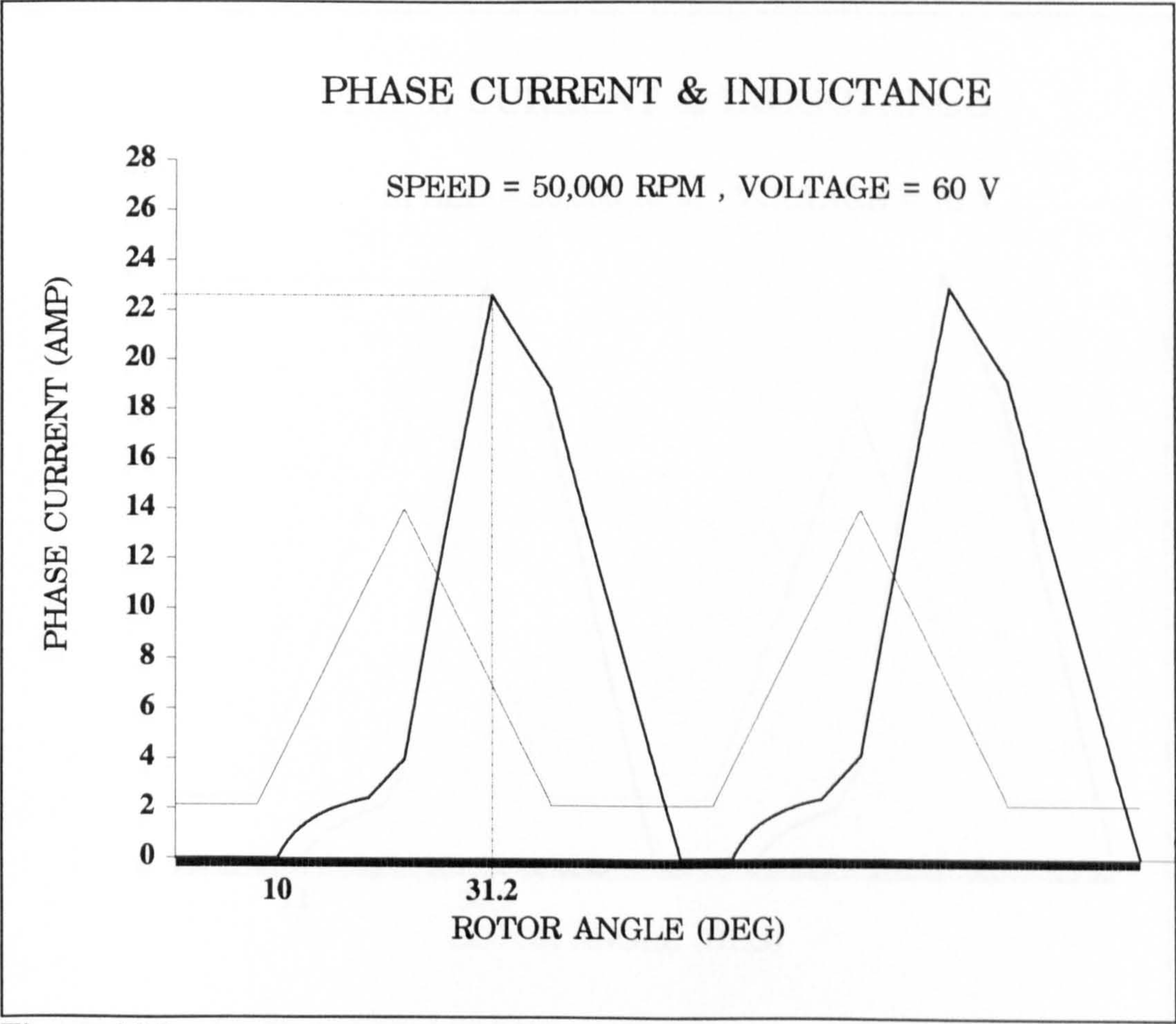


Figure A3.8

CASE 3 , VOLTAGE = 70 VOLTS

Switching Angles: Theta_dly = 12.00 , Theta_com = 30.95 ** Theta_on = 18.95
Dis-Continuous Phase Current I_peak = 23.794 Amp
Step used for theta = 0.050 , Peak Flux Density Bpk = 0.510
Max Flux Density 0.51 is 2.22 times Bsat!
Number of Phase Current Pulses = 2 Inductance Scale = 20000
Rotor Speed = 50 krpm Excitation Ve = 70 volts O/P Vo = 70 volts
Input Power per phase = 215.239 W Isw_rms/phase = 6.641 AMP
Output Load Power/phase = 351.515 W IL_rms/phase = 11.445 AMP
Total Power generated = 272.551 W
EFFICIENCY = 71.04% steps = 1859

*****0C

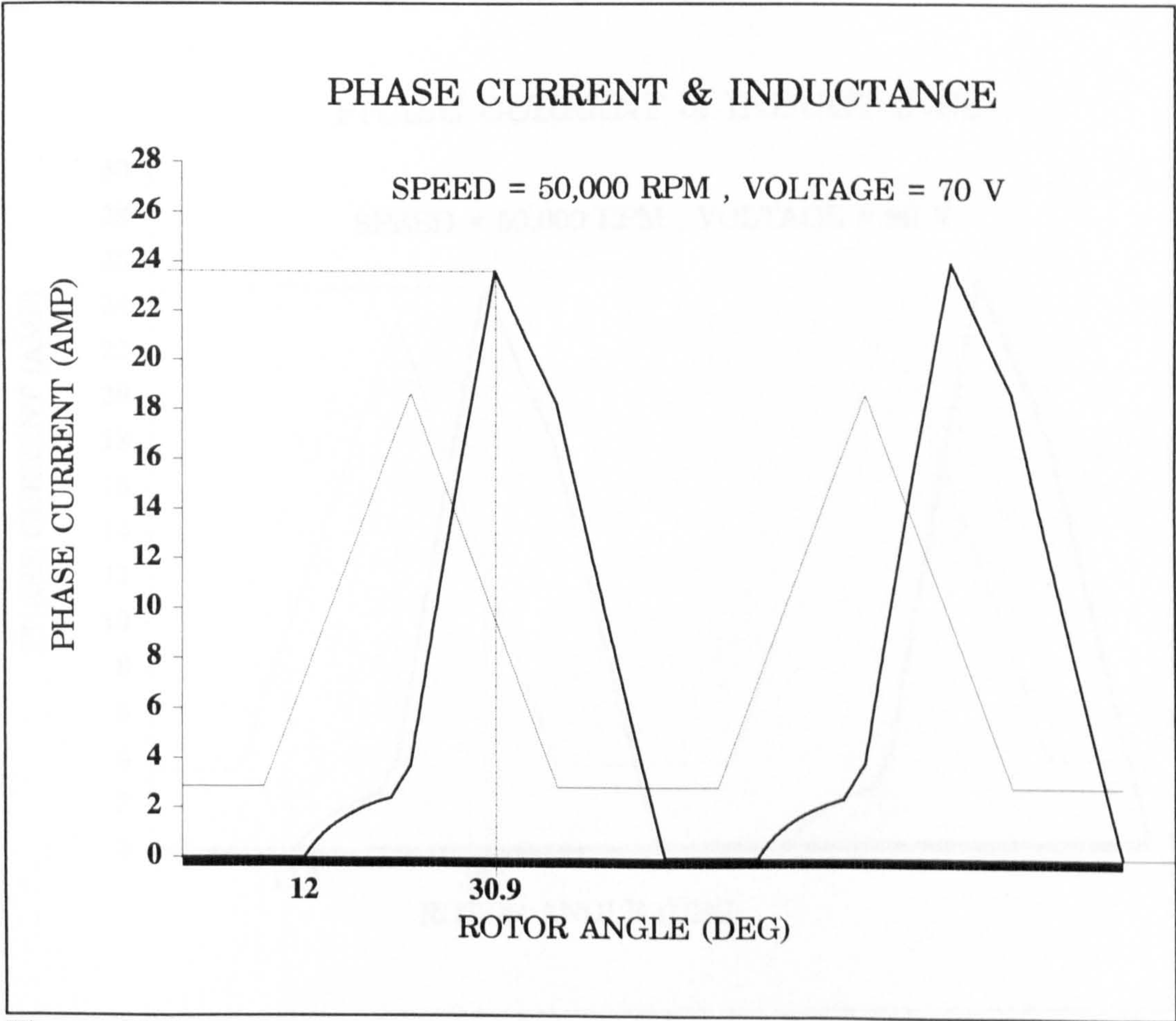


Figure A3.9

CASE 4 , VOLTAGE = 80 VOLTS

Switching Angles: Theta_dly = 13.20 , Theta_com = 30.50 ** Theta_on = 17.30
Dis-Continuous Phase Current I_peak = 24.796 Amp
Step used for theta = 0.050 , Peak Flux Density Bpk = 0.535
Max Flux Density 0.53 is 2.32 times Bsat!
Number of Phase Current Pulses = 2 Inductance Scale = 20000
Rotor Speed = 50 krpm Excitation Ve = 80 volts O/P Vo = 80 volts
Input Power per phase = 239.929 W Isw_rms/phase = 6.736 AMP
Output Load Power/phase = 383.410 W IL_rms/phase = 11.433 AMP
Total Power generated = 286.961 W
EFFICIENCY = 72.08% steps = 1824

*****0

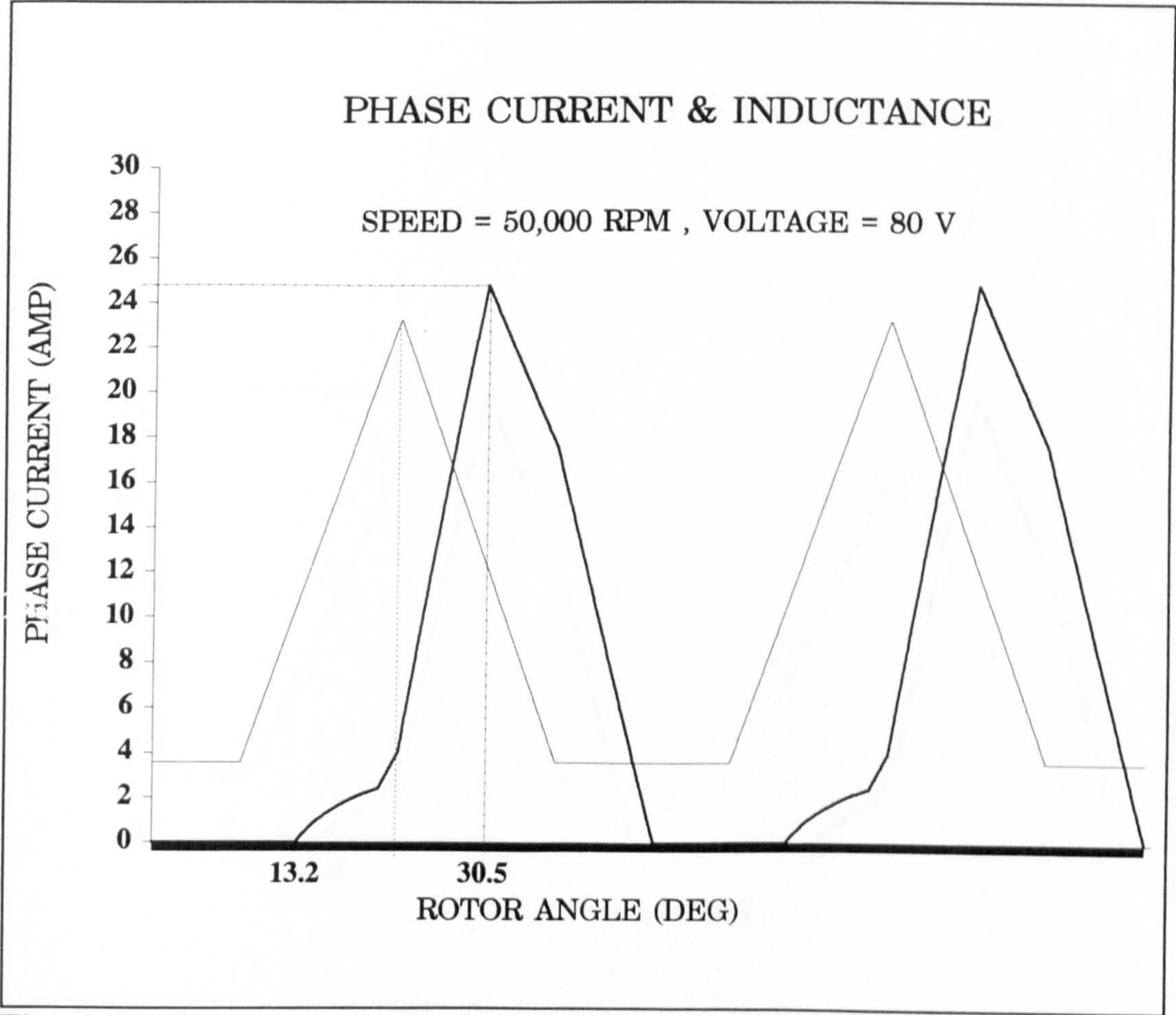


Figure A3.10

CASE 5 , VOLTAGE = 100 VOLTS

Switching Angles: Theta_dly = 14.50 , Theta_com = 29.50 ** Theta_on = 15.00
Dis-Continuous Phase Current I_peak = 26.619 Amp
Step used for theta = 0.050 , Peak Flux Density Bpk = 0.583
Max Flux Density 0.58 is 2.53 times Bsat!
Number of Phase Current Pulses = 2 Inductance Scale = 25000
Rotor Speed = 50 krpm Excitation Ve = 100 volts O/P Vo = 100 volts
Input Power per phase = 292.224 W Isw_rms/phase = 6.916 AMP
Output Load Power/phase = 444.317 W IL_rms/phase = 11.429 AMP
Total Power generated = 304.185 W
EFFICIENCY = 73.16% steps = 1766

*****Of

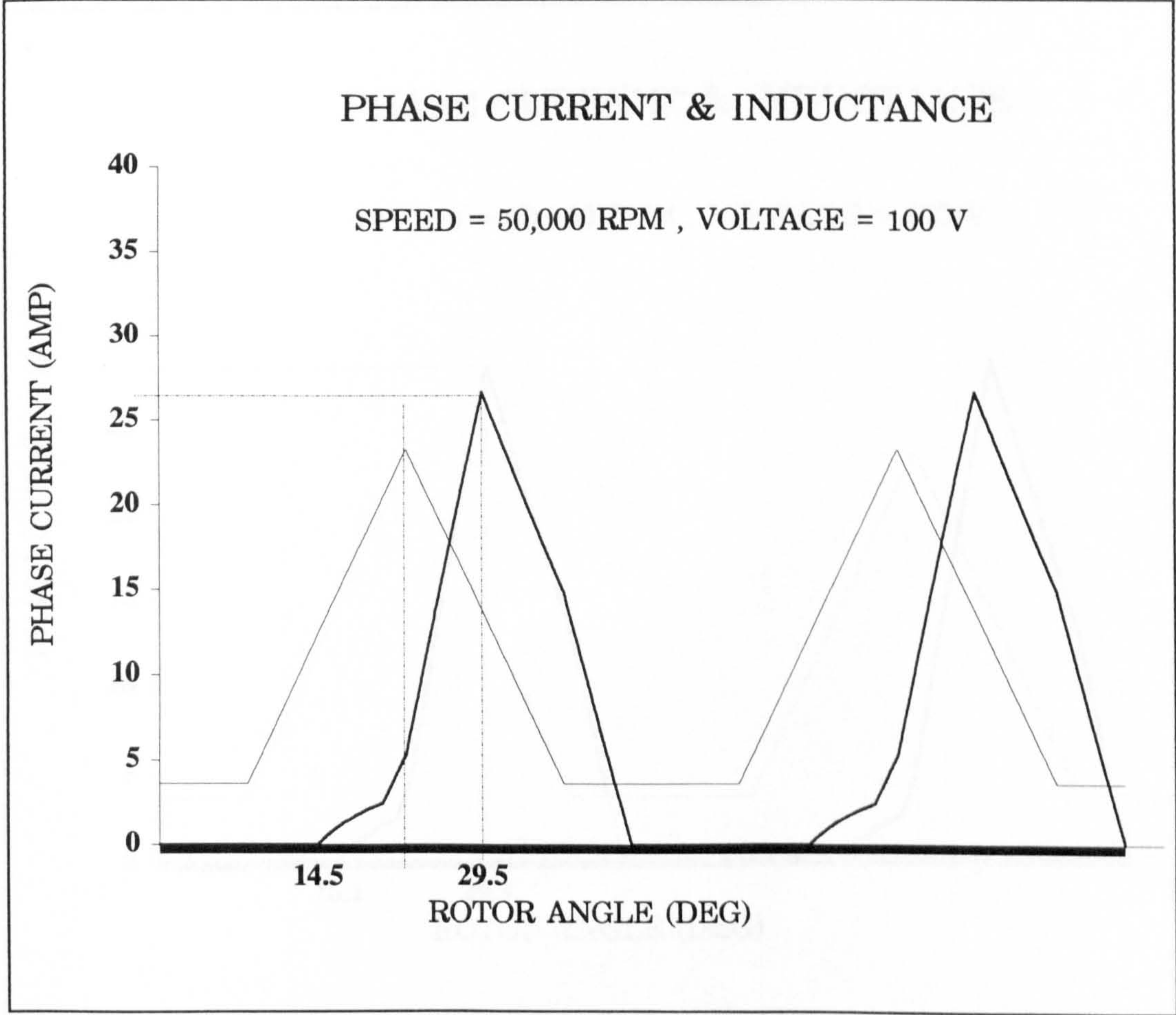


Figure A3.11

CASE 6 , VOLTAGE = 120 VOLTS

Switching Angles: Theta_dly = 16.10 , Theta_com = 29.30 ** Theta_on = 13.20
Dis-Continuous Phase Current I_peak = 28.465 Amp
Step used for theta = 0.050 , Peak Flux Density Bpk = 0.618
Max Flux Density 0.62 is 2.69 times Bsat!
Number of Phase Current Pulses = 2 Inductance Scale = 25000
Rotor Speed = 50 krpm Excitation Ve = 120 volts O/P Vo = 120 volts
Input Power per phase = 340.807 W Isw_rms/phase = 7.111 AMP
Output Load Power/phase = 495.854 W IL_rms/phase = 11.459 AMP
Total Power generated = 310.094 W
EFFICIENCY = 73.35% steps = 1732

*****0D

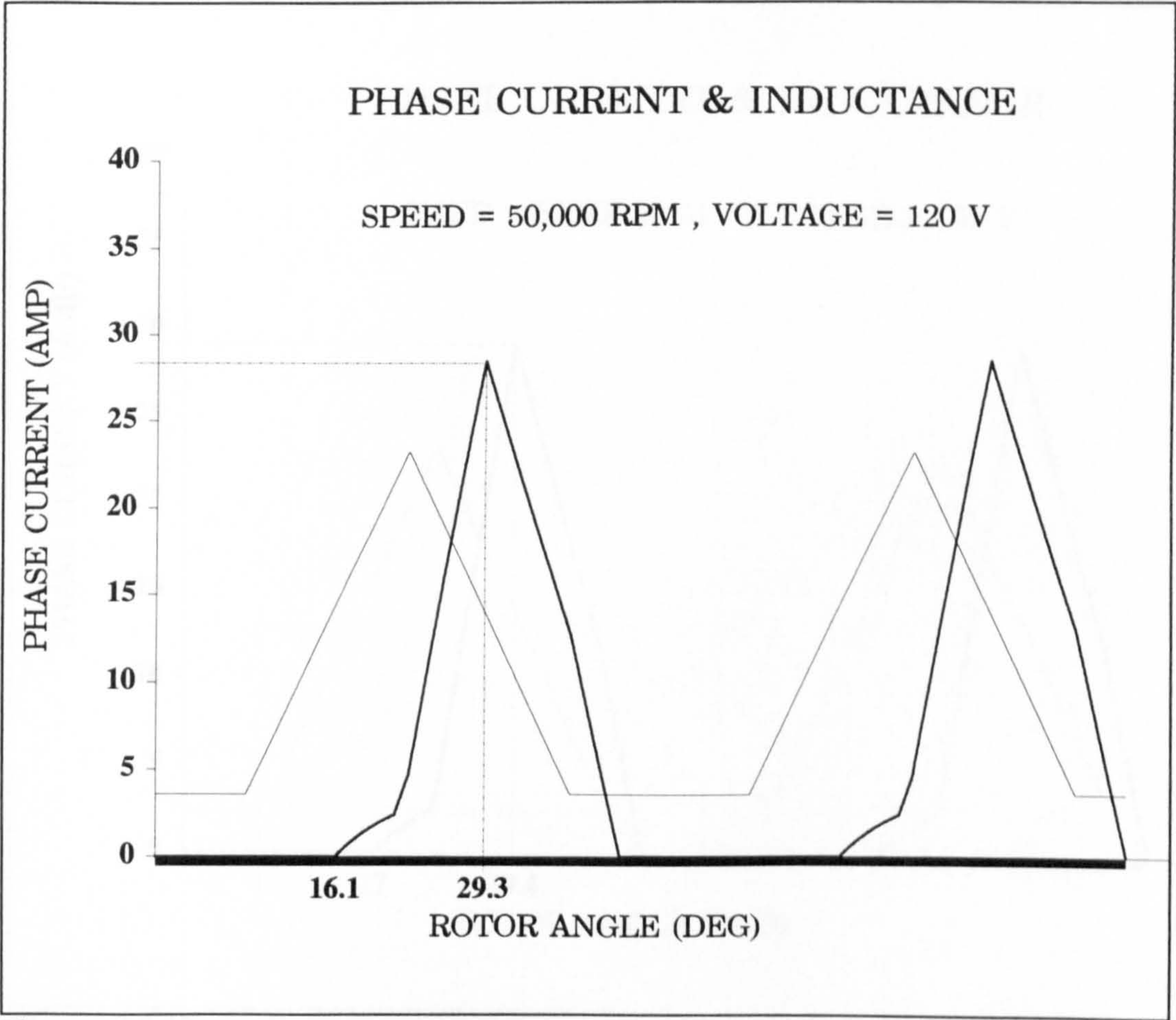


Figure A3.12

CASE 7 , VOLTAGE = 130 VOLTS

Switching Angles: Theta_dly = 17.00 , Theta_com = 29.40 ** Theta_on = 12.40
Dis-Continuous Phase Current I_peak = 29.270 Amp
Step used for theta = 0.050 , Peak Flux Density Bpk = 0.631
Max Flux Density 0.63 is 2.74 times Bsat!
Number of Phase Current Pulses = 2 Inductance Scale = 25000
Rotor Speed = 50 krpm Excitation Ve = 130 volts O/P Vo = 130 volts
Input Power per phase = 362.429 W Isw_rms/phase = 7.173 AMP
Output Load Power/phase = 516.551 W IL_rms/phase = 11.436 AMP
Total Power generated = 308.244 W
EFFICIENCY = 73.27% steps = 1720
*****08

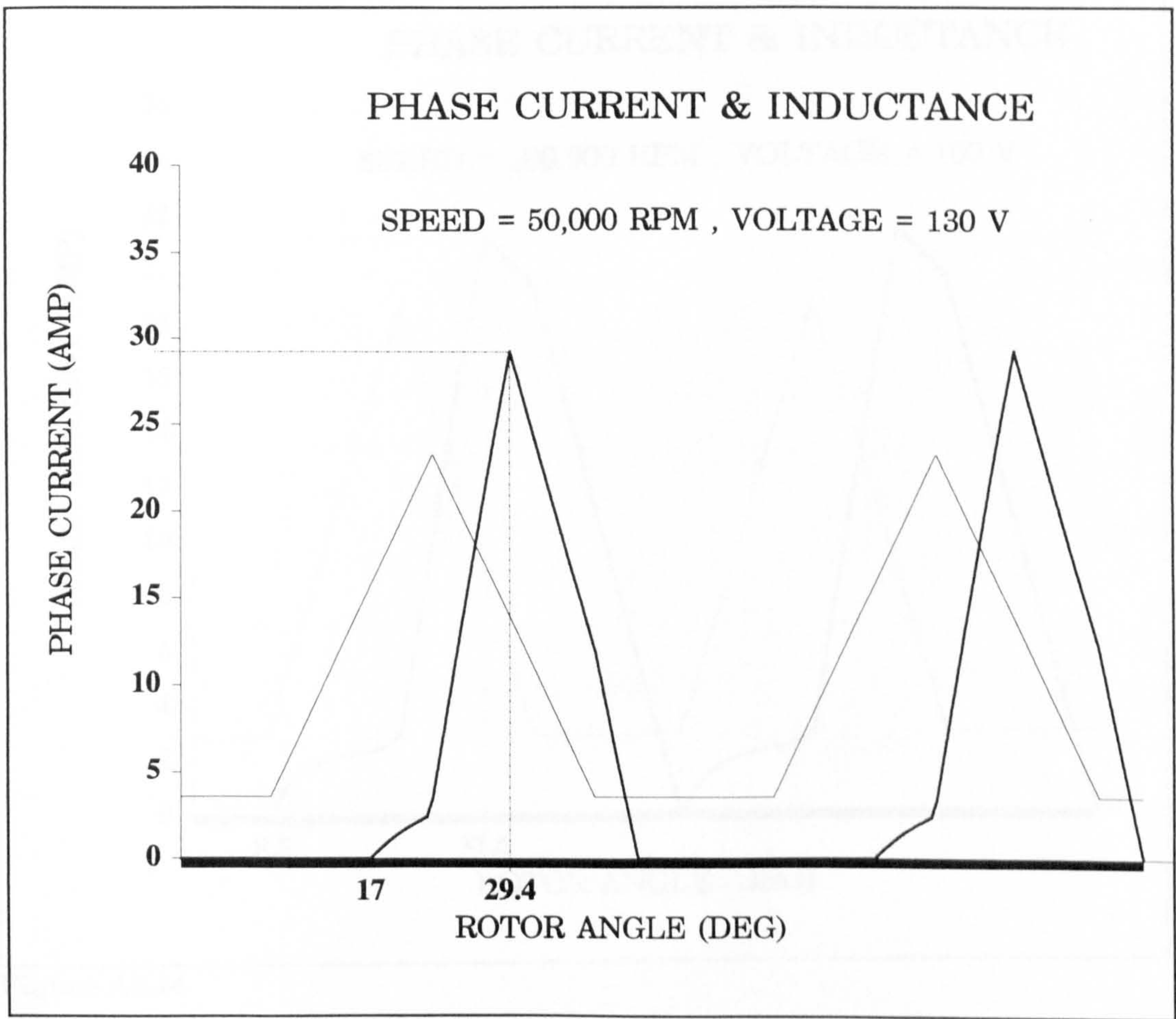


Figure A3.13

CASE 8; SPEED= 100,000 RPM , VOLTAGE = 100 VOLTS

Switching Angles: Theta_dly = 8.50 , Theta_com = 31.60 ** Theta_on = 23.10

Dis-Continuous Phase Current I_peak = 21.161 Amp

Step used for theta = 0.050 , Peak Flux Density Bpk = 0.455

Number of Phase Current Pulses = 2 Inductance Scale = 20000

Rotor Speed = 100 krpm Excitation Ve = 100 volts O/P Vo = 100 volts

Input Power per phase = 307.815 W Isw_rms/phase = 6.087 AMP

Output Load Power/phase = 586.733 W IL_rms/phase = 11.431 AMP

Total Power generated = 557.836 W

EFFICIENCY = 83.62% steps = 1965

*****0-

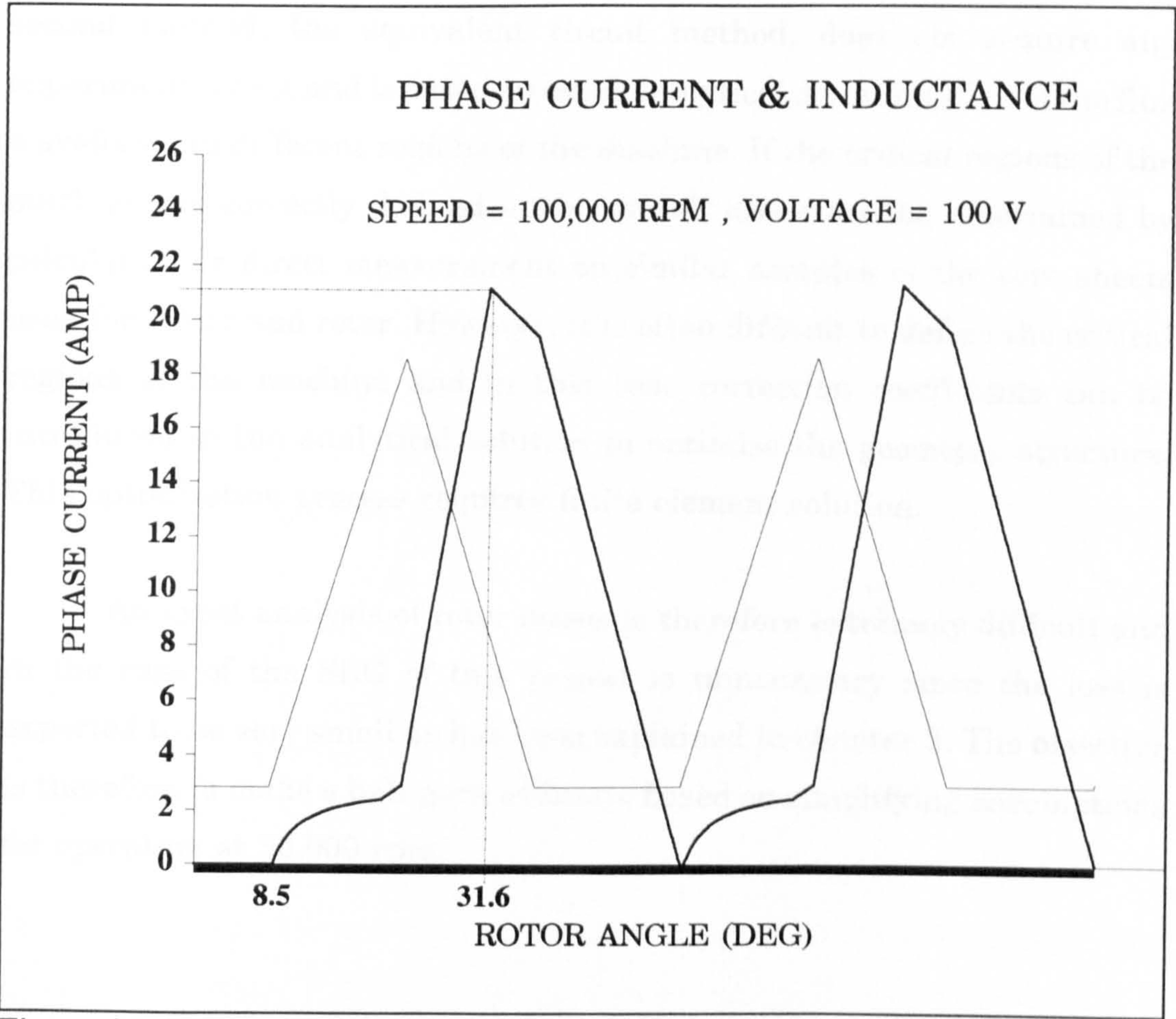


Figure A3.14

APPENDIX A3.5

ESTIMATION OF EDDY CURRENT LOSSES

A3.5.1 Introduction

Different methods have been in use to determine core losses in SR machines. They can be categorised as; the empirical method, the equivalent magnetic circuit method and the finite element method [1]. The first method requires the knowledge of the constants included in the basic equation. These constants are determined from the constructed machine itself. The second method, the equivalent circuit method, does not require any experimental data and is based on exact analytical determination of the flux waveforms in different regions of the machine. If the critical regions of the machine are correctly defined in the model, losses can be determined by calculation or direct measurement on similar samples of the core sheets used for stator and rotor. However, it is often difficult to define the critical regions of the machine and in this case correction coefficients can be introduced in the analytical solution to optimise the geometry structure. This optimisation process requires finite element solution.

An exact analysis of rotor losses is therefore extremely difficult and in the case of the SRG of this project is unnecessary since the loss is expected to be very small as has been explained in chapter 3. The objective is therefore to make a ball-park estimate based on simplifying assumptions for operation at 50,000 rpm.

A3.5.2 Assumption for Rotor Flux Distribution

Figure 3.14 in chapter 3 is repeated here for convenience as Figure A3.15. It shows the flux distribution in the rotor according to the assumptions explained below.

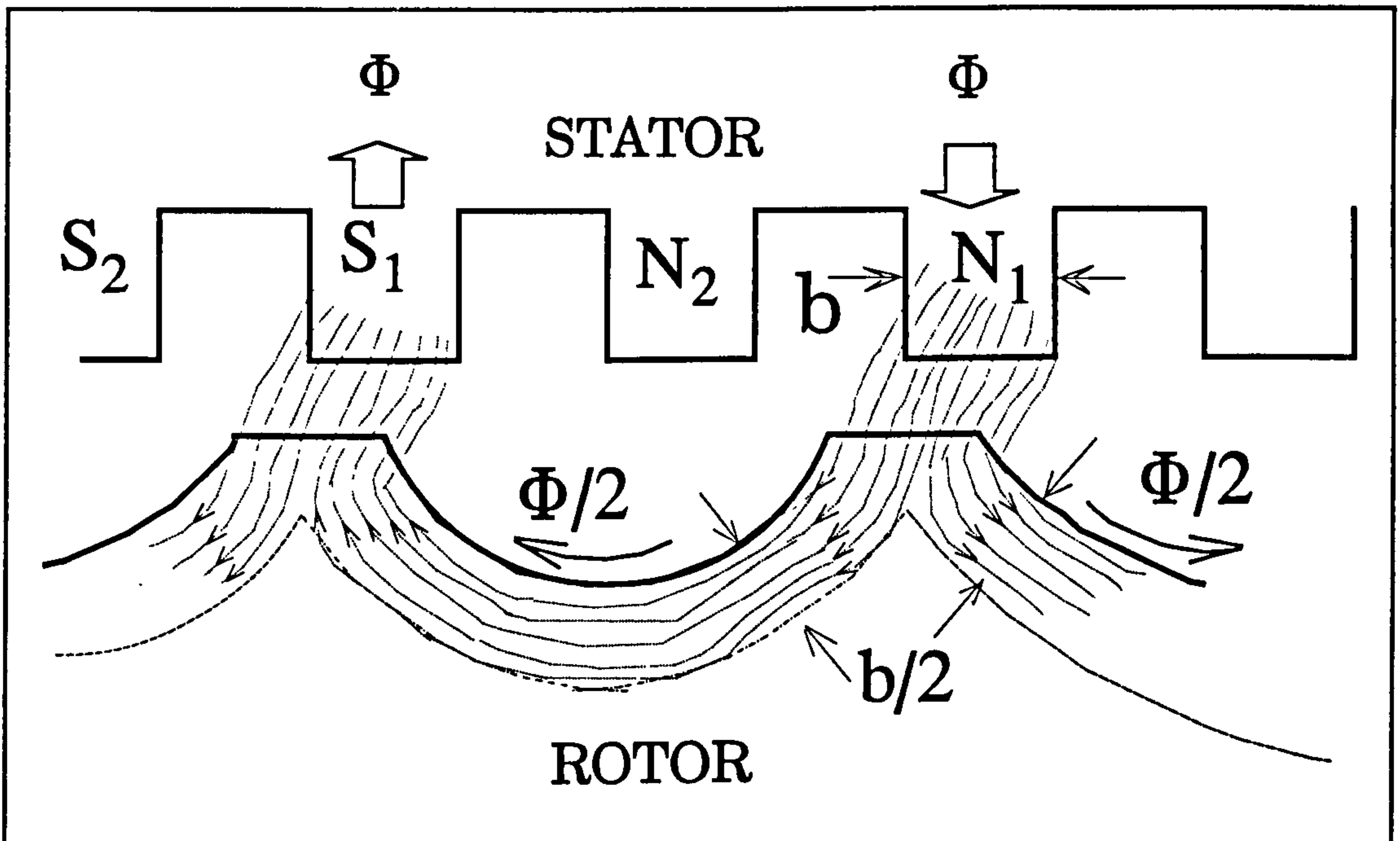


Figure A3.15: Flux distribution in the rotor.

An assumption is made that the overall flux density in the rotor for the region carrying the flux is the same as in the stator. In practice the rotor flux would distribute more into the rotor material giving lower losses. The estimate will therefore be rather conservative. Note also that the flux density at the rotor pole tips may be greater for parts of the repetitive cycle. However, this represents a relatively small area (or volume) and the effect will therefore be not very significant.

It is also assumed that the rotor flux due to the other phase winding (i.e. stator poles N_2S_2 as given in Figure A3.15) divides evenly and is superimposed on the flux for N_1S_1 . For the position shown in the figure above, the N_2S_2 will be much smaller.

A3.5.3 Assumption for Stator Flux

Figure A3.16 shows the flux waveform in the stator pole. An assumption is made first that stator flux variation with time is symmetrically triangular.

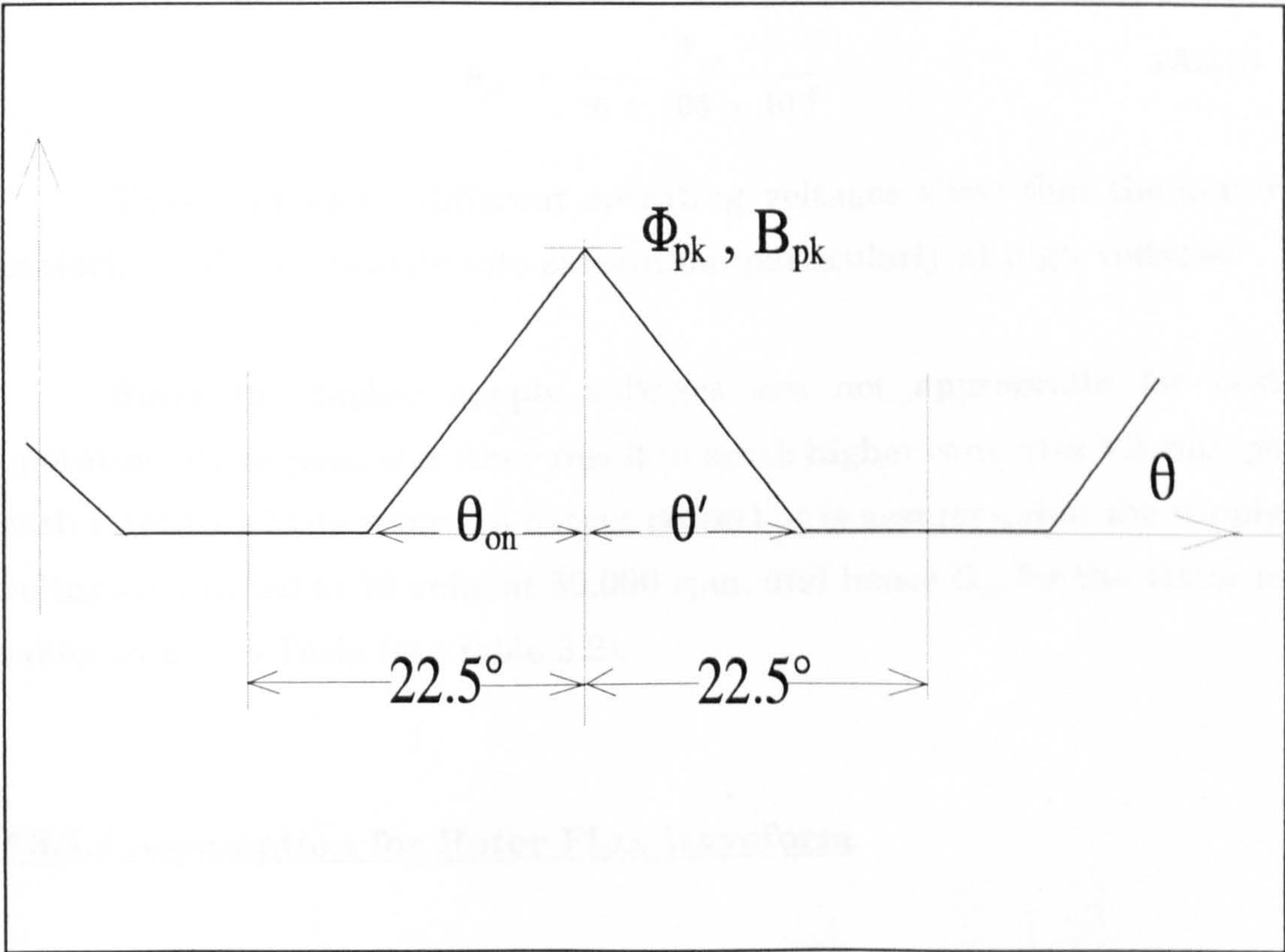


Figure A3.16: Flux waveform in the stator pole.

Due to the effect of the winding resistance, the flux waveform will not be symmetrical, i.e. θ_{on} in Figure A3.16 will be larger than θ' . However, to a reasonable approximation θ_{on} can be taken as half the duration of the pulse.

Values of B_{pk} can be obtained from the estimated peak flux linkage Ψ_{pk} for a phase, using (2.14) and substituting I_{pk} for i . $\Delta\Psi$ can be determined from (2.15) by substituting $(2\theta_m - \theta_{com})$ for θ if θ_{com} is larger than θ_m , which is likely to be the case, or by θ_{com} if it is smaller. Equation (2.14) will then be:

$$\Psi_{pk} = I_{pk} L_{\min} + I_{sat} L'_{\max} K (2\theta_m - \theta_{com} - \theta_r) \quad (\text{A3.1})$$

Since the pole area is $A = 106 \text{ mm}^2$, and there are $8 \times 9.5 = 76$ turns, then the peak flux density for the stator pole B_{pk} is:

$$B_{pk} = \frac{\Psi_{pk}}{76 \times 106 \times 10^{-6}} \quad (\text{A3.2})$$

These values for different operating voltages show that the stator material is driven heavily into saturation, particularly at high voltages.

Since the higher supply voltages are not appropriate for best operation of the generator (they result in much higher converter VA ratings with relatively little return in output power), it is assumed that the supply voltage is limited to 70 volts at 50,000 rpm, and hence B_{pk} for the stator is taken to be 0.5 Tesla (see table 3.2).

A3.5.4 Assumption for Rotor Flux Waveform

CASE-1: Full Power

The simplifying assumption is made here that the stator flux waveform is fully opened, i.e. $\theta_{sn} = 22.5^\circ$ with $B_{pk} = 0.5$ Tesla, and that the corresponding rotor flux density waveform, for the two phases is as shown in Figure A3.17.

This is also a conservative assumption since a significant proportion of the stator flux under heavily saturated conditions will not be carried by the rotor material anyway.

Φ_1 and Φ_2 , in Figure A3.17, represent the flux in the rotor material due to each of the two phases. B_r is the resultant variation in flux density for the rotor material carrying the flux. The corresponding waveform for B' is determined simply from dB_r/dt :

$$B'_{pk} = \frac{2 B_{r(pk)}}{\Delta t} \tag{A3.3}$$

and $B'_{rms} = \frac{B'_{pk}}{\sqrt{2}}$

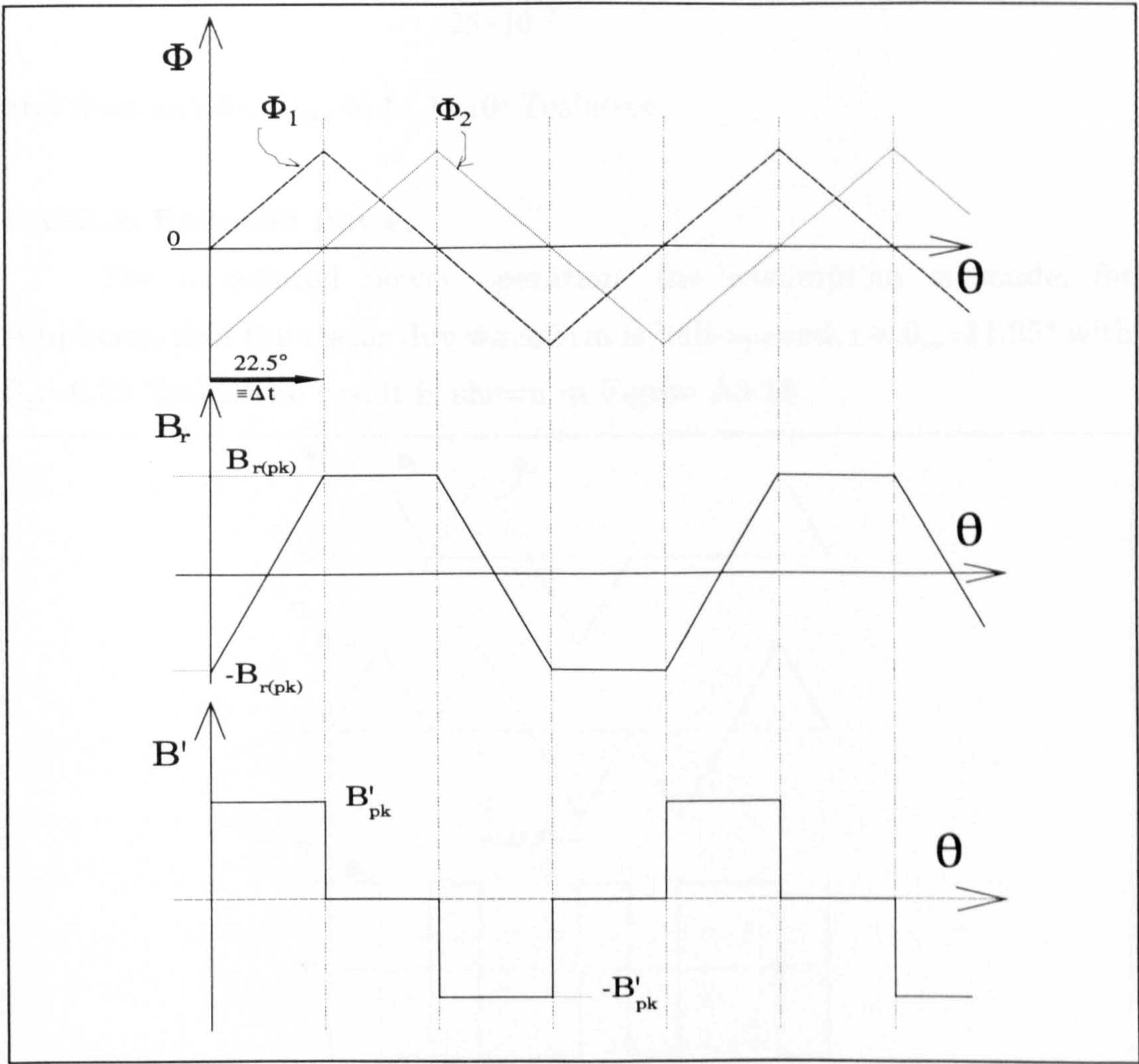


Figure A3.17: Rotor flux waveform at full power.

Since 50,000 rpm corresponds to 300°/ms, then Δt, which is equivalent to 22.5°, is 75 μsec. Also, the proportion of lamination in the rotor is a factor λ (which is < 1), making the flux density in the rotor material B_r, 1/λ higher than B in the stator. Hence:

$$\begin{aligned} B_{r(pk)} &= \frac{B_{pk}}{\lambda} = \frac{0.5}{\frac{\text{no. of lamin.} \times \text{lamin. thickness}}{l_c}} \\ &= \frac{0.5}{\frac{550 \times 30 \times 10^{-6}}{25 \times 10^{-3}}} = 0.75 \text{ Tesla} \end{aligned} \tag{A3.4}$$

and from (A3.3), B'_{rms} is 14.1×10³ Tesla/sec.

CASE-2: Reduced Power

For a reduced power operation, the assumption is made, for simplicity, that the stator flux waveform is half-opened, i.e. θ_{on}=11.25° with B_{pk}=0.25 Tesla. The result is shown in Figure A3.18.

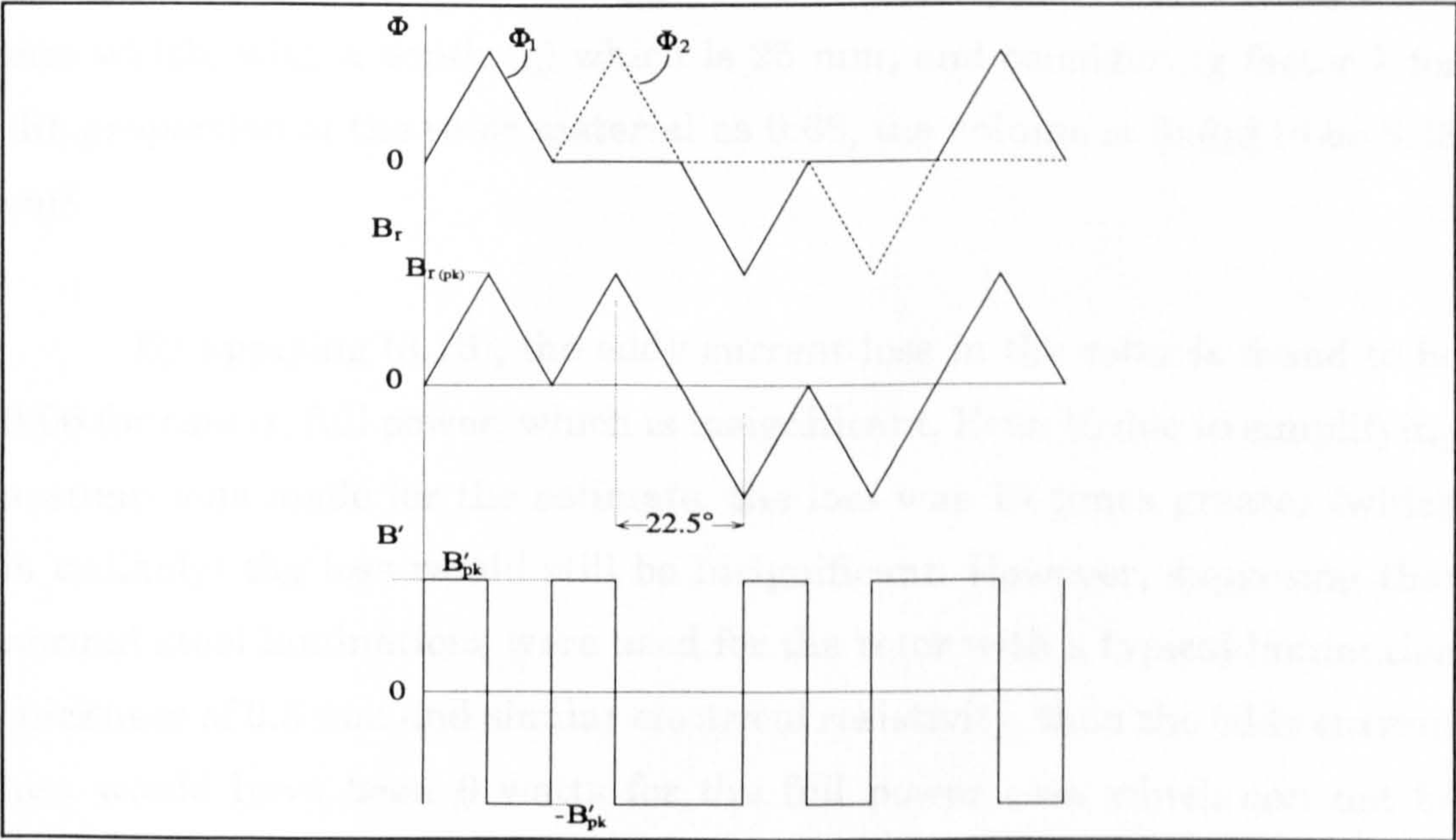


Figure A3.18: Rotor flux waveform at reduced power.

By applying (A3.3) and (A3.4) and substituting for B_{pk} in the stator by 0.25 Tesla, the resultant B'_{rms} is 10×10^3 Tesla/sec.

A3.5.5 Volume of Rotor Material Carrying Flux

Figure A3.19 shows the approximate geometry of the rotor strip assumed to be carrying the rotor flux.

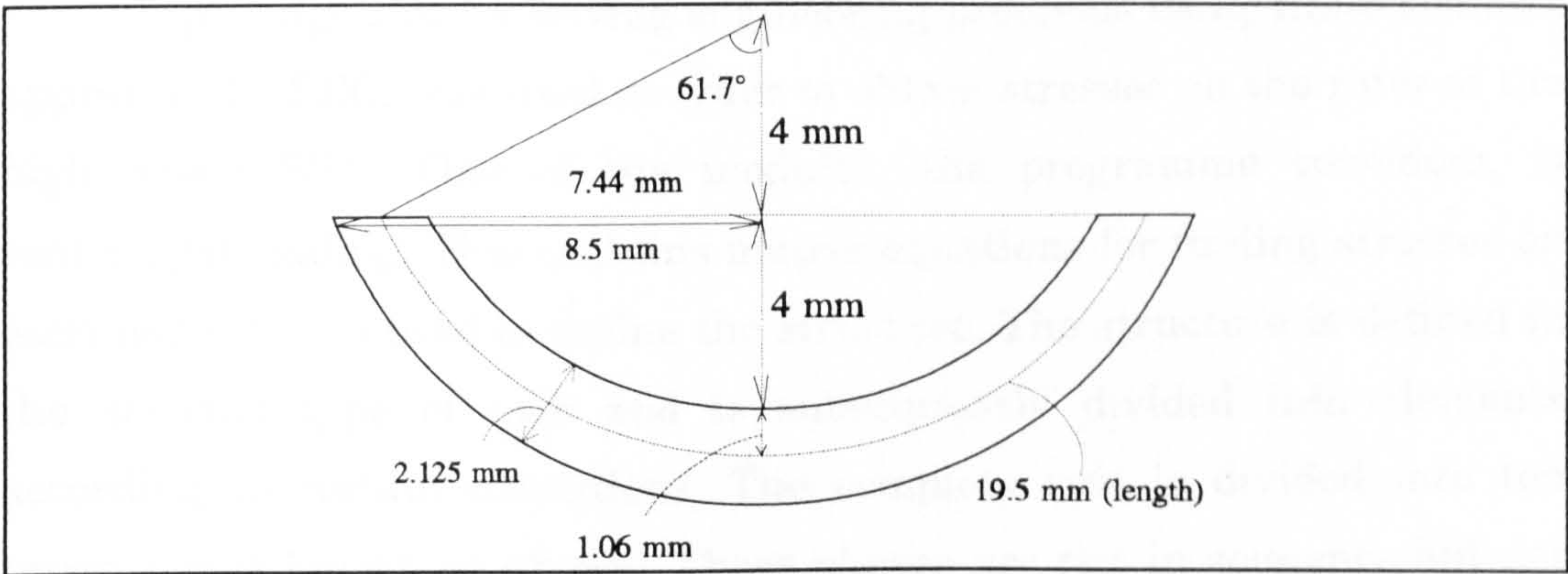


Figure A3.19: Geometry of the rotor strip assumed to be carrying the rotor flux.

The total volume of 8 segments (strips) of 19.55 mm length, 2.125 mm width, with a depth (l_c) which is 25 mm, and considering factor λ for the proportion of the rotor material as 0.66, the volume is found to be 5.48 cm^3 .

By applying (3.16), the eddy current loss in the rotor is found to be 0.06 for case-1, full power, which is insignificant. Even if, due to simplifying assumptions made for the estimate, the loss was 10 times greater (which is unlikely) the loss would still be insignificant. However, supposing that normal steel laminations were used for the rotor with a typical lamination thickness of 0.3 mm and similar electrical resistivity, then the eddy current loss would have been 6 watts for the full power case which can not be neglected. The use of the very thin amorphous laminations for the rotor is thus significantly reducing the rotor losses.

APPENDIX A4.1

GENERAL DESCRIPTION OF THE PAFEC PACKAGE WITH AN ILLUSTRATED LISTING OF DATA INPUT FOR STRESS ANALYSIS ON SEGMENT OF THE ROTOR

A package suit for solving engineering problems using finite element approach, PAFEC, was used in order to obtain stresses on the rotor of the high speed SRG. One of the modules, the programme considers, is centrifugal loading. This contains matrix equations for finding stresses on each node that is used to define the structure. The structure is defined in the selected type of axis and is subsequently divided into elements according to certain definitions. The complete suit is divided into ten programmes known as phases. These phases are run in sequence but not all of them are essential for every required solution. Phase one starts with reading the data. Phase two generates the mesh. Phase three is used to draw the un-loaded structure (to ensure correct mesh has been generated). Phase four considers the restraints. Phase seven solves equations for displacements and other primary conditions. Phase eight draws the displaced structure. In phase nine stresses are found and consequently drawn as contours over the complete (or segment of) structure in the last phase.

A special module is provided by the programme known as the CONTROL module. This is used to act as a qualifier to the mesh or it is used as an aid to guide a particular job through the various paths of PAFEC should the automatic sequence need to be modified in any way. It was used, for example, to skip check and validation of geometry and restraints for repetitive run of the programme at different speeds.

RPAFEC(DIGFILE=*SRC.PROG3)
TITLE STRESS ANALYSIS

**CALL THE PACKAGE AND SAVE THE DRAWING CODE.*

CONTROL
 STRESS
 TOLERANCE=10E-07
CONTROL.END

**CONTROL THE PROGRAMME FLOW BY CHANGING TOLERANCE DEFAULT.*

NODES
AXIS=3

**FIRST MODULE DEFINING THE GEOMETRY OF THE SEGMENT.
THE AXIS IS CHOSEN FOR POLAR COORDINATES. X IS IN METRE AND Y IS ANGLE IN DEGREES.

NODE.NUMBER	X	Y
1	8E-03	0
2	17.75E-03	0
3	8E-03	8.4375
4	18.40E-03	8.4375
5	8E-03	16.875
6	21.625E-03	16.875
7	8E-03	22.5
8	21.625E-03	22.5
9	8E-03	28.125
10	21.625E-03	28.125
11	8E-03	36.5625
12	18.4E-03	36.5625
13	8E-03	45
14	17.75E-03	45

ARC.NODES
LIST.OF.NODES.ON.ARC
1,3,5,7,9,11,13
2,4,6
6,8,10
10,12,14

**MORE DEFINITION OF GEOMETRY.*

MATERIAL

**PROPERTIES OF SEGMENT (ROTOR) MATERIAL. E, CORRESPONDS TO YIELD STRENGTH IN N/SQUARE M; NU, TO POISSONS RATIO AND RO TO WEIGHT DENSITY IN GM/CUBE CM.*

MATERIAL.NUMBER	E	NU	RO
11	150E09	0.3	7.7E03

PAFBLOCKS

**THIS MODULE IS FOR PREPARING THE REQUIRED MESH BY SUBDIVIDING THE SEGMENT INTO THREE MAIN BLOCKS. THE NUMBERS FOR N1 AND N2 GIVE A REFERENCE FOR THE NUMBER OF ELEMENTS REQUIRED IN TWO DIRECTIONS. N1 GIVES REFERENCE TO ELEMENTS IN THE X-AXIS AND N2 FOR ELEMENTS IN THE Y-AXIS DIRECTION.*

TYPE=1			
ELEMENT.TYPE=36210			
BLOCK.NUMBER	N1	N2	TOPOLOGY
1	1	2	1,2,5,6,0,3,4
2	1	2	5,6,9,10,0,7,8
3	1	2	9,10,13,14,0,11,12

MESH

**THIS MODULE IS FOR GENERATING THE REQUIRED MESH. THE SPACING LIST GIVES THE NUMBER OF ELEMENTS REQUIRED IN EACH DIRECTION ACCORDING TO ITS REFERENCE FROM THE PREVIOUS MODULE.*

REFERENCE	SPACING.LIST
1	27
2	20

CENTRIFUGAL

**THIS MODULE PREPARES THE CALCULATION REQUIRED TO DETERMINE CENRIFUGAL STRESSES ON EACH NODE, ELEMENT AND THEN CATERS FOR AVERAGING THE STRESS CALCULATIONS. THE Z.FREQ REFERS TO THE ROTATIONAL SPEED OF THE ROTOR IN REV/SEC.*

LOAD.CASE	Z.FREQ
1	1700

PLATES.AND.SHELLS

PLATE.NUMBER	THICKNESS
1	25E-03

AXES

**DEFINING NEW AXES FOR FOR LOCAL DIRECTIONS IN ORDER TO SPECIFY RESTRAINTS OF THE SEGMENT IN CERTAIN DIRECTIONS. THREE LOCAL AXES ARE REQUIRED SINCE THERE THREE MAIN BLOCKS IN GEOMETRY.*

AXISNO	ANG1		
10	16.875		
20	28.125		
30	45		
LOCAL.DIRECTIONS			
NODE	LOCAL	PLANE	AXIS
5	10	2	10
9	20	2	20
13	30	2	30

RESTRAINTS NODE	AXIS	PLANE	DIRECTION
1	1	2	2
5	10	2	2
9	20	2	2
13	30	2	2

IN.DRAW

**SPECIFYING SELECTIONS FOR THE DRAWING OF THE DIVIDED STRUCTURE OF THE SEGMENT. ELEMENT NUMBERS WERE SELECTED TO BE DISPLAYED IN THE PLOT.*

TYPE	INFORMATION.NUMBER
3	3

OUT.DRAW

**SPECIFYING SELECTIONS FOR THE STRUCTURE WITH THE OUTPUT RESULT REQUIRED TO BE SHOWN AS: A GRAPHICAL REPRESENTATION OF DISPLACEMENT DUE TO STRESSES AND AS STRESS COTOURS SHOWING MAXIMUM PRICIPAL STRESSES ON THE PLOTTED SEGMENT.*

PLOT.TYPE
1
30
END.OF.DATA
++++
EJ

APPENDIX A4.2

DATA PREPARATION LISTING FOR OPERATING
PAFEC TO CALCULATE STRESSES ON THE
COMPLETE ROTOR STRUCTURE AT 100 KRPM

RPAFEC(DIGFILE=*SRC.STRESS)
TITLE STRESS ANALYSIS VERY HIGH SPEED
CONTROL
TOLERANCE=10E-07
STRESS
PIGS.STRESS.FILE
CONTROL.END
NODES
AXIS=3

NODE.NUMBER	X	Y

1	7.5E-03	0
2	17E-03	0
3	7.5E-03	9.5
4	17E-03	9.5
5	7.5E-03	22.5
6	20.5E-03	9.5
7	20.5E-03	22.5
8	20.5E-03	35.5
9	7.5E-03	35.5
10	17E-03	35.5
11	7.5E-03	45
12	17E-03	45
13	7.5E-03	54.5
14	17E-03	54.5
15	7.5E-03	67.5
16	20.5E-03	54.5
17	20.5E-03	67.5
18	20.5E-03	80.5
19	7.5E-03	80.5
20	17E-03	80.5
21	7.5E-03	90
22	17E-03	90
23	7.5E-03	99.5
24	17E-03	99.5
25	7.5E-03	112.5
26	20.5E-03	99.5
27	20.5E-03	112.5
28	20.5E-03	125.5
29	7.5E-03	125.5
30	17E-03	125.5
31	7.5E-03	135

CHAPTER 4

APPENDICES

32	17E-03	135
33	7.5E-03	144.5
34	17E-03	144.5
35	7.5E-03	157.5
36	20.5E-03	144.5
37	20.5E-03	157.5
38	20.5E-03	170.5
39	7.5E-03	170.5
40	17E-03	170.5
41	7.5E-03	180
42	17E-03	180
43	7.5E-03	189.5
44	17E-03	189.5
45	7.5E-03	202.5
46	20.5E-03	189.5
47	20.5E-03	202.5
48	20.5E-03	215.5
49	7.5E-03	215.5
50	17E-03	215.5
51	7.5E-03	225
52	17E-03	225
53	7.5E-03	234.5
54	17E-03	234.5
55	7.5E-03	247.5
56	20.5E-03	234.5
57	20.5E-03	247.5
58	20.5E-03	260.5
59	7.5E-03	260.5
60	17E-03	260.5
61	7.5E-03	270
62	17E-03	270
63	7.5E-03	279.5
64	17E-03	279.5
65	7.5E-03	292.5
66	20.5E-03	279.5
67	20.5E-03	292.5
68	20.5E-03	305.5
69	7.5E-03	305.5
70	17E-03	305.5
71	7.5E-03	315
72	17E-03	315
73	7.5E-03	324.5
74	17E-03	324.5
75	7.5E-03	337.5
76	20.5E-03	324.5
77	20.5E-03	337.5
78	20.5E-03	350.5
79	7.5E-03	350.5
80	17E-03	350.5

APPENDIX A4.2

MATERIAL				
MATERIAL.NUMBER		E	NU	RO
11			150E09	0.3
7.7E03				
PAFBLOCKS				
TYPE=1				
ELEMENT.TYPE=36210				
BLOCK.NUMBER	N1	N2	TOPOLOGY	
1		1	2	79,80,3,4,0,1,2
2		3	4	3,6,9,8,0,5,7
3		1	2	9,10,13,14,0,11,12
4		3	4	13,16,19,18,0,15,17
5		1	2	19,20,23,24,0,21,22
6		3	4	23,26,29,28,0,25,27
7		1	2	29,30,33,34,0,31,32
8		3	4	33,36,39,38,0,35,37
9		1	2	39,40,43,44,0,41,42
10		3	4	43,46,49,48,0,45,47
11		1	2	49,50,53,54,0,51,52
12		3	4	53,56,59,58,0,55,57
13		1	2	59,60,63,64,0,61,62
14		3	4	63,66,69,68,0,65,67
15		1	2	69,70,73,74,0,71,72
16		3	4	73,76,79,78,0,75,77
MESH				
REFERENCE	SPACING.LIST			
1	4			
2	2			
3	5			
4	3			
CENTRIFUGAL				
LOAD.CASE	Z.FREQ			
1	1700			
PLATES.AND.SHELLS				
PLATE.NUMBER	THICKNESS			
1	3E-05			
AXES				
AXISNO	ANG1			
11	9.5			
12	35.5			
13	54.5			
14	80.5			
15	99.5			
16	125.5			
17	144.5			
18	170.5			


```
LOCAL.DIRECTIONS
PLANE=2
NODE          LOCAL      AXIS
3             11         11
9             12         12
13            13         13
19            14         14
23            15         15
29            16         16
33            17         17
39            18         18
RESTRAINTS
PLANE=2
DIRECTION=2
NODE          AXIS
1             1
3             11
9             12
13            13
19            14
23            15
29            16
33            17
39            18
IN.DRAW
TYPE          INFORMATION.NUMBER
3             3
OUT.DRAW
PLOT.TYPE
1
30
END.OF.DATA
++++
EJ
```


APPENDIX A5.1

DETERMINATION OF HEAT SINKING REQUIREMENTS FOR THE POWER SWITCHES

A matt black heat sink operated by natural convection of ambient air and in a horizontal mounting position, to dissipate heat out of the IRF640 power MOSFET is considered here.

The maximum junction temperature of the device, $T_{j\max}$, is 125°C and ambient air temperature is considered 25°C. Maximum power dissipation in the transistor P_{diss} is determined from:

$$P_{diss} = I_{sw-rms}^2 \times R_{ds-on} \quad (A5.1)$$

where I_{sw-rms} is the maximum expected r.m.s. current in the power transistor, estimated from the model as 7 Amp, and R_{ds-on} is given as 0.18 Ω , however approximated here, due to temperature rise, to be 0.2 Ω . P_{diss} from (A5.1) will approximately be 10 watts.

Using the thermal equation:

$$P_{diss} = \frac{T_{j\max} - T_a}{R_{\theta j-a}} \quad (A5.2)$$

$$\text{where, } R_{\theta j-a} = \frac{125 - 25}{10} = 10^\circ\text{C/watt}$$

is the thermal resistance between the device junction and air, and with heat sink will be:

$$R_{\theta j-a} = R_{\theta j-c} + R_{\theta c-s} + R_{\theta s-a} \quad (A5.3)$$

The first two terms relate to the thermal resistance of junction-to-case, given as $1^{\circ}\text{C}/\text{W}$, and case-to-sink, given as $1.2^{\circ}\text{C}/\text{W}$ for Teflon insulator.

The sink-to-air thermal resistance $R_{\theta_{s-a}}$ will then be $7.8^{\circ}\text{C}/\text{W}$. The matt black heat sink of $1.1^{\circ}\text{C}/\text{W}$ is very sufficient for cooling the power transistor as well as the accompanying power diode even if a 20% derating for horizontal mounting position is applied.

APPENDIX A5.2

PCB PRODUCTION DIAGRAM FOR THE
CONTROLLER OF FIGURE 5.7

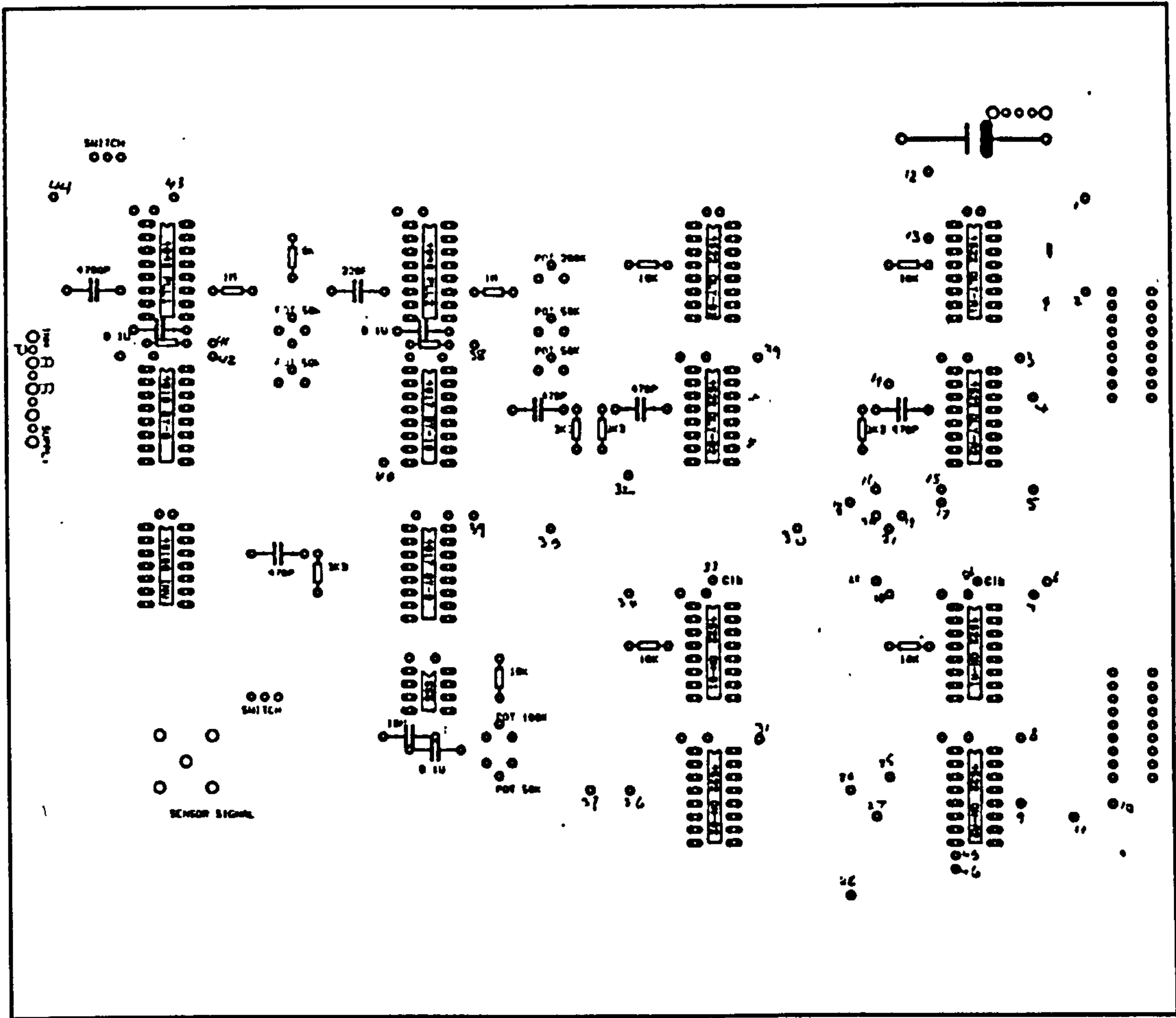


Figure A5.1: Covering sheet. Components and IC function definition for the controller of Figure 5.7.

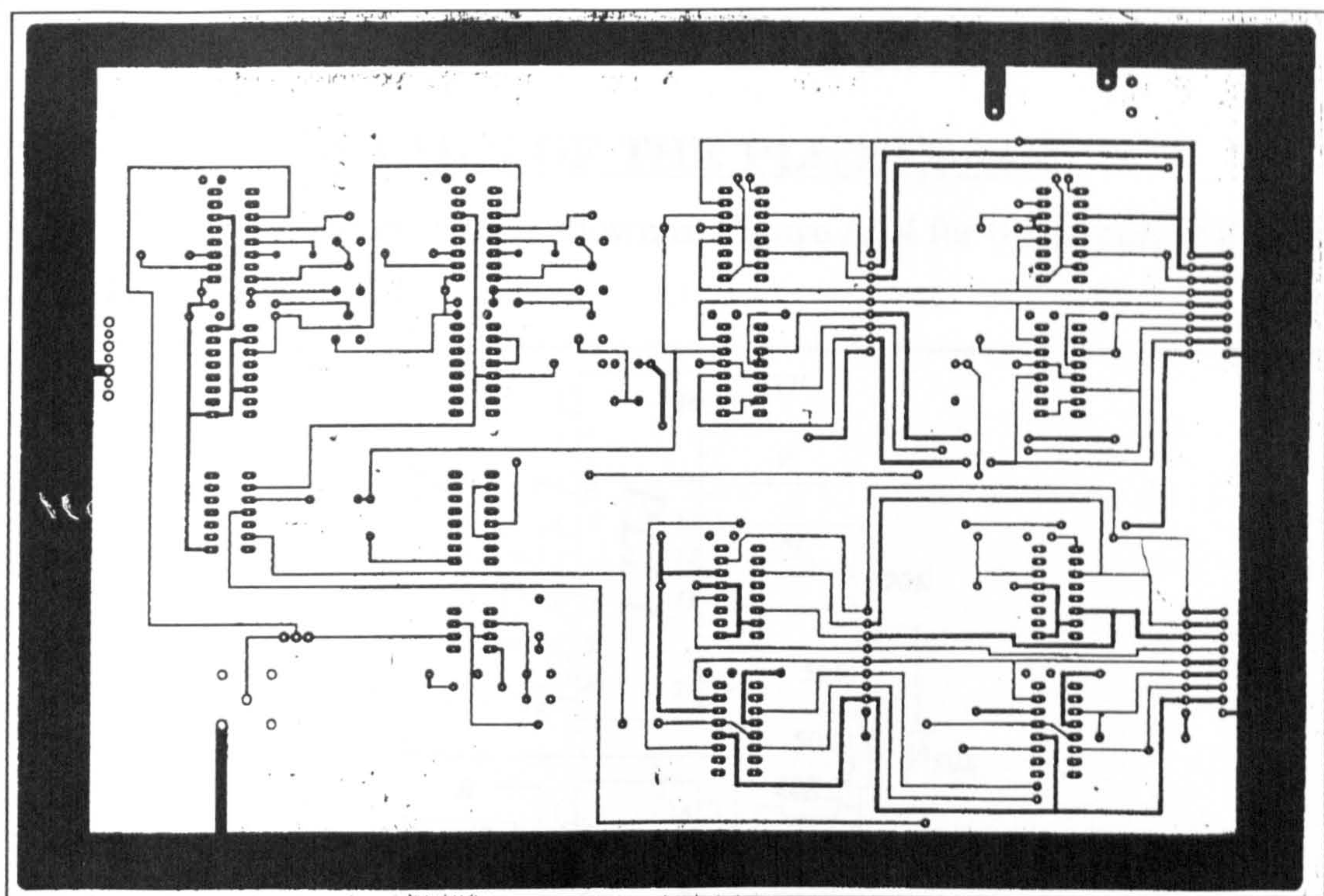


Figure A5.2: Upper layer of the PCB diagram of the controller circuit.

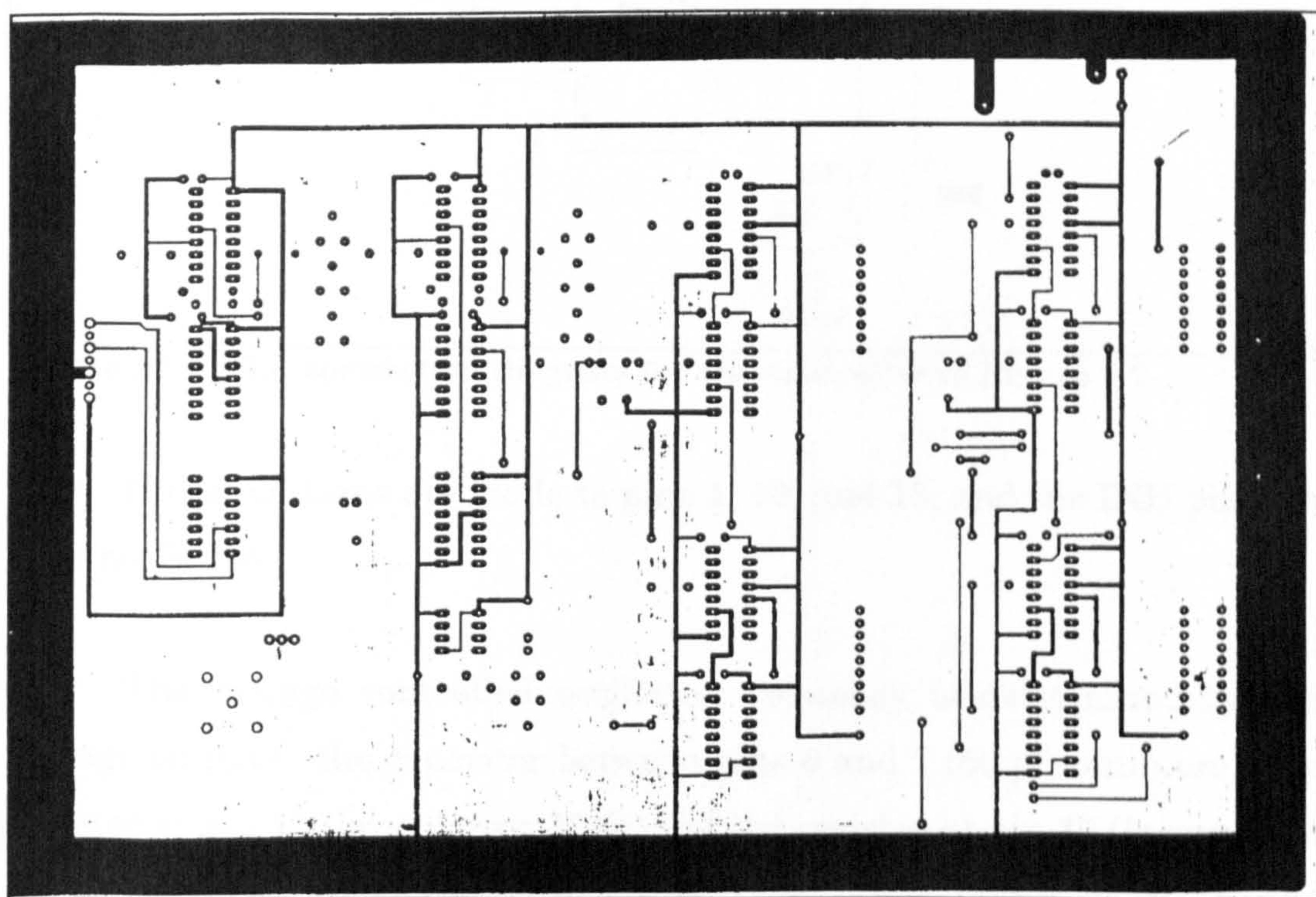


Figure A5.3: Bottom layer of the PCB diagram of the controller circuit.

APPENDIX A5.3

DETAILS OF THE PLL DESIGN

The pin arrangement is shown in Figure A5.4 for the circuit of Figure 5.7, the two-stage PLL.

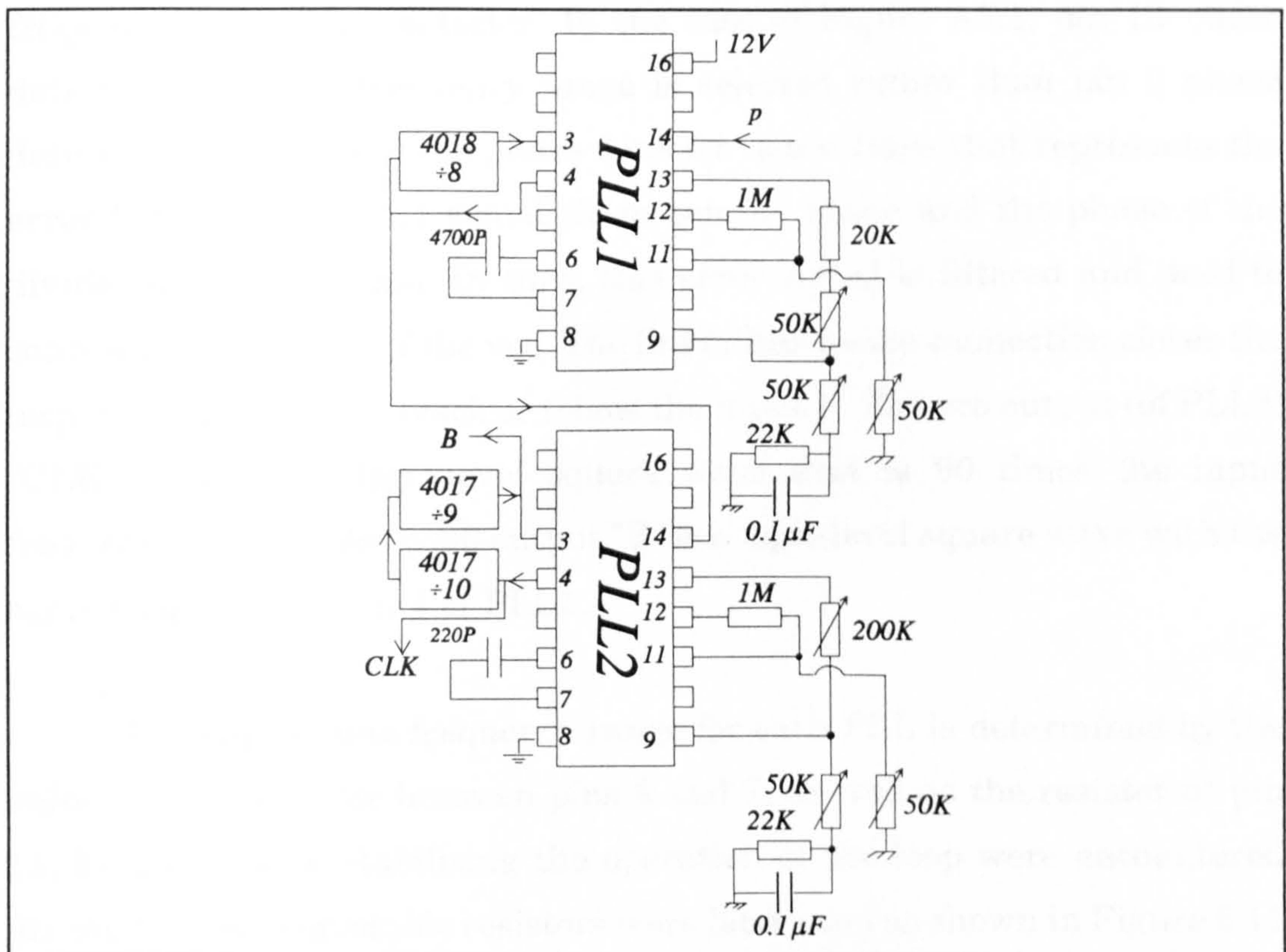


Figure A5.4: PLL connection diagram for the controller of Figure 5.7.

No connections are made to pins 1, 10, and 15, and the INH pin (pin 5) is made low.

The voltage controlled oscillator frequency is determined by the voltage on pin 9, the capacitor between pins 6 and 7 (50 pf minimum), the resistor at pin 11 (larger than 10K), and the resistor at pin 12 (larger than that at pin 11) [163]. The output appears at pin 4, and is routed to the comparator input (pin 3) via a divide-by-n counter. The divider used with

PLL1 is 4018 to divide by 8. Two stages of 4017 are used with PLL2 to divide by 90. These counters are configured as was shown in the circuit diagram used for PCB production in Appendix A5.2.

The output of the divide-by-n counter is compared to the input frequency in a phase detector. In the case of Figure A5.1, pin 13 phase detector with wide frequency range is selected rather than pin 2 phase detector. The output of the phase detector is a voltage that represents the error between the input signal (from sensor) phase and the phase of the divided-down vco signal. In turn, this error signal is filtered and used to control the frequency of the vco. The final filter-to-vco connection closes the loop, forcing the vco to track or follow the input P. The vco output (of PLL2) "CLK" is a clean, logic-level square wave that is 90 times the input frequency. The divide-by-90 output "B" is a logic-level square wave with the same frequency as pin 4 of PLL1.

The appropriate frequency range for each PLL is determined by the value of the capacitor between pins 6 and 7, as well as the resistor at pin 11. Problems with stabilising the operation of the loop were encountered during testing. Adjustable resistors were later used as shown in Figure 5.11 in order to experimentally fine tune the loop operation. The same for the low-pass filter resistors at pin 9; these were first given as fixed resistors. However, at different speeds (frequencies of the input signal) there are some optimum values for these resistors which will produce a stable and jitter-free signal at "B" and "CLK". Data sheets information of the 4046 IC were useful for initial design of the loop. Alterations that led to connection diagram shown in Figure 5.11 were made after running and testing the actual machine and converter.

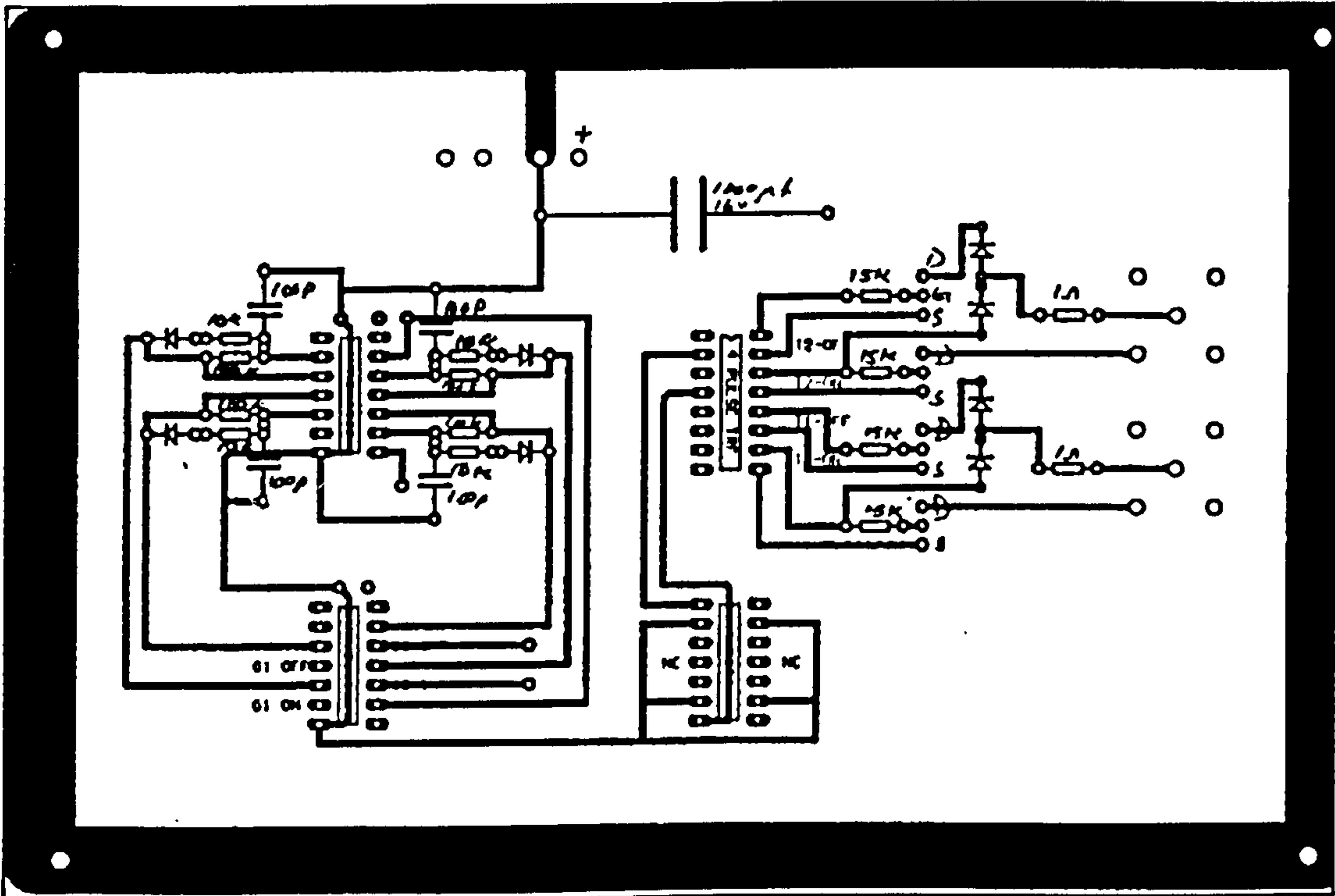


Figure A5.6: Upper layer of the PCB diagram of the gate drive circuit.

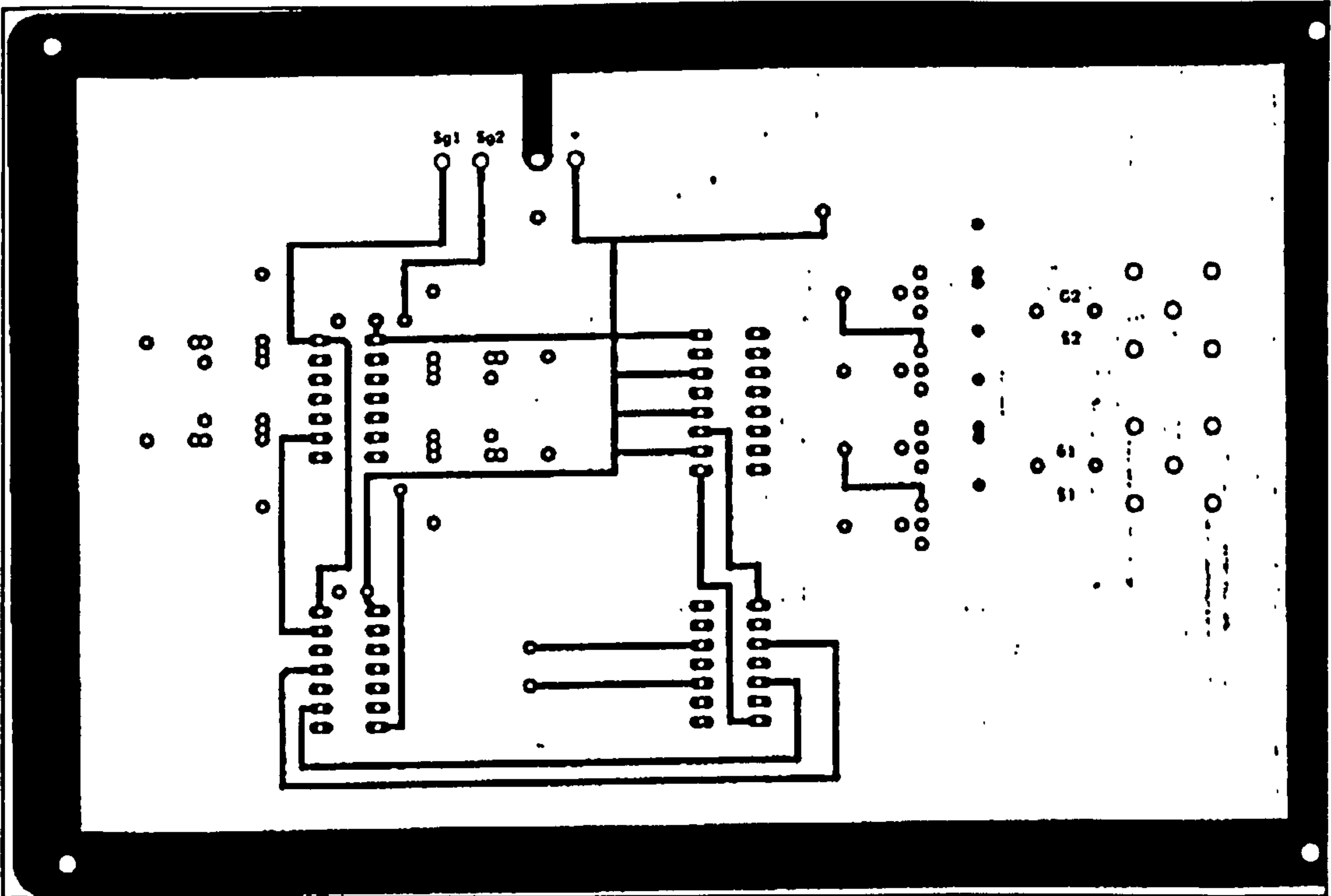


Figure A5.7: Bottom layer of the PCB diagram of the gate drive circuit.

APPENDIX A6.1

VOLUME AND WEIGHT OF THE

ELECTROMAGNETIC UNIT

To estimate the power density (power/weight) or (power/volume), of the SRG, the weight and the volume of the electromagnetic unit, i.e. the SR machine comprising the stator, the rotor, and the copper winding (but not the power converter) is to be determined.

By referring to Figure 3.1, the volume of 16 slots of the stator ferrite core is determined from the slot dimensions; $(4.25 \times 7 \times 25)$ times 16 slots. The volume density of the ferrite is given in Appendix A3.1 as 4.8 gm/cm^3 . The total weight of two stator ferrite cores is found to be 220 gm. Note that a similar stator made of steel would weight about 320 g assuming 0.9 stacking factor for the steel laminations and 7.8 g/cm^3 weight density for the steel.

The total weight of the stator is found by adding the weight of the copper in the machine. As the wire length needed for making a phase winding is 5.3 m (from section 3.4.3), and for 22 SWG the weight/length is given as 3.532 gm/m , then for two phases total copper weight will be 37.4 gm. Therefore, the total weight of the stator part of the SRG will approximately be 260 gm.

The estimation of the likely load on the bearing of the gas turbine requires the determination of the weight of the rotor of the SRG. Before completing the rotor assembly, its weight can be worked out from the rotor dimensions as selected in chapter 3 and from material data as given in Appendix A3.2. The dimensions are given as follows:

r_o , the outer radius = 21.62 mm

r_i , the inner radius = 8.00 mm

R , the distance between the rotor centre and the centre of the circle used for profiling the rotor = 25.75 mm

Using trigonometric relations, the area which represents one of eight cut parts from a circular cross section of the rotor is found to be 35 mm².

Since the rotor is profiled with eight poles, and the central hole is 8 mm in radius:

$$\begin{aligned} \text{Total cross section area of a rotor lamination} &= \pi r_o^2 - 35 \times 8 \\ &= 988 \text{ mm}^2 \end{aligned}$$

Total weight of the 550 amorphous laminations (of 7.7 gm/cm³ density) is:

$$\begin{aligned} 988 \text{ mm}^2 \times 0.03 \text{ mm} \times 7.7 \times 10^{-3} \frac{\text{gm}}{\text{mm}^3} \times 550 \\ = 125.5 \text{ gm} \end{aligned}$$

Adding 10% to the weight of the laminations to allow for the resin, and 50 gm for the steel stub shaft (as was determined), the total static bearing loading is not expected to be more than 190 gm.

The total weight of the electromagnetic unit is: 260 + 190 = 450 gm. Weight measurements could confirm these figures to a large extent.

The total volume is assumed as $(6.95/2 \text{ cm})^2 \pi \times 2.5 \text{ cm} = 94.8 \text{ cm}^3$ which is equivalent to 6 in³. Note that 6.95 cm is the OD of the stator.

APPENDIX A6.2

DATA OF THE GAS TURBINE AND DETERMINATION OF THE AIR SUPPLY DEMAND

The required volume flow rate \underline{V} in Litre/sec of the air delivered by the air blower at a relative air pressure of 500 mbar is found from the dynamometer performance curves of the air turbine given in Figure A6.1. The ambient temperature is assumed 25°C, and the temperature rise ΔT of the air delivered by the blower at 500 mbar (relative) is initially assumed 50°C. ΔT can, however, be corrected later after referring to the performance curves of the blower (given in Appendix A6.3). Thus for a target speed of 100,000 rpm, the normalised speed figure becomes:

$$\begin{aligned} \text{Normalised Speed} &= \frac{N}{\sqrt{T}} \\ &= \frac{100,000/60}{\sqrt{(25 + 273 + 50)}} \approx 88 \frac{\text{rev}}{\text{sec} \cdot \sqrt{K}} \end{aligned} \quad (\text{A6.1})$$

The curve corresponding to an expansion ratio of 1.5 is not shown in Figure A6.1. The curve which corresponds to 1.8 was used instead, with the ratio assumed for this curve to be 1.5. This needed extrapolation to find the corresponding value of $\underline{M}\sqrt{T}/P$. \underline{M} is the mass flow rate of air given on the performance curves in lb/min, T is the temperature of air in °K, and P is the total inlet air pressure given in psi. $\underline{M}\sqrt{T}/P$ is found as in Figure A6.1:

$$\frac{\underline{M}\sqrt{T}}{P} = 18 \quad (\text{A6.2})$$

Since the total pressure P is approximated 1.5 bar (or 1.5×14.5 psi), and \sqrt{T} is as given above, \underline{M} is then found as 20.9 lb/min (or 0.158 Kg/sec), from which the required air volume flow rate \underline{V} is found to be 88.5 Litre/sec.

This is also equivalent to 317 m³/hour. Other data from the manufacturer of the turbine are given in Figure A6.2 for basic dimensions and ratings, and Figure A6.3 for some dynamic tests results conducted by the manufacturer.

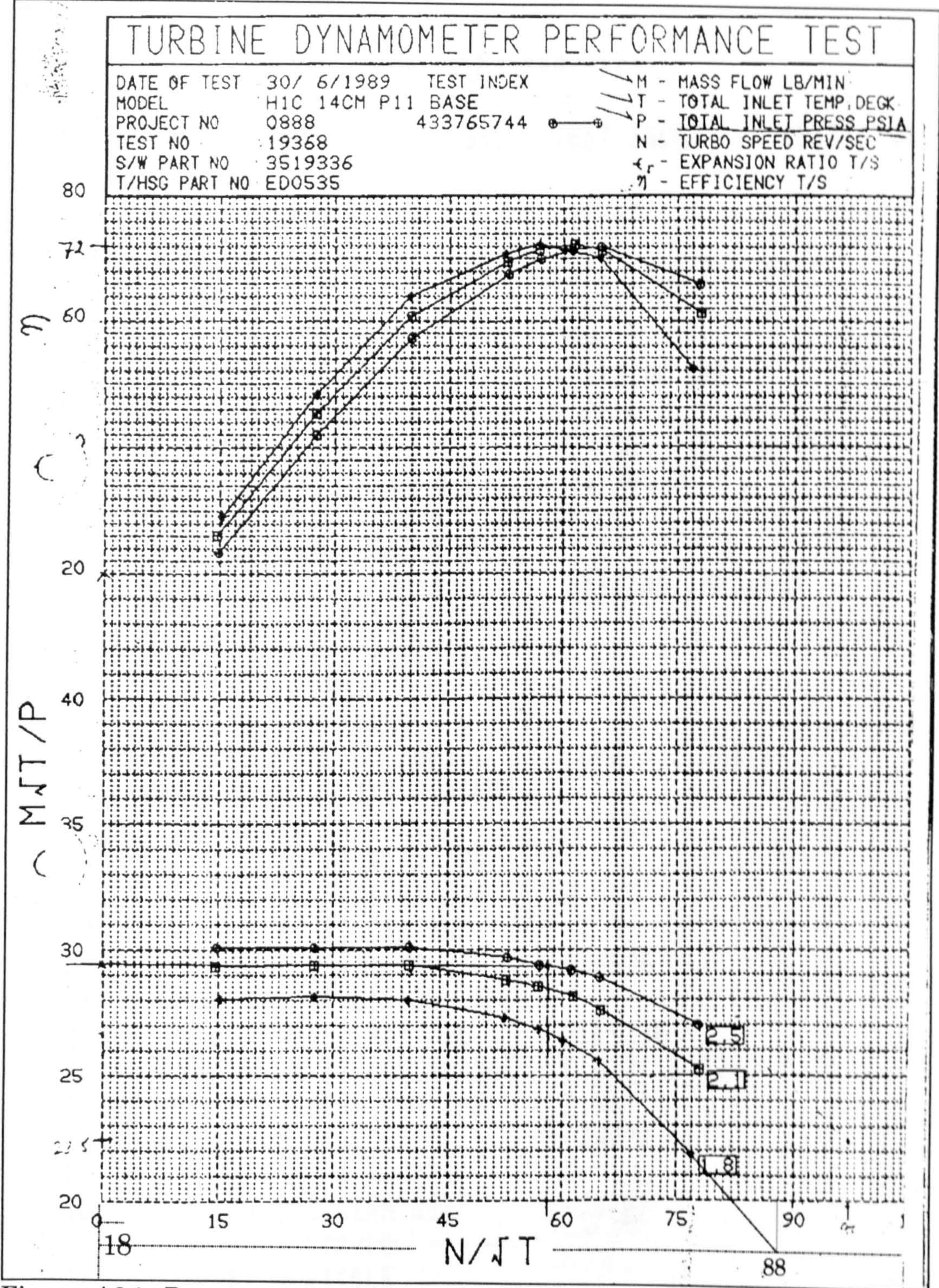


Figure A6.1: Dynamometer performance curves for determining air supply demand.

RAW DATA FROM		CELL 2

DATE SIGNED OFF	30/ 6/1989	TEST INDEX 433765744
1	TEST NUMBER	19368
2	PROJECT NUMBER	0888
3	TURBO MODEL	H1C 14CM P11 BASE
4	ENGINE MODEL	N/A
5	TESTER NAME	BM
6	TEST DESCRIPTION	TURBINE MAP
7	TEST DESCRIPTION	CELL 2
8	SPECIAL FEATURES	DY/BRG F80 000 PSI
9	DATE LAST CALIBRATED	24 AUG 87
10	TURBO PART NUMBER	
11	COMP COVER NUMBER	
12	COMP WHEEL NUMBER	3518200/IMPELLER
13	AIR ORIFICE DIAMETER	
14	COMP OUTLET PIPE DIA	
15	F.W.C. (INS)	
16	DIFF. GAP (INS)	
17	COMP WHEEL OD.(MM)	65MM = 2.559INS
18	COMP WHEEL IND DIA(MM)	
19	SPECIFIC GRAV FUEL	0.842
20	TURB. INLET AREA INS	0.39 : 3.24
21	MASSFLOW VENTURI DIA	0.657
22	LEG VENTURI DIA INS	1.5 : 1.38
23	TURBINE HSING NO.	ED0535
24	TRBINE HSING FLOW TIME	
25	SHAFT WHEEL PART NO.	3519336
26	TRBINE WHEEL CLEARANCE	F.022" 8.029
27	TRBINE WHEEL O/D INS	2.761"
28	MAXIMUM SPEED RPM	130000
29	NOZZLE RING NUMBER	
30	MFLOW UPSTREAM DIA	2.070"
31	SPARE VARIABLE	
32	SPARE VARIABLE	
33	SPARE VARIABLE	

Figure A6.2: Manufacturer's data: Basic data of the Holset gas turbine.

TURBINE DYNAMOMETER PERFORMANCE TEST													CELL 2	

MODEL H1C 14CM P11 BASE PROJECT NO 0888													TEST NO 19368	
TESTED ON 30/ 6/1989													TEST INDEX 433765744	
TESTED BY BH													* Denotes manual override	
SPECIAL FEATURES DY/BRG F80 R80 PSI														
HOUSING PART NUMBER ED0535														
SHAFT AND WHEEL PART NUMBER ... 3519336														
FRONT TURBINE CLEARANCE (IN) .. F.022" B.029"														
HOUSING FLOW TIME (SEC)														
TURBINE WHEEL O.DIA (IN) 2.761"														
MAX. TURBO SPEED 130000														
NOZZLE RING NUMBER..... 0.0														
DATE LAST CALIBRATED 24 AUG 87														
Mass Flow Parameter and Non-Dimensional Speed based on Total temperatures and pressures														
+ Denotes Difference between Total(Average)T/I Temp And One Of The Other T/I Temp IS GT 10.0 DEG C														
NO EXP. RATIO	NO MASS FLOW	N.D. SPEED	EFFY T/S	U/C	POWER KW	MASS FLOW KG/S	AIR/ FUEL	TURB IN PRESS BAR	TURB IN STATIC C	TORQUE N/M	BARO-METER MBAR	TURB OUT PRESS BAR*	TURB IN TOTAL C	
T/S	LB/MIN* SQT(K)/ PSIA	RPS/ SQT (K)												
1	2.494	30.11	14.81	0.12	13.29	0.315	163.24	1.642	496.	5.146	1009.0	0.054	496.9	
2	2.507	27.02	77.87	0.62	32.59	0.271	155.41	1.532	499.	2.397	1009.0	0.004	499.5	
3	2.505	28.90	64.96	0.52	30.19	0.290	154.85	1.541	502.	3.359	1009.0	0.009	502.9	
4	2.503	29.70	52.80	0.42	36.98	0.301	157.78	1.560	499.	4.010	1009.0	0.017	499.5	
5	2.508	30.10	57.22	0.32	32.28	0.309	159.66	1.595	501.	4.612	1009.0	0.029	502.0	
6	2.496	30.09	27.54	0.22	23.62	0.311	163.23	1.607	496.	4.917	1009.0	0.039	497.4	
7	2.501	29.21	61.48	0.49	38.08	0.294	156.89	1.541	497.	3.564	1009.0	0.010	498.5	
8	2.506	29.38	57.06	0.45	37.75	0.297	157.55	1.550	497.	3.792	1009.0	0.012	498.1	
9	2.097	29.37	14.76	0.13	9.97	0.252	153.00	1.176	503.	3.859	1009.2	0.033	503.8	
10	2.092	25.23	70.05	0.68	19.46	0.213	156.45	1.126	498.	1.429	1009.2	0.011	498.6	
11	2.107	27.60	65.14	0.57	25.10	0.232	153.48	1.124	504.	2.198	1009.3	0.004	504.8	
12	2.095	28.82	52.68	0.46	25.19	0.242	155.24	1.110	497.	2.740	1008.7	0.006	498.3	
13	2.103	29.40	40.11	0.35	22.83	0.249	152.03	1.141	499.	3.258	1008.7	0.013	499.7	
14	2.100	29.41	27.61	0.24	17.10	0.251	156.28	1.154	498.	3.548	1008.8	0.021	498.7	
15	2.096	28.14	61.48	0.54	25.51	0.236	153.35	1.112	496.	2.380	1008.8	0.003	497.1	
16	2.102	28.53	56.86	0.50	25.80	0.240	155.76	1.122	498.	2.598	1008.7	0.005	499.2	
17	1.035	28.07	15.23	0.15	7.20	0.204	154.01	0.834	497.	2.711	1008.7	0.010	497.9	
18	1.001	21.03	77.01	0.75	10.06	0.150	161.19	0.827	500.	0.747	1008.7	0.011	500.3	
19	1.004	25.60	64.04	0.63	15.79	0.185	145.38	0.821	500.	1.394	1008.7	0.005	501.0	
20	1.000	27.32	52.34	0.51	17.04	0.197	149.02	0.819	502.	1.860	1008.7	0.002	502.7	
21	1.000	28.00	39.05	0.30	15.01	0.202	150.60	0.823	502.	2.267	1008.6	0.004	502.8	
22	1.002	20.13	27.54	0.27	12.01	0.204	152.32	0.829	498.	2.497	1008.7	0.011	493.3	
23	1.000	26.39	60.22	0.59	16.40	0.189	156.64	0.811	501.	1.557	1008.5	0.003	501.7	
24	1.006	26.83	56.83	0.55	16.78	0.193	151.45	0.800	495.	1.694	1008.5	0.003	496.0	

Figure A6.3: Manufacturer's data: Results of dynamic tests of the gas turbine.

APPENDIX A6.3

AIR BLOWER DETAILS, SELECTION, DATA SHEETS, AND DETERMINATION OF DRIVE DEMANDS

General information on the air blower are provided in the sheet of Figure A6.4. The HR-12 positive displacement air blower was selected on the basis of the required air pressure, in mbar, as given in the selection sheet of Figure A6.5, and the required volume flow rate in m³/hour found in Appendix A6.2. At 500 mbar (relative pressure) the HR-12 blower delivers 471 m³/hour. This is shown in the (blower performance table) given in the sheet of Figure A6.5. Blower package unit description is given in the sheet of Figure A6.6.

The sheet of Figure A6.7 is used to determine the required power to drive the blower at the required pressure and air flow. If 320 m³/hour is selected on the performance curve of Figure A6.7, then the required blower speed is found as 1550 rpm and the corresponding absorbed power is about 7.5 KW. These figures are also valid after correcting the value of ΔT in equation (A6.1), Appendix A6.2, from 50°C to 70°C, as found in the performance curves of Figure A6.7.

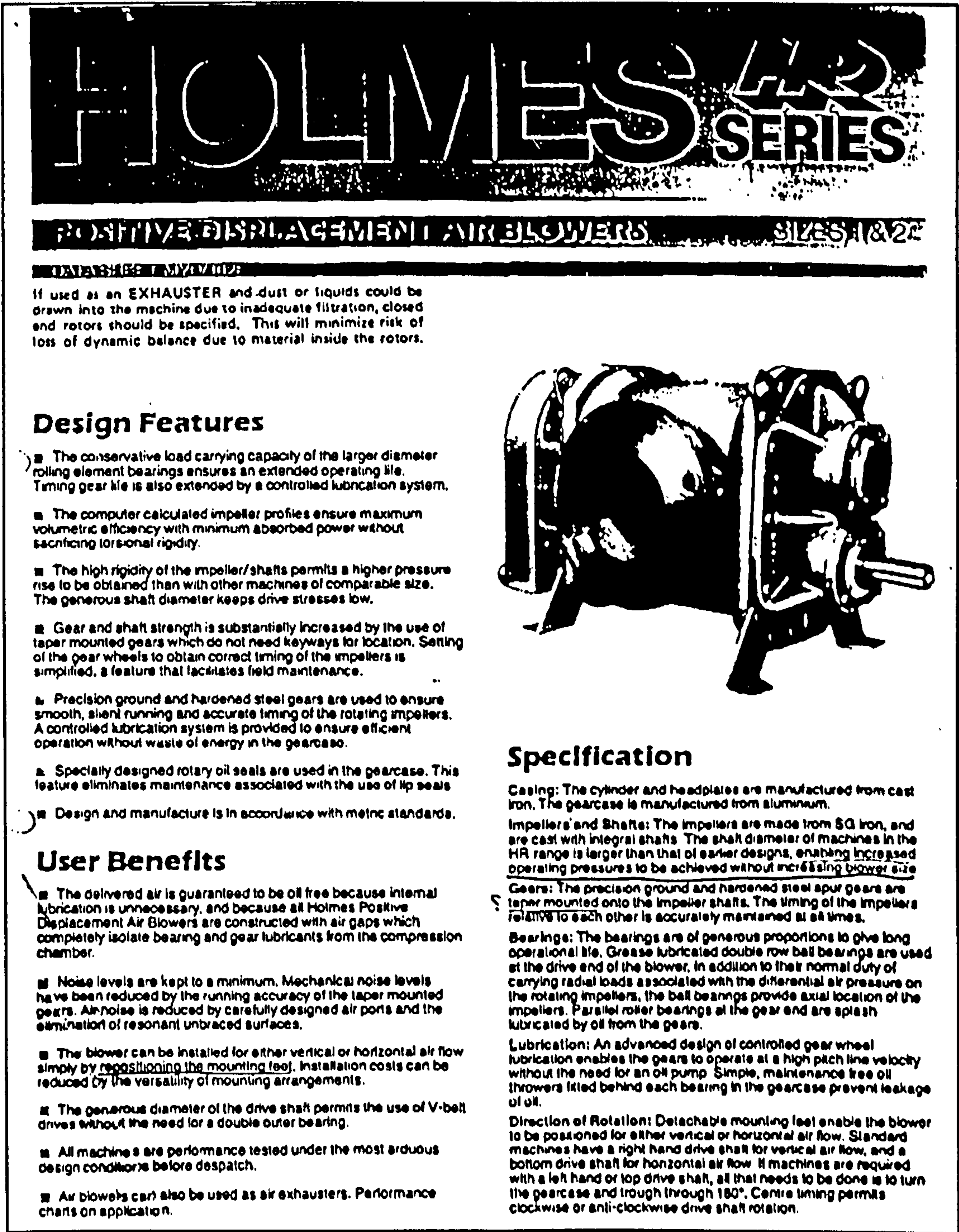


Figure A6.4: Manufacturer's Data: General information on the Peabody Holmes Air Blowers.

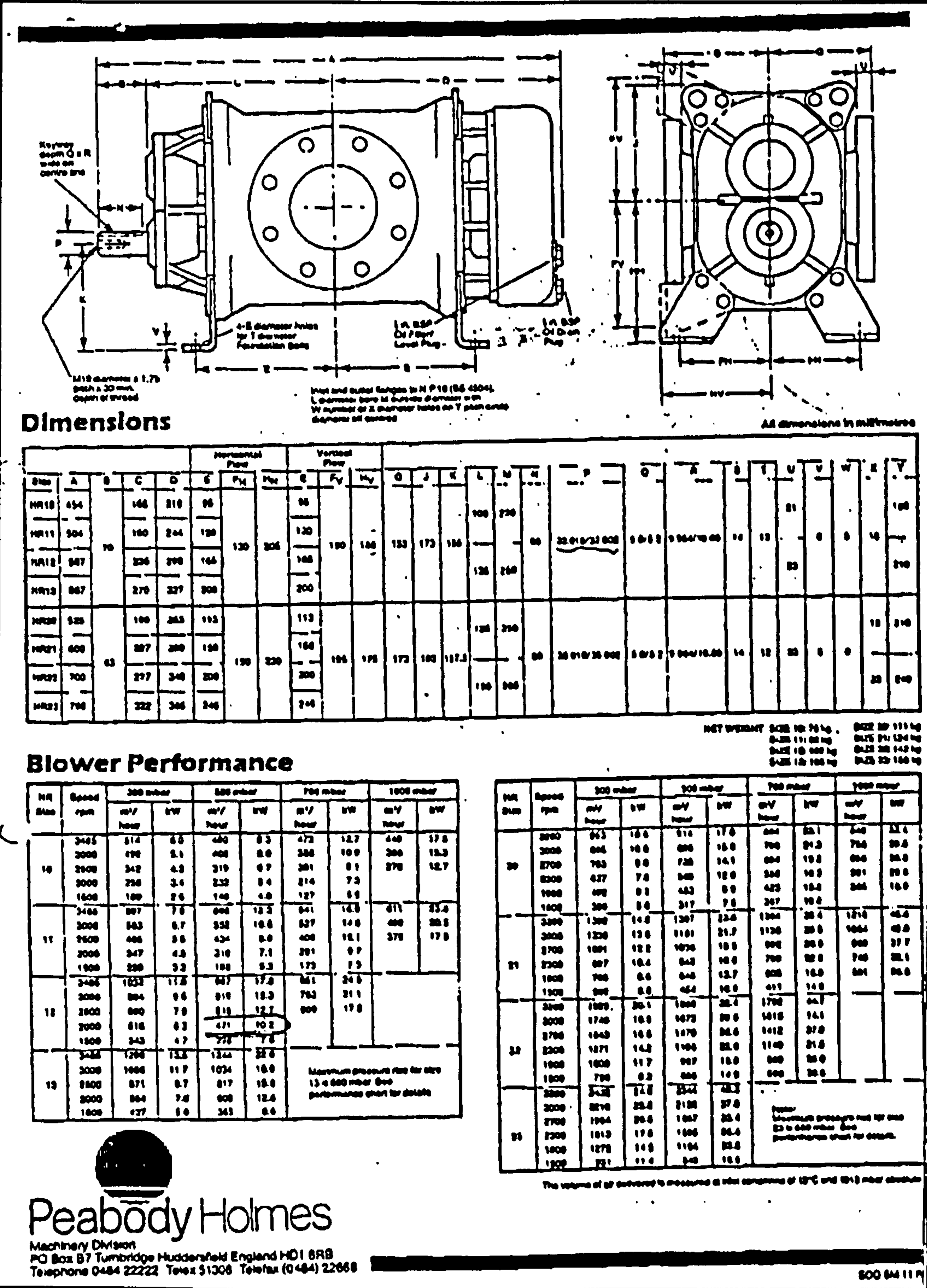


Figure A6.5: Manufacturer's Data: Selection sheet for a range of available air blowers.

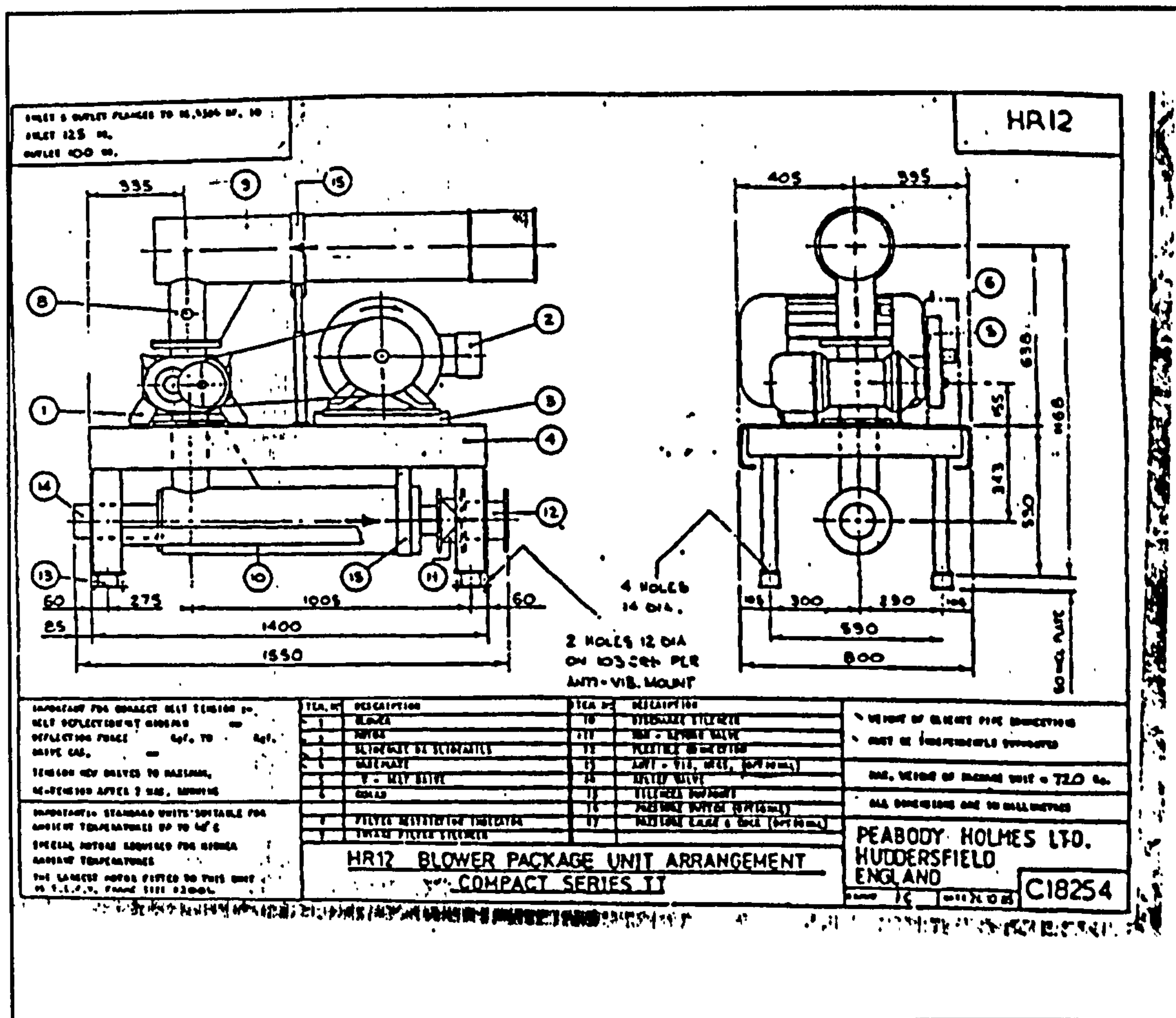


Figure A6.6: Manufacturer's Data: Blower package Unit description and dimensions.

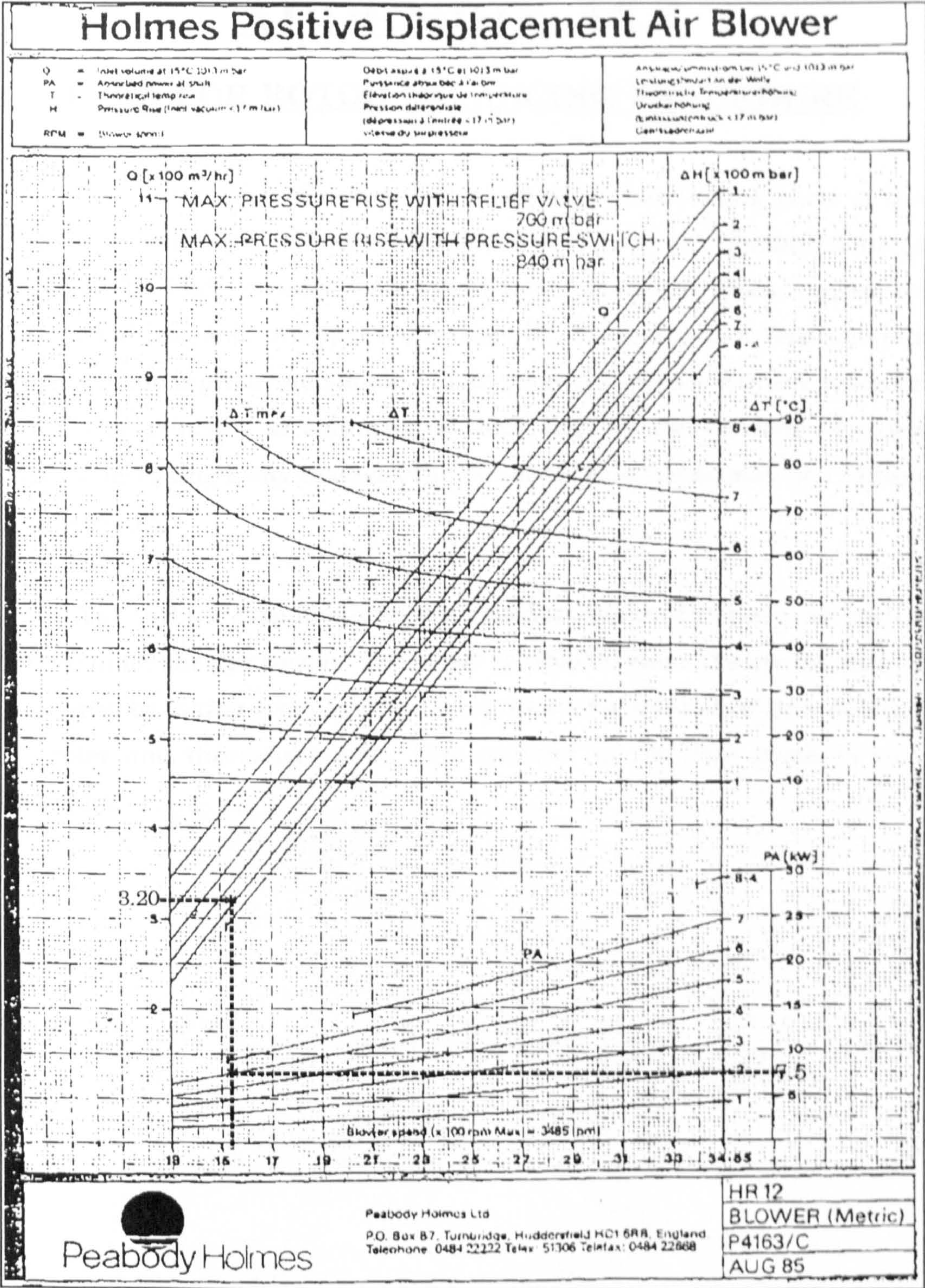


Figure A6.7: Blower performance sheet used for the determination of the required drive for the blower.

APPENDIX A6.4

DATA FOR ROTOR BALANCING PROCEDURE

The importance of dynamically balancing the rotating parts of the high speed rotating machine was indicated in chapter 4. Unbalanced forces can lead to high stresses and vibrations. These are often caused by magnetic forces and improper balancing [90]. Balancing is a very complex operation and is often hand made which requires experience by the operator [146]. The principle of balancing is such that by the addition of extra masses (or taking away masses), the out-of balance forces may be reduced or eliminated.

The turbine manufacturer was asked in this case to run a balancing operation for the gas turbine at a speed of 100,000 rpm. The operation was performed by taking away material from the steel stub shaft after mounting the rotor and the sensor disk. This resulted in the data given in this Appendix.

----- HOLSET DEVELOPMENT HUDDERSFIELD -----	
operator : results run 1	20.03.91 12:10 file name : JOHN rotor : ORIGINAL ROTOR bal. speed: 2507. C/min
<div>plane 1</div> <div>20.1 moz at 333 deg 20.1 = tol</div>	<div>plane 2</div> <div>1.04 moz at 332 deg 1.0 = tol</div>

ROTOR BEFORE BALANCE

----- HOLSET DEVELOPMENT HUDDERSFIELD -----	
operator : results run 5	20.03.91 12:40 file name : rotor : SHAFT + WHEEL bal. speed: 2807. C/min
<div>plane 1</div> <div>0.36 moz at 206 deg in tol</div>	<div>plane 2</div> <div>0.53 moz at 338 deg in tol</div>

BALANCING SHAFT AND WHEEL (SENSOR DISK)

----- HOLSET DEVELOPMENT HUDDERSFIELD -----	
operator : results run 1	20.03.91 09:10 file name : rotor : ROTOR AFTER BALANCE bal. speed: 2000. C/min
<div>plane 1</div> <div>1.73 moz at 46 deg in tol</div>	<div>plane 2</div> <div>0.70 moz at 13 deg in tol</div>

ROTOR AFTER BALANCE

APPENDIX A7.1

TABLES FOR STATIC TEST MEASUREMENT
RESULTS FOR DETERMINING THE MAGNETIC
CHARACTERISTICS OF THE SRG

	$\theta = 8$		$\theta = 12$	
I	Ψ V. μ s	L μ H	Ψ V. μ s	L μ H
0.1	18	180	42	420
0.2	37	185	82	410
0.3	54	180	124	413
0.4	73	182	160	400
0.5	93	186	197	394
0.6	112	186	236	394
1.0	183	183	417	417
1.5	264	176	-	-
2	280	176	820	410
4	720	190	1280	320
7	1250	180	1750	250
10	1920	178	2200	220

Table A7.1: Flux Linkage - Current Measurements at 8 and 12 deg.

	$\theta = 17$		$\theta = 22.5$	
I	$\Psi \text{ V.}\mu\text{s}$	L μH	$\Psi \text{ V.}\mu\text{s}$	L μH
0.2	136	680	158	790
0.3	205	683	-	-
0.4	265	662	312	780
0.5	305	610	390	780
0.6	354	590	480	800
1.0	603	603	906	906
2	1120	560	1480	740
3	1590	530	1865	620
4	1944	486	2240	560
5	2095	419	2460	492
7	2559	365	3010	430
10	3300	330	3750	375

Table A7.2: Flux linkage - Current Measurements at 17 and 22.5 deg.

APPENDIX A8.1

TABLES FOR DYNAMIC TEST MEASUREMENT RESULTS

The procedure of obtaining the dynamic tests results is fully explained in chapter 7. In this Appendix, the results are presented in tabulated form. At a particular set of speed and voltage, the pulse width of the firing angle, referred to as θ_{on} , is fixed by the thumb wheel (or push button switch) at a low value, starting from 10° first, which represents 22% of the phase switching period, whereas the position of the firing angle is taken from a minimum (that which results into a commutation angle θ_{com} of 26°) up to a maximum (that which results into θ_{com} of 38°) into seven steps. The pulse width θ_{on} is then increased by 2° and the process is repeated. The maximum value of θ_{on} is 22° which corresponds to half the phase switching period. This will result into six sets. Each set of particular speed and voltage contains seven separate tables each for a particular value of θ_{on} . In each table seven readings are given in which the only variable input parameter is the position of the firing angle. Measured values of r.m.s. currents per phase in both the phase winding I_{L-rms} , and the power switch I_{sw-rms} are given. From these the term P_{LOSS} (in the tables) is determined which represents the losses including copper losses in the phase winding and the power switch conduction losses, but excluding the on-state diode losses which were added later to determine the efficiency as shown in chapter seven. Measurements for mean current values I_{out} and I_{in} are also given, from which the net generated power P_{gen} is determined.

SPEED = 40,000 RPM VOLTAGE = 30V $\theta_{ON} = 10 \text{ DEG}$

θ_{dly} deg	θ_{com} deg	P_{gen} WATT	$\eta\%$	P_{LOSS} WATT	I_{out} AMP	I_{in} AMP	I_{L-rms} AMP	I_{sw-rms} AMP
16	26	1.2	57.0	0.5	0.58	0.54	0.83	0.48
18	28	7.5	83.9	0.86	0.83	0.58	1.11	0.55
20	30	14.1	83.7	1.9	1.16	0.69	1.67	0.77
22	32	17.4	80.5	3.2	1.43	0.85	2.15	0.99
24	34	16.2	69.1	6.1	1.64	1.1	2.98	1.42
26	36	10.2	56.3	6.7	1.74	1.4	3.06	1.67
28	38	1.2	11.5	8.0	1.74	1.7	3.27	2.04

SPEED = 40,000 RPM VOLTAGE = 30V $\theta_{ON} = 12 \text{ DEG}$

θ_{dly} deg	θ_{com} deg	P_{gen} WATT	$\eta\%$	P_{LOSS} WATT	I_{out} AMP	I_{in} AMP	I_{L-rms} AMP	I_{sw-rms} AMP
14	26	7.2	80.2	1.1	0.97	0.73	1.27	0.7
16	28	16.2	84.3	2.1	1.32	0.78	1.78	0.8
18	30	24.3	84.4	3.3	1.69	0.88	2.23	0.96
20	32	28.5	81.1	5.2	2.04	1.09	2.75	1.24
22	34	27.0	74.6	7.6	2.3	1.4	3.33	1.57
24	36	19.8	59.2	11.9	2.46	1.8	4.0	2.38
26	38	8.1	35.5	13.0	2.45	2.18	4.17	2.54

SPEED = 40,000 RPM VOLTAGE = 30V $\theta_{ON} = 14 \text{ DEG}$

θ_{dly} deg	θ_{com} deg	P_{gen} WATT	$\eta\%$	P_{LOSS} WATT	I_{out} AMP	I_{in} AMP	I_{L-rms} AMP	I_{sw-rms} AMP
12	26	12.3	81.5	1.8	1.41	1.0	1.63	0.83
14	28	24.3	83.7	3.4	1.9	1.09	2.26	0.86
16	30	36.3	83.7	5.4	2.38	1.17	2.87	1.1
18	32	41.1	79.4	8.7	2.84	1.46	3.6	1.52
20	34	39.0	74.4	11.2	3.13	1.83	4.03	1.87
22	36	30.3	62.8	15.6	3.34	2.33	4.67	2.49
24	38	15.6	42.7	18.6	3.37	2.85	5.07	2.82

SPEED = 40,000 RPM VOLTAGE = 30V $\theta_{ON} = 16 \text{ DEG}$

θ_{dly} deg	θ_{com} deg	P_{gen} WATT	$\eta\%$	P_{LOSS} WATT	I_{out} AMP	I_{in} AMP	I_{L-rms} AMP	I_{sw-rms} AMP
10	26	20.4	81.2	3.3	2.05	1.37	2.2	1.0
12	28	38.4	82.3	6.4	2.64	1.36	3.12	1.2
14	30	50.7	81.6	9.2	3.22	1.53	3.73	1.35
16	32	56.1	77.8	13.4	3.7	1.83	4.5	1.77
18	34	51.6	71.6	17.6	4.02	2.3	5.07	2.31
20	36	40.5	60.9	23.0	4.22	2.87	5.73	2.85
22	38	23.7	43.6	27.6	4.28	3.49	6.1	3.6

SPEED = 40,000 RPM VOLTAGE = 30V $\theta_{ON} = 18 \text{ DEG}$

θ_{dly} deg	θ_{com} deg	P_{gen} WATT	$\eta\%$	P_{LOSS} WATT	I_{out} AMP	I_{in} AMP	I_{L-rms} AMP	I_{sw-rms} AMP
8	26	29.4	77.4	6.6	2.86	1.88	3.09	1.46
10	28	54.0	81.2	10.0	3.6	1.80	3.90	1.45
12	30	67.2	80.3	13.6	4.15	1.91	4.57	1.65
14	32	72.3	76.0	19.5	4.66	2.25	5.43	2.04
16	34	66.0	69.5	25.5	4.98	2.78	6.13	2.64
18	36	51.3	59.7	31.0	5.11	3.40	6.67	3.30
20	38	33.3	44.7	37.5	5.18	4.07	7.2	3.97

SPEED = 40,000 RPM VOLTAGE = 30V $\theta_{ON} = 20 \text{ DEG}$

θ_{dly} deg	θ_{com} deg	P_{gen} WATT	$\eta\%$	P_{LOSS} WATT	I_{out} AMP	I_{in} AMP	I_{L-rms} AMP	I_{sw-rms} AMP
6	26	36.9	71.9	11.8	3.76	2.53	4.13	1.95
8	28	65.1	78.4	14.8	4.50	2.33	4.73	1.85
10	30	84.0	77.2	21.2	5.22	2.42	5.67	2.18
12	32	87.0	73.8	27.0	5.64	2.74	6.37	2.55
14	34	81.3	67.9	34.2	6.00	3.27	7.1	3.09
16	36	65.4	59.7	39.9	6.1	3.92	7.67	3.33
18	38	40.8	43.4	49.0	6.07	4.71	8.27	4.4

SPEED = 40,000 RPM

VOLTAGE = 30V

θ_{ON} = 22 DEG

θ_{dly} deg	θ_{com} deg	P_{gen} WATT	$\eta\%$	P_{LOSS} WATT	I_{out} AMP	I_{in} AMP	I_{L-rms} AMP	I_{sw-rms} AMP
4	26	41.1	68.6	15.5	4.77	3.40	4.67	2.43
6	28	75.3	75.1	21.0	5.68	3.17	5.60	2.26
8	30	95.7	75.9	26.0	6.30	3.11	6.27	2.36
10	32	100.8	71.7	35.0	6.74	3.38	7.27	2.86
12	34	93.6	66.4	42.4	7.10	3.98	7.90	3.43
14	36	78.0	56.2	55.7	7.30	4.70	9.00	4.10
16	38	48.6	42.4	61.0	7.10	5.48	9.20	4.97

SPEED = 40,000 RPM VOLTAGE = 40V $\theta_{ON} = 10 \text{ DEG}$

θ_{dly} deg	θ_{com} deg	P_{gen} WATT	$\eta\%$	P_{LOSS} WATT	I_{out} AMP	I_{in} AMP	I_{L-rms} AMP	I_{sw-rms} AMP
16	26	8.8	83.9	1.14	0.78	0.56	1.23	0.77
18	28	19.2	88.2	1.8	1.08	0.6	1.59	0.84
20	30	29.6	87.7	3.1	1.47	0.73	2.11	1.03
22	32	36.4	85.1	5.1	1.84	0.93	2.72	1.35
24	34	33.2	78.5	7.7	2.05	1.22	3.28	1.78
26	36	25.2	68.5	10	2.23	1.6	3.67	2.17
28	38	11.2	44.1	12.6	2.31	2.03	4.03	2.69

SPEED = 40,000 RPM VOLTAGE = 40V $\theta_{ON} = 12 \text{ DEG}$

θ_{dly} deg	θ_{com} deg	P_{gen} WATT	$\eta\%$	P_{LOSS} WATT	I_{out} AMP	I_{in} AMP	I_{L-rms} AMP	I_{sw-rms} AMP
14	26	9.6	74.5	2.38	1.29	1.05	1.8	1.03
16	28	29.6	85.1	3.9	1.81	1.07	2.37	1.15
18	30	44	82.6	6.9	2.35	1.25	3.2	1.37
20	32	50	80.3	10.3	2.79	1.54	3.83	1.9
22	34	46.4	73.7	14.4	3.12	1.96	4.5	2.34
24	36	34	61.4	19.1	3.3	2.45	5.1	2.95
26	38	16.4	39.0	23.3	3.37	2.96	5.6	3.33

SPEED = 40,000 RPM VOLTAGE = 40V $\theta_{ON} = 14 \text{ DEG}$

θ_{dly} deg	θ_{com} deg	P_{gen} WATT	$\eta\%$	P_{LOSS} WATT	I_{out} AMP	I_{in} AMP	I_{L-rms} AMP	I_{sw-rms} AMP
12	26	27.6	81.1	5.0	2.06	1.37	2.67	1.3
14	28	50.8	84.4	7.5	2.7	1.43	3.33	1.41
16	30	66.8	82.3	12	3.34	1.67	4.2	1.8
18	32	72	78.5	17	3.85	2.05	5.0	2.25
20	34	65.5	72.5	21.9	4.2	2.56	5.57	2.84
22	36	50.8	62.1	27.9	4.41	3.14	6.23	3.33
24	38	28.8	43.7	34	4.5	3.78	6.77	4.03

SPEED = 40,000 RPM VOLTAGE = 40V $\theta_{ON} = 16 \text{ DEG}$

θ_{dly} deg	θ_{com} deg	P_{gen} WATT	$\eta\%$	P_{LOSS} WATT	I_{out} AMP	I_{in} AMP	I_{L-rms} AMP	I_{sw-rms} AMP
10	26	53.2	83.3	8.5	3.08	1.75	3.5	1.68
12	28	82.8	83.8	13.3	3.82	1.75	4.47	1.74
14	30	99.6	81.9	18.9	4.48	1.99	5.27	2.31
16	32	104.4	78.3	25.4	4.97	2.36	6.13	2.57
18	34	97.2	73.1	32	5.33	2.9	6.77	3.27
20	36	78.8	65	38.5	5.55	3.58	7.23	4.13
22	38	50.8	50.4	46	5.56	4.29	7.77	4.93

SPEED = 40,000 RPM VOLTAGE = 40V $\theta_{ON} = 18 \text{ DEG}$

θ_{dly} deg	θ_{com} deg	P_{gen} WATT	$\eta\%$	P_{LOSS} WATT	I_{out} AMP	I_{in} AMP	I_{L-rms} AMP	I_{sw-rms} AMP
8	26	67.2	78.9	15	4.23	2.55	4.67	2.17
10	28	121.2	82.9	21.4	5.09	2.06	5.67	2.3
12	30	124.4	79.8	27.5	5.73	2.62	6.43	2.5
14	32	129.2	75.4	37.8	6.32	3.09	7.53	3.04
16	34	117.2	69.7	46.4	6.63	3.7	8.2	3.83
18	36	98.4	61.8	56	6.84	4.38	8.83	4.77
20	38	65.2	47.9	66	6.88	5.25	9.33	5.8

SPEED = 40,000 RPM VOLTAGE = 40V $\theta_{ON} = 20 \text{ DEG}$

θ_{dly} deg	θ_{com} deg	P_{gen} WATT	$\eta\%$	P_{LOSS} WATT	I_{out} AMP	I_{in} AMP	I_{L-rms} AMP	I_{sw-rms} AMP
6	26	75.6	72.1	25.4	5.55	3.66	6.00	3.03
8	28	121.2	76.3	33.2	6.47	3.44	7.00	3.01
10	30	146	75.9	41.4	7.19	3.54	7.9	3.04
12	32	154	73.1	51.3	7.72	3.87	8.73	3.53
14	34	140.4	66.8	64.2	8.00	4.49	9.63	4.43
16	36	117.2	58.2	78.5	8.28	5.35	10.57	5.13
18	38	76.8	44.9	88.5	8.17	6.25	11.05	6.03

SPEED = 40,000 RPM

VOLTAGE = 40V

θ_{ON} = 22 DEG

θ_{dly} deg	θ_{com} deg	P_{gen} WATT	$\eta\%$	P_{LOSS} WATT	I_{out} AMP	I_{in} AMP	I_{L-rms} AMP	I_{sw-rms} AMP
4	26	71.2	62.2	38.4	6.88	5.1	7.3	3.87
6	28	126.4	71.0	46	7.83	4.67	8.2	3.33
8	30	159.2	72.0	55.8	8.66	4.68	9.03	3.67
10	32	168.4	68.0	72.8	9.40	5.0	10.33	4.43
12	34	150.0	61.4	87.7	9.50	5.75	11.33	4.90
14	36	117.2	50.9	106.3	9.60	6.67	12.33	5.87
16	38	73.6	36.7	120	9.66	7.82	12.97	6.67

SPEED = 50,000 RPM

VOLTAGE = 40V

θ_{ON} = 10 DEG

θ_{dly} deg	θ_{com} deg	P_{gen} WATT	$\eta\%$	P_{LOSS} WATT	I_{out} AMP	I_{in} AMP	I_{L-rms} AMP	I_{sw-rms} AMP
16	26	8	87.3	0.7	0.66	0.46	0.97	0.6
18	28	16	88.7	1.4	0.91	0.51	1.4	0.75
20	30	25.2	89.5	2.1	1.23	0.6	1.75	0.85
22	32	30	86.0	3.8	1.54	0.79	2.29	1.24
24	34	28	80.6	5.5	1.75	1.05	2.75	1.53
26	36	20	69.2	7.6	1.87	1.37	3.2	1.88
28	38	9.2	46.4	9.3	1.91	1.68	3.47	2.29

SPEED = 50,000 RPM

VOLTAGE = 40V

θ_{ON} = 12 DEG

θ_{dly} deg	θ_{com} deg	P_{gen} WATT	$\eta\%$	P_{LOSS} WATT	I_{out} AMP	I_{in} AMP	I_{L-rms} AMP	I_{sw-rms} AMP
14	26	17.6	87.2	1.8	1.1	0.66	1.57	0.91
16	28	30.8	88.6	2.9	1.49	0.72	2.03	0.97
18	30	42.4	88.4	4.2	1.91	0.85	2.48	1.15
20	32	46.8	85.1	6.6	2.28	1.11	3.06	1.55
22	34	44.0	80.5	8.9	2.51	1.41	3.50	1.95
24	36	33.2	70.2	12.2	2.66	1.83	4.03	2.47
26	38	18.8	52.1	15.4	2.72	2.25	4.47	2.88

SPEED = 50,000 RPM

VOLTAGE = 40V

θ_{ON} = 14 DEG

θ_{dly} deg	θ_{com} deg	P_{gen} WATT	$\eta\%$	P_{LOSS} WATT	I_{out} AMP	I_{in} AMP	I_{L-rms} AMP	I_{sw-rms} AMP
12	26	31.6	87.4	3.33	1.72	0.93	2.18	1.08
14	28	50.8	88.0	5.36	2.24	0.97	2.79	1.29
16	30	64.4	87.2	7.50	2.75	1.14	3.33	1.44
18	32	68.4	83.3	11.5	3.16	1.45	4.07	1.96
20	34	62.4	78.2	15.0	3.43	1.87	4.57	2.43
22	36	48.8	70.0	18.4	3.56	2.34	4.97	2.97
24	38	29.2	54.4	21.8	3.61	2.88	5.37	3.33

SPEED = 50,000 RPM

VOLTAGE = 40V

θ_{ON} = 16 DEG

θ_{dly} deg	θ_{com} deg	P_{gen} WATT	$\eta\%$	P_{LOSS} WATT	I_{out} AMP	I_{in} AMP	I_{L-rms} AMP	I_{sw-rms} AMP
10	26	48.4	88.0	4.8	2.52	1.31	2.67	1.14
12	28	73.6	87.9	7.9	3.17	1.33	3.47	1.23
14	30	88.0	85.6	12.2	3.72	1.52	4.30	1.50
16	32	92.0	82.6	16.4	4.16	1.86	4.93	2.07
18	34	84.4	77.3	21.65	4.43	2.32	5.57	2.67
20	36	68.0	69.0	27.3	4.62	2.92	6.20	3.20
22	38	45.6	56.4	31.9	4.67	3.53	6.53	3.90

SPEED = 50,000 RPM

VOLTAGE = 40V

θ_{ON} = 18 DEG

θ_{dly} deg	θ_{com} deg	P_{gen} WATT	$\eta\%$	P_{LOSS} WATT	I_{out} AMP	I_{in} AMP	I_{L-rms} AMP	I_{sw-rms} AMP
8	26	64.4	83.4	10.4	3.46	1.85	3.93	1.63
10	28	95.6	84.6	14.4	4.21	1.82	4.67	1.73
12	30	111.6	82.1	19.5	4.79	2.00	5.43	2.02
14	32	116.8	80.5	24.6	5.25	2.33	6.1	2.29
16	34	106.8	75.7	30.3	5.54	2.87	6.67	2.90
18	36	86.8	68.2	36.4	5.74	3.57	7.27	3.33
20	38	58.8	55.7	42.7	5.77	4.30	7.63	4.30

SPEED = 50,000 RPM

VOLTAGE = 40V

θ_{ON} = 20 DEG

θ_{dly} deg	θ_{com} deg	P_{gen} WATT	$\eta\%$	P_{LOSS} WATT	I_{out} AMP	I_{in} AMP	I_{L-rms} AMP	I_{sw-rms} AMP
6	26	78.0	80.5	15.7	4.53	2.58	4.77	2.20
8	28	117.2	82.6	20.8	5.41	2.48	5.60	2.11
10	30	136.0	80.8	28.0	6.00	2.60	6.53	2.30
12	32	138.4	77.5	35.6	6.46	3.00	7.30	2.88
14	34	127.6	72.4	43.8	6.76	3.57	7.97	3.67
16	36	102.8	65.0	50.5	6.88	4.31	8.50	4.10
18	38	70.8	52.4	59.4	6.93	5.16	9.17	4.90

SPEED = 50,000 RPM

VOLTAGE = 40V

θ_{ON} = 22 DEG

θ_{dly} deg	θ_{com} deg	P_{gen} WATT	$\eta\%$	P_{LOSS} WATT	I_{out} AMP	I_{in} AMP	I_{L-rms} AMP	I_{sw-rms} AMP
4	26	87.6	76.3	23.5	5.72	3.53	5.80	2.77
6	28	131.6	78.8	30.7	6.67	3.38	6.27	2.71
8	30	157.5	78.3	38.37	7.33	3.39	7.60	2.84
10	32	162.0	75.2	48.0	7.82	3.77	8.47	3.33
12	34	149.2	70.4	57.2	8.03	4.30	9.12	3.93
14	36	122.4	62.6	67.5	8.16	5.10	9.83	4.67
16	38	83.2	50.2	76.8	8.08	6.00	10.33	5.47

SPEED = 50,000 RPM

VOLTAGE = 50V

θ_{ON} = 10 DEG

θ_{dly} deg	θ_{com} deg	P_{gen} WATT	$\eta\%$	P_{LOSS} WATT	I_{out} AMP	I_{in} AMP	I_{L-rms} AMP	I_{sw-rms} AMP
16	26	13.5	89.4	1.0	0.86	0.59	1.14	0.67
18	28	27.0	90.5	2.0	1.20	0.66	1.7	0.84
20	30	41.5	90.7	3.1	1.62	0.79	2.15	0.90
22	32	46.5	87.4	5.3	1.97	1.04	2.78	1.30
24	34	42.0	81.8	7.8	2.21	1.37	3.33	1.67
26	36	30.0	71.1	10.4	2.55	1.75	3.77	2.15
28	38	13.5	47.9	13.0	2.40	2.13	4.13	2.61

SPEED = 50,000 RPM

VOLTAGE = 50V

θ_{ON} = 12 DEG

θ_{dly} deg	θ_{com} deg	P_{gen} WATT	$\eta\%$	P_{LOSS} WATT	I_{out} AMP	I_{in} AMP	I_{L-rms} AMP	I_{sw-rms} AMP
14	26	30.0	87.9	3.1	1.48	0.88	2.11	1.05
16	28	51.5	89.4	4.7	2.00	0.97	2.63	1.16
18	30	67.0	88.1	7.3	2.52	1.18	3.28	1.42
20	32	70.5	84.7	10.7	2.92	1.51	3.97	1.75
22	34	63.5	79.3	14.3	3.19	1.92	4.47	2.36
24	36	46.5	67.8	19.7	3.33	2.40	5.20	2.93
26	38	25.0	49.6	23.0	3.40	2.90	5.57	3.33

SPEED = 50,000 RPM

VOLTAGE = 50V

θ_{ON} = 14 DEG

θ_{dly} deg	θ_{com} deg	P_{gen} WATT	$\eta\%$	P_{LOSS} WATT	I_{out} AMP	I_{in} AMP	I_{L-rms} AMP	I_{sw-rms} AMP
12	26	53.0	87.4	6.0	2.32	1.26	2.97	1.28
14	28	80.5	89.4	7.5	2.96	1.35	3.33	1.44
16	30	97.0	85.1	14.5	3.57	1.63	4.60	2.05
18	32	101.0	82.8	18.2	4.02	2.00	5.13	2.38
20	34	91.0	77.2	23.8	4.33	2.51	5.83	2.94
22	36	66.5	68.5	27.4	4.49	3.16	6.00	3.73
24	38	36.5	49.7	33.7	4.53	3.80	6.67	4.10

SPEED = 50,000 RPM

VOLTAGE = 50V

 $\theta_{ON} = 16 \text{ DEG}$

θ_{dly} deg	θ_{com} deg	P_{gen} WATT	$\eta\%$	P_{LOSS} WATT	I_{out} AMP	I_{in} AMP	I_{L-rms} AMP	I_{sw-rms} AMP
10	26	81.0	84.7	11.0	3.46	1.84	4.07	1.67
12	28	112.0	84.6	17.5	4.22	1.98	5.17	1.83
14	30	125.0	83.0	22.2	4.83	2.33	5.73	2.37
16	32	127.0	78.9	30.3	5.27	2.73	6.63	2.93
18	34	108.5	72.5	37.3	5.58	3.41	7.23	3.73
20	36	88.0	66.0	41.2	5.76	4.00	7.53	4.10
22	38	51.5	49.6	48.2	5.78	4.75	7.93	5.00

SPEED = 50,000 RPM

VOLTAGE = 50V

 $\theta_{ON} = 18 \text{ DEG}$

θ_{dly} deg	θ_{com} deg	P_{gen} WATT	$\eta\%$	P_{LOSS} WATT	I_{out} AMP	I_{in} AMP	I_{L-rms} AMP	I_{sw-rms} AMP
8	26	103.0	82.9	18.0	4.7	2.64	5.33	1.44
10	28	142.5	82.1	26.7	5.55	2.70	6.33	2.42
12	30	162.5	80.2	35.7	6.18	2.93	7.33	2.77
14	32	161.5	76.6	44.6	6.66	3.43	8.13	3.33
16	34	140.5	70.0	55.3	6.93	4.12	8.90	4.23
18	36	107.5	60.7	64.5	7.15	5.01	9.50	4.93
20	38	69.0	47.4	71.6	7.16	5.78	9.90	5.50

SPEED = 50,000 RPM

VOLTAGE = 50V

 $\theta_{ON} = 20 \text{ DEG}$

θ_{dly} deg	θ_{com} deg	P_{gen} WATT	$\eta\%$	P_{LOSS} WATT	I_{out} AMP	I_{in} AMP	I_{L-rms} AMP	I_{sw-rms} AMP
6	26	114.5	75.0	34.0	6.08	3.79	7.07	3.10
8	28	165.5	77.4	43.5	7.05	3.74	8.07	3.17
10	30	180.0	74.7	55.5	7.72	4.00	9.17	3.33
12	32	175.0	70.1	69.0	8.24	4.74	10.13	4.10
14	34	161.5	65.0	80.9	8.50	5.27	10.90	4.67
16	36	124.0	56.2	90.6	8.68	6.20	11.27	5.80
18	38	79.0	44.4	93.0	8.33	6.75	11.33	6.13

SPEED = 50,000 RPM

VOLTAGE = 50V

θ_{ON} = 22 DEG

θ_{dly} deg	θ_{com} deg	P_{gen} WATT	$\eta\%$	P_{LOSS} WATT	I_{out} AMP	I_{in} AMP	I_{L-rms} AMP	I_{sw-rms} AMP
4	26	100.5	65.1	48.6	7.55	5.54	8.33	4.00
6	28	164.5	70.0	63.0	8.54	5.25	9.67	3.97
8	30	207.0	72.9	70.5	9.31	5.17	10.07	4.17
10	32	205.5	67.6	91.4	9.81	5.70	11.63	4.80
12	34	165.5	59.7	104.5	10.05	6.47	12.40	5.26
14	36	125.5	48.4	127.0	10.00	7.49	13.53	6.27
16	38	70.0	34.5	126.2	9.84	8.44	13.33	6.73

SPEED = 60,000 RPM VOLTAGE = 40V $\theta_{ON} = 14 \text{ DEG}$

θ_{dly} deg	θ_{com} deg	P_{gen} WATT	$\eta\%$	P_{LOSS} WATT	I_{out} AMP	I_{in} AMP	I_{L-rms} AMP	I_{sw-rms} AMP
12	26	22	90.2	1.5	1.27	0.73	1.43	0.69
14	28	38	91.9	2.2	1.65	0.70	1.8	0.72
16	30	54	91.2	3.7	2.12	0.78	2.34	0.89
18	32	64	89.5	5.7	2.57	0.97	2.9	1.12
20	34	62	86.4	7.8	2.82	1.27	3.34	1.5
22	36	56	81.1	10.9	3.1	1.7	3.80	2.18
24	38	52	76.6	13.6	3.2	1.9	4.2	2.3

SPEED = 60,000 RPM VOLTAGE = 40V $\theta_{ON} = 16 \text{ DEG}$

θ_{dly} deg	θ_{com} deg	P_{gen} WATT	$\eta\%$	P_{LOSS} WATT	I_{out} AMP	I_{in} AMP	I_{L-rms} AMP	I_{sw-rms} AMP
10	26	29	88.0	2.7	1.77	1.05	1.9	0.97
12	28	53	90.1	4.2	2.3	0.98	2.46	1.0
14	30	72	88.9	7.0	2.85	1.05	3.23	1.1
16	32	83	87.9	9.1	3.32	1.25	3.67	1.37
18	34	80	83.7	13.0	3.62	1.62	4.34	1.83
20	36	71	79.1	16.0	3.95	2.17	4.67	2.48
22	38	55	71.7	18.9	3.97	2.60	5.0	2.9

SPEED = 60,000 RPM VOLTAGE = 40V $\theta_{ON} = 18 \text{ DEG}$

θ_{dly} deg	θ_{com} deg	P_{gen} WATT	$\eta\%$	P_{LOSS} WATT	I_{out} AMP	I_{in} AMP	I_{L-rms} AMP	I_{sw-rms} AMP
8	26	43	85.7	5.4	2.5	1.42	2.76	1.3
10	28	72	87.8	7.76	3.2	1.41	3.34	1.22
12	30	93	88.9	9.0	3.75	1.42	3.67	1.32
14	32	106	86.4	13.6	4.3	1.65	4.5	1.58
16	34	101	82.2	18.6	4.65	2.12	5.2	2.06
18	36	82	74.9	25.0	4.82	2.78	6.0	2.59
20	38	77	70.7	28.4	5.1	3.17	6.2	3.34

SPEED = 60,000 RPM VOLTAGE = 40V $\theta_{ON} = 22 \text{ DEG}$

θ_{dly} deg	θ_{com} deg	P_{gen} WATT	$\eta\%$	P_{LOSS} WATT	I_{out} AMP	I_{in} AMP	I_{L-rms} AMP	I_{sw-rms} AMP
4	26	97	82.9	17.2	5.23	2.4	5.0	2.02
6	28	133	83.7	21.7	6.0	2.7	5.67	2.00
8	30	147	81.0	30.0	6.42	2.75	6.67	2.38
10	32	144	78.9	33.8	6.67	3.0	7.0	2.86
12	34	132	72.8	44.3	7.0	3.7	8.0	3.34
14	36	102	65.3	49.3	7.0	4.45	8.3	4.00
16	38	66	53.9	51.6	6.95	5.3	8.4	4.37

SPEED = 60,000 RPM

VOLTAGE = 50V

θ_{ON} = 10 DEG

θ_{dly} deg	θ_{com} deg	P_{gen} WATT	$\eta\%$	P_{LOSS} WATT	I_{out} AMP	I_{in} AMP	I_{L-rms} AMP	I_{sw-rms} AMP
16	26	9.3	89.3	0.64	0.68	0.50	0.90	0.51
18	28	22.0	92.8	1.1	0.88	0.44	1.24	0.61
20	30	33.8	92.5	1.9	1.2	0.53	1.64	0.75
22	32	42.5	91.2	3.0	1.56	0.72	2.06	0.97
24	34	43.5	87.9	4.7	1.82	0.95	2.5	1.2
26	36	36.6	85.4	4.9	1.9	1.18	2.9	1.6
28	38	17.7	65.7	7.94	1.84	1.48	3.1	2.0

SPEED = 60,000 RPM

VOLTAGE = 50V

θ_{ON} = 12 DEG

θ_{dly} deg	θ_{com} deg	P_{gen} WATT	$\eta\%$	P_{LOSS} WATT	I_{out} AMP	I_{in} AMP	I_{L-rms} AMP	I_{sw-rms} AMP
14	26	12	86.8	1.2	0.89	0.65	1.23	0.75
16	28	29.8	92.9	1.4	1.23	0.63	1.4	0.77
18	30	50.7	93.2	2.5	1.73	0.71	1.89	0.84
20	32	63.0	91.6	4.3	2.13	0.87	2.46	1.15
22	34	66.4	89.0	6.5	2.49	1.16	3.0	1.53
24	36	44.7	73.6	14	2.9	2.0	4.3	2.58
26	38	25.0	59.5	15	2.9	2.2	4.35	2.7

SPEED = 60,000 RPM

VOLTAGE = 50V

θ_{ON} = 14 DEG

θ_{dly} deg	θ_{com} deg	P_{gen} WATT	$\eta\%$	P_{LOSS} WATT	I_{out} AMP	I_{in} AMP	I_{L-rms} AMP	I_{sw-rms} AMP
12	26	50.4	92.1	3.0	1.92	0.91	2.08	0.95
14	28	75.5	91.2	5.2	2.49	0.98	2.76	1.1
16	30	90.2	90.1	7.8	3.0	1.19	3.34	1.45
18	32	94.0	87.3	11.3	3.41	1.53	3.96	1.92
20	34	87.2	83.8	14.3	3.72	1.97	4.4	2.36
22	36	67.5	76.3	18.3	3.85	2.5	4.86	3.0
24	38	44	64.2	22.0	3.58	2.7	5.15	3.35

SPEED = 60,000 RPM

VOLTAGE = 50V

θ_{ON} = 16 DEG

θ_{dly} deg	θ_{com} deg	P_{gen} WATT	$\eta\%$	P_{LOSS} WATT	I_{out} AMP	I_{in} AMP	I_{L-rms} AMP	I_{sw-rms} AMP
10	26	74.3	91.2	5.5	2.79	1.3	2.81	1.22
12	28	106.7	89.8	9.7	3.5	1.36	3.77	1.45
14	30	123.5	88.1	13.9	4.0	1.6	4.5	1.78
16	32	130.4	86.9	19.3	4.6	2.0	5.26	2.26
18	34	114.4	81.0	23.4	4.82	2.53	5.73	2.68
20	36	93.0	75.4	26.8	4.97	3.11	6.0	3.34
22	38	61.0	63.2	32	5.0	3.78	6.36	4.10

SPEED = 60,000 RPM

VOLTAGE = 50V

θ_{ON} = 18 DEG

θ_{dly} deg	θ_{com} deg	P_{gen} WATT	$\eta\%$	P_{LOSS} WATT	I_{out} AMP	I_{in} AMP	I_{L-rms} AMP	I_{sw-rms} AMP
8	26	104	88.3	11	3.93	1.85	4.0	1.67
10	28	137	87.8	15.8	4.62	1.88	4.8	1.9
12	30	156	86.6	20.5	5.25	2.11	5.46	2.14
14	32	158	82.9	28.5	5.74	2.57	6.4	2.74
16	34	145	80.0	32	6.04	3.14	6.67	3.34
18	36	118	72.6	40.3	6.02	3.84	7.34	4.14
20	38	81	62.2	45	6.02	4.58	7.67	4.56

SPEED = 60,000 RPM

VOLTAGE = 50V

θ_{ON} = 20 DEG

θ_{dly} deg	θ_{com} deg	P_{gen} WATT	$\eta\%$	P_{LOSS} WATT	I_{out} AMP	I_{in} AMP	I_{L-rms} AMP	I_{sw-rms} AMP
6	26	120	85.7	16.5	5.08	2.68	4.86	2.06
8	28	166	86.2	22.5	5.94	2.62	5.73	2.24
10	30	188	84.3	30.3	6.56	2.8	6.67	2.55
12	32	192	80.8	40.5	7.1	3.26	7.66	3.13
14	34	177	77.2	47	7.36	3.82	8.2	3.64
16	36	146	70.5	55.8	7.56	4.64	8.7	4.67
18	38	100	59.1	64	7.5	5.5	9.2	5.34

SPEED = 60,000 RPM VOLTAGE = 50V $\theta_{ON} = 22 \text{ DEG}$

θ_{dly} deg	θ_{com} deg	P_{gen} WATT	$\eta\%$	P_{LOSS} WATT	I_{out} AMP	I_{in} AMP	I_{L-rms} AMP	I_{sw-rms} AMP
4	26	131	78.5	31.3	6.44	3.82	6.63	3.13
6	28	188	82.1	35.8	7.32	3.56	7.16	3.06
8	30	217	80.3	47.6	8.02	3.68	8.34	3.27
10	32	223.5	78.6	54.7	8.55	4.08	8.83	3.9
12	34	204	73.8	66.2	8.8	4.72	9.63	4.56
14	36	171	66.2	81	8.92	5.5	10.5	5.43
16	38	118	56.2	85.7	8.82	6.46	10.67	6.1

SPEED = 60,000 RPM VOLTAGE = 60V $\theta_{ON} = 10 \text{ DEG}$

θ_{dly} deg	θ_{com} deg	P_{gen} WATT	$\eta\%$	P_{LOSS} WATT	I_{out} AMP	I_{in} AMP	I_{L-rms} AMP	I_{sw-rms} AMP
16	26	22	92.0	1.3	0.86	0.5	1.31	0.68
18	28	37.9	93.5	1.8	1.21	0.58	1.62	0.72
20	30	47	92.7	2.7	1.4	0.62	1.92	0.95
22	32	59.8	89.5	5.5	2.0	1.02	2.76	1.34
24	34	54	85.0	8	2.21	1.31	3.34	1.67
26	36	47	79.8	10.3	2.27	1.49	3.5	2.1
28	38	23	62.6	12.4	2.27	1.87	3.9	2.6

SPEED = 60,000 RPM VOLTAGE = 60V $\theta_{ON} = 12 \text{ DEG}$

θ_{dly} deg	θ_{com} deg	P_{gen} WATT	$\eta\%$	P_{LOSS} WATT	I_{out} AMP	I_{in} AMP	I_{L-rms} AMP	I_{sw-rms} AMP
14	26	27	88.5	2.7	1.15	0.7	1.96	0.92
16	28	51	92.6	2.9	1.64	0.78	2.03	0.95
18	30	79	92.0	5.3	2.27	0.95	2.75	1.22
20	32	90	90.1	8	2.71	1.2	3.34	1.58
22	34	90	86.8	11.6	3.0	1.57	4.0	2.03
24	36	68.4	77.0	18.1	3.38	2.24	4.9	2.81
26	38	42	64.4	20.9	3.3	2.6	5.0	3.33

SPEED = 60,000 RPM VOLTAGE = 60V $\theta_{ON} = 14 \text{ DEG}$

θ_{dly} deg	θ_{com} deg	P_{gen} WATT	$\eta\%$	P_{LOSS} WATT	I_{out} AMP	I_{in} AMP	I_{L-rms} AMP	I_{sw-rms} AMP
12	26	61	90.6	4.8	2.2	1.18	2.6	1.21
14	28	97.4	91.2	7.4	2.84	1.21	3.29	1.28
16	30	122	90.1	11	3.47	1.44	4.0	1.64
18	32	129.4	87.7	15.4	3.92	1.76	4.67	2.13
20	34	126.2	84.0	21	4.34	2.23	5.43	2.59
22	36	100.8	77.4	26.3	4.55	2.87	5.93	3.32
24	38	67	65.0	32.9	4.62	3.5	6.5	4.06

SPEED = 60,000 RPM

VOLTAGE = 60V

θ_{ON} = 16 DEG

θ_{dly} deg	θ_{com} deg	P_{gen} WATT	$\eta\%$	P_{LOSS} WATT	I_{out} AMP	I_{in} AMP	I_{L-rms} AMP	I_{sw-rms} AMP
10	26	107	89.7	9.8	3.52	1.74	3.73	1.65
12	28	148	89.6	14.2	4.27	1.8	4.53	1.88
14	30	168	88.2	19.1	4.88	2.08	5.2	2.37
16	32	170.4	84.1	28.4	5.4	2.56	6.3	3.04
18	34	155	79.3	36.3	5.75	3.17	6.96	3.9
20	36	121	71.0	45.2	5.98	3.97	7.7	4.56
22	38	73.6	57.4	50.4	5.98	4.75	7.93	5.3

SPEED = 60,000 RPM

VOLTAGE = 60V

θ_{ON} = 18 DEG

θ_{dly} deg	θ_{com} deg	P_{gen} WATT	$\eta\%$	P_{LOSS} WATT	I_{out} AMP	I_{in} AMP	I_{L-rms} AMP	I_{sw-rms} AMP
8	26	138	86.1	18.8	4.84	2.54	5.16	2.34
10	28	187	87.1	23.8	5.67	2.55	5.86	2.41
12	30	210	84.0	35.5	6.34	2.84	7.16	2.93
14	32	212.7	81.4	43.8	6.9	3.36	7.87	3.63
16	34	194.2	77.3	52	7.27	4.03	8.46	4.34
18	36	159	70.5	61.3	7.5	4.85	9.0	5.2
20	38	110	60.6	68	4.85	5.67	9.34	5.84

SPEED = 60,000 RPM

VOLTAGE = 60V

θ_{ON} = 20 DEG

θ_{dly} deg	θ_{com} deg	P_{gen} WATT	$\eta\%$	P_{LOSS} WATT	I_{out} AMP	I_{in} AMP	I_{L-rms} AMP	I_{sw-rms} AMP
6	26	161	82.9	28.8	6.4	3.72	6.43	3.03
8	28	222	83.9	37.5	7.34	3.64	7.4	3.26
10	30	249	83.1	45	7.95	3.8	8.16	3.34
12	32	250.8	78.6	62.3	8.53	4.35	9.5	4.34
14	34	230	75.0	70.2	8.94	5.1	10.0	4.86
16	36	188	64.2	98.5	9.03	5.9	10.7	5.73
18	38	112	49.5	108	8.94	7.06	11.53	6.67

SPEED = 60,000 RPM

VOLTAGE = 60V

θ_{ON} = 22 DEG

θ_{dly} deg	θ_{com} deg	P_{gen} WATT	$\eta\%$	P_{LOSS} WATT	I_{out} AMP	I_{in} AMP	I_{L-rms} AMP	I_{sw-rms} AMP
4	26	163.9	73.6	53	8.34	5.6	8.7	4.17
6	28	231.5	78.2	58.2	9.1	5.25	9.13	4.34
8	30	277.6	77.7	72.7	9.7	5.08	10.4	4.4
10	32	273.8	76.1	78.8	10.3	5.72	10.7	4.9
12	34	231	69.5	94.2	10.5	6.65	11.0	6.0
14	36	192	61.2	114.4	10.4	7.2	12.1	6.67
16	38	108	43.7	132	10.5	8.7	12.5	7.6

SAMPLE OF BLOWER SPEED MEASUREMENT RESULTS

	SPEED = 40,000 RPM		SPEED = 50,000 RPM	
ANGLE SET deg $\theta_{dly}/\theta_{com}$	VOLTAGE 30 V	VOLTAGE 40 V	VOLTAGE 40 V	VOLTAGE 50 V
4/26	15.9	16.8	19.4	19.4
6/28	16.3	17.0	19.6	20.0
8/30	16.6	17.4	19.8	20.5
10/32	16.65	17.8	19.9	20.5
12/34	16.5	17.5	19.8	20.4
14/36	16.4	17.4	19.6	20.3
16/38	16.3	17.0	19.5	20.0

BLOWER SPEED MEASUREMENT RESULTS, SPEED IS IN Hz

APPENDIX A8.2

SOME RESULTS OF THE MODELLING PROGRAMME FOR COMPARISON WITH DYNAMIC TEST RESULTS

Several cases were considered in chapter 8 to validate the modelling programme by comparing it to the measured results which were presented fully in Appendix A8.1. Details of the programme solutions for some of these cases are given in this Appendix.

Case-1: Operating at 60 volt Sink and 50 volt Source

*****0
Switching Angles: Theta_dly = 14.00 , Theta_com = 32.00 ** Theta_on = 18.00
Dis-Continuous Phase Current I_peak = 12.381 Amp
Step used for theta = 0.050 , Peak Flux Density Bpk = 0.295
Number of Phase Current Pulses = 2 Inductance Scale = 12000
Rotor Speed = 60 krpm Excitation Ve = 50 volts O/P Vo = 50 volts
Input Power per phase = 61.724 W Isw_rms/phase = 2.883 AMP
Output Load Power/phase = 140.917 W IL_rms/phase = 5.990 AMP

Total Power generated = 158.386 W
EFFICIENCY = 83.65% steps = 1874
*****0R
*****0^T

Switching Angles: Theta_dly = 14.00 , Theta_com = 32.00 ** Theta_on = 18.00
Dis-Continuous Phase Current I_peak = 12.381 Amp
Step used for theta = 0.050 , Peak Flux Density Bpk = 0.295
Number of Phase Current Pulses = 2 Inductance Scale = 12000
Rotor Speed = 60 krpm Excitation Ve = 50 volts O/P Vo = 60 volts
Input Power per phase = 61.794 W Isw_rms/phase = 2.883 AMP
Output Load Power/phase = 140.080 W IL_rms/phase = 5.536 AMP

Total Power generated = 156.571 W
EFFICIENCY = 85.38% steps = 1821
*****0^]

Case-2: 60,000 rpm, 60 volts Results for $\theta_{on} = 22^\circ$

*****0

Switching Angles: Theta_dly = 4.00 , Theta_com = 26.00
SET NO. 20 , RUN NO. 1 : Theta_on = 22.00
Dis-Continuous Phase Current I_peak = 14.213 Amp
Step used for theta = 0.050 , Peak Flux Density Bpk = 0.423
Number of Phase Current Pulses = 2 Inductance Scale = 15000
Rotor Speed = 60 krpm Excitation Ve = 60 volts O/P Vo = 60 volts
Input Power per phase = 180.228 W Isw_rms/phase = 4.699 AMP
Output Load Power/phase = 243.575 W IL_rms/phase = 8.199 AMP

Total Power generated = 126.693 W
EFFICIENCY = 68.27% steps = 1819
*****0^[

*****0^[

Switching Angles: Theta_dly = 6.00 , Theta_com = 28.00
SET NO. 20 , RUN NO. 2 : Theta_on = 22.00
Dis-Continuous Phase Current I_peak = 16.207 Amp
Step used for theta = 0.050 , Peak Flux Density Bpk = 0.426
Number of Phase Current Pulses = 2 Inductance Scale = 15000
Rotor Speed = 60 krpm Excitation Ve = 60 volts O/P Vo = 60 volts
Input Power per phase = 159.728 W Isw_rms/phase = 4.595 AMP
Output Load Power/phase = 269.645 W IL_rms/phase = 8.826 AMP

Total Power generated = 219.833 W
EFFICIENCY = 76.87% steps = 3678
*****0^

*****0^

Switching Angles: Theta_dly = 8.00 , Theta_com = 30.00
SET NO. 20 , RUN NO. 3 : Theta_on = 22.00
Dis-Continuous Phase Current I_peak = 18.109 Amp
Step used for theta = 0.050 , Peak Flux Density Bpk = 0.427
Number of Phase Current Pulses = 2 Inductance Scale = 15000
Rotor Speed = 60 krpm Excitation Ve = 60 volts O/P Vo = 60 volts
Input Power per phase = 150.809 W Isw_rms/phase = 4.949 AMP
Output Load Power/phase = 288.888 W IL_rms/phase = 9.565 AMP

Total Power generated = 276.159 W
EFFICIENCY = 78.21% steps = 5577
*****0I

Switching Angles: Theta_dly = 10.00 , Theta_com = 32.00
SET NO. 20 , RUN NO. 4 : Theta_on = 22.00
Dis-Continuous Phase Current I_peak = 19.838 Amp
Step used for theta = 0.050 , Peak Flux Density Bpk = 0.425
Number of Phase Current Pulses = 2 Inductance Scale = 15000
Rotor Speed = 60 krpm Excitation Ve = 60 volts O/P Vo = 60 volts
Input Power per phase = 162.986 W Isw_rms/phase = 5.585 AMP
Output Load Power/phase = 299.268 W IL_rms/phase = 10.264 AMP

Total Power generated = 272.565 W
EFFICIENCY = 75.39% steps = 7513
*****0Y

Switching Angles: Theta_dly = 12.00 , Theta_com = 34.00
SET NO. 20 , RUN NO. 5 : Theta_on = 22.00
Dis-Continuous Phase Current I_peak = 21.523 Amp
Step used for theta = 0.050 , Peak Flux Density Bpk = 0.423
Number of Phase Current Pulses = 2 Inductance Scale = 15000
Rotor Speed = 60 krpm Excitation Ve = 60 volts O/P Vo = 60 volts
Input Power per phase = 181.787 W Isw_rms/phase = 6.290 AMP
Output Load Power/phase = 304.220 W IL_rms/phase = 10.876 AMP

Total Power generated = 244.866 W
EFFICIENCY = 70.80% steps = 9487
*****0^O

Switching Angles: Theta_dly = 14.00 , Theta_com = 36.00
SET NO. 20 , RUN NO. 6 : Theta_on = 22.00
Dis-Continuous Phase Current I_peak = 23.189 Amp
Step used for theta = 0.050 , Peak Flux Density Bpk = 0.420
Number of Phase Current Pulses = 2 Inductance Scale = 15000
Rotor Speed = 60 krpm Excitation Ve = 60 volts O/P Vo = 60 volts
Input Power per phase = 204.463 W Isw_rms/phase = 7.034 AMP
Output Load Power/phase = 303.460 W IL_rms/phase = 11.393 AMP

Total Power generated = 197.995 W
EFFICIENCY = 63.76% steps = 11498
*****0j

Switching Angles: Theta_dly = 16.00 , Theta_com = 38.00
SET NO. 20 , RUN NO. 7 : Theta_on = 22.00
Dis-Continuous Phase Current I_peak = 23.972 Amp
Step used for theta = 0.050 , Peak Flux Density Bpk = 0.429
Number of Phase Current Pulses = 2 Inductance Scale = 15000
Rotor Speed = 60 krpm Excitation Ve = 60 volts O/P Vo = 60 volts
Input Power per phase = 245.869 W Isw_rms/phase = 8.213 AMP
Output Load Power/phase = 319.575 W IL_rms/phase = 12.445 AMP

Total Power generated = 147.413 W
EFFICIENCY = 51.89% steps = 13606

APPENDIX A9.1

MODEL RESULTS FOR SOME OF THE ALTERNATIVE CASES OF STATOR SIZE, MATERIAL, AND POLE CONFIGURATION

CASE-1 The Case of Maximum Power at 80,000 rpm

stator poles = 16 rotor poles = 8 no. of phases m = 2
stator arc = 11.340 rotor arc = 11.250 Fringing factor = 1.400
Important Values of theta in (deg) which define L profile are :
thm = 22.500, thr = 8.004, thf = 36.996
thm1 = 22.455, thm2 = 22.545

stator inner dia id = 4.374E-02 m core (axial) length = 2.500E-02 m
sat flux density B = 0.230 Tesla Air gap g = 1.250E-04 m
Inductance ratio = 6.500 no. of turns N = 9.5

A = 1.082129E-04 sqm, Isat = 2.408266 Amp,
La = 7.854459E-04 H, Lmin = 1.428083E-04 H , k = 3.965
*****0
Switching Angles: Theta_dly = 11.10 , Theta_com = 30.20 ** Theta_on = 19.10
Dis-Continuous Phase Current I_peak = 20.821 Amp
Step used for theta = 0.050 , Peak Flux Density Bpk = 0.470
Max Flux Density 0.47 is 2.05 times Bsat!
Number of Phase Current Pulses = 2 Inductance Scale = 8000
Rotor Speed = 80 krpm Excitation Ve = 100 volts O/P Vo = 100 volts
Input Power per phase = 255.581 W Isw_rms/phase = 5.552 AMP
Output Load Power/phase = 481.634 W IL_rms/phase = 10.272 AMP
Total Power generated = 452.106 W
EFFICIENCY = 83.60% steps = 1863

CASE-2 The Case of a 16/8 All-Steel SRG

stator poles = 16 rotor poles = 8 no. of phases $m = 2$
 stator arc = 11.340 rotor arc = 11.250 Fringing factor = 1.400
 Important Values of theta in (deg) which define L profile are :
 thm = 22.500, thr = 8.004, thf = 36.996
 thm1 = 22.455, thm2 = 22.545

stator inner dia id = 4.374E-02 m core (axial) length = 2.500E-02 m
 sat flux density B = 1.000 Tesla Air gap g = 1.250E-04 m
 Inductance ratio = 6.500 no. of turns N = 9.5

A = 1.082129E-04 sqm, Isat = 10.470720 Amp,
 La = 7.854459E-04 H, Lmin = 1.428083E-04 H , k = 3.965

(A) Solution for very high current density, i.e. infinite cooling:

*****0

Switching Angles: Theta_dly = 13.00 , Theta_com = 32.00 ** Theta_on = 19.00

Dis-Continuous Phase Current I_peak = 97.630 Amp

Step used for theta = 0.050 , Peak Flux Density Bpk = 2.042

Max Flux Density 2.04 is 2.04 times Bsat!

Number of Phase Current Pulses = 2 Inductance Scale = 8000

Rotor Speed = 50 krpm Excitation Ve = 280 volts O/P Vo = 280 volts

Input Power per phase = 3453.511 W Isw_rms/phase = 27.066 AMP

Output Load Power/phase = 5730.217 W IL_rms/phase = 46.784 AMP

Total Power generated = 4553.412 W

EFFICIENCY = 72.05% steps = 1880

*****0X

(B) Solution for lower current density:

*****0

Switching Angles: Theta_dly = 13.00 , Theta_com = 32.00 ** Theta_on = 19.00

Dis-Continuous Phase Current I_peak = 64.920 Amp

Step used for theta = 0.050 , Peak Flux Density Bpk = 1.474

Number of Phase Current Pulses = 2 Inductance Scale = 8000

Rotor Speed = 50 krpm Excitation Ve = 200 volts O/P Vo = 200 volts

Input Power per phase = 1432.979 W Isw_rms/phase = 16.207 AMP

Output Load Power/phase = 2929.001 W IL_rms/phase = 31.499 AMP

Total Power generated = 2992.042 W

EFFICIENCY = 79.31% steps = 1883

CASE-3 The case of a 2-Phase 4/2 All-Steel SRG

stator poles = 4 rotor poles = 2 no. of phases m = 2
stator arc = 22.500 rotor arc = 22.500 Fringing factor = 1.200
Important Values of theta in (deg) which define L profile are :
thm = 90.000, thr = 56.250, thf = 123.750

stator inner dia id = 4.374E-02 m core (axial) length = 2.500E-02 m
sat flux density B = 1.000 Tesla Air gap g = 1.250E-04 m
Inductance ratio = 8.000 no. of turns N = 70.0

A = 2.147082E-04 sqm, Isat = 1.421026 Amp,
La = 2.115313E-02 H, Lmin = 3.021876E-03 H , k = 1.698
*****0
Switching Angles: Theta_dly = 52.00 , Theta_com = 120.00 ** Theta_on = 68.00
Dis-Continuous Phase Current I_peak = 19.622 Amp
Step used for theta = 0.050 , Peak Flux Density Bpk = 2.084
Max Flux Density 2.08 is 2.08 times Bsat!
Number of Phase Current Pulses = 2 Inductance Scale = 8000
Rotor Speed = 50 krpm Excitation Ve = 280 volts O/P Vo = 280 volts
Input Power per phase = 588.256 W Isw_rms/phase = 4.912 AMP
Output Load Power/phase = 1052.038 W IL_rms/phase = 8.693 AMP
Total Power generated = 927.563 W
EFFICIENCY = 91.11% steps = 7320
*****0^X

CASE-4 The Case of a Maximum Power at 50,000 rpm for 25 mm and 75 mm Core length 16/8 SRG

(A) Solution for core length = 25

*****0

Switching Angles: $\theta_{dly} = 13.10$, $\theta_{com} = 30.30$ ** $\theta_{on} = 17.20$
Dis-Continuous Phase Current $I_{peak} = 20.708$ Amp
Step used for $\theta = 0.050$, Peak Flux Density $B_{pk} = 0.466$
Max Flux Density 0.47 is 2.03 times B_{sat} !
Number of Phase Current Pulses = 2 Inductance Scale = 8000
Rotor Speed = 50 krpm Excitation $V_e = 70$ volts O/P $V_o = 70$ volts
Input Power per phase = 163.156 W $I_{sw_rms/phase} = 5.356$ AMP
Output Load Power/phase = 286.726 W $I_{L_rms/phase} = 9.517$ AMP

Total Power generated = 247.139 W
EFFICIENCY = 76.25% steps = 1819

*****0^[

(B) Solution for core length = 75 mm

*****0^A

Switching Angles: $\theta_{dly} = 11.30$, $\theta_{com} = 31.50$ ** $\theta_{on} = 20.20$
Dis-Continuous Phase Current $I_{peak} = 22.373$ Amp
Step used for $\theta = 0.050$, Peak Flux Density $B_{pk} = 0.476$
Max Flux Density 0.48 is 2.07 times B_{sat} !
Number of Phase Current Pulses = 2 Inductance Scale = 8000
Rotor Speed = 50 krpm Excitation $V_e = 180$ volts O/P $V_o = 180$ volts
Input Power per phase = 525.220 W $I_{sw_rms/phase} = 6.223$ AMP
Output Load Power/phase = 948.735 W $I_{L_rms/phase} = 11.217$ AMP

Total Power generated = 847.029 W
EFFICIENCY = 80.97% steps = 1905

*****0q

LIST OF REFERENCES

- [1] Lawrenson P.J. et al, "Variable-speed switched reluctance motors", *IEE proc.*, vol.127, Pt.B, no.4, July 1980, pp 253-265.
- [2] Fitzgerald A.E., Kingsley C., Umans S.D., "Electric Machinery", chapter ten, McGraw-Hill ©, London, 5th ed, 1992.
- [3] Miller T.J.E., "Brushless Permanent-magnet and reluctance motor drives", chapter seven, Clarendon Press ©, Oxford 1989.
- [4] Oljaca M., Corda, J., "An investigation of control of SRM supplied by AC pulses". *EPE'91, Florence*, vol.1, pp 404-406.
- [5] Garlish G., "An idea 100 years old comes to fruition", *Financial Times, Technology section*, Jan. 26 1983.
- [6] Gray C.B., "Electrical machines and drive systems", Longman Scientific & Technical © 1989.
- [7] Stephenson J.M., Corda J., "Computation of torque and current in doubly salient reluctance motors from non-linear magnetisation data", *IEE proc.* vol.126, no.5, pp 393-396, May 1979.
- [8] Arumugam R., et al, "Magnetic field analysis of a switched reluctance motor using a two-dimensional finite element model", *IEEE T-MAG*, vol.MAG-21, no.3, Sept 1985, pp 1183-1185.
- [9] Lindsay J.F., et al, "Finite element analysis characterisation of a switched reluctance motor with multi-tooth per stator pole", *IEE proc.*, vol.33 Pt.B, no.6, Nov. 1986.
- [10] Stephenson J.M., El-Khazendar, "Saturation in doubly salient reluctance motors", *IEE proc.*, vol.136, Pt.B, no.1, January 1989, pp 50-58.
- [11] Lang J.H. and Vallese F.J., "Variable reluctance motor drives for electric vehicle propulsion", *MIT Final report, DOE/CS-54209-26*, May 1985.
- [12] Torrey DA, "Excitation of variable reluctance motor drives", *Electric machines and power systems*, vol.19, no.6, Nov-Dec 1991, 19:713-729.
- [13] Elmas C., and Dela Parra, "A DSP controlled switched reluctance motor drive system for wide range of operating speeds", *PESC'92*, pp 844-850.
- [14] Lawrenson PJ, et al, "Controlled speed SR motors, present status and future potential", *Proc. 1st Europ. Conf. on Elect. Drives / Motors / Controls*, University of Leeds, June 1982.
- [15] Miller TJE, Bower PG, Becerra R, and Ehsani M, "Four quadrant brushless reluctance motor drive", *Proc. IEE Conf on PEVD*, 13-15 July 1988, London, Conf pub 291, pp 273-276.
- [16] Ilic-Spong M, et al, "Feedback linearizing control of switched reluctance motors", *IEEE Transactions on Automatic Control*, vol. AC-32, no.5, May 1987 pp 371-379.
- [17] Sudgen DM, Randall SP, and Webster PD, "Low-power controlled-speed drives using SR motors", *IEE conf on PEVD*, 13-15 July 1988, London, Conf publ 291, pp 269-272.

REFERENCES

- [18] Kamper MJ, "Four quadrant control of a 20 W switched reluctance motor drive for near servo applications", *EPE conf, Florence, Sept 1991, vol.1, pp 386-389.*
- [19] Miller TJE, Bower PG, Becerra R, and Ehsani M, "Four quadrant brushless reluctance motor drive", *Proc. IEE Conf on PEVD, 13-15 July 1988, London, Conf pub 291, pp 273-276.(the same as [15]).*
- [20] Lawrenson P, "Switched reluctance drives' applications and potential", *Seminar on electrical industrial drives, Coventry May 1989, pp B1-B7.*
- [21] Ray WF and Davis R, "Inverter drive for doubly salient reluctance motor: its fundamental behaviour, linear analysis and cost implications", *IEE proc. electric power applications, Dec. 1979, vol.2, no.6. pp 185-193.*
- [22] Chappel PH, Ray WF, Blake RJ, "Microprocessor control of a variable reluctance motor", *IEE proc, vol.131, Pt.B, no.2, March 1984, pp 51-60.*
- [23] Krishnan R, Mang X, Bharadwaj AS, "Design and performance of a microcontroller-based switched reluctance motor drive system", *Electric machines and power systems, vol.18, 1990, pp 359-373.*
- [24] Ehsani M, et al, "Development of a unipolar converter for variable reluctance motor drives", *IEEE - IAS Annual meeting Sept. 1985 pp 1062-1068.*
- [25] Mang X, et al, "Design and performance of an interactive personal computer controller for switched reluctance motor drives", *Conf record of the IEEE IAS Annual meeting Oct 1988, pp 515-519.*
- [26] Davis R, et al, "Inverter drive for switched reluctance motor: circuits and components ratings", *Proc IEE Pt.B, vol.128, no.2, March 1981, pp 126-136.*
- [27] Stiebler M, "A low voltage switched reluctance motor with experimentally optimised control", *ICEM'92 pp 532-536.*
- [28] Ilic-Spong M, et al, "Feedback linearizing control of switched reluctance motors", *IEEE Transactions on Automatic Control, vol. AC-32, no.5, May 1987 pp 371-379.(the same as [16]).*
- [29] Taylor D, "An experimental study on composite control of switched reluctance motors", *IEEE Control systems Feb 1991 pp 31-36.*
- [30] Rochford, et al, "Development of smooth torque in switched reluctance motors using self-learning techniques", *EPE'93 vol.6, pp 14-19.*
- [31] Buja GS, et al, "Variable structure control of an SRM drive", *IEEE T-Industrial electronics, vol.140, no.1, Feb 93, pp 56-63.*
- [32] Reay, Green, and Williams, "Neural networks used for torque ripple minimisation for a switched reluctance motor", *EPE'93 vol.6, pp 1-5.*
- [33] Krishnan R, Materu P, "Analysis and design of a new converter topology for switched reluctance motor drives", *IEEE Proc IAS conf, San Diego, Oct 1989, pp 1181-1185.*
- [34] Pulle DWJ, "Performance of split-coil SR drives", *IEE proc, vol.135, no.6, Nov.88, pp 318-323.*

REFERENCES

- [35] Liang F, Liao Y, Lipo TA, "A new variable reluctance motor utilizing an auxiliary commutation winding", *IEEE proc IAS'92, Houston, Texas, Oct 1992, vol.1, pp 219-225.*
- [36] Vukosavic S, Stefanvic VR, "SRM inverter topologies: A comparative evaluation", *IEEE Trans on Indust. App., vol.27, no.6, 1991, pp 1034-1047.*
- [37] Stephenson JM, "High performance switched reluctance drives" *Drives, motors and controls '85, Conf proc, July 15-17, 1985.*
- [38] Pollock C, Williams B, "A unipolar converter for a switched reluctance motor", *IEEE Trans IA, vol.26, no.2, March/April 1990, pp 222-228.*
- [39] Stephenson JM, Blake RJ, "The design and performance of a range of a general-purpose industrial SR drives for 1 kW to 110 kW", *Proc IEEE IAS conf, San Diego, California, Oct 1989, pp 99-107.*
- [40] Miles AR, "Design of 5 MW, 9000 V, switched reluctance motor", *IEEE T-EC, vol.6, no.3, Sept 1991, pp 484-491.*
- [41] Moallem M, Ong CM, "Predicting the steady-state performance of a switched reluctance machine", *Proc IEEE IAS conf, San Diego, California, Oct 1989, pp 529-537.*
- [42] Torrey DA, Lang J, "Modelling a non-linear variable reluctance motor", *Proc. IEE, vol.137, Pt.B, no.5, Sept 1990, pp 314-326.*
- [43] Veltman A, Bosch P, "A universal method for modelling electrical machines", *Proc. IEE 5th ICEM conf. 1991, London, pp 193-197.*
- [44] Staton D, McGlip, Miller TJE, Gray G, "High speed PC-based CAD for motor drives", *EPE'93, vol.6, pp 26-31.*
- [45] Tohumco M, Ertan HB, "Prediction of performance of switched reluctance motor for design purposes", *Proc. of ICEM '88 conf., Pisa Italy, 12-14 Sept. 1988, vol.2, pp 551-556.*
- [46] Pulle DWJ, "New data base for switched reluctance drive simulation", *Proc. IEE, Pt.B, vol.138, no.6, Nov. 91, pp 331-337.*
- [47] Mohgbelli H, "Analysis of the switched reluctance motor drive using finite element method to predict steady state performance", *PhD Dissertation, University of Missouri-Columbia, May 1989.*
- [48] Mohgbelli H, Adams GE, Hoft RG, "Prediction of the instantaneous and the steady state torque of the switched reluctance motor using the finite element method", *Conf. record of the IEEE IAS Annual meeting, Pittsburgh, Oct. 2-7, 1988, pp 59-70.*
- [49] Faiz J, "Prediction of static magnetisation characteristics of switched reluctance motors for general rotor positions", *EPE'91, Florence, vol.1, pp 355-359.*
- [50] Pulle DWJ, "Magnetic analysis of a switched reluctance motor using a finite difference method" *EPE'91, Florence, vol.1, pp 366-368.*
- [51] Ray WF et al, "High performance switched reluctance brushless drives", *IEEE T-IAS, vol.IA-22, no.4, July/August 1986, pp 722-730.*
- [52] Miller TJE, "Converter volt-ampere requirements of the switched reluctance drive" *IEEE T-IAS, vol.IA-21, 1985, pp 1136-1144.*

REFERENCES

- [53] Acarnley PP et al, "Detection of rotor position in stepping and switched reluctance motors by monitoring of current waveform", *IEEE T-Indust. Electronics*, vol.IE-32, no.3, Aug 1985, pp 215-222.
- [54] "Discussion on variable-speed switched-reluctance motor systems", *IEE Proc.*, vol.128, Pt.B, no.5, Sept. 1981, pp 260-268.
- [55] Hucker D, Semlow R, Glennon G, "Development of a family of light-weight short duration turbo-alternator power supplies", *Intersociety energy conv. conf.*, Florida USA 1967, pp 517-526.
- [56] MacMinn SR, Jones Wd, "A very high speed switched-reluctance starter-generator for aircraft engine applications", *Proc. of IEEE NAECON'89*, Dayton Ohio, May 1989, pp 1758-1764.
- [57] Finch JW, Metwally HMB, Harris MR, "Switched reluctance motor excitation current: scope for improvement", *Proc. of PEVD conf.*, Birmingham, Nov. 1986, *IEE conf. publ.* 264, pp 196-199.
- [58] Faiz J, et al "The multi-tooth per stator pole switched reluctance motor: four teeth per pole", *Proc. of ICEM '88 conf.*, Pisa Italy, 12-14 Sept. 1988, vol.2, pp 563-568.
- [59] Welburn R, "Ultra high torque motor system for direct drive robotics", *Proc. of Robots conf.*, Detroit, MI, June 4-7 1984, vol.2, pp 19/63-19/71.
- [60] Fink D, and Beaty H, [ed.], "Standard handbook for electrical engineers", New York, McGraw-Hill, 12th ed. 1987.
- [61] Beauchamp ED, "Aircraft electrical control systems", *Proc. of NAECON'85*, vol.2, pp 1527-1535.
- [62] Lindsay OL, "Direct-drive turbo alternators", *Proc. IEEE conf. IAS Annual meeting*, vol.2, pp 320-328, 1989.
- [63] Jahns TM, Maldonado MA, "A new resonant link aircraft power generating system", *IEEE T-AES*, Jan. 1993.
- [64] Slobodan Cuk, "Integrated magnetics versus conventional power filtering", *9th inter. telecom. energy conf. INTELEC'87*, vol.9 pp 61-75.
- [65] Malmquist A, et al, "Development of a small gas turbine-driven high speed generator", *Conf. on high-speed technology*, Finland 1988, pp 187-198.
- [66] Millner R, "High-speed high-efficiency permanent magnet motor-generator", *3rd Int. workshop on rare earth cobalt magnets and their applications*, Univ. of California San Diego 1978, pp 139-153.
- [67] Gutt H, "Development of small very high speed AC drives and considerations about their upper speed/ output limit", *Conf. on high-speed technology*, Finland 1988, pp 199-215.
- [68] Jokl AL, "Electric generators: technology status", *IEEE AES systems magazine*, Dec. 1991, vol.6, no.12, pp 56-59.
- [69] Amaratunga G, et al, "Optimum magnetic circuit configurations for permanent magnet aerospace generators", *IEEE T-AES*, March 1985, vol.AES-21, no.2, pp 230-255.
- [70] Marcusson B, "The gas turbine as a prime mover for standby power applications", *9th inter. telecom. energy conf. INTELEC'87*, vol.9 pp 424-429.

REFERENCES

- [71] Mackay R, Noe J, "High efficiency low cost, small gas turbines", 1991 *ASME COGEN-TURBO, IGTI-vol.6*, pp 163-167.
- [72] Bressani M, et al, "High-speed, large-power, induction motors for direct coupling to variable speed gas compressors", *EPE'93, vol.5*, pp 366.
- [73] Dillman TL, "brushless excitation", *IEEE Spectrum* 3/1972.
- [74] Lindgren O, "Experiments on high speed generator design and magnetisation", *Conf. on high-speed technology, Finland 1988*, pp 217-230.
- [75] Vaidya JG, "Electrical machines technology for aerospace power generators", *IECEC'91, Aug 4-9 1991, Boston-MA-USA*, pp 7-12.
- [76] Baily L, Richter E, "Development report on a high-speed permanent-magnet generator of the 200 kVA rating class utilizing rare-earth cobalt magnets", *2nd Int. workshop on rare earth cobalt magnets and their applications, Univ. of Dayton Ohio 1976*, pp 235-250.
- [77] Beauchamp ED, "Aircraft electrical control systems", *Proc. of NAECON'85, vol.2*, pp 1527-1535.(the same as [61]).
- [78] Mhango LMC, "Benefits of Nd-Fe-B magnet in brushless DC motor design for aircraft applications", pp 76-79.
- [79] Jack AG, Acarnly PP, Jowett PT, "The design of small high speed brushless DC drives with precise speed stability", *IEEE T-IAS, 1988*, pp 500-505.
- [80] Defreita DM, "High performance electrical power systems for unmanned airborne vehicles", 1988, pp 40-51.
- [81] Binns KJ, Kurdali A, "Permanent magnet AC generators", *Proc. IEE, vol.126, no.7, July 1979*, pp 960-996.
- [82] Weh H, Boules N, "Field analysis of a high-power, high-speed permanent magnet synchronous machine of the disc construction type", *Electrical mach. and Electromagnetics 1980*, pp 25-37.
- [83] Arkadan AA, Vyas R, "Effects of toothless stator design on dynamic model parameters of permanent magnet generators", *IEEE T-EC, June 1993*.
- [84] Vaidya JG, Glennon TF, "Self-regulating permanent magnet generators for aerospace applications", *Intermag conf., 1990*, pp GC-02.
- [85] Millner R, "High-speed high-efficiency permanent magnet motor-generator", *3rd Int. workshop on rare earth magnets, 1978*.(the same as [66]).
- [86] Dishner B, "A novel electromechanical approach to constant frequency power generation", *Proc. of IEEE NAECON'89, Dayton Ohio, May 1989*, pp 1756-1769.
- [87] Mcgee D, "A breakthrough in brushless motor design", *16th Ann. symp. Int. motion control systems and drives, 1987*, pp 327-332.
- [88] Binns KJ, Lisboa PJ, Al-Din M, "The use of canned rotors in high speed permanent magnet machines", *5th int. conf. on elec. mach. and drives, Sept 1991*, pp 21-25.
- [89] West JGW, "DC, Induction, Reluctance, and PM motors for electric vehicles", *IEE colloq., 15 April-1993*, pp 1/1 - 1/11.
- [90] Pynhonen J, "Some aspects of high speed rotor design in electrical machines", *Conf. on high-speed technology, Finland 1988*, pp 231-246.

REFERENCES

- [91] Steen, "Flux switched inductor alternator", *US patent* 3,912,958, 1975.
- [92] Walker JH, "The theory of inductor alternator", *Proc. IEE-89, Pt.II, June 1942*, pp 227-241.
- [93] Mitchen AJ, Jack AG, Mecro BC, "High performance permanent magnet drive for electric vehicles", *IEE colloq.*, 15 April-1993, pp 8/1 - 8/3.
- [94] Wiart A, et al, "New high-speed high-power machines with converter power supply", *Proc. Int. Motorcon conf., MOTORCON'82, vol.3, Sept. 1982*, pp 354-365.
- [95] Jokinen T, Luomi J, "High speed electrical machines", *Conf. on high-speed technology, Finland 1988*, pp 175-185.
- [96] Hippner M, Harley R, "High speed synchronous homopolar and permanent magnet machines comparative study", *Conf. record of the IEEE IAS Annual meeting, Houston TX/USA, Oct. 4-5, 1992*, pp 75-78.
- [97] Gasielles PG, Zarauza L, Sanz J, "Analysis and design of wind turbine driven self-excited induction generator", *Conf. record of the IEEE IAS Annual meeting, Pittsburgh, USA, Oct. 2-7, 1988*, pp 116-123.
- [98] Osheiba AM, et al, "Performance analysis of self-excited induction and reluctance generators", *Elect. mach. and power sys.*, 1991, 19:477-499.
- [99] Fukao T, Taka K, "A self-cascaded induction generator combined with a separately excited inverter and a synchronous condenser", *Conf. record of the IEEE IAS Annual meeting, Seattle/USA, Oct. 7-12, 1990*, pp 310-317.
- [100] Murthy SS, Rai HC, Tandon AK, "A novel self-excited self-regulated single phase induction generator - Part I: Basic system & theory, Part II: Experimental investigation", *IEEE T-EC, vol.8, no.3, Sept. 1993*, pp 377-387.
- [101] Perera BSP, Smith BH, "Brushless constant frequency generation using single frame cascaded induction machines", *Elec. mach. and power sys.*, 1991, 19:399-413.
- [102] Kawamura, "Reluctance rotary machine", *US patent*, 4,769,568, 1988.
- [103] Bleijs CA, et al, "Optimisation of a high speed solid rotor asynchronous machine in view of reducing rotor losses and improving the converter utilisation factor", *Elec. mach. and power sys.*, 1984, 9:375-386.
- [104] Pyrhonen J, "The high speed induction motor: calculating the effects of solid rotor material on machine characteristics", *PhD thesis, Lappeenranta University of Technology, Finland, April 1991*.
- [105] Nagrial MH, Rahman MA, "Operation and characteristics of self-excited reluctance generator", *Conf. record of the IEEE IAS Annual meeting, Pittsburgh, Oct. 2-7, 1988*, pp 55-58.
- [106] Abdel-Kader FE, "The reluctance machine as a self-excited reluctance generator", *Elect. mach. and power sys.*, 1985, 10:141-148.
- [107] Fukao T, et al, "Voltage control of super high speed reluctance generator system with a PWM voltage source converter", *IEEE T-IA, vol.28, no.4, July/Aug 1992*, pp 880-886.

REFERENCES

- [108] Mohamadein AL, Rahim YHA, "Steady state performance of self excited reluctance generators", *Proc. IEE, Pt.B, vol.137, no.5, Sept. 1990, pp 293-298.*
- [109] Fukao T, "Principles and output characteristics of super high-speed reluctance generator system", *IEEE T-IA, vol.IA-22,, no.4, July/Aug 1986, pp 702-707.*
- [110] Boldea I, Nasar SA, "Emerging electric machines with axially laminated anisotropic rotors: A review", *Elect. mach. and power sys., 1991, 19:673-703.*
- [111] Lipo TA, "Synchronous reluctance machines - a viable alternative for AC drives", *Elect. mach. and power sys., 1991, 19:659-671.*
- [112] Yang ZQ, et al, "Direct output power control for PWM converter based super high speed reluctance generator", *Conf. record of the IEEE IAS Annual meeting, San Diego CA/USA, Oct. 1989, pp 662-667.*
- [113] Stephens CM, "Fault detection and management system for fault tolerant SR motor drives", *Conf. record of the IEEE IAS Annual meeting, San Diego CA/USA, Oct. 1989, pp 574-578.*
- [114] Cronin MJ, "The all-electric (secondary power) airplane", *Journal of Aerospace Engineering, April 1989, pp 17-19.*
- [115] Richter E, "Switched reluctance machines for high performance operations in a harsh environment - a review paper", *Proc. ICEM,90, MIT Cambridge MA/UAS, 13-15 Aug. 1990, pp 18-24.*
- [116] Koch WH, Nasar SA, "A new two-phase reluctance generator for DC loads", *IEEE Trans on PAS 1974, pp 1449-1452.*
- [117] Cameron DE, Lang JH, "The control of high speed variable reluctance generators in electric power systems", *Applied power electronics conf. APEC, Feb. 1992, Boston MA, pp 121-125.*
- [118] Cameron DE, Lang JH, Belanger D, "The computer aided design of variable reluctance generators", *Applied power electronics conf. APEC, Feb. 1992, Boston MA, pp 114-120.*
- [119] Radun AV, "High power density SR motor drive for aerospace applications", *Conf. record of the IEEE IAS Annual meeting, San Diego CA/USA, Oct. 1989, pp 568-573.*
- [120] MacMinn SR, Sember JW, "Control of a switched reluctance aircraft engine starter-generator over a very wide speed range", *Proc. of IECEC'89, Washington DC, Aug. 1989, pp 631-638.*
- [121] Richter E, "High temperature lightweight, switched reluctance motors and generators for future aircraft engine applications", *Proc. of 1988 American Control Conf., Atlanta, June 1988, vol.3, pp 1846-1851.*
- [122] Soohoo RF, "Theory and Application of Ferrites", *Englewood Cliffs NJ, ©1960.*
- [123] Roess E, "Soft magnetic ferrites and applications in telecommunication and power converters", *IEEE T-MAG, vol.MAG-18, no.6, Nov. 1982, pp 1529-1535.*
- [124] Kaga A, Anazawa Y, Akagami H, "A research of efficiency improvement by means of wedging with soft ferrite in small induction motors", *IEEE T-MAG, vol.MAG-18, no.6, Nov. 1982, pp 1547-1549.*

REFERENCES

- [125] Chan S, Bolton HR, "Development of sub-kW single phase switched reluctance motor drives", *Proc. of International Conf on Electrical Machines ICEM'92, 15-17 Sept. 1992, Manchester, UK, vol.2, pp 527-531.*
- [126] Chan S, Bolton HR, "Performance enhancement of single-phase switched reluctance motor by DC link voltage boosting", *Proc. IEE, Pt.B, vol.140, no.5, Sept. 1993, pp 316-322.*
- [127] Lovatt HC, Stephenson JM, "Influence of number of poles per phase in switched reluctance motors", *Proc. IEE, Pt.B, vol.139, no.4, July 1992, pp 307-314.*
- [128] Arumugam R, Lindsay JF, Krishnan R, "Sensitivity of pole arc/pole pitch ratio on switched reluctance motor performance", *Conf. record of the IEEE IAS Annual meeting, Pittsburgh, USA, Oct. 2-7, 1988, pp 50-54.*
- [129] Allano S, et al, "Design and tests of amorphous magnetic circuits for high speed medium frequencies for motors", *Physica Scripta, vol.40, 1989, pp 307-310.*
- [130] Higgins RA, "Materials For The Engineering Technician", *Edward Arnold 2nd ed. © 1987.*
- [131] Johnson LA, et al, "Applications of low loss amorphous metals in motors and transformers", *IEEE power engineering society 1981, transformation and distribution conf. and exposition.*
- [132] Smith CH, "Magnetic shielding to multi-gigawatt magnetic switches, ten years of amorphous magnetic applications", *IEEE T-MAG, vol.MAG-18, no.6, Nov. 1982, pp 1376-1381.*
- [133] March NH, Street RA, Tosi M, "Amorphous Solids and Liquid State", *Plenum Press NY ©1985.*
- [134] "Amorphous Metals VITROVAC® Alloys And Applications", *Catalogue (PV-006) by VAC Vacuumshmeleze, Germany.*
- [135] Yagi M, Sawa T, "Soft magnetic properties of ultrathin Co-based amorphous alloy ribbons with thickness of 2-10 μm ", *IEEE T-MAG, 1990, vol.26, no.5, pp 1409-1411.*
- [136] Warlimont H, "The impact of amorphous metals on the field of soft magnetic materials", *Materials Science and Engineering, 99 (1988), pp 1-10.*
- [137] Fukao T, et al, "Super high speed reluctance motor using amorphous iron", *IEEE T-IA, vol.25, no.1, Jan/Feb 1989, pp 119-125.*
- [138] Lawrenson PJ, et al, "Controlled speed reluctance motors: present status and future potential", *Proc. of 1st european conf. on electrical drives/motors/controls 1982, University of Leeds, 29 June-1 July 1982.*
- [139] Corda J, Stephenson JM, "Analytical estimation of the minimum and maximum inductances for doubly salient motor", *Proc. of Int conf on stepping motors and systems, 1979, pp 50-59.*
- [140] Materu P, Krishnan R, "Analytical prediction of SRM inductance profile and steady-state average torque", *Proc. of IEEE IAS conf., Seattle, 7 -12 Oct. 1990, pp 214-223.*
- [141] Cossar C, Miller T, "Electromagnetic testing of Switched reluctance motor", *Proc. of International Conf on Electrical Machines ICEM'92, 15-17 Sept. 1992, Manchester, UK, vol.2, pp 470-474.*

REFERENCES

- [142] Krishnan R, Materu P, "Measurement and instrumentation of switched reluctance motor", *Conf. record of the IEEE IAS Annual meeting, San Diego CA/USA, Oct. 1989*, pp 116-121.
- [143] Stephenson JM, Lovatt HC, "Measurement of magnetic characteristics of switched reluctance motor", *Proc. of International Conf on Electrical Machines ICEM'92, 15-17 Sept. 1992, Manchester, UK, vol.2*, pp 465-470.
- [144] Ferrero A, Raciti A, "A digital method for the determination of the magnetic characteristics of variable reluctance motors", *IEEE T-Inst. Meas.*, vol.39, Aug. 1990, pp 604-608.
- [145] Ferrero A, Raciti A, Urzi C, "An indirect test method for the characterisation of variable reluctance motors", *IEEE T-Inst. Meas.*, vol.42, no.6, pp 1020-1025.
- [146] Boglietti A, et al, "About the design of very high frequency induction motors for spindle applications", *IEEE proc IAS'92, Houston, Texas, Oct 1992, vol.1*, pp 25-32.
- [147] Fiorito C, "High-speed high-power spindles for flexible manufacturing systems: Applications and results", *Robotics and Computer Integrated Manufacturing*, vol.4, no.2, 1988, pp 155-163.
- [148] Boglietti A, et al, "Test procedure for very high speed spindle motors", *Conf. record of the IEEE IAS Annual meeting, Seattle/USA, Oct. 7-12, 1990, Pt. I*, pp 102-108.
- [149] Moritomo S, Ota M, "Present high speed machine tool spindles, 200,000 rpm", *Bull. Japan Society of Precision Eng.*, vol.20, no.1, March 1986, pp 1-6.
- [150] Volkman WK, Jackson DC, "AC spindle drives for machine tools", *IEEE T-IA*, vol.IA-21, no.5, 1985, pp 1263-1267.
- [151] Obreg E (ed.), et al, "Machinery's Handbook: A Reference Book For The Mechanical Engineer, Draftsman, Toolmaker And Machinist", *Industrial Press NY*, 19th ed. 1971.
- [152] "PAFEC; Data Preparation 7.1, User Manual", *Cripps Computing Centre, University of Nottingham*.
- [153] Faupel JH, Fisher FE, "Engineering Design, A Synthesis of Stress Analysis And Materials Engineering", *John Wiley & Sons*, 2nd ed., 1981.
- [154] Skeist I, "Handbook of Adhesives", *Van Nostrnad Reinhold NY*, 2nd ed., 1977.
- [155] De Lollis NJ, "Adhesives For Metals, Theory and Technology", *Chapter 5, Industrial Press NY*, 1970.
- [156] Koshal D, "Manufacturing Engineers' Referencer Book", *Butterworth Heinmann*, 1993.
- [157] Brandes EA (ed.), Brook GB (ed.), "Smithells, Metals Reference Book", *Butterworth Heinmann*, 7th ed., 1993.
- [158] Kalpajian S, "Manufacturing Engineering and Technology", *Addison-Wesley Pub. Co.*, 2nd ed., ©1992.
- [159] Rothbart HA, *Mechanical Design and Systems Handbook*, *McGraw Hill*, 1964.
- [160] Byrne JV, McMullin MF, "Design of a reluctance motor as a 10 kW spindle drive", *Proc. MOTOCON'82, Sept. 1982*, pp 10-25.

REFERENCES

- [161] Williamson S, Shaikh AA, "Three dimensional effects in λi diagram for switched reluctance motors", *Proc. of International Conf. on Electrical Machines ICEM'92*, 15-17 Sept. 1992, Manchester, UK, vol.2, pp 489-493.
- [162] Materu PN, "Design and Steady-State Analysis of The Switched Reluctance Motor Drives", *PhD Dissertation, Dept. of Elect. Eng., VPI & SU, Blacksburge Virginia VA 24661 USA, July 1989*.
- [163] Lancaster D, "CMOS Cookbook", *Howard W. Sams & Company USA, 2nd ed., 1988*.
- [164] Richter E, et al, "An integrated electrical starter/generator system for gas turbine application, design and test results", *Proc. of Int. Conf. on Electrical Machines ICEM'94*, Sept. 1994, France, pp 286-291.